Langmuir Films of Perfluoroalkylalkanes: Multiscale Insights on Molecular Structure, Mixing, and Subphase Deformability Effects

Pedro Manuel Ribeiro Silva

UNIVERSIDADE DE LISBOA
INSTITUTO SUPERIOR TÉCNICO

SORBONNE UNIVERSITÉ
INSTITUT DES NANOSCIENCES DE PARIS

Langmuir Films of Perfluoroalkylalkanes: Multiscale Insights on Molecular Structure, Mixing, and Subphase Deformability Effects

Pedro Manuel Ribeiro Silva

Supervisor: Doctor Eduardo Jorge Morilla Filipe
Co-Supervisor: Doctor Michel Goldmann
Co-Supervisor: Doctor Pedro Jorge Rodrigues Morgado

Thesis approved in public session to obtain the PhD Degree in

Chemistry

Jury final classification: Pass with Distinction and Honour

President of the jury: Doctor José Nuno Canongia Lopes

July 2024

UNIVERSIDADE DE LISBOA
INSTITUTO SUPERIOR TÉCNICO
SORBONNE UNIVERSITÉ
INSTITUT DES NANOSCIENCES DE PARIS

Langmuir Films of Perfluoroalkylalkanes: Multiscale Insights on Molecular Structure, Mixing, and Subphase Deformability Effects

Pedro Manuel Ribeiro Silva

Supervisor: Doctor Eduardo Jorge Morilla Filipe
Co-Supervisor: Doctor Michel Goldmann
Co-Supervisor: Doctor Pedro Jorge Rodrigues Morgado

Thesis approved in public session to obtain the PhD Degree in

Chemistry

Jury final classification: Pass with Distinction and Honour

Jury

Chairperson: Doctor José Nuno Canongia Lopes, Instituto Superior Técnico, Universidade de Lisboa
Members of the Committee:

Doctor Matthew Paige, Department of Chemistry, College of Arts and Science, University of Saskatchewan, Canada

Doctor Michel Goldmann, Institut des NanoSciences de Paris (INSP), Sorbonne Université, Paris, France

Doctor José Paulo Barbosa Mota, Faculdade de Ciências e Tecnologia, Universidade Nova de Lisboa

Doctor José Nuno Aguiar Canongia Lopes, Instituto Superior Técnico, Universidade de Lisboa

Doctor Marie-Claude Fauré, Institut des NanoSciences de Paris (INSP), Sorbonne Université, Paris, France

Doctor Benilde de Jesus Vieira Saramago, Instituto Superior Técnico, Universidade de Lisboa

Funding Institutions

Fundação para a Ciência e a Tecnoclogia (FCT) grant number SFRH/BD/149192/2019

July 2024

É um átomo a mais que se animou...
in *Cântico Negro*, José Régio (1926)

Abstract

Perfluoroalkylalcanes (PFAAs; $C_nF_{2n+1}C_mH_{2m+1}$; FnHm) are diblock molecules formed by a hydrogenated (CH) and a perfluorinated (CF) blocks, both hydrophobic and mutually phobic. Despite lacking a terminal polar group, these primitive surfactants form Langmuir films on water or hydrophilic substrates. The films comprise hexagonally ordered, monodisperse hemimicelles as shown by AFM and GIXD. The hemimicelles' diameter is linked to molecular structure. However, the effects of varying the chains' lengths (n and/or m), mixing in binary films and the physicochemical properties of the liquid subphase on the structure and ordering of the Langmuir films are still left untapped.

Previous computational (Molecular Dynamics (MD) simulation) studies elucidated the pure F8H16 hemimicelles' internal structure; herein, this is extended to other FnHm. The molecules' fan-like arrangement within the hemimicelles explains the variation of their diameter with molecular architecture, specifically the mismatching CH/CF chains' cross-sectional areas and relative lengths of the CH/CF chains. A model based on geometrical arguments is proposed. Furthermore, the hemimicelles' central pit results from both the CH_2-CF_2 dipoles intermolecular interaction and the liquid substrate's deformability. The formation of ordered hemimicelles of FnHm was found to be possible on other liquid subphases (short-chain CH/CF alcohols).

The structure of mixed F8H14:F8H20 films was probed by surface pressure-molecular area isotherms, GISAXS and GIXD. The lattice parameter of the hemimicelles' network is between those of the pure cases, indicating either mixing at the molecular level or of two types of pure hemimicelles.

These promising results enlighten the fundamental principles driving the self-assembling and, ultimately, the prediction and control of the morphology of the nanostructured PFAA films, envisaging practical applications. Future work should focus on further characterising the mixed binary films, including with different n/m, to discern between the proposed scenarios. Moreover, the studies should advance towards studying mixed films and emulsions of PFAAs with relevant biomolecules (e.g. phospholipids).

Keywords: Soft-Matter, Langmuir Films, Perfluoroalkylalkanes, Self-assembly, Molecular Dynamics Simulation, Atomic Force Microscopy, Grazing Incidence X-Ray Diffraction

Resumo

Perfluoroalquilalcanos (PFAAs; $C_nF_{2n+1}C_mH_{2m+1}$; FnHm) são moléculas dibloco formadas por blocos hidrogenados (CH) e perfluorados (CF), ambos hidrofóbicos e mutuamente fóbicos. Apesar de não possuírem um grupo polar, esses surfactantes primitivos formam filmes de Langmuir sobre água ou substratos hidrofílicos. Os filmes são formados por hemimicelas monodispersas, ordenadas hexagonalmente, conforme mostrado por AFM e GIXD. O diâmetro das hemimicelas depende da estrutura molecular, existindo porém lacunas acerca dos seus efeitos concretos (variação n/m), da mistura em filmes binários e das propriedades físico-químicas da subfase líquida na estrutura/ordenação desses filmes.

Estudos computacionais anteriores (simulação de Dinâmica Molecular (MD)) elucidaram a estrutura interna de hemimicelas de F8H16 puro, estendendo-se aqui o estudo a outros FnHm. Verificou-se que o arranjo em leque das moléculas dentro das hemimicelas explica a variação do seu diâmetro com a arquitetura molecular, especificamente a incompatibilidade das secções das cadeias CH/CF e os comprimentos relativos CH/CF, propondo-se um modelo baseado em argumentos geométricos. Ademais, a depressão central das hemimicelas resulta da interação intermolecular dos dipolos CH_2-CF_2 e da deformabilidade do substrato líquido. Descobriu-se que as hemimicelas formam-se sobre outras subfases líquidas (álcoois CH/CF curtos).

A estrutura dos filmes mistos F8H14:F8H20 foi estudada por isotérmicas de pressão superficial-área molecular, GISAXS e GIXD. Verificou-se que o parâmetro de rede da rede de hemimicelas está entre os dos casos puros, indicativo de mistura a nível molecular ou de dois tipos de hemimicelas puras.

Estes resultados promissores esclarecem sobre os princípios fundamentais subjacentes à automontagem e, em última análise, a previsão e controle da morfologia dos filmes nanoestruturados de PFAAs, perspectivando a sua aplicação prática. Futuramente, a caracterização dos filmes binários deve prosseguir, inclusive variando n/m, para discernir entre os cenários propostos. Além disso, os estudos deverão avançar no sentido de estudar filmes mistos e emulsões de PFAAs com biomoléculas relevantes (por exemplo, fosfolípidos).

Palavras-Chave: Matéria Mole, Filmes de Langmuir, Perfluoroalquilalcanos, Auto-montagem, Simulação de Dinâmica Molecular, Microscopia de Força Atómica, Difracção de Raios-X a Incidência Rasante

Résumé

Les perfluoroalkylalcanes (PFAAs ; $C_nF_{2n+1}C_mH_{2m+1}$; FnHm) sont des molécules formées d'un bloc hydrogéné (CH) et d'un bloc perfluoré (CF), hydrophobes et mutuellement phobiques. Bien qu'ils n'aient pas de groupe terminal polaire, ces tensioactifs « primitifs » forment des monocouches sur l'eau (film de Langmuir) ou sur substrats hydrophiles. Les films sont constitués d'hémimicelles monodisperses, organisées sur un réseau hexagonal, comme cela a été démontré par GISAXS et AFM. Le diamètre des hémimicelles dépend de la longueur des blocs. Cependant, l'origine de cette variation n'était pas élucidée jusqu'à présent. Dans ce travail, les effets de la structure moléculaire (variation de n et/ou m) ont été étudiés. Nous avons également débuté l'étude des films binaires et les propriétés de la sous-phase liquide (nature, déformation) sur la structure et l'ordre des films. Des approches expérimentale et numérique ont été mises en œuvre pour progresser dans la compréhension de ces systèmes.

Des simulations de dynamique moléculaire (MD) avaient proposé une structure interne en éventail des hémimicelles de F8H16. Nous avons étendu cette approche à d'autres FnHm avec n et m variables. Il a été constaté que cette structure en éventail est à l'origine de la variation du diamètre des hémimicelles avec l'architecture moléculaire, notamment en raison des aires différentes des sections transverses des blocs CH et CF et de leur longueur relative. De plus, nous avons retrouvé le puits central qui avait été mis en évidence par des mesures AFM. Nous avons développé un modèle basé sur des arguments géométriques qui justifie la variation de diamètre avec l'architecture moléculaire. En outre, nous montrons que l'origine du puits est liée à l'interaction intermoléculaire des dipôles CH_2-CF_2 et à la capacité du substrat liquide à se déformer.

La structure des films mixtes F8H14 :F8H20 a été sondée expérimentalement par des isothermes de pression de surface-aire moléculaire ainsi que par des mesures de GISAXS et GIXD. Nous avons montré que le paramètre de maille du réseau d'hémimicelles se situe entre ceux des cas purs, indiquant soit un mélange au niveau moléculaire, soit un mélange de deux types d'hémimicelles pures et excluant le scénario d'une ségrégation d'hémimicelles pures.

Ces résultats prometteurs contribuent à éclaircir les principes fondamentaux qui gouvernent l'auto-assemblage des PFAAs et, à terme, permettront le contrôle de leur morphologie ; par exemple, ceux des films mixtes de PFAAs et de phospholipides déjà utilisés dans un contexte médical.

Mots Clés: Matière Molle, Films de Langmuir, Perfluoroalkylalcanes, Auto-assemblage, Simulations de Dynamique Moléculaire, Microscopie à Force Atomique, Diffraction des Rayons-X à Incidence Rasante

Resumo Alargado

Os Perfluoroalquilalcanos (PFAA; $C_nF_{2n+1}C_mH_{2m+1}$; FnHm) são moléculas constituídas por um bloco hidrogenado (CH) e por um bloco perfluorado (CF), ambos hidrofóbicos e mutuamente fóbicos. Estas moléculas são de interesse potencial como substitutos do sangue, dada a sua notável capacidade de dissolver oxigénio. Apesar de não possuírem um grupo polar terminal, contrariamente às moléculas anfifílicas usuais, estes surfactantes "primitivos" formam monocamadas sobre água (filmes de Langmuir) ou sobre substratos hidrofílicos. Os filmes são constituídos por hemimicelas monodispersas organizadas numa rede hexagonal a 2 dimensões, conforme demonstrado por medições de difusão de raios-X de superfície (GISAXS) e microscopia de força atómica (AFM). É sabido que o diâmetro das hemimicelas depende do comprimento dos blocos. No entanto, a origem desta variação estava por elucidar, tendo sido um dos temas estudados neste trabalho. Além disso, foi caracterizado o efeito da subfase (natureza físico-química e deformação), na organização dos filmes. Também se iniciou o estudo de filmes binários. Foram implementadas abordagens experimentais e computacionais para progredir na compreensão das propriedades destes filmes.

Um estudo de simulação de dinâmica molecular (MD) anterior já tinha proposto uma estrutura interna em forma de leque para as hemimicelas F8H16. Neste trabalho, esta abordagem foi estendida ao estudo de outros FnHm com n e m variáveis. Verificou-se que a estrutura em leque está na origem da variação do diâmetro das hemimicelas com a arquitectura molecular, nomeadamente devido às diferenças nas áreas das secções transversais dos blocos CH e CF e ao seu comprimento relativo. Além disso, reproduziu-se a existência da depressão ou "pit" central que havia sido posto em evidência pelas medições de AFM. Desenvolveu-se um modelo, baseado em argumentos geométricos, que propõe uma explicação para a variação de diâmetro com a arquitetura molecular. Mostra-se, igualmente, que a origem da depressão central deve-se à interação intermolecular dos dipolos CH_2-CF_2 e à capacidade do substrato líquido de se deformar.

A formação de hemimicelas de PFAAs (F8H16 ou F8H18) na presença de álcoois gordos com cadeias CH (octadecanol) ou CF (perfluorooctadecanol) foi estudada por simulação de MD. Observa-se uma tendência para a segregação nestes filmes e o colapso das monocamadas provoca a subida das moléculas de PFAA sobre as de álcool. Além disso, a simulação de uma hemimicela depositada sobre um filme de álcool gordo (CH ou CF), à superfície da água, origina a estrutura em leque com a típica depressão central, devido à deformação do filme de álcool e da água.

A influência da natureza físico-química da subfase, na organização dos PFAAs, foi estudada por simulação de MD e experimentalmente. Uma solução de PFAAs foi depositada por *spin coating* sobre um substrato previamente coberto de uma camada líquida de álcool de cadeia curta CH (metanol, etanol ou butanol) ou CF (trifluoro-1H,1H-etanol). A presença de hemimicelas nos filmes assim preparados foi confirmada por AFM. Verificou-se que a morfologia e a organização 2D das hemimicelas são semelhantes às das formadas pelo mesmo procedimento sobre água. Estes resultados demonstram que a água não é imprescindível para a formação destas estruturas.

Os filmes de Langmuir de misturas binárias de F8H14:F8H20 foram estudados por isotérmicas de pressão superficial-área molecular (π–A) e por difusão de raios-X de superfície (GISAXS e GIXD). Verificou-se que as isotérmicas π–A dos filmes mistos são semelhantes às dos sistemas puros. Em particular, aquelas apresentam apenas uma única pressão de colapso, intermédia às dos sistemas puros. Isto exclui a hipótese de segregação total das moléculas no filme. Da mesma

forma, os resultados de GISAXS mostram a presença de uma rede hexagonal 2D de hemimicelas, cujo parâmetro de malha é intermédio aos obtidos para os sistemas puros. Isto indica que os filmes mistos são constituídos ou por uma mistura de hemimicelas puras ou por hemimicelas mistas de tamanho intermédio. Observa-se, ainda, a presença de uma segunda rede associada a um estado meta-estável das moléculas de F8H14, tanto no filme puro, como nos filmes mistos. Por fim, analisou-se a evolução do parâmetro de malha da rede de hemimicelas em função da composição molar do filme. Verificou-se que a área da malha do filme misto é sistematicamente inferior à prevista pela lei de Vegard. Estes resultados sugerem que as interações moleculares cruzadas são preferenciais ou que as hemimicelas, e em particular as de maiores dimensões, se deformam aquando da compressão lateral dos filmes mistos.

Por outro lado, os resultados de GIXD permitiram determinar a organização das moléculas de PFAA no seio das hemimicelas. Os espectros de difracção dos filmes de F8H14 ou de F8H20 puros permitiram validar os calculados a partir das estruturas obtidas por simulação de MD. Os espectros de difracção dos filmes mistos apresentam três picos: um associado à organização dos blocos CF e dois à dos blocos CH, sendo um destes específico dos blocos H20. A largura deste último pico corresponde a um comprimento característico (ξ) da ordem de algumas dezenas de nm, comparado com alguns nm para o ξ deduzido dos outros dois picos. Observa-se, ainda, uma variação na intensidade do pico associado à organização dos blocos CF, em função das componentes no plano (Q_{xy}) e fora do plano (Q_z) do vector de difusão, em concordância com a estrutura em leque proposta. O pico associado à organização dos blocos H20 é observado logo a partir de uma reduzida concentração de F8H20 na mistura. Por outro lado, este pico é instável ao longo do tempo, o que é indicativo de uma evolução na organização dos blocos CH. Os resultados de GIXD são compatíveis com a mistura das duas moléculas dentro das hemimicelas.

O último capítulo é dedicado a um estudo preliminar de misturas de cadeias CH e cadeias CF em fase líquida, em particular para a caracterização das cavidades intersticiais. Estas desempenharão um papel de relevo nas propriedades de automontagem dos PFAAs. Simularam-se, por MD, misturas de hexano (H6) e perfluorohexano (F6), em função da composição molar (x_{F6}) e temperatura (T). O estudo focou-se em cavidades de tamanho suficiente para conter uma molécula de oxigénio. Estas aumentam em número e em volume com x_{F6} e T. Além disso, evoluem de formas mais compactas e esféricas para outras mais complexas e alongadas, com o aumento de x_{F6}. Verificou-se, ainda, que estas cavidades estão localizadas preferencialmente perto dos grupos terminais das cadeias moleculares. O volume absoluto do espaço intersticial vazio aumenta com x_{F6} e com T, com um desvio positivo face à média dos valores obtidos para sistemas puros. Estes resultados correlacionam-se com a expansão de misturas líquidas de alcanos e perfluoroalcanos (que apresentam volumes de excesso de mistura positivos) e com a expansão térmica dos sistemas estudados. Por fim, estendeu-se a metodologia a sistemas de interesse biomédico (F6H6 e 1-bromoperfluorooctano, F8Br). Verificou-se que as cavidades de tamanho relevante também se encontram próximas dos grupos terminais das moléculas de F6H6 e de F8Br.

Estes resultados são promissores, contribuindo para o esclarecimento dos princípios fundamentais que regem a automontagem de PFAAs e que, em última análise, permitirão o controle da sua morfologia. Por exemplo, estes conhecimentos são relevantes para o estudo das propriedades de filmes mistos de PFAAs e fosfolipídios, já utilizados em contexto médico.

Résumé Substantiel

Les perfluoroalkylalcanes (PFAA ; $C_nF_{2n+1}C_mH_{2m+1}$; FnHm) sont des molécules formées d'un bloc hydrogéné (CH) et d'un bloc perfluoré (CF), hydrophobes et mutuellement phobiques. Ces molécules présentent un intérêt potentiel comme substitut du sang vu leur capacité à physisorber l'oxygène. Bien qu'ils n'aient pas de groupe terminal polaire contrairement aux molécules amphiphiles usuelles, ces tensioactifs « primitifs » forment des monocouches sur l'eau (film de Langmuir) ou sur substrats hydrophiles. Les films sont constitués d'hémimicelles monodisperses et organisées sur un réseau hexagonal, comme cela a été démontré par des mesures de diffusion de rayons X de surface (GISAXS) et de microscopie à force atomique (AFM). Il a été démontré que le diamètre des hémimicelles dépendait de la longueur des blocs. Cependant, l'origine de cette variation n'était pas élucidée. Dans ce travail, l'effet de la sous-phase (nature, et déformation) sur l'organisation des films a été caractérisé. Nous avons également débuté l'étude des films binaires. Des approches expérimentale et numérique ont été mises en œuvre pour progresser dans la compréhension de ces films.

Des simulations de dynamique moléculaire (MD) avaient proposé une structure interne en éventail des hémimicelles de F8H16. Nous avons étendu cette approche à d'autres FnHm avec n et m variables. Il a été constaté que cette structure en éventail au sein des hémimicelles est à l'origine de la variation de leur diamètre avec l'architecture moléculaire, notamment en raison des différences des aires des sections transverses des blocs CH et CF et de leur longueur relative. De plus, nous avons retrouvé le puits central qui avait été mis en évidence par des mesures AFM. Nous avons développé un modèle basé sur des arguments géométriques qui justifie la variation de diamètre avec l'architecture moléculaire. De plus, nous montrons que l'origine du puits est liée à l'interaction intermoléculaire des dipôles CH_2-CF_2 et à la capacité du substrat liquide à se déformer.

La formation d'hémimicelles de PFAAs (F8H16 ou F8H18) en présence d'alcools gras à chaînes hydrocarbonées (octadécanol) ou fluorocarbonées (perfluorooctadécanol) a été étudiée par simulation de MD. On observe une tendance à la ségrégation dans ces films et le collapse correspond à la montée des PFAAs sur les molécules d'alcools. Par ailleurs, la simulation d'une hémimicelle déposée au-dessus d'un film d'alcool gras (CH ou CF) sur l'eau redonne la structure en éventail ainsi que le puits, du fait de la déformation du film d'alcool et de l'eau.

L'influence de la nature de la sous-phase sur l'organisation des PFAAs a été étudiée par simulation de MD et expérimentalement. Pour cela, une solution de PFAAs a été déposée par spin coating sur un substrat recouvert d'un film d'alcool à chaînes courtes CH (méthanol, éthanol ou butanol) ou CF (trifluoro-1H,1H-éthanol). La présence d'hémimicelles a été confirmée par AFM. Leur morphologie et leur organisation 2D sont similaires à celles des hémimicelles formées par la même procédure avec de l'eau. Ceci démontre que l'eau n'est pas impérative pour la formation de ces structures.

Les films de Langmuir binaires de F8H14:F8H20 ont été étudiés par des isothermes de pression de surface-aire moléculaire (π–A) et par des mesures de diffusion de rayons X de surface (GISAXS et GIXD). Les isothermes π–A ont une allure similaire à celles des systèmes purs. En particulier, elles ne présentent qu'une seule pression de collapse, intermédiaire à celles de ces cas purs. Ce résultat exclut la ségrégation totale des molécules au sein du film. De même,

les expériences de GISAXS montrent la présence d'un réseau hexagonal d'hémimicelles dont le paramètre de maille est intermédiaire à ceux déterminés sur les cas purs. Ceci indique que les films mixtes sont formés soit d'un mélange d'hémimicelles pures, soit d'hémimicelles mixtes. Il est à noter que l'on observe la présence d'un second réseau associé à un état métastable des molécules de F8H14 aussi bien dans le film pur que dans des films mixtes. Nous avons analysé l'évolution du paramètre du réseau des hémimicelles en fonction de la composition molaire du film. On obtient une aire de maille du film mixte systématiquement inférieure à celle prédite par la loi de Vegard. Ceci suggère soit des interactions croisées préférentielles, soit une déformation des grandes hémimicelles.

D'autre part, les résultats de GIXD ont permis de déterminer l'organisation des molécules PFAA au sein des hémimicelles. Les spectres de diffraction des films de F8H14 ou F8H20 purs ont permis de valider ceux calculés à partir des structures obtenues par simulation. Les spectres de diffraction des films de mélanges présentent trois pics, l'un associé à l'organisation des blocs CF et deux à celle des blocs CH dont l'un caractéristique des blocs H20. La largeur de ce dernier pic correspond à une longueur caractéristique de l'ordre de quelques dizaines de nm contre quelques nm pour celle déduite des deux autres pics. De plus, on observe une variation de l'intensité du pic lié à l'organisation des blocs CF en fonction des composantes dans le plan (Q_{xy}) et hors plan (Q_z) du vecteur de diffusion, en accord avec la structure en éventail. Le pic associé à l'organisation des blocs CH du F8H20 est observé dès une faible concentration de cette molécule dans le mélange. En revanche, ce pic est instable au cours du temps ce qui indique une évolution de l'organisation des blocs CH. Les résultats de GIXD sont compatibles avec un mélange des deux molécules au sein des hémimicelles.

Le dernier chapitre est consacré à une étude préliminaire des mélanges 3D de chaînes CH et de chaînes CF en phase liquide et en particulier de la caractérisation du vide interstitiel. En effet, ce dernier joue probablement un rôle dans les propriétés d'auto-assemblage des PFAAs. Nous avons simulé (MD) des mélanges d'hexane (H6) et de perfluorohexane (F6), en fonction de la composition molaire (x_{F6}) et de la température (T). Nous nous sommes concentrés sur les cavités de taille suffisante pour accueillir une molécule d'oxygène. Ces cavités augmentent en nombre et en volume avec x_{F6} et T. De plus, ces interstices évoluent de formes plus compactes et sphériques à des formes plus complexes et allongées avec l'augmentation de x_{F6}. Nous avons établi également que ces interstices sont préférentiellement situés à proximité des groupes terminaux des chaînes moléculaires. Le volume absolu d'espace interstitiel vide augmente avec x_{F6} et de T, avec un écart positif par rapport à la moyenne des valeurs obtenus pour les systèmes purs. Ces résultats ont été corrélés avec la dilatation de mélanges liquides d'alcanes et de perfluoroalcanes (qui présentent des volumes d'excès positifs) et avec la dilatation thermique des systèmes étudiés. Enfin, nous avons étendu la méthodologie aux systèmes d'intérêt biomédical (F6H6 et 1-bromoperfluorooctane, F8Br). De même, nous avons vérifié que des interstices de taille pertinente se trouvent à proximité des groupes terminaux des molécules F6H6 et F8Br.

Ces résultats prometteurs contribuent à éclaircir les principes fondamentaux qui gouvernent l'auto-assemblage des PFAAs et, à terme, permettront le contrôle de leur morphologie ; par exemple, ceux des films mixtes de PFAAs et de phospholipides déjà utilisés dans un contexte médical.

Acknowledgements

I would like to thank Doctor Eduardo Filipe, who welcomed me in his research team and provided the opportunity to develop the work presented here, with utmost care and ability to communicate his vast expertise in both experimental and computational domains. I truly appreciate his personal endeavours and preoccupation to promote a welcoming environment in the lab and outside of it. I would also like to express my deep gratitude towards Doctor Michel Goldmann for sharing his knowledge and guidance, with particular emphasis on the subjects of characterisation of Langmuir films and X-ray diffraction. Moreover, I truly appreciate the good-humoured environment fomented as well as the many film suggestions and intakes on French history, provided on several opportune occasions. I thank very much Doctor Pedro Morgado for his patience, the thorough discussions and for sharing insightful advice throughout this work, highlighting the hands-on and tireless introduction to the realms of Molecular Dynamics simulations and managing a scientific computation cluster. His much appreciated and thoughtful music recommendations complemented this work in the most harmonious and pleasant way.

I would like to direct a special thanks to Doctor Marie-Claude Fauré for all the dedication in passing valuable know-how about Langmuir films, and particularly those of Perfluoroalkylalkanes, and her thorough and reassuring scientific rigour. I immensely value her personal touch, sympathy and patience when explaining the functioning of the equipment and also when discussing experimental results, as well as her sincere moral support. My thank you would not be complete without addressing the insightful knowledge and taste shared on French cheeses and pastries, which were (and still are) delightfully appreciated. I would also like to thank Doctor Sylvie Spagnoli for her time and for sharing her knowledge on the experimental characterisation of Langmuir films. Furthermore, her wordplays and pointing out curious intricacies of the French language animated the trips to the synchrotron facilities in a remarkable way.

I thank Doctors Hervé Cruguel, Yoann Prado, Bumedijen Raka and Kamal Sbargoud for all the support, the training to use the facilities and equipment at Institut des NanoSciences de Paris in all safety and effectiveness and making sure all the reactants and devices were available and functional. Yoann Prado and Kamal Sbargoud are acknowledged for the synthesis, purification and characterisation of some of the Perfluoroalkylalkane molecules used in the scope of this work.

For discussing my work and making sure I had all the conditions necessary to do it, material and other, I thank Doctors José Nuno Lopes, Pedro Paulo and Luís Martins for kindly accepting to be part of my Comissão de Acompanhamento de Tese (CAT) at Universidade de Lisboa, and Doctors Maria Chamarro, Benoit Coasne and Jessem Landoulsi for kindly accepting to be part of my Comission de Suivi Individuel (CSI) at Sorbonne Université.

The X-ray diffraction experiments presented in this document were conducted at the Source Optimisée de Lumière d'Énergie Intermédiaire du LURE (SOLEIL) and European Synchrotron Radiation Facility (ESRF) synchrotrons. I would like to thank in particular Doctors Philippe Fontaine and Arnaud Hemmerle, the scientists at the SOLEIL synchrotron responsible for the SIRIUS beamline, and Doctors Oleg Konovalov and Maciej Jankowski, the scientists at the ESRF synchrotron responsible for the ID10 beamline.

I would like to thank the other PhD students, whether current or former, with whom I shared a laboratory, an office, creative discussions, knowledge, beam time, banana bread, moments of more anxiety and others of more laughter. I would like to thank in particular Tiago Eusébio, Diogo Machacaz and Gonçalo Silva, from Universidade de Lisboa, and Azmat Ali, Alexia Bistintzanos, Angéline Dileseigres, Guillaume Diot, Lamya Essaoui, Laurita Floréan, Maria Kandyli, Luis Lechaptois and Jean-de-Dieu Niyonzima and post-doc researcher Fredrik Johansson, from Sorbonne Université.

I thank the then MSc students Guilherme Damião, José Fonseca, Diogo Gaspar, Ricardo Luís, Duarte Nova, Milton Ponte and João Rodrigues, with whom I had the pleasure to work side-by-side, for their initiative, active participation, will to learn and fruitful contributions and input that were invaluable in the course of this work.

I'd like to extend a special thanks to the people who have made so far this journey memorable, insightful and who contributed to my personal growth, one way or another. Without their helping hand, patience, love and advice, this work would not have been possible and, most importantly, I would not be the person I am today. To them, I am truly grateful and indebted. I would like to thank, in particular: Mafalda Santos, for her kind words of motivation and wisdom, in all aspects of life and work, for being someone I truly admire and find inspiring; João Saraiva, for his immense patience and for taking time to personally tutor me with his characteristic passion and thoroughness in all things scientific programming and Python, but also for his invaluable words of advice, support and understanding, both work wise and personally; Miguel Filipe, for his camaraderie and patience in listening to me endlessly discoursing about any and everything (and, fortunately, never holding back on putting his two cents in); and Prerna Ajwani and Haoran Chen, who have made my stay in Paris homey and much enjoyable, for their invaluable and close support, and who have profoundly marked me in a very personal and dear way.

And this journey would not be complete without its beginning. My deepest gratitude goes to my family, for their unconditional support and for being the source of strength and the solid base from which my whole self draws from and is built on top of.

This work was conducted at Centro de Química Estrutural (Instituto Superior Técnico, Universidade de Lisboa, Lisboa, Portugal) and at Institut des Nanosciences de Paris (Sorbonne Université, Paris, France) in a joint international collaboration between the two hosting institutions. Funding from Fundação para a Ciência e a Tecnologia (FCT) for the PhD grant SFRH/BD/149192/2019 (https://doi.org/10.54499/SFRH/BD/149192/2019) is gratefully acknowledged. Funding from the hosting institutions and from the doctoral school 397 (ED 397 – Physique et Chimie des Matériaux) that covered part of the travelling expenses and enrolling in training programs, summer schools and scientific meetings is gratefully acknowledged. In particular, I thank ED 397 for financial support for two fruitful semesters of French lessons.

Contents

List of Tables

List of Figures

Acronyms and Symbols

2D two-dimensional. 3, 5, 6, 67, 69, 70, 140, 143, 148, 159, 162–168, 170, 185–187, 235

2DFT 2-Dimensional Fourier Transform. 61, 130, 139–144, 146

3D three-dimensional. 3, 5, 6, 67, 68, 159

AA All-Atom. 28–30, 48, 79, 81, 82, 94, 128, 198, 233

AFM Atomic Force Microscopy. 12–14, 19, 20, 22–27, 30, 31, 55–61, 79, 83, 95, 104, 111, 112, 114, 116–118, 127, 138–149, 168, 188, 231, 232, 234, 236, 237

AIBN 2,2'-azobis(isobutyronitrile). 15

BAM Brewster Angle Microscopy. 21, 22

BuOH Butanol. 126, 142, 143, 145, 147–149, 232, 234

CF perfluorinated. 7–13, 15–30, 81, 82, 93, 94, 97, 99–101, 103–105, 107, 109–114, 116, 117, 119–121, 125–128, 132–137, 144, 148, 149, 159, 174, 175, 177, 179, 180, 184–188, 191, 192, 198, 204, 205, 218, 220, 225, 231–236, XXII, XXVII

CG Coarse-Grained. 29, 48, 79, 80, 86, 93, 233, 236

CH hydrogenated. 7–9, 11–13, 15–20, 22–26, 28–30, 81, 82, 93, 94, 97, 101, 103–105, 107, 109–114, 116, 117, 119–121, 125–129, 132–137, 141, 143, 148, 149, 155, 174, 175, 177, 179, 180, 186–188, 191, 192, 198, 204, 218, 220, 225, 231–236, XXII, XXVII

DPPE Dipalmitoylphosphatidylethanolamine. 127, 137, 149

ESP Equilibrium Spreading Pressure. 118, 161

ESRF European Synchrotron Radiation Facility. 71, 156

EtOH Ethanol. 126, 128, 131–133, 142, 143, 147–149, 232, 234

Fn-COOH Perfluorinated n-Carboxylic 1-Acid. 8, 11, 12, 18, 20

Fn-OH n-Perfluoro 1H,1H-Alkan-1-ol. 11, 13

FnHm-COOH n-Perfluoroalkyl m-Carboxylic 1-Acid. 8, 118

FnHm-OH n-Perfluoroalkyl m-Alkan-1-ol. 8

FF Force Field. 27–30, 48, 50, 51, 79–84, 86, 87, 93, 94, 127, 128, 198, 199, 205, 233, 236

FWHM Full Width at Half Maximum. 162, 163, 170, 171, XXXVI, XXXVIII

GISAXS Grazing Incidence Small Angle X-Ray Scattering. 21, 23, 27, 30, 31, 71, 83, 104, 116, 117, 140, 145–147, 156–158, 162–167, 169–171, 178, 179, 182, 183, 185, 187, 231, 232, 234–237, XXXV–XXXVIII

GIXD Grazing Incidence X-Ray Diffraction. 18, 22, 27, 29, 70, 79, 83, 108–110, 121, 126, 127, 157, 168, 169, 172–178, 185–188, 231–237, IV, XIII–XX, XXX–XXXIII, XXXIX–XLII

GROMACS Groningen Machine for Chemical Simulation. 82, 94, 198

Hn-COOH Hydrogenated n-Carboxylic 1-Acid. 8, 11, 12, 20

Hn-OH Hydrogenated n-Alkan-1-ol. 8, 11–13

HOPG Highly Oriented Pyrolytic Graphite. 24

IRRAS Infrared Reflection-Absorption Spectroscopy. 23

IUPAC International Union of Pure and Applied Chemistry. 50, 51, 96, 102, 115, XXVI

KFM Kelvin Force Microscopy. 24

LB Langmuir-Blodgett. 61, 82, 145–147

LC Liquid Condensed. 6, 18, 21, 161

LE Liquid Expanded. 6

LJ Lennard-Jones. 27, 49–51, 82, 195, 199, 211, 215

LS Langmuir-Schaefer. 61, 147

MC Monte Carlo. 46

MD Molecular Dynamics. 19, 27–31, 46, 47, 51, 53, 78, 80, 81, 83, 84, 86–88, 93–97, 99–111, 113, 115, 116, 120, 126–128, 135–137, 143, 147–149, 180, 184, 186, 191, 192, 194, 198–200, 202, 205, 208, 224, 226, 231–237, III, IV, XIV–XX, XXVII, XXVIII, XXX–XXXIII, XLVIII, XLIX

MeOH Methanol. 126, 128, 131, 132, 141, 143, 145, 147, 148, 232, 234, 237

n-A Normal Alkane. 7–9, 16, 17, 19–21, 30, 191, 213, 224

NMR Nuclear Magnetic Resonance. 156, 168

OPLS Optimised Potential for Liquid Simulations. 51, 79, 81–85, 94, 128, 198, 233

PBC Periodic Boundary Condition. 28, 29, 52, 53, 128

PFA Perfluoroalkane. 7–9, 16–20, 30, 128, 191, 213, 224

PFAA Perfluoroalkylalkane. 7–9, 15–31, 59, 71, 79–81, 85–88, 93–99, 101–105, 107–121, 125–133, 135–140, 145–149, 155, 156, 161, 163, 168, 173, 174, 179–181, 183–185, 187, 188, 192, 215, 218, 231–237, XIV–XX, XXVI, XXVII, XXX–XXXIII

PFOA Perfluorooctanoic Acid. 10

PFOS Perfluorooctane Sulfonate. 10

PL Phospholipid. 11, 127, 237

PME Particle-mesh Ewald. 52, 82

PrOH Propanol. 128, 131–133, 143, 148, 232, 234

PS-PEO Polystyrene-poly(ethylene oxide). 27

PTFE Polytetrafluoroethylene. 15, 156, 157

RB Ryckaert-Bellemans. 50

RDF Radial Distribution Function. 195, 199, 210–217, 219, 221–224, LII–LXXI

RMSD Root-mean-square Deviation. 195

SDF Spacial Distribution Function. 82, 85, 94, 113, 114, XXII

SFA Semifluorinated Alkane. 15

SOLEIL Source Optimisée de Lumière d'Énergie Intermédiaire du LURE. 71, 72, 157

SPC/E Extended Simple Point Charge. 82, 128

SPICA Surface Property fItting Coarse grAining. 30

STM Scanning Tunnelling Microscopy. 55

TFE 2,2,2-trifluoroethanol. 126, 128, 131, 132, 142, 144, 147–149, 232, 234

TraPPE Transferable Potentials for Phase Equilibria. 81–86, 233

TRAVIS Trajectory Analyzer and Visualizer. 82, 94

UA United Atom. 27, 48, 81, 82

UCST Upper Critical Solution Temperature. 8

vdW van der Waals. 9, 17, 25, 49

VMD Visual Molecular Dynamics. 82, 94, 127, 199

XRR X-Ray Reflectivity. 18–20

A Molecular Area. 5, 6, 14, 17–19, 21–23, 25, 27, 126, 127, 137, 156, 158, 159, 161, 168, 169, 171, 184–188, 232, 234, 236

H^E Excess Enthalpy of Mixing. 7, 8

π Surface Pressure. 5, 6, 11–14, 17–23, 27, 31, 93, 110, 116, 126, 127, 137, 156, 158, 159, 161–179, 182, 183, 185–188, 232, 234–236, XXXV–XLII

$\pi_{\mathbf{collapse}}$ Surface Pressure of Collapse. 6, 159–161, 163, 165, 169, 185, 234

$\pi_{\mathbf{transf}}$ Surface Pressure of Transfer. 12, 20, 22

γ Surface Tension. 4, 5, 19, 29, 30, 233

T Temperature. 5, 11–15, 17, 31, 158–160, 162–167, 170, 172, 173, 177, 178, 198, 200, 201, 203–205, 208–212, 214, 216, 224, 234, 235, XXXV–XLII

ΔV Surface Potential. 19, 24

V^E Excess Volume of Mixing. 7, 8, 191, 224, 235

Part I

Context and Motivation

Chapter 1

Langmuir Films

1.1 Formation of Langmuir Films

It is known since classical antiquity that thin films of organic oils spread on top of water have a calming effect on the waves of ponds. Observations of this phenomenon by Benjamin Franklin and then by Lord Rayleigh note that the thickness of the film of grease would be about the same as the length of the organic molecules constituent of the oils (in the order of tens of Å) [1]. But it was the self-taught physicist Agnes Pockels who, in the end of the 19^{th} century, first proposed an experimental apparatus capable of containing and systematically varying the surface area of a monomolecular thin film spread at the air–water interface. At a time when women had limited recognition in scientific research, her achievements were acknowledged through Lord Rayleigh's sponsorship of a publication in *Nature*, based on a letter she sent him detailing some of her work [2]. Later, Irving Langmuir modified Pockels' device, creating what is known today as a surface balance or, more commonly, a Langmuir trough. He used this apparatus to study films of pure water-insoluble substances (rather than natural oils) spread at the surface of water, which also became known as Langmuir films. He determined that the thickness of these films was equal to the chain length of the organic molecules comprising them and that the area occupied by each molecule in the compressed film was the same for molecules that varied only in chain length [3]. Langmuir's experiments also led him to conclude that those molecules contain two moieties: one usually formed by a strongly polar group that tends to be directed towards the water surface and are thus "water loving" (hydrophilic) and another one that is oriented away from water, usually made of aliphatic chains of varying length, rendering it "water hating" (hydrophobic). This dual character is at the origin of the name of these substances: amphipathic or amphiphilic (from the Greek *amphi*, "dual", *pathos*, "feeling" and *philos*, "loving") [4].

For quite some time, Langmuir films remained laboratory curiosities in fundamental two-dimensional (2D) physics studies, but their importance was rapidly recognised in pure and applied sciences. Since then, they have served as models for the study of the structure and function of biological membranes, have been employed in the elucidation of the structure of three-dimensional (3D) crystals and, evidently, have proved useful in the understanding of the molecular packing within the Langmuir films themselves [5]. They also find practical everyday-life applications, for instance in reducing the rate of evaporation of water in reservoirs [4]. Additionally, Langmuir

films can be transferred onto solid substrates whether as a single layer of molecules (monolayer) or, through the successive transfer of multiple layers, as a multilayered structure (see Section 6.4). This opens a broad range of possible applications for Langmuir films, in areas as varied as medicine, electronics, sensors, optical devices and nanopatterning of surfaces [6, 7].

1.2 Surface Pressure–Molecular Area Isotherms

Surface chemistry consists in the study of the effects of the finitude of physical systems on their thermodynamic properties. It is well established that molecules in bulk have a markedly different environment than molecules near a surface of contact to another bulk phase of a different nature (*e. g.* a liquid in contact with air saturated with its vapour). The transition region between the two different phases has a thickness comparable to the size of individual molecules and the name *interface* is used to designate it. The interface is a region of higher energy, since the molecules experience less intermolecular like interactions there. Therefore, it requires work to reversibly increase the interfacial area, being that work proportional to the increase in area. The proportionality constant is called interfacial tension and depends on the nature of the contacting phases. When one of the phases is a gas, the term Surface Tension (γ) is often employed and, for low to moderate pressures, is practically independent of the nature of the gas. The γ can be viewed as a measure of the energy per unit area of the interface or of the tangential force required per unit length to reversibly expand the interface (accordingly, the International System of Units unit for γ is J m^{-2} = N m^{-1}) [4].

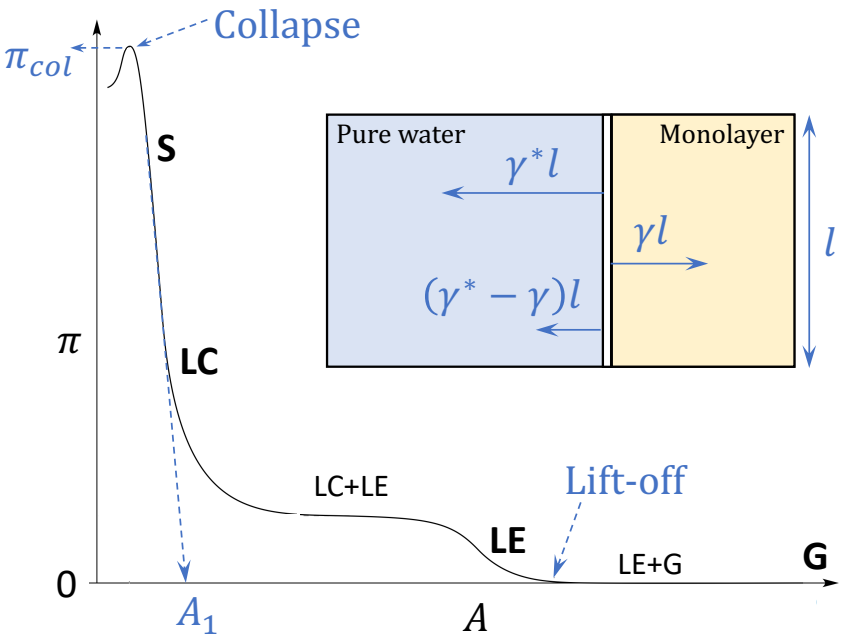

Figure 1.1: Example of a generic surface pressure – molecular area (π–A) isotherm. The inset is a schematic representation of a surface balance of side l, where the arrows depict the force balance exerted on a float separating a pure water surface from another one covered with a monolayer. The resulting force $(\gamma^* - \gamma)l = \pi l$ is proportional to the surface pressure (π). Adapted from [8].

The amphiphiles studied by Langmuir, having long hydrocarbon tails, are poorly soluble in water and, at room temperature, exist as solids or as liquids with low vapour pressure. Thus, when spread on top of water, the amounts that dissolve in the subphase and evaporate are negligible, compared to the amount that accumulates at the interface. For this reason, the amphiphiles readily adsorb at the interface and lower its γ. Solutes that significantly lower the γ are called surface-active agents or surfactants [4]. The Langmuir films are usually obtained by dissolving the amphiphile molecules in a volatile solvent (*e. g.* chloroform or hexane) and depositing the spreading solution on top of the liquid substrate with the help of a microsyringe. The solution spreads on the surface and the solvent is allowed to evaporate, forming a film at the interface [1, 6].

A Langmuir trough is essentially a device capable of isolating a region of known area of the surface of a liquid substrate covered with a molecular film and of measuring the associated changes in γ. Its design may vary, but the contention is usually achieved with one or more adjustable floating barriers, as illustrated on the inset of Figure 1.1. The γ can be measured by a number of methods, one of the simplest and most practical being the Wilhelmy method[1]. In Figure 1.1, the balance of forces exerted on the barrier due to the presence of the surfaces of pure water (left of the barrier) and of the monolayer-covered water (right of the barrier) is depicted. As mentioned previously, the existence of an interface increases the energy of the system and its surface area tends to be minimised. The forces exerted on each side of the barrier are thus in the sense of minimising the surface on the side they refer to, being proportional to the surface tension of the interface on the same side of the barrier. Denoting the surface tension of pure water by γ^* and the surface tension of the monolayer-covered surface by γ, and since $\gamma < \gamma^*$, there is a net force per unit length on the barrier of $\gamma^* - \gamma$ toward the left. This quantity is called the Surface Pressure (π) [4]. The Langmuir monolayers are characterised by the thermodynamic variables of Temperature (T), Surface Pressure (π) and Molecular Area (A). These are analogous to the variables used to characterise 3D systems, namely: temperature (T, which is essentially the same as in the 2D case), pressure (p) and volume (V) [6].

If the barrier in Figure 1.1 is moved to the right, reducing the area available to the monolayer molecules, these are further adsorbed to the surface and the π increases [4]. By dividing the total available area right of the barrier by the number of molecules spread to make the monolayer, the Molecular Area (A) is retrieved. The π can be plotted versus A at constant temperature as a surface pressure–molecular area (π–A) isotherm. A generic π–A isotherm is presented in Figure 1.1. In this isotherm, several 2D phases characteristic of Langmuir films are identified. Depending on the type of molecules constituting the film and the temperature, some phases might not be observable [6].

In a film spread at a low molecular density and surface pressure, the molecules are far apart from one another (A is large compared to the molecules' cross-sectional area). This way, the state of the monolayer is analogous to a 2D gas (G in Figure 1.1). In the limit of low density, an equation of state analogous to the ideal gas law is applicable: $\pi A = RT$. However, this state is generally not observed experimentally since the transition to the condensed phase (see below)

[1] In simple terms, with this method, the vertical force exerted on a thin plate (usually paper or roughened metal to promote wetting and thus minimise the contact angle) submerged in the liquid is measured and, from it, γ is computed. This method is well established and is described in more detail elsewhere [1].

appears at very low π. When the film is compressed, A decreases and the gaseous phase can condense to a Liquid Expanded (LE) phase via a first-order transition (and so at constant π; sometimes a subtle increase in π is observed). In these phases, the chains are interacting, but disordered and with *gauche* defects. Throughout the transition, the two phases coexist in a form analogous to the 3D vapour-liquid condensation. Within the LE phase, the molecules remain disordered (the phase is characteristically 2D isotropic). The relatively steep increase in π that usually follows is termed lift-off. Upon further compression, other first-order transitions can occur and a Liquid Condensed (LC) phase is formed. These phases appear at lower values of A, closer to the molecules' cross-sectional area. In these phases, the chains are extended and rather parallel to one another. The molecules are arranged with short-range positional order and long-range orientational order. Continuing the compression, the molecules become tightly packed together in a solid phase (S), occurring a steep increase in π characteristic of a poorly compressible phase. At this point, called the Pockels point, the molecules are closely organised and the molecular area extrapolated to $\pi = 0\,\mathrm{mN\,m^{-1}}$ (A_1) gives an estimate of the cross-sectional area per molecule. Upon further compression, the film might not possess enough area to have its molecules remaining assembled in a monolayer, and thus the film collapses and either it forms a 3D multilayered film or the molecules submerge in the liquid subphase. This is usually visible on a π–A compression isotherm plot, due to an abrupt halt on the increase in π after surpassing the collapse molecular area. Moreover, after the film's collapse, the π can decrease slightly owing to a partial relaxation of the collapsed film. The π at which the collapse occurs is the film's Surface Pressure of Collapse (π_{collapse}), although this is not always clearly experimentally discernible [1, 4, 6].

The monolayer isothermal compressibility (χ) is defined in Equation 1.1, analogously to the bulk compressibility [9].

$$\chi = -\frac{1}{A}\left.\frac{\partial A}{\partial \pi}\right|_T = -\left.\frac{\partial \ln A}{\partial \pi}\right|_T \tag{1.1}$$

Because π doesn't change with A for a pure surface (or in the limit of an infinitely diluted Langmuir film), χ diverges to infinity in such circumstances. To circumvent this mathematical particularity, the properties of the monolayers are usually characterised resorting to the compression modulus (C_S), which is essentially the inverse of χ (Equation 1.2) [9].

$$C_S = \frac{1}{\chi} = -A\left.\frac{\partial \pi}{\partial A}\right|_T \tag{1.2}$$

Chapter 2

Fluorinated surfactants: properties and applications

Fluorinated surfactants are substances that display significant surface activity and contain fluorine atoms in their composition [10]. Evidently, this is a broad definition and, in the scope of this thesis, the focus will be mainly on specific subcategories of these compounds: Perfluoroalkanes (PFAs), Perfluoroalkylalkanes (PFAAs) and partially and perfluorinated (CF) alkan-1-ols and carboxylic 1-acids, as well as mixtures with their hydrogenated (CH) analogues. Whenever pertinent and where applicable, a comparison will be established between these molecules and their CH analogues, given the usually more abundant and deeper knowledge on the latter. An emphasis is put on interfacial properties, particularly of the adsorption at the air–water interface. To facilitate the reading and to serve as a reference guide, the nomenclature and structural formulae of the chemical compounds recurrently mentioned in the text are summarised in Table 2.1.

2.1 Perfluorinated (CF) *vs.* hydrogenated (CH) chains

Despite the similarities between PFAs and *n*-As (most notably their carbon atom backbone), these are quite different classes of chemical compounds and even exhibit significant mutually phobic behaviour. In fact, the liquid mixtures of CH and CF compounds are highly non-ideal: they display large and positive Excess Enthalpies of Mixing (H^E) [12, 13] and Excess Volumes of Mixing (V^E) [14–19] (nearing $5\,\mathrm{cm^3/mol}$ for the equimolar mixture of F6+H6 at 25 °C); they have broad regions of liquid–liquid immiscibility [14, 15, 20]; they display significant positive deviations from Raoult's law [18, 21–23]. The mutually

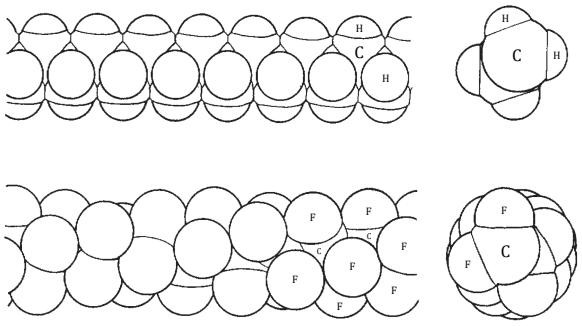

Figure 2.1: Illustration of the minimum energy configurations of alkyl (CH, top) and of perfluoroalkyl (CF, bottom) chains. The carbon, hydrogen and fluorine atoms are labelled C, H and F, respectively. Adapted from [11].

Table 2.1: Reference guide compiling the definition, structural formulae and notation of the chemical compounds which are the subject of this monograph. The attention of the reader is drawn to the fact that some of the cited references employ their own notation, which might differ from the one below. Where pertinent, the information from the literature was adapted in conformity to this table.

Name	**Abbreviation**	**Structural Formula**	**Notation**
Normal Alkane	*n*-A	$H(CH_2)_nH$	Hn
Perfluoroalkane	PFA	$F(CF_2)_nF$	Fn
Perfluoroalkylalkane	PFAA	$F(CF_2)_n(CH_2)_mH$	FnHm
Hydrogenated *n*-Alkan-1-ol	H*n*-OH	$H(CH_2)_nOH$	HnOH
n-Perfluoroalkyl *m*-Alkan-1-ol	F*n*H*m*-OH	$F(CF_2)_n(CH_2)_mOH$	FnHmOH
Hydrogenated *n*-Carboxylic 1-Acid	H*n*-COOH	$H(CH_2)_{n-1}COOH$	HnCOOH
Perfluorinated *n*-Carboxylic 1-Acid	F*n*-COOH	$F(CF_2)_{n-1}COOH$	FnCOOH
n-Perfluoroalkyl *m*-Carboxylic 1-Acid	F*n*H*m*-COOH	$F(CF_2)_n(CH_2)_{m-1}COOH$	FnHmCOOH

Note: the closest fluorinated analogue to H*n*-OHs, i.e. perfluorinated alcohols, are $1H$,$1H$ substituted because the fully fluorinated compounds are chemically unstable.

phobic behaviour is also found in other more subtle instances: the presence of F6 in liquid mixtures of F6+H6 at 25 °C (which are monophasic, since the mixture's Upper Critical Solution Temperature (UCST) is 21 °C [17]) induces the coiling of H6, favouring more globular states of the latter by increasing the proportion of *gauche* conformations, which has been interpreted as a solvophobic effect [24]. Overall, the described behaviour suggests the like interactions are considerably favoured and stronger compared to the unlike ones, in binary mixtures of CF and CH chains.

The mutually phobic behaviour of CF and CH chains has been studied for decades, but the fundamental reasons for its occurrence are yet to be fully understood. This behaviour is usually interpreted as a sign of weak intermolecular dispersion forces between CF and CH chains [17, 25–29]. Some insights have emerged from theoretical modelling, in which reproducing experimental results (*e.g.* V^E and H^E of mixtures of PFAs and *n*-As) require the use of corrective parameters that lower the heteromolecular dispersion interactions relative to those predicted with usual combining rules (*e.g.* Lorentz-Berthelot) [18, 24, 30–33]. On the other hand, it has been suggested based on first principles calculations that the CF–CH dispersive interactions might not be disfavoured after all, relative to the average of the homomolecular interactions [34], meaning that the introduction of corrective parameters would work only in an effective way. Other factors, such as the structural differences between the rigid CF chains and the flexible CH chains, might thus be contributing to the underlying causes of the observed behaviour [35]. The lack of a definitive picture demonstrates that this remains an active area of research.

Concerning the respective molecular structures, the rigid CF chains are known to adopt a characteristic helical conformation, as is schematised in Figure 2.1, with equally likely left and right helices [36]. The origin of such conformation has been attributed to: hindered C_F–C_F bond rotations due to steric repulsion between adjacent fluorine atoms (which have a larger van der Waals (vdW) radius – 0.135 nm – compared to that of hydrogen atoms – 0.11 nm to 0.12 nm) [11]; electrostatic repulsion between fluorine atoms [37]; and orbital hyperconjugation [38]. This is unlike the CH chains, which have a minimum conformational energy for the all-*trans* or zigzag structure [11, 36]. Thus, the conformational freedom of the CF chains is greatly reduced compared to that of the CH chains, the former having a *trans*/*gauche* interchange enthalpy at least 25% higher than the latter [36]. The hindered internal reorientation about the C–C bonds and reduced occurrence of *gauche* defects facilitate the stacking, ordering and crystallisation of CF chains [36]. CF chains are also bulkier than CH chains: they have cross sections of 0.27 nm^2 to 0.30 nm^2 and 0.18 nm^2 to 0.21 nm^2, respectively, the value depending on the packing situation [36]. The larger surface area of the CF chains also contributes to their enhanced hydrophobicity and surface activity, relative to CH chains [39].

In their condensed states, PFAs are less cohesive than *n*-As. This results in the vapour pressures of PFAs being higher than those of *n*-As of comparable molecular weight and PFAs displaying narrower liquid regions than those of the corresponding *n*-A. PFAs also display lower surface energy (surface tension), polarisability, and dielectric constant, but higher density, viscosity, and critical temperature than their *n*-A counterparts. These specificities essentially reflect the stronger intramolecular bonding and weaker intermolecular interactions found in PFAs relative to the corresponding *n*-As. Ultimately, these properties relate to the behaviour of CF and CH chains: both are classified as hydrophobic, but the former are lipophobic and the latter are fluorophobic as well [36].

2.2 Applications and environmental fate of fluorinated surfactants

Fluorinated compounds, especially those containing long CF chains in their structure, are usually chemically inert, are generally biocompatible, thermally stable and display a strikingly low surface energy, which drastically reduces their affinity for both hydrophobic and hydrophilic materials. These characteristics arise from the high electronegativity of fluorine that makes the C–F bond one of the strongest bond to carbon in organic chemistry [35, 38]. This surrounds the backbone of carbon atoms by a dense and electron-rich coating, resulting in very low intermolecular interactions. PFAs and related compounds are important for applications where low surface energy and inertness are key whether in the medical, biotechnological and industrial fields, including in: stain-repellent textiles, food-wrapping paper and fire-fighting foams [10], in targeted drug delivery [40, 41], as materials for eye surgery and as carriers of poorly soluble corneal drugs [42, 43] and as agents for contrast ultrasound imaging [44, 45]. Other attractive properties of fluorinated compounds include: their high gas-dissolving capacity, which elicits interest in using them in artificial blood and oxygen delivery formulations [46–48]; and their remarkable self-assembly properties, especially PFAAs and partially fluorinated acids and alcohols, which

self assemble into regular structures at the air–water interface and can be used as templates for surface nanopatterning [7, 49, 50]. The variety of fields of application highlights the ubiquitous presence and remarkable versatility of fluorinated compounds [51].

However, the widespread use of highly fluorinated compounds also has significant drawbacks. These compounds tend to be persistent in the environment and bioaccumulative [10, 52]. Fluorinated compounds, with particular emphasis on Perfluorooctanoic Acid (PFOA) and Perfluorooctane Sulfonate (PFOS), which are used as precursors for the fabrication of surface coatings and in other applications, have been found in environmental and biological samples from around the world [53], including in human blood [54]. The uptake and bioaccumulation along the food chain has also been documented [55]. Other uptake routes include food-contact materials, drinking water, air dust and even breast milk [10, 55]. The stability of these compounds is also a downside for bioremediation efforts, making their separation or degradation very challenging [56].

The research for alternatives to replace harmful or persistent CF compounds is thus of great importance, preferably for ones that should combine the attractive properties of CF moieties (inertness, stability, low cohesiveness and surface energy) with a better environmental fate, easier processability and low toxicity [10, 52]. For instance, compounds containing a shorter CF chain (usually shorter than 6 carbon atoms) are considered less bioaccumulative [10] and modified chains might be more biodegradable while maintaining the attractive properties of CF chains (*e.g.* perfluoropolyether chains [57] or "comblike" polymers containing short – 4 carbon atom-long – CF chains [58]).

Chapter 3

Long-chain carboxylic acids and alcohols

Simple long-chain fatty acids and alcohols are among the most extensively investigated amphiphiles and are often used as model film-forming substances [59, 60]. Mixed Langmuir films of long-chain acids or alcohols can also be used as model systems to study the effects of the mutual CF/CH incompatibility, of molecules in 2D confinement at the air–water interface. Through a careful balance of different factors, such as film composition and/or CH/CF chain lengths (illustrated in Figure 3.1), π, subphase Temperature (T), subphase composition, *etc.*, the structure of the mixed films can be varied for fundamental studies or for a myriad of applications, particularly for the nanopatterning of surfaces (*e.g.* changing the length of the CH and/or the CF molecules can impact the line tension, and thus the film morphology [61]).

The characteristics, organisation and thermodynamic properties of several CH amphiphiles (Hn-OHs, Hn-COOHs, Phospholipids (PLs) and others) are well established [1, 59, 62]. CF amphiphiles are ubiquitous and well known, but studies of Langmuir films of these molecules have been less systematic and scarcer, compared to their CH analogues [63]. Gaines refers the special difficulty in finding a convenient spreading solvent as a reason for this [59]. Moreover, some areas within the field are more explored than others: data of Langmuir films of some molecules (like Fn-COOHs) are more common than of others (which is the case of n-Perfluoro 1H,1H-Alkan-1-ols (Fn-OHs)). Nevertheless, there have been recent efforts in establishing experimental and theoretical frameworks to describe and interpret phase transitions and molecular organisation in Langmuir films of several CF acids, alcohols and phospholipids [7, 61, 64–67].

Pure perfluorinated alcohols spread at the air–water interface form stable Langmuir films and assemble at low surface density in discrete polygonal domains, a manifestation of a remarkable supramolecular organisation behaviour [68]. Under the same thermodynamic conditions, CH alcohols form Langmuir films comprised of homogeneous and circular domains. Surprisingly, similarly organised structures have been reported by other authors, but in phase-separated, compressed Langmuir films of mixtures of Hn-COOH and Fn-COOH [69–75] and of mixtures of Hn-OH and Fn-OH [76, 77]. The subject has been recently reviewed [61, 78, 79].

Whilst in the case of Hn-COOH the size of the hydrophilic –COOH head is larger than the diameter of the aliphatic chain, for Hn-OH the opposite happens with its –OH polar head [60]. Thus, the film packing and tilt angle of the molecules are more dependent on the packing of the –COOH heads in acids, while those properties are determined by the packing of the chains in the case of alcohols. Moreover, hydrogen bonding interactions are stronger than in the case of the –OH heads and it is possible to promote ion pairing interactions between the –COOH heads and solutes added to the subphase. The phase diagrams of Langmuir films of CH acids have been studied in greater detail and are deemed richer than those of the corresponding alcohols [60, 80].

3.1 Carboxylic acids

In general, mixed films of Fn-COOH and Hn-COOH are stable and immiscible [61] (*i.e.* the film separates into a CF-rich and a CH-rich phases at the liquid–air and solid–air interfaces), although there are also reports of miscible binary systems [69, 72]. Various factors, including the π (and Surface Pressure of Transfer (π_{transf})) [70, 81–83], the subphase T [81, 82, 84], the subphase composition (notably the subphase pH, in case the surfactant headgroup is ionisable, as in a carboxylic acid) [50, 85, 86], the solubility of the amphiphiles in the subphase [82, 87], the spreading solvent [70, 71, 73] and domain growth kinetics [82, 88], often acting subtly and together, affect the molecular organisation and morphology of the Langmuir film. The type of amphiphiles, the relative length of their nonpolar chains and the molar fractions in which they are present are also determinant for the variety of observed mixed film morphologies [75, 77]. Paige *et al.* state that when the difference between the number of carbon atoms in the CH and the CF molecules (denoted $\Delta_{\text{H-F}}$) is +6 or larger, the film is typically comprised of discrete, compact domains surrounded by a continuous matrix of a different height [61, 75]. Conversely, for $\Delta_{\text{H-F}} \leq +5$, the film structure is dominated by elongated or stripe-like domains disposed parallelly to one another. This rule, albeit empirical, is useful to predict and interpret the structure of the phase-separated films.

Usually, in the binary phase-separated Langmuir film, the molecule with the longest carbon backbone concentrates in the discrete domains (when these are formed) and the continuous matrix is enriched in the shorter molecule [61, 70, 71, 73, 75]. This was uncovered resorting to a clever experimental setup: the topography of the trans-

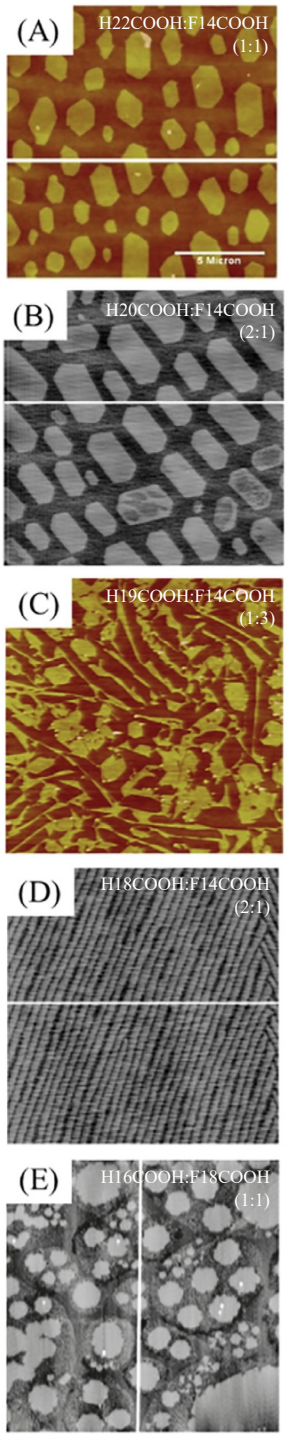

Figure 3.1: AFM images of phase-separated mixed monolayer systems (composition in top-right corners; image sides 5 µm (D), 10 µm (C, E), 15 µm (A) and 20 µm (B)). Adapted from [61].

ferred mixed monolayers was analysed by AFM before and after the incubation with a solvent that selectively dissolves the CH compound; the CH-rich domains were identified as those that would dissolve and were absent in the images of the second scan [61, 73]. Regarding the shape of the domains, there are reports of: 1) vertically aligned, CH-enriched polygonal domains (*e.g.* mixed films of docosanoic (H22COOH) and perfluorotetradecanoic acid (F14COOH), for which $\Delta_{\text{H-F}} = +8$ [75], and in mixed films of eicosanoic acid (H20COOH) and F14COOH, for which $\Delta_{\text{H-F}} = +6$ [71, 73], depicted in Figures 3.1a and 3.1b, respectively); 2) vertically aligned, CH-enriched stripe domains (*e.g.* mixed films of nonadecanoic acid (H19COOH) and F14COOH, for which $\Delta_{\text{H-F}} = +5$ [77], and in mixed films of octadecanoic acid (H18COOH) and F14COOH, for which $\Delta_{\text{H-F}} = +4$ [83], illustrated in Figures 3.1c and 3.1d, respectively); 3) vertically aligned, amorphous or rounded CH-enriched domains (*e.g.* mixed films of H20COOH and perfluorooctadecanoic acid (F18COOH), for which $\Delta_{\text{H-F}} = +2$ [70]); 4) vertically aligned, CF-enriched polygonal domains (*e.g.* mixed films of hexadecanoic acid (H16COOH)[1] and F18COOH, for which $\Delta_{\text{H-F}} = -2$ [87], shown in Figure 3.1e). The variety of morphologies of the mixed Langmuir films has been broadly attributed to a balance of the line tension between different phases (which favours the formation of large domains with compact or discrete shapes) and the dipole-dipole repulsion between the charged or polar headgroups (which favours the formation of small or extended domains) [61, 89].

The literature provides another interesting example of varying the subphase T and the chain length of the film-forming substances to control the morphology of mixed Langmuir films of carboxylic acids [90]. By mixing HnCOOH (n = 18, 20, 22, 24) with a perfluoropolyether surfactant ($F(CF(CF_3)CH_2O)_3CF(CF_3)COOH$, abbreviated PFPE) at the air–water interface, the mobility of the former determined the resulting film morphology: shorter CH molecules or increased T originated circular domains, whilst an interconnected network of ribbons would form if a lower T or longer molecules were employed. Rounded domains, once formed, are not deformed into ribbons, which suggests there is an interplay between thermodynamic and kinetic aspects that determine the morphology of the film. This example is illustrative of the possibilities for tailoring film morphologies, by modulating the experimental conditions and intermolecular interactions, and where the incompatibility between CF and CH chains plays an important role.

3.2 Alcohols

The properties of Langmuir films of mixtures of H*n*-OH and F*n*-OH have also been characterised, to some extent [76, 77, 81, 91, 92]. The Langmuir films of both acids and alcohols are known to be crystalline-like and sufficiently organised to produce an X-ray diffraction pattern, even at π=0 mN m^{-1} [65, 68, 81, 93, 94], attesting the molecular are prone to organisation at the air–water interface. The modification of the head group changes the morphology of the transferred films to discrete elliptical CH-enriched domains in a CF-enriched matrix, in mixed films of nonadecan-1-ol (H19OH) and F14COOH (compared to discrete polygonal domains for the H19COOH+14COOH system), as is illustrated in Figure 3.2. However, the acid- and the

[1] In this case, H16COOH has a reportedly finite solubility in the subphase, which might be indicative of additional kinetic effects affecting the formation and structure of this mixed film.

alcohol-containing films display minimal differences when comparing the respective thermodynamic mixing properties: in both cases small, near ideal values of excess Gibbs energy of mixing and excess molecular area of mixing are reported [77]. This is consistent with near total immiscibility of the film components and suggests that any difference in the extent of head group interactions (OH/COOH *vs.* COOH/COOH) is negligible in comparison with the dispersion interactions between the apolar chains.

In the case of a mixed film of 1,1,2,2-tetrahydrohenicosafluorododecanol (F10H2OH) and H14OH, both components seem mutually miscible at low π, in the expanded phase, and completely segregate in the compressed film [76]. Although both components phase separate and crystallise at the surface of water and perpendicularly to it, the film was not transferred and thus its morphology has not been determined. It remains unclear what shape might the transferred domains present, if these are formed at all. Overall, despite the important efforts reported so far, most of the characterisation work has been done on compressed mixed films at low values of A, and the same holds for the mixed Langmuir films of carboxylic acids. This leaves out some information concerning the formation of the observed domains, the structure of the low-surface density films and also the characteristics and organisation of the pure compounds spread at the surface of water.

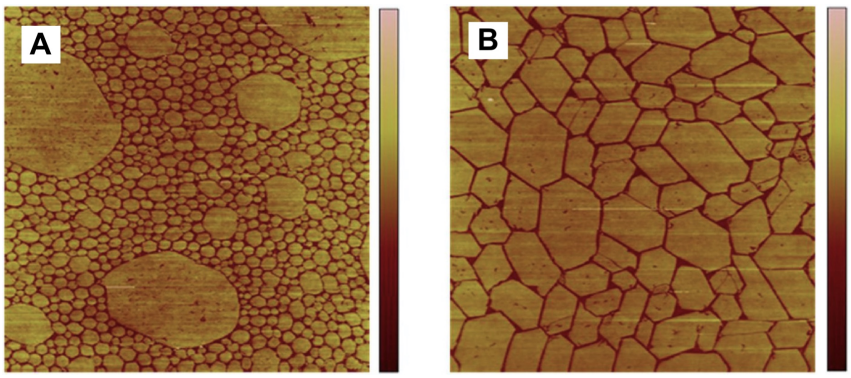

Figure 3.2: AFM topographic images of mixed monolayers of H19OH:F14COOH 4:1 (A) and H19COOH:F14COOH 4:1 (B) transferred onto silicon wafers at $T = 22\,^{\circ}\mathrm{C}$ and $\pi = 30\,\mathrm{mN\,m^{-1}}$ (image side 15 µm; height scales 3 nm (A) and 5 nm (B)). Adapted from [77]. See text for further details.

Chapter 4

Perfluoroalkylalkanes (PFAAs)

PFAAs have been known for decades, but recent interest on them has spurred due to novel observations of their remarkable biological inertness, self-assembling properties and high gas-dissolving capacities. PFAAs, sometimes referred to as Semifluorinated Alkanes (SFAs)[1], possess a fluorinated carbon chain (CF chain or block) covalently bonded to a hydrogenated carbon chain (CH chain or block), making them essentially low molecular weight block copolymers [95]. Their structural formula is thus $F(CF_2)_n(CH_2)_mH$ (denoted FnHm for short).

4.1 Synthesis and historical perspective

The first communication reporting the synthesis of PFAAs is from Tiers in 1962 [96], although some unpublished work might have been developed around the same time, namely by Walter Mahler at Du Pont [95]. Only in the 1980's a series of PFAA homologues with varying chain lengths were synthesised and studied in the solid state by Rabolt and coworkers at IBM as models for alternating copolymers of the type $(-(CF_2)_n(CH_2)_m-)_x$ [97, 98]. These studies were aimed at characterising a series of compounds with a high T stability approaching that of Polytetrafluoroethylene (PTFE) while at the same time maintaining the processability of polyethylene. The semiflexible partially fluorinated polymers are thermally stable, have superior mechanical and dielectric properties and are more soluble in various common solvents.

Although the main focus of this work is not on the discussion of the synthetic routes for the production of PFAAs (or other molecules), the topic is mentioned in brief, for context and historical perspective. The process described by Rabolt *et al.* [97] remains the most common synthetic route for the production of PFAAs. This is achieved in two steps:

1. Radical addition of a perfluoroalkyl iodide to a 1-alkene, in the presence of an azonitrile-type radical-generating chain initiator, usually 2,2'-azobis(isobutyronitrile) (AIBN):

$$F(CF_2)_nI \;+\; CH_2{=\!=}CH\cdot(CH_2)_{m-2}H \xrightarrow{\text{AIBN}} F(CF_2)_n\text{-}CH_2CHI\text{-}(CH_2)_{m-2}H$$

[1]The prefix "semi" does not imply the CF and CH chains must be equal in length (*i.e.* n and m in $F(CF_2)_n(CH_2)_mH$ or FnHm don't need to be equal).

2. Dehalogenation by reduction of the iodinated adduct with gaseous hydrochloric acid and zinc powder, in ethanol:

$$F(CF_2)_n\text{-}CH_2CHI\text{-}(CH_2)_{m-2}H \xrightarrow[EtOH]{HCl(g),Zn(s)} F(CF_2)_n\text{-}(CH_2)_mH$$

In the past decades, the study of PFAAs has raised quite some attention in the scientific community due to these compounds' peculiar characteristics and self-assembling properties. Several review articles have been published, systematising the knowledge on these compounds. Some of those reviews are cited here for reference: a few are focused on the characterisation of the self-assembly and physicochemical characteristics of PFAAs [7, 36, 99, 100]; others are devoted to the potential uses of these compounds, especially in the biomedical field [42, 101, 102]; additionally, some others still are dedicated to the systematisation of the nomenclature of this class of compounds and also their environmental impact [10, 55].

4.2 PFAAs are (a)polar species

PFAAs are generally considered apolar molecules, since they do not have a polar or hydrophilic moiety in their structure [36]. However, these compounds have a significant molecular dipole moment character, mostly due to the electrically asymmetrical CH_2–CF_2 junction, a consequence of the electron-withdrawing CF chain. The CF_3 and CH_3 termini also contribute to the molecular dipole, although to a lesser extent. The total dipole moment of the molecule is at an angle with its principal axis, closely aligned with the CH_2–CF_2 bond, and its magnitude is significant: literature values vary from 2.3 D to 3.4 D [103–108] (the range is mostly due to differences in the methods used for the measurement or calculation of this property; varying the length of the CF or CH chains has a comparatively smaller impact on the molecular dipole).

The molecular dipole of PFAAs is responsible for some of the peculiar properties of these substances. For instance, the shorter the PFAAs are, the higher is the relative importance of the dipole–dipole interactions that increase the cohesiveness of the molecules, which translates into a lower vapour pressure compared to *n*-As and PFAs of similar chain lengths [108]. Also, the significant electrostatic interactions at the liquid–liquid interface between water and PFAAs explain why the interfacial tensions of PFAAs with water are lower than those of similar-length PFAs or *n*-As with water [109]. The molecular dipole of PFAAs can also explain why these compounds are more soluble in methanol than *n*-As and PFAs of similar chain length [95].

4.3 Discovery and characterisation of surfactant properties

PFAAs merge two markedly different and, as explained above, largely incompatible moieties. As such, they have been described as "chemical mixtures of two mutually phobic segments" [22]. Since the reciprocal incompatibility of the CF and CH chains cannot be relieved by macro-phase separation, some rather interesting properties arise from this combination [110]. By combining the two blocks, these molecules display the dual character of amphiphiles [111]. They behave like functionally *primitive surfactants* [112], a designation that highlights their lack of a polar head, a usual feature in amphiphiles [59].

The driving force for PFAAs' supramolecular organisation, smectogenic character and surfactant behaviour is the subtle balance between weak dispersion forces between CH chains and even weaker ones between CF chains [110, 113]. That differs from common surfactants, which self-organise in great part due to the strong interaction between polar or ionic groups and water [113]. The surfactant behaviour of the water–insoluble PFAAs is reflected on their capacity of forming aggregates in bulk and in solution [110, 114], of assembling into micelles in both perfluorinated [112] and hydrogenated liquids [115] and of forming a variety of smectic liquid crystalline phases [116, 117]. The formation of Langmuir films of PFAAs at the air–water interface has been amply documented [6, 80, 91, 92, 95, 106, 111, 118–133], as well as the adsorption at the air–*n*-A interface [114, 134, 135] (but not at the air–PFA interface [114], since that would increase, rather than decrease, the surface energy of the CF compound). The adsorption of PFAAs at the water–PFA [136], water–*n*-A [114, 136, 137] and PFA–*n*-A [114] interfaces have been studied too.

Overall, PFAAs have been called **amphiphilic** (because the CH and CF moieties display unlike affinities), **amphisteric** (since the chains have different cross-section, preferential conformations and spacial requirements) and **amphidynamic** (contrasting the behaviour of the rigid and crystallisation-prone CF moieties with the behaviour of the more flexible CH chains) [36, 100].

4.4 Ability to form Langmuir films

As mentioned above, PFAAs form Langmuir films at the air–water interface. Given the lack of a polar or hydrophilic head in the structure of PFAAs, this was not foreseen. The first studies that uncovered this behaviour of PFAAs were conducted by Gaines in 1991 [95]. Upon compression of the PFAA Langmuir films, the author noticed the π remained practically constant and approximately null until a sudden increase occurred at a value of A close to that of the CF chain's cross-sectional area, as can be seen in Figure 4.1. This behaviour can be explained based on the fact that, although the PFAA molecules display a significant dipole due to the CH_2–CF_2 bond, they interact mainly through vdW forces. Since these forces are short-ranged, they are felt most intensely when the molecules are tightly packed, which explains the sudden and steep lift-off observed around a value of A characteristic of close-packed CF chains [131]. The stability of PFAA Langmuir films increases with increasing chain length and with decreasing T [6, 128, 131, 138, 139], which sometimes conditions the study of these systems. Nevertheless, they continued to spur interest in the scientific community for the years that followed.

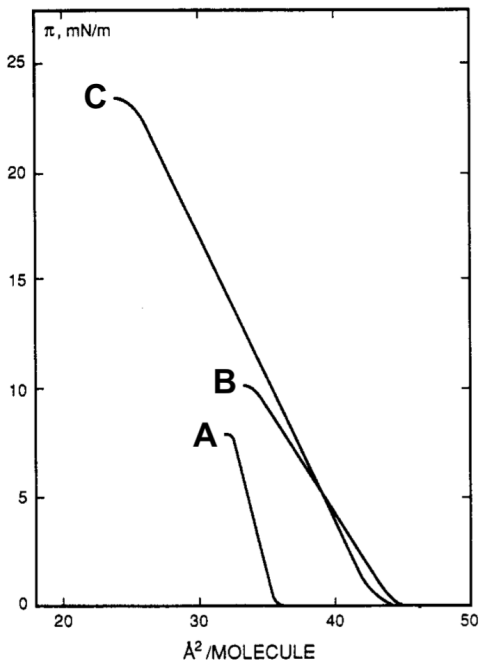

Figure 4.1: Surface Pressure – Molecular Area (π–A) compression isotherms for the PFAAs spread at the air–water interface at $T = 24\,°C$: F12H8 (A), F10H12 (B) and F12H18 (C). Adapted from [95].

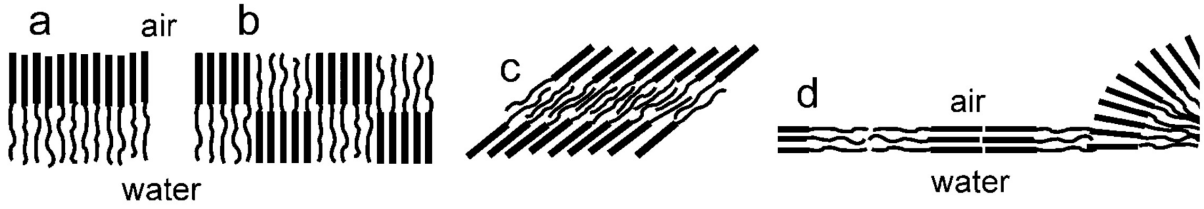

Figure 4.2: Schematic representation of the ordering of PFAAs in Langmuir monolayers proposed by different authors: (a) CF up–CH down 2-slab laterally-homogeneous monolayer, in which the molecules are vertically oriented, having their CF and CH chains in contact with air and water, respectively; (b) clustering of the molecules in nanodomains with alternating antiparallel orientation, with approximately half of the molecules having their CF chains facing the water subphase and the other half having the reverse orientation; (c) 3-slab model (smectic bilayer) with an antiparallel molecular arrangement forming an inner slab of interleaved CH chains and 2 outer slabs of CF chains in contact with both air and water; (d) coexistence of surface micelles having a CF up–CH down molecular orientation, with a LC parallel (P) phase in which the molecules lay parallel to the surface in stripes of alternate molecular orientation. Adapted from [36]. See text for further details.

4.5 Early Langmuir film characterisation studies

Because PFAAs do not possess a polar group and are built of two hydrophobic moieties, it is not a trivial problem which of them is oriented toward the air and which is in contact with water [131]. Gaines initially suggested that, because of the significant CH_2–CF_2 dipole, the PFAA molecules might arrange in a folded configuration, extending both the CH and the CF hydrophobic chains upward and leaving the polar junction in contact with water [95]. However, based on π–A isotherms' data, the molecules wouldn't have enough surface area to be organised in such a way. Instead, the author suggested the molecules might be vertically ordered with the CF chain extending upward and the CH chain immersed in the aqueous subphase, based on the relative order of hydrophobicity of the chains. At that time, there was no experimental structural evidence to support this conjecture.

Based on Grazing Incidence X-Ray Diffraction (GIXD) data of a F12H18 Langmuir monolayer at the air–water interface, Huang *et al.* observed that the CF chains were ordered and close packed according to a hexagonal lattice, whilst the CH chains remained only weakly organised [138]. A diffraction peak characteristic of the organisation of CF chains was visible even at zero π, although it was broad and had low intensity, indicating a weak organisation of the film. It was concluded that the monolayer was organised, although not as much as in other CF systems such as Fn-COOHs [65] or PFAs [140]. The authors also conducted X-Ray Reflectivity (XRR) studies of the F12H18 monolayer and these revealed a CF up–CH down orientation of the molecules. The monolayer was considered to be mostly featureless (as schematised in Figure 4.2a), only displaying some "surface inhomogeneities", *i.e.* the thickness of the monolayer fluctuated.

Combining data from π–A isotherms and XRR experiments of Langmuir films of F8H18, El Abed *et al.* later proposed that the PFAA molecules would pack in a smectic homogeneous bilayer for values of A indicative of a densely packed film (around $0.3\,\mathrm{nm^2\,molecule^{-1}}$) [141]. The proposed molecular organisation consisted in an antiparallel bilayer where the CF chains comprised the external slabs and the internal slab contained fully interleaved CH chains (as in

Figure 4.2c). The CF chains would then be slightly tilted, since the experimentally determined thickness of the CF layer was smaller than the length of a fully stretched CF chain. In a subsequent work, the same research team measured the Surface Potential (ΔV) of the same system for values of A in the range $1.0\,\mathrm{nm^2\,molecule^{-1}}$ to $0.2\,\mathrm{nm^2\,molecule^{-1}}$ in compression mode [104]. The ΔV remained practically null during the compression until a A of about $0.45\,\mathrm{nm\,molecule^{-1}}$, at which point it decreased linearly (*i.e.* became increasingly more negative) until the collapse of the monolayer at around $0.30\,\mathrm{nm\,molecule^{-1}}$, remaining constant upon further compression. The negative sign of the ΔV supports the CF up–CH down orientation of the molecules. Putting together all the experimental results, the researchers proposed the film would organise in a mosaic monolayer with clusters of molecules aligned in opposite directions for $A \geq 0.45\,\mathrm{nm^2\,molecule^{-1}}$ (Figure 4.2b); half the clusters would have the PFAA molecules oriented CF up–CH down and the remainder would display the opposite orientation. Upon compression, the domains would coalesce and originate the aforementioned smectic bilayer (Figure 4.2c). The mosaic model was supported by early Molecular Dynamics (MD) simulation results [142, 143], but more recent ones have provided additional insights contradicting it (*cf.* Subsection 4.12).

Other subsequent measurements of ΔV [131] supported the model proposed by Gaines [95] to the detriment of the mosaic model proposed by El Abed *et al.* [104]: for the entire studied range of A and for different PFAA molecules, the new ΔV measurements displayed a negative sign. An increase in magnitude of ΔV upon compression of the monolayer was also reported, in line with the former results. This way, the CF up–CH down orientation should always be preferred, since a monolayer with mixed domains would display, on average, $\Delta V = 0\,\mathrm{mV}$.

Another argument for the CF up–CH down orientation within the Langmuir films of PFAAs comes from the difference in the interfacial energies of n-As and PFAs: for instance, at room temperature, the surface tension of H6 is $17.8\,\mathrm{mN\,m^{-1}}$ [144], while F6's is $12.2\,\mathrm{mN\,m^{-1}}$ [145]. On the other hand, the liquid–liquid interfacial tensions of H6 and F6 with water are $50.4\,\mathrm{mN\,m^{-1}}$ [146] and $54.0\,\mathrm{mN\,m^{-1}}$ [109], respectively. This way, the energetically favoured configuration of the PFAA film can be inferred to be the CH chains in contact with water and the CF chains facing the air, in agreement with Gaines' line of thought (who we recall reasoned solely from π-A isotherms' data!) [95]. In fact, as a last example, thin liquid films of H6+F6 mixtures at the surface of silicon wafers display an enrichment of the liquid–vapour interface with F6, the compound with the lowest γ [147]. Throughout the years, other experimental [148, 149] and computer simulation [113, 136, 150, 151] results have supported the CF up–CH down orientation of the PFAA molecules.

4.6 Evidence of nanostructuration of Langmuir films of PFAAs

Some time after Gaines' work was known, it was suggested that the Langmuir films of PFAAs could present nanodomains, in part because such nanostructuration had been described for monolayers of partially fluorinated fatty acids [152, 153]. The first evidence in that sense was reported by Maaloum *et al.* [154]. In this work, a F8H16 Langmuir monolayer was transferred at non-zero π from the air–water interface onto a solid substrate and studied by AFM and XRR. The AFM images revealed that the monolayer was formed by monodisperse and approximately circular dome-

shaped surface micelles, tightly packed in a hexagonal pattern. The authors reported a set of other important findings, namely that the size of the surface micelles was controlled by the length of the PFAA molecules and that the micelle density increased upon film compression, but their size and shape remained practically unchanged throughout that process. Also, no coalescence of micelles was verified. The XRR results suggested the film was comprised of two "slabs" of different electronic density consistent with a CF up–CH down molecular orientation (as in Figure 4.2d). Finally, the dome shape of the nanodomains was interpreted as a way of relieving the low packing density of the CH chains, which originates in the mismatch of the CH and CF chains' cross-sectional areas. This way, both CH and CF moieties could be close-packed within the domains and their interactions could thus be maximised.

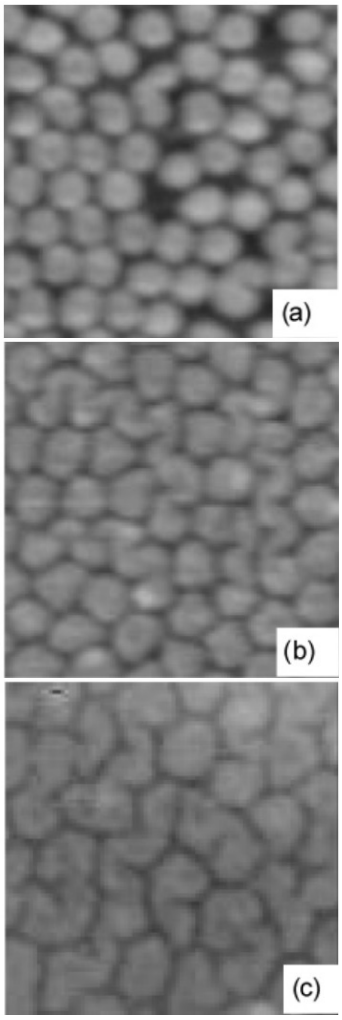

Figure 4.3: AFM topographic images of the PFAA monolayers transferred onto silicon wafers at $\pi = 5\,\mathrm{mN\,m^{-1}}$: F8H16 (a), F8H18 (b) and F8H20 (c) (image side 0.25 µm; no information on height scale). Adapted from [128].

The results reported by Maaloum *et al.* were later extended to monolayers of a series of PFAA molecules with different chain lengths [123, 128]. The new AFM images of the transferred monolayers also exhibited hexagonally packed monodisperse domains (*cf.* Figure 4.3). Some additional features were reported, namely the existence of elongated or worm-like micelles, as well as circular pit- or tip-centred micelles. The area fraction of the monolayers covered by elongated micelles was found to increase with both CH and CF chain lengths and to decrease with increasing π_{transf}, the latter reportedly being a reversible phenomenon. The authors confirmed that the π_{transf} practically did not affect the size of the observed domains, this being controlled mainly by the length of the CH chain (the CF chain length had a comparably little effect on domain size). Based on the obtained results, the authors proposed the circular micelles could result from the partitioning and closing of the elongated micelles, an idea supported by other researchers' findings [148]. The pit-centred micelles would result from the complete closing of the elongated micelles, whilst the tip-centred ones would result from an incomplete closing process, as is schematised in Figure 4.4. The effect of the CF and CH chain lengths on the morphology and on the size of the aggregates was later confirmed by other researchers [121].[2]

The driving force for the self-assembling process of nanostructured rather than homogeneous monolayers seems specific to PFAA molecules, because it is not observed for other similar short-chain organic amphiphiles. On one hand, *n*-As usually form multilayers on the surface of water or simply do not spread (forming droplets) and PFAs, F*n*-COOHs, and H*n*-COOHs form

[2]For reference, a series of aggregate size values obtained from the study of different PFAA monolayers is compiled in Table 4.1, on page 31. See also Figure 9.9, on page 104, for a visual representation of selected values.

homogeneous monolayers [78, 124, 140, 155]. On the other hand, the formation of surface micelles in monolayers of semifluorinated fatty acids has been reported [152, 153]. However, the domains made from simple PFAA molecules are better organised than those made from semifluorinated fatty acids with similar hydrophobic chains. This is an indication that the carboxylic headgroup, when present in the amphiphile, plays little or no role in the formation of hemimicelles and might even be a factor of disorder [128]. Finally, perfluoroeicosane (F20) forms a stable, crystalline Langmuir film at the surface of water that is able to diffract grazing X-rays even at zero π [140], while a n-A spread at the air–water interface requires a chain with at least 36 carbon atoms – hexatriacontane (H36) – to form stable, crystalline monolayers capable of diffracting X-rays [155]. These facts suggest the organisation and stabilisation tendencies of the Langmuir films mentioned above is, to a significant extent, due to the interaction, cohesion and crystallisation of the hydrophobic moieties, especially the CF chains [64].

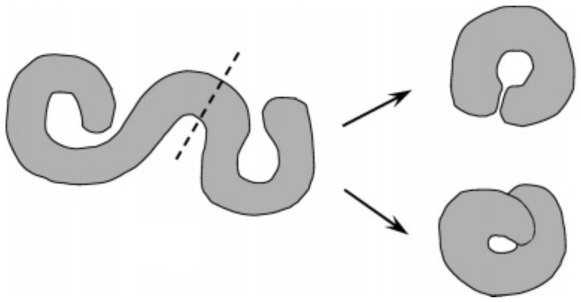

Figure 4.4: Schematic representation of the partitioning of an elongated micelle (left) that closes, upon compression of the monolayer, and yields pit-centred (top) or tip-centred (bottom) circular micelles. Adapted from [128].

At this point, it should be highlighted that the existence of nanodomains within the Langmuir monolayers of PFAAs was not foreseeable neither from π–A isotherms of different PFAAs [128] nor from early Brewster Angle Microscopy (BAM) experiments that studied the compression of F8H16 monolayers [131]. Both techniques only provided evidence of a gaseous and a liquid phases coexisting at high A that, upon compression and after a lift-off around $A \approx 0.3\,\mathrm{nm^2\,molecule^{-1}}$, give way to a LC phase. The film eventually collapses and a thick multilayered structure is formed.

4.7 Evidence of the existence of nanodomains at the air–water interface

Despite the extensive characterisation studies described above, these did not confirm the existence of the nanodomains directly at the surface of water, casting the doubt whether they could be an artefact of the process of transfer onto the solid substrates. That changed when Fontaine *et al.* performed Grazing Incidence Small Angle X-Ray Scattering (GISAXS) measurements of a F8H16 Langmuir film at the air–water interface and reported that it comprised hemimicelles arranged in a regular hexagonal lattice [122]. The fact that the nanodomains arranged in a 2D crystalline structure, originating a diffraction signal, is a demonstration of the monodispersity of the domain sizes [124]. For $\pi \approx 0\,\mathrm{mN\,m^{-1}}$ no diffraction occurred, but, as the authors noted, that does not mean the micelles do not exist at large values of surface area (for which $\pi \approx 0\,\mathrm{mN\,m^{-1}}$); they might just not be sufficiently organised in order to diffract the X-ray beam. The domains were about 30 nm in diameter, much larger than what's usually reported for hemimicelles made from molecular surfactants ($\approx 5\,\mathrm{nm}$) [122].

The results obtained by Fontaine *et al.* were later extended to other F8Hm molecules [120]. In this work, the authors refer the domains presented two levels of organisation: interdomain or long-range order (reflected in the lateral organisation of the domains in a hexagonal diffracting lattice) and intradomain. The latter level of organisation was assessed with GIXD experiments that revealed the CF chains and, to a lesser extent, the CH chains organised in 2 diffracting lattices, in agreement with previous reports by Huang *et al.* [138]. Each of the intradomain diffracting structures (stacking of CF and CH chains) was indexed to a 2D hexagonal lattice, with a coherence length (a measure of the lattice order) in the order of magnitude of the domains' size. The calculated size of the domains increased with the CH chain length [120]. The F8H20 Langmuir film was further characterised by BAM [120]. Upon compression, the condensed phase seen before the collapse of the monolayer was described as being fragmented in regions with sharp edges, forming angles consistent with an underlying hexagonal symmetry. Finally, the authors contrast the crystalline order of the hemimicelles necessary for the diffraction of X-rays with the lack of long-range order seen in AFM images of transferred films of PFAA monolayers: although the imaged domains appear closely packed, their impaired long-range order could be due to relaxation occurring upon the process of transfer [120].

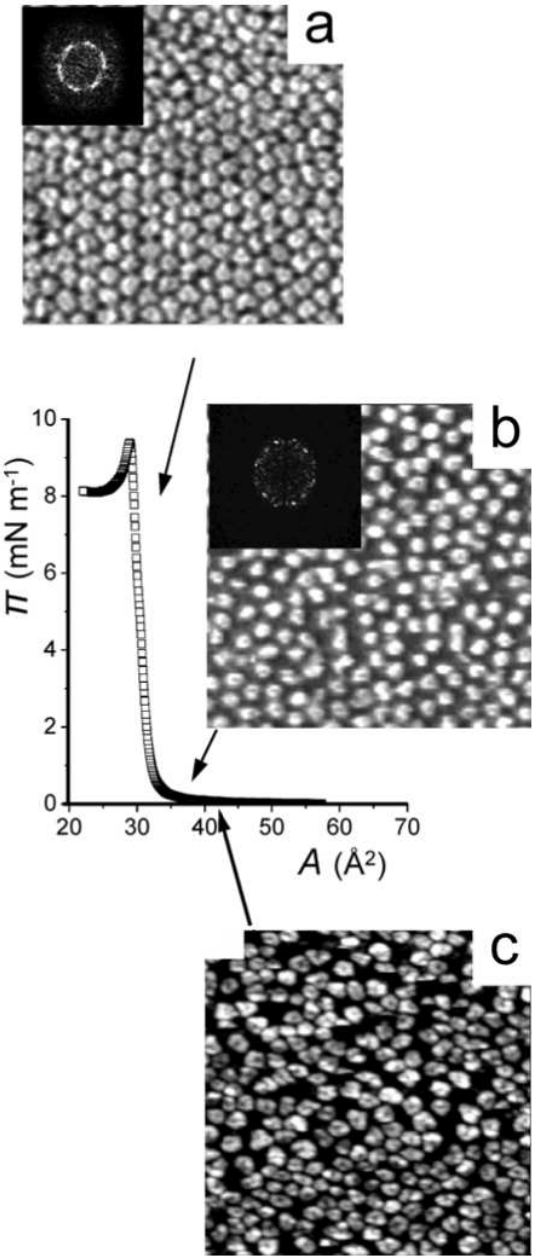

Figure 4.5: AFM topographic images of the F12H16 Langmuir films prepared at 20 °C and transferred onto silicon wafers at π values of $7\,\mathrm{mN\,m^{-1}}$ (a), $0.5\,\mathrm{mN\,m^{-1}}$ (b) and $0\,\mathrm{mN\,m^{-1}}$ (c), the latter corresponding to $A = 0.41\,\mathrm{nm^2\,molecule^{-1}}$ (image sides 0.5 µm; height range 5 nm). At large values of A, $\pi \approx 0\,\mathrm{mN\,m^{-1}}$. The insets represent the 2D Fourier Transforms of the AFM images, showing 2 (a), 1 (b) or 0 (c) rings, which confirm the decreasing lateral order of the films with decreasing π_{transf}. Adapted from [36], with data from [121, 154, 156]. See text for further details.

4.8 Evidence of the existence of nanodomains at low molecular density

Evidence that the domains are formed and exist even at low molecular density surged with AFM images of monolayers of F8H14 and of F8H16 transferred onto silicon wafers at $\pi = 0\,\mathrm{mN\,m^{-1}}$ (at A around $0.4\,\mathrm{nm^2\,molecule^{-1}}$ to $0.5\,\mathrm{nm^2\,molecule^{-1}}$), which displayed the distinct nanostructures, as is represented in Figure 4.5 [121]. The diameter of

the domains transferred at null surface pressure was similar to the diameter of those transferred at high π and their morphology was unaffected by compression [121, 127]. Evidence of the existence of the domains directly at the air–water interface at large A has also been provided from Infrared Reflection-Absorption Spectroscopy (IRRAS) studies of a Langmuir film of F8H16 [127]. This study also showed that the CH chains are not liquid-like and are actually quite ordered, assuming a preferential all-*trans* conformation (independently of A). Moreover, the CH chains should be tilted by $\approx 30^\circ$ relative to the film's normal in order to compensate for the larger space requirements of the CF chains, which should remain normal to the surface of water.

Progressively, more information about the structure of PFAA Langmuir films and details of the molecular packing within the aggregates surged. The resilience of the domains was attested by further AFM and GISAXS investigations in which it was verified that these structures would not coalesce upon film compression and even upon film collapse [124, 139]. Additionally, their size and shape would remain fairly unchanged independently of π, which implies the PFAA aggregates resist deformation due to strong repulsive interdomain interactions [126]. The mismatch of the CH and CF chains' cross-sectional areas was reiterated as the driving force for the assembly of curved or dome-shaped domains [124, 148].

4.9 Effect of the substrate on the nanostructuration of the Langmuir films

The formation of the domains is remarkably dependent on the nature of the underlying substrate. There are reports of PFAA nanodomains obtained on polar substrates, such as water [120], mica [148, 157], liquid crystals [158], wet silicon wafers [159] and amphiphilic block copolymers [111]. On the contrary, no evidence of nanostructuring has been observed at the surface of bulk PFAA liquids [160] or on dry silicon wafers [111]. Additionally, the collapsed Langmuir films of PFAAs at the air–water interface have been studied by AFM after transfer onto a solid substrate [139] and by GISAXS [124]. Upon compression beyond collapse (*i.e.* for values of A too low to be consistent with the existence of a monolayer), the monolayers do not dissolve or randomly disrupt, rather a trilayer is formed: the collapsed film forms a structureless bilayer on top of a first monolayer that rests in contact with water. Interestingly, the lower monolayer remains composed of regularly organised, hexagonally packed surface micelles. These observations attest the nanodomains' resilience, as they remain visible (in the AFM images) in the first layer that is partially covered with the collapsing and disordered film, they don't coalesce and their size and shape remain practically unaltered compared to before the collapse of the film. Furthermore, the interactions with air and other PFAA molecules are not the driving force for the observed self-organisation, since the upper layers are in contact with those media and are not nanostructured. That said, the in-plane interactions alone (as between CH_2–CF_2 dipoles) seem insufficient to induce self-assembly and nanostructuration of the films. These results demonstrate the importance of rigorously describing the interactions among the PFAA molecules and also between those and the different substrates (particularly with water), to enable the formation of regular and organised domains.

Gallyamov *et al.* reported the formation of organised domains of F12H19 and F14H18 at the surfaces of mica and of HOPG by deposition from a decalin solution or by precipitation through decompression of supercritical carbon dioxide solutions [157]. When the substrate was mica, round domains with a hole in the centre would always form (the authors call them "toroids"). The fact that domains are formed even without the influence of an evaporating or support liquid on the self organisation suggests this process is a true molecular self-assembly process. When the substrate was HOPG, the formation of aggregates is also observed, but these tended to be oriented along specific (crystalline) directions (especially when the samples were slightly annealed or the decompression rate was slow – compare Figures 4.6A and 4.6B), which is an indication of a strong interaction of the CH chains with the substrate. However, the mechanism of formation of the nanostructures or toroidal assemblies might differ from that occurring in the Langmuir films, since the height of the domains deposited from supercritical carbon dioxide was higher than the length of the fully stretched PFAAs (the authors suggest the observed structures are stacked double discs, with the CF chains facing the outside, as represented in Figure 4.8).

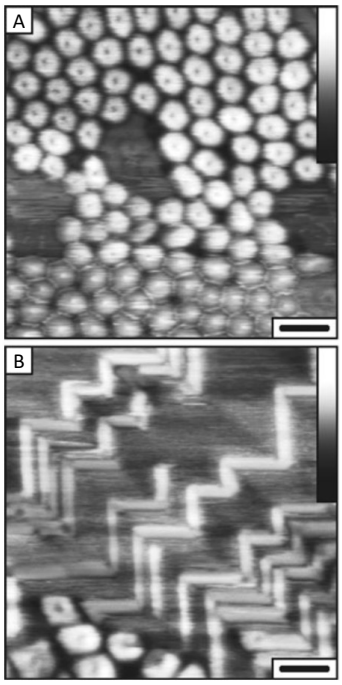

Figure 4.6: AFM topographic images of the F12H19 films deposited on mica (A) and on HOPG (B), upon slow depressurisation of a supercritical carbon dioxide solution (scale bar 75 nm; image side 0.5 µm; height scale 10 nm). Adapted from [157]. See text for further details.

In another study, the topography and the ΔV of films of F12H8 or F14H20 on mica, graphite or silicon wafers (obtained by spin-coating from perfluorodecalin solutions) were studied using Kelvin Force Microscopy (KFM) [161]. All substrates revealed the existence of curved domains with different gnarled shapes (ribbons, spirals, toroids), but always displaying a negative surface potential, consistent with a CF up–CH down orientation of the molecules. Only the films deposited on graphite displayed regions of lamellar organisation, which was attributed to the tendency of PFAAs to orient along the basal plane of the substrate. Unlike the curved domains, the lamella were considered to be formed by horizontally stacked molecules resulting from a compromise between unfavourable proximity of CF and CH chains and the CH affinity to the substrate. The curved shapes resemble the elongated domains reported by other authors [128, 148]. Interestingly, the F14H20 adsorbate on a silicon substrate formed a compact network of ribbons upon deposition, but these would spread out upon 24 h exposure to a humid atmosphere (relative humidity $> 90\%$). The prolongation of the exposure to humid air for another 24 h period induced the conversion of the ribbons into circular aggregates (toroids) with $\approx$45 nm in diameter.

These two studies demonstrate that the organisation of PFAAs is a true self-assembling process, which happens in the absence of water (*i.e.* the formation of a Langmuir film at the air–water interface is not mandatory prior to transferring the film). However, they also reveal that the interactions of PFAA molecules with the substrate (or with water, after the adsorption onto the solid substrate) still strongly influence the outcome of the self-assembling process.

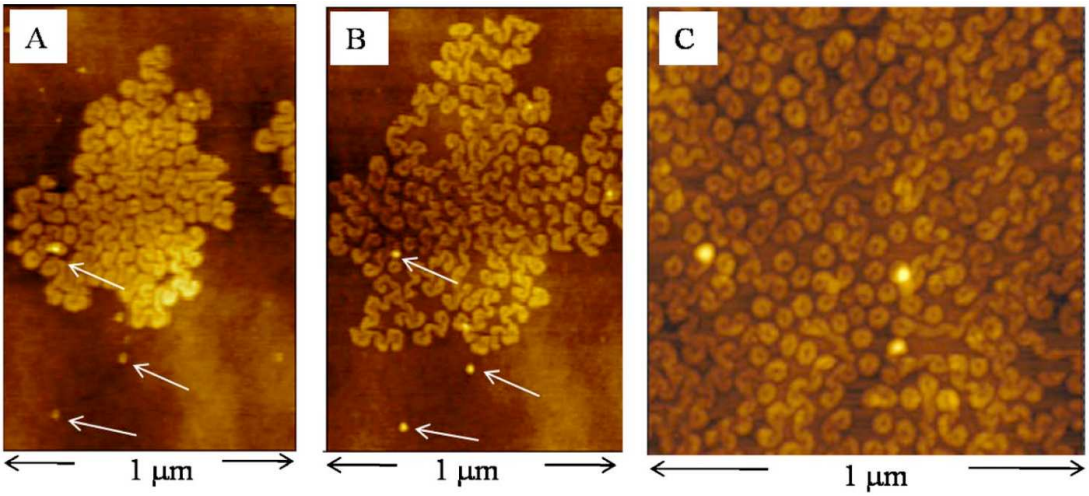

Figure 4.7: AFM topographic images obtained at the same location of F14H20 adsorbate spin-coated on a silicon wafer after 0 h (A), 24 h (B) and 48 h (C) exposure to humid air (relative humidity $> 90\%$). Adapted from [161]. See text for further details.

4.10 Theory and modelling of the formation of PFAA Langmuir films

The study of the formation of hemimicelles within the PFAA Langmuir monolayers is an intricate subject. Envisaging a rational description this phenomenon, Semenov *et al.* proposed a theoretical model with an analytical framework based on a balance of intermolecular vdW and dipolar interactions [162]. The model treats the water subphase as a structureless supporting medium, and so the interactions among PFAA molecules are in-plane only. The PFAA molecules lie parallel to the surface for high A and stand up under compression via a first-order phase transition. The surface micelles surge as a result of a liquid–liquid (rather than the experimentally observed gas–liquid) phase separation and comprise only upright, vertically aligned PFAA molecules, oriented in a CF chain up/CH chain down configuration, and packed hexagonally. The aggregates of vertical molecules coexist with a dilute phase (named parallel or P phase) consisting of horizontal molecules. The size of the domains is limited by the interaction of the domains' total dipoles with one another, which result from the sum of the vertical dipole moments of the CH_2–CF_2 bonds of each individual molecule. The model is able to describe a series of the features of PFAA Langmuir monolayers, but also predicts others that have not been confirmed by experiments. That is the case of the transition between the lying and standing phases. Also, the repulsive interactions between the domains' dipoles are considered to limit the size of the domains, suppress the micelle size polydispersity and prevent their coalescence, which has not been experimentally confirmed [125, 126]. Moreover, the model does not explain the dependency of the domain size on the length of the CH block (the dipole remains essentially the same when this is varied). Finally, the model does not account for the observed differences of stability and morphologies of the domains, which are markedly dependent on molecular architecture and on the nature of the upper phase and subphase.

The monodispersity of the hemimicelles suggests a link between hemimicelle size and molecular structure [157]. Early observations of these self-assembled structures were indicative that the size of the hemimicelles is essentially determined by the lengths of the CH and CF chains of PFAAs [154]. Some models have been proposed to rationalise the structure and size of the aggregates by establishing a relation between the CH and CF chain lengths with those properties. A disklike model was proposed in the already mentioned work by Zhang *et al.* [128], in which the radius of the aggregates is computed based on the interfacial area of the CF and CH moieties and the cross-sectional area and the lengths of the CF and CH chains. The predicted values compare well with those calculated from the authors' AFM results, although these appear to be slightly underestimated compared to other literature values (cf. Table 4.1 on page 31 and Figure 9.9 on page 104). The model adequately conveys that a change in the CF chain length increases the aggregates' size less substantially than a similar change in the CH chain length. However, it does not provide any information about the aggregates' internal structure and molecular organisation.

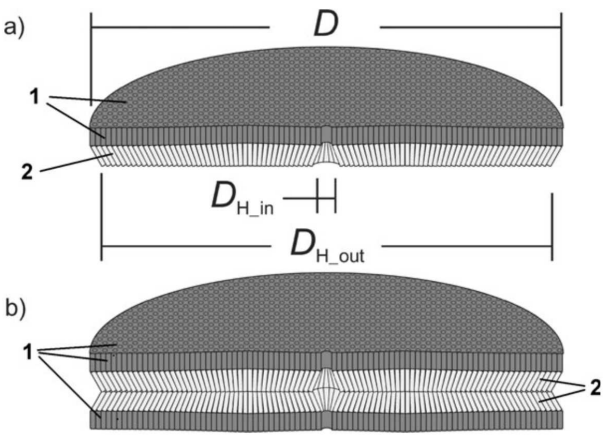

Figure 4.8: Schematic representation of the packing of the PFAA molecules in a toroid, according to Gallyamov *et al.*, with the CF and CH moieties labelled 1 and 2, respectively. The structure presents a hole in the centre of the hydrogenated layer, a consequence of a mismatch between the CF and CH chains' cross-sectional areas. Adapted from [157]. See text for further details.

Gallyamov and co-workers proposed the self-assembly of PFAAs to be governed by molecular close-packing effects, in the communication already cited above [157]. Hemimicelles are described as discs in which the CF chains are tightly packed and the CH chains are straight, but tilted to compensate the mismatch in the cross-sectional areas. The close packing of the CH moieties is achieved by the formation a hole in the centre of the disc, originating a toroidal structure. The diameter of these discs is computed considering the number of chains in the CH discs is limited by the maximum angle between the CF and CH chains, attained at the edge of the discs. While this model reportedly underestimates the diameter of the hemimicelles, the authors attribute that to the assumption that the chains are very closely packed, while the packing might be looser in reality. The maximum angle between the CF and CH chains is also assumed to be ≈90°, which constitutes an even cruder approximation. Even though the model explicitly considers the existence of a central hole in the hemimicelles, which could be related to the experimentally observed pit, it underperforms both quantitatively, by underestimating the dimensions of the hemimicelles, and qualitatively, since varying the CF chain does not affect the calculated diameter.

4.11 Existence of lying molecules between domains (P phase)

The existence of lying molecules between domains or P phase, as represented in Figure 4.2d, has been predicted by theory [162] and there are experimental [6, 111, 120, 125, 159] and MD simulation [151] results supporting its existence. However, the debate over this subject remains a controversial topic. The P phase is thought to stabilise the hemimicelles and prevent their coalescence upon compression of the Langmuir monolayer [159]. The existence of lying molecules has been suggested based on AFM observations of a "bump" between tightly packed nanodomains in monolayers of pure PFAAs [159] and in mixed Langmuir monolayers of PFAAs with the amphiphilic block copolymer Polystyrene-poly(ethylene oxide) (PS-PEO) [111]. In the latter case, the "bump" could be an accumulation of PS-PEO molecules at the boundaries of the domains. π–A isotherms [120] and of GISAXS spectra [125] of the Langmuir monolayers of PFAAs have also been interpreted in support of the existence of the P phase. The interaction of the lying molecules' dipoles with the dipoles of water molecules is the driving force proposed for this structuring of the films. The existence of lying molecules also provides an explanation for the stability of the nanostructures that persist under compression at the surface of polar substrates and its non-observation at the surface on neutral substrates [125]. These molecules, which occupy a larger A than upright molecules, would also explain why the lift-off value of A from π–A isotherms of PFAAs is slightly larger than the cross-sectional area of CF chains [6].

The compressibility of several Langmuir monolayers of PFAAs has been calculated from both GIXD and GISAXS spectra obtained at different values of π [120]. The compression of the films led to the compression of the domains closer together, though not so much of the molecules within the aggregates. Whilst the compressibility of the hexagonal lattice of the domains compared well with the monolayer compressibility retrieved from π–A isotherms, the compressibility of the stacked chains was two orders of magnitude lower. The authors concluded the compression of the film is due to the compression of the domains since the 2D pressure is not transmitted to the close-packed structure inside the domains [120]. This behaviour can be associated with the capacity of the CF chains to promote self-assembly and ordering, which helps converting the compression of layers of molecules into the compression of arrays of nanodomains [139]. These results are consistent with the existence of lying PFAA molecules between domains [120].

4.12 Computational studies

Given the complexity of the subject and the limitations on the resolution of the experimental techniques, it is hard to obtain a detailed characterisation of the molecular arrangement of the Langmuir films of PFAAs. This problem can be tackled, at least in part, by conducting computer simulations of those Langmuir films. Some of the earliest contributions in this sense include the works by Kim *et al.* [142, 143]. The authors employed a United Atom (UA) Force Field (FF) to model an F8H18 monolayer, describing each of the CF_3, CF_2, CH_2 and CH_3 groups by a single uncharged Lennard-Jones (LJ) interactive centre connected by rigid bonds. Moreover, the molecular structure of the substrate was neglected, being treated as a continuous medium truncated at a planar surface (known as a 9–3 repulsive wall), and the con-

formations of both the CF and CH chains were modelled by a dihedral potential that considered the energy minima for the all-*trans* conformations. The molecular area was kept relatively low at 0.35 nm molecule^{-1}. The results showed the spontaneous organisation from a random initial configuration of the molecules in a monolayer with a collective tilt of 40° to 45°, which was attributed to the small size of the system coupled with the use of Periodic Boundary Condition (PBC). The molecules displayed a mixed CF up–CH down and CH up–CF down orientation (as in Figure 4.2b), although the former appeared to be slightly favoured. The clustering of molecules with the same orientation was also reported. The authors suggest that the monolayers could be formed by large CF up–CH down domains separated by smaller ones with the reverse orientation. However, the studied systems were small (with just 100 PFAA molecules), used a relatively simplistic model (with uncharged interacting centres, neglecting the molecular structure of the aqueous subphase and not considering the helical structure of CF chains) and the duration of the simulations was short (10 ns), due to limitations in computational power. The authors recognised that more extensive simulations using larger systems should be performed.

The liquid–liquid interface of water and F8H8 was later studied by MD simulation, using an All-Atom (AA) FF to model both the aqueous and the organic phases [136]. The authors reported that the liquid phases were immiscible in all cases, displaying high values of interfacial tension and sharp interfaces. The interface was enriched with CH chains of F8H8, which was attributed to the lower hydrophobicity of the CH compared to that of the CF chains (in agreement with more recent MD simulation studies [109]).

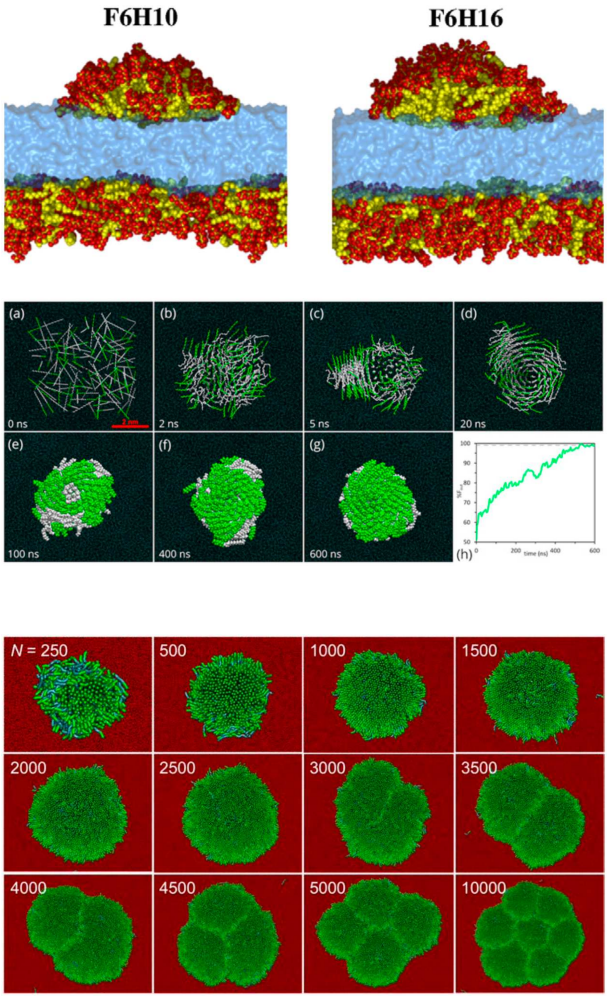

Figure 4.9: Snapshots of simulated aggregates of PFAAs at the air–water interface from different computational studies reported in the literature. Top: side view of two monolayers, each consisting of 160 F6H10 (left) or 160 F6H16 (right), one on each side of a slab of water (10 nm side; CF, CH and water moieties in red, yellow and blue, respectively); middle: top views of time evolution of 100 F8H16 molecules from a random starting configuration and plot of the time evolution of the percentage of molecules with a CF up–CH down orientation (scale bar 2 nm; CF, CH and water moieties in green, white and blue, respectively); bottom: top view of the final state of F8H16 aggregates with varying numbers N of molecules (varying scale, the diameter of the $N = 250$ aggregate is ≈ 9 nm and the linear dimension of the $N = 10\,000$ aggregate is ≈ 60 nm; CF, CH and water moieties in green, cyan and red, respectively). Adapted from [150], [113] and [151], respectively. See text for further details.

In a different work, Piñeiro *et al.* studied Langmuir films of F6H10 and F6H16 at the air–water interface, using an AA FF including explicit water molecules for the subphase [150]. The authors reported the aggregation of PFAA molecules in immiscible clusters and the formation of elongated surface micelles that, upon compression, would reorganise into multilayers. The molecules displayed a CF up–CH down orientation and the surface micelles had a rounded shape (*cf.* Figure 4.9 (top)). However, no electrostatic interactions involving the PFAA molecules were considered in this study and, as presented above, those seem determinant to the properties and behaviour of these systems (particularly to model the interaction with water). Additionally, the formation of elongated micelles could be an artefact resulting from: the small size of the simulation box; the use of PBCs; and the small number of PFAA molecules used (160 for each simulated monolayer), which is about one order of magnitude lower than that found in the experimentally observed hemimicelles ($\approx 10^3$ molecules per hemimicelle [120]).

A more recent work studied the self-assembling and structural properties of aggregates with varying numbers of F8H16 molecules at the surface of water, at low surface density [113]. An AA FF was used to model both the organic molecules and water, and electrostatic interactions were explicitly considered in the form of partial atomic charges. The authors demonstrated that the molecules spontaneously aggregate into rounded surface domains and that the CF up–CH down orientation is achieved from molecules randomly dispersed at the surface of water, as is represented in Figure 4.9 (middle). Compared to the study by Kim *et al.* mentioned above, the difference in the obtained molecular orientation can be attributed to the slow process of organisation, which is only achievable through longer simulations that were technically inaccessible at the time. The molecules assembled into a spiralling arrangement within the aggregates to maximise the interactions and the occupation of space, a phenomenon quantified by the computation of an average azimuthal angle. This angle decreased with increasing aggregate size until it 0° was attained for an aggregate with dimensions and morphology resembling the experimentally observed hemimicelles (named limit-size aggregate). The limit-size aggregate had a round shape, a pit in its centre and a diameter of about 31 nm to 32 nm, in agreement with experimental results (cf. Table 4.1 on page 31 and Figure 9.9 on page 104). The GIXD pattern of the limit-size aggregate was calculated from the corresponding simulation trajectory and it also compared favourably with experimental results. The molecules were disposed in concentric rings in almost hexagonal packing, this not being achieved due to the occurrence of defects/tilting, the mobility of the molecules, and the aggregates not being flat. The coalescence of 2 small (100 molecules) aggregates was demonstrated, while the compression of 2 large (1763 molecules), near limit-size aggregates resulted in deformation at the contacting edges and no coalescence was observed for the duration of the simulation. This provided insights into the mechanism of formation of the nanostructured Langmuir films and also into the remarkable sturdiness of the domains. Finally, the organisation of the molecules was found to be conditioned by a number factors, namely: the mismatch of the CF and CH chains' cross sections; the relative hydrophobicity and lengths of the CF and CH chains; the lower γ of CF chains; the interaction between the PFAA dipole and water; the segregation between CF and CH chains.

In order to probe the ordering of the PFAA Langmuir films at larger length and longer time scales through MD simulations, the use of Coarse-Grained (CG) FFs can be of great utility, if

not imperative for technical reasons. Yadav *et al.* conducted 1 µs-long MD simulations to study the formation and the organisation of aggregates containing up to 10 000 F8H16 molecules at the air–water interface, using a purposely developed extension of the Surface Property fItting Coarse grAining (SPICA)[3] FF for PFAA compounds [151]. The authors report that, for all studied systems, the PFAA molecules self-assembled in approximately circular surface aggregates, with the molecules showing a preferred CF up–CH down orientation. The authors estimated the aggregation number of the limit-size aggregate to be between 2500 and 3000 molecules, in agreement with the AA simulations mentioned above [113], considering that the systems containing $\leq$ 2500 molecules formed a single aggregate, whereas larger systems spontaneously organised in multiple-lobed aggregates, as can be seen in Figure 4.9 (bottom). The diameter of the 2500-molecule aggregate was estimated to be about 27 nm, which is close to the reported experimental values. This aggregate was round and dome shaped, but did not display the experimentally observed pit in its centre. The molecules were found to be packed in a pseudo-hexagonal network inside the aggregates. The authors also report on the existence of a lower density P phase of laid-down molecules that accumulate in between the aggregates for systems larger than the limit-size hemimicelle. The authors also propose a mechanism of hemimicelle formation based on simulations conducted at very high molecular area ($\approx 1\,\mathrm{nm}^2$/molecule) which consists on the condensation of a dilute 2D gas into transient P phase strips, which turn into transient PFAA islands surrounded by an extremely dilute 2D gas phase; the islands eventually merge through a collision-coalescence (fusion) mechanism to form hemimicelles of saturated sizes.

4.13 Compilation of pure PFAA surface aggregate size values from literature

Some literature values of diameter of the pure PFAA surface aggregates are compiled in Table 4.1. These values vary slightly depending on the method by which they were determined. In the case of AFM, the values are likely an underestimation of the real size of the hemimicelles, mostly for two reasons: first, the AFM tip has a finite width and, adding to the tip-sample interactions that can disturb the structure of soft substrates, the determined topography of the samples can by slightly distorted; second, the calculation of the diameter of the aggregates is usually done using image analysis software, through the detection of domains with a height higher than a certain threshold, the computation of their cross sectional area and the determination of the diameter of a circle with the same area. This procedure can underestimate the size of the domains if the threshold is too high and domains whose shape is highly non-circular can have their dimensions miscalculated as well. In the case of GISAXS, the values are likely to be closer to the real diameter of the surface aggregates or to err by a slight overestimation. It is clear from these data that the domain size increases with increasing chain length, particularly with the CH chain.[4] This trend had already been identified before [128].

[3] This FF models the molecules as beads that interact exclusively through dispersion interactions, using a predominantly 3-to-1 mapping of heavy atoms to interaction centres (including for water). The FF is parametrised to reproduce room-temperature liquid densities and γs of water, *n*-As, PFAs and PFAAs, as well as interfacial tensions of the organic compounds with water.

[4] *Cf.* Figures 9.9 and 9.20 on pages 104 and 117, respectively, as well for a graphical representation of a selection of these points, for a few CH and CF chain lengths.

Table 4.1: Domain size of the pure FnHm nanostructures formed at the air–water interface, determined by different techniques. The values of Surface Pressure (π) correspond to the π at which: the Langmuir film was transferred, in the case of the results obtained by AFM; the Langmuir film was probed, in the case of the results obtained by GISAXS; the simulations were conducted, in the case of the results obtained by MD simulation.

Molecule	π (mN m^{-1})	Domain size (nm)	Technique	Reference	Observations
F6H16	0	31.3 ± 0.1	MD	–	a)
	5	25.3 ± 0.8	AFM	[128]	b)
F8H14	0	26 ± 3	AFM	[121]	–
		26.5 ± 0.1	MD	–	a)
	0.5	24 ± 3	AFM	[121]	–
	2	27.8 ± 1.0	AFM	[128]	–
		28.7 ± 0.3	GISAXS	[120]	–
	5	19.9 ± 1.6	AFM	[128]	–
		27.8 ± 0.6	GISAXS	[120]	–
		28 ± 4	GISAXS	[126]	–
F8H16	0	30 ± 3	AFM	[121]	–
		32 ± 2	AFM	[127]	–
		31.7 ± 0.2	MD	[113]	–
	0.5	33 ± 3	AFM	[121]	–
	2	27.8 ± 1.0	AFM	[128]	–
	3	32.3 ± 0.3	GISAXS	[120]	–
	5	24.6 ± 2.3	AFM	[128]	–
		≈ 33.5	GISAXS	[122]	–
		32.8 ± 0.3	GISAXS	[120]	–
		29 ± 5	GISAXS	[126]	–
	7	30 ± 2	AFM	[154]	–
F8H18	undetermined	≈ 35	AFM	[159]	c)
	0	35.7 ± 0.1	MD	–	a)
	0.5	41 ± 5	AFM	[121]	–
	2	27.5 ± 0.7	AFM	[128]	–
	5	27.2 ± 1.6	AFM	[128]	–
		40.3 ± 1.5	GISAXS	[120]	–
		32 ± 5	GISAXS	[126]	–
F8H20	0	39.4 ± 0.1	MD	–	a)
	0.5	43 ± 5	AFM	[121]	–
	3	40.8 ± 1.8	GISAXS	[120]	–
	5	33.9 ± 2.4	AFM	[128]	–
		40.7 ± 1.2	GISAXS	[120]	–
		36 ± 7	GISAXS	[126]	–
F10H14	0	27.0 ± 0.1	MD	–	a)
	5	27.9 ± 0.4	GISAXS	–	a)
F10H16	0	32.5 ± 0.2	MD	–	a)
	3	35.3 ± 1.0	GISAXS	[6]	–
	5	25.4 ± 3.4	AFM	[128]	–
		34.5 ± 0.5	GISAXS	[6]	–
		30 ± 5	GISAXS	[126]	–
		31.8 ± 0.4	GISAXS	–	a)
F10H18	0	37.3 ± 0.1	MD	–	a)
	5	34 ± 6	GISAXS	[126]	–
		35.9 ± 0.6	GISAXS	–	a)
F10H20	0	39.5 ± 0.1	MD	–	a)
	5	41.1 ± 1.0	GISAXS	–	a)
F12H12	2	≈ 30	AFM	[149]	–
F12H16	0	36.6 ± 0.1	MD	–	a)
	5	33 ± 5	GISAXS	[126]	–
		≈ 35.9	GISAXS	–	a)
F12H19	undetermined	48 ± 4	AFM	[157]	d)
F12H20	2	≈ 50	AFM	[149]	–
	5	≈ 53.3	GISAXS	–	a)
F14H18	undetermined	52 ± 5	AFM	[157]	d)
F14H20	undetermined	≈ 45	AFM	[161]	e)
	4.9	≈ 60	AFM	[148]	f)

Notes: a) original (preliminary) results; b) F6H16 is reported to not form stable Langmuir monolayers at the air–water interface and at room T (a stable π value is not obtained upon film compression) although it is still possible to transfer a film of F6H16 onto a solid substrate and image it by AFM; c) monolayer formed by spin-coating a wet silicon wafer, a method by which the surface pressure is neither controlled nor measured; d) deposition of the PFAA molecules from a supercritical CO_2 solution onto a solid substrate (mica) (see text for details); e) the samples were obtained by spin-coating onto silicon substrates and exposed to a humid atmosphere for 2 days prior to imaging; f) the authors report the existence of either ribbons or close-packed spirals on the transferred film. The indicated size is the reported packing periodicity of the spirals.

References

[1] A. W. Adamson and A. P. Gast. *Physical Chemistry of Surfaces*. 6th ed. Hoboken, New Jersey, USA: John Wiley & Sons, Inc., 1997. ISBN: 978-0-471-14873-9.

[2] A. Pockels. 'Surface Tension'. In: *Nature* 43.1115 (1891), pp. 437–439. DOI: 10.1038/043437b0.

[3] I. Langmuir. 'The Constitution and Fundamental Properties of Solids and Liquids. II. Liquids.' In: *Journal of the American Chemical Society* 39.9 (1917), pp. 1848–1906. DOI: 10.1021/ja02254a006.

[4] I. N. Levine. *Physical Chemistry*. 4th ed. ISBN 0-07-037528-3. New York, USA: McGraw-Hill, 1995. ISBN: 0-07-037528-3.

[5] J. Als-Nielsen et al. 'Principles and Applications of Grazing-Incidence X-Ray and Neutron-Scattering from Ordered Molecular Monolayers at the Air–Water Interface'. In: *Physics Reports – Review Section of Physics Letters* 246.5 (1994), pp. 252–313. DOI: 10.1016/0370-1573(94)90046-9.

[6] L. Bardin. 'Monocouches d'alcanes semi-fluorés'. PhD thesis. Paris, France: Université Pierre et Marie Curie, 2010.

[7] M. P. Krafft and M. Goldmann. 'Monolayers made from fluorinated amphiphiles'. In: *Current Opinion in Colloid and Interface Science* 8.3 (2003), pp. 243–250. DOI: 10.1016/S1359-0294(03)00046-3.

[8] *Example of a compression isotherm*. File licensed under the Creative Commons Attribution-Share Alike 4.0 International license. Wikimedia Commons. URL: https://commons.wikimedia.org/wiki/File:Isotherme_de_compression_1.png (visited on 19/09/2022).

[9] D. Vollhardt and V. B. Fainerman. 'Progress in charecterization of Langmuir monolayers by consideration of compressibility'. In: *Advances in Colloid and Interface Science* 127.2 (2006), pp. 83–97. DOI: 10.1016/j.cis.2006.11.006.

[10] R. C. Buck et al. 'Perfluoroalkyl and Polyfluoroalkyl Substances in the Environment: Terminology, Classification, and Origins'. In: *Integrated Environmental Assessment and Management* 7.4 (2011), pp. 513–541. DOI: 10.1002/ieam.258.

[11] C. W. Bunn and E. R. Howells. 'Structures of Molecules and Crystals of Fluorocarbons'. In: *Nature* 174.4429 (1954), pp. 549–551. DOI: 10.1038/174549a0.

[12] R. D. Dunlap et al. 'Liquid-Vapor Equilibrium for the System: Perfluoro-*n*-hexane–*n*-Hexane'. In: *Journal of the American Chemical Society* 81.12 (1959), pp. 2927–2930. DOI: 10.1021/ja01521a002.

[13] A. G. Williamson and R. L. Scott. 'Heats of mixing of non-electrolyte solutions. II. Perfluoro-*n*-heptane + isooctane and perfluoro-*n*-hexane + *n*-hexane'. In: *Journal of Physical Chemistry* 65.2 (1961), pp. 275–279. DOI: 10.1021/j100820a022.

[14] R. G. Bedford and R. D. Dunlap. 'Solubilities and Volume Changes Attending Mixing for the System: Perfluoro-*n*-hexane–*n*-Hexane'. In: *Journal of the American Chemical Society* 80.2 (1958), pp. 282–285. DOI: 10.1021/ja01535a007.

[15] J. H. Hildebrand, B. B. Fisher and H. A. Benesi. 'Solubility of Perfluoro-*n*-heptane with Benzene, Carbon Tetrachloride, Chloroform, *n*-Heptane and 2,2,4-Trimethylpentane'. In: *Journal of the American Chemical Society* 72.10 (1950), pp. 4348–4351. DOI: 10.1021/ja01166a003.

[16] L. Lepori et al. 'Volume changes on mixing perfluoroalkanes with alkanes or ethers at 298.15 K'. In: *Fluid Phase Equilibria* 201.1 (2002), pp. 119–134. DOI: 10.1016/S0378-3812(02)00069-9.

[17] C. Duce et al. 'VLE and LLE of perfluoroalkane + alkane mixtures'. In: *Fuid Phase Equilibria* 199.1–2 (2002), pp. 197–212. DOI: 10.1016/S0378-3812(01)00815-9.

[18] P. Morgado, C. McCabe and E. J. M. Filipe. 'Modelling the phase behaviour and excess properties of alkane + perfluoroalkane binary mixtures with the SAFT–VR approach'. In: *Fluid Phase Equilibria* 228 (2005), pp. 389–393. DOI: 10.1016/j.fluid.2004.08.002.

[19] R. A. Khairulin, S. V. Stankus and V. A. Gruzdev. 'Liquid–Liquid Coexistence Curve of n-Perfluorohexane–n-Hexane System'. In: *International Journal of Thermophysics* 28.4 (2007), pp. 1245–1254. DOI: 10.1007/s10765-007-0237-4.

[20] M. J. P. de Melo et al. 'Liquid–liquid equilibrium of (perfluoroalkane + alkane) binary mixtures'. In: *Fluid Phase Equilibria* 242.2 (2006), pp. 210–219. DOI: 10.1016/j.fluid.2006.02.003.

[21] D. G. LeGrand and G. L. Gaines Jr. 'Immiscibility and Interfacial-Tension Between Polymer Liquids – Dependence on Molecular-Weight'. In: *Journal of Colloid and Interface Science* 50.2 (1975), pp. 272–279. DOI: 10.1016/0021-9797(75)90230-1.

[22] P. Morgado et al. 'Systems Involving Hydrogenated and Fluorinated Chains: Volumetric Properties of Perfluoroalkanes and Perfluoroalkylalkane Surfactants'. In: *Journal of Physical Chemistry B* 115.50 (2011), pp. 15013–15023. DOI: 10.1021/jp207567y.

[23] P. Morgado et al. 'Perfluoroalkanes and perfluoroalkylalkane surfactants in solution: Partial molar volumes in n-octane and hetero-SAFT-VR modelling'. In: *Fluid Phase Equilibria* 306.1 (2011), pp. 76–81. DOI: 10.1016/j.fluid.2011.02.020.

[24] P. Morgado et al. 'Alkane Coiling in Perfluoroalkane Solutions: A New Primitive Solvophobic Effect'. In: *Langmuir* 33.42 (2017), pp. 11429–11435. DOI: 10.1021/acs.langmuir.7b02516.

[25] J. H. Simons and R. D. Dunlap. 'The Properties of n-Pentforane and Its Mixtures with n-Pentane'. In: *Journal of Chemical Physics* 18.3 (1950), pp. 335–346. DOI: 10.1063/1.1747628.

[26] E. M. D. Siebert and C. M. Knobler. 'Interaction Virial Coefficients in Hydrocarbon–Fluorocarbon Mixtures'. In: *Journal of Physical Chemistry* 75.25 (1971), pp. 3863–3870. DOI: 10.1021/j100694a014.

[27] S. Brode and I. R. McDonald. 'Excess thermodynamic properties of liquid mixtures of methane and perfluoromethane'. In: *Molecular Physics* 65.4 (1988), pp. 1007–1012. DOI: 10.1080/00268978800101561.

[28] M. Schoen, C. Hoheisel and O. Beyer. 'Liquid CH_4, liquid CF_4 and the partially miscible liquid mixture CH_4/CF_4'. In: *Molecular Physics* 58.4 (1986), pp. 699–709. DOI: 10.1080/00268978600101511.

[29] G. M. Schneider. 'High-pressure phase equilibria and spectroscopic investigations up to 200 MPa on fluid mixtures containing fluorinated compounds: a review'. In: *Fluid Phase Equilibria* 199.1–2 (2002), pp. 307–317. DOI: 10.1016/S0378-3812(01)00803-2.

[30] W. Song, P. J. Rossky and M. Maroncelli. 'Modeling alkane+perfluoroalkane interactions using all-atom potentials: Failure of the usual combining rules'. In: *Journal of Chemical Physics* 119.17 (2003), pp. 9145–9162. DOI: 10.1063/1.1610435.

[31] A. M. A. Dias et al. 'SAFT Modeling of the Solubility of Gases in Perfluoroalkanes'. In: *Journal of Physical Chemistry B* 108.4 (2004), pp. 1450–1457. DOI: 10.1021/jp036225o.

[32] L. Zhang and J. I. Siepmann. 'Pressure Dependence of the Vapor–Liquid–Liquid Phase Behavior in Ternary Mixtures Consisting of n-Alkanes, n-Perfluoroalkanes, and Carbon Dioxide'. In: *Journal of Physical Chemistry B* 109.7 (2005), pp. 2911–2919. DOI: 10.1021/jp0482114.

[33] P. Morgado et al. 'Liquid Mixtures Involving Hydrogenated and Fluorinated Alcohols: Thermodynamics, Spectroscopy, and Simulation'. In: *Journal of Physical Chemistry B* 120.38 (2016), pp. 10091–10105. DOI: 10.1021/acs.jpcb.6b04297.

[34] S. Tsuzuki and T. Uchimaru. 'Magnitude of attraction in CF_4-CH_4 interactions: Are CF_4-CH_4 interactions weaker than average of CF_4-CF_4 and CH_4-CH_4 interactions?' In: *Journal of Fluorine Chemistry* 231 (2020), Article No. 109468. DOI: 10.1016/j.jfluchem.2020.109468.

[35] P. Lo Nostro. 'Phase Separation Properties of Fluorocarbons, Hydrocarbons and their Copolymers'. In: *Advances in Colloid and Interface Science* 56 (1995), pp. 245–287. DOI: 10.1016/0001-8686(95)00234-H.

[36] M. P. Krafft and J. G. Riess. 'Chemistry, Physical Chemistry, and Uses of Molecular Fluorocarbon-Hydrocarbon Diblocks, Triblocks, and Related Compounds – Unique "Apolar" Components for Self-Assembled Colloid and Interface Engineering'. In: *Chemical Reviews* 109.5 (2009), pp. 1714–1792. DOI: 10.1021/cr800260k.

[37] S. S. Jang et al. 'The Source of Helicity in Perfluorinated N-Alkanes'. In: *Macromolecules* 36.14 (2003), pp. 5331–5341. DOI: 10.1021/ma025645t.

[38] R. A. Cormanich, D. O'Hagan and M. Bühl. 'Hyperconjugation Is the Source of Helicity in Perfluorinated n-Alkanes'. In: *Angewandte Chemie – International Edition* 56.27 (2017), pp. 7867–7870. DOI: 10.1002/anie.201704112.

[39] P. Mukerjee. 'Fluorocarbon–hydrocarbon interactions in micelles and other lipid assemblies, at interfaces, and in solutions'. In: *Colloids and Surfaces A: Physicochemical and Engineering Aspects* 84.1 (1994), pp. 1–10. DOI: 10.1016/0927-7757(93)02682-5.

[40] J. J. Rychak and A. L. Klibanov. 'Nucleic acid delivery with microbubbles and ultrasound'. In: *Advanced Drug Delivery Reviews* 72 (2014), pp. 82–93. DOI: 10.1016/j.addr.2014.01.009.

[41] C. Tsagogiorgas et al. 'Impact of different emulsifiers on biocompatibility and inflammatory potential of Perfluorohexyloctane (F6H8) emulsions for new intravenous drug delivery systems'. In: *Drug Design, Development and Therapy* 13 (2019), pp. 2097–2110. DOI: 10.2147/DDDT.S195954.

[42] H. Meinert and T. Roy. 'Semifluorinated alkanes – A new class of compounds with outstanding properties for use in ophthalmology'. In: *European Journal of Ophtalmology* 10.3 (2000), pp. 189–197. DOI: 10.1177/112067210001000301.

[43] P. Agarwal et al. 'Semifluorinated alkane based systems for enhanced corneal penetration of poorly soluble drugs'. In: *International Journal of Pharmaceutics* 538.1–2 (2018), pp. 119–129. DOI: 10.1016/j.ijpharm.2018.01.019.

[44] S. Sirsi and M. Borden. 'Microbubble Compositions, Properties and Biomedical Applications'. In: *Bubble Science Engineering and Technology* 1.1–2 (2009), pp. 3–17. DOI: 10.1179/175889709X446507.

[45] J. G. Riess. 'Fluorocarbon-based injectable gaseous microbubbles for diagnosis and therapy'. In: *Current Opinion in Colloid and Interface Science* 8.3 (2003), pp. 259–266. DOI: 10.1016/S1359-0294(03)00047-5.

[46] J. G. Riess and M. Le Blanc. 'Solubility and Transport Phenomena in Perfluorochemicals Relevant to Blood Substitution and other Biomedical Applications'. In: *Pure and Applied Chemistry* 54.12 (1982), pp. 2383–2406. DOI: 10.1351/pac198254122383.

[47] J. G. Riess. 'Perfluorocarbon-based Oxygen Delivery'. In: *Artificial Cells, Blood Substitutes and Biotechnology* 34.6 (2006), pp. 567–580. DOI: 10.1080/10731190600973824.

[48] M. P. Krafft and J. G. Riess. 'Therapeutic oxygen delivery by perfluorocarbon-based colloids'. In: *Advances in Colloid and Interface Science* 294 (2021), Article No. 102407. DOI: 10.1016/j.cis.2021.102407.

[49] E. Charrault et al. 'A Facile Route to Homogeneous High Density Networks of Metal Nanoparticles'. In: *Langmuir* 25.19 (2009), pp. 11285–11288. DOI: 10.1021/la9026915.

[50] S. Kataoka, Y. Takeuchi and A. Endo. 'Nanometer-Sized Domains in Langmuir–Blodgett Films for Patterning SiO_2'. In: *Langmuir* 26.9 (2010), pp. 6161–6163. DOI: 10.1021/la100998h.

[51] E. Kissa. 'Fluorinated Surfactants'. In: *Fluorinated Surfactants and Repellents*. Ed. by A. T. Hubbard. 2nd ed. Vol. 97. Surfactant Science Series. New York, NY, USA: Marcel Dekker, 2001. ISBN: 978-0824704728.

[52] M. P. Krafft and J. G. Riess. 'Per- and polyfluorinated substances (PFASs): Environmental challenges'. In: *Current Opinion in Colloid and Interface Science* 20.3 (2015), pp. 192–212. DOI: 10.1016/j.cocis.2015.07.004.

[53] J. P. Giesy and K. Kannan. 'Global Distribution of Perfluorooctane Sulfonate in Wildlife'. In: *Environmental Science and Technology* 35.7 (2001), pp. 1339–1342. DOI: 10.1021/es001834k.

[54] K. J. Hansen et al. 'Compound-Specific, Quantitative Characterization of Organic Fluorochemicals in Biological Matrices'. In: *Environmental Science and Technology* 35.4 (2001), pp. 766–770. DOI: 10.1021/es001489z.

[55] W. D'Hollander et al. 'Perfluorinated Substances in Human Food and Other Sources of Human Exposure'. In: *Reviews of Environmental Contamination and Toxicology, Vol. 208: Perfluorinated Alkylated Substances*. Ed. by D. M. Whitacre and P. De Voogt. Vol. 208. Reviews of Environmental Contamination and Toxicology. ISBN 978-1-4419-6879-1. DOI: 10.1007/978-1-4419-6880-7_4. New York: Springer, 2010, pp. 179–215. ISBN: 978-1-4419-6879-1. DOI: 10.1007/978-1-4419-6880-7_4.

[56] L. A. M. Pereira et al. 'Diffusion Coefficients of Fluorinated Surfactants in Water: Experimental Results and Prediction by Computer Simulation'. In: *Journal of Chemical and Engineering Data* 59.10 (2014), pp. 3151–3159. DOI: 10.1021/je500211w.

[57] J. E. Black et al. 'Perfluoropolyethers: Development of an All-Atom Force Field for Molecular Simulations and Validation with New Experimental Vapor Pressures and Liquid Densities'. In: *Journal of Physical Chemistry B* 121.27 (2017), pp. 6588–6600. DOI: 10.1021/acs.jpcb.7b00891.

[58] J. Guo et al. 'Alternative Fluoropolymers to Avoid the Challenges Associated with Perfluorooctanoic Acid'. In: *Industrial and Engineering Chemistry Research* 47.3 (2008), pp. 502–508. DOI: 10.1021/ie0703179.

[59] G. L. Gaines Jr. *Insoluble Monolayers at Liquid–Gas Interfaces*. 1st ed. New York, NY, USA: John Wiley & Sons, 1966. ISBN: 978-0470289204.

[60] D. Vollhardt et al. 'Phase Transition in Monolayers of Straight Chain and 2-Methyl Branched Alcohols at the Air–Water Interface'. In: *Langmuir* 18.17 (2002), pp. 6571–6577. DOI: 10.1021/la0201671.

[61] M. F. Paige and A. F. Eftaiha. 'Phase-separated surfactant monolayers: Exploiting immiscibility of fluorocarbons and hydrocarbons to pattern interfaces'. In: *Advances in Colloid and Interface Science* 248 (2017), pp. 129–146. DOI: 10.1016/j.cis.2017.07.023.

[62] V. M. Kaganer, H. Möhwald and P. Dutta. 'Structure and phase transitions in Langmuir monolayers'. In: *Reviews of Modern Physics* 71.3 (1999), pp. 779–819. DOI: 10.1103/RevModPhys.71.779.

[63] E. Kissa. 'Fluorinated Surfactants'. In: *Fluorinated Surfactants: Synthesis, Properties, Applications*. Ed. by A. T. Hubbard. 1st ed. Vol. 50. Surfactant Science Series. New York, NY, USA: Marcel Dekker, 1994. ISBN: 978-0824790110.

[64] M. Goldmann, P. Nassoy and F. Rondelez. 'Search for perfectly ordered dense monolayers'. In: *Physica A* 200.1–4 (1993), pp. 688–695. DOI: 10.1016/0378-4371(93)90576-P.

[65] A. A. Acero et al. 'Molecular packing in water supported monolayers of $F(CF_2)_{11}COOH$ and $F(CF_2)_{10}CH_2COOH$'. In: *Journal of Chemical Physics* 99.9 (1993), pp. 7214–7220. DOI: 10.1016/10.1063/1.465438.

[66] N. C. Yoder et al. 'Nanoscale Patterning in Mixed Fluorocarbon–Hydrocarbon Phospholipid Bilayers'. In: *Journal of the American Chemical Society* 129.29 (2007), pp. 9037–9043. DOI: 10.1021/ja0709501.

[67] P. Fontaine et al. 'Structure of Langmuir Monolayers of Perfluorinated Fatty Acids: Evidence of a New 2D Smectic C Phase'. In: *Molecules* 24.19 (2019), Article No. 3590. DOI: 10.3390/molecules24193590.

[68] P. Silva et al. 'Langmuir Films of Perfluorinated Fatty Alcohols: Evidence of Spontaneous Formation of Solid Aggregates at Zero Surface Pressure and Very Low Surface Density'. In: *Nanomaterials* 10.11 (2020), Article No. 2257. DOI: 10.3390/nano10112257.

[69] O. Shibata et al. 'Mixed Monolayer Properties of Tetradecanoic Acid with *n*-Perfluorocarboxylic Acids with 10, 12, 14, 16, and 18 Carbon Atoms'. In: *Journal of Colloid and Interface Science* 184.1 (1996), pp. 201–208. DOI: 10.1006/jcis.1996.0612.

[70] T. Imae, T. Takeshita and M. Kato. 'Phase Separation in Hybrid Langmuir–Blodgett Films of Perfluorinated and Hydrogenated Amphiphiles. Examination by Atomic Force Microscopy'. In: *Langmuir* 16.2 (2000), pp. 612–621. DOI: 10.1021/la9902237.

[71] M. Matsumoto et al. 'Structure of Phase-Separated Langmuir-Blodgett Films of Hydrogenated and Perfluorinated Carboxylic Acids Investigated by IR Spectroscopy, AFM, and FFM'. In: *Langmuir* 19.7 (2003), pp. 2802–2807. DOI: 10.1021/la020849o.

[72] N. Rontu and V. Vaida. 'Miscibility of Perfluorododecanoic Acid with Organic Acids at the Air–Water Interface'. In: *Journal of Physical Chemistry C* 111.27 (2007), pp. 9975–9980. DOI: 10.1021/jp0718395.

[73] S. E. Qaqish and M. F. Paige. 'Structural and Compositional Mapping of a Phase-Separated Langmuir–Blodgett Monolayer by Atomic Force Microscopy'. In: *Langmuir* 23.5 (2007), pp. 2582–2587. DOI: 10.1021/la062890n.

[74] S. Christensen et al. 'Structural and compositional mapping of a phase-separated Langmuir–Blodgett monolayer by X-ray photoelectron emission microscopy'. In: *Journal of Electron Spectroscopy and Related Phenomena* 162.3 (2008), pp. 107–114. DOI: 10.1016/j.elspec.2007.12.003.

[75] J. Rehman et al. 'Morphology and Composition of Structured, Phase-Separated Behenic Acid – Perfluorotetradecanoic Acid Monolayer Films'. In: *Langmuir* 32.21 (2016), pp. 5341–5349. DOI: 10.1021/acs.langmuir.6b01104.

[76] T. Takiue and D. Vollhardt. 'Miscibility of alkanol and fluoroalkanol in Langmuir film at the air/water interface'. In: *Colloids and Surfaces A: Physicochemical and Engineering Aspects* 798 (2002), pp. 797–804. DOI: 10.1016/S0927-7757(01)01003-2.

[77] D. Sowah-Kuma and M. F. Paige. 'The influence of surfactant head group on miscibility in mixed hydrocarbon-perfluorocarbon monolayers'. In: *Colloids and Surfaces A* 556 (2018), pp. 157–166. DOI: 10.1016/j.colsurfa.2018.08.025.

[78] C. Bernardini et al. 'Colloids in Flatland: a perspective on 2D phase-separated systems, characterisation methods, and lineactant design'. In: *Chemical Society Reviews* 42.5 (2013), pp. 2100–2129. DOI: 10.1039/c2cs35269a.

[79] C. Yan and M. F. Paige. 'Pattern Formation in Phase-Separated Langmuir and Langmuir Monolayer Films'. In: *Langmuir* 37.28 (2021), pp. 8357–8369. DOI: 10.1021/acs.langmuir.1c00642.

[80] A. L. S. Gamboa. 'Ordering in Langmuir and Langmuir-Blodgett Films: Effect of the Presence of Fluorocarbon and Hydrocarbon Chains'. PhD thesis. Lisboa, Portugal: Universidade Técnica de Lisboa – Instituto Superior Técnico, 2006.

[81] M. C. Shih et al. 'X-ray diffraction study of heneicosanol monolayers on the surface of water'. In: *Journal of Chemical Physics* 97.6 (1992), pp. 4485–4488. DOI: 10.1063/1.463891.

[82] S. E. Qaqish and M. F. Paige. 'Mechanistic Insight into Domain Formation and Growth in a Phase-Separated Langmuir-Blodgett Monolayer'. In: *Langmuir* 23.20 (2007), pp. 10088–10094. DOI: 10.1021/la701413m.

[83] S. E. Qaqish and M. F. Paige. 'Rippled Domain Formation in Phase-Separated Mixed Langmuir-Blodgett Films'. In: *Langmuir* 24.12 (2008), pp. 6146–6153. DOI: 10.1021/la8002146.

[84] S. Watanabe et al. 'Effect of subphase temperature on the phase-separated structures of mixed Langmuir and Langmuir–Blodgett films of fatty acids and hybrid carboxylic acids'. In: *Journal of Colloid and Interface Science* 363.1 (2011), pp. 379–385. DOI: 10.1016/j.jcis.2011.07.069.

[85] M. C. Shih et al. 'Pressure and *p*H dependence of the structure of a fatty acid monolayer with calcium ions in the subphase'. In: *Journal of Chemical Physics* 96.2 (1992), pp. 1556–1559. DOI: 10.1063/1.462139.

[86] R. Johann, D. Vollhardt and H. Möhwald. 'Shifting of Fatty Acid Monolayer Phases Due to Ionization of the Headgroups'. In: *Langmuir* 17.15 (2001), pp. 4569–4580. DOI: 10.1021/la001781k.

[87] S. E. Qaqish et al. 'Phase Separation of Palmitic Acid and Perfluorooctadecanoic Acid in Mixed Langmuir–Blodgett Monolayer Films'. In: *Langmuir* 25.13 (2009), pp. 7401–7409. DOI: 10.1021/la900308b.

[88] S. E. Qaqish and M. F. Paige. 'Characterization of domain growth kinetics in a mixed perfluorocarbon-hydrocarbon Langmuir–Blodgett monolayer'. In: *Journal of Colloid and Interface Science* 325.1 (2008), pp. 290–293. DOI: 10.1016/j.jcis.2008.06.022.

[89] H. M. McConnell and R. de Koker. 'Note on the Theory of the Sizes and Shapes of Lipid Domains in Monolayers'. In: *Journal of Physical Chemistry* 96.17 (1992), pp. 7101–7103. DOI: 10.1021/j100196a048.

[90] K. Iimura, T. Shiraku and T. Kato. 'Micro-Phase Separation in Binary Mixed Langmuir Monolayers of *n*-Alkyl Fatty Acids and a Perfluoropolyether Derivative'. In: *Langmuir* 18.26 (2002), pp. 10183–10190. DOI: 10.1021/la020643n.

[91] M. Broniatowski and P. Dynarowicz-Łatka. 'Semifluorinated Chains at the Air/Water Interface: Studies of the Interaction of a Semifluorinated Alkane with Fluorinated Alcohols in Mixed Langmuir Monolayers'. In: *Langmuir* 22.6 (2006), pp. 2691–2696. DOI: 10.1021/la0533009.

[92] M. Broniatowski, N. V. Romeu and P. Dynarowicz-Łatka. 'Two-Dimensional Miscibility Studies – The Analysis of Interaction between Long-Chain Alcohols and Semifluorinated Alkanes'. In: *Journal of Physical Chemistry B* 110.7 (2006), pp. 3078–3087. DOI: 10.1021/jp055986j.

[93] B. Lin et al. 'Phase Diagram of a Lipid Monolayer on the Surface of Water'. In: *Physical Review Letters* 65.2 (1990), pp. 191–194. DOI: 10.1103/PhysRevLett.65.191.

[94] D. Sowah-Kuma et al. 'Molecular-Level Structure and Packing in Phase-Separated Arachidic Acid – Perfluorotetradecanoic Acid Monolayer Films'. In: *Langmuir* 34.36 (2018), pp. 10673–10683. DOI: 10.1021/acs.langmuir.8b02291.

[95] G. L. Gaines Jr. 'Surface Activity of Semifluorinated Alkanes: $F(CF_2)_m(CH_2)_nH$'. In: *Langmuir* 7.12 (1991), pp. 3054–3056. DOI: 10.1021/la00060a025.

[96] G. van D. Tiers. 'Some Free Radical-Catalyzed Additions of Perfluoroalkyl Iodides to Olefins'. In: *Journal of Organic Chemistry* 27.6 (1962), pp. 2261–2262. DOI: 10.1021/jo01053a537.

[97] J. F. Rabolt, T. P. Russell and R. J. Twieg. 'Structural Studies of Semifluorinated *n*-Alkanes. 1. Synthesis and Characterization of $F(CF_2)_m(CH_2)_nH$ in the Solid State'. In: *Macromolecules* 17.12 (1984), pp. 2786–2794. DOI: 10.1021/ma00142a060.

[98] T. P. Russell et al. 'Structural Characterization of Semifluorinated *n*-Alkanes. 2. Solid–Solid Transition Behaviour'. In: *Macromolecules* 19.4 (1986), pp. 1135–1143. DOI: 10.1021/ma00158a035.

[99] M. Broniatowski and P. Dynarowicz-Łatka. 'Semifluorinated alkanes – Primitive surfactants of fascinating properties'. In: *Advances in Colloid and Interface Science* 138.2 (2008), pp. 63–83. DOI: 10.1016/j.cis.2007.11.002.

[100] X. Liu, J. G. Riess and M. P. Krafft. 'Self-Organization of Semifluorinated Alkanes and Related Compounds at Interfaces: Thin Films, Surface Domains and Two-Dimensional Spherulites'. In: *Bulletin of the Chemical Society of Japan* 91.5 (2018), pp. 846–857. DOI: 10.1246/bcsj.20170431.

[101] J. G. Riess. 'Fluorous micro- and nanophases with a biomedical perspective'. In: *Tetrahedron* 58.20 (2002), pp. 4113–4131. DOI: 10.1016/S0040-4020(02)00262-4.

[102] M. P. Krafft. 'Fluorine in medical microbubbles – Methodologies implemented for engineering and investigating fluorocarbon-based microbubbles'. In: *Journal of Fluorine Chemistry* 177 (2015), pp. 19–28. DOI: 10.1016/j.jfluchem.2015.02.013.

[103] R. G. Shulman, B. P. Dailey and C. H. Townes. 'Molecular Dipole Moments and Stark Effects. III. Dipole Moment Determinations'. In: *Physical Review* 78.2 (1950), pp. 145–148. DOI: 10.1103/PhysRev.78.145.

[104] A. El Abed et al. 'Experimental evidence for an original two-dimensional phase structure: An antiparallel semifluorinated monolayer at the air-water interface'. In: *Physical Review E* 65.5 (2002), Article No. 051603. DOI: 10.1103/PhysRevE.65.051603.

[105] A. El Abed et al. 'Assembling and compressing a semifluorinated alkane monolayer on a hydrophobic surface: Structural and dielectric properties'. In: *Physical Review E* 70.5 (2004), Article No. 051607. DOI: 10.1103/PhysRevE.70.051607.

[106] M. Broniatowski et al. 'Langmuir Monolayers Characteristic of (Perfluorodecyl)-Alkanes'. In: *Journal of Physical Chemistry B* 108.35 (2004), pp. 13403–13411. DOI: 10.1021/jp0402481.

[107] P. Dynarowicz-Łatka et al. 'Structural Investigation of Langmuir and Langmuir–Blodgett Monolayers of Semifluorinated Alkanes'. In: *Journal of Physical Chemistry B* 110.12 (2006), pp. 6095–6100. DOI: 10.1021/jp057270u.

[108] P. Morgado et al. 'Vapor Pressure of Perfluoroalkylalkanes: The Role of the Dipole'. In: *Journal of Physical Chemistry B* 119.4 (2015), pp. 1623–1632. DOI: 10.1021/jp5109448.

[109] P. Morgado, J. Gaspar and E. J. M. Filipe. 'Liquid–liquid interfaces: Water–perfluoroalkanes and water–perfluoroalkylalkanes, experimental interfacial tensions and molecular simulation'. In: *Journal of Molecular Liquids* 312 (2020), Article No. 113385. DOI: 10.1016/j.molliq.2020.113385.

[110] P. Lo Nostro. 'Aggregates from semifluorinated *n*-alkanes: how incompatibility determines self-assembly'. In: *Current Opinion in Colloid and Interface Science* 8.3 (2003), pp. 223–226. DOI: 10.1016/S1359-0294(03)00052-9.

[111] A. L. S. Gamboa, E. J. M. Filipe and P. Brogueira. 'Nanoscale Pattern Formation in Langmuir-Blodgett Films of a Semifluorinated Alkane and a Polystyrene-Poly(Ethylene Oxide) Diblock Copolymer'. In: *Nano Letters* 2.10 (2002), pp. 1083–1086. DOI: 10.1021/nl025698o.

[112] M. P. Turberg and J. E. Brady. 'Semifluorinated hydrocarbons: primitive surfactant molecules'. In: *Journal of the American Chemical Society* 110.23 (1988), pp. 7797–7801. DOI: 10.1021/ja00231a034.

[113] G. M. C. Silva et al. 'Spontaneous self-assembly and structure of perfluoroalkylalkane surfactant hemimicelles by molecular dynamics simulations'. In: *Proceedings of the National Academy of Sciences of the United States of America* 116.30 (2019), pp. 14868–14873. DOI: 10.1073/pnas.1906782116.

[114] B. P. Binks et al. 'Adsorption and Aggregation of Semifluorinated Alkanes in Binary and Ternary Mixtures with Hydrocarbon and Fluorocarbon Solvents'. In: *Langmuir* 13.25 (1997), pp. 6669–6682. DOI: 10.1021/la970408i.

[115] J. Höpken et al. 'Melting, crystallization, and solution behavior of chain molecules with hydrocarbon and fluorocarbon segments'. In: *Makromolekulare Chemie – Macromolecular Chemistry and Physics* 189.4 (1988), pp. 911–925. DOI: 10.1002/macp.1988.021890422.

[116] W. Mahler, D. Guillon and A. Skoulios. 'Smectic Liquid Crystal from (Perfluorodecyl)Decane'. In: *Molecular Crystals and Liquid Crystals* 2.3–4 (1985), pp. 111–119. DOI: 10.1080/01406566.1985.10767000.

[117] C. Viney et al. 'Transitions to Liquid Crystalline Phases in a Semifluorinated Alkane'. In: *Molecular Crystals and Liquid Crystals* 168 (1989), pp. 63–82. DOI: 10.1080/00268948908045960.

[118] M. Broniatowski and P. Dynarowicz-Łatka. 'Interactions of a Fluoroaryl Surfactant with Hydrogenated, Partially Fluorinated, and Perfluorinated Surfactants at the Air/Water Interface'. In: *Langmuir* 22.15 (2006), pp. 6622–6628. DOI: 10.1021/la060421f.

[119] M. Broniatowski et al. 'Nucleation and Growth in the Collapsed Langmuir Monolayers from Semifluorinated Alkanes'. In: *Journal of Physical Chemistry B* 111.44 (2007), pp. 12787–12794. DOI: 10.1021/jp0748462.

[120] L. Bardin et al. 'Long-Range Nanometer-Scale Organization of Semifluorinated Alkane Monolayers at the Air/Water Interface'. In: *Langmuir* 27.22 (2011), pp. 13497–13505. DOI: 10.1016/10.1021/la201802x.

[121] A. González-Pérez, C. Contal and M. P. Krafft. 'Experimental evidence for a surface concentration-dependent mechanism of formation of hemimicelles in Langmuir monolayers of semi-fluorinated alkanes'. In: *Soft Matter* 3.2 (2007), pp. 191–193. DOI: 10.1039/b613265k.

[122] P. Fontaine et al. 'Direct Evidence for Highly Organized Networks of Circular Surface Micelles of Surfactant at the Air-Water Interface'. In: *Journal of the American Chemical Society* 127.2 (2005), pp. 512–513. DOI: 10.1021/ja044779e.

[123] G. Zhang et al. 'Surface micelles of semifluorinated alkanes in Langmuir–Blodgett monolayers'. In: *Physical Chemistry Chemical Physics* 6.7 (2004), pp. 1566–1569. DOI: 10.1039/b314764a.

[124] P. Fontaine et al. 'Evidence for Interaction with the Water Subphase As the Origin and Stabilization of Nano-Domain in Semi-Fluorinated Alkanes Monolayer at the Air/Water Interface'. In: *Langmuir* 30.50 (2014), pp. 15193–15199. DOI: 10.1021/la5038124.

[125] P. Fontaine et al. 'Evidence of lying molecules in the structure of the most condensed phase of semifluorinated alkane monolayers'. In: *Nanoscale* 10.5 (2018), pp. 2310–2316. DOI: 10.1039/c7nr07415h.

[126] M. Veschgini et al. 'Size, Shape, and Lateral Correlation of Highly Uniform, Mesoscopic, Self-Assembled Domains of Fluorocarbon–Hydrocarbon Diblocks at the Air/Water Interface: A GISAXS Study'. In: *ChemPhysChem* 18.19 (2017), pp. 2791–2798. DOI: 10.1002/cphc.201700325.

[127] C. Schwieger, X. Liu and M. P. Krafft. 'Self-assembled mesoscopic surface domains of fluorocarbon-hydrocarbon diblocks can form at zero surface pressure: tilting of solid-like hydrocarbon moieties compensates for cross-section mismatch with fluorocarbon moieties'. In: *Physical Chemistry Chemical Physics* 19.35 (2017), pp. 23809–23816. DOI: 10.1039/c7cp02432k.

[128] G. Zhang et al. 'Occurrence, Shape, and Dimensions of Large Surface Hemimicelles Made of Semifluorinated Alkanes. Elongated versus Circular Hemimicelles. Pit- and Tip-Centered Hemimicelles'. In: *Journal of the American Chemical Society* 127.29 (2005), pp. 10412–10419. DOI: 10.1021/ja0510515.

[129] M. Broniatowski et al. 'Two-dimensional miscibility between a semifluorinated hydrocarbon and hydrogenated alcohols'. In: *Colloids and Surfaces A: Physicochemical and Engineering Aspects* 249.1–3 (2004), pp. 3–9. DOI: 10.1016/j.colsurfa.2004.08.039.

[130] M. Broniatowski, J. Miñones Jr. and P. Dynarowicz-Łatka. 'Semifluorinated chains in 2D-(perfluorododecyl)-alkanes at the air/water interface'. In: *Journal of Colloid and Interface Science* 279.2 (2004), pp. 552–558. DOI: 10.1016/j.jcis.2004.06.080.

[131] M. Broniatowski, I. Sandez Macho and P. Dynarowicz-Łatka. 'Study of perfluorooctyl-*n*-alkanes monolayers at the air–water interface'. In: *Thin Solid Films* 493.1–2 (2005), pp. 249–257. DOI: 10.1016/j.tsf.2005.05.034.

[132] M. Broniatowski, P. Dynarowicz-Łatka and W. Witko. 'Critical influence of the alkane length in surface and liquid–crystalline properties of perfluorodecyl-*n*-alkanes'. In: *Journal of Fluorine Chemistry* 126.1 (2005), pp. 79–86. DOI: 10.1016/j.jfluchem.2004.10.045.

[133] M. Broniatowski et al. 'Properties of Langmuir monolayers from semifluorinated alkanes'. In: *Applied Surface Science* 246.4 (2005), pp. 342–347. DOI: 10.1016/j.apsusc.2004.11.038.

[134] Y. Hayami and G. H. Findenegg. 'Surface Crystallization and Phase Transitions of the Adsorbed Film of $F(CF_2)_{12}(CH_2)_{16}H$ at the Surface of Liquid Hexadecane'. In: *Langmuir* 13.18 (1997), pp. 4865–4869. DOI: 10.1021/la9702446.

[135] Y. Hayami and H. Sakamoto. 'Surface crystallization and phase transitions of the adsorbed film of $F(CF_2)_{12}(CH_2)_{16}H$ at the surface of liquid tetradecane'. In: *Colloid and Polymer Science* 282.5 (2004), pp. 461–467. DOI: 10.1007/s00396-003-0969-z.

[136] F. Pierce et al. 'Liquid–Liquid Interfaces of Semifluorinated Alkane Diblock Copolymers with Water, Alkanes, and Perfluorinated Alkanes'. In: *Journal of Physical Chemistry B* 112.50 (2008), pp. 16012–16020. DOI: 10.1021/jp805574f.

[137] B. P. Binks et al. 'Adsorption of Semifluorinated Alkanes at Hydrocarbon–Air Surfaces'. In: *Langmuir* 11.3 (1995), pp. 977–983. DOI: 10.1021/la00003a047.

[138] Z. Huang et al. 'Structural studies of semifluorinated hydrocarbon monolayers at the air/water interface'. In: *Journal of the Chemical Society – Faraday Transactions* 92.4 (1996), pp. 545–552. DOI: 10.1039/ft9969200545.

[139] C. G. Lux et al. 'Compression of Self-Assembled Nano-Objects: 2D/3D Transitions in Films of (Perfluoroalkyl)Alkanes – Persistence of an Organized Array of Surface Micelles'. In: *Chemistry – A European Journal* 16.24 (2010), pp. 7186–7189. DOI: 10.1002/chem.200903535.

[140] M. Li et al. 'Formation of an ordered Langmuir monolayer by a non-polar chain molecule'. In: *Nature* 367.6459 (1994), pp. 151–153. DOI: 10.1038/367151a0.

[141] A. El Abed et al. 'Air-water interface-induced smectic bilayer'. In: *Physical Review E* 62.5 (2000), R5895–R5898. DOI: 10.1103/PhysRevE.62.R5895.

[142] N. Kim and S. Shin. 'Formation of ordered structure in Langmuir monolayers of semifluorinated hydrocarbons: Molecular dynamics simulations'. In: *Journal of Chemical Physics* 110.21 (1999), pp. 10239–10242. DOI: 10.1063/1.478956.

[143] N. Kim and S. Shin. 'Molecular dynamics studies of semifluorinated hydrocarbon monolayers'. In: *Journal of Chemical Physics* 111.14 (1999), pp. 6556–6564. DOI: 10.1063/1.480010.

[144] B. A. Grigoryev et al. 'Surface Tension of Normal Pentane, Hexane, Heptane, and Octane'. In: *International Journal of Thermophysics* 13.3 (1992), pp. 453–464. DOI: 10.1007/BF00503882.

[145] M. G. Freire et al. 'Surface Tension of Liquid Fluorocompounds'. In: *Journal of Chemical and Engineering Data* 51.5 (2006), pp. 1820–1824. DOI: 10.1021/je060199g.

[146] S. Zeppieri, J. Rodríguez and A. L. López de Ramos. 'Interfacial Tension of Alkane + Water Systems'. In: *Journal of Chemical Engineering Data* 46.5 (2001), pp. 1086–1088. DOI: 10.1021/je000245r.

[147] W. Prange et al. 'The structure of hexane/perfluorohexane thin liquid films'. In: *Journal of Physics: Condensed Matter* 13.21 (2001), pp. 4957–4972. DOI: 10.1088/0953-8984/13/21/321.

[148] A. Mourran et al. 'Self-Assembly of the Perfluoroalkyl-Alkane F14H20 in Ultrathin Films'. In: *Langmuir* 21.6 (2005), pp. 2308–2316. DOI: 10.1021/la048069y.

[149] L. de Viguerie et al. 'Effect of the Molecular Structure on the Hierarchical Self-Assembly of Semifluorinated Alkanes at the Air/Water Interface'. In: *Langmuir* 27.14 (2011), pp. 8776–8786. DOI: 10.1021/la201377f.

[150] Á. Piñeiro et al. 'Surface films of short fluorocarbon–hydrocarbon diblocks studied by molecular dynamics simulations: Spontaneous formation of elongated hemimicelles'. In: *Journal of Colloid and Interface Science* 329.2 (2009), pp. 351–356. DOI: 10.1016/j.jcis.2008.10.018.

[151] H. O. S. Yadav et al. 'Hemimicelle formation of semi-fluorocarbon chains at air–water interface: coarse-grained molecular dynamics study with an extension of the SPICA force field'. In: *Molecular Physics* 119.19–20 (2021), Article No. e1910355. DOI: 10.1080/00268976.2021.1910355.

[152] T. Kato et al. 'Monodisperse Two-Dimensional Nanometer Size Clusters of Partially Fluorinated Long-Chain Acids'. In: *Langmuir* 14.7 (1998), pp. 1786–1798. DOI: 10.1021/la970951z.

[153] Y. Ren et al. 'Surface Micelles of $CF_3(CF_2)_7(CH_2)_{10}COOH$ on Aqueous La^{3+} Subphase Investigated by Atomic Force Microscopy and Infrared Spectroscopy'. In: *Journal of Physical Chemistry B* 105.19 (2001), pp. 4305–4312. DOI: 10.1021/jp004502a.

[154] M. Maaloum, P. Muller and M. P. Krafft. 'Monodisperse Surface Micelles of Nonpolar Amphiphiles in Langmuir Monolayers'. In: *Angewandte Chemie – International Edition* 41.22 (2002), pp. 4331–4334. DOI: 10.1002/1521-3773(20021115)41:22<4331::AID-ANIE4331>3.0.CO;2-J.

[155] S. P. Weinbach et al. 'Self-Assembled Crystalline Monolayers and Multilayers of *n*-Alkanes on the Water Surface'. In: *Advanced Materials* 7.10 (1995), pp. 857–862. DOI: 10.1002/adma.19950071009.

[156] M. Maaloum, P. Muller and M. P. Krafft. 'Lateral and Vertical Nanophase Separation in Langmuir-Blodgett Films of Phospholipids and Semifluorinated Alkanes'. In: *Langmuir* 20.6 (2004), pp. 2261–2264. DOI: 10.1021/la030312q.

[157] M. O. Gallyamov et al. 'Self-assembly of (perfluoroalkyl)alkanes on a substrate surface from solutions in supercritical carbon dioxide'. In: *Physical Chemistry Chemical Physics* 8.22 (2006), pp. 2642–2649. DOI: 10.1039/b602959k.

[158] X. Feng et al. 'AFM Study of Gibbs Films of Semifluorinated Alkanes at Liquid Crystal/Air Interfaces'. In: *ChemPhysChem* 14.9 (2013), pp. 1801–1805. DOI: 10.1002/cphc.201300173.

[159] L. Bardin et al. 'Highly organized crystalline monolayer of a semi-fluorinated alkane on a solid substrate obtained by spin-coating'. In: *Thin Solid Films* 519.1 (2010), pp. 414–416. DOI: 10.1016/j.tsf.2010.07.065.

[160] O. Gang et al. 'Surface phases of semi-fluorinated alkane melts'. In: *Europhysics Letters* 49.6 (2000), pp. 761–767. DOI: 10.1209/epl/i2000-00216-4.

[161] J. Alexander, S. Magonov and M. Moeller. 'Topography and surface potential in Kelvin force microscopy of perfluoroalkyl alkanes self-assemblies'. In: *Journal of Vacuum Science and Technology B* 27.2 (2009), pp. 903–911. DOI: 10.1116/1.3079675.

[162] A. N. Semenov et al. 'Theory of Surface Micelles of Semifluorinated Alkanes'. In: *Langmuir* 22.21 (2006), pp. 8703–8717. DOI: 10.1021/la060638+.

Part II

Experimental and Computational Techniques

Chapter 5

Molecular Dynamics Simulations

5.1 Computational Chemical Simulations

Computational chemistry is the use of computational techniques in chemistry, from the scale of quantum mechanics of single molecules to the dynamics of large molecular aggregates. The field is very useful to study a variety of chemical systems, their structure and microscopic interactions among assemblies of molecules, often with atomic resolution. It is based on molecular modelling, that is describing complex chemical systems in terms of a realistic atomic model, aiming at comprehending and predicting macroscopic system properties [1]. Therefore, the simulation of chemical systems can serve as a bridge between the microscopic phenomena and the macroscopic laboratory world. By modelling the interactions at the molecular scale, the bulk properties can be predicted or studied as accurately as computationally possible [2]. These properties can be divided into two categories: static equilibrium properties, which include the density or the radial distribution function of a liquid, the binding constant of an inhibitor to an enzyme or the interfacial tension in a multi-phase system; and dynamic or non-equilibrium properties, such as the viscosity of a liquid, the kinetics of chemical reactions or the diffusion through membranes [1].

5.1.1 The link between Experiments, Models and Theory

The approach described above is a useful complement to experimental techniques. However powerful the latter may be, resolving fine details of physical systems might require resorting to theoretical and simulation calculations. This way, a link between experiments, theory and simulation is found. Experimental measurements permit the development of models to mimic the system of interest. Having established a specific model, a theory can be devised by the introduction of mathematical formalism and approximations so simulations can be carried out. The latter are exact for a specific model and thus can serve to corroborate or refute the approximations made in the theory. Moreover, the simulation results, when compared with experimental ones, can test the accuracy of the model. The information can also flow in the other sense, since an accurate model can help devise and interpret future experiments. Beyond its academic interest, a model can also be technologically useful, for instance to predict (and optimise) the properties of materials prior to their synthesis and to help perform simulations under conditions that are difficult to achieve experimentally (*e. g.* extremes of temperature and/or pressure) [2–4].

5.1.2 The Basis: Statistical Mechanics

Chemical simulations based on sound molecular models provide a detailed characterisation of the interactions and structure of a given system. These may be the positions, velocities, momenta, potential energies and so on of the atoms or molecules making up the system. In the meantime, it is desired to retrieve the thermodynamic properties of the macroscopic system (temperature, pressure, specific heat, *etc.*) that that assembly of molecules constitutes [4]. The link between the microscopic (mechanical) and the macroscopic (thermodynamic) properties is founded on the theoretical basis of *statistical mechanics* or *statistical thermodynamics* [5]. The discipline is named statistical mechanics because it deals with the average behaviour of a system, linking that with the macroscopic properties intended to be interpreted and, as far as possible, predicted [4]. The macroscopic properties are ensemble averages over a representative statistical ensemble of molecular systems [1].

While some problems in statistical mechanics are exactly soluble, meaning the complete specification of the microscopic properties of a system leads directly to a set of macroscopic properties of interest, that does not hold up for all systems, particularly complex and larger ones [4]. The use of computer simulations provides a numerical solution for several of those complex problems in statistical mechanics, provided a sound molecular model is used. The theoretical framework for the simplifications in the treatment of a simulation with atomistic detail, in order to retrieve the macroscopical properties of interest, is also within the domain of statistical mechanics [1].

5.1.3 The two main types of Computational Chemical Simulations

There are two main families of simulation techniques used to generate representative statistical ensembles, namely Molecular Dynamics (MD) and Monte Carlo (MC). The first is based on numerically solving the equations of motion for the system of interest whilst the second relies on repeated random sampling to obtain numerical results of the properties characterising the system [2]. Although Monte Carlo (MC) simulations are simpler than MD (because the computation of forces is unnecessary in the former), only the latter is appropriate to generate non-equilibrium ensembles. Apart from that advantage, both methods provide similar quality statistics in a given amount of computer time, making MD a more universal technique [1]. The simulations carried out in the scope of this work belong to the MD family.

5.1.4 Molecular Dynamics Simulations

In essence, MD simulations consist in numerically solving the equations of motion, provided the initial conditions and the potentials of interaction of the system are known [1]. Classically, motion is a response to an applied force, which is conveyed in Newton's second law of motion (Equation 5.1) [3]. This law relates the resulting force on a particle i ($\overrightarrow{F_i}$) with the particle's mass (m_i) and acceleration ($\frac{\partial^2 \overrightarrow{r_i}}{\partial t^2}$), where $\overrightarrow{r_i}$ denotes the particle's position in an appropriate coordinates system.

$$\overrightarrow{F_i} = m_i \frac{\partial^2 \overrightarrow{r_i}}{\partial t^2} \tag{5.1}$$

Within the Born-Oppenheimer approximation[1], the Hamiltonian of a system is expressed as a function of the nuclear variables, being assumed the electrons adjust their dynamics instantly and their motion is averaged out when atomic positions change [4]. In a classical description, the Hamiltonian H of an isolated system corresponds to its total energy E, which is conserved [3]. E is the sum of kinetic (K) and potential (U) energy functions of the set of coordinates r_i and momenta p_i of each particle i [4].

Considering a system of N particles at an instant t, their positions and momenta correspond to a point in the $6N$-dimensional phase space (3 position and 3 momentum coordinates per particle) describing the microscopic state of a system [3, 4]. The interactions between particles are modelled by an Interaction Potential (U). The forces acting on the particles are related to U by Equation 5.2. In the scope of this work, for simplicity, an atomic description is used (the interacting particles are atoms).

$$\overrightarrow{F_i} = -\frac{\partial U}{\partial \overrightarrow{r_i}} \tag{5.2}$$

The principles on which MD simulations are based have been summarised up to this point. These are implemented, in general, by following the algorithm that is schematically presented in Figure 5.1.

1. Input initial conditions

Define the potentials of interaction (U) as a function of atom positions; state the initial positions ($\overrightarrow{r}$) and velocities ($\overrightarrow{v}$) of all atoms

⇓

Repeat 2, 3 and 4 for the necessary number of simulation steps:

2. Compute forces

Based on Equation 5.2, encompassing non-bonded pair-wise interactions, bonded interactions and possible constraints and/or external forces

⇓

3. Update configuration

The movement of the atoms is simulated by numerically solving Newton's equations of motion

⇓

4. Output step (if required)

Export positions and velocities of atoms and other system information (temperature, energies, ...)

Figure 5.1: Global MD algorithm. Adapted from [1].

[1]The Born–Oppenheimer approximation (after Max Born and J. Robert Oppenheimer) consists in the assumption that the motion of atomic nuclei and electrons in a molecule can be treated separately. This is based on the fact that the electrons are orders of magnitude lighter and move much faster than the nuclei [3].

5.2 Definition and Calculation of the Interaction Potentials

5.2.1 Force Field

In computer simulations, a Force Field (FF) comprehends two components, namely: the mathematical description (the set of equations) used to convey the interaction potential energies and, by means of Equation 5.2, the forces acting on the system; and the parameters used in those equations [1]. The implementation of a FF is usually done by summing all the contributions from the different interaction potentials, each of which is defined and calculated in separate [3]. The role of a FF is to describe an entire class of molecules with reasonable accuracy. Hence, the parameters of a FF are usually determined by a combination of quantum chemical calculations and by adjusting parameters to reproduce experimental data, the fit being performed for a limited number of molecules and then used for the simulation of a wider set of molecules and structures [2, 3]. The number of atom types to parameterise is greater than the number of elements because the chemical surroundings are very influential on the parameters. For instance, the parameters used to effectively describe the interactions involving a carbon atom in an alkyl chain differ considerably from those used to parameterise the interaction potential functions of the carbon atoms in a benzene ring [6].

There are two main types of FFs: the All-Atom (AA) and the Coarse-Grained (CG) [1]. In the first type, the molecules are represented by all their constituent atoms, and each atom is modelled as an interaction centre for the calculation of the different interaction potentials. In the second type, the molecules comprise of an adequate number of "beads" or interaction centres, each one representing a group of "merged" atoms. These groups can be as simple as CH_3 or CH_2 groups (in this case, the FF is usually dubbed United Atom (UA)) or other larger and more complex ones (*e. g.* whole segments of alkyl chains) [1, 2]. Although CG FFs lack the atomic resolution of their AA counterparts, they are useful because they considerably simplify and reduce the computational load required to perform simulations [1, 3].

5.2.2 Bonded and Non-bonded Interactions

The total potential energy of the system (U) can be calculated as the sum of several terms, each describing a specific type of interaction [3]. For molecular systems, these interactions can be between chemically bonded atoms, originating the bonded part of the potential energy (U_{bonded}), or between non-bonded atoms, which make up the corresponding non-bonded part of the potential energy ($U_{\text{non-bonded}}$). The bonded interactions are treated separately due to their markedly quantum mechanical nature and so they are treated separately, usually by using distinct potential functions or by constraining the bonds to a fixed length and/or angle to save computational effort [1, 2].

5.2.2.1 Non-bonded Interactions

For a system with N atoms, the non-bonded interaction potential energy can be computed as the sum of the terms dependent on the coordinates of individual atoms, atom pairs, triplets of atoms and so on (Equation 5.3) [4].

$$U_{\text{non-bonded}} = \sum_i u_1(\overrightarrow{r_i}) + \sum_i \sum_{j>i} u_2(\overrightarrow{r_i}, \overrightarrow{r_j}) + \sum_i \sum_{j>i} \sum_{k>j>i} u_3(\overrightarrow{r_i}, \overrightarrow{r_j}, \overrightarrow{r_k}) + ... \tag{5.3}$$

The summations in Equation 5.3 are extended over all distinct pairs ij, triplets ijk, *etc.* excluding multiple counting. The first term accounts for externally applied fields (*e. g.* the effect of container walls). The second term is the most important and stands for the pair potential, depending only on the distance between each pair ij of interacting centres (r_{ij}). The higher order terms, which account for the interactions between three and more bodies, albeit important, are relatively less significant. Because it is computationally expensive to calculate the latter, they are usually not included in computer simulations. Instead, a pairwise approximation is used in which these higher order terms are accounted for in an effective pair potential (u_2^{eff}) representing all the many-body effects (Equation 5.4). In this case, $U_{\text{non-bonded}}$ only depends on the coordinates of each atom ($\overrightarrow{r_i}$) and the pairwise distances (r_{ij}) [4].

$$U_{\text{non-bonded}} \approx \sum_i u_1(\overrightarrow{r_i}) + \sum_i \sum_{j>i} u_2^{\text{eff}}(r_{ij}) \tag{5.4}$$

The pair potentials normally employed in computer simulations intend to purport all the many-body effects. Therefore, in order to reproduce experimental data, u_2^{eff} might vary with density, temperature or other factors (whilst u_2 inherently does not). The pair potentials used are usually simple and more idealised, intending to reflect relevant characteristics of the interactions [4]. As a consequence of how they are defined, and because they are a function of r_{ij} only, the non-bonded interactions are pair-additive (the interaction potential of a particle i with all remaining particles is equal to the sum of the pairwise interactions of i with the remaining particles) and centre-symmetric (the force exerted on two interacting particles i and j obeys $F_i = -F_j$) [1].

The non-bonded interactions are usually subdivided in vdW (dispersion) interactions and electrostatic interactions [1]. The vdW interactions are commonly modelled by a Lennard-Jones (LJ) potential (U_{LJ}; Equation 5.5) [2]. This potential has two parameters: well depth or energy (ε_{ij}) and wall distance or diameter (σ_{ij}). The LJ parameters are usually obtained for the homologous interactions from pure components' experimental data, such as liquid densities and enthalpies of vaporisation, *i.e.* ε_{ii} and σ_{ii} are parameterised for every atom type i. The unlike interaction parameters can be approximated according to some combination rule, such as the geometric rules (Equation 5.6) or the Lorentz-Berthelot rules (Equation 5.7) [1, 4].

$$U_{\text{LJ}}(r_{ij}) = 4\varepsilon_{ij}\left(\left(\frac{\sigma_{ij}}{r_{ij}}\right)^{12} - \left(\frac{\sigma_{ij}}{r_{ij}}\right)^{6}\right) \tag{5.5}$$

$$\sigma_{ij} = \sqrt{\sigma_{ii}\sigma_{jj}} \quad \text{and} \quad \varepsilon_{ij} = \sqrt{\varepsilon_{ii}\varepsilon_{jj}} \tag{5.6}$$

$$\sigma_{ij} = \frac{\sigma_{ii} + \sigma_{jj}}{2} \quad \text{and} \quad \varepsilon_{ij} = \sqrt{\varepsilon_{ii}\varepsilon_{jj}} \tag{5.7}$$

The electrostatic interactions are modelled according to the classical Coulomb point charge potential (U_{Coulomb}; Equation 5.8). This has three parameters, namely the point charge intensities q_i and q_j and the relative permittivity of the medium ε_r (ε_0 is the absolute permittivity of vacuum) [3]. To describe the molecular charge distribution (which accounts for the existence of dipoles within the molecules) in an approximate and computationally simpler way, a set of partial point charges is often used. Although not mandatorily, these usually are as many as and coincide with the positions of the nuclei (LJ interaction sites alike) to reduce the computational burden of calculating more site–site distances. They often take on non-integer (effective) values, chosen to yield a better description of the structural and thermodynamic properties of the system [2, 4].

$$U_{\text{Coulomb}}(r_{ij}) = \frac{q_i q_j}{4\pi\varepsilon_0\varepsilon_r r_{ij}^2} \tag{5.8}$$

5.2.2.2 Bonded Interactions

Four types of bonded interactions can be discerned: covalent bond-stretching (pair interaction), angle bending (3-body interaction), proper dihedrals and improper dihedrals (both 4-body interactions). The improper dihedral is a special type of interaction used to prevent the transition of atoms to a configuration of opposite chirality or to restrict their position within a planar configuration [1]. In the scope of this work, this was not used and is not elaborated further.

The bond stretching between two covalently bonded atoms j and k is usually modelled by a harmonic potential [1, 2]. Harmonic potentials are formally simple, but adequate to describe the structures and energies of several common molecules, which explains their ubiquitous implementation in several FFs [3]. For simulations performed near room temperature, this is usually adequate since the bonds are strong and fluctuate only slightly around the equilibrium values in those conditions [6]. The harmonic potential (U_{bond}; Equation 5.9) allows the distance between the atoms (r_{jk}, *cf.* Figure 5.2) to oscillate around an equilibrium value (r_{jk}^0), with a force constant (k_{jk}^b) similar to that of a Hookean spring [1, 3]. The r_{jk}^0 and k_{jk}^b are usually optimised based on quantum chemistry calculations or X-ray and vibrational frequency data [6].

$$U_{\text{bond}}(r_{jk}) = \frac{1}{2}k_{jk}^b(r_{jk} - r_{jk}^0)^2 \tag{5.9}$$

The oscillation of the angle formed by three covalently bonded atoms in sequence j, k and l (θ_{jkl}, *cf.* Figure 5.2) around an equilibrium value (θ_{jkl}^0) is also commonly modelled using a harmonic potential [2]. The form of this potential (U_{angle}; Equation 5.10) is the same, being the force constant in this case denoted k_{jkl}^θ [1].

$$U_{\text{angle}}(\theta_{jkl}) = \frac{1}{2}k_{jkl}^\theta(\theta_{jkl} - \theta_{jkl}^0)^2 \tag{5.10}$$

The (proper) dihedral angle is defined as the angle between the planes formed by atoms: i, j and k; and j, k and l (ϕ_{ijkl}, *cf.* Figure 5.2). According to the International Union of Pure and Applied Chemistry (IUPAC) convention $\phi_{ijkl} = 0°$ for the *cis* configuration [1]. The oscillation of ϕ_{ijkl} is usually modelled by a torsional potential involving an expansion of periodic functions truncated at a certain term [2]. The Ryckaert-Bellemans (RB) potential (U_{RB}; Equation 5.11) is often used and corresponds to a series expansion of $\cos\varphi_{ijkl}$ up to the 5^{th} order term [1, 7].

As is implemented in some FFs, this potential is a function of the supplementary angle to ϕ_{ijkl}: $\varphi_{ijkl} = 180° - \phi_{ijkl}$. The parameters in U_{RB} are the constants in the series expansion (C_n).

$$U_{\mathrm{RB}}(\varphi_{ijkl}) = \sum_{n=0}^{5} C_n(\cos\varphi_{ijkl})^n \qquad (5.11)$$

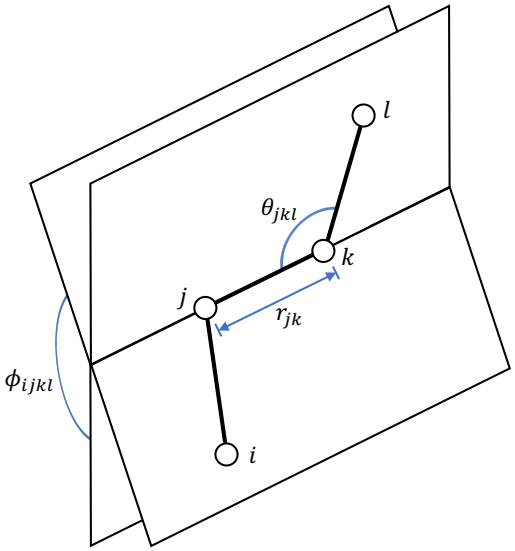

Figure 5.2: Bond length (r_{jk}), bond angle (θ_{jkl}) and dihedral angle (ϕ_{ijkl}) definitions for a sequence of four covalently bonded atoms i, j, k and l. The ϕ_{ijkl} follows the IUPAC convention, for which $\phi_{ijkl} = 0°$ for the *cis* configuration. However, the implementation of this angle in some FFs is based on the supplementary angle $\varphi_{ijkl} = 180° - \phi_{ijkl}$.

As mentioned above, the interactions between an atom i and its immediate first and second neighbours (j and k in Figure 5.2, respectively) are mainly quantum mechanical and are poorly modelled by a LJ potential. This way, the atoms separated by one or two bonds are usually considered to be unaffected by dispersion interactions between one another (nor electrostatic ones, for that matter) and their interaction is modelled exclusively using the harmonic potentials presented above. Even the LJ interactions between third neighbours (i and l in Figure 5.2) are often too strong and might cause the deformation or rupture of molecules due to significant internal strain. For this reason, these interactions (called 1–4 interactions) are scaled to half their normal value in several FFs, including in the Optimised Potential for Liquid Simulations (OPLS) FF [1], the one most extensively used in this work.

Finally, U_{bonded} is obtained by summing all the aforementioned contributions, as presented in Equation 5.12. The summations are extended to all the existing covalent bonds, bond angles and proper dihedrals in the system under study.

$$U_{\mathrm{bonded}} = \sum_{\mathrm{bonds}} U_{\mathrm{bond}} + \sum_{\mathrm{angles}} U_{\mathrm{angle}} + \sum_{\mathrm{dihedrals}} U_{\mathrm{RB}} \qquad (5.12)$$

5.2.3 Periodic Boundary Conditions (PBCs)

The implementation of MD simulations requires the definition of a simulation cell containing all the N simulated particles [3]. This is a finite geometrical representation of the system under study, its size being limited by the available storage on the host computer [4]. The simulation box is an artificial construction with a lot of unnatural boundaries with vacuum or, sometimes, container walls. Either way, the molecules near those boundaries experience a significantly different environment compared to those well inside the box. Those differences are non-negligible when simulating bulk systems and are usually overcame by surrounding the simulation box by

virtual replicas of itself, a strategy aptly named Periodic Boundary Conditions (PBCs). This creates an infinite lattice throughout space and eliminates, to some extent, the aforementioned unnatural boundaries [1, 4].

Throughout the simulation, the particles inside the original box and their periodic images move exactly alike. Thus, when a molecule leaves the box through one side, it (or its periodic image) immediately enters through the opposite side, conserving the system's number density [4]. This way, the artefacts created by the unwanted boundaries of an isolated cluster of molecules disappear and are replaced by the artefacts of periodic conditions. Although that introduces some errors, particularly for non-periodic systems like isotropic liquids or solutions, those are usually much less severe than the errors arising from the unnatural boundaries with vacuum and become less significant for larger systems. Importantly, PBCs have little effect on the equilibrium thermodynamic and structural properties of fluids not undergoing phase transitions [1, 3].

The PBCs are often implemented following the minimum image convention: each atom interacts with only one (the nearest) atom or image in the periodic array, for the computation of short-range non-bonded interactions [1, 2]. In practice, this limits the range of the pairwise interaction calculations to a sphere of, at most, half the box's smallest linear dimension [4]. However, this distance is sometimes too short for an accurate estimation of the interaction intensities (particularly for electrostatic interactions) [1].

5.2.4 Short- and Long-range interactions

Evaluating every possible pairwise interaction when computing the non-bonded interactions' contributions to the potential energy of a system of particles carries too high a computational cost to be practical. This way, the non-bonded interactions with respect to a particle i are usually computed only up to a certain distance r_c, called cut-off radius. Only the interactions with the particles inside the sphere of radius r_c are explicitly computed, being the interaction potential set to zero for $r_{ij} \geq r_c$ [2]. The list of particles inside this sphere is called a neighbour list and it evolves throughout the simulation. The neighbour lists of each atom are updated regularly, but usually not at every simulation step, because doing so involves an overhead in the computation of pair-wise distances [1, 8]. The rationale behind this approach is that the largest contributions to the non-bonded potentials and forces are short-ranged and originate in the interactions with the particles closely neighbouring the particle of interest [3]. The value of r_c should be large enough in order to introduce the smallest perturbation to the system while also not violating the minimum image convention, but small enough to minimise the computational burden. Evidently, applying a spherical cut-off to the non-bonded interactions introduces some degree of error and the simulation results using it will differ from other simulations that don't [4].

Despite the (relatively small) negative implications arising from the implementation of a cut-off distance for the non-bonded interactions, some corrective methods are available to recover the information lost with this approximation. For homogeneous systems, the use of analytical tail corrections for energy and pressure to the dispersion terms is common. The Particle-mesh Ewald (PME) is another of those methods, often used to calculate non-bonded interactions beyond r_c. The PME method is particularly useful for the estimation of the long-range electrostatic interactions, which decay slower with distance [1, 8].

5.3 Running a simulation and extracting the system's properties

As mentioned above, the instantaneous mechanical state of a system of N particles is characterised by a $6N$ ($3N$ position + $3N$ momentum) dimensional point in the phase space. The properties (temperature, potential energy, etc.) of the system are a function of the coordinates in the phase space. As the system evolves in time, so do those coordinates and, consequently, the system's properties. The experimentally observable properties can be seen as a time average of the system's properties over a long time interval (in the limit, an infinitely long one). In computer simulations, the accessible time scales are limited (and, evidently, finite) due to computational power constraints and also due to the limited numerical precision of the calculations, which might cap the precision especially of long simulations. In practice, the average of the desired properties is taken over a (preferably) large, albeit finite, simulation time interval [4].

The problem of the finite sampling of the phase space is in part overturned by the replacement of the time average by an ensemble average. The ensemble is a representative collection of points in the phase space. These points are obtained by allowing the simulation to be carried out for a sufficient number of steps and, provided the initial conditions (positions and velocities of the system's particles) are sensible, the ensemble averages should provide a reasonable insight into the computation of the macroscopic properties of interest [4].

In computer simulations, the most common and useful ensembles are those where a set of thermodynamic variables is specified and the remainder are probed either by means of ensemble averaging or derived from thermodynamic laws. Some examples of those ensembles are the NVT (the number of particles, volume and temperature are specified) and NpT (the number of particles, pressure and temperature are specified) [4]. When performing MD simulations, that is achieved by keeping the number of particles N in the simulated system constant (often recurring to PBC) and by setting the simulation box's dimensions to constant values (thus maintaining V constant). In the case of keeping either T or p constant, some specific algorithms are used, known as thermostats and barostats (to control T and p, respectively) [1].

A thermostat is required for the temperature control in MD simulations because, even if the initial velocities of the particles correctly follow a Maxwell-Boltzmann distribution, some significant deviations are likely to occur throughout the course of the simulation run [3]. These might arise from drifts during the equilibration of the system, numerical errors due to truncation in the calculation of forces and integration errors, among other factors. Thermostat algorithms vary in form but essentially act by comparing the system's instantaneous T, obtained from the velocity distribution of the particles, with a reference value and subsequently changing some or all particles' velocities in order to "guide" the system towards the desired temperature (or rather the intended average kinetic energy per particle). This might be achieved, for instance, by re-scaling the particles' velocities and, sometimes, affecting them by some additional stochastic terms to ensure the velocity distributions are physically sound. Pressure coupling follows a similar rationale, although p is controlled by successively altering one or more of the dimensions of the simulation box in the course of the simulation [1].

References

[1] M. J. Abraham et al. *GROMACS User Manual version 2018.2*. URL: https://ftp.gromacs.org/pub/manual/manual-2018.2.pdf (visited on 10/07/2022).

[2] M. P. Allen. 'Computational Soft Matter: From Synthetic Polymers to Proteins, Lecture Notes'. In: vol. 23. MIC Series. ISBN 3-00-012641-4. http://www.fz-juelich.de/nic-series/volume23. Jülich: John von Neumann Institute for Computing, 2004. Chap. *Introduction to Molecular Dynamics Simulation*, pp. 1–28. ISBN: 3-00-012641-4.

[3] J. T. Chin. 'Molecular Dynamics Simulation of Linear Perfluorocarbon and Hydrocarbon Liquid–Vapor Interfaces'. PhD thesis. Cambridge, MA, USA: Massachusetts Institute of Technology, 1999.

[4] M. P. Allen and D. J. Tildesley. *Computer Simulation of Liquids*. 1st ed. Oxford, UK: Oxford University Press, 1989. ISBN: 0-19-855645-4.

[5] G. S. Rushbrooke. *Introduction to Statistical Mechanics*. 1st ed. ISBN 978-0-470-20910-3. London, UK: Oxford University Press, 1960. ISBN: 978-0-470-20910-3.

[6] *Max Planck Institute for Polymer Research – Journal Club Page on the OPLS Forcefield*. URL: https://www2.mpip-mainz.mpg.de/~andrienk/journal_club/opls.pdf (visited on 10/07/2022).

[7] J.-P. Ryckaert and A. Bellemans. 'Molecular Dynamics of Liquid Alkanes'. In: *Faraday Discussions* 66 (1978), pp. 95–106. DOI: 10.1039/dc9786600095.

[8] M. P. Allen and D. J. Tildesley. *Computer Simulation of Liquids*. 2nd ed. Oxford, UK: Oxford University Press, 2017. ISBN: 0-19-880320-1.

Chapter 6

Atomic Force Microscopy

Atomic Force Microscopy (AFM) is a technique that permits at its core to measure surface structure with extremely high resolution and accuracy. Its development can be traced back to the development of the Scanning Tunnelling Microscopy (STM), a related but different technique and for whose invention Binnig and Rohrer shared the Nobel Prize in physics in 1986 [1]. Albeit a powerful technique that is still widely used today, because the functioning principle of STM relies on measuring an electrical current between a sharp scanning probe and the sample, this limits its use to conductive samples [2]. The same researchers eventually proposed an alternative device to probe the topography of virtually any surface, conductive or insulating, in which a probe connected to a cantilever sweeps the surface and the measurement of the deflection of the cantilever permits to retrieve the topographical features of the sample [3]. Nowadays, the basic working principle of AFM remains the same, even if the available technology has permitted attaining much faster imaging speeds, higher resolutions and even simultaneous access to properties of the sample other than the topography [2].

6.1 The Atomic Force Microscope

An AFM is different from other microscopes, inasmuch as it does not form an image of the sample resorting to focusing light or electrons onto a surface, like optical or electron microscopes. Rather, it works by scanning a probe over the sample surface, building up a map of the height or topography of the surface as it goes along [2]. This makes its principle of functioning quite different from other microscopes, but the direct access to height data makes it simple to grasp topological features of a sample and measure their heights, linear dimensions, areas or volumes. Adapted experimental setups make it possible to image samples of different natures (biological, organic, mineral, etc.) and in various environments, such as air, vacuum, controlled atmosphere and liquid medium, attesting the breadth and versatility of the technique [2, 4].

The main components of an AFM include the microscope stage itself, the control electronics and a computer interface. The core of the microscope stage of an AFM is represented in Figure 6.1. This contains the scanner or the mechanism for moving the tip relative to the sample, the sample holder and a force sensor, to hold and monitor the tip. The stage usually also includes an integrated optical microscope to view the sample and tip. Although it is not a mandatory piece

for the functioning of the AFM, an optical microscope is useful for the purposes of tip alignment and finding the region for scanning, and can also be combined with the AFM measurements themselves to simultaneously probe additional optical properties of the sample. Often, the microscope stage is supported on a vibration isolation platform to reduce noise and increase the attainable resolution. The control unit usually takes the form of a box containing the necessary electronics interfaced to both the microscope stage and the computer. The electronics generate the signals used to drive the scanner and any other motorised components in the microscope stage. They also digitise the signals coming from the AFM so that they can be displayed and recorded by the computer. Software in the computer is used by the operator to acquire and display AFM images. The user operates the software program, and the relevant acquisition parameters are passed onto the control electronics box [2].

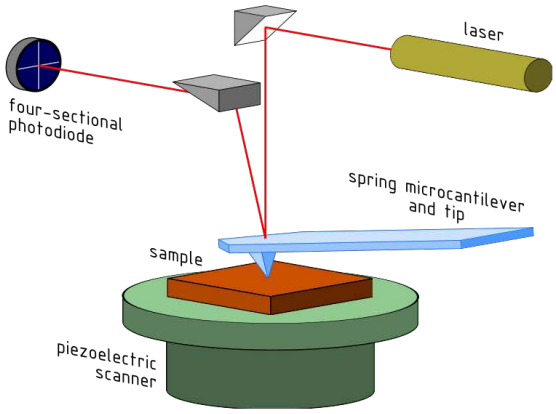

Figure 6.1: Schematic representation of the main components constituting an Atomic Force Microscope (not to scale). Adapted from [5].

To obtain an AFM image, the sample is placed in the sample holder and the tip is approached very close to the surface until the sample-tip interactions cause the cantilever to start deflecting (see Section 6.2). The deflection of the tip indicates the proximity to the surface, and the image acquisition can begin. The tip then sweeps the sample by means of the extremely precise movements of piezoelectric transducers (devices made of materials whose dimensions vary by the application of an electrical current). Several imaging modes exist, of which the most commonly used are listed in Section 6.2. In most AFM instruments nowadays, the deflection of the (reflective) cantilever is measured by shining a laser on it and capturing the laser's reflection on a four-sectional photodiode (see Figure 6.1). The force is measured by monitoring the change in light detected by the four quadrants of the photodiode. This setup magnifies small movements of the cantilever, creating large movements at the photodiode and is at the core of the high sensitivity of the technique. A feedback control loop then adjusts the vertical position of the cantilever in real time to maintain a fixed force between the tip and the sample, which also effectively maintains a fixed tip-sample distance. Ultimately, the map of the height of the cantilever permits to reconstruct the topography of the sample [2, 4].

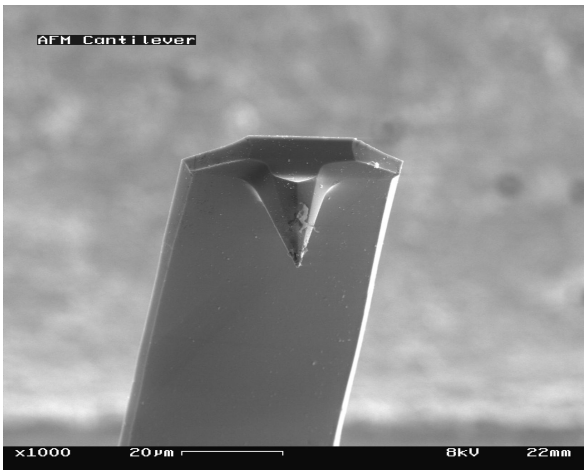

Figure 6.2: View of an AFM cantilever and tip obtained by Scanning Electron Microscopy. Sourced from [6].

The cantilever used in the AFM force sensor contains a probing element or tip at its end (Figure 6.2). This should be as sharp as

possible (in the limit, with just one atom at its end), to sense the surface at the highest attainable resolution. In principle, an AFM probe should last forever but, in practice, the tip is often blunted when it touches the surface and it can get contaminated especially from soft samples. Nowadays, it is possible to fabricate cantilevers at a relatively low cost and these are considered disposable parts of the AFM [2].

6.2 Imaging modes

The basis of AFM as a microscopic technique is that it measures the topography of the sample, and so its main output is a map of height measurements. Several topographic modes have been developed for this purpose, essentially divided into two categories: those that measure the static deflection of the cantilever and those that measure the dynamic oscillation of the cantilever. The differences between these are not only conceptual and practical, but also in what concerns the suitability for different samples, the information they provide and the interpretation of the results. Other modes, usually combining more intricate experimental setups and sometimes even requiring some modifications of the AFM device, allow the access to other properties of the sample (e.g. friction, electrical or thermal conductivities, chemical nature, among others). For historical reasons, these advanced modes are named spectroscopic or non-topographic modes; they fall outside the scope of this work and are not covered in this document. The available topographic modes are: the Contact (C) mode, based on the measurement of the static deflection of the cantilever; the Non-Contact (NC; also named Close-Contact) mode and the Intermittent-Contact (IC) or Tapping mode, both based on the measurement of the dynamic oscillation of the cantilever [2].

6.2.1 Force-distance Curve

The sample–tip interactions are quite complex and significantly depend on the nature of the sample and the tip and the distance between them. The deflection of the cantilever provides a measurement of the tip-sample interaction forces. The plot of the interaction force versus the distance of the tip from the sample is called a force-distance curve [2]. A scheme of a generic force-distance curve is represented in Figure 6.3. For larger distances, the long-range forces are attractive and usually result from van der Waals and capillary interactions; as the distance shortens, the attractions become repulsive and contact occurs (the part of the curve with a steep slope for short distances) when the electron orbitals of the interacting objects begin to overlap [7]. The different modes of operation or imaging in AFM can be matched with different parts of the curve [2, 7]. These are further explained below.

6.2.2 Contact Mode

The Contact mode was the first mode developed for AFM. Conceptually, it is also the simplest mode and it can be regarded as the basis for the later modes [2]. It works by approaching the AFM tip very close to the surface of the sample until they touch, that is, until the sample–tip distance is in the repulsive part of the curve in Figure 6.3 (identified with “C”). In other words, the tip is always touching the sample in this mode. This has practical implications, namely

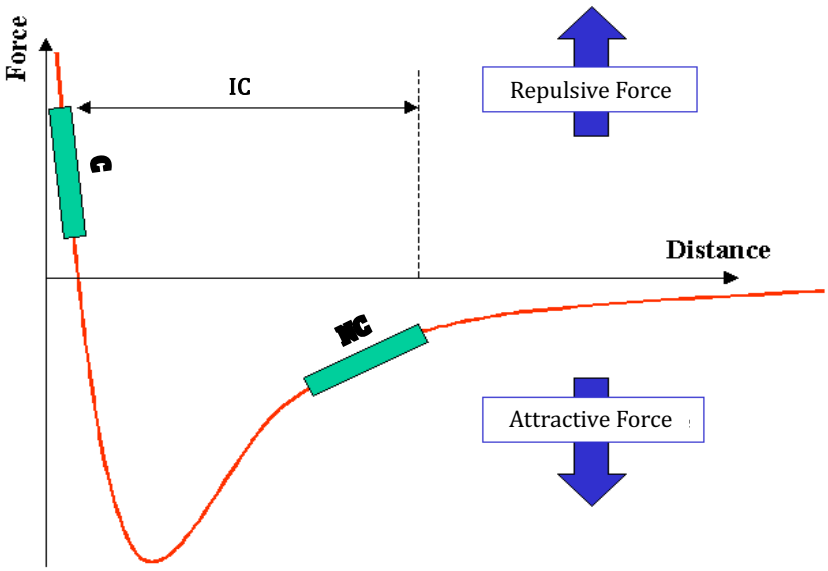

Figure 6.3: Simplified force-distance curve and scheme of the main available imaging (topographic) modes in AFM: Non-Contact (NC) mode, that places the cantilever oscillating close to the surface of the sample, but at a relatively large distance corresponding to the attractive region of the curve; Contact (C) mode, which approaches the non-oscillating cantilever to position the probe tip at a distance from the sample in the repulsive region of the curve; Intermittent-Contact (IC) or "Tapping" mode, in which the cantilever is oscillated with an amplitude that approaches the tip to the surface of the sample at distances sweeping an interval that includes regions of the curve in the attractive and repulsive regimes. Adapted from [4].

that such intense repulsive forces might damage or otherwise change the sample during the scan. Conversely, the probe tip can easily be blunted or soiled too. Most commonly, this mode is implemented with a feedback loop that maintains a constant or static cantilever deflection during the scan (and therefore a constant force applied by the tip on the sample), by adjusting the probe height accordingly. Contact mode is capable of obtaining high resolution images, but it's applicability to fragile or soft surfaces (like solid-supported organic layers) is limited [2, 4].

6.2.3 Intermittent-Contact or Tapping Mode

One of the major advantages of oscillating or dynamic modes in AFM is the fact that they can decrease the magnitude of tip–sample forces, while still being highly sensitive to the sample topography. The Intermittent-Contact or Tapping mode works by vertically oscillating the cantilever at or near its resonance frequency and monitoring the changes in the oscillatory behaviour as the cantilever approaches the sample. The amplitude of oscillation is relatively high (usually in the 1 nm to 100 nm range [2]) and is chosen such that the tip goes from large distances in the attractive part of the curve in Figure 6.3 to short distances corresponding to repulsive forces (identified with "IC"). A feedback loop is used to maintain the probe–tip interaction constant, usually by keeping a constant amplitude of oscillation. In addition to height and amplitude data, the phase shift between the free oscillation and the oscillation when in contact with the sample can

also be recorded. The oscillatory behaviour of the cantilever depends on the interactions with the sample which, themselves, vary with the chemical nature of the sample. Therefore, phase shift data can be useful to distinguish materials [2, 4]. Because of the oscillatory behaviour, tip–sample repulsive interactions still occur, but for shorter periods of time. This greatly reduces tip and sample damage. This comes with a modest loss in attainable resolution, compared to Contact mode, but provides gains in versatility, information (namely the phase shift data) and applicability [2, 4, 7]. Soft samples can usually be imaged in this mode, including films of PFAAs [8–11], but the mode used in the scope of this work was the Non-Contact mode.

6.2.4 Non-Contact Mode

In Non-Contact mode, the cantilever oscillates at its resonance frequency and sufficiently close to the surface of the sample, with a low amplitude (in the order of 10 nm [2]) to avoid passing into the repulsive regime used in Contact mode [2, 4, 7]. This is identified with a "NC" in the scheme shown on Figure 6.3. The changes in the amplitude and phase shift of the oscillation are recorded and used to reconstruct the height map of the sample. This mode of operation is sometimes called Close-Contact mode because, in reality, the principle of measurement of AFM always requires some degree of sample–tip interaction so that the tip can "sense" the surface of the sample. The advantage of this mode is the fact that these interactions are minimised and thus tip sharpness and sample integrity are more easily preserved, albeit with some degree of compromise in the attainable resolution. Because of this, Non-Contact mode is highly versatile in the type of samples it can be used for and is quite commonly used. Under the right circumstances, it can produce more consistent and reproducible results compared to Intermittent-Contact mode, due to lower tip wear [2].

6.3 Data processing

The data obtained from an AFM measurement is seldom used in its raw state. Several processing steps may be performed to clarify the information already within the data. In other words, processing AFM images intends to make it easier to observe and interpret the features that have been measured [2].

6.3.1 Data correction

The first and most common step in the treatment of the AFM data is levelling or background subtraction [2]. This is required because the AFM measures sample height and the background of the sample (such as the substrate on which the sample is deposited) can have a considerable tilt in it. This tilt can mask the changes in height associated with actual features from the sample. Background subtraction can be done resorting to different algorithms whose suitability will depend on the characteristics of the image, such as polynomial fitting (a polynomial is fitted and subtracted line-by-line) or two-dimensional plane fitting or plane levelling (the whole image is used to fit a background plane, which is then subtracted to produce the levelled image). Polynomial fitting is ubiquitous and very useful, but can introduce some artefacts in images with features having a significantly different height (with respect to the background). Plane

fitting is conceptually simple and often very satisfactory for samples with a very flat background, producing less of the artefacts that affect polynomial fitting [2].

The data can be further processed to smooth out any undesirable errors or occurrences deriving from the functioning of the AFM. These include the removal of streaks or scars caused by unwanted vibrations and acoustic noise and the line-by-line alignment to compensate for any drift or change in the imaging conditions during the scan. Because the scan is done line-by-line, sometimes the images are populated with a high-frequency periodic noise that can reduce the quality of the final images. This noise and, in general, any sources of errors should be minimised by improving the imaging conditions (correct calibration of the AFM parts and laser beam alignment, optimisation of the feedback loop controller parameters, install proper vibration insulation, etc.), but the use of image processing techniques can also help in removing such undesirable traits (for instance a low-pass filter to remove the traits in the direction of the scan) [2].

Depending on the data that is being analysed, not all processing steps mentioned above might be necessary, or others might be more suitable. Regardless, all processing steps of AFM data should be done carefully and be well documented, as they necessarily introduce changes in the data that might condition the interpretation of the final results [2].

6.3.2 Feature extraction

Depending on the intended purpose of the AFM experiment, the data can be further worked to extract valuable information about the sample. Listed below are a few analyses that are commonly used in characterising AFM height data [2].

- When the aim of the experiment is to characterise the topography of a substrate, as is the case in this work, the data can be rendered using a 3D perspective or as a **false colour image**, where a colour scale is used to map the sample height. This provides a visual clue to the viewer about the topography of the sample and the shape and size of its morphological features;

- Some **height profiles** along arbitrary linear segments of these images can also be retrieved and plotted separately, to get a quantitative grasp of the local topography along those lines. The dimensions of the features of the sample (*e.g.* steps, nano-objects, etc.) can be estimated from these height profiles;

- In the case of samples comprising discrete particles or grains, **particle analysis and counting** algorithms can be used to identify, count and characterise them. This is particularly useful for large samples or samples with a large number of particles, for which retrieving quantitative information from height profiles can be cumbersome. Statistical information on the particles' linear dimensions, height, diameter, area and volume can be computed from this. Different algorithms use different procedures to isolate the particles from the background, usually by specifying a height threshold. However, these algorithms might underperform, for instance if the background is not flat or if the height differences between the particles and the background are small (e.g. in very dense samples with tightly-packed particles);

- The order and periodicity of the sample's topographic features can be analysed by computing the **2-Dimensional Fourier Transform (2DFT)** of the height images. This is a mathematical operation that converts the image from the spatial (direct) domain to the frequency (Fourier) domain. This is particularly useful to identify any repeating patterns in the image, and, from those, estimate the characteristic dimensions of such patterns. The inverse operation is also possible, namely using information from just a subset of the calculated frequency domain. This can be useful to filter out noise with a well-defined characteristic frequency (e.g. removal of streaking along the fast direction of scanning). However, as in any other processing step, this should be used with caution to avoid introducing artificial patterns in the reconstituted image or masking true features from the underlying sample.

6.4 Sample Preparation

The AFM is a powerful tool to probe the surface morphology and other properties of different materials. In the field of soft-matter and surfactant science, this is an invaluable tool for the structural characterisation of Langmuir films. A Langmuir film is a monomolecular-thin film of insoluble molecules or amphiphiles, formed at the air–water interface (or, more generally, at the air–liquid interface). Due to their "soft" nature and because they exist at the surface of a liquid, Langmuir films cannot be imaged directly by AFM and must be transferred onto a solid substrate prior to imaging. There are several techniques to accomplish so, the most common of which is the Langmuir-Blodgett (LB) technique. Samples can also be prepared by spin coating the solid substrate with the film to be studied, among other techniques.

6.4.1 Langmuir-Blodgett Films

The most common way to transfer of Langmuir films from the air–liquid surface to a solid substrate has come to be known as LB deposition, after its developers [12, 13]. This technique involves dipping a solid substrate oriented perpendicularly to the liquid surface. The molecules are transferred with an orientation dependent on the sense of the dipping, the nature of the substrate (hydrophilic or hydrophobic) and the number of cycles of deposition. An alternative method exists, which has the same fundamental principle at its core, but in which the solid substrate is oriented parallel to the water surface: the Langmuir-Schaefer (LS) technique [13]. These methods are mentioned here due to their importance and widespread use, but they were not the ones used in the scope of this work.

6.4.2 Spin coating

An alternative method for the preparation of an organic film at the surface of a solid substrate for imaging by AFM, and the one used in this work, is by spin coating the substrate (Figure 6.4). This consists in depositing a known volume of the spreading solution on a silicon wafer previously wet with a certain volume of ultrapure water [11] or, as it was the scope of this work, other liquids constituting the subphase of interest. The system is then put in rotation in a spin coater and left to dry at room temperature.

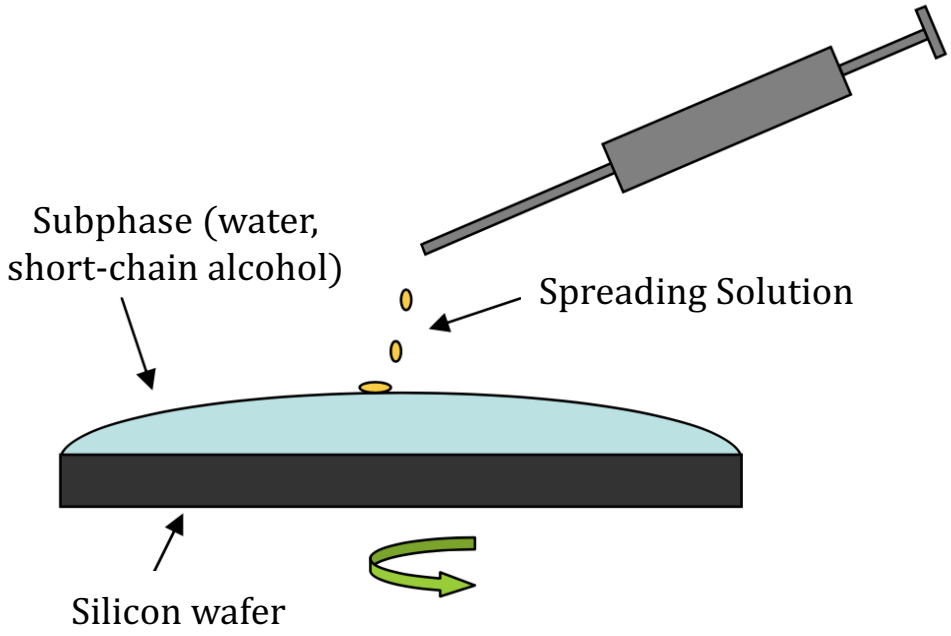

Figure 6.4: Scheme of the experimental protocol used for the preparation of the samples by spin coating. Adapted from [4].

References

[1] *The Nobel Prize in Physics 1986*. URL: https://www.nobelprize.org/prizes/physics/1986/summary/ (visited on 27/02/2024).

[2] P. Eaton and P. West. *Atomic Force Microscopy*. 1st ed. New York, USA: Oxford University Press, 2010. ISBN: 978-0-19-957045-4.

[3] G. Binnig, C. F. Quate and Ch. Gerber. 'Atomic Force Microscope'. In: *Physical Review Letters* 56.9 (1986), pp. 930–933. DOI: 10.1103/PhysRevLett.56.930.

[4] L. Bardin. 'Monocouches d'alcanes semi-fluorés'. PhD thesis. Paris, France: Université Pierre et Marie Curie, 2010.

[5] *Schematic of an atomic force microscope with optical detection of the deflection of the microcantilever*. File licensed under the Creative Commons Attribution-Share Alike 3.0 Unported license. URL: https://simple.m.wikipedia.org/wiki/File:AFM_schematic_(EN).svg (visited on 13/10/2019).

[6] Materialscientist. *View of cantilever in Atomic Force Microscope (magnification 1000x)*. File licensed under the Creative Commons Attribution-Share Alike 3.0 Unported license. URL: https://commons.wikimedia.org/w/index.php?curid=7305670 (visited on 01/03/2024).

[7] JPK Instruments AG®. *NanoWizard® AFM Handbook*. (v. 2.2a). JPK Instruments AG®. 2012. URL: https://www.nanophys.kth.se/nanolab/afm/jpk/manuf-manuals/handbook-2.2a.pdf.

[8] G. Zhang et al. 'Occurrence, Shape, and Dimensions of Large Surface Hemimicelles Made of Semifluorinated Alkanes. Elongated versus Circular Hemimicelles. Pit- and Tip-Centered Hemimicelles'. In: *Journal of the American Chemical Society* 127.29 (2005), pp. 10412–10419. DOI: 10.1021/ja0510515.

[9] A. Mourran et al. 'Self-Assembly of the Perfluoroalkyl-Alkane F14H20 in Ultrathin Films'. In: *Langmuir* 21.6 (2005), pp. 2308–2316. DOI: 10.1021/la048069y.

[10] M. O. Gallyamov et al. 'Self-assembly of (perfluoroalkyl)alkanes on a substrate surface from solutions in supercritical carbon dioxide'. In: *Physical Chemistry Chemical Physics* 8.22 (2006), pp. 2642–2649. DOI: 10.1039/b602959k.

[11] L. Bardin et al. 'Highly organized crystalline monolayer of a semi-fluorinated alkane on a solid substrate obtained by spin-coating'. In: *Thin Solid Films* 519.1 (2010), pp. 414–416. DOI: 10.1016/j.tsf.2010.07.065.

[12] A. W. Adamson and A. P. Gast. *Physical Chemistry of Surfaces*. 6th ed. Hoboken, New Jersey, USA: John Wiley & Sons, Inc., 1997. ISBN: 978-0-471-14873-9.

[13] O. N. Oliveira Jr., L. Caseli and K. Ariga. 'The Past and the Future of Langmuir and Langmuir–Blodgett Films'. In: *Chemical Reviews* 122.6 (2022), pp. 6459–6513. DOI: 10.1021/acs.chemrev.1c00754.

Chapter 7

X-Ray Diffraction (GIXD/GISAXS)

The use of light, and X-rays in particular, which have a wavelength in the order of magnitude of interatomic and intermolecular distances in a Langmuir film, permits the determination of the structure of crystalline materials resorting to X-ray diffraction experiments. The physical principles underlying such measurements are briefly visited in the following pages. In particular, the use of synchrotron X-ray sources for the study of Langmuir films is mentioned, given its utility and importance in the present work.

7.1 Coherent X-ray scattering by a density of charges

X-rays are electromagnetic waves characterised by a high frequency (in the 3×10^{16} Hz to 6×10^{19} Hz range). When they interact with atoms in matter, they accelerate their constituent charged particles (namely their electrons), that are set in vibration by the incident wave field [1]. The frequency of movements of the charges due to the incident wave is large when compared to the frequency of the movements due to interactions between charges; the latter can be then considered an assembly of free charges that scatter radiation individually [2, 3]. To understand the process of scattering of X-rays by a spatial charge distribution given by a charge density $\rho(\overrightarrow{r})$, it is thus important to understand how X-rays are scattered by a single charged particle. Considering an incident plane, linearly polarised electromagnetic field $\overrightarrow{E_i}$, characterised by its angular frequency ω and wave vector $\overrightarrow{k_i}$, using the notation in Figure 7.1, the electric field $E_s(\overrightarrow{R})$ at point M, associated with $\overrightarrow{R}$, by a single particle of charge q and mass m_q is given by Equation 7.1 (Thompson's formula) [2–4]:

$$E_s(\overrightarrow{R}) = \frac{q^2}{m_q c^2 R} E_0 \sin\theta \cdot e^{i\left(\omega t - \overrightarrow{k_s}\overrightarrow{R}\right)} \tag{7.1}$$

where $\overrightarrow{k_s}$ is the wave vector of the scattered wave and c is the speed of light in vacuum.

Knowing that the scattered intensity is given by the square of the amplitude of the electric field of the scattered wave, it follows from Equation 7.1 that this is inversely proportional to the square of the mass of the scattering particle. Knowing that the mass of an electron (9.1×10^{-31} kg) is orders of magnitude smaller than the mass of a proton (1.67×10^{-27} kg), the scattered intensity by atoms arises essentially from the scattering by their electrons. That said, the elemental electric

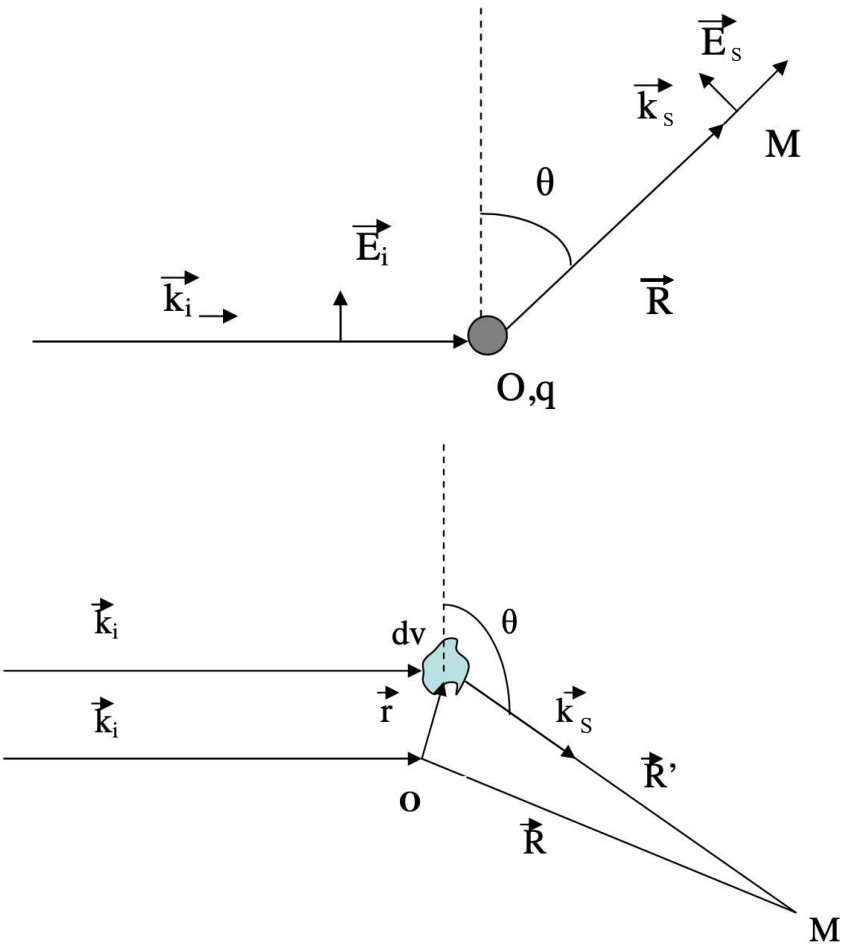

Figure 7.1: Scheme depicting the scattering of X-rays by a single charged particle q (top) and by a volume element dv of a charge density $\rho\,(\overrightarrow{r})$ (bottom). Adapted from [4].

field dE_s, at point M associated with $\overrightarrow{R'}$ (see Figure 7.1), due to scattering by a volume element dv of a charge (or, essentially, electron) density positioned at $\overrightarrow{r}$ i

$$dE_s(\overrightarrow{R'}) = \frac{e^2\rho\,(\overrightarrow{r})\,dv}{m_e c^2 R'}\left(E_0 e^{-i\overrightarrow{k_i}\,\overrightarrow{r}}\right)\sin\theta\cdot e^{i\left(\omega t-\overrightarrow{k_s}(\overrightarrow{r})\overrightarrow{R'}\right)} \tag{7.2}$$

where e is the electron's elementary charge, m_e is the mass of the electron and $E_0 e^{-i\overrightarrow{k_i}\,\overrightarrow{r}}$ is the amplitude of the incident wave at point $\overrightarrow{r}$.

Given that $\overrightarrow{R} = \overrightarrow{r} + \overrightarrow{R'}$ and that $r << R$ and R', Equation 7.2 becomes:

$$dE_s(\overrightarrow{R}) = \left\{\frac{e^2 dv}{m_e c^2 R}E_0\sin\theta\cdot e^{i\left(\omega t-\overrightarrow{k_s}\,\overrightarrow{R}\right)}\right\}\rho\,(\overrightarrow{r})\,e^{i\overrightarrow{Q}\,\overrightarrow{r}} \tag{7.3}$$

where $\overrightarrow{Q} = \overrightarrow{k_s} - \overrightarrow{k_i}$ is the scattering vector or the momentum transfer vector. By integrating Equation 7.3 over the whole volume of the charge distribution V, the scattered electric field E_s becomes:

$$E_s(\overrightarrow{R}) = \underbrace{\left\{ \frac{e^2}{m_e c^2 R} E_0 \sin\theta \cdot e^{i\left(\omega t - \overrightarrow{k_s}\overrightarrow{R}\right)} \right\}}_{E_e} \underbrace{\int_V \rho\left(\overrightarrow{r}\right) e^{i\overrightarrow{Q}\overrightarrow{r}} dv}_{FT(\rho)} \tag{7.4}$$

It is clear that E_s is given by the product of two terms, the first (E_e) being the scattered intensity by a single electron or Thompson's formula (*cf.* Equation 7.1) and the second ($FT\left(\rho\right)$) being the Fourier transform of the charge density. The scattered intensity I is given by the squared modulus of E_s (Equation 7.5), and this is proportional to the square of the modulus of $FT\left(\rho\right)$:

$$I = E_s \cdot E_s^* = |E_e|^2 \cdot |FT\left(\rho\right)|^2 \tag{7.5}$$

7.2 Diffraction by a perfect 3D crystal

The term *scattering* is generic and refers to different types of experiments aiming at determining different kinds of correlations in charge density. In the case of a Langmuir film spread at the air–water interface, the regular arrangement of the molecules in a 2D solid or liquid condensed phases gives rise to significant and periodical fluctuations in the electron density. The scattering resulting from the molecules in such arrangement is concentrated in the directions for which the scattered waves from each row of molecules are in phase, resulting in constructing interference. In that case, the scattering spectrum contains peaks, equivalent to the Bragg peaks in 3D, corresponding to those specific directions. This phenomenon is named diffraction [3, 4].

Diffraction results from the constructive interference of the scattered waves by organised matter, when this is irradiated by electromagnetic radiation with the right wavelength and in the appropriate geometry. Considering what was laid out in the previous section, the scattering of X-rays by an ensemble of charges originates coherent scattered waves, that may interfere constructively and originate a diffraction pattern [4]. In the case of the crystalline state, this is characterised by the spatial periodicity of the atomic arrangements, which in turn corresponds to periodical variations in charge density [2, 3]. In a perfect infinite 3D crystal, this periodicity is represented by a structural motif (unit cell) that is infinitely repeated in space defined by three basis vectors, $\overrightarrow{a}$, $\overrightarrow{b}$ and $\overrightarrow{c}$ [2, 4]. The periodicity is of the same order of magnitude as the wavelength of X-rays, and so crystals can act as diffraction gratings for X-rays [2, 3]. If the electronic density of the structural motif is denoted ρ_0 and the total electronic density of the crystal is denoted $\rho\left(\overrightarrow{r}\right)$, the latter is given by the sum of the contributions of all structural motifs, taking into account their respective translations (Equation 7.6):

$$\rho\left(\overrightarrow{r}\right) = \sum_{j=1}^{\infty} \rho_0 \left(\overrightarrow{r} - \overrightarrow{R_j}\right) \tag{7.6}$$

where the vector $\overrightarrow{R_j} = n_1\overrightarrow{a} + n_2\overrightarrow{b} + n_3\overrightarrow{c}$ gives the position of the unit cell j (n_1, n_2 and n_3 are integers). The Fourier transform of the electronic density of the crystal becomes:

$$FT\left(\rho\left(\overrightarrow{r}\right)\right) = \int_V \left(\sum_{j=1}^{\infty} \rho_0 \left(\overrightarrow{r} - \overrightarrow{R_j} \right) \cdot e^{i\overrightarrow{Q}\left(\overrightarrow{r}-\overrightarrow{R_j}\right)} \right) dv = \\ = \underbrace{\sum_{j=1}^{\infty} e^{i\overrightarrow{Q}\overrightarrow{R_j}}}_{S\left(\overrightarrow{Q}\right)} \underbrace{\int_V \rho_0 \left(\overrightarrow{r} - \overrightarrow{R_j} \right) \cdot e^{i\overrightarrow{Q}\left(\overrightarrow{r}-\overrightarrow{R_j}\right)} dv}_{F\left(\overrightarrow{Q}\right)} \quad (7.7)$$

The Fourier transform of $\rho\left(\overrightarrow{r}\right)$ is thus the product of two terms, namely:

- $F\left(\overrightarrow{Q}\right)$, the Fourier transform of the electronic density of the structural motif or the *structure factor*. It represents the electronic density of the structural motif of the unit cell;

- $S\left(\overrightarrow{Q}\right)$, the *sum of the lattice*. It represents the periodicity of the structural motif.

For a perfect, infinite 3D crystal, $S\left(\overrightarrow{Q}\right)$ is given by Equation 7.8:

$$S(\overrightarrow{Q}) = \sum_{n_1=1}^{\infty} e^{in_1\overrightarrow{Q}\overrightarrow{a}} \cdot \sum_{n_2=1}^{\infty} e^{in_2\overrightarrow{Q}\overrightarrow{b}} \cdot \sum_{n_3=1}^{\infty} e^{in_3\overrightarrow{Q}\overrightarrow{c}} \quad (7.8)$$

Constructive interference of the scattering by all unit cells of the crystal, and consequently non zero diffraction intensity, occurs only for a discrete set of scattering vectors $\overrightarrow{Q}$ that satisfy the Laue conditions [2, 4]: $\overrightarrow{Q} \cdot \overrightarrow{a} = 2\pi h$, $\overrightarrow{Q} \cdot \overrightarrow{b} = 2\pi k$ and $\overrightarrow{Q} \cdot \overrightarrow{c} = 2\pi l$ (h, k and l are integers known as the Miller indices).

The set of vectors for which the diffraction intensity is non zero are called *diffraction peaks*, *Bragg peaks* or *reflections* [2–4]. The set of vectors $\overrightarrow{Q}_{hkl} = h\overrightarrow{a}^* + k\overrightarrow{b}^* + l\overrightarrow{c}^*$ that verify Laue's conditions define a reciprocal lattice in the space of scattering vectors, and whose base vectors $\overrightarrow{a}^*$, $\overrightarrow{b}^*$ and $\overrightarrow{c}^*$ satisfy: $\overrightarrow{a}^* \cdot \overrightarrow{a} = 2\pi$, $\overrightarrow{a}^* \cdot \overrightarrow{b} = 0$, $\overrightarrow{a}^* \cdot \overrightarrow{c} = 0$; $\overrightarrow{b}^* \cdot \overrightarrow{a} = 0$, $\overrightarrow{b}^* \cdot \overrightarrow{b} = 2\pi$, $\overrightarrow{b}^* \cdot \overrightarrow{c} = 0$; and $\overrightarrow{c}^* \cdot \overrightarrow{a} = 0$, $\overrightarrow{c}^* \cdot \overrightarrow{b} = 0$, $\overrightarrow{c}^* \cdot \overrightarrow{c} = 2\pi$.

In the case of a perfect, but finite crystal, a more realistic case, the structural motif is repeated N_1, N_2 and N_3 times in the three directions given by $\overrightarrow{a}$, $\overrightarrow{b}$ and $\overrightarrow{c}$. Consequently, the diffraction intensity arising from a perfect finite crystal is not entirely located in the nodes of the reciprocal lattice (in the form of Dirac peaks), but also in the vicinity of those positions; the diffraction intensity, in this case, will be proportional to the product of one interference function per direction of the system, *i.e.* basis vector. In other words, the diffraction peaks will have non-zero width, for a perfect finite crystal [2–4].

An additional note concerning $F(\overrightarrow{Q})$ should be mentioned. Because the diffraction intensity is also a function of $F(\overrightarrow{Q})$, this results in an additional modulation of the peak intensity that may lead to the extinction of some of them, under certain conditions. This is not deepened in the context of this work, but further information can be found elsewhere [2, 3, 5].

7.3 Diffraction by a perfect 2D crystal

In an analogous way, by applying the reasoning presented in the preceding section to a perfect 2D infinite crystal (*i.e.* the periodic repetitions of the structural motif are in-plane only, being described in the space defined by only 2 basis vectors $\overrightarrow{a}$ and $\overrightarrow{b}$), the sum of lattice becomes:

$$S\left(\overrightarrow{Q}\right) = \sum_{n_1=1}^{\infty} e^{in_1 \overrightarrow{Q}\,\overrightarrow{a}} \cdot \sum_{n_2=1}^{\infty} e^{in_2 \overrightarrow{Q}\,\overrightarrow{b}} \tag{7.9}$$

The Laue conditions, in this case, for diffraction to occur are: $\overrightarrow{Q} \cdot \overrightarrow{a} = 2\pi h$ and $\overrightarrow{Q} \cdot \overrightarrow{b} = 2\pi k$. This way, in the reciprocal space, the diffraction intensity is zero except for a set of scattering vectors $\overrightarrow{Q}_{hk}$ that satisfy these conditions (not regarding the eventual effects of $F(\overrightarrow{Q})$). This has an important implication, which is the fact that the sum of lattice does not depend on the out-of-plane component Q_z of the scattering vector: the Bragg peaks become *Bragg rods* in the reciprocal space corresponding to a perfect infinite 2D crystal.

7.4 Ordering within a (finite) 2D crystal

The existence of a perfect, infinite 2D crystal has been proven theoretically to be impossible [2, 3]. To get a quantitative grasp on the extent to which the positional order is preserved in a 2D crystal, the formalism of the auto-correlation function of the charge density, $C(\overrightarrow{r}) = \langle \rho(\overrightarrow{r}) \rho(\overrightarrow{r} + \overrightarrow{r}') \rangle$, is commonly employed. In this framework, the crystal is thought of as an assembly of domains with characteristic size ξ: the *correlation length*. Inside each domain (in practice, for small distances compared to ξ), the auto-correlation function tends to unity. This means that the position of the atoms can be predicted by the application of translations of the lattice. Conversely, between domains (in practice, for large distances compared to ξ) $C(\overrightarrow{r})$ becomes zero [2, 3]. While the exact form of the auto-correlation form is unknown, two forms are usually admitted for analytical purposes: Gaussian or exponential decay. This implicitly determines the shape of the diffraction peaks: if $C(\overrightarrow{r})$ is given by a Gaussian function, then the diffraction peaks will also have a Gaussian shape; if $C(\overrightarrow{r})$ is given by an exponential decay function, then the diffraction peaks will have a Lorentzian shape [3]. If a Lorentzian shape is assumed for the diffraction peak, ξ is given by Equation 7.10; for Gaussian-shaped diffraction peaks, ξ can be estimated using Scherrer's relation (Equation 7.11) [2, 4, 6].

$$\xi = \frac{2}{\mathrm{FWHM}^{\mathrm{Lorentz}}} \tag{7.10}$$

$$\xi = \frac{0.88 \times 2\pi}{\mathrm{FWHM}^{\mathrm{Gauss}}} \tag{7.11}$$

It should be emphasised that what is experimentally accessible to characterise a Langmuir film is a *coherence length*, determined by applying the formulas above using data from the functions fitted to the experimental diffraction spectra. The correlation length is associated with a correlation function, whereas a coherence length is a measured quantity [3]. This distinction is important and relevant, since the measurement of a diffraction peak is perturbed by a number of

factors that affect its shape, starting with the fact that the shape of the peak is convoluted with the experimental resolution. Consequently, the measurements of coherence length in particular, but other peak properties too, should be interpreted and compared between experiments made with the same experimental setup and, ideally, the same Langmuir film, so that the observed changes reflect the evolution of the Langmuir film itself rather than differences in experimental resolution or others [3, 4].

7.5 Diffraction by a 2D powder

The Langmuir films are usually not monocrystalline, comprising instead an ensemble of up to µm-size 2D crystals or crystallites at the water surface, with completely uncorrelated relative orientations: a 2D powder [2, 3]. In the reciprocal space, each crystallite originates a reciprocal lattice that is itself also randomly oriented in the plane. Collectively, these turn the assembly of the corresponding diffraction rods into *diffraction rings*. The radius of each ring is equal to the modulus of the in-plane wave vector component of a rod in the reciprocal lattice of a single crystal. Therefore, in a 2D powder diffraction experiment, a given wave vector $\overrightarrow{Q}$ gives rise to a diffraction peak if the modulus of its in-plane component ($Q_{\mathrm{xy}} = \sqrt{Q_{\mathrm{x}} + Q_{\mathrm{y}}}$) is equal to the modulus of a vector of the reciprocal lattice of the single crystal $\overrightarrow{Q}_{hk}$, regardless of the sense and direction of $\overrightarrow{Q}$; the out-of-plane component (Q_{z}) only influences the form of the rod. The latter arises from the fact that the Langmuir films are not 2D systems, strictly speaking, and have instead a finite thickness [2–4].

7.6 Grazing Incidence X-Ray Diffraction (GIXD)

The intensity measured in an X-ray scattering experiment is proportional to the irradiated sample volume. For X-rays, the penetration depth of the radiation can range from a few µm to a few mm, depending on the how absorbing the material is. This poses a practical problem when studying Langmuir films, which are typically a few nm thick, and are supported by a bulk liquid. To minimise the scattering from the liquid subphase and restricting the penetration depth to the surface region, that is in order to have an experimental setup that is sensitive to the structural properties of the interface rather than the bulk, the phenomenon of total external reflection is exploited [2, 3]. In practice, this requires shining the incident X-ray beam on the film covered surface at an angle below the critical angle of total external reflection (α_c), creating an evanescent wave that propagates parallel to the interface and is diffracted by the film molecules. The transmitted wave penetrates only to a depth in the order of 1 nm to 10 nm, which minimises the background scattering by water [2, 4].

Because of their specificity, that is because the light strikes the sample at *grazing incidence*, this type of experiments is called Grazing Incidence X-Ray Diffraction (GIXD). The diffracted intensity is measured as a function of the in-plane (Q_{xy}) and out-of-plane (Q_{z}) components of the scattering vector, by varying the diffraction angle 2θ (horizontally) and θ_z (vertically), respectively [2, 4]. The information from the diffractograms permits to infer the structural properties of the ordered Langmuir films. Finally, depending on the geometry of the experiment, which also

conditions the technical and practical aspects of the experimental setup, the range of sampled 2θ (for typical wavelengths in the order of $\lambda = 0.155\,\text{nm}$) determines the order at the molecular scale is probed (*i.e.* the packing of the molecules relative to one another). The experiments can also be conducted to measure small angles of diffraction, to assess the order of supramolecular nanostructures such as in the case of the surface hemimicelles of PFAAs. In this case, the experiments are named Grazing Incidence Small Angle X-Ray Scattering (GISAXS) [4]. Because the evanescent wave has a very weak intensity and there is only little amount of material of the film in the footprint of the illuminated monolayer that diffracts light, these experiments cannot be conducted using conventional X-ray sources and require the use of the high-intensity, low-divergence radiation sources produced in a synchrotron environment [2, 4].

7.7 X-ray diffraction experiments in a synchrotron environment

The principle of functioning of a synchrotron light source is that charged particles, when accelerated, emit radiation. This way, by accelerating electrons up to relativistic speeds (*i.e.* near the speed of light) and maintaining them in a quasi-circular orbit in a storage ring permits to exploit this phenomenon for the production of high intensity, low divergence sources of light. The spectral distribution that can be attained with this technology ranges from the infrared to the X-ray frequencies. Typically, the electrons are first accelerated linearly from an electron gun, and their trajectory leads them to a first, smaller accelerator ring. The electrons are injected from this accelerator ring into the storage ring, which is essentially a sequence of straight and curved sections that form a closed loop, as depicted in Figure 7.2. In the curved sections, a bending magnet accelerates the electrons to deflect their trajectory from one straight section to the next. This causes the emission of a "white" beam of light in the tangential direction of the trajectory. The use of additional devices such as wigglers or undulators in the straight sections of the storage ring in between two bending magnets can be exploited to increase the flux of emitted photons. A beamline can thus be placed at each point where a bending magnet is found to source the emitted light and perform experiments. The specificities of each beamline will depend on the type of experiment to be performed, on the required sample environment and the region of the electromagnetic spectrum that is used to probe matter [2, 4, 7].

In the case of experiments performed to probe the structure and other properties of Langmuir films using X-rays, the incident beam must strike the sample at a grazing incidence angle, as mentioned above. This poses specific technical challenges and requirements, because the X-ray beam that is sourced from the storage ring is horizontal and it must be deflected and focused onto the sample, which is liquid and thus mandatorily horizontal as well. The beamlines SIRIUS at Source Optimisée de Lumière d'Énergie Intermédiaire du LURE (SOLEIL) and ID10 at European Synchrotron Radiation Facility (ESRF) are specifically equipped for this kind of experiments, possessing a set of mirrors that bend the incident wave in a very precise way for this effect, given the alignment of the beam towards the sample cannot be done by rotation and/or translation of the latter [2–4].

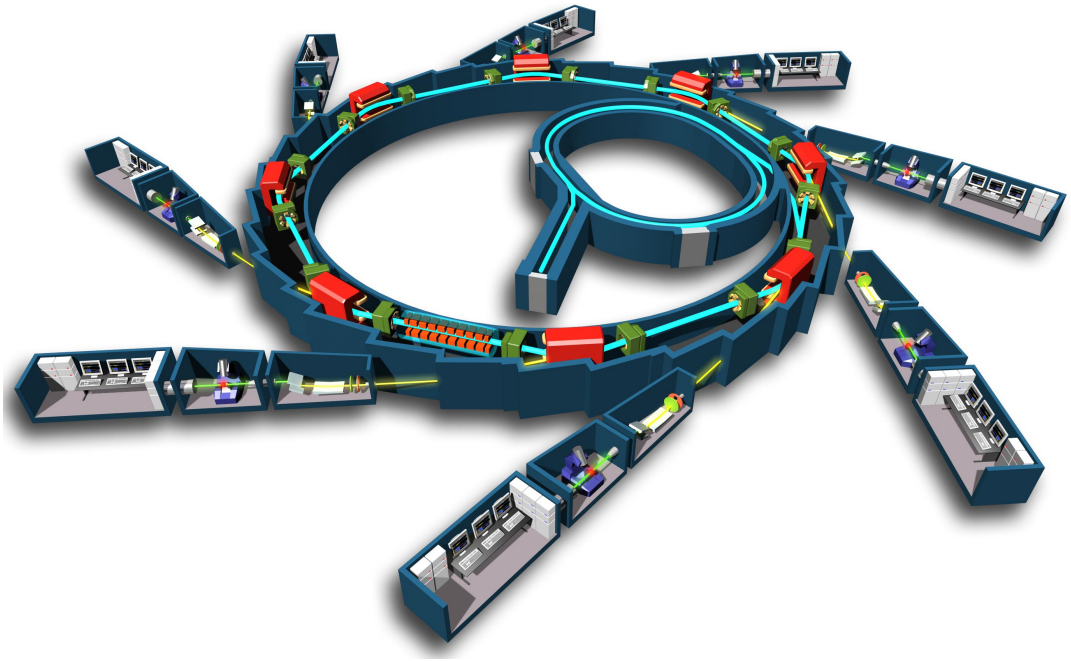

Figure 7.2: Scheme of the main components and functioning of a synchrotron light source, specifically of synchrotron SOLEIL. Electrons are accelerated first in a linear accelerator, then in a smaller booster ring and only then they are injected in the main storage ring. The latter is the outer circular ring or synchrotron, a particle accelerator that brings electrons (whose trajectory is depicted by the light blue line) to relativistic speeds. The electrons are linearly accelerated by electric fields in the straight sections between the green elements. The red boxes are magnets that bend the beam. When the beam is bent the electrons emit radiation (in yellow); this is recovered by various beam lines (the laboratories placed tangently the synchrotron). Sourced from [8].

References

[1] J. Als-Nielsen et al. 'Principles and Applications of Grazing-Incidence X-Ray and Neutron-Scattering from Ordered Molecular Monolayers at the Air–Water Interface'. In: *Physics Reports – Review Section of Physics Letters* 246.5 (1994), pp. 252–313. DOI: 10.1016/0370-1573(94)90046-9.

[2] A. L. S. Gamboa. 'Ordering in Langmuir and Langmuir-Blodgett Films: Effect of the Presence of Fluorocarbon and Hydrocarbon Chains'. PhD thesis. Lisboa, Portugal: Universidade Técnica de Lisboa – Instituto Superior Técnico, 2006.

[3] P. Fontaine. *Grazing Incidence X-ray Diffraction on Langmuir Monolayers*. Lecture notes (in French). Synchrotron SOLEIL. Dec. 2014.

[4] L. Bardin. 'Monocouches d'alcanes semi-fluorés'. PhD thesis. Paris, France: Université Pierre et Marie Curie, 2010.

[5] M. M. Woolfson. *An introduction to X-ray crystallography*. 2nd ed. ISBN 0-521-42359-7. Cambridge, UK: Cambridge University Press, 1997. ISBN: 0-521-42359-7.

[6] L. Bardin et al. 'Long-Range Nanometer-Scale Organization of Semifluorinated Alkane Monolayers at the Air/Water Interface'. In: *Langmuir* 27.22 (2011), pp. 13497–13505. DOI: 10.1016/10.1021/la201802x.

[7] F. Johansson. 'Core-hole Clock Spectroscopy Using Hard X-rays'. PhD thesis. Uppsala, Sweden: Uppsala Universitet, 2020. ISBN: 978-91-513-0915-6.

[8] *General diagram of Synchrotron SOLEIL*. Copyright © EPSIM 3D/JF Santarelli, Synchrotron SOLEIL. Synchrotron SOLEIL. URL: https://upload.wikimedia.org/wikipedia/commons/6/60/Sch%C3%A9ma_de_principe_du_synchrotron.jpg (visited on 04/05/2024).

Part III

Results and Discussion

Chapter 8

Origin of the central pit in hemimicelles of perfluoroalkylalkanes

How molecular dipoles and substrate deformation can determine supra-molecular morphology

This chapter has been published in the form of an open-access paper, as cited below. The paper is presented herein in full form, with only minor formatting modifications for consistency with the rest of the document.

P. Silva, G. M. C. Silva, P. Morgado, M.-C. Fauré, M. Goldmann and E. Filipe. 'Origin of the central pit in hemimicelles of semifluorinated alkanes: How molecular dipoles and substrate deformation can determine supra-molecular morphology'. In: *Journal of Colloid and Interface Science* 655 (2023), pp. 576–583. DOI: 10.1016/j.jcis.2023.11.007.

The author of this thesis performed all the simulations and analyses presented in the following pages, with the exception of the simulation of the F8H16 hemimicelle over unconstrained water (named "OPLS aggregate" herein), which was performed by G. M. C. Silva as his own original work. All the authors of the article contributed to the discussion of the results and writing of the manuscript.

Abstract

Hypothesis: Semifluorinated alkanes amphiphiles spontaneously form highly monodispersed hemimicelles at the surface of water. The origin of the formation and complex structure of these surprising supramolecular aggregates were only recently clarified using Molecular Dynamics (MD) simulations. The existence of a pit at the centre of these aggregates made up of almost 3000 molecules was indeed reproduced by the MD simulations, but not understood.

Method: A careful strategy of atomistic MD simulations comparing non-electrostatic force fields with force fields that include electrostatic forces, thus bearing an implicit or explicit dipole, allowed demonstrating the roles of dipolar interactions and interactions with the liquid subphase on the morphology of the aggregates.

Findings: The simulation results clearly show that within the hemimicelles the strong molecular dipoles located at the CH_2-CF_2 junctions tend to align, leading to a collective shift of the PFAA molecules relatively to each other. This shift is responsible for the curvature of the hemimicelles and originates the central pit, provided the possibility of deforming the surface of the water sub-phase. Comparisons with non-electrostatic force field results further contribute to understand the origin of the self-assembling process. The results directly connect for the first time a molecular property with a mesoscopic structural feature. Given the molecular simplicity of these "primitive" amphiphiles compared to the common hydrophilic/hydrophobic surfactants, the results contribute to understand self-assembly in general.

Keywords: Self-assembly, Molecular Dynamics, Semifluorinated Alkanes, Hemimicelles

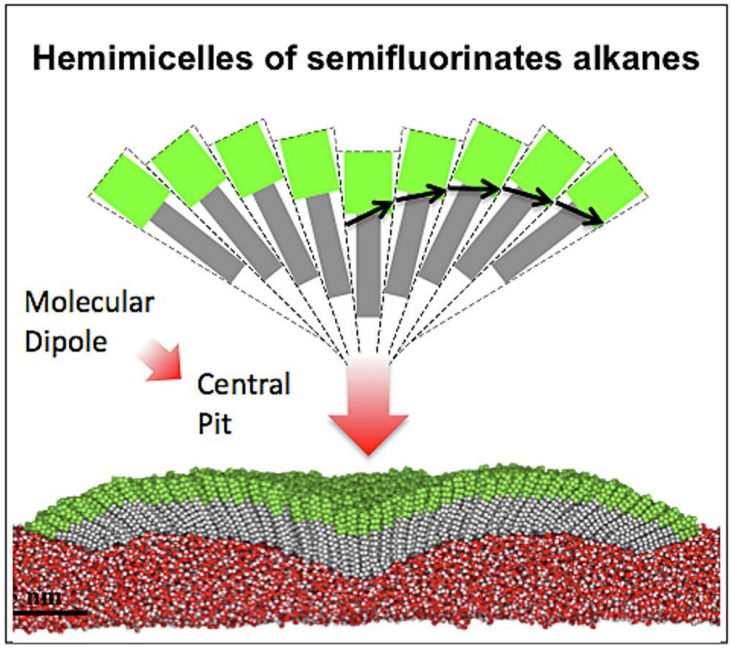

Figure 8.1: Graphical abstract.

8.1 Introduction

Perfluoroalkylalkane (PFAA) amphiphiles are known to spontaneously self-assemble forming hemimicelles (Langmuir films) at the surface of water [1–3]. These surprising supramolecular aggregates are potential candidates for numerous exciting applications as medical devices [4–6] and in material sciences, as highly organised templates for the precise nanopatterning of surfaces using bottom-up methods.

PFAAs, also known as semifluorinated alkanes and often called "primitive surfactants", are formed by two mutually phobic perfluorinated and hydrogenated segments covalently bonded forming a single molecule (general formula $F(CF_2)_n(CH_2)_mH$ or FnHm). The mutual phobicity between hydrogenated and perfluorinated chains is well documented but still poorly understood. It is responsible, for example, for large positive excess properties, liquid–liquid immiscibility and nanosegregation in mixtures of alkanes and perfluoroalkanes [7–10]. Anomalies in transport [11], surface [12], and conformational [13, 14] properties of these mixtures are also known. Phase separation in bi-dimensional systems has also been reported, e.g. for mixtures of hydrogenated and perfluorinated surfactants, such as long-chain alcohols and carboxylic acids spread at the air–water interface [15]. The amphiphilic character of PFAAs is further evidenced by their ability to form micelles in hydrocarbon [16, 17] and fluorocarbon [18] solutions, complex anisotropic fluids [19], liquid crystalline phases and, as previously described, surface aggregates or hemimicelles at the air–water interface [1, 2, 20, 21].

Despite all efforts, the principles governing the formation and structure of PFAA hemimicelles at the surface of water have been a subject of debate over the years. Their spontaneous formation at zero surface pressure and their resistance to coalescence, even under strong compression, were particularly puzzling [22–26]. Indeed, until very recently it was not at all clear why monolayers of PFAA are not uniform, especially considering the size and aggregation number of the formed hemimicelles. These are highly monodisperse aggregates, each containing between 2000 and 5000 molecules, with an average diameter ranging between 30 and 40 nm, depending on chain length.

In recent work we have succeeded in simulating the spontaneous formation of F8H16 hemimicelles using atomistic molecular dynamics (MD) simulations [27]. The All-Atom (AA) Optimised Potential for Liquid Simulations (OPLS) was used, a force field that includes electrostatic interactions. The simulated hemimicelles remarkably reproduce all observed experimental details, namely size, dome shape and central pit. Moreover, the internal structure of the simulated hemimicelle leads to "diffraction peaks" that agree with the spectra obtained by Grazing Incidence X-Ray Diffraction (GIXD), fully validating the simulation results and methodology. But perhaps more importantly, a detailed structural analysis of the simulated hemimicelles enabled, for the first time, a comprehensive understanding of the physical principles that explain the formation of the aggregates.

More recently, Yadav *et al.* have also simulated the formation of F8H16 surface aggregates using a Coarse-Grained (CG) Force Field (FF), a method that allowed performing microsecond-long simulations of larger systems, up to 10 000 PFAA molecules [28]. Although the simulated aggregates generally have the correct shape and similar aggregation number, they lack the characteristic central pit experimentally observed by Atomic Force Microscopy (AFM). Since the used

CG FF does not include electrostatic interactions explicitly, this underlines the need to elucidate the role of these forces in the self-assembly process and structure of the aggregates, and in particular the influence of the dipole located at the CH_2-CF_2 junction. Indeed, while hydrogenated and perfluorinated chains interact essentially through dispersion forces, PFAA additionally display important dipole–dipole interactions. The molecular dipole of PFAA is rather strong (literature values lie between 2.3 D to 3.4 D [29–34] depending on n, m and on the methods employed for the measurement or calculation of this property) and its orientation does not coincide with the molecular axis, aligning instead with the electronically asymmetric CH_2-CF_2 bond.

The importance of the dipole to the self-assembling process has been addressed by Semenov *et al.* [35] who developed a 2D theoretical model of the FnHm monolayers, taking into account dispersive and dipolar interactions, and treating the water subphase as a structure-less supporting surface. The model predicts the formation of aggregates as a liquid/liquid phase separation in the Langmuir film. According to the model, at low surface density, the FnHm molecules would lie parallel to the water surface, but stand-up under compression via a first order phase transition. In the vertical phase, the molecules self-assemble in domains whose size would be limited by the interactions between the final dipole carried by each domain. In this model, the vertical component (perpendicular to the interface) of the dipole carried by each molecule at the CH_2-CF_2 bonds is summed to determine the value of the final dipole of the domain. Repulsive interactions between the dipoles of the domains would limit growth and prevent coalescence. The model is thus able to describe a number of features of the FnHm films, but is unable to explain others, such as the dependence of hemimicelle diameter with chain length.

It should be emphasised that alkyl and perfluoroalkyl chains display very different physical properties, all of which contribute to the overall behaviour of the systems. While hydrogenated chains are flexible and tend to adopt an all-*trans* conformation, perfluorinated chains are rigid and display a stable helical conformation. The cross section of perfluorinated chains is larger than that of hydrogenated ones. Consequently, the molar volumes of perfluorinated substances are higher than those of equivalent hydrogenated substances, and so is their density and viscosity. On the contrary, the surface tension of perfluorinated compounds is much lower than that of their hydrogenated counterparts. Finally, both types of chains are highly hydrophobic and mutually phobic. In recent years we have accomplished a systematic experimental, computational and theoretical study on the thermophysical properties of liquid PFAA, either pure or mixed with alkanes, perfluoroalkanes and water. We have reported a number of properties of pure liquid PFAA (liquid density [36, 37], vapour pressure [34], viscosity [38] and surface tension [39]) and their mixtures (partial molar volume at infinite dilution [40, 41], solubility of water [42] and interfacial tension [43]) as a function of temperature, pressure and relative length of the hydrogenated and fluorinated segments. All these results and experience were crucial for developing, parameterising and testing molecular models and force fields to be used in computer simulations and molecular-based theoretical calculations.

In this work, we report an MD simulation study of the F8H16 hemimicelles at the air–water interface, aimed at uncovering the connection between the existence of the molecular dipole at the CF_2-CH_2 bond and the morphology and internal structure of the formed hemimicelles. The adopted strategy compares the simulation results from two well established force fields, one in

which electrostatic interactions are explicitly taken into account by including partial charges in all interactive sites, thus leading to presence of dipoles (the OPLS-AA force field used in previous work) and another in which electrostatic interactions are absent (the United Atom (UA) Transferable Potentials for Phase Equilibria (TraPPE)). Both FFs are known to accurately model the energetic interactions between hydrogenated (CH) and perfluorinated (CF) chains and their conformations and structure, and have been thoroughly tested and validated for a variety of molecules and systems. Since the TraPPE FF models the PFAA molecules as electrically neutral entities, this allowed including a dipole in the form of point charges at the junction between segments, "turning on" the dipole and adding this interaction on top of the dispersive forces. Comparing the results from the different models, the direct influence of the molecular dipole on the morphology and inner structure of the hemimicelles can be unambiguously assessed.

8.2 Methods, MD simulation details

Each studied system consists of an aggregate of 2500 F8H16 molecules (mimicking an isolated experimentally observed hemimicelle) placed on one of the surfaces of a water slab. Construction of the simulation boxes followed a previously established procedure [27]. Briefly, simulation boxes of equilibrated slabs of water (a film of liquid water with 2 explicit water-vacuum interfaces perpendicular to the z axis) were prepared at the desired temperature and density. The vertically aligned F8H16 molecules, in their minimum energy configuration, were packed in a cylinder using the open-source software Packmol (v. 20.2.2) [44] and placed near the surface of water, with the CH chains facing the water surface. The system was then equilibrated in the NVT ensemble for at least 2 ns, followed by 20 ns NVT production runs, always at 298.15 K and with periodic boundary conditions in all directions. We have previously [27] demonstrated that: the aggregates thus constructed are structurally similar to those formed starting from a random configuration but self-assemble over 100 times faster; 2500 molecules is a reasonable estimation of the aggregation number for this system. The dimensions of the simulation box and the thickness of the water slab were large enough to ensure: the proper sampling of the interface; that the periodic images of the system did not interact significantly in the z direction; and that the in-plane interactions of the aggregate with its periodic images were negligible (the simulations were conducted at an area $> 0.50\,\mathrm{nm^2\,molecule^{-1}}$; specifically, at $0.5776\,\mathrm{nm^2\,molecule^{-1}}$ (2500 F8H16 on a 38 nm × 38 nm surface), essentially at null surface pressure). A snapshot of a typical simulation box displaying the water layer and a hemimicelle is shown in Figure A.3.

The systems were modelled using one of three FFs: an atomistic force field based on the OPLS–AA framework [45–47] (for the OPLS–AA FF the details of the MD simulations are described elsewhere [27]; this is referred to as OPLS–AA aggregate); the united atom TraPPE FF for the CH [48] and CF [49][1] segments of the PFAA molecules (TraPPE aggregate); the TraPPE FF with added point partial charges at the 2 groups comprising the CH_2-CF_2 bond to mimic a dipole (TraPPE + dipole aggregate). The dipole moment magnitude μ for a pair of equal point charges q but with opposite signs, separated by a distance l, is given by $\mu = ql$ [50]. The length of the CH_2-CF_2 bond is 0.154 nm in the TraPPE FF and a dipole moment of 2.8 D

[1]Note: two FF models are provided in this article; the one labelled "model-T" was used.

was chosen. This value is quite large (for comparison the dipole moment of water is 1.85 D), and was chosen based on a literature survey and is in line with our own quantum calculations. Thus, the magnitude of the point charges placed at the CH_2 and CF_2 groups was fixed at 0.3785 e, with opposite signs.

Within the UA TraPPE FF, each of the CH_3, CH_2, CF_2 and CF_3 groups is represented by a single interaction centre or pseudoatom. These interact exclusively through dispersion forces, which are modelled by Lennard-Jones (LJ) potentials. Only atoms separated by more than 3 bonds or belonging to different molecules interact through dispersion interactions. The C–H chemical bonds and, in the case of the water molecules also the bond angles, are constrained to their equilibrium positions using the LINCS algorithm [51]. The potential energy varies with the dihedral angles according to a Fourier series (truncated after the 3rd term) or a truncated cosine power series (up to the 7th degree term), for the CH and CF chains, respectively. A cutoff of 1.4 nm and Particle-mesh Ewald (PME) calculations were used for both dispersion and electrostatic interactions. The unlike dispersion interactions are calculated using the Langmuir-Blodgett (LB) combining rules, according to the TraPPE FF, except for the interactions between hydrogenated and fluorinated pseudoatoms. In those cases, the unlike interaction energy (ε_{HF}) is reduced by 11 % and the unlike interaction size (σ_{HF}) is increased by 1 % relative to the values calculated using the LB combining rules to account for the large positive excess volumes and the immiscibility envelope of mixtures of alkanes and perfluoroalkanes [52, 53]. In the case of the OPLS–AA FF the unlike dispersion interactions are calculated using geometric combining rules, except for the interactions between hydrogenated and fluorinated atoms; the unlike energy interaction (ε_{HF}) is reduced by 23 % and the unlike size interaction (σ_{HF}) is increased by 3.5 %. As in previous work, the Extended Simple Point Charge (SPC/E) [54] water model was used for all systems. Although the purpose of this work did not include testing different water models, a simulation run was made using the TIP4P/2005. The obtained hemimicelle displays a similar structure as those simulated over SPC/E water (Figure A.4). All used parameters are collected in Section A.2 of Appendix A.

The simulations were performed using the Groningen Machine for Chemical Simulation (GROMACS) (version 2020.6) [55] open-source software. The simulation conditions and remaining algorithms are the same as those used before for the simulations of the OPLS aggregate [27]. For some of the simulations, a planar and non-deformable water surface has been generated by restraining the water molecules to a well-defined layer in the z direction. This was achieved by subjecting the water molecules to a position dependent potential, that is zero in the central region of the layer and then increases steeply, according to a harmonic function (force constant $= 1000\,\mathrm{kJ\,mol^{-1}\,nm^{-1}}$), as the frontiers of the slab are reached. The width of the slab was chosen according to the experimental density of water. The simulation trajectories were analysed using GROMACS built-in capabilities, in-house written programs and, for the computation of Spacial Distribution Functions (SDFs), the open-source software Trajectory Analyzer and Visualizer (TRAVIS) (version May 4, 2020) [56, 57]. The snapshots of the simulations were rendered using the open-source web viewer Mol* [58] and the SDFs' representations were obtained using the Visual Molecular Dynamics (VMD) (version 1.9.4) [59] open-source software.

8.3 Results and discussion

8.3.1 Simulation results: aggregate morphology

Height profiles of hemimicelles computed from the MD simulations using the three different models are presented in Fig. 8.2. The morphology of the hemimicelle obtained using the OPLS FF (model including electrostatics), shown as a red line, is identical to that previously reported and described in detail [27]. As can be seen, it has an approximately circular dome shape, a diameter of (31.5±0.1) nm and displays a sharp deep central pit, (1.44±0.09) nm deep. Within the aggregate, the molecules are packed in a pseudo-hexagonal lattice, with the perfluorinated segments oriented away from the water surface. These features are in quantitative agreement with experimental results, obtained with a variety of techniques (AFM, GIXD, Grazing Incidence Small Angle X-Ray Scattering (GISAXS)) [27]. The shape of the simulated hemimicelle is compared with an experimental AFM image in Figure A.1 of Appendix A. The simulated X-ray diffraction spectrum was found to be in excellent agreement with that experimentally obtained by GIXD, fully validating the simulation methodology. The two spectra are shown in Figure A.2 of Appendix A.

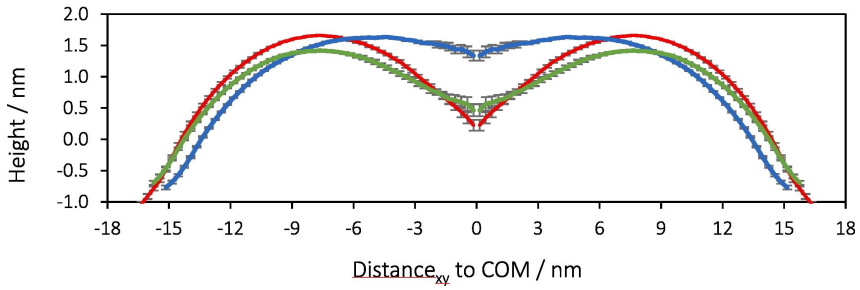

Figure 8.2: Height profile as a function of the distance in the x0y plane (Distance$_{xy}$) to the centre of mass (COM) of each aggregate: OPLS aggregate (red); TraPPE aggregate (blue); TraPPE + dipole aggregate (green). The height is defined relative to the height of the COM and the water molecules are excluded from the analysis. The total simulation production time was 20 ns. The error bars were estimated from 2 ns long block averages.

The height profile of the aggregate obtained with the TraPPE FF, which does not include electrostatic interactions, is also presented in Fig. 8.2 (blue line). The overall characteristics of the hemimicelle are quite similar to the previous one, namely the molecular orientation at the air–water interface and the circular shape. The diameter is slightly smaller, (29.7 ± 0.1) nm despite that the same number of molecules was used in the simulation. In this case, however, the sharp central pit is absent. Instead, a shallow depression ((0.30 ± 0.08) nm) is observed, which could be more easily perceived as a fluctuation or rugosity of the surface.

Finally, the height profile obtained for the aggregate simulated with the TraPPE + dipole FF can also be observed in Fig. 8.2 (green line). With this model the central pit is clearly recovered, although having a slightly shallower depth than that observed for the OPLS model ((0.95 ± 0.10) nm). The hemimicelle displays the same diameter ((31.4 ± 0.1) nm) and a very similar morphology to the OPLS aggregate, although the curvature and volume of the toroidal cavity under the hemimicelle (see Fig. 8.3) are slightly less pronounced.

Representative snapshots of the final state of the MD simulations are presented in Fig. 8.3 for the three models. Side views of cross-sections cut through the middle of the hemimicelles are presented. These visually illustrate the features quantitatively obtained from the analysis of the MD simulation trajectories. The pit at the centre of the hemimicelle obtained using the OPLS FF is well seen. In the case of the aggregate obtained with the TraPPE FF, the hemimicelle is essentially flat, although a shallow depression at the centre is visible. The (TraPPE + dipole) aggregate is very similar to the OPLS aggregate, although it is seen that the volume of the cavity is less pronounced, as previously described. However, the important observation is the presence of a central pit. It is worth noting that additional simulation runs were conducted to test and assure the inter-conversion of pit-less hemimicelles to hemimicelles with a pit and vice-versa. Pit-less hemimicelles, obtained from a TraPPE simulation, developed a pit after including the dipole, which disappeared once the dipole was removed. Two animations are included as Supplementary Information in which a sequence of snapshots is presented showing the formation and disappearance of the pit.[2] In the first case the pit-less hemimicelle obtained with the TraPPE FF was used as initial configuration. When the dipole is introduced, the evolution of the system is clearly seen: the pit fully forms in approximately 1 ns to 2 ns and remains during another 6 ns. When the dipole is removed the hemimicelles recover their initial pit-less form in approximately the same simulation time.

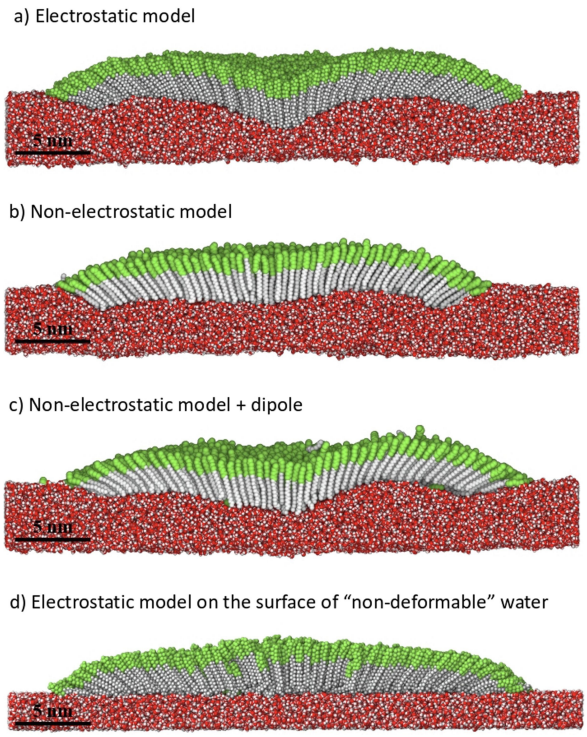

Figure 8.3: Representative snapshots of the final state of the MD simulation trajectories, illustrating a side view of a cross-section cut through the middle of the surface aggregates: a) Electrostatic model (OPLS); b) Non-electrostatic model (TraPPE); c) Non-electrostatic model + dipole (TraPPE + CH_2-CF_2 dipole); d) Electrostatic model at the surface of "non-deformable" water. Carbon atoms (OPLS) are coloured grey, fluorine atoms (OPLS) and fluorinated pseudoatoms (CF_2 and CF_3 groups in TraPPE) are coloured green and hydrogen atoms (OPLS) and hydrogenated pseudoatoms (CH_2 and CH_3 groups in TraPPE) are coloured white. Water molecules are coloured red and white (oxygen and hydrogen atoms, respectively).

Analysis of Fig. 8.3 provides an additional interesting and important information. As can be observed, the water molecules completely fill the cavity of the hemimicelle. Thus, a deformable liquid sub-phase seems to be essential to the formation of the pit. This hypothesis was tested running a simulation using the electrostatic model in which the movements of the water molecules

[2]These animations are freely available at https://doi.org/10.1016/j.jcis.2023.11.007 [online: 02/01/2024]. A sequence of snapshots representative of these animations is presented in Fig. A.5 of Appendix A.

were constrained to obtain a planar and non-deformable surface. As can be seen in Fig. 8.3d), in this case the pit did not form, confirming the hypothesis. These results are remarkable, as they demonstrate that electrostatics, in the form of the explicit dipole, associated to the possibility of deforming the surface of the sub-phase, are responsible for morphological characteristics of the aggregates at the mesoscale.

The results may help to explain the formation of PFAA hemimiceles at the surface of wet silicon wafers by spin coating, which was not fully understood [20]. Water remaining at the surface of the silicon wafer, could provide deformability to the surface (and thus the possibility of pit formation) and mobility to the PFAA molecules allowing the formation of the hemimicelles. However, this hypothesis should be tested in the future by carrying out simulations on a wet silicon surface. It is also known that traces of water can hinder the crystallisation of hydrogenated chains [60], a fact that in the case of the hydrogenated segments of the PFAA molecules could also contribute to the formation of the aggregates.

8.3.2 Simulation results: dipole–dipole interactions

To better understand and visualise the effect of the dipole–dipole interactions on the local organisation of the PFAA molecules, SDFs of the carbon atoms (or pseudoatoms in the case of the TraPPE simulations) at the CH_2-CF_2 junction were computed and are shown in Fig. 8.4.[3]

In the case of the OPLS aggregate (Fig. 8.4a), the molecules clearly display a preferential packing direction that favours the alignment of the CH_2-CF_2 dipole. Two regions of higher particle density can be seen in the vicinity of the PFAA molecules at the ends of the CH_2-CF_2 junction. This creates a misalignment between adjacent PFAA molecules along their principal molecular axes, relative to each other. This shift thus seems to be a direct consequence of the alignment of the CH_2-CF_2 dipoles of neighbouring molecules. More importantly, this shift gives rise to the curvature of the aggregate and is thus the origin of the dome and formation of the pit. This can be better visualised in a close up scheme shown in Fig. 8.5.

The SDF calculated for the TraPPE aggregate (Fig. 8.4b) shows that, in this case, molecules uniformly surround the reference molecule with nearly radial symmetry, without showing a preferential orientation, i.e. without aligning the CH_2-CF_2 junctions. Thus, no molecular shift occurs, as described for the OPLS aggregate. This explains the absence of a pit at the centre of the TraPPE aggregate.

Finally, the SDF computed for the (TraPPE + dipole) aggregate recovers, qualitatively, the results obtained for the OPLS aggregate. In this case, the molecules are again oriented in a way that promotes the alignment of the CH_2-CF_2 junctions, which now bear an explicit dipole of significant magnitude. Again, this alignment of the dipoles is accompanied by a shift of neighbouring molecules relatively to one another, leading to the formation of the pit at the centre of the (TraPPE + dipole) aggregate.

[3] Complementary visual representations of the SDFs obtained for the OPLS aggregate are presented in Appendix B, including for hemimicelles of different FnHm. These results are further discussed in Chapter 9.

8.3.3 Discussion

The MD simulation results, in particular the comparison between the results obtained using models with and without electrostatic forces, unambiguously demonstrate the alignment of the strong dipoles at the CH_2-CF_2 junction of PFAA molecules, with important structural consequences. The results also show that maximising the interactions between dipoles leads to a constant shift of the PFAA molecules relatively to one another. This shift, allied to the conical-like shape of the molecules (resulting from the different diameters of the hydrogenated and fluorinated segments), naturally gives rise to the curvature of the hemimicelle. Fig. 8.5 eloquently illustrates this relation. The deformation of the sub-phase surface then enables the formation of the central pit. In conclusion, the link between the localised molecular dipole and the central pit is established.

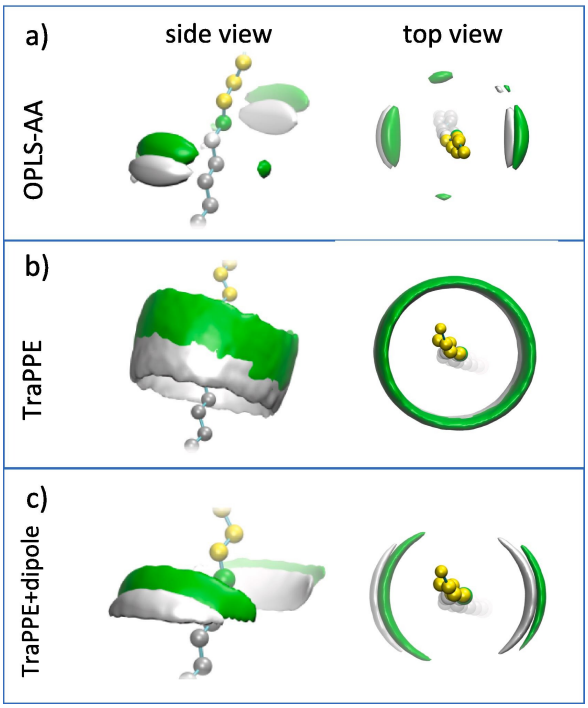

Figure 8.4: Spatial distribution functions (SDF) of the hydrogenated (white) and fluorinated (green) carbon atoms around the CH_2-CF_2 junction of a reference PFAA molecule, simulated using a) OPLS-AA, b) TraPPE, c) TraPPE + dipole; (left image) side view; (right image) top view, along approximately the principal axis of the reference molecule. The remaining carbon atoms of the reference molecule are coloured silver and yellow. The contour surfaces envelop the regions in space where the probability of finding the selected atoms within the aggregate is highest. The images show that when a dipole is present, neighbour molecules surround the reference molecule along preferential directions, correctly oriented. When no dipole exists, molecules pack without any preferential directions.

The results obtained with the TraPPE FF, namely the formation of aggregates and the observation of a central shallow depression/fluctuation, provide important information to understand the very formation of the hemimicelles. First of all, the fact that the non-electrostatic model also predicts the formation of hemimicelles proves that these forces are not essential to the aggregation process. This result corroborates those of Yadav *et al.* [28] who also use a non-electrostatic CG FF. Secondly, having established the link between the dipoles and the central pit, one could expect that in the absence of electrostatic interactions or dipoles, the surface of the aggregates should be completely flat. This is in fact not true, as a flat surface would imply the stability of a continuous and homogeneous monolayer of PFAA molecules, consequently, no spontaneous formation of hemimicelles. The observed fluctuations are likely the result of local tilting of the molecules relatively to one another when in contact, adding cohesion to the otherwise less dense layer of hydrogenated chains. As can be seen, the fluctuations are mainly observed on the central part of the aggregate, while on the borders, the curvature of the hemimicelle inherently approaches the hydrogenated chains.

The present results further demonstrate that the tendency to spontaneously form finite aggregates is directly related to molecular shape, with the additional contribution of a number of factors related to the properties of each type of segment: 1 – the relative hydrophobicity of the hydrogenated and perfluorinated segments. 2 – the mutual phobicity between hydrogenated and perfluorinated segments. 3 – the enhanced tendency of perfluorinated chains to crystallise [61, 62]. The self-assembling process is finally "crowned" by the formation of the pit, following the alignment of the dipoles and the deformation of the sub-phase surface.

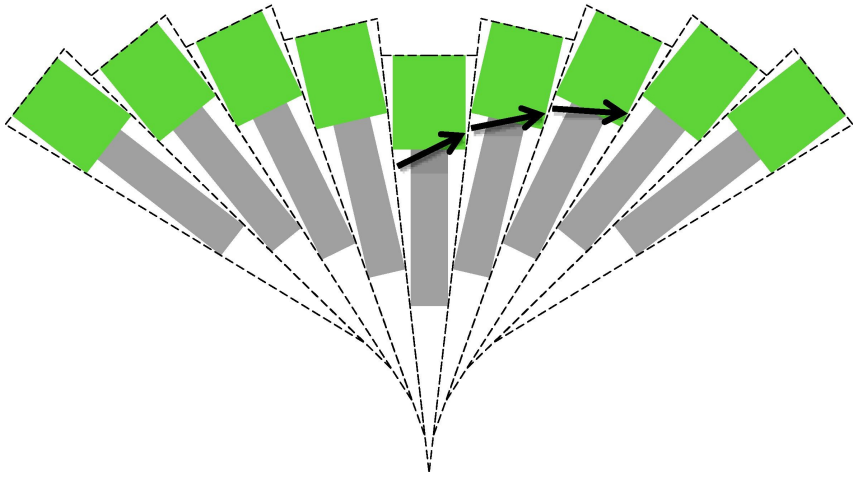

Figure 8.5: Geometrical relation between the conical-like shape of the PFAA molecules, the shift of the molecules relatively to each other, trying to align the dipoles at the CH_2-CF_2 junctions, and the consequent development of the dome's curvature and formation of the central pit. The green and grey rectangles represent the fluorinated and the hydrogenated chains, respectively (not to scale). The dashed lines purport the conical shape of the PFAA molecules; the water molecules are not represented.

8.4 Conclusions

The spontaneous formation of PFAA hemimicelles remained a perplexing yet fascinating self-assembling process since the aggregates were first observed [1, 2, 20] and despite all efforts to rationalise it [22–26]. Recently MD simulations succeeded to reproduce the process, supporting a rational justification for the first time [27, 28], but the peculiar shape of the aggregates, namely the sharp central pit, although reproduced by the simulations, remained unexplained.

We now show, using atomistic MD simulations with a FF that includes electrostatic forces (implicit dipole), that the strong molecular dipoles located at the CH_2-CF_2 junctions tend to align, leading to a systematic shift of the PFAA molecules relatively to one another. This systematic shift, allied to the conical-like molecular shape, naturally develops the curvature of the hemimicelles and ultimately originates the central pit if the sub-phase is deformable. MD simulations using a non-electrostatic force field do not reproduce the central pit, in agreement with literature results [28], but nevertheless contribute to understand the origin of the self-assembling process.

A direct link between a specific molecular dipole and the morphology of the supramolecular aggregates has thus been established. Previous visions about the role of the dipole have been considerably expanded [34, 35].

It should be emphasised that the dipole is localised at the centre of an essentially apolar, relatively long, linear chain of 24 carbon atoms. Aligning and maximising these dipole–dipole interactions suffice to trigger a collective shift and reorganisation of approximately 3000 molecules and deform the surface of the liquid sub-phase, which can be considered remarkable. The resulting shape of the hemimicelle, with a sharp central pit, is now fully understood.

Linking a specific molecular property to a mesoscopic-scale observation on a self-assembled system is not frequent, as molecular interactions are often interdependent and difficult to isolate. In this case, a judicious use of MD simulations allows isolating the different physical contributions, and the simple molecular structure of the PFAA "primitive surfactants" definitely contributes to build a clear structure–property relationship.

The ultimate goal of this project is controlling and designing the formation of the PFAA hemimicelles and related systems. Understanding the role of the dipole and the interactions with the sub-phase is an obvious important step. Our on-going investigations are now focused on demonstrating the influence of relative chain length of the hydrogenated and fluorinated segments on the size and shape of the hemimicelles. Aggregates formed by mixtures of amphiphiles and their diffusion within the hemimicelles, are also being studied. Finally, efforts to functionalise the hemimicelles for specific purposes are underway. These questions will be addressed in future communications.

References

[1] M. Maaloum, P. Muller and M. P. Krafft. 'Monodisperse Surface Micelles of Nonpolar Amphiphiles in Langmuir Monolayers'. In: *Angewandte Chemie – International Edition* 41.22 (2002), pp. 4331–4334. DOI: 10.1002/1521-3773(20021115)41:22<4331::AID-ANIE4331>3.0.CO;2-J.

[2] A. L. S. Gamboa, E. J. M. Filipe and P. Brogueira. 'Nanoscale Pattern Formation in Langmuir-Blodgett Films of a Semifluorinated Alkane and a Polystyrene-Poly(Ethylene Oxide) Diblock Copolymer'. In: *Nano Letters* 2.10 (2002), pp. 1083–1086. DOI: 10.1021/nl025698o.

[3] M. P. Krafft and J. G. Riess. 'Chemistry, Physical Chemistry, and Uses of Molecular Fluorocarbon-Hydrocarbon Diblocks, Triblocks, and Related Compounds – Unique "Apolar" Components for Self-Assembled Colloid and Interface Engineering'. In: *Chemical Reviews* 109.5 (2009), pp. 1714–1792. DOI: 10.1021/cr800260k.

[4] C. Tsagogiorgas et al. 'Impact of different emulsifiers on biocompatibility and inflammatory potential of Perfluorohexyloctane (F6H8) emulsions for new intravenous drug delivery systems'. In: *Drug Design, Development and Therapy* 13 (2019), pp. 2097–2110. DOI: 10.2147/DDDT.S195954.

[5] M. P. Krafft and J. G. Riess. 'Selected physicochemical aspects of poly- and perfluoroalkylated substances relevant to performance, environment and sustainability–Part one'. In: *Chemosphere* 129 (2015), pp. 4–19. DOI: 10.1016/j.chemosphere.2014.08.039.

[6] M. P. Krafft. 'Large Organized Surface Domains Self-Assembled from Nonpolar Amphiphiles'. In: *Accounts of Chemical Research* 45.4 (2012), pp. 514–524. DOI: 10.1021/ar200178a.

[7] J. H. Simons and R. D. Dunlap. 'The Properties of *n*-Pentforane and Its Mixtures with *n*-Pentane'. In: *Journal of Chemical Physics* 18.3 (1950), pp. 335–346. DOI: 10.1063/1.1747628.

[8] S. Brode and I. R. McDonald. 'Excess thermodynamic properties of liquid mixtures of methane and perfluoromethane'. In: *Molecular Physics* 65.4 (1988), pp. 1007–1012. DOI: 10.1080/00268978800101561.

[9] C. Duce et al. 'VLE and LLE of perfluoroalkane + alkane mixtures'. In: *Fuid Phase Equilibria* 199.1–2 (2002), pp. 197–212. DOI: 10.1016/S0378-3812(01)00815-9.

[10] P. Morgado, L. F. G. Martins and E. J. M. Filipe. 'From nano-emulsions to phase separation: evidence of nano-segregation in (alkane + perfluoroalkane) mixtures using ^{129}Xe NMR Spectroscopy'. In: *Physical Chemistry Chemical Physics* 21.7 (2019), pp. 3742–3751. DOI: 10.1039/c8cp06509h.

[11] P. Morgado et al. 'Viscosity of liquid systems involving hydrogenated and fluorinated substances: Liquid mixtures of (hexane + perfluorohexane)'. In: *Fluid Phase Equilibria* 358 (2013), pp. 161–165. DOI: 10.1016/j.fluid.2013.07.060.

[12] T. Handa and P. Mukerjee. 'Surface Tensions of Nonideal Mixtures of Fluorocarbons and Hydrocarbons and Their Interfacial Tensions against Water'. In: *Journal of Physical Chemistry* 85.25 (1981), pp. 3916–3920. DOI: 10.1021/j150625a042.

[13] P. Morgado et al. 'Alkane Coiling in Perfluoroalkane Solutions: A New Primitive Solvophobic Effect'. In: *Langmuir* 33.42 (2017), pp. 11429–11435. DOI: 10.1021/acs.langmuir.7b02516.

[14] P. Morgado et al. 'Liquid Mixtures Involving Hydrogenated and Fluorinated Alcohols: Thermodynamics, Spectroscopy, and Simulation'. In: *Journal of Physical Chemistry B* 120.38 (2016), pp. 10091–10105. DOI: 10.1021/acs.jpcb.6b04297.

[15] C. Yan and M. F. Paige. 'Pattern Formation in Phase-Separated Langmuir and Langmuir Monolayer Films'. In: *Langmuir* 37.28 (2021), pp. 8357–8369. DOI: 10.1021/acs.langmuir.1c00642.

[16] M. P. Turberg and J. E. Brady. 'Semifluorinated hydrocarbons: primitive surfactant molecules'. In: *Journal of the American Chemical Society* 110.23 (1988), pp. 7797–7801. DOI: 10.1021/ja00231a034.

[17] J. Höpken et al. 'Melting, crystallization, and solution behavior of chain molecules with hydrocarbon and fluorocarbon segments'. In: *Makromolekulare Chemie – Macromolecular Chemistry and Physics* 189.4 (1988), pp. 911–925. DOI: 10.1002/macp.1988.021890422.

[18] B. P. Binks et al. 'Adsorption and Aggregation of Semifluorinated Alkanes in Binary and Ternary Mixtures with Hydrocarbon and Fluorocarbon Solvents'. In: *Langmuir* 13.25 (1997), pp. 6669–6682. DOI: 10.1021/la970408i.

[19] P. Morgado, J. Barras and E. J. M. Filipe. 'From nano-seggregation to mesophases: probing the liquid structure of perfluoroalkylalkanes with ^{129}Xe NMR spectroscopy'. In: *Physical Chemistry Chemical Physics* 22.26 (2020), pp. 14736–14747. DOI: 10.1039/d0cp02123g.

[20] L. Bardin et al. 'Highly organized crystalline monolayer of a semi-fluorinated alkane on a solid substrate obtained by spin-coating'. In: *Thin Solid Films* 519.1 (2010), pp. 414–416. DOI: 10.1016/j.tsf.2010.07.065.

[21] L. Bardin et al. 'Long-Range Nanometer-Scale Organization of Semifluorinated Alkane Monolayers at the Air/Water Interface'. In: *Langmuir* 27.22 (2011), pp. 13497–13505. DOI: 10.1016/10.1021/la201802x.

[22] P. Fontaine et al. 'Evidence for Interaction with the Water Subphase As the Origin and Stabilization of Nano-Domain in Semi-Fluorinated Alkanes Monolayer at the Air/Water Interface'. In: *Langmuir* 30.50 (2014), pp. 15193–15199. DOI: 10.1021/la5038124.

[23] C. G. Lux et al. 'Stacking of Self-Assembled Surface Micelles in Ultrathin Films'. In: *ChemPhysChem* 13.6 (2012), pp. 1454–1462. DOI: 10.1002/cphc.201101030.

[24] C. G. Lux et al. 'Compression of Self-Assembled Nano-Objects: 2D/3D Transitions in Films of (Perfluoroalkyl)Alkanes – Persistence of an Organized Array of Surface Micelles'. In: *Chemistry – A European Journal* 16.24 (2010), pp. 7186–7189. DOI: 10.1002/chem.200903535.

[25] X. Liu et al. '2D Spherulites of a Semi-Fluorinated Alkane: Controlled Access to Either Radial Or Ring-Banded Morphologies'. In: *ChemPhysChem* 19.1 (2018), pp. 29–33. DOI: 10.1002/cphc.201701064.

[26] P. Fontaine et al. 'Evidence of lying molecules in the structure of the most condensed phase of semi-fluorinated alkane monolayers'. In: *Nanoscale* 10.5 (2018), pp. 2310–2316. DOI: 10.1039/c7nr07415h.

[27] G. M. C. Silva et al. 'Spontaneous self-assembly and structure of perfluoroalkylalkane surfactant hemimicelles by molecular dynamics simulations'. In: *Proceedings of the National Academy of Sciences of the United States of America* 116.30 (2019), pp. 14868–14873. DOI: 10.1073/pnas.1906782116.

[28] H. O. S. Yadav et al. 'Hemimicelle formation of semi-fluorocarbon chains at air–water interface: coarse-grained molecular dynamics study with an extension of the SPICA force field'. In: *Molecular Physics* 119.19–20 (2021), Article No. e1910355. DOI: 10.1080/00268976.2021.1910355.

[29] R. G. Shulman, B. P. Dailey and C. H. Townes. 'Molecular Dipole Moments and Stark Effects. III. Dipole Moment Determinations'. In: *Physical Review* 78.2 (1950), pp. 145–148. DOI: 10.1103/PhysRev.78.145.

[30] A. El Abed et al. 'Experimental evidence for an original two-dimensional phase structure: An antiparallel semifluorinated monolayer at the air-water interface'. In: *Physical Review E* 65.5 (2002), Article No. 051603. DOI: 10.1103/PhysRevE.65.051603.

[31] A. El Abed et al. 'Assembling and compressing a semifluorinated alkane monolayer on a hydrophobic surface: Structural and dielectric properties'. In: *Physical Review E* 70.5 (2004), Article No. 051607. DOI: 10.1103/PhysRevE.70.051607.

[32] M. Broniatowski et al. 'Langmuir Monolayers Characteristic of (Perfluorodecyl)-Alkanes'. In: *Journal of Physical Chemistry B* 108.35 (2004), pp. 13403–13411. DOI: 10.1021/jp0402481.

[33] P. Dynarowicz-Łątka et al. 'Structural Investigation of Langmuir and Langmuir–Blodgett Monolayers of Semifluorinated Alkanes'. In: *Journal of Physical Chemistry B* 110.12 (2006), pp. 6095–6100. DOI: 10.1021/jp057270u.

[34] P. Morgado et al. 'Vapor Pressure of Perfluoroalkylalkanes: The Role of the Dipole'. In: *Journal of Physical Chemistry B* 119.4 (2015), pp. 1623–1632. DOI: 10.1021/jp5109448.

[35] A. N. Semenov et al. 'Theory of Surface Micelles of Semifluorinated Alkanes'. In: *Langmuir* 22.21 (2006), pp. 8703–8717. DOI: 10.1021/la060638+.

[36] P. Morgado et al. 'Liquid Phase Behavior of Perfluoroalkylalkane Surfactants'. In: *Journal of Physical Chemistry B* 111.11 (2007), pp. 2856–2863. DOI: 10.1021/jp063136d.

[37] P. Morgado et al. 'Systems Involving Hydrogenated and Fluorinated Chains: Volumetric Properties of Perfluoroalkanes and Perfluoroalkylalkane Surfactants'. In: *Journal of Physical Chemistry B* 115.50 (2011), pp. 15013–15023. DOI: 10.1021/jp207567y.

[38] P. Morgado et al. 'Viscosity of Liquid Perfluoroalkanes and Perfluoroalkylalkane Surfactants'. In: *Journal of Physical Chemistry B* 115.29 (2011), pp. 9130–9139. DOI: 10.1021/jp201364k.

[39] P. Morgado et al. 'SAFT-γ force field for the simulation of molecular fluids: 8. Hetero-segmented coarse-grained models of perfluoroalkylalkanes assessed with new vapour–liquid interfacial tension data'. In: *Molecular Physics* 114.18 (2016), pp. 2597–2614. DOI: 10.1080/00268976.2016.1218077.

[40] P. Morgado et al. 'Solution Behavior of Perfluoroalkanes and Perfluoroalkylalkane Surfactants in n-Octane'. In: *Journal of Physical Chemistry C* 111.43 (2007), pp. 15962–15968. DOI: 10.1021/jp073758e.

[41] P. Morgado et al. 'Perfluoroalkanes and perfluoroalkylalkane surfactants in solution: Partial molar volumes in n-octane and hetero-SAFT-VR modelling'. In: *Fluid Phase Equilibria* 306.1 (2011), pp. 76–81. DOI: 10.1016/j.fluid.2011.02.020.

[42] P. Morgado, J. Barras and E. J. M. Filipe. 'Solubility of water in perfluoroalkylalkanes surfactants: Evidence of specific interaction between water and the surfactant molecule'. In: *Fluid Phase Equilibria* 522 (2020), Article No. 112754. DOI: 10.1016/j.fluid.2020.112754.

[43] P. Morgado, J. Gaspar and E. J. M. Filipe. 'Liquid–liquid interfaces: Water–perfluoroalkanes and water–perfluoroalkylalkanes, experimental interfacial tensions and molecular simulation'. In: *Journal of Molecular Liquids* 312 (2020), Article No. 113385. DOI: 10.1016/j.molliq.2020.113385.

[44] L. Martínez et al. 'PACKMOL: A Package for Building Initial Configurations for Molecular Dynamics Simulations'. In: *Journal of Computational Chemistry* 30.13 (2009), pp. 2157–2164. DOI: 10.1002/jcc.21224.

[45] W. L. Jorgensen, D. S. Maxwell and J. Tirado-Rives. 'Development and Testing of the OPLS All-Atom Force Field on Conformational Energetics and Properties of Organic Liquids'. In: *Journal of the American Chemical Society* 118.45 (1996), pp. 11225–11236. DOI: 10.1021/ja9621760.

[46] E. K. Watkins and W. L. Jorgensen. 'Perfluoroalkanes: Conformational Analysis and Liquid-State Properties from ab Initio and Monte Carlo Calculations'. In: *Journal of Physical Chemistry A* 105.16 (2001), pp. 4118–4125. DOI: 10.1021/jp004071w.

[47] S. W. I. Siu, K. Pluhackova and R. A. Böckmann. 'Optimization of the OPLS-AA Force Field for Long Hydrocarbons'. In: *Journal of Chemical Theory and Computation* 8.4 (2012), pp. 1459–1470. DOI: 10.1021/ct200908r.

[48] M. G. Martin and J. Ilja Siepmann. 'Transferable Potentials for Phase Equilibria. 1. United-Atom Description of *n*-Alkanes'. In: *Journal of Physical Chemistry B* 102.14 (1998), pp. 2569–2577. DOI: 10.1021/jp972543+.

[49] S.T. Cui et al. 'Intermolecular potentials and vapor–liquid phase equilibria of perfluorinated alkanes'. In: *Fluid Phase Equilibria* 146.1 (1998), pp. 51–61. DOI: 10.1016/S0378-3812(98)00216-7.

[50] J. N. Israelashvili. *Intermolecular and Surface Forces*. 2nd ed. ISBN 0123751810. San Diego, C, USA: Academic Press, 1991. ISBN: 0123751810.

[51] B. Hess. 'P-LINCS: A Parallel Linear Constraint Solver for Molecular Simulation'. In: *Journal of Chemical Theory and Computation* 4.1 (2008), pp. 116–122. DOI: 10.1021/ct700200b.

[52] L. Zhang and J. I. Siepmann. 'Pressure Dependence of the Vapor–Liquid–Liquid Phase Behavior in Ternary Mixtures Consisting of *n*-Alkanes, *n*-Perfluoroalkanes, and Carbon Dioxide'. In: *Journal of Physical Chemistry B* 109.7 (2005), pp. 2911–2919. DOI: 10.1021/jp0482114.

[53] P. Morgado, C. McCabe and E. J. M. Filipe. 'Modelling the phase behaviour and excess properties of alkane + perfluoroalkane binary mixtures with the SAFT–VR approach'. In: *Fluid Phase Equilibria* 228 (2005), pp. 389–393. DOI: 10.1016/j.fluid.2004.08.002.

[54] H. J. C. Berendsen, J. R. Grigera and T. P. Straatsma. 'The Missing Term in Effective Pair Potentials'. In: *Journal of Physical Chemistry* 91.24 (1987), pp. 6269–6271. DOI: 10.1021/j100308a038.

[55] M. J. Abraham et al. 'GROMACS: High performance molecular simulations through multi-level parallelism from laptops to supercomputers'. In: *SoftwareX* 1–2 (2015), pp. 19–25. DOI: 10.1016/j.softx.2015.06.001.

[56] M. Brehm and B. Kirchner. 'TRAVIS - A Free Analyzer and Visualizer for Monte Carlo and Molecular Dynamics Trajectories'. In: *Journal of Chemical Information and Modeling* 51.8 (2011), pp. 2007–2023. DOI: 10.1021/ci200217w.

[57] M. Brehm et al. 'TRAVIS–A free analyzer for trajectories from molecular simulation'. In: *Journal of Chemical Physics* 152.16 (2020), Article No. 164105. DOI: 10.1063/5.0005078.

[58] D. Sehnal et al. 'Mol* Viewer: modern web app for 3D visualization and analysis of large biomolecular structures'. In: *Nucleic Acids Research* 49.W1 (2021), W431–W437. DOI: 10.1093/nar/gkab314.

[59] W. Humphrey, A. Dalke and K. Schulten. 'VMD: Visual Molecular Dynamics'. In: *Journal of Molecular Graphics & Modelling* 14.1 (1996), pp. 33–38. DOI: 10.1016/0263-7855(96)00018-5.

[60] Y. Qiu and V. Molinero. 'Strength of Alkane-Fluid Attraction Determines the Interfacial Orientation of Liquid Alkanes and Their Crystallization through Heterogeneous or Homogeneous Mechanisms'. In: *Crystals* 7.3 (2017), p. 86. DOI: 10.3390/cryst7030086.

[61] P. Silva et al. 'Langmuir Films of Perfluorinated Fatty Alcohols: Evidence of Spontaneous Formation of Solid Aggregates at Zero Surface Pressure and Very Low Surface Density'. In: *Nanomaterials* 10.11 (2020), Article No. 2257. DOI: 10.3390/nano10112257.

[62] P. Fontaine et al. 'Structure of Langmuir Monolayers of Perfluorinated Fatty Acids: Evidence of a New 2D Smectic C Phase'. In: *Molecules* 24.19 (2019), Article No. 3590. DOI: 10.3390/molecules24193590.

Chapter 9

Modelling the internal structure and size of PFAA hemimicelles

It is well established that PFAAs form stable Langmuir films at the air–water interface. These films are nanostructured, comprising discrete domains (surface aggregates or hemimicelles). As was discussed in the previous chapter, the hemimicelles are monodisperse, round-shaped and display a characteristic pit in their centre. Herein, the influence of the CH and the CF chain lengths on the size of the hemimicelles is probed by a systematic MD simulations study. The results are further rationalised in terms of model describing the internal structure of the hemimicelles, based on geometrical considerations.

9.1 Introduction

The structure of the Langmuir films of PFAAs has been a subject of controversy and active investigation for decades [1–7]. It has been well established that they are not homogeneous and, in fact, comprise discrete, monodisperse surface aggregates or hemimicelles. The monodispersity of the hemimicelles suggests a correlation between hemimicelle size and molecular structure [8]. Early observations of these self-assembling structures were indicative that the size of the hemimicelles is essentially determined by the lengths of the CH and CF chains of their constituent molecules and is relatively unaffected by changes in Surface Pressure (π) [3, 9].

As it was mentioned in Section 4.10, the literature provides examples of efforts to rationalise the formation, structure and size (the diameter or D) of the hemimicelles of PFAAs as a function of the CH and CF chains lengths [8, 9]. Zhang *et al.* have provided a model that adequately conveys that the CH chain length impacts D more than the CF chain length, but it falls short in detailing the hemimicelles' internal structure [9]. Gallyamov *et al.* rationalise the packing of the PFAA molecules according to a model that explicitly considers the existence of a pit-like feature in the centre of the hemimicelles, but it also considers that the CF chains are tightly and vertically packed and that varying their length does not impact D at all, which are claims that are not consistent with available experimental evidence [8]. A recent MD simulation study has also provided insights on this matter, but using a CG FF that didn't consider explicit electrostatic interactions [10]. As it was demonstrated in the previous chapter, these are paramount for the

detailed description of the self-assembled supramolecular structures that ultimately arise from them, namely the existence of a central pit in the hemimicelles. Moreover, the authors mention that the size of the aggregates is determined by the PFAA molecules' chains lengths, but don't provide a rationale for it, and only aggregates of one type of PFAA (F8H16) were studied, so the effect of varying n and/or m in FnHm was left untapped.

In a recent study, the formation and internal structure of F8H16 surface aggregates was studied by MD simulations using an AA FF considering explicit electrostatic interactions [11, 12]. This was the starting point for the work presented herein. The investigations were extended to systems of PFAAs with different CH and CF chains lengths. The effects of molecular architecture on the size and morphology of the hemimicelles are thus elucidated. Combining information from the different simulated systems, a model is proposed relating those variables with the hemimicelles' size, based on geometric arguments to describe the packing of the PFAA molecules.

9.2 Methods

The simulation conditions are the same as those described in Section 8.2 of the previous chapter (OPLS–AA aggregate), to which the reader is referred for further details, with the exception that the production NVT production runs were typically 10 ns to 12 ns-long (minimum 8 ns or 4 2 ns-long blocks for analysis).

The preparation of the initial configurations also followed the procedure described in the previous chapter and in a former publication [11]. Briefly, in all cases, this consists in placing the vertically aligned, cylinder-packed PFAA molecules (prepared using the open-source software Packmol (v. 20.2.2) [13]) near one of the surfaces of an equilibrated water slab with their CH chains facing the water surface. In the case of the surface aggregates of F8H14, these were simulated in increasing order of number of molecules, starting by simulating an aggregate of 100 molecules. This was carried on until an average molecular azimuthal angle ($\bar{\theta}_{\mathrm{Az}}$) of 0° was attained, specifically for an aggregate of 1700 molecules. As has been presented before [11] and is further discussed in Section 9.3, this is a reasonable way of estimating the limit size of the hemimicelles of PFAAs formed at the air–water interface. For the remaining aggregates, an estimation of their limit diameter and aggregation number were obtained based on the geometrical model described below. This way, these aggregates were studied by performing standalone simulations, *i.e.* starting from an initial configuration with the estimated aggregation number. It was confirmed that the $\bar{\theta}_{\mathrm{Az}}$ for such aggregates was 0° within a reasonable margin of error, as is discussed in Section 9.3 (and further simulations with a different number of molecules were performed until that condition was satisfied), being thus considered limit-size hemimicelles.

All the analyses were performed using GROMACS (v. 5.0.3 [14]) built-in functions and in-house written Python (v. 3.10) programs, part of which are credited to Gonçalo Silva. These programs draw extensively from the following packages: Numpy (v. 1.26.3 [15, 16]), pandas (v. 2.0.1 [17, 18]), Matplotlib (v. 3.7.1 [19, 20]), MDAnalysis (v. 2.6.1 [21–23]). The diffraction patterns calculated from the simulation trajectories were obtained using a modified version of Pedro Lourenço's program [11, 24]. The snapshots of the simulations were rendered using the VMD open-source software package (v. 1.9.3, 2016 [25], including those of the SDFs presented in Appendix B (computed using the open-source TRAVIS software (version May 4 2020 [26, 27])).

9.3 Results and Discussion

9.3.1 Surface aggregates of F8H14 with varying numbers of molecules

Part of the simulations presented in this Subsection were performed in the scope of the MSc Thesis of the author of the present document, whose results can be found in Reference [28].

9.3.1.1 Mean azimuthal angle ($\bar{\theta}_{Az}$)

When aggregates containing a number of PFAA molecules below that corresponding to a limit-size aggregate (equivalent to the experimentally observed hemimicelles), the molecules are arranged in a spiral relative to one another. This is quantified by the average azimuthal angle ($\bar{\theta}_{Az}$), defined as the average angle between the PFAA molecules' end-to-end vector (projected on the xy plane) and the radius of the aggregate, as schematised on the inset of Figure 9.1. The same methodology was used to perform a series of MD simulations of surface aggregates with varying numbers of F8H14 molecules. The obtained results of $\bar{\theta}_{Az}$ as a function of the diameter of the F8H14 aggregates (D_{agg}) are presented in Figure 9.1. D_{agg} and all values of aggregate or hemimicelle diameter reported herein were calculated from the MD simulation trajectories by estimating the top-view surface area of the aggregates and back-calculating the diameter of a circle with the same area [11, 28].

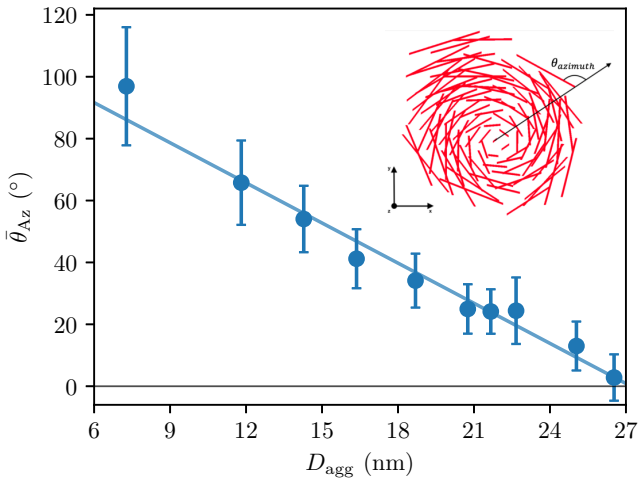

Figure 9.1: Mean azimuthal angle ($\bar{\theta}_{Az}$) as a function of the diameter of the simulated F8H14 aggregates (D_{agg}). The inset illustrates the definition of $\bar{\theta}_{Az}$ (adapted from [12]. The error bars correspond to one standard deviation, similarly to what is presented in Table 9.2. The weighted linear regression line is given by the equation $\bar{\theta}_{Az} = -4.321 \times D_{agg} + 117.6$ ($R^2 = 0.971$), the weights being taken as the inverse of the standard deviation.

It is clear that $\bar{\theta}_{Az}$ decreases linearly with D_{agg}, for the simulated surface aggregates of F8H14. The largest simulated aggregate had $D_{agg} = (26.5 \pm 0.1)$ nm, which compares well with experimental data reported in the literature (about 24 nm to 29 nm; *cf.* Figure 9.9 and Table 4.1, on page 31). This aggregate comprises 1700 F8H14 molecules, corresponding to the experimentally observed hemimicelles or limit-size aggregate. Indeed, $\bar{\theta}_{Az} \approx 0°$ for this aggregate and its morphology is similar to that obtained from AFM measurements, with emphasis on the existence of a central pit (*cf.* Figures 9.15 and 9.16). It is reiterated that the analysis of $\bar{\theta}_{Az}$ provides a quantitative indication of the limit size of the aggregates [11].

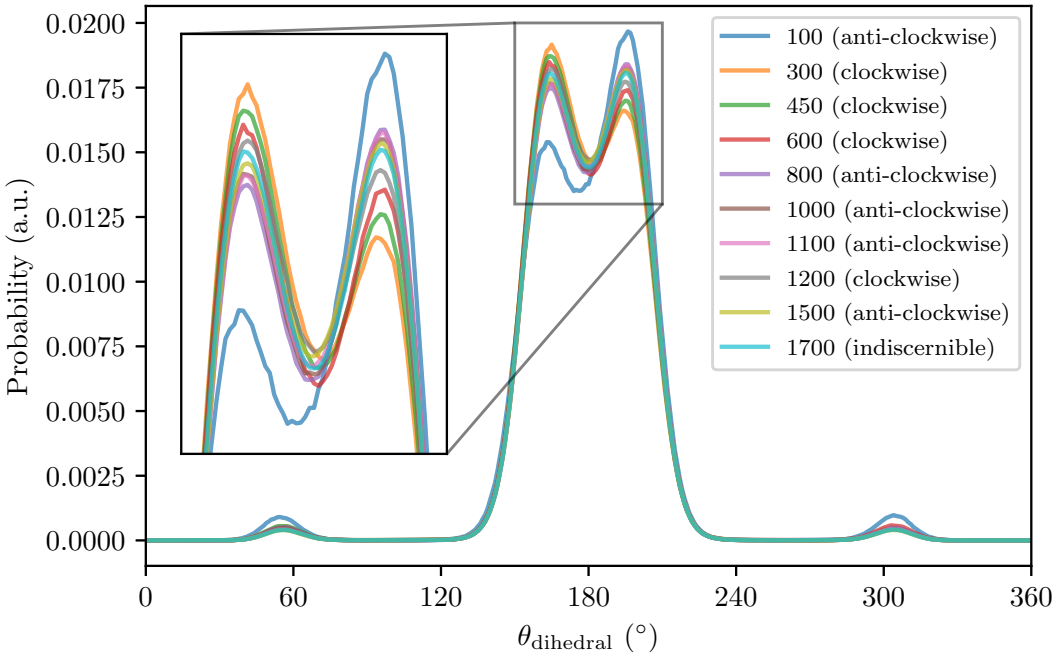

Figure 9.2: Distribution of the C_F–C_F–C_F–C_F dihedral angles (θ_{dihedral}) for aggregates of F8H14 of different sizes (*i.e.* with different numbers of molecules). The θ_{dihedral} follows the IUPAC convention, for which $\theta_{\text{dihedral}} = 0°$ for the *cis* conformation. The asymmetry (around 180°) of the relative maxima of these distributions correlate with the aggregates' spiralling sense (indicated in brackets in the legend and highlighted in the inset).

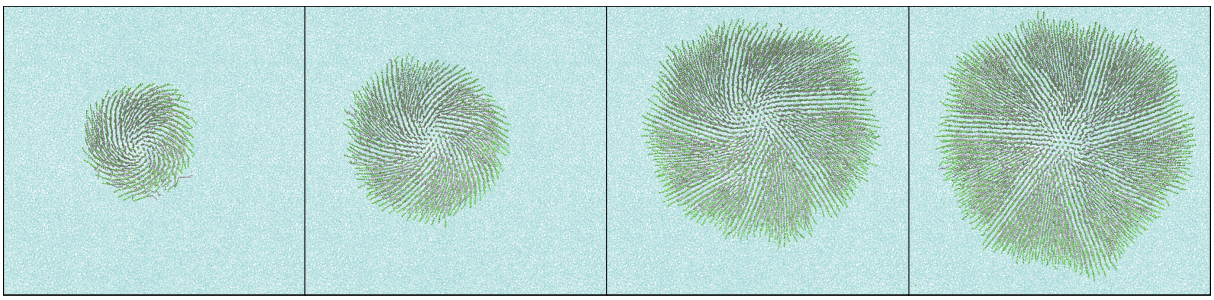

Figure 9.3: Top-view snapshots of the final configuration of the MD simulations of F8H14 sub-limit-size aggregates of 300, 600, 1200 and 1500 molecules, from left to right. Each image measures 31.5 nm of side. The water molecules are represented as cyan points and the carbon atom backbone of the PFAA chains are represented by lines coloured according to their respective moiety (green and grey for the fluorinated and hydrogenated carbon atoms, respectively). Hydrogen and fluorine atoms of the PFAA molecules are omitted for clarity.

9.3.1.2 C_F–C_F–C_F–C_F dihedral angle ($\theta_{dihedral}$)

The CF chains adopt a preferential helical conformation that correlates with the sense of winding of the sub-limit-size aggregate's spiral [11]. This is clear from the distribution of the dihedral angles of the CF chains' carbon atom backbone (C_F–C_F–C_F–C_F dihedral or $\theta_{dihedral}$), presented in Figure 9.2. For the clockwise-winding aggregates, the CF chain helix conformations with $\theta_{dihedral} < 0°$ are more frequent. Conversely, helices having $\theta_{dihedral} > 0°$ are more frequent in aggregate whose spiral is anti-clockwise. This winding phenomenon has also been verified in *ab initio* studies of dimers of fluorinated alcohols [29] and of PFAAs [30], whose molecules tend to adopt a double helix conformation. A parallel can be drawn between those studies on dimers and the results presented herein, inasmuch as the wrapping of the molecules around one another can be interpreted as an additional way of maximising the interactions among the PFAA molecules, within the sub-limit-size aggregates. This is anticipated to favour molecular conformations that permit a closer proximity of the CF moieties. In the case of the limit-size aggregates, left- and right-winding helices of the CF chains are equally frequent. This further supports the attainment of the limit size and can be considered to be another criterion for the verification of such condition.

9.3.1.3 Illustrative snapshots of the MD simulations

Figure 9.3 depicts some top-view snapshots of the final state of the MD simulations of a few F8H14 sub-limit-size aggregates with different numbers of molecules. These illustrate in a qualitative and visual way the preceding quantitative remarks concerning the winding of the molecules in spirals for aggregates below the limit size. This effect is ever less noticeable with decreasing number of PFAA molecules.

9.3.2 Modelling the internal structure of the hemimicelles

Drawing on the accumulated knowledge about the internal structure of the PFAA aggregates at the air–water interface, obtained through the MD simulations reported herein and priorly [11], a model describing the packing of the molecules within the hemimicelles was conceived. This model, referred to in short as geometrical model, is described in the paragraphs below.

9.3.2.1 Description of the geometrical model

The PFAA molecules were modelled as two rigid cylinders connected by their bases in a way that their central axes are collinear, as is schematised in Figure 9.4. One cylinder corresponds to the CF chain and the other to the CH chain, represented in green and in grey in Figure 9.4, respectively. The radius of the CH cylinder (r_H) is obtained from the value of cross-sectional area of the CH chain (A_H), according to Equation 9.1. Likewise, the radius of the CF cylinder (r_F) is given by Equation 9.2, considering the appropriate value of cross-sectional area of the CF chain (A_F). The length of each cylinder was calculated as the contour length of the fully stretched chains, as outlined in Reference [31]. The CH and CF chains' lengths are given by Equations 9.3 and 9.4, respectively. The values of the bond lengths and angles, as well as of the Van der Waals radii, used in the calculations are presented in Table 9.1.

$$r_H = \sqrt{\frac{A_H}{\pi}} \tag{9.1}$$

$$r_F = \sqrt{\frac{A_F}{\pi}} \tag{9.2}$$

$$l_H = r_{\mathrm{H}} + l_{\mathrm{CH}} \cdot \sin\frac{\widehat{\mathrm{CCH}}}{2} + \left(m - \frac{1}{2}\right) \cdot l^{\mathrm{H}}_{\mathrm{CC}} \cdot \sin\left(\frac{\widehat{\mathrm{CCC}}_{\mathrm{H}}}{2}\right) \tag{9.3}$$

$$l_F = r_{\mathrm{F}} + l_{\mathrm{CF}} \cdot \sin\frac{\widehat{\mathrm{CCF}}}{2} + \left(n - \frac{1}{2}\right) \cdot l^{\mathrm{F}}_{\mathrm{CC}} \cdot \sin\left(\frac{\widehat{\mathrm{CCC}}_{\mathrm{F}}}{2}\right) \tag{9.4}$$

In describing the molecules, as can be seen in Figure 9.4, there are a few points outlining some similar triangles, most notably: $[ABC]$, $[CDE]$ and $[AGF]$. The angles $B\hat{C}A$, $D\hat{E}C$ and $G\hat{F}A$ are equal and their value is denoted by θ. Focusing on triangle $[CDE]$, the lengths of its sides $\overline{CD}$ and $\overline{DE}$ are computed according to Equations 9.5 and 9.6, respectively. These parameters are combined in Equation 9.7 in order to retrieve $\tan\theta$. Finally, the value of d is attained using Equation 9.8.

$$\overline{CD} = r_F - r_H \tag{9.5}$$

$$\overline{DE} = l_H \tag{9.6}$$

$$\tan\theta = \frac{\overline{CD}}{\overline{DE}} = \frac{r_F - r_H}{l_H} \tag{9.7}$$

$$d = \frac{r_{\mathrm{H}}}{\tan\theta} \tag{9.8}$$

Having specified the dimensions of the model cylinders as functions of a few parameters, the aggregates' internal structure is described recursively, as is schematised in Figure 9.5. The geometrical construction of the aggregates' inner structure is conceived starting from the centre towards the periphery. This corresponds to the regular stacking of the model molecules, whose shape reduces the problem to the stacking of a set of geometrically identical cones (*cf.* Figure 9.4). The central molecule of the aggregate is considered to be vertically oriented

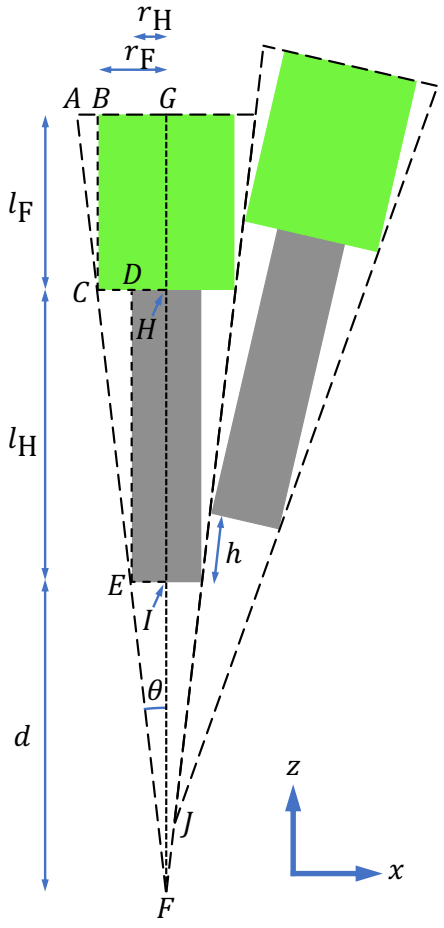

Figure 9.4: Longitudinal cross-section of the two-cylinder geometrical construction considered for the PFAA molecules. The capital letters mark some relevant points. The symbols and notation are presented in the text.

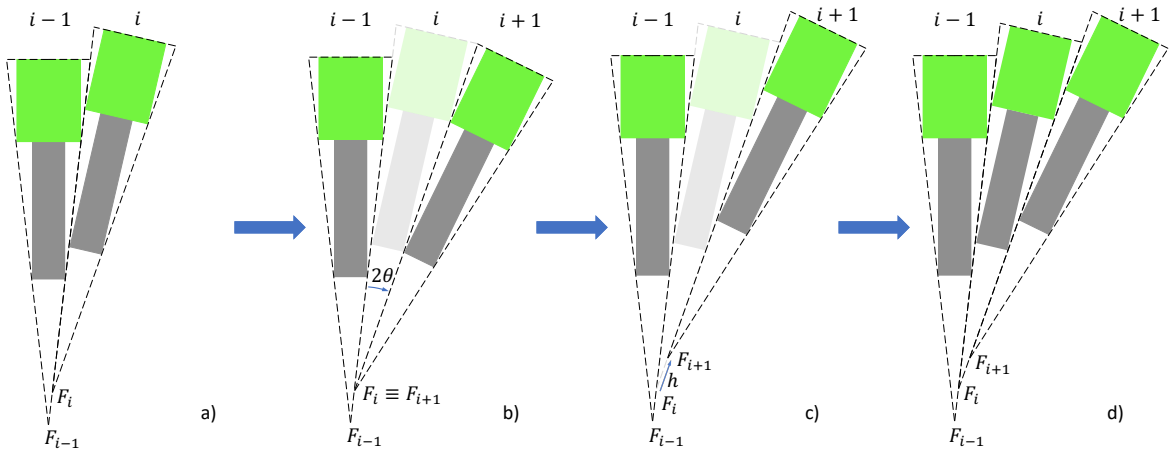

Figure 9.5: Recursive method used to calculate the coordinates of the molecules.

and aligned with the z axis. Along a given radial direction (here, the x axis), the PFAA molecules are successively packed in layers. Each layer is generated via a rotation by 2θ, followed by a translation by a distance h, of the previous layer. The process is repeated until the outermost layer achieves a specified value of tilt angle (θ_{Tilt} – the angle between the molecule's central axis and the z axis), namely $\theta_{\text{Tilt,F}} = 65°$. This value was found to be approximately constant based on the MD simulation results of the F8H14 and the F8H16 surface aggregates with different numbers of molecules. The applicability of this observation to other FnHm aggregates is analysed below. The recursive juxtaposition of the molecules is carried out n_{layers} times so as to have to have $\theta_{\text{Tilt},n_{\text{layers}}-1} < \theta_{\text{Tilt,F}} \leq \theta_{\text{Tilt},n_{\text{layers}}}$. The value of h was adjusted based on results from the MD simulations in order to reproduce the diameter and the internal structure of the simulated F8H14 and F8H16 limit-size aggregates. The best fit was obtained for $h = 0.383\,\text{nm}$, which corresponds to about 2.5 times the C–C bond length. Both parameters ($\theta_{\text{Tilt,F}}$ and h) were then assumed to be constant and transposable for aggregates of PFAAs with different chain lengths. Finally, some further important definitions are presented in Figure 9.6.

The hemimicelles are assumed to have a circular shape of radius R. As a first approximation, the number of molecules packed in a circular shape of radius r ($N(r)$) is given by the area of a circle of radius r ($A_\circ(r) = \pi r^2$) divided by the cross-sectional area of the CF chains (A_{CF}), conveyed in Equation 9.9.

$$N(r) = \frac{A_\circ(r)}{A_{\text{CF}}} = \frac{\pi}{A_{\text{CF}}} r^2 \tag{9.9}$$

The tilt angle of the molecules (θ_{Tilt}) is considered to vary linearly as a function of the radial distance r from the centre of the pure hemimicelles. The rate of variation of θ_{Tilt} with r for a pure hemimicelle of FnHm is denoted Δ_{FnHm}. θ_{Tilt} varies between 0° for $r = 0$ and a limit value $\theta_{\text{Tilt,F}}$ for $r = R$. These premises are founded on MD simulation results, as is further elaborated below. The radius of a pure hemimicelle R_{FnHm} relates to $\theta_{\text{Tilt,F}}$ and Δ_{FnHm} by Equation 9.10.

$$\theta_{\text{Tilt,F}} = \Delta_{\text{FnHm}} \times R_{\text{FnHm}} \Leftrightarrow R_{\text{FnHm}} = \frac{\theta_{\text{Tilt,F}}}{\Delta_{\text{FnHm}}} \Leftrightarrow \Delta_{\text{FnHm}} = \frac{\theta_{\text{Tilt,F}}}{R_{\text{FnHm}}} \tag{9.10}$$

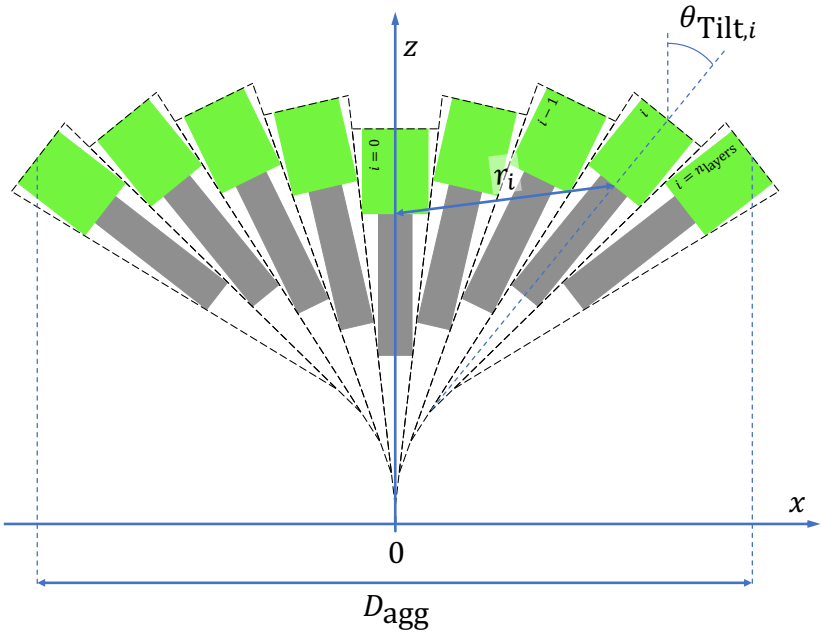

Figure 9.6: Schematic representation of the aggregates constructed according to the geometrical model. The diameter of the aggregates (D_{agg}) is defined as twice the x coordinate of the centre of the CF cylinder top (point G in Figure 9.4) of the outermost molecule. The tilt angle of a molecule in a layer i ($\theta_{\mathrm{Tilt},i}$) is defined as the angle between its central axis and the z axis. The distance of the molecules to the centre of the aggregate (r_i) is defined as the straight distance between the midpoint of that molecule's CH_2-CF_2 junction (point H in Figure 9.4) and that of the central molecule. This is coherent with the definition used for the analyses of the MD simulation results, which is based on the coordinates of the fluorinated carbon atom of the CH_2-CF_2 junction.

Table 9.1: Parameters and the respective numerical values used in the geometrical model.

Parameter	Symbol	Value	Units	Ref.
CH chain cross-sectional area	A_{H}	0.20	nm^2	[32]
CF chain cross-sectional area	A_{F}	0.30	nm^2	[32]
Van der Waals radius of organic hydrogen	r_{H}	0.120	nm	[33]
Van der Waals radius of organic fluorine	r_{F}	0.135	nm	[33]
C–H bond length	l_{CH}	0.110	nm	[34]
C–C bond length (hydrogenated)	$l^{\mathrm{H}}_{\mathrm{CC}}$	0.1532	nm	[34]
C–C bond length (fluorinated)	$l^{\mathrm{F}}_{\mathrm{CC}}$	0.154	nm	[33]
C–F bond length	l_{CF}	0.138	nm	[33]
C–C–H bond angle	$\widehat{\mathrm{CCH}}$	110	°	[33]
C–C–C bond angle (hydrogenated)	$\widehat{\mathrm{CCC}}_{\mathrm{H}}$	110	°	[33]
C–C–C bond angle (fluorinated)	$\widehat{\mathrm{CCC}}_{\mathrm{F}}$	116	°	[33]
C–C–F bond angle	$\widehat{\mathrm{CCF}}$	110	°	[33]
Final tilt angle	$\theta_{\mathrm{Tilt,F}}$	≈65	°	This work
Longitudinal shift	h	0.383	nm	This work

9.3.3 Surface hemimicelles of FnHm of varying chain lengths

9.3.3.1 Mean azimuthal angle ($\bar{\theta}_{\mathbf{Az}}$)

Table 9.2: Summary of the parameters of the Gaussian curves (mean ± standard deviation or $\mu_{\mathrm{Az}} \pm \sigma_{\mathrm{Az}}$) fitted to the signed azimuthal angle (θ_{Az}) distribution for each of the simulated PFAA limit-size aggregates. The number of PFAA molecules comprising the simulated limit-size aggregates (n_{mol}) and the uncertainty on n_{mol} (Δ_{mol}) are also presented. Δ_{mol} is estimated as the number of molecules comprising the outermost layer of the simulated aggregates, calculated as the perimeter of the aggregates divided by the diameter of the CF chain ($d_{\mathrm{F}} = 2\sqrt{A_{\mathrm{F}}/\pi}$).

FnHm	D (nm)	$\mu_{\mathrm{Az}} \pm \sigma_{\mathrm{Az}}$ (°)	n_{mol}	Δ_{mol}
F8H14	26.5 ± 0.1	0.03 ± 7.32	1700	135
F8H16	31.7 ± 0.2	-2.96 ± 6.32	2500	161
F8H18	35.7 ± 0.1	-1.16 ± 7.92	3200	182
F8H20	39.4 ± 0.1	3.16 ± 5.09	3900	200
F6H16	31.3 ± 0.1	3.51 ± 7.25	2486	159
F10H16	32.5 ± 0.2	-0.97 ± 5.99	2550	165
F12H16	36.6 ± 0.1	0.14 ± 5.15	3200	186

The geometrical model was used to predict the diameter of hemimicelles of PFAAs of varying CH and CF chains' lengths. A series of PFAA molecules with a constant CH chain (m = 16) and varying CF chain length (FnH16: F6H16, F8H16, F10H16 and F12H16) and a series of PFAA molecules with a constant CF chain (n = 8) and varying CH chain length (F8Hm: F8H14, F8H16, F8H18 and F8H20) were selected, based on the interest in exploring the influence of varying both chains' lengths and the availability of literature data on their Langmuir films to which the MD simulation results could be compared. The number of molecules for each aggregate was estimated using Equation 9.9 and an initial configuration for the MD simulation was prepared as described in Section 9.2. This standalone MD simulation or one-shot approach eschewed the need to simulate progressively larger aggregates until $\theta_{\mathrm{Az}} \approx 0°$, significantly reducing the computational effort. Nevertheless, this criterion was always checked and, in case it was not fulfilled (as it happened for F12H16, as is further elaborated in Subsection 9.3.4), new simulations were conducted with a different number of molecules until a limit-size aggregate was attained. This was done by computing the θ_{Az} distributions from the MD simulation trajectories; this information was condensed in histograms and a bell-shaped distribution was obtained in each case, to which a Gaussian curve was then fitted. A summary of the mean (μ_{Az}) and standard deviation (σ_{Az}) of the fits obtained for the limit-size aggregates is presented in Table 9.2. The diameter (D; see also Figure 9.9), number of PFAA molecules comprising the simulated limit-size aggregates (n_{mol}) and the estimated uncertainty on n_{mol} (Δ_{mol}) are also compiled in this table.

As can be seen on Table 9.2, the θ_{Az} distributions are centred around a value close to 0° and, in all cases, $\theta_{\mathrm{Az}} = 0°$ is within less than $1 \times \sigma_{\mathrm{Az}}$ of μ_{Az}, i.e. $|\mu_{\mathrm{Az}} - 0°| < \sigma_{\mathrm{Az}}$. Given the uncertainties and the dispersion of the results inherent to the MD simulations, namely on D_{agg} and Δ_{mol}, it is reasonable to say that the simulated aggregates are limit-size ones.

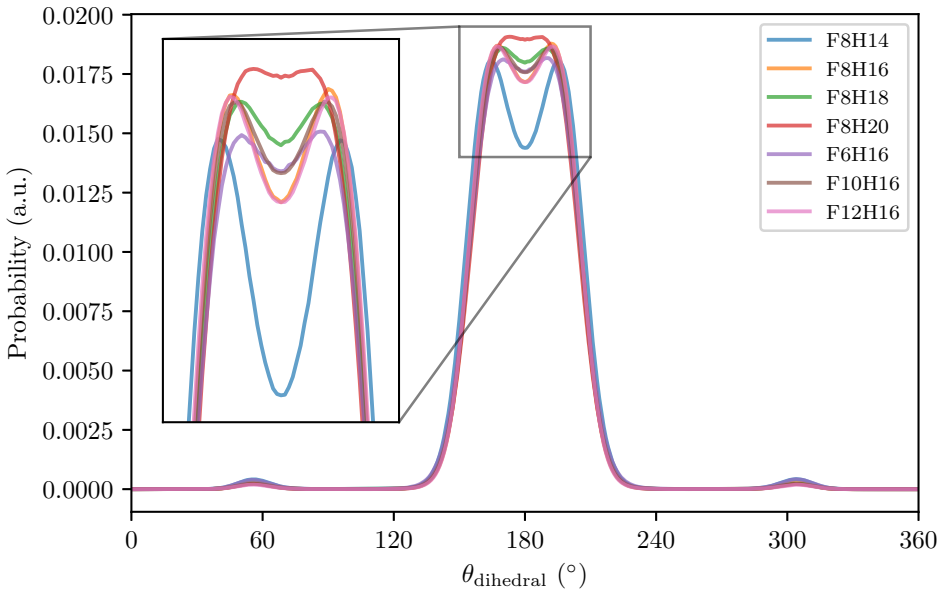

Figure 9.7: Distribution of the C_F–C_F–C_F–C_F dihedral angles (θ_{dihedral}) for hemimicelles of different PFAA molecules (FnHm, indicated in brackets in the legend and highlighted in the inset). The θ_{dihedral} follows the IUPAC convention, for which $\theta_{\text{dihedral}} = 0°$ for the *cis* conformation. The symmetry (around 180°) of these distributions are indicative of the attainment of the limit size of the aggregates.

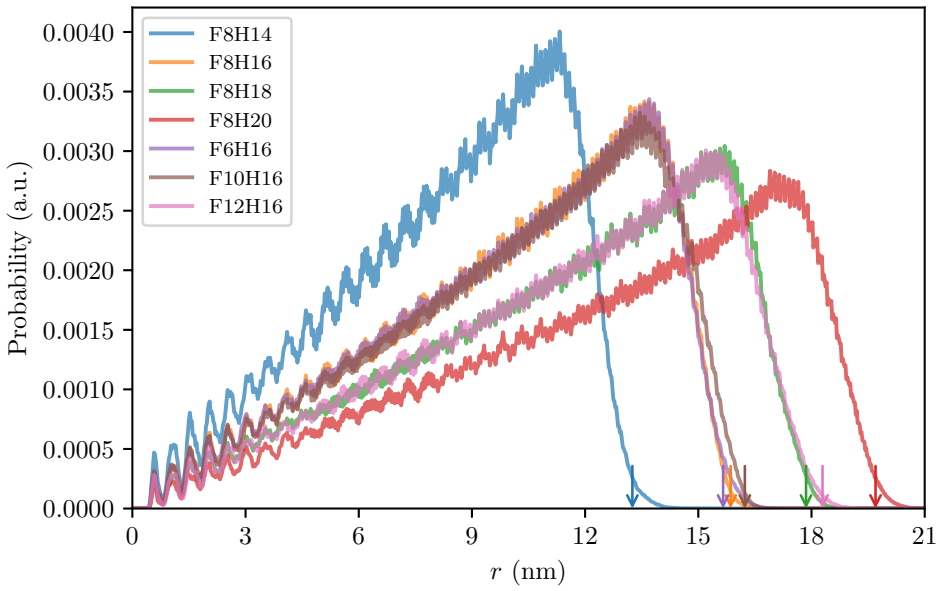

Figure 9.8: Distribution of the probability of finding a PFAA molecule as a function of the radial distance (r) from the centre of the limit-size aggregates or hemimicelles. The arrows mark the radii of the hemimicelles computed from the MD simulation trajectories, using the same colour coding as the one presented in the legend.

9.3.3.2 C_F–C_F–C_F–C_F dihedral angle ($\theta_{dihedral}$)

The $\theta_{dihedral}$ angle distribution was computed from the MD simulation trajectories for the limit-size aggregates, being presented in Figure 9.7. The obtained distributions are essentially symmetrical around $\theta_{dihedral} = 180°$, which serves as an additional check of the attainment of the limit size of the aggregates.

9.3.3.3 Hemimicelle size and molecular packing

The probability of finding a molecule as a function of the radial distance from the centre of the hemimicelles (r) was calculated from the simulation trajectories; the obtained distributions are presented in Figure 9.8. Local maxima are discernible at approximately regular intervals. This is in line with previous findings for the F8H16 hemimicelle [11] and arises from the disposition of the PFAA molecules in approximately concentric layers resembling 2D hexagonal packing. This is not strictly attained due to the occurrence of defects, the mobility and trapezoidal shape of the PFAA molecules, and because the aggregate is not flat. These regular variations are better defined for shorter distances, which can be attributed to the fact that inter-molecular order is more significant at a local level and is gradually lost for longer distances. Save for this oscillatory behaviour, the probability distributions increase roughly linearly up until approximately the radii of the hemimicelles are attained, falling off rapidly for distances beyond this point. This observation is important as it substantiates the approximations made in the development of Equation 9.9.

The diameter of the hemimicelles (D) was estimated from the MD simulation trajectories and is plotted as a function of n or m in Figure 9.9. The values of D predicted by the geometrical model and some experimental values from the literature are represented in the same figure, for comparison. In general, the calculated D values using the geometrical model are in agreement with the available experimental values. The same can be said for the values obtained from the MD simulations, with two added remarks. First, there is a discrepancy between the D predicted by the geometrical model and the value computed from the MD simulation trajectories for the F8H14 hemimicelle, which is relatively significant by comparison to the remaining points of the F8Hm data set. However, given that both the D values from MD simulation and geometrical model display similar and coherent trends, this was attributed to the inherent dispersion of the MD simulation results as well as the approximations made in the development of the geometrical model (namely that of considering the molecules as rigid cylinders). Second, the F12H16 hemimicelle is also an apparent outlier in the FnH16 dataset, inasmuch as the value of D obtained from the MD simulations is significantly higher than the one predicted by the geometrical model and it also is not aligned with the trend that follows from the remaining points in this dataset. In fact, the system of the F12H16 hemimicelle appears to have a peculiar behaviour compared to the remaining ones. This is the object of further discussion in Subsection 9.3.4.

The geometrical model and the MD simulation results correctly purport the relative influence of the CH and CF chain lengths on D_{agg}. This is clear by calculating the slope of the trend line obtained for each data set. As for the influence of the CF chain length or n (left plot), this is $\text{slope}_{CF} = 0.24\,\text{nm}\,\text{Atom}_C^{-1}$ (geometrical model) or $\text{slope}_{CF} = (0.29 \pm 0.05)\,\text{nm}\,\text{Atom}_C^{-1}$ (MD simulations, excluding the F12H16 data point). This means that the addition of a carbon

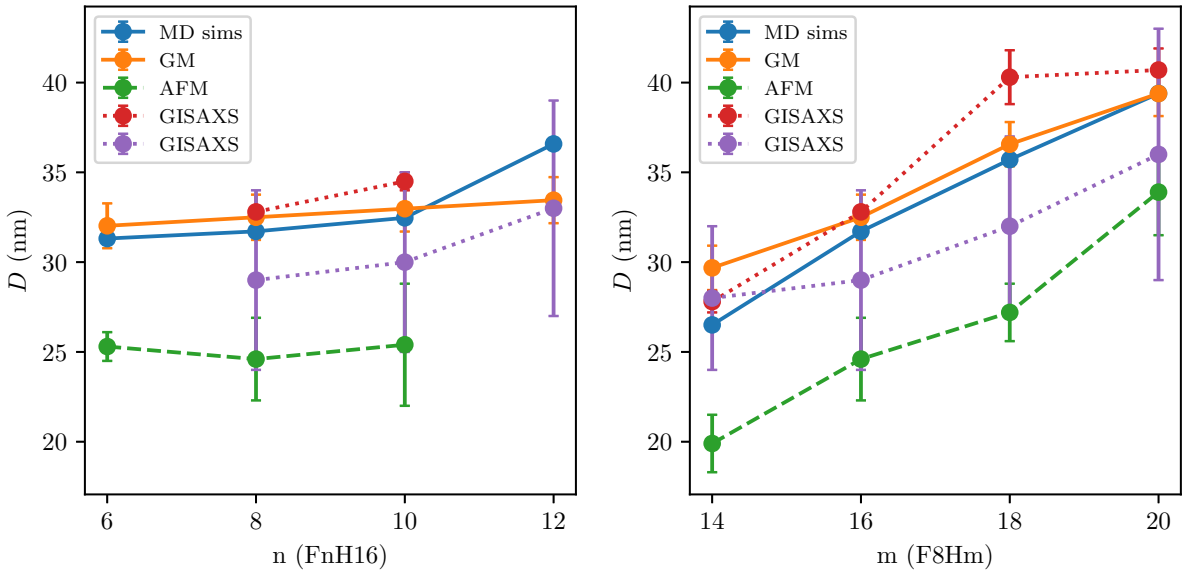

Figure 9.9: Diameter (D) of the PFAA hemimicelles formed at the air–water interface estimated with the geometrical model (orange, full lines) and computed from the simulation trajectories of the limit-size aggregates (blue, full lines) as functions of: the number of carbon atoms in the CF chain or n, for m=16 (FnH16; left); the number of carbon atoms in the CH chain or m, for n=8 (F8Hm; right). For comparison, other literature results obtained using different experimental techniques are also shown, namely: AFM (green, dashed lines), from Ref. [9], and GISAXS, from Refs. [5, 35] (red, dotted lines) and [36] (purple, dotted lines). The lines are guides to the eye.

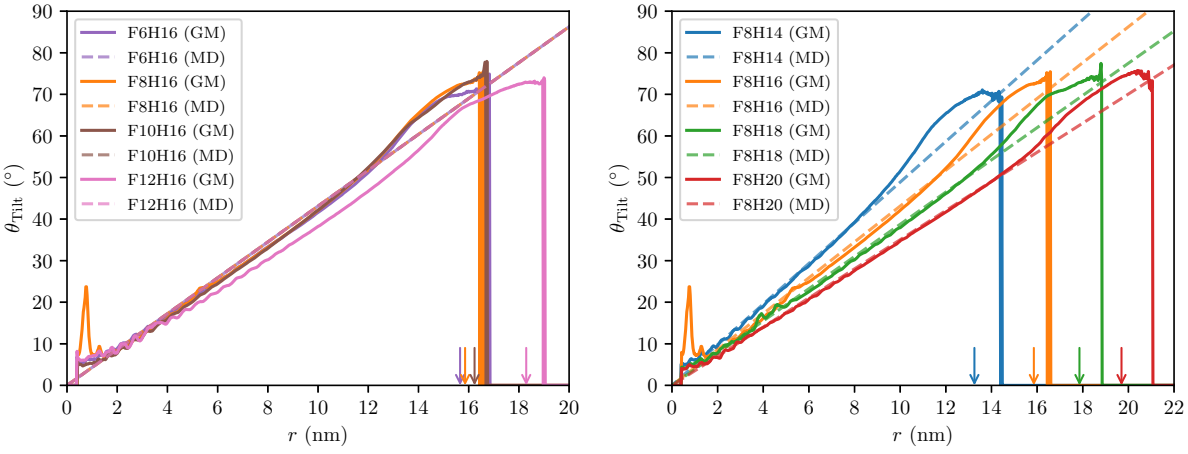

Figure 9.10: Average tilt angle (θ_{Tilt}, full lines) as a function of the radial distance to centre of the aggregate (r) for the simulated limit-size aggregates or hemimicelles of FnH16 (n = 6, 8, 10, 12; left) and of F8Hm (m = 14, 16, 18, 20; right). The dashed lines represent the corresponding dependency of θ_{Tilt} on r predicted with the geometrical model. The arrows mark the radii of the hemimicelles computed from the MD simulation trajectories, using the same colour coding as the one presented in the legend.

atom to the CF chain increases D_{agg} by about 0.24 nm, according to the geometrical model, which is roughly twice the C–C bond length (*cf.* Table 9.1). Conversely, the influence of the CH chain length or m (right plot) is $\text{slope}_{CH} = (1.66 \pm 0.09)\,\text{nm}\,\text{Atom}_C{}^{-1}$ (geometrical model) or $\text{slope}_{CH} = (2.13 \pm 0.12)\,\text{nm}\,\text{Atom}_C{}^{-1}$ (MD simulations). By computing the ratio of these values, the CH chain length is approximately 7.0 ± 0.4 or 7.4 ± 1.4 times more influential than the CF chain length in determining the size of the hemimicelles, respectively based on the results from the geometrical model or from the MD simulations. This is in line with experimental results and confirms previous reports[1]: Zhang *et al.* reported $\text{slope}_{CF} \approx 0.25\,\text{nm}\,\text{Atom}_C{}^{-1}$ and $\text{slope}_{CH} \approx 1.4\,\text{nm}\,\text{Atom}_C{}^{-1}$ [9] and Gallyamov *et al.* reported $\text{slope}_{CH} \approx 2.0\,\text{nm}\,\text{Atom}_C{}^{-1}$ (the latter don't account for the influence of the CF chain length on the size of the hemimicelles in their model, i.e. $\text{slope}_{CF} = 0\,\text{nm}\,\text{Atom}_C{}^{-1}$) [8]. These results are remarkable and important in explaining the dependence of D on the CH and CF chains' lengths as the product of packing and geometrical constraints.

9.3.3.4 Tilt angle (θ_{Tilt})

Because the PFAA molecules have a trapezoidal shape, they are not simply juxtaposed side by side and vertically oriented within the monolayer; instead, they display a variable angle relative to the normal to the water surface – a tilt angle (θ_{Tilt}) – and arrange in discrete structures or hemimicelles. This is illustrated in Figure 9.6 and it has been described for the F8H16 hemimicelle, based on the prior MD simulation study [11]. This maximises the interactions and minimises the free space between the PFAA molecules. To gain a quantitative insight into this phenomenon, the θ_{Tilt} was computed as a function r, for the simulated limit-size aggregates. These results are presented in Figure 9.10.

It's clearly observable that θ_{Tilt} increases with r within the hemimicelles. This is consistent with the bouquet-like packing of the molecules, originating a dome-shaped structure (*cf.* Figure 9.16). Moreover, this dependency is strikingly linear, particularly for intermediate values of r. For small values of r, the fluctuations of θ_{Tilt} can be attributed to the reduced number of molecules near the centre of the aggregate, and thus those molecules' thermal agitation leads to a higher variability in θ_{Tilt}. For large values of r , the slight increase of θ_{Tilt} is due to the added mobility of the molecules near the rim of the aggregates and because θ_{Tilt} is defined based on an end-to-end vector, from the carbon atom in the CH_3 group to the carbon atom in the CF_3 group; the molecules have conformational freedom to form an angle between the CH and CF chains, which explains the increase of θ_{Tilt} at the edge of the hemimicelles.

The molecules in the outermost layer of the aggregates are tilted by a constant value of θ_{Tilt}, which is smaller than 90°, meaning the outermost molecules do not lie flat on the surface of the water. This final θ_{Tilt} (denoted $\theta_{\text{Tilt,F}}$) is similar for all aggregates and $\theta_{\text{Tilt,F}} \approx 65°$ (see Subsection 9.3.2). This value is estimated as the θ_{Tilt} value at a distance r equal to the aggregate's radius or R_{FnHm} (marked by the arrows in Figure 9.10; the plots extend beyond R_{FnHm} because of fluctuations in the molecules' positions and the fact that the hemimicelles are not strictly circular). The fact that $\theta_{\text{Tilt,F}}$ is roughly the same regardless of the composition and size of the

[1]Some of the values presented herein were calculated from data from the cited references, being presented in a different way compared to the original publications.

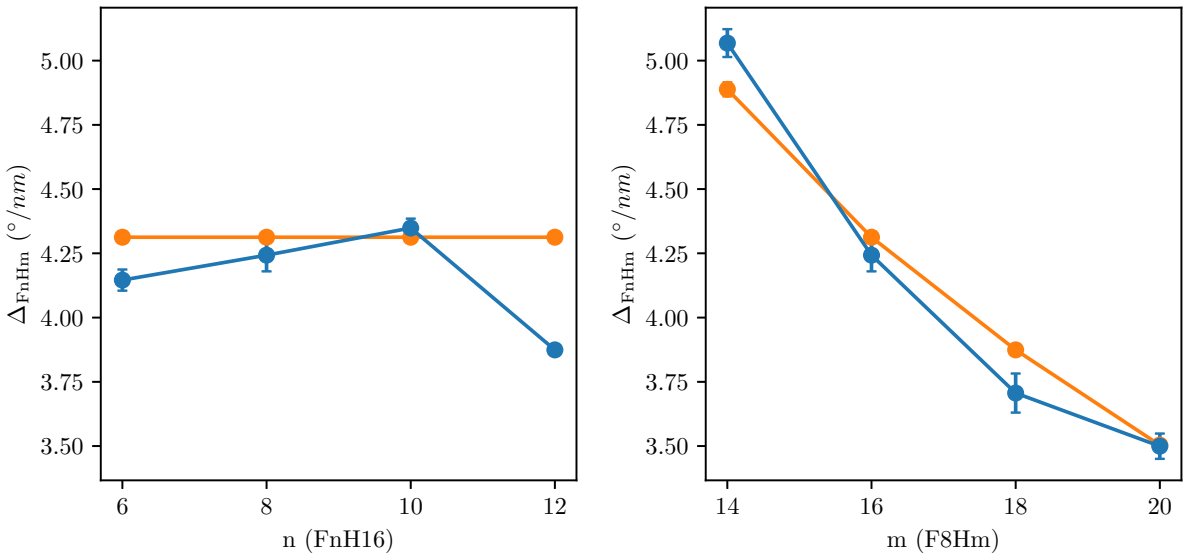

Figure 9.11: Slope of the plots of average tilt angle as a function of the radial distance to centre of the aggregate (presented in Figure 9.10) for the simulated hemimicelles of FnH16 (n = 6, 8, 10, 12; left) and of F8Hm (m = 14, 16, 18, 20; right): predicted by the geometrical model (orange) and obtained from the MD simulation results (blue).

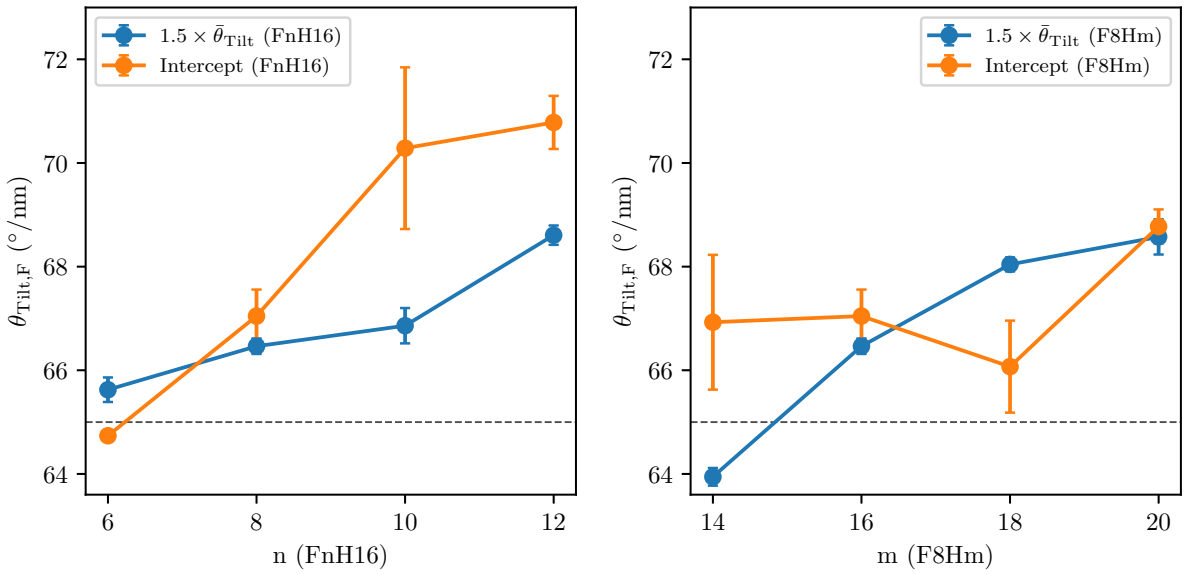

Figure 9.12: Final tilt angle ($\theta_{\mathrm{Tilt,F}}$) estimated from the MD simulation results for the hemimicelles of FnH16 (n = 6, 8, 10, 12; left) and of F8Hm (m = 14, 16, 18, 20; right): calculated as the interception of the straight line going through the linear region in Figure 9.10 with the vertical line for the radius of the corresponding hemimicelle ("Intercept"; orange); and calculated as 1.5 times the average θ_{Tilt} ("$1.5 \times \bar{\theta}_{\mathrm{Tilt}}$"; blue), as presented in Equation 9.11. The dashed line marks the $\theta_{\mathrm{Tilt,F}} = 65°$ value that was assumed in the development of the geometrical model (*cf.* Subsection 9.3.2).

aggregates suggests this upper limit has its origins in fundamental principles, namely the balance of forces between the PFAA and the water molecules (as a way to minimise the disturbance of the water surface while permitting a close interaction of the PFAA chains). The lateral packing of the PFAA molecules induces a curvature of the water surface, which is counteracted by the surface tension of the subphase, which has a planarizing effect on the hemimicelle shape and, ultimately, determines its size [10]. These results point once more to the preponderance of the geometry of the molecules in conditioning the shape of the aggregates. This is in contrast with other previous findings that suggested the size and shape of the PFAA domains is determined by the balance between the line tension and inter-domain dipole repulsions [36–38].

The rates of variation of θ_{Tilt} with r (denoted Δ_{FnHm}) can be estimated from the slope of the linear region of the plots in Figure 9.10. These can be compared with the predictions of the geometrical model. Both results are presented in Figure 9.11. The values of Δ_{FnHm} obtained from the MD simulation are generally agreement with those predicted by the geometrical model, with the exception of F12H16 (see Subsection 9.3.4). In particular, the Δ_{FnHm} is very similar among the F6H16, F8H16 and F10H16 hemimicelles. Conversely, Δ_{FnHm} decreases with increasing m in the F8Hm systems. This is a consequence of the molecular packing being constrained by the bulkier CF chains, but determined essentially by the CH chain length: the longer the latter is, the more layers are needed to attain $\theta_{\text{Tilt,F}}$, and so Δ_{FnHm} is lower. By varying n for a constant CH chain (FnH16 group), it is clear that the CF chain has a comparatively smaller impact on Δ_{FnHm} and, to that extent, a smaller influence on the molecular packing and, ultimately, the hemimicelles' diameter.

$\theta_{\text{Tilt,F}}$ can be calculated from Δ_{FnHm} and R_{FnHm} through Equation 9.10. This equates to finding the θ_{Tilt} for each hemimicelle at the respective radius R_{FnHm}, which is marked by the coloured arrows in Figure 9.8. However, for a circular aggregate whose molecules present a constant Δ_{FnHm} and for which the number of molecules at a distance r from its centre is given by Equation 9.9, the average θ_{Tilt} ($\bar{\theta}_{\text{Tilt}}$) is related to $\theta_{\text{Tilt,F}}$ through Equation 9.11. Knowing that $\bar{\theta}_{\text{Tilt}}$ is a quantity directly accessible from the simulation trajectories, the estimation of $\theta_{\text{Tilt,F}}$ through Equation 9.11 provides a means of checking the consistency of the assumptions made before. Figure 9.12 shows the $\theta_{\text{Tilt,F}}$ values obtained using the two methods.

$$\bar{\theta}_{\text{Tilt}} = \frac{\int_0^R \theta_{\text{Tilt}}(r) \times n(r)\, dr}{\int_0^R n(r)\, dr} = \frac{\int_0^R \frac{\theta_{\text{Tilt,F}}}{R} r \times Cr\, dr}{\int_0^R Cr\, dr} = \frac{C\frac{\theta_{\text{Tilt,F}}}{R}\left[\frac{r^3}{3}\right]_0^R}{C\left[\frac{r^2}{2}\right]_0^R} = \frac{2}{3}\theta_{\text{Tilt,F}} \Leftrightarrow$$

$$\Leftrightarrow \theta_{\text{Tilt,F}} = \frac{3}{2}\bar{\theta}_{\text{Tilt}} \quad (9.11)$$

The obtained $\theta_{\text{Tilt,F}}$ values are mostly within $\approx 3°$ of the initial approximation of $\theta_{\text{Tilt,F}} \approx 65°$. In particular, the values for the F8H14 and the F8H16 hemimicelles, the ones used to obtain initial estimates for the parameters to set up the geometrical model, are very close to 65°. This validates the initial approximation, within the boundaries of the simulation conditions and range of chain lengths of the studied systems. In relative terms, both methods of estimating $\theta_{\text{Tilt,F}}$ provide results in agreement with each other. This shows consistency in the calculations and

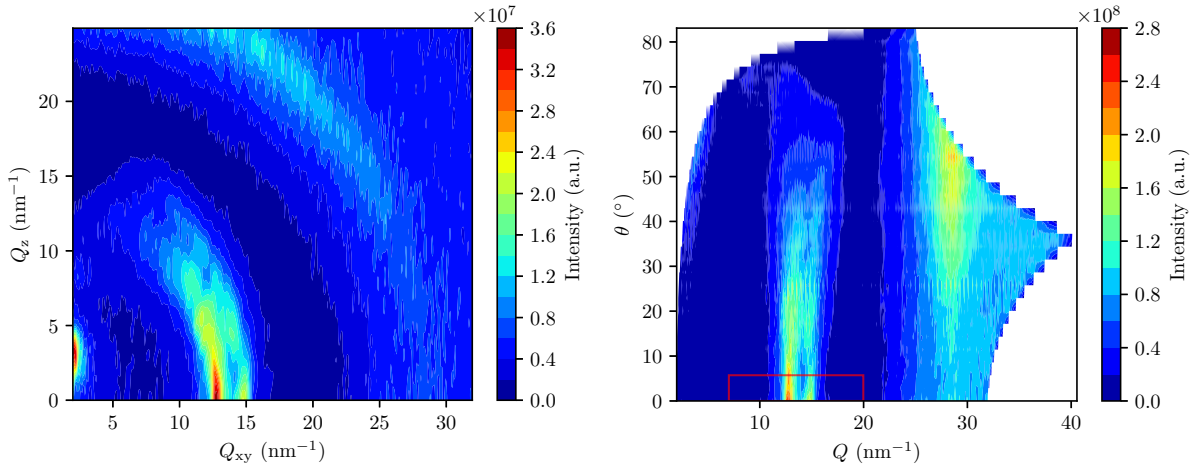

Figure 9.13: Left: contour plot of the diffraction intensity as a function of the in-plane (Q_{xy}) and out-of-plane (Q_z) components of the scattering vector calculated from the final configuration of the MD simulation trajectory of the pure F8H16 hemimicelle, which contained 2500 molecules of PFAA. Right: the same dataset, but represented in polar coordinates, that is the contour plot of the diffraction intensity as a function of the modulus of the scattering vector (Q) and the out-of-plane angle with the interface (θ). The red rectangle patch marks the integration region considered for the computation of the θ-integrated diffractogram presented in Figure 9.14.

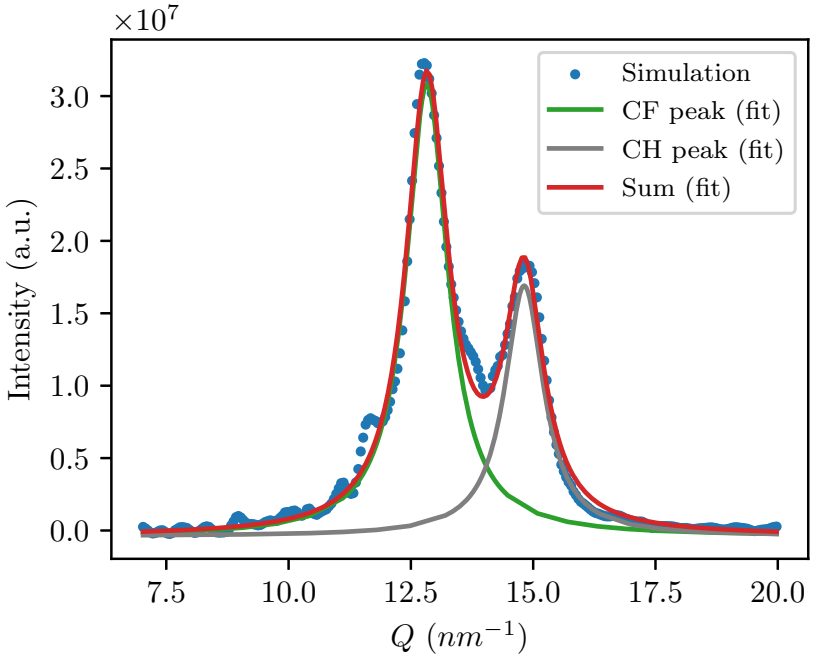

Figure 9.14: GIXD θ-integrated diffractogram for small values of θ (*i.e.* the intensity presented in Figure B.3 integrated along θ in the range of 0 rad to 0.1 rad, or about 0° to 5.73°, as a function of Q), calculated from the final configuration of the MD simulation trajectory of the pure F8H16 hemimicelle, which contained 2500 molecules of PFAA. The blue circles represent the data points retrieved from the calculation and the curves represent the fitted Lorentzian peaks corresponding to the proposed structures, labelled "CF peak" (green) and "CH peak" (grey). The red curve is the cumulative sum of the remaining fitted curves.

supports the conjectures and approximations made in the reasoning and modelling presented herein. However, for the F10H16 and the F12H16 hemimicelles, the obtained $\theta_{\mathrm{Tilt,F}}$ using the "Intercept" method (orange points in Figure 9.12) are somewhat outliers, since they are $\approx 5°$ or more above the $\theta_{\mathrm{Tilt,F}} = 65°$ mark. Moreover, $\theta_{\mathrm{Tilt,F}}$ generally increases with increasing n but not so much with increasing m, for the "Intercept" method. These observations might be an effect of the calculation itself: the hemimicelles of the FnH16 data set have very similar numbers of molecules and diameters. Further, the distances from the centre of the hemimicelles are computed from the positions of the CH_2CF_2 fluorinated carbon atom. Therefore, changing the length of the CF chain increases the hemimicelle area (and D), but not so much the relative positions of the reference atoms. This results in the interception occurring at higher R for systems with similar Δ_{FnHm}, and thus higher $\theta_{\mathrm{Tilt,F}}$ values are retrieved. Finally, concerning the values calculated using Equation 9.11 (blue points in Figure 9.12), it appears that $\theta_{\mathrm{Tilt,F}}$ increases with increasing n and m. This might be an effect of the added mobility of the simulated molecules, compared to the rigid construction assumed by the geometrical model: the simulated hemimicelle is more flexible and can probably be "flattened" in the simulation. This should be a direct consequence of the planarizing effect of the water surface, which is linked to its high surface tension [10]. As the hemimicelles are flatter, the molecules can lie down flatter too and can ultimately attain a higher $\theta_{\mathrm{Tilt,F}}$.

9.3.3.5 Diffraction pattern from the simulation trajectories

The GIXD patterns were estimated by computing the structure factor or the diffracted intensity in Cartesian coordinates, that is as a function of the in-plane (Q_{xy}) and out-of-plane (Q_{z}) components of the scattering vector. These calculations were performed from the final configurations of each of the MD simulation trajectories of the pure hemimicelles, using an adapted version of the code developed by Pedro Lourenço [24]. The diffracted intensity was also computed in polar coordinates[2], that is as a function of the modulus of the scattering vector (Q) and the out-of-plane angle with the interface (θ). Figure 9.13 presents these results, obtained for the pure F8H16 hemimicelle of 2500 PFAA molecules. In line with the treatment of the experimental data presented in Chapter 11, the θ-integrated spectra were obtained for small values of θ (*i.e.* the diffraction intensity integrated along θ in the range of 0 rad to 0.1 rad, or about 0° to 5.73°, – the region marked with the rectangular patch in Figure 9.13 – and represented as a function of Q) and fitted with Lorentzian curves. The results obtained for the pure F8H16 hemimicelle are presented in Figure 9.14. The corresponding plots obtained for the remaining simulated hemimicelles are provided as Supplementary Information in Appendix B.

As illustrated in Figure 9.13, the calculated GIXD patterns present two peaks in the plane: one centred at $Q_{\mathrm{xy}} \approx 12.5\,\mathrm{nm}^{-1}$ which can be associated with the close packing of CF chains (and thus named "CF peak", being represented in green in Figure 9.14); and another one centred at $Q_{\mathrm{xy}} \approx 14.5\,\mathrm{nm}^{-1}$ which can be associated with the close packing of CH chains (and thus named "CH peak", being represented in grey in Figure 9.14). This is in line with the available experimental data on Langmuir films of PFAAs [1, 5, 35] and as is further discussed in Chapter 11. One remarkable observation is the fact that the GIXD pattern that arises from the MD

[2]See Equations 11.2 and 11.3 in Subsection 11.3.3, on page 173.

Table 9.3: Positions of the 2 peaks fitted to the results of the GIXD pattern calculated from the MD simulation trajectories: a first peak corresponding to the stacking of the CF chains (CF peak) and a second one to the stacking of the CH chains (CH peak). The MD simulation results for the F8H16 system were taken from Reference [11]. The experimental data, where available, are reported for the monolayers compressed to $\pi = 5\,\mathrm{mN\,m^{-1}}$. The values marked with a) are original work, which is presented in detail in Chapter 11. The value marked with an asterisk corresponds to the "CH chain (generic)" peak (*cf.* Chapter 11).

Molecule	MD Simulation		Experimental		
	CF peak ($\mathrm{nm^{-1}}$)	CH peak ($\mathrm{nm^{-1}}$)	CF peak ($\mathrm{nm^{-1}}$)	CH peak ($\mathrm{nm^{-1}}$)	Ref.
F8H14	12.72	14.77	12.53	14.35	a)
F8H16	12.83	14.82	12.56	14.07	[5]
F8H18	12.75	14.82	12.54	14.23	[5]
F8H20	12.72	14.83	12.47	15.10	[5]
			12.52	14.38*	a)
F6H16	12.90	14.84	-	-	-
F10H16	12.71	14.78	12.45	14.20	[35]
F12H16	12.76	14.86	-	-	-

simulation trajectories reproduces the experimentally observed feature of the shift of the position of the maximal diffraction intensity to lower Q_{xy} values with increasing Q_z (*i.e.* the peaks "turn" counter-clockwise; *cf.* leftmost plot in Figure 9.13). The change to polar coordinates (*cf.* rightmost plot in Figure 9.13) gives rise to peaks with their maximal diffraction intensity at an approximately constant value of Q with varying θ. This is consistent with the existence of two diffracting structures (one per identified diffraction peak) of chains packed with an approximately constant lattice parameter and with a progressively increasing tilt angle. This is in line with the proposed geometrical model and with the remaining analyses presented in this chapter, with particular highlight for the results presented in Subsubsection 9.3.3.4. Higher order peaks seem to be present approximately in the $25\,\mathrm{nm^{-1}}$ to $30\,\mathrm{nm^{-1}}$ range. These appear to be out of the plane, although no reason could be put forward to explain such effect.

The positions of the peaks obtained from the fits to the simulated GIXD patterns of each of the simulated hemimicelles of PFAAs are summarised in Table 9.3, together with experimental results for comparison when these are available. The complete set of parameters obtained from the fits to the MD simulation results is provided in Appendix B, in Tables B.1 and B.2. The obtained simulation results are in general agreement with the experimental ones, inasmuch as two peaks are usually identified at similar positions from experiments. However, contrarily to what is experimentally observed, the position of the "CH peak" appears slightly but systematically overestimated, which might be an indication of the CH chains being excessively cohesive or even solid-like in the MD simulations, compared to the real systems. Furthermore, in the case of the F8H20 Langmuir film, a third diffraction peak at higher Q ($\approx 15.0\,\mathrm{nm^{-1}}$) is proposed based on the analyses of the experimental data obtained in the course of this work (see Chapter 11), which has been interpreted as the diffraction signal of a third structure arising from closer packed CH chains. However, only 2 diffraction peaks can be identified in the GIXD pattern calculated from the MD simulation trajectory of the F8H20 hemimicelle. This might be an

indication that the structure that is detected experimentally is not present in the simulations, at least for the duration and size of the simulated systems. Nevertheless, given the qualitative (and even quantitative, to a significant extent) agreement between simulation and experiments, this validates the MD simulation results and confirms and expands the previous findings [11].

9.3.3.6 Illustrative snapshots of the MD simulations

According to the geometrical model, the hemimicelles are reduced to a single row of molecules disposed along a given radial direction, which serves as a proxy for the whole hemimicelle's structure. This can be viewed as an effective way of accommodating the trapezoidal-shaped molecules in a quasi-hexagonal structure, a tendency that can be related to the CF chains propensity to crystallise at the surface of water in hexagonal close-packed lattices [39, 40]. Starting from the central vertical molecule around which the remaining molecules are layered: in the first layer, exactly 6 molecules can be packed, taking their geometry into account; in the subsequent layers, the molecules are unable to pack strictly hexagonally since they become ever more tilted towards the edge of the aggregates. Therefore, the close packing of the molecules is anticipated to be preferred along 6 radial directions and the position of the molecules is adjusted in intermediate directions to maximise the interactions and minimise the free space among the chains. This rationale is illustrated in Figure 9.17. This is substantiated with the observation of the trajectories of the MD simulations of limit-size aggregates, in which the molecules apparently subdivide in about 6 or 7 regular segments within the aggregates. The top-view snapshots of the final state of those simulations illustrate this fact, in Figure 9.15. From this perspective, 6 or 7 directions of molecular alignment are visible, corresponding to the frontiers of the segments. As an illustrative example, an AFM-like topography image of the hemimicelle of 3200 F8H18 molecules is also presented in Figure 9.15, in which the approximate location of the frontiers between the segments is highlighted with white dashes. The segments are slightly protuberant, compared to the rest of the aggregate, as though the latter comprises several lobes. This is in accordance with previously reported experimental AFM data of PFAA monolayers transferred onto solid substrates, in which an array of monodisperse hemimicelles is visible, each apparently made of 5 or 6 lobes fused together [41]. However, as is further discussed in Subsection 9.3.4, experimentally this is more clearly marked for some PFAAs than others, which might be attributed to a self-assembling behaviour dependent on n and m in FnHm.

Figure 9.16 shows some snapshots of the cross-section cuts of the final state configurations of the simulated PFAA hemimicelles, together with a superimposed visual representation of the corresponding structure constructed using the geometrical model, for comparison. The morphological and structural features already described for the F8H16 hemimicelle [11] are retrieved here for the FnH16 and the F8Hm series of hemimicelles: the PFAA molecules are preferentially oriented with their CH chains facing the water and the CF chains facing the air; the aggregates have a rounded dome shape; the dome has a characteristic pit in its centre, as pointed out in Chapter 8; the water surface is deformed, acquiring a shape that resembles the negative imprint of the bottom side of the hemimicelles, which was also mentioned in Chapter 8; the progressively increasing θ_{Tilt}, from the centre towards the rim of the aggregates, is striking; the molecules are arranged in successive, approximately concentric layers, and each layer presents

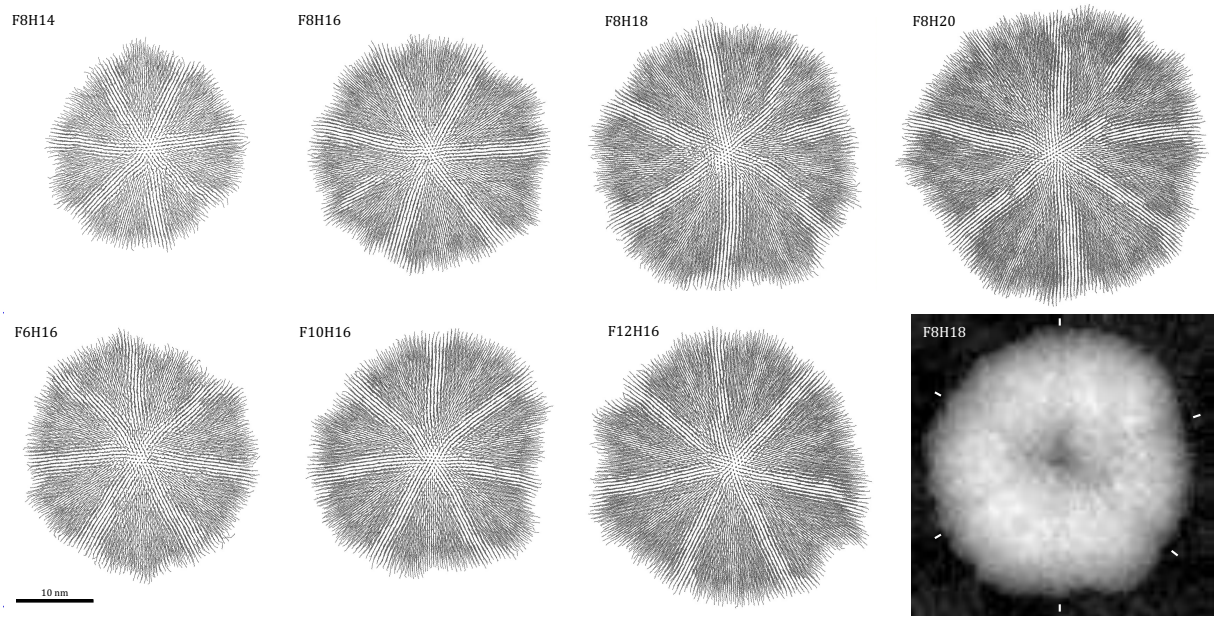

Figure 9.15: Top-view snapshots of the final state configurations of the simulated PFAA limit-size aggregates or hemimicelles. Only the carbon atom backbones of the PFAA molecules are depicted as solid black lines (the water molecules are omitted for clarity). The bottom right image is a topography (AFM-like) image of the F8H18 hemimicelle, highlighting the pit or depression in its centre. The white dashes mark the approximate locations of the borders of the segments or lobes mentioned in the text. All images are to the same scale.

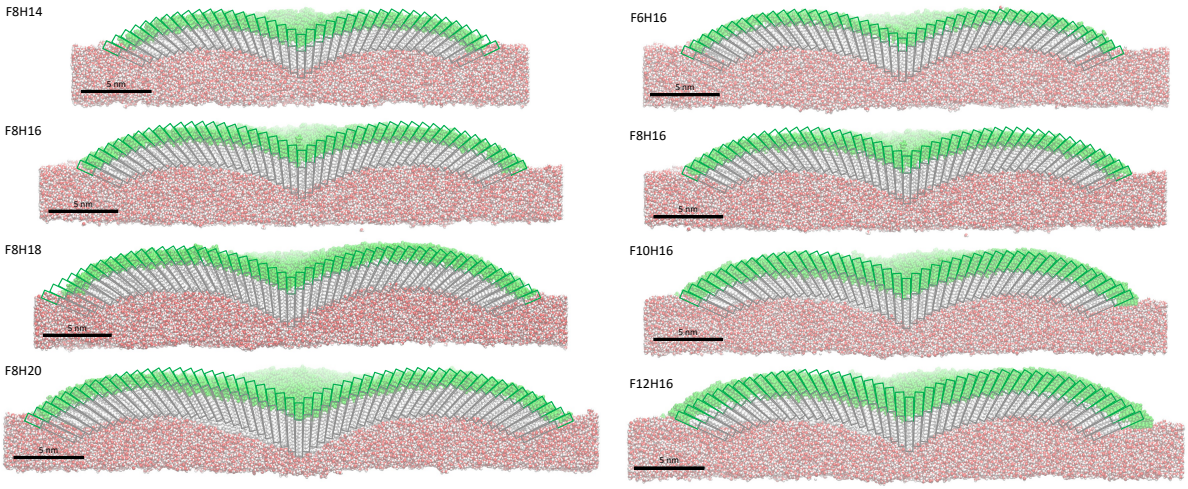

Figure 9.16: Snapshots of the final state configurations of the cross-section cuts through the centre of the simulated PFAA limit-size aggregates or hemimicelles. The atoms pertaining to the CH and CF chains are represented in a space fill model and coloured white and green, respectively. The water molecules are represented in a space fill model and their oxygen and hydrogen atoms are coloured red and white, respectively. The corresponding hemimicelle structures constructed using the geometrical model are superimposed for comparison, representing the CH and CF chains as grey and green rectangles, respectively. All images are to the same scale.

a shift along the molecular axis relative to the preceding layer (denoted h in Figures 9.4 and 9.5), which results from the alignment of the CH_2–CF_2 dipole (*cf.* Chapter 8 and Subsubsection 9.3.3.7). Moreover, the qualitative agreement of the superposition of the structure given by the geometrical model with that obtained from the MD simulation trajectories complements the quantitative agreement already discussed above. Finally, Figure 9.16 retrieves in graphical form what was concluded above regarding the dependence of the size and the internal structure of the PFAA hemimicelles on the lengths of the CH and the CF chains: varying the length of the CH chain by a certain number of carbon atoms impacts the size and the internal structure of the hemimicelles to a greater extent than an equal change in the length of the CF chain.

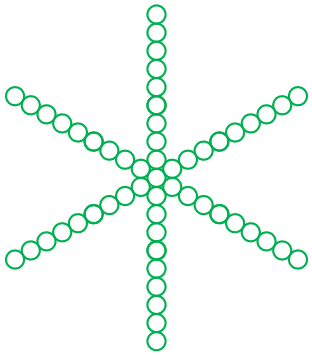

Figure 9.17: Illustration of the packing of the PFAA molecules within the hemimicelles along 6 preferential radial directions.

9.3.3.7 Spatial Distribution Functions of the carbon atoms in CH_2–CF_2

In Chapter 8, it was demonstrated that the molecules comprising the F8H16 hemimicelle display a level of ordering that favours a head-to-tail disposition of the CH_2–CF_2 dipoles. This reasoning was founded on the computed SDFs of the carbon atoms in the CH_2–CF_2 of the molecules constituting the hemimicelle (*cf.* Fig. 8.4 on page 86). This analysis was also performed for the remaining simulated hemimicelles, for which the results are presented in Appendix B (Figures B.15 to B.21). The pictures present the contour surfaces at different values of constant particle density (named isovalues therein). The CH_2–CF_2 dipole ordering effect is general, as it is observed for all the simulated hemimicelles. This is evident when analysing the snapshots at high isovalue (corresponding to a higher particle density). At lower isovalues, the disposition of the molecules in concentric layers surrounding one another is clear, a result that complements the observations made in prior work [11] and in Subsubsection 9.3.3.3.

9.3.4 Surface aggregates of F12H16 of varying numbers of molecules

9.3.4.1 Mean azimuthal angle ($\bar{\theta}_{Az}$)

As was mentioned previously, the simulations of the limit size aggregates were prepared and run by predicting the diameter and the number of molecules in those aggregates and simulating them directly. This significantly reduced the computational burden of simulating increasingly larger systems until the limit size would be attained. Nevertheless, the condition of attainment of the limit size (*i.e.* $\bar{\theta}_{Az} \approx 0°$) was always checked in the end. In the case of the F12H16 aggregates, it was found that the initial prediction (of about 2650 molecules) resulted in an aggregate with $D \approx 30\,\text{nm}$, which was found to be below the limit size according to the $\bar{\theta}_{Az}$ criterion. Several simulations with increasingly larger systems (2750, 2900 and 3200 molecules) as well as one significantly smaller system (1500 molecules) were performed to understand the apparently disparate behaviour of this particular PFAA at the water–vacuum interface. The obtained $\bar{\theta}_{Az}$ values are presented as a function of the calculated D in Figure 9.18.

The dependence of $\bar{\theta}_{Az}$ on D for the F12H16 aggregates is not strikingly linear, as it was observed for the F8H14 aggregates (*cf.* Figure 9.1). Nonetheless, it is clear that smaller aggregates have a higher $\bar{\theta}_{Az}$ and that $\bar{\theta}_{Az} \approx 0°$ is obtained for an aggregate of about (36.6 ± 0.1) nm, with 3200 F12H16 molecules.

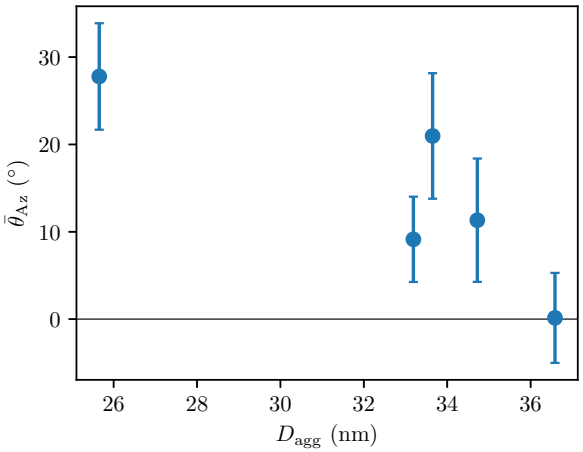

Figure 9.18: Mean azimuthal angle ($\bar{\theta}_{Az}$) as a function of the diameter of the simulated F12H16 aggregates (D_{agg}).

9.3.4.2 C_F–C_F–C_F–C_F dihedral angle ($\theta_{dihedral}$)

As an additional check, the C_F–C_F–C_F–C_F dihedral angle ($\theta_{dihedral}$) distributions were calculated for the simulated aggregates of F12H16, and these are presented in Figure 9.19. The analyses presented in Figures 9.18 and 9.19 indicate that all the simulated aggregates are below the limit size, except the largest one. This was considered to be the limit-size aggregate or hemimicelle, for which $\bar{\theta}_{Az} \approx 0°$ and the $\theta_{dihedral}$ distribution is symmetrical around $\theta_{dihedral} = 180°$. The latter result can be related to the top-view snapshot of this aggregate, presented in Figure 9.15, for which no spiralling arrangement of the molecules is seen.

As it was noted above, the results obtained for the simulated F12H16 hemimicelle fall outside the trends observed for the remaining systems. This is indicative that this particular system might have different dynamics or that, above a certain length of the CF chain (in absolute terms or relatively to the length of the CH chain of the PFAA molecule), the intermolecular interactions and the packing of the molecules within the hemimicelles might be subject to different constraints. The obtained hemimicelle diameter is nonetheless comparable to the only experimental data point found in the literature for this system ((33 ± 5) nm [36]), although the uncertainty of this measurement is relatively high. The subdivision of the hemimicelle in segments is observed in the simulation, since the dividing frontiers between segments with remarkably consistent molecular orientation are discernible in Figure 9.15. This phenomenon has been observed very markedly for F12H12, which has been described to comprise about 5 smaller primary aggregates, but not for F12H20 [41]. It is possible that the F12H16 hemimicelle might display an intermediate behaviour, but further experimental studies (including AFM imaging of the transferred films) should be conducted to assess it. Notwithstanding the particularities of this system, the performed analyses and checks are consistent among them: the attainment of a limit-size aggregate was confirmed based on the symmetry of the $\theta_{dihedral}$ distribution and the fact that $\bar{\theta}_{Az} \approx 0°$; the computed SDFs (*cf.* Figure B.15) show the ordering of the CH_2-CF_2 dipoles; the molecules are disposed in concentric layers within the hemimicelle (*cf.* Figure 9.8); the molecular orientation and the hemimicelle morphology are in line with the remaining systems (*cf.* Figure 9.16); the obtained $\theta_{Tilt,F}$ is slightly above, but still close to 65° (*cf.* Figure 9.12); the dependency of θ_{Tilt} with r is approximately linear and, based on the obtained value for Δ_{F12H16} (Figure 9.11) and the overall top-view appearance of the hemimicelle (Figure 9.15), the round shape of the aggregate and the approximations arising from there are reiterated.

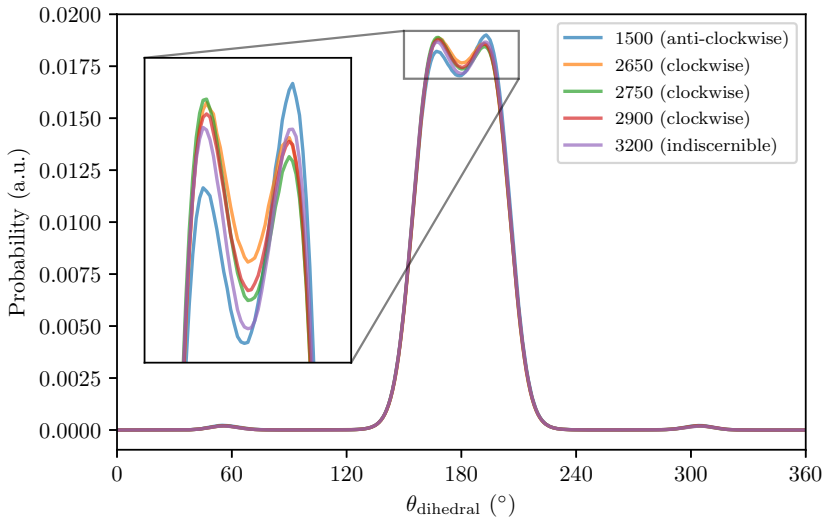

Figure 9.19: Distribution of the C_F–C_F–C_F–C_F dihedral angles (θ_{dihedral}) for aggregates of F12H16 of different sizes (*i.e.* with different numbers of molecules). The θ_{dihedral} follows the IUPAC convention, for which $\theta_{\text{dihedral}} = 0°$ for the *cis* conformation. The asymmetry (around 180°) of the relative maxima of these distributions correlate with the aggregates' spiralling sense (indicated in brackets in the legend and highlighted in the inset).

9.3.5 Extending the methodology to other PFAAs

Having established a methodology for the systematic study by MD simulation of the hemimicelles of PFAAs, this was extended to the investigation of hemimicelles of other molecules that were not part of the original data sets described above. This was done to provide further information on the self-assembling phenomenon under study and to assess the capacity of the geometrical model and of the MD simulations in reproducing experimental results for molecules that are different form those used in the initial set up of the model. That said, two additional series of PFAA hemimicelles were simulated at the water–vacuum interface, according to the procedure described above. These were the F10Hm (F10H14, F10H16, F10H18 and F10H20) and the F12Hm (F12H16 and F12H20) series. The specific molecules were chosen based on the availability of experimental data for comparison and to have some overlap with the preexisting results, to maximise their use. The mean (μ_{Az}) and standard deviation (σ_{Az}) of the fits obtained for the F10Hm and F12Hm series are presented in Table 9.4. The diameter (D), number of PFAA molecules comprising the simulated limit-size aggregates (n_{mol}) and the estimated uncertainty on n_{mol} (Δ_{mol}) are also compiled in this table. According to the established criterion of attainment of the limit size, the simulated aggregates are within $1 \times \sigma_{\text{Az}}$ of $\mu_{\text{Az}} = 0°$, so it is plausible that the performed simulations correspond to the experimentally observed hemimicelles.

The remaining analyses that were performed for the F8Hm and the FnH16 data sets were also conducted for the F10Hm and F12Hm series, whose results are presented in Section B.3 of Appendix B. In particular, the attention of the reader is drawn to the θ_{dihedral} distributions presented in Figure B.22, which are essentially symmetrical around θ_{dihedral} 180° and are consistent with the attainment of the limit size. The values of D obtained for the F10Hm and

Table 9.4: Summary of the parameters of the Gaussian curves (mean ± standard deviation or $\mu_{Az} \pm \sigma_{Az}$) fitted to the signed azimuthal angle (θ_{Az}) distribution for each of the simulated PFAA limit-size aggregates of the F10Hm and the F12Hm series. The number of PFAA molecules comprising the simulated limit-size aggregates (n_{mol}) and the uncertainty on n_{mol} (Δ_{mol}) are also presented. Δ_{mol} is estimated as the number of molecules comprising the outermost layer of the simulated aggregates, calculated as the perimeter of the aggregates divided by the diameter of the CF chain ($d_F = 2\sqrt{A_F/\pi}$).

FnHm	D (nm)	$\mu_{Az} \pm \sigma_{Az}$ (°)	n_{mol}	Δ_{mol}
F10H14	27.0 ± 0.1	-0.15 ± 6.10	1850	137
F10H16	32.5 ± 0.2	-0.97 ± 5.99	2550	165
F10H18	37.3 ± 0.1	2.06 ± 7.17	3400	189
F10H20	39.5 ± 0.1	-3.37 ± 5.02	3900	201
F12H16	36.6 ± 0.1	0.14 ± 5.15	3200	186
F12H20	39.9 ± 0.1	-1.83 ± 6.55	3900	203

F12Hm series are represented in graphical form in Figure 9.20, together with the corresponding predictions from the geometrical model and some experimental values from the literature, for comparison. The values marked as original work are preliminary results obtained in the scope of the studies presented in Chapter 11. These correspond to the hexagonal lattice parameter obtained from GISAXS measurements of the pure F10Hm and F12Hm films compressed to approximately $\pi = 5\,\mathrm{mN\,m^{-1}}$, according to the experimental procedure described therein.

In general, the obtained D results are in agreement with the available experimental data. Moreover, the predictions made from the geometrical model are similar to the values obtained from the MD simulations. The relatively more significant impact of varying the length of the CH chain on D is reiterated, compared to a similar variation of the length of the CF chain. However, apart from the discrepancies occurring for the F12H16 hemimicelle and that were the subject of a more detailed analysis in Subsection 9.3.4, the F12H20 hemimicelle also appears to be an outlier. The sizes predicted from the geometrical model and estimated from the MD simulations for this aggregate are significantly below the available experimental values. The morphology of the transferred film of F12H20 has been characterised by AFM, and this comprises hemimicelles with a varying degree of lateral order [41]. The existence of worm-like or elongated aggregates is also reported and these tend to enlarge the dimensions of the aggregates. This could explain why the D determined for F12H20 is significantly larger than expected, but such effect is unlikely: worm-like or elongated aggregates have been reported for F8H20 as well [9, 35], but this molecule organises according to a lattice of a size comparable to those predicted by the geometrical model and estimated by MD simulation. Moreover, the reported experimental size of ≈50 nm (*cf.* Table 4.1) corresponds to the diameter of the rounded hemimicelles [41], and also it has been suggested that the presence of elongated hemimicelles might be a transient effect that is suppressed upon the compression of the monolayer [9] or it might be an artefact of the process of transferring the film onto a solid substrate [36]. That said, similarly to what has been discussed for the case of F12H16, it is possible that the structure of the hemimicelles of F12H20 might diverge with the elongation of the molecule past a certain threshold. Although it is less likely, in light of the

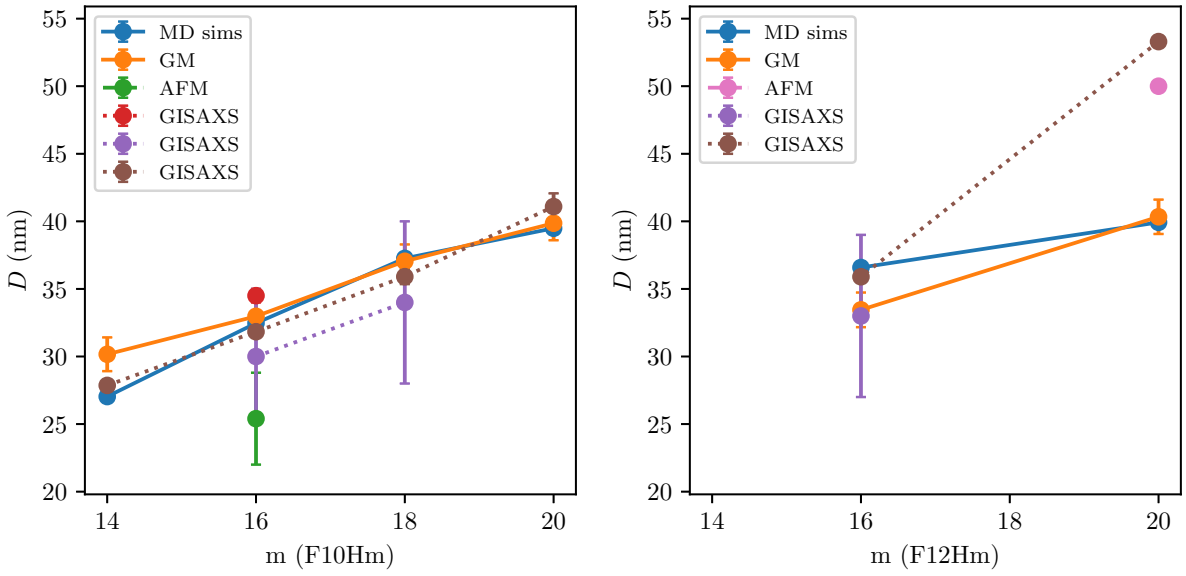

Figure 9.20: Diameter (D) of the PFAA hemimicelles formed at the air–water interface estimated with the geometrical model (orange, full lines) and computed from the simulation trajectories of the limit-size aggregates (blue, full lines) as functions of the number of carbon atoms in the CH chain or m, for n=10 (F10Hm) and for n=12 (F12Hm). For comparison, other literature results obtained using different experimental techniques are also shown, namely: AFM, from Refs. [9] (green, dashed lines) and [41] (pink, dashed lines); and GISAXS, from Refs. [5, 35] (red, dotted lines), [36] (purple, dotted lines) and original preliminary results (brown, dotted lines; see text for details). The lines are guides to the eye.

aforementioned AFM results [41], other aggregate morphologies that might result from a different balance of forces at the liquid–air interface have been reported, such as spiralling aggregates of F14H20 [42], which could effectively result in a larger D.

Overall, extending the study to the F10Hm and F12Hm series provides further insights into the phenomenon of self-assembling of PFAAs at the air–water interface. The obtained results are satisfactory and reiterate the conclusions drawn in the previous sections.

9.3.6 General discussion

Within the framework of the geometrical model, the PFAA hemimicelles are constructed starting from a central vertical molecule and the subsequent accretion of layers of molecules until a certain threshold value of θ_{Tilt} is attained ($\theta_{\mathrm{Tilt,f}}$). The juxtaposed trapezoidal-shaped molecules form an angle 2θ (*cf.* Figure 9.4) – ultimately, this is the origin of θ_{Tilt} – and display a longitudinal shift (h); otherwise, the stacking of the molecules would result in spherical or hemispherical structures. As explained in the previous chapter, this shift occurs as a consequence of the ordering of the CH_2-CF_2 dipoles. The molecules pack closely together and adopt a conformation that favours the mutual segregation of the CH and CF moieties and minimises the surface area of the hydrophobic PFAA molecules exposed to the aqueous subphase, subject to the constraints imposed by the molecules' architecture and intermolecular interactions (*cf.* Figure 9.6).

The overall balance of the subtle factors mentioned above results in the formation of the monodisperse round aggregates. Kato *et al.* have conducted AFM studies of Langmuir films of *n*-Perfluoroalkyl *m*-Carboxylic 1-Acid (F*n*H*m*-COOH), with varying n and m, and reported the formation of rounded, nanometre-sized and monodisperse surface aggregates [43, 44]. The morphology of the observed aggregates is strikingly similar to that of the PFAA hemimicelles, exhibiting a central pit and hexagonal ordering of the film. The authors propose the formation of the aggregates can be described by a mechanism of nucleation and growth, upon deposition of the spreading solution and quick solvent evaporation. The molecules, initially covering the surface area evenly, would gather in clusters or nuclei that grow rapidly by the incorporation of further molecules. The growth is limited by the exhaustion of monomers, substantiated by the low Equilibrium Spreading Pressure (ESP) of PFAAs. This is in line with the model proposed herein, which also describes the molecular packing through the accretion of layers of molecules. However, the arguments presented for the finite size and monodispersity of the aggregates are dissimilar: whilst Kato *et al.* base their reasoning on kinetics and availability of free molecules, the attainment of $\theta_{\mathrm{Tilt,f}}$ for the outermost layer of molecules limits the size of the aggregates, according to the geometrical model.

The self-assembling of amphiphiles in solution into supramolecular structures such as micelles and bilayers has been the subject of studies in physical chemistry for decades [45]. The morphology of the micellar aggregates of classical surfactants in solution can be predicted based on a geometrical packing parameter (P), given by $P = v_{\mathrm{t}}/(a_{\mathrm{h}} l_{\mathrm{c}})$, where v_{t}, a_{h} and l_{c} are the volume, average area of the (hydrophilic) head group and the length of the (hydrophobic) tail of the amphiphile molecule, respectively [45, 46]. This rationalises the self-assembling of dissolved amphiphiles and can help to predict, *e.g.*, whether a given surfactant forms spherical or cylindrical micelles or bilayers, all based on parameters characterising the geometry of the molecules. However, this reasoning is usually approximate and it's hard to define the cutoffs for P separating one micelle morphology from another. Still, P provides a rational approach for the adjustment of the medium conditions (*e.g.* *p*H or T) that might condition the molecular conformations and, ultimately, favour the formation of a specific kind of supramolecular structure [46].

Transposing this knowledge onto the study of the entirely hydrophobic "primitive surfactants" that are PFAAs, an analogy can be made between the packing parameter and the geometrical model. The latter describes the morphology and the internal structure of the PFAA hemimicelles and predicts their size solely based on parameters characterising the geometry of the individual molecules (chain lengths and cross-sectional areas) and the lateral ordering arising from the CH_2-CF_2 dipole interactions (the longitudinal shift or h), which is specific of this system. Another parallel can be drawn with the phenomenon of self-assembling at a much larger length scale of rod-like "mesoscopic amphiphiles" in solution [47]. These are µm-long building blocks made of two axis-collinear cylinders of materials with different affinities: a wider ($\approx 400\,\mathrm{nm}$ in diameter), hydrophilic, gold cylinder connected to a thinner ($\approx 360\,\mathrm{nm}$ in diameter), hydrophobic, polymer cylinder. Under the right conditions, these rigid structures form curved sheets or tubes, the size of which being determined by the relative lengths of the cylinders. The mutual segregation of the cylinders is a paramount driving force for this phenomenon. This is another example highlighting how the geometry of relatively simple building blocks can give rise to remarkable

self-assembled, organised structures at a much larger length scale, just like the hemimicelles of the trapezoidal PFAAs, with their mutually phobic CH and CF chains.

Finally, in the development and analysis of the geometrical model, some assumptions were made, and these deserve a few comments:

- The molecules are modelled as stacked rigid cylinders (one for each chain). This might be a reasonable approximation in the case of the stiff and helical CF chain, but a cruder one when it comes to the CH chain. Even though there is evidence that the CH chains are not liquid-like and are ordered within the monolayer [48], the CH chains are more mobile and that is not accounted for in the geometrical model (*e.g.* they might form an angle with the CF chain [8, 42, 48]);

- The model is based on a simple geometric construction, and no energetic or entropic factors are explicitly considered in its development. Most notably, the model does not predict the shape or the stability of the aggregates, rather a circular shape is assumed in its development, regardless of the type of PFAA considered. This way, the model does not predict whether the aggregates are formed or not and, even if they are (*i.e.* there is experimental evidence of their formation), their real morphology might differ;

- There are no limits to the validity of the model in terms of the length of either chain. Besides, the parameters used in the model (h, $\theta_{\mathrm{Tilt,f}}$) are assumed to be constant and transposable, regardless of the chemical composition of the aggregates. These assumptions might not hold up for aggregates too different from those studied by MD simulations herein and on whose results the model was founded. In fact, the different morphologies reported for some PFAAs, such as worm-like spirals and ribbons for F14H20 [42], might be the result of other factors that are unaccounted for (including kinetic ones) and that result in different constraints in the molecular packing;

- Still regarding the limits of the geometrical model, this considers the close packing of the CF chains for virtually any value of n. However, as the value of n increases, the divergence of the model in the close packing of the CF chains is ever more significant. This occurs because the geometrical model considers the molecules as 2 rigid, axis-collinear cylinders and does not compensate for the elongation of the CF chains, for instance in the form of an angle between the CH and the CF chains, to ensure their tight packing. This might be a reasonable approximation for shorter CF chains (in absolute terms or relative to the CH chain's length), but perhaps the peculiar behaviour reported herein for the F12H16 system is indicative of the start of a diverging behaviour with increasing n;

- Only pure component PFAA hemimicelles are considered and no prediction is possible for mixed aggregates, at least without added information or further assumptions.

Notwithstanding the aforementioned remarks and within the boundaries of the studied simulation conditions and range of chain lengths, the geometrical model provides a rational description for the packing of the molecules, an interpretation for the relative importance of the CH and CF chain lengths on D and a framework that complements the explanation for the existence of a central pit within the aggregates.

9.4 Concluding remarks

In this work, the influence of the hydrogenated (CH) and the perfluorinated (CF) chain lengths on the size of the hemimicelles was probed by a systematic Molecular Dynamics (MD) simulations study. Several Perfluoroalkylalkane (PFAA) molecules or FnHm with fixed CF chain length (n) and varying CH chain length (m) – F8Hm data set: F8H14, F8H16, F8H18, F8H20 – and with fixed m and varying n – FnH16 data set: F6H16, F8H16, F10H16, F12H16 – were studied, covering a representative range of molecular structures. The results were compared with available experimental data and were further rationalised in terms of a model describing the internal structure of the hemimicelles based on geometrical considerations. From a methodological point of view, this model enabled the estimation of the diameter and the number of molecules comprising a hemimicelle, being used in a predictive way for the preparation of the starting configurations of the MD simulation runs. Several conclusions can be drawn from this study:

- An initial study of aggregates with a varying number of F8H14 molecules reiterated the previous finding [11] that the mean azimuthal angle ($\bar{\theta}_{\mathrm{Az}}$) for a limit-size aggregate, corresponding to the experimentally observable hemimicelles, approaches the value of 0°. This is interpreted as a way of maximising the interactions and minimising the free space among the PFAA molecules. This also validates the method of verification of the attainment of the limit size by means of computing $\bar{\theta}_{\mathrm{Az}}$ from the θ_{Az} distribution;

- The rationalisation of the intramolecular structure and packing of the PFAA molecules in terms of a model based on geometric arguments pins the origin of the observed supramolecular self-assembled structure to fundamental principles, namely the conformational and geometrical characteristics of its constituting molecules. The implementation of such model in a predictive way was successful and its findings compare well with experiments, namely the predicted hemimicelle diameter and its dependence on the CH and CF chain lengths and the existence of a central pit;

- The study of the F8Hm and FnH16 data sets permitted to attain limit-size aggregates with $\bar{\theta}_{\mathrm{Az}} \approx 0°$, a C_F–C_F–C_F–C_F dihedral angle ($\theta_{\mathrm{dihedral}}$) distribution symmetrical around 180° and a molecular disposition within the aggregates in a non-spiralling bouquet. These were all reiterated as evidence of the attainment of the limit size of the aggregates;

- It was found that the molecules are disposed in a CF chain up-CH chain down configuration, in concentric layers and forming a tilt angle (θ_{Tilt}) that increases linearly with the radial distance from the centre of the hemimicelles (r), up to a limit value $\theta_{\mathrm{Tilt,F}} \approx 65°$. This limit value was found to be similar for all aggregates, suggesting it might arise from fundamental principles that ultimately determine the size of the hemimicelles, such as the counteraction of the curvature of the water surface induced by the packing of the PFAA molecules by the planarizing effect of the high surface tension of water [10];

- Considering a constant shift along the molecular axes (h) in the packing of consecutive layers gives rise to the existence of the central pit of the hemimicelles. Together with the fact that the variation of θ_{Tilt} with r is linear, these results are in support of the morphology

and size of the observed supramolecular structures being determined by molecular geometry (the mismatch of the CH and CF chains' cross-sectional areas and their relative chain lengths) and intermolecular interactions (with emphasis on the CH/CF chain antipathy and the ordering of the CH_2-CF_2 dipoles);

- The Grazing Incidence X-Ray Diffraction (GIXD) pattern was calculated from the simulation trajectories. The results are generally in agreement with available experimental data. Moreover, they shed light on the latter by reproducing the shift of the maximal diffraction intensity to lower Q_{xy} values with increasing Q_z. This was linked to the fan-like molecular arrangement within the aggregates and the constant rate of change of θ_{Tilt} with r;

- The F12H16 hemimicelle was found to be larger than the size predicted with the geometrical model and, in general, the results obtained for this system fell somewhat outside the trends observed for the remaining systems. This was attributed to probably different dynamics or the fact that, above a certain length of the CF chain (as this was the studied molecule with the longest CF chain), the intermolecular interactions and the molecular packing within the hemimicelles might be subject to different constraints. Nevertheless, in an analogy to a scaling effect, these results were still found to be consistent with the remaining ones obtained for the different PFAA molecules;

- The computational methodology was extended to investigate the structural properties of hemimicelles of other PFAA molecules not featured in the initial study and in the development of the geometrical model. These were the F10Hm (F10H14, F10H16, F10H18 and F10H20) and the F12Hm (F12H16 and F12H20) series. The results obtained for the F10Hm series fall within the trends described above and reiterate those findings. The F12H20 was found to be smaller than what has been determined experimentally. As it was pointed out for the F12H16 system, this is an indication that the F12H20 system might also present different dynamics or its packing might be subject to other constraints that were not accounted for in this study. Nevertheless, extending this study complemented the findings obtained with the F8Hm and FnH16 series, providing furhter insights into the phenomenon of self-assembling of PFAAs at the air–water interface.

Overall, the results reported herein provide a rational basis for a better understanding of the self-assembling process of PFAA molecules into discrete hemimicelles in Langmuir films prepared at the air–water interface.

References

[1] Z. Huang et al. 'Structural studies of semifluorinated hydrocarbon monolayers at the air/water interface'. In: *Journal of the Chemical Society – Faraday Transactions* 92.4 (1996), pp. 545–552. DOI: 10.1039/ft9969200545.

[2] A. El Abed et al. 'Experimental evidence for an original two-dimensional phase structure: An antiparallel semifluorinated monolayer at the air-water interface'. In: *Physical Review E* 65.5 (2002), Article No. 051603. DOI: 10.1103/PhysRevE.65.051603.

[3] M. Maaloum, P. Muller and M. P. Krafft. 'Monodisperse Surface Micelles of Nonpolar Amphiphiles in Langmuir Monolayers'. In: *Angewandte Chemie – International Edition* 41.22 (2002), pp. 4331–4334. DOI: 10.1002/1521-3773(20021115)41:22<4331::AID-ANIE4331>3.0.CO;2-J.

[4] A. González-Pérez, C. Contal and M. P. Krafft. 'Experimental evidence for a surface concentration-dependent mechanism of formation of hemimicelles in Langmuir monolayers of semi-fluorinated alkanes'. In: *Soft Matter* 3.2 (2007), pp. 191–193. DOI: 10.1039/b613265k.

[5] L. Bardin et al. 'Long-Range Nanometer-Scale Organization of Semifluorinated Alkane Monolayers at the Air/Water Interface'. In: *Langmuir* 27.22 (2011), pp. 13497–13505. DOI: 10.1016/10.1021/la201802x.

[6] P. Fontaine et al. 'Evidence for Interaction with the Water Subphase As the Origin and Stabilization of Nano-Domain in Semi-Fluorinated Alkanes Monolayer at the Air/Water Interface'. In: *Langmuir* 30.50 (2014), pp. 15193–15199. DOI: 10.1021/la5038124.

[7] P. Fontaine et al. 'Evidence of lying molecules in the structure of the most condensed phase of semi-fluorinated alkane monolayers'. In: *Nanoscale* 10.5 (2018), pp. 2310–2316. DOI: 10.1039/c7nr07415h.

[8] M. O. Gallyamov et al. 'Self-assembly of (perfluoroalkyl)alkanes on a substrate surface from solutions in supercritical carbon dioxide'. In: *Physical Chemistry Chemical Physics* 8.22 (2006), pp. 2642–2649. DOI: 10.1039/b602959k.

[9] G. Zhang et al. 'Occurrence, Shape, and Dimensions of Large Surface Hemimicelles Made of Semifluorinated Alkanes. Elongated versus Circular Hemimicelles. Pit- and Tip-Centered Hemimicelles'. In: *Journal of the American Chemical Society* 127.29 (2005), pp. 10412–10419. DOI: 10.1021/ja0510515.

[10] H. O. S. Yadav et al. 'Hemimicelle formation of semi-fluorocarbon chains at air–water interface: coarse-grained molecular dynamics study with an extension of the SPICA force field'. In: *Molecular Physics* 119.19–20 (2021), Article No. e1910355. DOI: 10.1080/00268976.2021.1910355.

[11] G. M. C. Silva et al. 'Spontaneous self-assembly and structure of perfluoroalkylalkane surfactant hemimicelles by molecular dynamics simulations'. In: *Proceedings of the National Academy of Sciences of the United States of America* 116.30 (2019), pp. 14868–14873. DOI: 10.1073/pnas.1906782116.

[12] G. M. C. Silva. 'The Fluorophobic Effect in Soft Matter'. PhD thesis. Lisboa, Portugal: Universidade de Lisboa – Instituto Superior Técnico, 2021.

[13] L. Martínez et al. 'PACKMOL: A Package for Building Initial Configurations for Molecular Dynamics Simulations'. In: *Journal of Computational Chemistry* 30.13 (2009), pp. 2157–2164. DOI: 10.1002/jcc.21224.

[14] M. J. Abraham et al. *GROMACS User Manual version 5.0.7*. URL: https://ftp.gromacs.org/manual/manual-5.0.7.pdf (visited on 10/07/2022).

[15] C. R. Harris et al. 'Array programming with NumPy'. In: *Nature* 585.7825 (2020), pp. 357–362. DOI: 10.1038/s41586-020-2649-2.

[16] T. E. Oliphant *et al. numpy 1.26.2*. Version 1.26.2. Nov. 2023. URL: https://pypi.org/project/numpy/1.26.2/.

[17] W. McKinney. 'Data Structures for Statistical Computing in Python'. In: *Proceedings of the 9th Python in Science Conference*. Ed. by S. van der Walt and J. Millman. 2010, pp. 56–61. DOI: 10.25080/Majora-92bf1922-00a.

[18] The pandas Development Team. *pandas-dev/pandas: Pandas*. Version 2.0.1. Apr. 2023. URL: https://doi.org/10.5281/zenodo.7857418.

[19] J. D. Hunter. 'Matplotlib: A 2D graphics environment'. In: *Computing in Science & Engineering* 9.3 (2007), pp. 90–95. DOI: 10.1109/MCSE.2007.55.

[20] T. A. Caswell et al. *matplotlib/matplotlib: REL: v3.7.1*. Version 3.7.1. Mar. 2023. URL: https://doi.org/10.5281/zenodo.7697899.

[21] N. Michaud-Agrawal et al. 'MDAnalysis: A Toolkit for the Analysis of Molecular Dynamics Simulations'. In: *Journal of Computational Chemistry* 32.10 (2011), pp. 2319–2327. DOI: 10.1002/jcc.21787.

[22] R. Gowers et al. 'MDAnalysis: A Python Package for the Rapid Analysis of Molecular Dynamics Simulations'. In: *Proceedings of the 15th Python in Science Conference*. Ed. by S. Benthall and S. Rostrup. 2016, pp. 98–105. DOI: 10.25080/Majora-629e541a-00e.

[23] The MDAnalysis Development Team. *MDAnalysis 2.6.1*. Version 2.6.1. Aug. 2023. URL: https://pypi.org/project/MDAnalysis/2.6.1/#history.

[24] P. A. C. Lourenço. 'Molecular Dynamics Simulations and Simulated Diffraction Spectra of Long Chain Fluorinated and Hydrogenated Substances at the Water-Air Interface'. Online (accessed 10/08/2019): https://fenix.tecnico.ulisboa.pt/cursos/meq/dissertacao/1691203502343168. MA thesis. Instituto Superior Técnico, 2018.

[25] W. Humphrey, A. Dalke and K. Schulten. 'VMD: Visual Molecular Dynamics'. In: *Journal of Molecular Graphics & Modelling* 14.1 (1996), pp. 33–38. DOI: 10.1016/0263-7855(96)00018-5.

[26] M. Brehm and B. Kirchner. 'TRAVIS - A Free Analyzer and Visualizer for Monte Carlo and Molecular Dynamics Trajectories'. In: *Journal of Chemical Information and Modeling* 51.8 (2011), pp. 2007–2023. DOI: 10.1021/ci200217w.

[27] M. Brehm et al. 'TRAVIS–A free analyzer for trajectories from molecular simulation'. In: *Journal of Chemical Physics* 152.16 (2020), Article No. 164105. DOI: 10.1063/5.0005078.

[28] P. Silva. 'Monolayers of hemi-micelles of semifluorinated alkanes at the air–water interface: influence of chain length on the self-assembling properties'. Online (accessed 30/10/2021): https://fenix.tecnico.ulisboa.pt/cursos/mebiol/dissertacao/846778572212315. MA thesis. Instituto Superior Técnico, 2019.

[29] Y. B. Vysotsky et al. 'Quantum Chemical Semiempirical Approach to the Structural and Thermodynamic Characteristics of Fluoroalkanols at the Air/Water Interface'. In: *Journal of Physical Chemistry B* 109.1 (2005), pp. 454–462. DOI: 10.1021/jp048240e.

[30] P. Dynarowicz-Łatka et al. 'Structural Investigation of Langmuir and Langmuir–Blodgett Monolayers of Semifluorinated Alkanes'. In: *Journal of Physical Chemistry B* 110.12 (2006), pp. 6095–6100. DOI: 10.1021/jp057270u.

[31] F. G. Tournilhac, P. Bassoul and R. Cortès. 'Structure of the Smectic B Phase Formed by Linear and Branched Perfluoroalkyl-Alkanes'. In: *Molecular Crystals and Liquid Crystals* 362 (2001), pp. 45–65. DOI: 10.1080/10587250108025759.

[32] J. G. Riess. 'Fluorous micro- and nanophases with a biomedical perspective'. In: *Tetrahedron* 58.20 (2002), pp. 4113–4131. DOI: 10.1016/S0040-4020(02)00262-4.

[33] P. de Santis et al. 'Stability of Helical Conformations of Simple Linear Polymers'. In: *Journal of Polymer Science: Part A* 1.4 (1963), pp. 1383–1404. DOI: 10.1002/pol.1963.100010426.

[34] Sir Derek Barton et al. 'Comprehensive Organic Chemistry'. In: 1st ed. Vol. I. ISBN 9780080213194. Oxford: Pergamon Press, 1979. Chap. *Hydrocarbons*. ISBN: 9780080213194.

[35] L. Bardin. 'Monocouches d'alcanes semi-fluorés'. PhD thesis. Paris, France: Université Pierre et Marie Curie, 2010.

[36] M. Veschgini et al. 'Size, Shape, and Lateral Correlation of Highly Uniform, Mesoscopic, Self-Assembled Domains of Fluorocarbon–Hydrocarbon Diblocks at the Air/Water Interface: A GISAXS Study'. In: *ChemPhysChem* 18.19 (2017), pp. 2791–2798. DOI: 10.1002/cphc.201700325.

[37] H. M. McConnell and R. de Koker. 'Note on the Theory of the Sizes and Shapes of Lipid Domains in Monolayers'. In: *Journal of Physical Chemistry* 96.17 (1992), pp. 7101–7103. DOI: 10.1021/j100196a048.

[38] A. N. Semenov et al. 'Theory of Surface Micelles of Semifluorinated Alkanes'. In: *Langmuir* 22.21 (2006), pp. 8703–8717. DOI: 10.1021/la060638+.

[39] M. Li et al. 'Formation of an ordered Langmuir monolayer by a non-polar chain molecule'. In: *Nature* 367.6459 (1994), pp. 151–153. DOI: 10.1038/367151a0.

[40] P. Silva et al. 'Langmuir Films of Perfluorinated Fatty Alcohols: Evidence of Spontaneous Formation of Solid Aggregates at Zero Surface Pressure and Very Low Surface Density'. In: *Nanomaterials* 10.11 (2020), Article No. 2257. DOI: 10.3390/nano10112257.

[41] L. de Viguerie et al. 'Effect of the Molecular Structure on the Hierarchical Self-Assembly of Semifluorinated Alkanes at the Air/Water Interface'. In: *Langmuir* 27.14 (2011), pp. 8776–8786. DOI: 10.1021/la201377f.

[42] A. Mourran et al. 'Self-Assembly of the Perfluoroalkyl-Alkane F14H20 in Ultrathin Films'. In: *Langmuir* 21.6 (2005), pp. 2308–2316. DOI: 10.1021/la048069y.

[43] T. Kato, M. Kameyama and M. Kawano. 'Two-dimensional micronodule structure in monolayers of a partially fluorinated long-chain acid observed by atomic force microscopy'. In: *Thin Solid Films* 273.1–2 (1996), pp. 232–235. DOI: 10.1016/0040-6090(95)06774-4.

[44] T. Kato et al. 'Monodisperse Two-Dimensional Nanometer Size Clusters of Partially Fluorinated Long-Chain Acids'. In: *Langmuir* 14.7 (1998), pp. 1786–1798. DOI: 10.1021/la970951z.

[45] J. N. Israelashvili. *Intermolecular and Surface Forces*. 3rd ed. ISBN 0-12-375182-9. Cambridge, MA, USA: Academic Press, 2011. ISBN: 0-12-375182-9.

[46] P. C. Hiemenz and R. Rajagopalan. *Principles of Colloid and Surface Chemistry*. 3rd ed. New York, USA: Marcel Dekker, 1997. ISBN: 978-0-8247-9397-5.

[47] S. Park et al. 'Self-Assembly of Mesoscopic Metal-Polymer Amphiphiles'. In: *Science* 303.5656 (2004), pp. 348–351. DOI: 10.1126/science.1093276.

[48] C. Schwieger, X. Liu and M. P. Krafft. 'Self-assembled mesoscopic surface domains of fluorocarbon-hydrocarbon diblocks can form at zero surface pressure: tilting of solid-like hydrocarbon moieties compensates for cross-section mismatch with fluorocarbon moieties'. In: *Physical Chemistry Chemical Physics* 19.35 (2017), pp. 23809–23816. DOI: 10.1039/c7cp02432k.

Chapter 10

Formation of hemimicelles of PFAAs in the presence of long- and short-chain alcohols

It has been proposed that the shape of the domains in a Langmuir film results from a balance between electrostatic repulsive forces between molecules of the same type (say between charged or polar headgroups of the amphiphiles forming the film) and the line tension between immiscible phases [1–3]. Line tension can be perceived as the 2D-analogue of surface tension, arising from the existence of a boundary between two immiscible 2D phases and being larger the more chemically different those phases are. Higher repulsive electrostatic forces favour the formation of smaller or extended (e.g. ribbon-like) domains, whereas a larger line tension favours the formation of large domains with compact shapes (to minimise the perimeter of the domain and the length of the contact line). This reasoning is commonly employed to interpret the morphology of domains in the 100 µm length scale, such as in phase-separated films of CH and CF carboxylic acids [4, 5], and it was the starting point in the rationale of this work.

10.1 Films of PFAAs on a liquid subphase of short-chain alcohols

PFAAs have a molecular structure that is atypical, in comparison to common amphiphiles. The latter usually contain a hydrophilic moiety or polar head that anchors the molecules at the air–water interface and a hydrophobic tail that renders the molecules insoluble [6]. When it comes to PFAAs, they lack a polar terminal group and their amphiphilic character derives instead from the mutual incompatibility of the CH and CF chains, and they have been termed "primitive surfactants" because of that [7–9]. PFAAs self-assemble into hemimicelles, each one constituting one domain whose shape can be expected *a priori* to also be controlled by the balance between electrostatic interactions and line tension (between the hemimicelles and the subphase free surface). The electrostatic interactions among PFAA molecules are essentially due to the CH_2–CF_2 dipoles buried in the middle of the chains [10–12]. These interactions can be considered to be constant regardless of the subphase composition, as a first approximation. However, by lowering the surface tension of the subphase, the line tension should be lowered as

Table 10.1: Surface tension at 293 K of the pure compounds used as subphase of the studied systems.

Compound	**Surface tension** ($\mathrm{mN\,m^{-1}}$)	**Ref.**
Water	72.74 ± 0.36	[15]
Methanol (MeOH)	22.73 ± 0.02	[16]
Ethanol (EtOH)	22.11 ± 0.09	[17]
Butanol (BuOH)	24.56 ± 0.10	[17]
2,2,2-trifluoroethanol (TFE)	20.02 ± 0.05	[17]

well. The formation of smaller domains or domains with a larger perimeter (e.g. worm-like) could be anticipated in such circumstances.[1]

A preliminary MD simulation study was conducted, suggesting that switching the subphase from water to short-chain alcohols should still allow the formation of stable, nanostructured PFAA films at the air–liquid interface [13]. The experimental extension of this investigation followed suit, to assess the effect of the nature of the liquid subphase on the morphology of the thin film of PFAA spread over it. The interactions between the subphase alcohol molecules and the PFAAs can be tweaked by varying the length of the alcohol side chain (herein, from 1 carbon atom in methanol to 4 carbon atoms in butanol) as well as its chemical composition (CH or CF alcohols). Ultimately, from a practical point of view, this work can be regarded as an exploratory study of this experimental variable towards the understanding, and thus the control, of the morphology of PFAA films for the preparation of highly ordered self-assembled templates for surface nanopatterning and other nanotechnology applications. Herein, samples were prepared by spin coating a spreading solution of PFAAs on solid substrates previously wet with different liquid subphases. Following previous work [8, 14], the molecule F8H18 was chosen for these studies. For reference, Table 10.1 compiles the values of surface tension at 293 K of the studied alcohols and water. At this temperature, water has a high surface tension ($(72.74 \pm 0.36)\,\mathrm{mN\,m^{-1}}$), whereas the surface tension of the studied alcohols is about 3 times lower, falling in the $20\,\mathrm{mN\,m^{-1}}$ to $25\,\mathrm{mN\,m^{-1}}$ range.

10.2 Mixed Langmuir films of PFAAs with long-chain alcohols

A different, although related, MD simulation study was conducted to investigate the structural features of mixed binary Langmuir films of PFAAs mixed with long-chain CH or CF alcohols. An experimental characterisation study of these systems has uncovered that the lateral segregation of the alcohol and the PFAA molecules is plausible [18]. Moreover, based on data from Surface Pressure (π)–Molecular Area (A) isotherms and GIXD experiments, it seems that the laterally segregated film reorganises upon compression beyond the point of collapse of the

[1] A note should be added concerning the electrostatic interactions between the molecules at the edge of the hemimicelles and the molecules of the subphase. The molecules at the rim of the hemimicelles are the only ones expected to have more significant electrostatic interactions with the subphase molecules. Because the PFAA molecules and the subphase molecules don't interact through strong polar interactions (such as hydrogen bonds), the effect of changing water for a liquid of decreasing polarity, like alcohols of different chain lengths, is expected to have a smaller influence on the size of the hemimicelles compared to the change in line tension.

monolayer. In such conditions, it is plausible that the PFAA molecules are ejected from the monolayer and accumulate on top of the alcohol molecules, which rest anchored onto the water subphase by their alcohol moieties. Depending on the molar proportion of PFAA to alcohol molecules, a loosely to densely packed monolayer or a multilayer of PFAA molecules may form on top of the alcohol monolayer. The formation of a monolayer seems to be favoured for systems containing long-chain CH alcohols, whereas a trilayer seems to be preferred for systems containing long-chain CF alcohols [18]. At the time, there was no evidence of nanostructuring (*i.e.* of the existence of hemimicelles of PFAA) of the mixed binary film. However, based on π–A isotherms, GIXD and Atomic Force Microscopy (AFM) results of related systems of mixed Langmuir films of F8H16 and a Phospholipid (PL) (Dipalmitoylphosphatidylethanolamine (DPPE)) [19, 20], that scenario seems plausible. For these F8H16/DPPE mixed films, the existence of a network of hemimicelles in coexistence with a monolayer of DPPE is reported. Moreover, a similar behaviour was observed, inasmuch as the PFAA molecules were vertically segregated upon compression and collapse of the film and the gliding of the F8H16 hemimicelles on top of the DPPE film was reported. Provided the adequate molar proportion of PFAA to DPPE molecules is employed, total coverage of the DPPE film by a network of hemimicelles is observed. A similar behaviour is therefore anticipated for the mixed binary films of PFAAs mixed with long-chain alcohols (at least for CH alcohols).

That said, the objective of this additional study was to investigate by MD simulation whether the proposed scenarios are plausible, specifically: starting from a water-supported laterally-segregated mixed binary film of a long-chain alcohol (1-octadecanol (H18OH) or 1H,1H-perfluoro-1-octadecanol (F17H1OH)) and a PFAA (F8H18), assess if the lateral compression of such system induces the vertical segregation of the PFAA molecules, *i.e.* if an aggregate of F8H18 molecules would glide on top of the monolayer of the long-chain alcohol; building an initial configuration of a vertically separated mixed binary film comprising a water-supported long-chain alcohol (H18OH or F17H1OH) dense monolayer and an aggregate of PFAA molecules (F8H16) on top of it, the latter in sufficient number (2500) to form a hemimicelle with a size and structural features similar to the equilibrium-size hemimicelles found in pure Langmuir films of F8H16 [21], assess whether the F8H16 aggregate would evolve to develop a structure resembling that of the pit-centred hemimicelles described before. In the scope of this work, these systems are designated designated monolayer- or bilayer-start systems, respectively.

10.3 Methods

10.3.1 MD simulations

The Force Field (FF) parameters and the method of preparation of the initial configurations for the simulations carried out within the scope of this study are described below. All the algorithms and simulation conditions are otherwise similar to the ones already described in Chapter 8. Except where noted differently, all simulations were performed at a temperature of 298.15 K. The featured snapshots were rendered using the Visual Molecular Dynamics (VMD) (version 1.9.4) [22] open-source software.

10.3.1.1 Films of PFAAs over a liquid subphase of short-chain alcohols

The MD simulations described herein were performed by MSc student Diogo Gaspar [13], within the broader framework of the studies presented in this thesis.

The short-chain hydrogenated alcohols were modelled with the Optimised Potential for Liquid Simulations (OPLS)-All-Atom (AA) FF [23]. The 2,2,2-trifluoroethanol (TFE) molecules were modelled based on the work of Duffy *et al.* [24, 25]. In this work, the alcohols Methanol (MeOH), Ethanol (EtOH), Propanol (PrOH) and TFE were studied. The Extended Simple Point Charge (SPC/E) model was used for the water molecules [26]. The L-OPLS based FF parameters described in Chapter 8 were used to model the PFAA molecules [23, 27–29], specifically F8H16, in this work.

Preequilibrated slabs (a film with 2 explicit liquid-vacuum interfaces perpendicular to the z axis) of liquid water, pure alcohols or a mixture of water and alcohol with a thickness of about 3.5 nm to 4.0 nm and 8 nm of side of were generated using the open-source software Packmol (v. 20.2.2) [30]. These were equilibrated in the NVT ensemble for at least 2 ns with Periodic Boundary Condition (PBC) in all directions. Whenever it was required, slabs with larger lateral dimensions were generated by replicating smaller equilibrated liquid slabs in the xy plane and further equilibrating the resulting system for at least 1 ns. In the case of the mixed water/alcohol systems, the composition of the liquid subphase was set by adjusting the number of molecules of water and of alcohol accordingly. The F8H16 molecules were then placed close to the liquid-vacuum interface of the preequilibrated liquid slabs, either in a random configuration or packed in a dense cylinder, the latter obtained using Packmol, with the CH chains facing the liquid.

10.3.1.2 Mixed Langmuir films of PFAAs with long-chain alcohols

The MD simulations described herein were performed by MSc students José Fonseca [31] and João Rodrigues [32], within the broader framework of the studies presented in this thesis.

The aliphatic chains of the long-chain CH alcohols were modelled with the L-OPLS FF [28]. The alcohol moiety for these molecules was modelled using the OPLS-AA FF parameters [23]. The fluorinated segments of the long-chain CF alcohols were modelled with an optimised version [33] of the OPLS FF for Perfluoroalkanes (PFAs) [27]. The alcohol moiety of the CF alcohols was modelled after the work of Duffy *et al.* on TFE [24, 25]. In this work, the alcohols 1-octadecanol (H18OH) and 1H,1H-perfluoro-1-octadecanol (F17H1OH) were studied. The SPC/E model was used for the water molecules [26]. The L-OPLS based FF parameters described in Chapter 8 were used to model the PFAA molecules [23, 27–29]. The molecules F8H16 and F8H18 were studied in this work.

The initial configurations were prepared in a way similar to that described in Chapter 8. Equilibrated water slabs were used as the subphase or supporting liquid substrate for the studied films. For the studies presented herein, two different types of initial configurations and simulation procedures were employed, designated Monolayer- or Bilayer-start systems.

Monolayer-start systems The Monolayer-start systems were obtained using the open-source software Packmol to prepare a densely packed block (cylinder or prism) with 795 molecules of either H18OH or F171HOH in their relaxed (energy-minimised) configuration. This block of

molecules was then placed close to an equilibrated water slab of appropriate lateral dimensions to produce a dense monolayer (molecular area $< 0.4\,\mathrm{nm\,molecule^{-1}}$), with the alcohol moieties facing the water slab. Separately, a cylinder of 300 tightly packed F8H18 molecules in their minimum energy configuration was prepared using the open-source software Packmol and placed (CH chains facing the liquid) near a preequilibrated water slab with the same lateral dimensions as the one used to prepare the alcohol monolayer, to form an aggregate of PFAA molecules. Both systems were equilibrated for at least 2 ns in the NVT ensemble before further use. The equilibrated systems were concatenated side-by-side, as is shown in Figures 10.3 and 10.4. The simulation protocol that followed, named intermittent anisotropic compression/equilibration protocol, consisted in performing alternate steps of: simulation in the NPT ensemble, applying an anisotropic barostat to control the pressure in order to reduce the linear dimension of the box corresponding to its largest side in the starting configuration (horizontal direction in the snapshot depicted in Figures 10.3a and 10.4a) by about 2 nm to 4 nm; simulation in the NVT ensemble for at least 3 ns for the relaxation and reequilibration of the resulting compressed system. The total simulation time required to produce the final state configurations was at least 32 ns.

Bilayer-start systems The Bilayer-start systems were obtained using the open-source software Packmol to prepare a densely packed block (prism) with a varying number of molecules of either H18OH or F171HOH in their relaxed (energy-minimised) configuration. The number of molecules of the long-chain alcohol was chosen to yield a dense film in a simulation box whose side measured approximately 8 nm. This block of molecules was then placed close to an equilibrated water slab, with the alcohol moieties facing the water slab, and the system was relaxed using the steepest descent energy-minimisation algorithm. Whenever needed, short simulations in the NPT ensemble followed, using a semiisotropic barostat to reduce the xy dimensions of the simulation box, to achieve a dense film (the values of area per molecule attained in the simulated pure alcohol monolayers varied between around $0.18\,\mathrm{nm\,molecule^{-1}}$ to $0.20\,\mathrm{nm\,molecule^{-1}}$ for H18OH and about $0.28\,\mathrm{nm\,molecule^{-1}}$ for F171HOH). These water-supported pure alcohol monolayers were then equilibrated in the NVT ensemble for at least 1 ns before being replicated in the xy plane, whenever larger systems were needed. These were further equilibrated for at least 1 ns more before any further use. A cylinder of 2500 F8H16 densely packed molecules in their minimum-energy configuration was prepared using the open-source software Packmol and placed on top of the previously prepared simulation boxes of dense monolayers of H18OH or F171HOH (CH chains facing the alcohol). The system was relaxed using the steepest descent energy-minimisation algorithm and the resulting system was used as the starting configuration of a simulation run of at least 10 ns in the NVT ensemble.

10.3.2 Experimental

Following previous work [34], the silicon wafers used to prepare the samples had an area of approximately $1\,\mathrm{cm^2}$. The silicon wafers were thoroughly cleaned by immersion in piranha solution (1/3 in volume of 30% hydrogen peroxide and 2/3 concentrated sulphuric acid) for 15 min. This cleans the wafers of any organic impurities and renders their surface hydrophilic. This procedure is necessary to make sure that the liquid subphase (pure water or short-chain

alcohols) spreads and holds at the surface of the solid substrate prior to depositing the spreading solution [34].

To prepare the samples by spin coating, one clean wafer (stored in ultrapure water) was placed on the spin coater and secured with a vacuum system. The remaining water was eliminated by blowing a nitrogen gust, before quickly depositing a known volume of liquid subphase (50 µL). The spreading solution (1 µL of a 2 mmol dm^{-3} solution of the FnHm in chloroform) was then deposited on top of the wet wafer. The amount of spreading solution was enough to form a dense monolayer of FnHm at the surface of the substrate. Various parameters characterise the functioning of a spin coater, including the acceleration, the rotation speed and interval of time during which this speed is maintained. In this work, the samples were accelerated at 60 rpm/s up to a speed of 600 rpm. This speed was kept constant for 5 min, after which the rotation was slowed to a halt at the same acceleration. Some of the samples were prepared differently, by a method referred here as simple evaporation. In these cases, the same protocol described above was followed except for the use of the spin coater. Rather, the samples were air-dried in a dust-protected environment.

The samples were imaged with a Park Systems NX20 Atomic Force Microscope working in Non-Contact mode.[2] The used cantilever chips were RTESPA-300 Silicon probes (Bruker, USA) with a force constant and a resonance frequency approximately equal to 40 N m^{-1} and 300 kHz, respectively. The obtained scans had an aspect ratio of 1:1 (square images) and measured about 0.5 µm to 2 µm and 128 pixel to 1024 pixel of side. All studied systems were imaged from at least two independent replicates and each replicate was sampled several times in different parts of its surface for representativeness. The data files were treated using the open-source software Gwyddion (v. 2.62) [35]. The height data was processed by removing the background plane and aligning the rows by their median height. The remaining analyses (image rendering, 2D FT, extraction of height profiles) were also performed using this software.

The size of the hemimicelles was estimated by sampling several images for height profiles and by computing the 2-Dimensional Fourier Transform (2DFT) (see Subsection 6.3.2). The first approach is more versatile and was used throughout this work, not least because it is applicable for images of samples with practically any morphology (including heterogeneous or weakly organised samples or images whose background is difficult to define or is not completely flat). However, height profiles only provide information at a local level, a drawback which is partially circumvented by sampling each image for several height profiles. The 2DFT is computed based on the entire image, so it can provide a more complete picture but, because of its definition, its performance degrades for heterogeneous and weakly organised samples. A third method was attempted, the particle analysis or counting described in Subsection 6.3.2. This is a common method to estimate the diameter of the round hemimicelles and has been used successfully before [14, 34, 36, 37]. This was not the case in the present work, due to problems in defining the threshold isolating the hemimicelles from the background. The methods used are noted on a case-by-case basis.

[2] In the context of this work, and following previous experiments, the samples of films of PFAAs were first imaged in Intermittent-Contact mode. However, difficulties in optimising the scanning conditions and signs of sample degradation (*e.g.* "dragging" molecules displaced by the tip during the scan) prompted the use of Non-Contact mode for its sample-preserving advantages (see Subsection 6.2.4).

10.4 Results and Discussion: MD Simulation

10.4.1 Films of PFAAs over a liquid subphase of short-chain alcohols

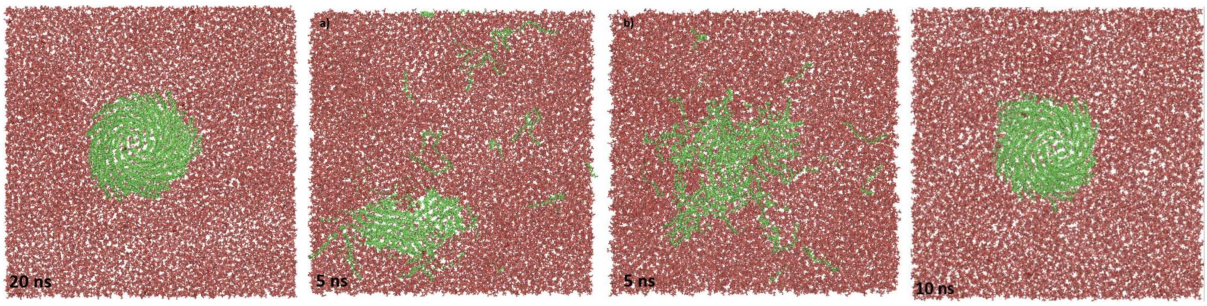

Figure 10.1: Top-view snapshots of the final state of the simulations of 100 F8H16 molecules at the surface of the pure alcohols (from left to right): MeOH, EtOH, PrOH and TFE. The PFAA molecules are coloured green and the alcohol molecules are coloured red. The bottom left corner of each image indicates the duration of the respective production simulation run. The simulation boxes measure 16 nm of side. Adapted from [13].

Figure 10.1 shows some top-view snapshots of the final state of the simulations of 100 F8H16 molecules at the surface of the investigated pure short-chain alcohols. The simulation of an aggregate with a relatively small number of molecules (about one order of magnitude below the typical aggregation number for hemimicelles of F8H16 formed at the air–water interface [21, 38]) had the purpose of assessing whether a stable, cohesive aggregate of PFAA molecules could be formed at the surface of the pure short-chain alcohols or whether the molecules would disaggregate and dissolve in the liquid subphase instead. In that regard, it can be observed that a round and cohesive aggregate is formed at the surface of pure MeOH and of pure TFE. Moreover, the molecules within these aggregates wind up in a spiral, a phenomenon which has been reported before for simulations performed over pure water and has been interpreted as indicative that the aggregate contains a number of molecules below the equilibrium aggregation number [21] (see also Chapter 9). On the other hand, the PFAA molecules at the surface of pure EtOH and of pure PrOH are partially dissolved in the liquid subphase. In these two cases, a stable aggregate is not obtained. Notwithstanding, the possibility of the PFAA molecules forming a film at the surface of these two liquids should not be discarded as this could still happen even if the molecules display a finite solubility in the subphase. In such case, the adsorption of PFAA molecules at the liquid–air interface would occur in equilibrium with the molecules dissolved in the bulk liquid (in what is known as a Gibbs film) and the possible nanostructuring of such film cannot be excluded.

Considering the obtained results, this study was extended to the investigation of films of pure PFAAs at the surface of liquid mixtures of water with each of the aforementioned short-chain alcohols. It was anticipated that these mixtures could provide a more suitable liquid subphase for the formation of stable aggregates of PFAAs. The mixtures with highest molar fraction of alcohol in water (x_{alcohol}) that were investigated were [13]: $x_{\text{MeOH}} = 1.0$ (pure MeOH); $x_{\text{EtOH}} = 0.2$; $x_{\text{PrOH}} = 0.2$; and $x_{\text{TFE}} = 1.0$ (pure TFE). Aggregates comprising 2500 F8H16 molecules were simulated at the liquid–vacuum interface of slabs of these liquids. Snapshots illustrating the cross-

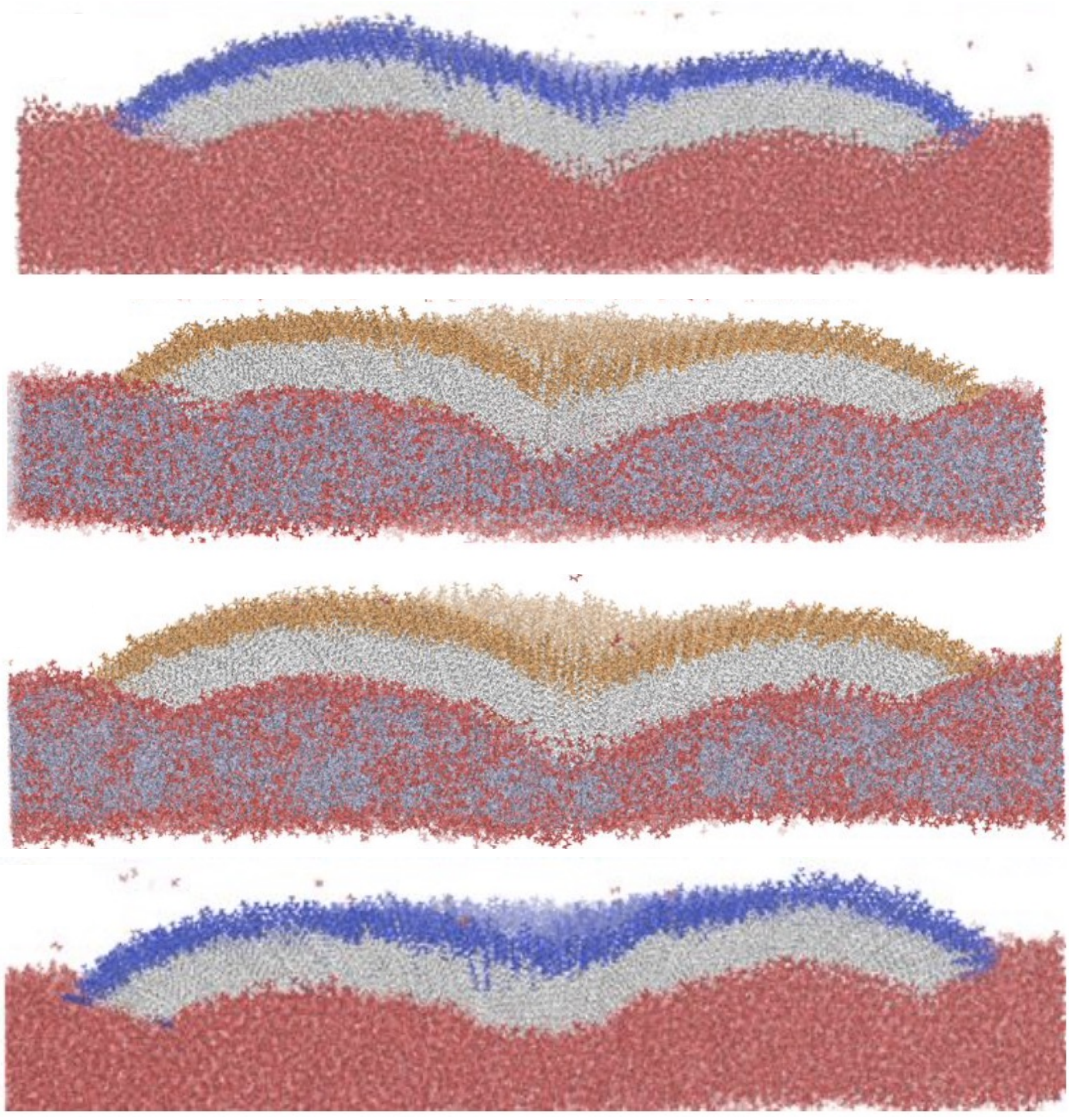

Figure 10.2: Snapshots of the cross-section cuts of the final state configuration of the aggregates comprising 2500 F8H16 molecules, highlighting the internal structure of the aggregates and their characteristic central pit, simulated at the surface of (from top to bottom): pure MeOH; a mixture of water and EtOH (with a molar fraction of EtOH of $x_{\mathrm{EtOH}} = 0.2$); a mixture of water and PrOH (with a molar fraction of PrOH of $x_{\mathrm{PrOH}} = 0.2$); pure TFE. The PFAA molecules are represented as sticks, with the CF chains coloured in navy blue (for the systems containing MeOH or TFE) or in orange (for the systems containing EtOH or PrOH) and the CH chains coloured in white. The alcohol molecules are depicted in red and the water molecules are represented in light blue. The simulation boxes measure 36 nm of side. Adapted from [13].

section cuts of the final state of those simulations are depicted in Figure 10.2. It is observed, for all systems, the formation of an aggregate with the morphological characteristics of the hemimicelles obtained at the surface of water (round, dome-shaped, with a central pit, with the molecules disposed in a fan-like arrangement, with the molecules displaying a CF chain up-CH chain down orientation). In the case of the systems with a subphase of EtOH+water or PrOH+water, some degree of adsorption of the alcohol molecules at the liquid–vacuum and liquid–PFAA interfaces is observed. Taken together, these results are indicative that the formation of nanostructured films at the surface of liquids other than water, specifically of short-chain alcohols, is plausible. This serves as the motivation for the experimental studies that followed, which will be presented in the following Section.

10.4.2 Mixed Langmuir films of PFAAs with long-chain alcohols

10.4.2.1 Monolayer-start systems

Figure 10.3 shows a few snapshots of the initial and final configurations of the monolayer-start systems of mixed films of F8H18 with H18OH. It can be observed that, upon compression, the density of the film increases and the F8H18 aggregate engages in lateral contact with the H18OH molecules, as the available surface area of free water decreases. Further compression leads to the presence of a highly organised H18OH monolayer that rests anchored to the surface of water by the alcohol moiety. A significant portion of the F8H18 aggregate is expelled from the water surface and glides on top of the H18OH monolayer, forming an aggregate. The F8H18 molecules within aggregate show some degree of lateral organisation and the characteristic segregation of the CH and CF chains (*cf.* Figure 10.3c). Importantly, most F8H18 molecules are oriented such that their CH chains are facing the H18OH monolayer and their CF chains are facing the vacuum. Some F8H18 molecules rest in contact with the water surface, possibly due to insufficient compression or a transient effect. Regardless, the overall trend of this system's behaviour upon lateral compression and collapse of the film has been asserted, namely that the PFAA molecules glide on top of the alcohol monolayer, in accord with experimental results [18].

Concerning the mixed binary films of F8H18 with F171HOH, Figure 10.4 shows a few snapshots of the initial and final configurations of the corresponding monolayer-start system. Similarly to was been described for the F8H18+H18OH system, the F8H18 and the F171HOH molecules come closer together upon the compression of the simulation box and reduction of the available surface area per molecule. As the compression is carried out further, the F171HOH monolayer rests highly organised and in contact with water, through the anchorage provided by the alcohol moieties. The F8H18 molecules are, for the most part, expelled from the water surface and glide on top of the F171HOH monolayer, the latter of which, as whole, appears to be somewhat deformed during the process. The F8H18 molecules rest quite organised and display a preferential orientation of their CH chains facing the F171HOH monolayer (cf. Figure 10.4c). This result is somewhat contradictory, as, on one hand, this leads to the unfavourable contact between the CH chains of the F8H18 and the CF chains of the F17H1OH molecules. On the other hand, the inversion of the orientation of the F8H18 molecules, leading to the more favourable contact of both types of CF chains, would also be unfavourable as the CH blocks present a higher surface energy, compared to that of the CF blocks. The formation of a multilayer (possibly a

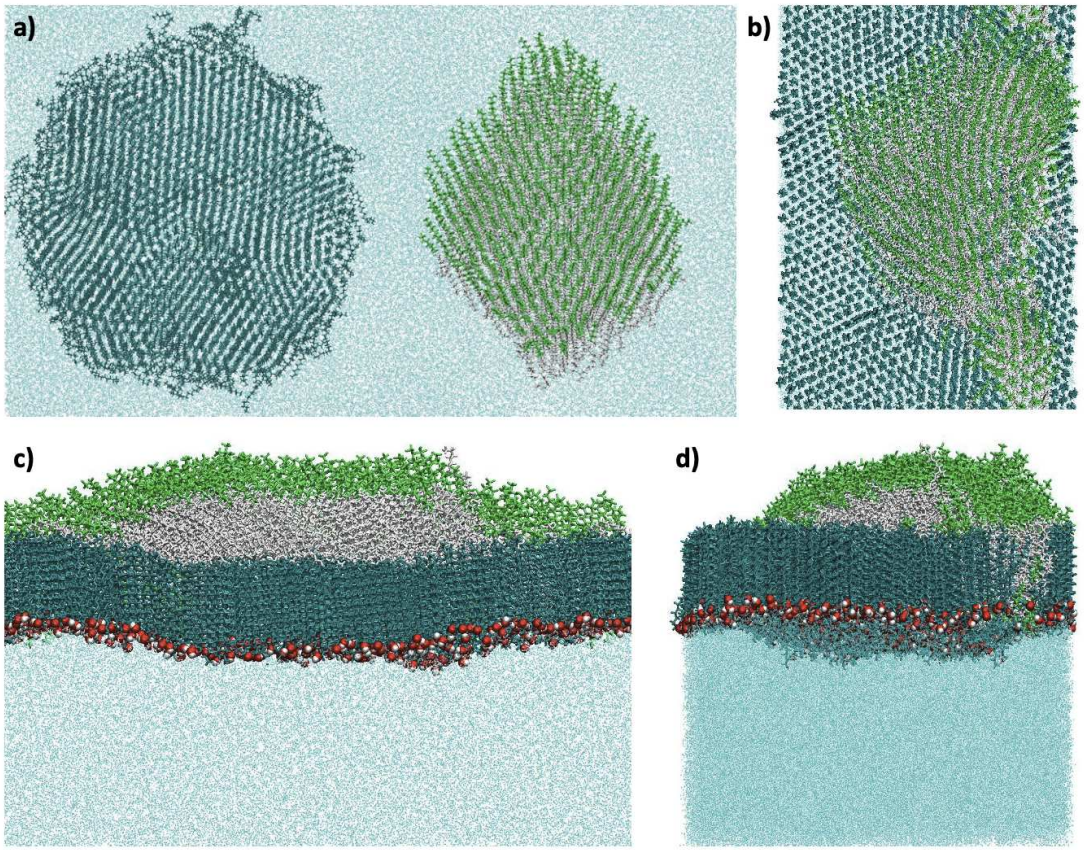

Figure 10.3: a) Top-view snapshot of the initial pre-equilibrated configuration of a system comprising 795 molecules of H18OH and 300 molecules of F8H18 at the air–water interface; b) Top-view snapshot of the final state of the same system, after 32 ns of simulation, during which the intermittent anisotropic compression/equilibration protocol was followed; c) Snapshot of the same configuration as b), but showcasing a cross-section cut of the system; d) Side view snapshot of the same configuration as b). The cyan dots represent the water molecules. The CH and the CF chains of the F8H18 molecules are coloured in white and green, respectively. The H18OH molecules are coloured in dark blue, with the oxygen and hydrogen atoms of the alcohol moiety represented by red and white spheres, respectively. Adapted from [31].

triple layer, as some experimental evidence points to [18]) could provide a means of avoiding these unfavourable contacts. However, such organisation of the collapsed film was not observed during the simulations, which could also be a consequence of insufficient lateral compression of the film, a transient effect or simply because the ratio of the number of F8H18 to the number of F171HOH molecules might not be high enough to permit it. That being said, the observed trend of the vertical segregation of the F8H18 molecules, which glide on top of the F171HOH monolayer upon compression and collapse of the mixed binary film, seems consistent with the available experimental data [18] and is otherwise a plausible scenario, since the F171HOH are more likely to remain in contact with the water surface in the event of the collapse of the film, being anchored by their alcohol moieties.

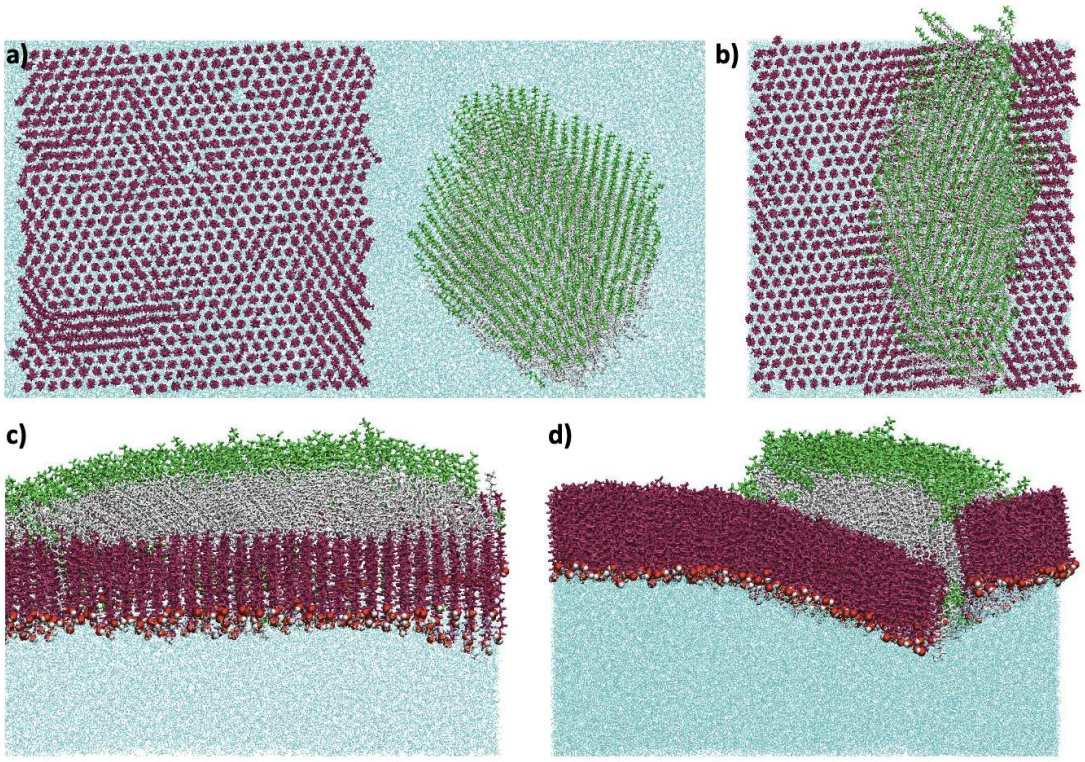

Figure 10.4: a) Top-view snapshot of the initial pre-equilibrated configuration of a system comprising 795 molecules of F171HOH and 300 molecules of F8H18 at the air–water interface; b) Top-view snapshot of the final state of the same system, after 32 ns of simulation, during which the intermittent anisotropic compression/equilibration protocol was followed; c) Snapshot of the same configuration as b), but showcasing a cross-section cut of the system; d) Side view snapshot of the same configuration as b). The cyan dots represent the water molecules. The CH and the CF chains of the F8H18 molecules are coloured in white and green, respectively. The F171HOH molecules are coloured in bordeaux, with the oxygen and hydrogen atoms of the alcohol moiety represented by red and white spheres, respectively. Adapted from [31].

10.4.2.2 Bilayer-start systems

The cross-sectional cut view snapshots of the final configuration of the MD simulations of the bilayer-start systems are featured in Figure 10.5. In both scenarios (H18OH+F8H16 and F171HOH+F8H16), the systems evolve into the formation of a round, dome-shaped, pit-centred aggregate on top of and fully in contact with the underlying alcohol monolayer. The internal structure of the aggregates resembles that of the hemimicelles formed at the surface of pure water [21] (see also Chapters 8 and 9): the molecules are oriented with the CF chains facing the vacuum and are, on average, upright in the centre of the aggregate, displaying a steadily increasing tilt the closer they are located near the rim of the aggregate. The most striking observation, however, is the fact that the physical forces at the origin of these morphological features are strong enough to induce the deformation of the alcohol monolayer and even propagate to the alcohol–water interface, which is also deformed to a shape that resembles a negative imprint of the bottom side of the PFAA aggregates. This probably occurs so that the close contact between the PFAA and the alcohol molecules is not broken, as it would likely be energetically unfavourable.

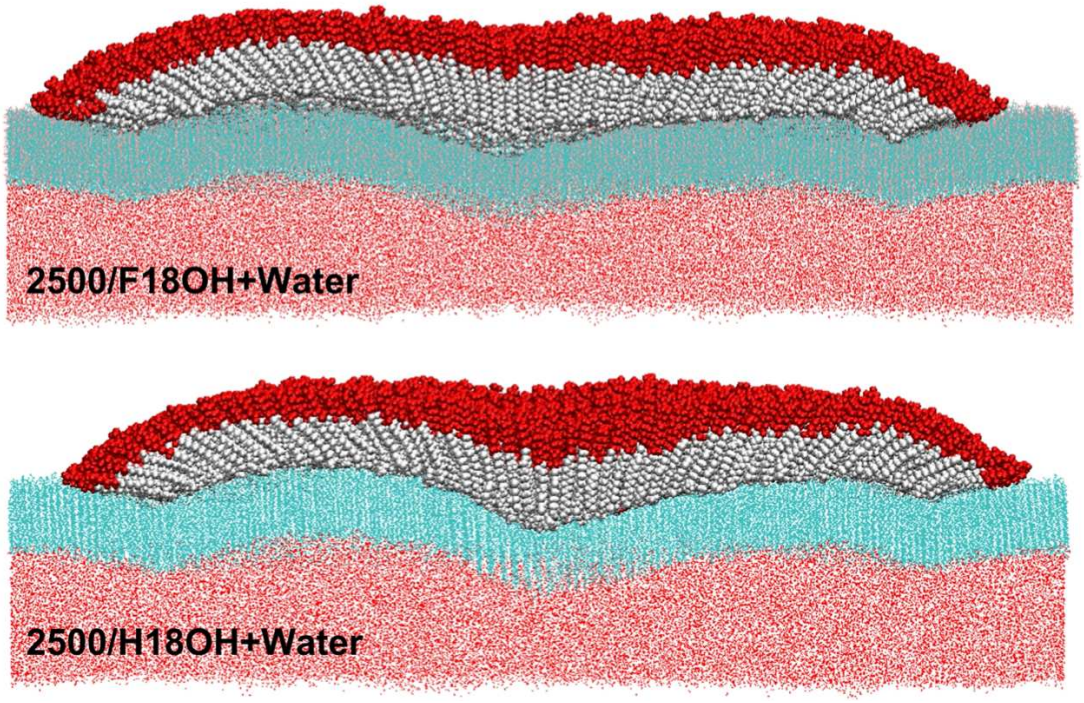

Figure 10.5: Cross-sectional cut view snapshots of the final configuration of the aggregates of 2500 F8H16 molecules, for the F171HOH (top) and H18OH (bottom) water-supported substrates (the notation used in the illustration for F17H1OH is different, but it refers to the same molecule). The PFAA molecules are represented in a spacefill visualisation and their CH and CF chains are coloured in white and red, respectively. The alcohols' carbon atom chains are represented as light blue sticks. The water molecules are represented by the red dots. The simulation boxes measure 36 nm of side. Adapted from [32].

One further set of simulation conditions was tested: the positions of the oxygen atoms of the long-chain alcohols were constrained[3] to a fixed height in the simulation box, in effect restraining the vertical movement of the densely packed long-chain alcohol molecules [32]. The same initial configuration of the PFAA molecules (2500 molecules packed in a cylinder, with their CF chains facing the vacuum) was placed near the restrained alcohol slab and the system was simulated under otherwise identical simulation conditions. The resulting final configurations for each system are depicted in Figure 10.6. It is clear that a dome-shaped aggregate is formed under these conditions as well, but its bottom is flat and the characteristic central pit is conspicuously absent in both cases. A parallel can be drawn between these results and the ones presented in Chapter 8, in which aggregates of F8H16 with similar morphological characteristics were retrieved in MD simulations conducted using a restrained slab of water molecules as subphase. It can thus be reiterated that the existence of a deformable substrate seems to be necessary for the formation of an aggregate with the morphological characteristics of the experimentally observed hemimicelles of PFAAs, namely one featuring a central pit or depression.

[3]This was achieved by subjecting the oxygen atoms of the long-chain alcohols to a position dependent potential, according to a harmonic function (with a force constant of $1000\,\mathrm{kJ\,mol^{-1}\,nm^{-1}}$), similarly to what was implemented in the MD simulations described in Chapter 8.

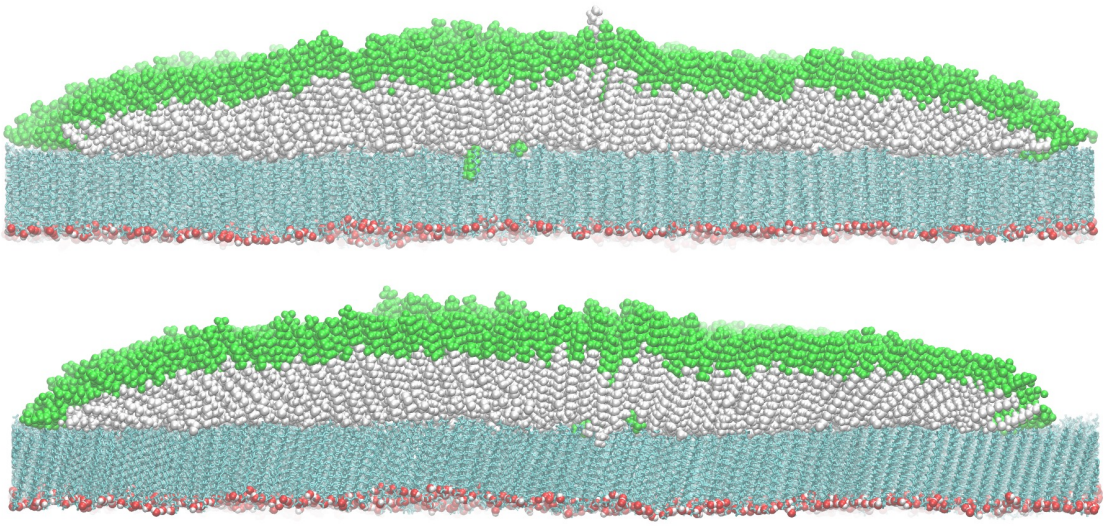

Figure 10.6: Cross-sectional cut view snapshots of the final configuration of the aggregates of 2500 F8H16 molecules, for the F171HOH (top) and H18OH (bottom) restrained substrates. The PFAA molecules are represented in a spacefill visualisation and their CH and CF chains are coloured in white and green, respectively. The alcohols' carbon atom chains are represented as light blue sticks. The oxygen and hydrogen atoms of the alcohol moieties are represented as red and white spheres, respectively. The simulation boxes measure 33 nm of side. Adapted from [32].

These results should be analysed in light of what was discussed in the preceding Subsubsection, namely the MD simulation results of the monolayer-start systems and the experimental results from the literature concerning the structural characterisation of the mixed Langmuir films of H18OH+F8H18 and of F171HOH+F8H18 [18]. It is clear that the most probable structure of the collapsed binary film comprises a monolayer of the densely-packed long-chain alcohol molecules in contact with water and another layer of PFAA molecules on top of it. Depending on the molar proportions of the constituting compounds, the thermodynamic conditions of the film (*i.e.* π and A) and the chemical nature of the long-chain alcohol, the PFAA molecules are anticipated to organise in a monolayer or a multilayer structure, the former appearing to be favoured in the presence of CH alcohols and the latter in the presence of CF alcohols. Regardless of the specific structure that is formed, the gregarious behaviour of the PFAA molecules and their tendency to form stable, self-assembled hemimicelles has been observed in a variety of experimental conditions, including, as mentioned above, in mixed films of F8H16 with other CH molecules (DPPE) [19, 20]. The main result that should be highlighted from this MD simulation study is that it is plausible that the formation of (pit-centred) hemimicelles can occur and their integrity, morphology and internal structure be maintained even when the PFAA molecules are not in contact with water, as when they are supported by monolayers of H18OH or F171HOH. In a broader sense, this provides a connection with the other sections of this chapter, inasmuch as they also address the formation of nanostructured films of PFAAs at the surface of substrates other than liquid water. It can be said that the ensemble of these results is in line with the rationale that the formation of hemimicelles of PFAAs can be perceived as a true self-assembling phenomenon driven by factors intrinsic to the PFAAs.

10.5 Results and Discussion: Experimental

10.5.1 Subphase: None (dry substrate)

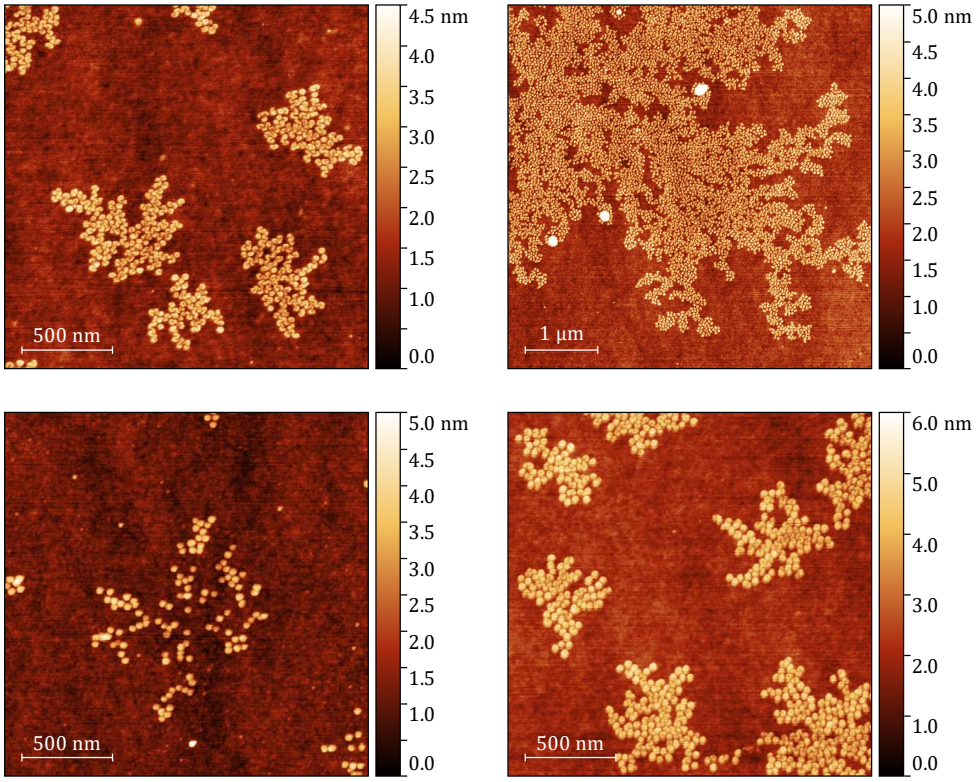

Figure 10.7: AFM height images of a F8H18 thin film spin-coated on a dry silicon wafer.

It has been noted that hemimicelles of PFAAs are only obtained on polar substrates, such as water [38], mica [39], liquid crystals [40], wet silicon wafers [14] and amphiphilic block copolymers [8]. On the contrary, no evidence of nanostructuring has been observed at the surface of bulk PFAA liquids [41] or on dry silicon wafers [8]. This seems indicative of the importance of having a polar substrate (and with emphasis on water) for the existence of hemimicelles of PFAAs. Therefore, the first experimental condition tested consisted in spreading the film directly on top of a clean wafer, without prior deposition of any liquid subphase, to verify such prerequisites.

Figure 10.7 shows some AFM height images of a F8H18 spin-coated on a dry silicon wafer. These images are representative of the areas on which some form of deposited film was found. However, it should be noted that about 2/3 of the sampled regions displayed no evidence of film deposition. From these images, we can observe that the density of the film is rather low and that hemimicelles are scarce. Most of the observed nanostructures are worm-like aggregates that tend to gather in clusters.

Given the somewhat arbitrary shape of the aggregates and the fact that they are far apart from one another, the quantification of their dimensions was performed by sampling different regions of the images for height profiles (see Subsection 6.3.2). From these, the diameter of the round hemimicelles and the thickness of the film were estimated. The round hemimicelles were found to have a diameter of (40.4 ± 2.6) nm and the film thickness was about (2.4 ± 0.3) nm.

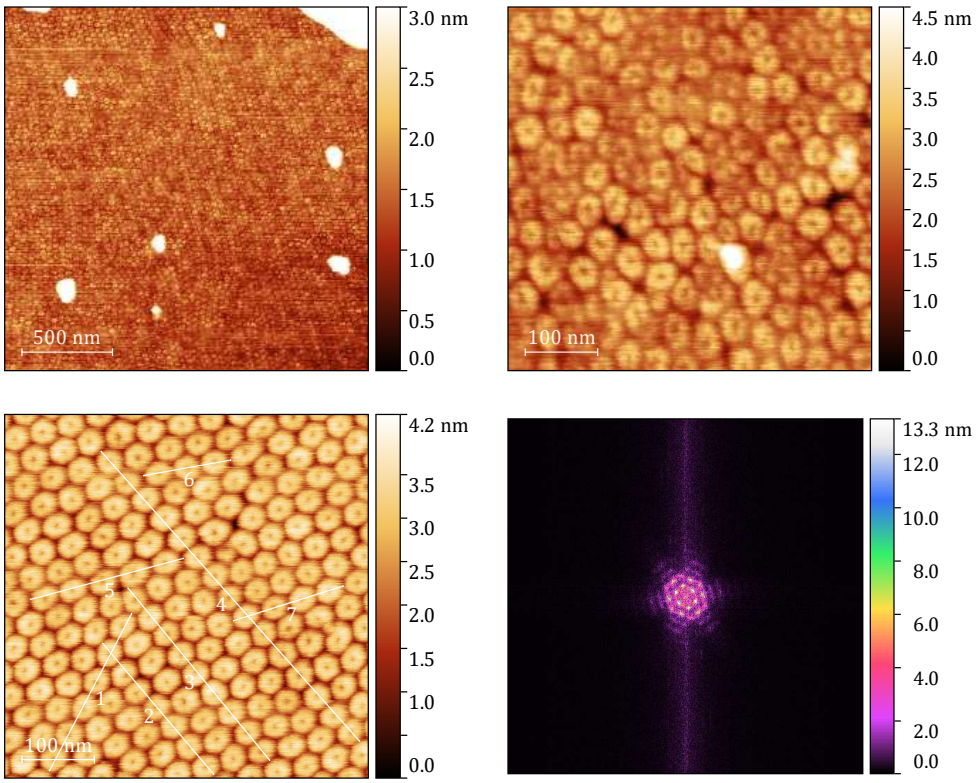

Figure 10.8: AFM height images of a F8H18 thin film spin-coated on a silicon wafer previously wet with pure water (top row and bottom left). The bottom right image shows the 2DFT of the bottom left AFM height image.

This is slightly lower than the fully-stretched F8H18 molecule (3.66 nm, estimated following the procedure outlined in [42]), being consistent with the existence of partially tilted molecules and in accord with literature data [9, 14, 34, 36, 43].

For these samples, the amount of spreading solution deposited was enough for the formation of a dense monolayer covering the entire surface of the substrate. The fact that a very low density film was found suggests that the spreading of the PFAA solution, the formation of the film and subsequent organisation into hemimicelles are impaired in the absence of a liquid water subphase. The fact that some closed, round hemimicelles were observed nonetheless somewhat contradicts previous observations attesting that the presence of liquid water was a requirement for their formation [8, 14, 34]. However, in another study, a film of F14H20 deposited directly at the surface of a silicon wafer displayed patches of worm-like aggregates [44]. These would morph and reorganise into round hemimicelles upon exposure to humid air. This suggests that the presence of at least some water molecules (possibly adsorbed as a thin film at the surface of the silicon wafer) is necessary to obtain the hemimicelle structures. Therefore, it can be hypothesised that it might be possible to form a film under these conditions, but a low-density one comprising aggregates with different morphological features and with impaired lateral ordering. The AFM images in Figure 10.7 display a mixture of both structures, which might be caused by some traces of adsorbed water remaining on the silicon wafer prior to the deposition of the PFAAs (these are stored immersed in water and dried under a stream of nitrogen before use – see Section 10.3).

10.5.2 Subphase: Pure Water

The preparation of a F8H18 ordered film by spin coating at the surface of a silicon wafer wet with water has been achieved before [14]. This served as a starting point for the following steps of this work. Figure 10.8 shows some AFM height images of a F8H18 thin film spin-coated on a silicon wafer previously wet with pure water. The film is ordered, dense and comprises tightly-packed pit-centred hemimicelles. The film appears to be a monolayer for the sampled regions, although some aggregates of bigger height are visible (cf. Figure 10.8 top left). The lateral organisation of the hemimicelles varies between regions of the sample, but the hemimicelles are, in general, organised according to a two-dimensional (2D) hexagonal lattice (cf. Figure 10.8 bottom row). Some packing defects and other aggregate morphologies, such as worm-like aggregates, are also to be noted (cf. Figure 10.8 top right).

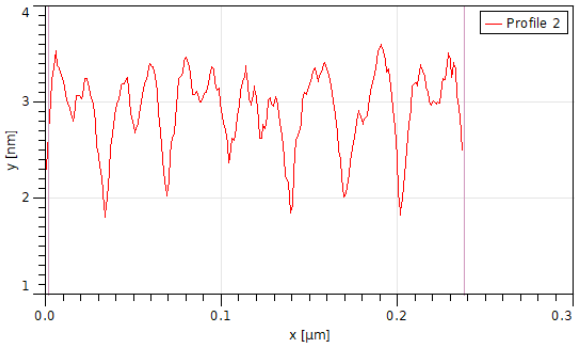

Figure 10.9: Height profile along the segment number 2 in Figure 10.8 (bottom left). The vertical lines mark the positions used to measure the distance corresponding to the lateral juxtaposition of 7 hemimicelles.

The diameter of the rounded hemimicelles was estimated to be about (37.0 ± 3.1) nm (from height profiles). As explained in Section 10.3, several images were sampled for this estimation and, for illustrative purposes, some of the segments whose height profiles were used in the computations are marked in Figure 10.8 (bottom left; lines 1 to 7). Also for illustrative purposes, the height profile along the segment number 2 of Figure 10.8 is presented in Figure 10.9. Each segment spans several hemimicelles, whose diameter is estimated to be the length of the segment divided by the number of hemimicelles it spans. Based on 2DFTs, the diameter of the hemimicelles was estimated to be 36.4 nm to 43.2 nm.

The variability in the diameter values can be attributed not only to the use of different methods, but also to the fact that the hemimicelles appear to be ellipsoidal rather than perfectly circular. This results in the dimensions of the hemimicelles being characterised by a long and a short axis (corresponding approximately to the lower and upper limits of the range of the 2DFT results). Conversely, this result can be interpreted as though the hemimicelles were packed in a distorted hexagonal lattice, instead of a regular hexagonal lattice (cf. Figure 10.8 bottom right). The existence of ellipsoidal hemimicelles has been suggested based on Grazing Incidence Small Angle X-Ray Scattering (GISAXS) measurements of Langmuir films of PFAAs at the air–water interface [45], but limits on the experimental uncertainty and other GISAXS measurements in support of a perfect hexagonal lattice [34, 38, 46, 47] contradict this. The observation of a distorted lattice and/or ellipsoidal hemimicelles could also be an artefact of the AFM measurements or a consequence of the centrifugal forces that affect the film during the spin coating procedure. The range of the computed diameter values could be perceived as an estimation of the experimental uncertainty. Regardless, the obtained film morphology and the computed hemimicelle size are overall in agreement with those reported in the literature for films of F8H18 (≈ 35 nm [14], see Subsection 10.5.4).

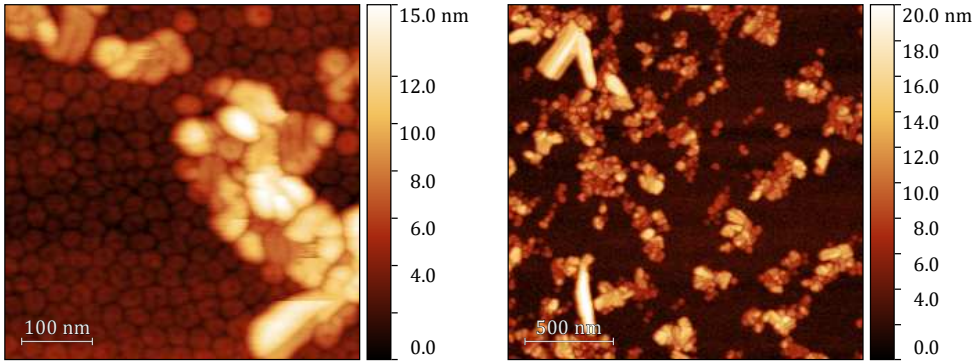

Figure 10.10: AFM height images of a F8H18 thin film prepared by simple evaporation on a silicon wafer previously wet with pure water.

Thin films of F8H18 on silicon wafers previously wet with pure water were also prepared by the method of simple evaporation. Some AFM height images obtained for such films are shown in Figure 10.10. It is clear that the film is less organised and that a significant portion of the surface of the wafer is covered with aggregates or multi layers. An underlying monolayer of pit-centred hemimicelles is nonetheless visible, but its order seems impaired and the existence of defects is also noticeable (e.g. with worm-like and multi-lobed aggregates). The average diameter of the hemimicelles was estimated to be of about (30.8 ± 1.7) nm, from height profile sampling.

10.5.3 Subphase: Short-chain alcohols

10.5.3.1 Methanol (MeOH)

The first short-chain alcohol to be tested as a replacement for water was Methanol (MeOH), the CH alcohol with the shortest side chain. Figure 10.11 (top) shows an AFM height image of a F8H18 thin film prepared by spin coating a silicon wafer previously wet with MeOH.

Similarly to the results presented for the water subphase, the film is quite ordered, dense and comprises tightly-packed pit-centred hemimicelles. The occurrence of packing defects and the existence of different aggregate morphologies (including worm-like aggregates) is also noteworthy. The sampled regions were covered with what can be anticipated to be a monolayer, with occasional thicker aggregates or "clumps" covering some spots (not shown in the presented AFM height images). The lateral order of the film was variable depending on the sampled region and

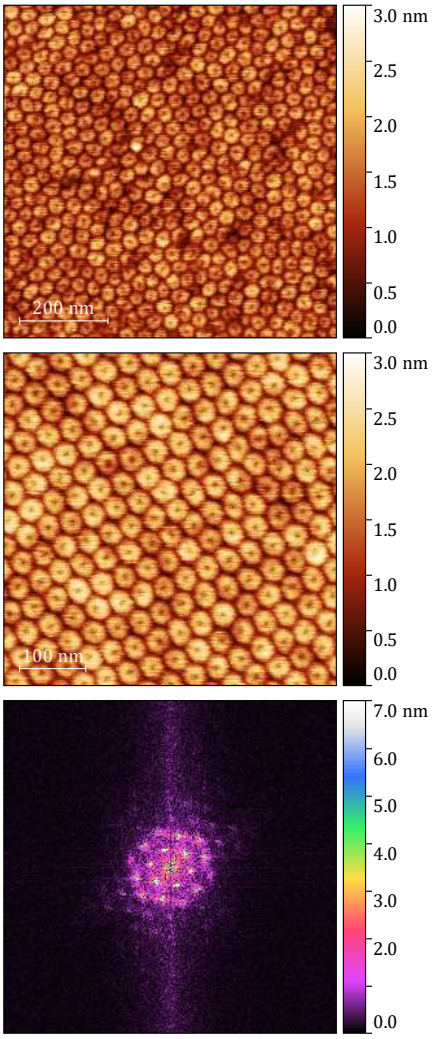

Figure 10.11: AFM height images of F8H18 thin films prepared by spin coating (top) or by simple evaporation (middle) on silicon wafers previously wet with Methanol (MeOH). The bottom image shows the 2DFT of the middle AFM height image.

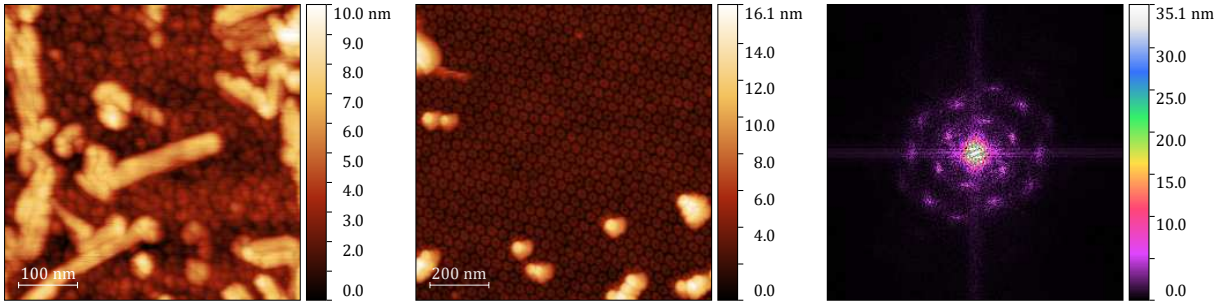

Figure 10.12: AFM height images of F8H18 thin films prepared by spin coating (left) or by simple evaporation (centre) on silicon wafers previously wet with Ethanol (EtOH). The right image shows the 2DFT of the middle AFM height image.

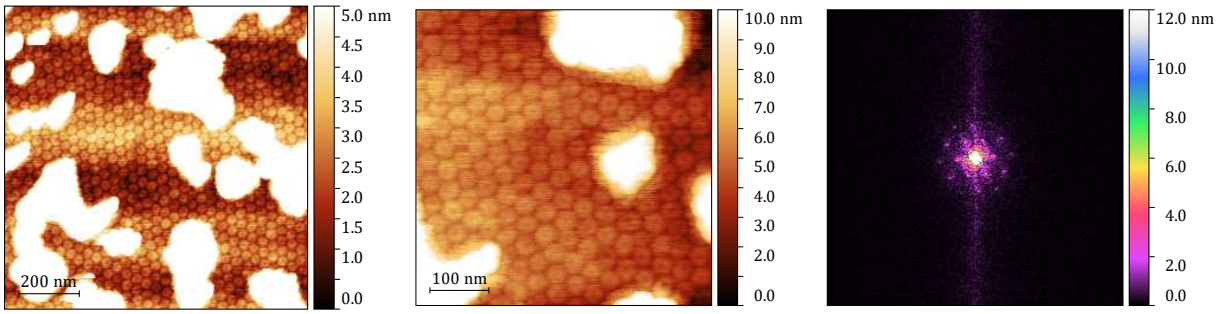

Figure 10.13: AFM height images of a F8H18 thin film prepared by simple evaporation on a silicon wafer previously wet with Butanol (BuOH). The right image shows the 2DFT of the middle AFM height image.

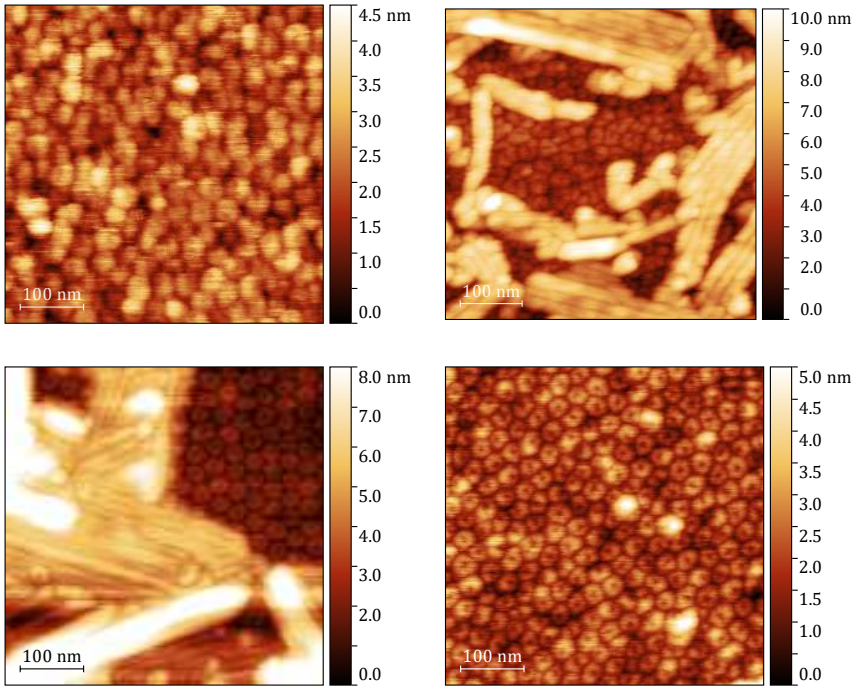

Figure 10.14: AFM height images of F8H18 thin films prepared by spin coating (top row) or by simple evaporation (bottom row) on silicon wafers previously wet with 2,2,2-trifluoroethanol (TFE).

this precluded the accurate computation of the size of the hemimicelles from 2DFTs. A rough estimation was nonetheless obtained from one single image (≈ 38.1 nm; 2DFT not shown), which compares well with the results obtained from height profile sampling: (35.4 ± 2.8) nm.

The method of simple evaporation was also employed to prepare MeOH-supported thin films of F8H18. An AFM height image of such film is presented in Figure 10.11 (middle), together with its 2DFT (bottom). The film is remarkably ordered and only rare spots of greater thickness (consistent with the existence of multilayered aggregates) were found in the sampled regions. The 2DFT shows six well defined first-order peaks consistent with a hexagonal lattice, with a slight distortion whose possible origin has been discussed above (although no centrifugal forces are present in this case). Higher order peaks are also discernible, attesting the organisation of the sample. From the 2DFTs, the size of the hemimicelles was estimated to be in the range of 35.4 nm to 40.3 nm; from the height profile sampling, a value of 38.7 nm was obtained.

10.5.3.2 Ethanol (EtOH)

An AFM height image of a F8H18 thin film prepared by spin coating a silicon wafer previously wet with Ethanol (EtOH) is presented in Figure 10.12 (left). A significant portion of the sample's surface is covered with aggregates or multi layers, although an underlying monolayer comprising pit-centred hemimicelles is still visible. However, the shapes of the latter appear more variable, being discernible a few rounded hemimicelles, worm-like aggregates and segmented hemimicelles. The existence of segmented hemimicelles has been reported before (for F12H12 [48]), but the effect could also be caused by a different mechanism (e.g. the forces acting during the spin coating and/or a subsequent relaxation effect [14]). The diameter of the rounded hemimicelles was estimated to be (36.1 ± 2.0) nm, using the height profile sampling method.

Figure 10.12 (centre) shows an AFM height image of a F8H18 film prepared on a EtOH-wet silicon wafer by simple evaporation, together with its 2DFT (right). The morphology of the film appears to be similar to others described above, inasmuch as a monolayer comprising laterally-ordered pit-centred hemimicelles is visible, covered with patches of thicker aggregates or multilayered structures. The film in the image is sufficiently ordered to produce a 2DFT showing diffraction peaks of a 2D hexagonal lattice. From these, the size of the hemimicelles was estimated to be 32.5 nm to 42.1 nm, compared to (36.1 ± 1.5) nm from height profile sampling.

10.5.3.3 Butanol (BuOH)

The longest CH alcohol to be studied was Butanol (BuOH) and the samples were prepared exclusively by simple evaporation, in this case. Considering the preliminary MD simulation results presented above, it should be remarked that the choice of BuOH as the longest CH alcohol (skipping PrOH, the one studied by MD simulation) was simply practical, as this solvent was available whereas PrOH was not. This was not perceived as a limitation, not least considering the results presented herein as a whole, in what is fundamentally a largely exploratory experimental study.

Figure 10.13 shows two AFM height images of these samples. A thin film (presumably a monolayer) of laterally-ordered pit-centred hemimicelles is visible. This film seems to be covered with patches of greater thickness, suggesting the presence of multilayered aggregates. The imaged

Table 10.2: Compilation of the obtained results of hemimicelle diameter for the different studied samples: experimental conditions (subphase composition); sample preparation technique (spin coating or simple evaporation); and analysis method (height profiles or 2DFT). The dashes mark the experimental conditions for which data is not available (the experiment or the analysis were not performed).

Subphase	**Diameter (nm)**			
	Spin coating		**Simple Evaporation**	
	Height profiles	2DFT	Height profiles	2DFT
Dry silicon wafer	40.4 ± 2.6	—	—	—
Pure water	37.0 ± 3.1	36.4 to 43.2	30.8 ± 1.7	—
MeOH	35.4 ± 2.8	≈ 38.1	38.7 ± 1.6	35.4 to 40.3
EtOH	36.1 ± 2.0	—	36.1 ± 1.5	32.5 to 42.1
BuOH	—	—	35.1 ± 0.9	34.3 to 37.5
TFE	35.7 ± 3.4	—	34.4 ± 2.8	32.3 to 37.3

film is sufficiently ordered to produce a 2DFT with diffraction peaks corresponding to a hexagonal network (see rightmost image of Figure 10.13). These results permitted to estimate the diameter of the hemimicelles as 34.3 nm to 37.5 nm. From height profiles, the diameter of the hemimicelles is (35.1 ± 0.9) nm.

10.5.3.4 Trifluoroethanol (TFE)

Lastly, the replacement of the water subphase with a CF alcohol was tested, specifically 2,2,2-trifluoroethanol (TFE). Figure 10.14 shows AFM height images of F8H18 thin films prepared by spin coating (top row) or by simple evaporation (bottom row) on silicon wafers previously wet with TFE. The morphology of the sampled regions was characterised by the presence of "patches" or aggregates of greater thickness, consistent with multilayered structures, that covered a significant portion of the surface. This was observed for all samples, regardless of the method of preparation. Most "patches" had a filamentous or ribbon-like appearance (cf. Figure 10.14). An underlying film (presumably a monolayer) of pit-centred hemimicelles with varying degrees of lateral order was also observed. The size of the hemimicelles was estimated from height profile sampling as (35.7 ± 3.4) nm and (34.4 ± 2.8) nm, respectively for the samples prepared by spin coating and by simple evaporation. Only for the samples prepared by simple evaporation an estimate of the hemimicelle diameter using the 2DFT methodology was successful, this being 32.3 nm to 37.3 nm.

10.5.4 General discussion

The results presented in this chapter permit to make some general remarks concerning the formation of organised films of F8H18 at the liquid–air interface. The obtained values of hemimicelle diameter for the various studied systems are compiled in Table 10.2. A compilation of literature data on the diameter of the hemimicelles in thin films of F8H18 is presented in Table 10.3, for comparison.

Table 10.3: Compilation of literature data on the diameter of the hemimicelles in thin films of F8H18. The π indicates the surface pressure at which were performed the transfer onto a solid substrate (see Section 6.4) or the GISAXS measurements. This is not applicable (n.a.) in the case of the samples prepared by spin coating, as the surface pressured is neither measured nor controlled in that situation.

π ($\mathrm{mN\,m^{-1}}$)	**Diameter** (nm)	**Characterisation Technique**	**Ref.**
n.a.	≈ 35	AFM (spin coating)	[14]
0.5	41 ± 5	AFM (Langmuir-Blodgett (LB) transfer)	[37]
2	27.5 ± 0.7	AFM (LB transfer)	[36]
5	27.2 ± 1.6	AFM (LB transfer)	[36]
5	40.3 ± 1.5	GISAXS	[38]
5	32 ± 5	GISAXS	[45]

Taking all results together, it is clear that the morphologies of the systems prepared with a liquid subphase differ substantially from those without one. A thin film (presumably a monolayer) of mostly rounded pit-centred hemimicelles, usually displaying a high degree of lateral order, is observed for the samples prepared on a wet substrate. However, if the spreading solution is deposited directly on the dry solid substrate, the morphology of the film is different and its order is impaired. In the latter case, a low-density film is observed, comprising gnarled structures and some regions covered with sparse disorganised pit-centred hemimicelles. This contradicts previous reports that mention the formation of a film was only possible at the surface of wet substrates [8, 14]. It is not clear whether the observation of rounded hemimicelles is an effect of residual adsorbed water at the surface of the solid substrate: it has been shown that a humid atmosphere is sufficient to induce the change of the morphology of F14H20 aggregates from worm-like to round [44]. Taken together, the results obtained herein and the examples in the literature provide evidence in the sense that the existence of rounded, pit-centred hemimicelles is at least favoured in the presence of a liquid subphase. Regardless, it is clear that the existence of a liquid subphase seems to be a *sine qua non* condition to permit the lateral ordering of these nanostructures.

By comparing the two methods employed (spin coating and simple evaporation) for the preparation of an organised film at the surface of a wet solid substrate, it is clear that the action of the spin coater is neither the driving force for the formation of the pit-centred round hemimicelles nor for their lateral ordering. Hemimicelles are formed regardless of the method employed for the sample preparation (except in the case of a BuOH subphase, for which spin coating was not attempted). Concerning the lateral ordering if the hemimicelles, this seems to vary between samples and the regions imaged by AFM, and the interpretation of the results is not obvious. For instance, when water is used as the subphase, a more ordered sample is obtained by spin coating, whereas a sample obtained by simple evaporation was more ordered in the case of a MeOH subphase. These results are in support of the fact that the formation of hemimicelles is a phenomenon intrinsic to PFAAs, provided that a liquid supporting surface is present. Their spontaneous lateral ordering is most likely a consequence of the hemimicelle monodispersity [47] and the spatial constraints imposed by a dense film.

Technical difficulties precluded the estimation of the diameter of the hemimicelles using the particle analysis and counting methodology (see Subsection 6.3.2), which is more ubiquitous [14, 34, 36, 37] and provides a statistical distribution of domain sizes based on several (tens, hundreds) particles. This was circumvented in part by sampling the images for height profiles and, in the cases where the lateral ordering was sufficient, by the computation of 2DFTs, estimating the diameter of the hemimicelles from these data. The advantage of these methods is that they are more robust and less sensitive to the choice of parameters of the analysis (e.g. the choice of a threshold separating the particles from the background). The height profile sampling has the disadvantage, however, that it will fail to capture whether the hemimicelle size distribution is centred around one single value (unimodal) or several (multimodal), as the results are an average from all the sampled hemimicelles. In theory, the 2DFT should not have the same problem, provided the hemimicelles of different sizes would organise in separate lattices (in which case each lattice would generate a separate set of diffraction peaks in the 2DFT), but if hemimicelles of different sizes are mixed together in one single ordered lattice, an average parameter would thus be obtained from a unique set of intermediate diffraction peaks. Limits on the resolution of the AFM also diminish the sensitivity of this method for this particular purpose. Regardless, these limitations are not expected to constitute a setback for the case in study, as pure F8H18 hemimicelles are anticipated to be monodisperse. Finally, unlike height profile sampling and particle analysis and counting, 2DFT can capture deviations of the hemimicelle shape from rounded to ellipsoidal (see Subsection 10.5.2). However, this can also be caused by experimental artefacts [14].

For the samples in which round pit-centred hemimicelles were observed, their estimated size seems to be close to $\approx 35\,\mathrm{nm}$, reported in the literature for a F8H18 film prepared by spin coating a silicon wafer wet with pure water [14] (cf. Tables 10.2 and 10.3). This size is similar to those reported for hemimicelles transferred by LB onto a solid substrate and imaged by AFM and those reported from GISAXS measurements directly at the air–water interface. The fact that the hemimicelles are formed and have an approximately constant size for the various tested conditions suggests this process is a true molecular self-assembly process [43]. Notwithstanding the importance of the in-plane interactions that ultimately determine the morphology of the films (see Section 10.1), the mechanisms underlying the formation of the hemimicelles appear to be more complex and be ruled by factors other than just the line tension between the aggregates (hemimicelles) and the subphase.

Overall, it is conceivable that the formation and the lateral ordering of the hemimicelles of PFAAs is a phenomenon intrinsic to this type of molecules, provided a "soft" anchoring support for the film is present. The formation of the pit in the centre of the hemimicelles is only possible because the underlying liquid subphase is deformable and is linked to the alignment of the CH_2-CF_2 dipoles within the hemimicelles [49]. It is therefore possible that the existence of a deformable substrate is a necessary condition for the formation of the entire structure of the hemimicelle, and not just its pit. The mobility conferred by a supporting liquid subphase might explain the improved ordering of the films, compared to those prepared on a dry substrate.

This study was part of a broader, fundamental characterisation work of the structure and self-assembling properties of PFAAs at the liquid–air interface. It served essentially as a proof

of concept of whether it would be possible to form hemimicelles, and in particular hexagonally-ordered hemimicelles, at the surface of liquids other than pure water. In that regard, a laterally-ordered film of hemimicelles was observed for all systems containing a liquid subphase, which supports the initial hypothesis. However, it should be noted that the studied systems differ from the usual Langmuir films of PFAAs, namely in their preparation method, size and chemical nature of the subphase. Several constraints prevented this exploratory study from being carried out in a Langmuir trough, including: practical (the amount of high-purity solvents required would be costly), safety (the used solvents are hazardous, so small volumes were preferred and the samples were handled under the fume hood) and technical (the use of a Langmuir trough requires a stable work bench and the suppression of air currents, which are difficult to achieve under a fume hood or in an otherwise well ventilated location). The following remarks should be taken into account:

- The method of preparation of a Langmuir film consists in spreading the amphiphile molecules, dissolved in an appropriate solvent, at the surface of a large volume of water (or, by extension, a liquid subphase). The typical volumes employed in such experiments are in the order of 100 µL of spreading solution to 100 mL of water (a factor of 1000). Herein, the volume of ≈ 1 µL of spreading solution was deposited on top of ≈ 50 µL of liquid subphase (a factor of 50). Differences due to finite size effects should thus not be ruled out. Ideally, a film of PFAA would be prepared over pure MeOH (the strongest candidate, given the obtained results and the aspects raised in the third point below). This film would then either be transferred by the LB or the Langmuir-Schaefer (LS) methods onto a solid substrate and imaged by AFM or be probed directly at the liquid–air interface by GISAXS. For the reasons mentioned above, the choices made for this exploratory work were a compromise between feasibility and safety;

- Related to the previous point, the PFAA molecules were dissolved in chloroform for the preparation of the spreading solution. This step is customary and needed to deposit small, precise amounts of the amphiphile at the surface of the liquid subphase [6]. However, whilst chloroform is immiscible with water, the same cannot be said for the studied alcohols. It is expected that the volatility of chloroform and the fact that very small volumes of spreading solution are used will at least circumvent this practical limitation (since the PFAA molecules cannot be spread directly at the liquid–air interface). The chloroform should spread and evaporate quickly, leaving the PFAA molecules at the surface to spontaneously self-assemble, but this should be kept in mind when interpreting the results;

- Finally, following both previous points, the solubility of the PFAA in each of the solvents is expected to be essentially null (water, MeOH, TFE) or low (EtOH, BuOH), following the preliminary MD simulation results [13]. This was not quantified in the scope of this work and the finite solubility of the amphiphiles in the subphase and kinetic effects in general, such as film relaxation and crystallisation or precipitation, might thus be factors at play. For example, these phenomena could mean that the observed morphologies are the result of the ordering of a Gibbs (rather than a Langmuir) film. Furthermore, the presence of multilayered aggregates is significant and increasingly visible in the samples prepared with EtOH, BuOH and TFE and, with the exception of TFE, is consistent with this reasoning.

In the case of TFE, a different mechanism might be at play, since this CF alcohol might interact preferentially with the CF chains of the PFAA, rather than with the CH chains as it may be anticipated for the CH alcohols.

One remark should be made concerning the specific PFAA molecule chosen for the bilayer-start systems investigated by MD simulation. This was F8H16, despite the fact that the available experimental data concerns systems containing F8H18 instead [18]. This was a decision based on the fact that this study is part of a broader investigation about the formation of films of PFAAs in a variety of experimental and simulation conditions, and that the molecule F8H16 has been used as a more transversal benchmark (not least because of its stability and the availability of experimental and simulation data on F8H16-containing systems [21, 34, 36–38, 45, 46, 50, 51]; see also Chapters 8 and 9). Nevertheless, the results obtained herein can be considered as a general exploration of these systems and might serve as a base for future investigations utilising other combinations of long-chain alcohol/PFAA molecules.

10.6 Concluding remarks

It is well established that PFAAs form stable Langmuir films at the air–water interface [9, 52]. These films are nanostructured, comprising a network of monodisperse surface hemimicelles, laterally ordered in a 2D hexagonal lattice [36, 38, 46]. This organisation has also been obtained by spin coating the spreading solution onto a solid substrate previously wet with pure water [14]. The possibility of forming hemimicelles of PFAAs at the surface of other liquids, namely short-chain CH or CF alcohols, was hypothesised based on results from a MD simulation study [13]. The aim of this exploratory work was to extend this computational study and to experimentally test this hypothesis, by preparing thin films of F8H18 at the surface of silicon wafers previously wet with MeOH, EtOH, BuOH or TFE by spin coating or by simple evaporation. AFM was used to probe the morphology of the films, to discern whether or not the existence of hemimicelles could be asserted in these conditions and to characterise the degree of their lateral ordering.

The results from the MD simulation study suggest that the PFAA molecules may form stable films comprising surface aggregates over pure MeOH and pure TFE. Partial dissolution of the PFAAs was observed for simulations with a subphase of pure EtOH and of pure PrOH. Nevertheless, even if the PFAA solubility in these liquids is finite, the formation of a (nanostructured) Gibbs film might still be possible. Large aggregates of PFAAs were obtained at the surface of pure MeOH, pure TFE and mixtures of EtOH or PrOH with water (with a molar fraction of alcohol of 0.2 in the liquid subphase). The morphology of the obtained aggregates resembles that of the hemimicelles obtained at the surface of water (round, dome-shaped, with a central pit, with the molecules in a fan-like arrangement in a CF chain up-CH chain down orientation).

It was then experimentally demonstrated that the formation of a low density, disordered film is possible on a dry substrate. The existence of pit-centred hemimicelles was also observed under these conditions, but they were not laterally ordered. However, it is not clear whether the existence of these nanostructures was due to the presence of residual traces of water on the surface of the substrate, as it has been demonstrated that exposure to humidity induces a change in aggregate morphology from worm-like to round hemimicelles [44].

It was further demonstrated that the formation of a film of hemimicelles occurs for all the studied experimental conditions (though with a variable degree of lateral order). In particular, the formation by spin coating of a highly ordered film of hemimicelles over a silicon wafer wet with water was replicated [14]. The replacement of the water subphase by the alcohols still resulted in the formation of a dense film of hemimicelles, which is in support of the initial hypothesis. However, the morphology of the films, in these cases, was marked by significant portions of the samples covered in thicker (possibly multilayered) structures, with increasing importance for EtOH, BuOH (only prepared by simple evaporation) and TFE. This could be an effect of the finite size of the system, of a finite solubility of F8H18 in the alcohols or the result of a different spreading behaviour or mechanism. It was further verified that the action of the spin coater is neither the driving force for the formation of the round pit-centred hemimicelles nor for their lateral ordering, as these are attainable by the method of simple evaporation as well.

In a parallel MD simulation study, the mixed Langmuir films of PFAAs with long-chain CH (H18OH) or CF (H171HOH) alcohols was investigated. The laterally segregated films seem to display a mechanism of collapse through which the PFAA molecules are expelled from the surface of water and glide on top of the alcohol monolayer, which rests anchored to the surface of water by the alcohol moieties. The PFAA molecules preserve the orientation of their CF chains facing the vacuum, which seems coherent with experimental results in the case of mixed films of H18OH but not of mixed films with H171HOH (a multilayer would be anticipated in such case, possibly a trilayer) [18]. The simulation of PFAA aggregates on top of a monolayer of H18OH or H171HOH, results in the formation of round, dome-shaped, pit-centred hemimicelles resting on top of and fully in contact with the underlying alcohol monolayer. Remarkably, the alcohol monolayer and the alcohol–water interface are deformed and assume a morphology resembling the negative imprint of the bottom side of the PFAA aggregates. This deformation was found to not occur if the alcohol molecules were restrained to a fixed vertical position, in which case the obtained PFAA aggregates presented a flat bottom and no central pit. A parallel was drawn with the results presented in Chapter 8, reiterating that the existence of a deformable supporting substrate seems necessary for the formation of an aggregate with the morphological characteristics of the experimentally observed hemimicelles of PFAAs. Overall, it is plausible that the formation of (pit-centred) hemimicelles can occur and their integrity, morphology and internal structure be maintained even when the PFAA molecules are not in contact with water, as when they are supported by monolayers of H18OH or F171HOH. This has been experimentally observed for mixed films of F8H16 with other CH molecules (DPPE) [19, 20]. In a broader sense, these results address the formation of nanostructured films of PFAAs at the surface of substrates other than liquid water. This is in line with the rationale that the formation of hemimicelles of PFAAs can be perceived as a true self-assembling phenomenon driven by factors intrinsic to the PFAAs.

In conclusion, the formation and, at least to some extent, the lateral ordering of hemimicelles of a PFAA were investigated by MD simulation and successfully obtained experimentally at the surface of liquid subphases other than pure water and characterised by AFM. These results are in support of the hypothesis that the formation of these nanostructures and their ordering are phenomena intrinsic to PFAAs, provided a “soft” anchoring support for the film is present.

References

[1] H. M. McConnell and R. de Koker. 'Note on the Theory of the Sizes and Shapes of Lipid Domains in Monolayers'. In: *Journal of Physical Chemistry* 96.17 (1992), pp. 7101–7103. DOI: 10.1021/j100196a048.

[2] C. Bernardini et al. 'Colloids in Flatland: a perspective on 2D phase-separated systems, characterisation methods, and lineactant design'. In: *Chemical Society Reviews* 42.5 (2013), pp. 2100–2129. DOI: 10.1039/c2cs35269a.

[3] M. F. Paige and A. F. Eftaiha. 'Phase-separated surfactant monolayers: Exploiting immiscibility of fluorocarbons and hydrocarbons to pattern interfaces'. In: *Advances in Colloid and Interface Science* 248 (2017), pp. 129–146. DOI: 10.1016/j.cis.2017.07.023.

[4] S. Trabelsi et al. 'Linactants: Surfactant Analogues in Two Dimensions'. In: *Physical Review Letters* 100.3 (2008), p. 037802. DOI: 10.1103/PhysRevLett.100.037802.

[5] D. Sowah-Kuma and M. F. Paige. 'The influence of surfactant head group on miscibility in mixed hydrocarbon-perfluorocarbon monolayers'. In: *Colloids and Surfaces A* 556 (2018), pp. 157–166. DOI: 10.1016/j.colsurfa.2018.08.025.

[6] A. W. Adamson and A. P. Gast. *Physical Chemistry of Surfaces*. 6th ed. Hoboken, New Jersey, USA: John Wiley & Sons, Inc., 1997. ISBN: 978-0-471-14873-9.

[7] M. P. Turberg and J. E. Brady. 'Semifluorinated hydrocarbons: primitive surfactant molecules'. In: *Journal of the American Chemical Society* 110.23 (1988), pp. 7797–7801. DOI: 10.1021/ja00231a034.

[8] A. L. S. Gamboa, E. J. M. Filipe and P. Brogueira. 'Nanoscale Pattern Formation in Langmuir-Blodgett Films of a Semifluorinated Alkane and a Polystyrene-Poly(Ethylene Oxide) Diblock Copolymer'. In: *Nano Letters* 2.10 (2002), pp. 1083–1086. DOI: 10.1021/nl025698o.

[9] M. P. Krafft and J. G. Riess. 'Chemistry, Physical Chemistry, and Uses of Molecular Fluorocarbon-Hydrocarbon Diblocks, Triblocks, and Related Compounds – Unique "Apolar" Components for Self-Assembled Colloid and Interface Engineering'. In: *Chemical Reviews* 109.5 (2009), pp. 1714–1792. DOI: 10.1021/cr800260k.

[10] A. El Abed et al. 'Experimental evidence for an original two-dimensional phase structure: An antiparallel semifluorinated monolayer at the air-water interface'. In: *Physical Review E* 65.5 (2002), Article No. 051603. DOI: 10.1103/PhysRevE.65.051603.

[11] M. Broniatowski et al. 'Langmuir Monolayers Characteristic of (Perfluorodecyl)-Alkanes'. In: *Journal of Physical Chemistry B* 108.35 (2004), pp. 13403–13411. DOI: 10.1021/jp0402481.

[12] P. Morgado et al. 'Vapor Pressure of Perfluoroalkylalkanes: The Role of the Dipole'. In: *Journal of Physical Chemistry B* 119.4 (2015), pp. 1623–1632. DOI: 10.1021/jp5109448.

[13] D. L. A. Gaspar. 'MD simulations of hemimicelles of F8H16 at the surface of alcohols and water/alcohol mixtures'. Online (accessed 27/02/2024): https://fenix.tecnico.ulisboa.pt/cursos/meq21/dissertacao/846778572213831. MA thesis. Instituto Superior Técnico, 2022.

[14] L. Bardin et al. 'Highly organized crystalline monolayer of a semi-fluorinated alkane on a solid substrate obtained by spin-coating'. In: *Thin Solid Films* 519.1 (2010), pp. 414–416. DOI: 10.1016/j.tsf.2010.07.065.

[15] *Revised Release on Surface Tension of Ordinary Water Substance*. IAPWS R1-76(2014). International Association for the Properties of Water and Steam. June 2014. URL: http://www.iapws.org/relguide/Surf-H2O-2014.pdf (visited on 23/03/2024).

[16] M. Součková, J. Klomfar and J. Pátek. 'Measurement and correlation of the surface tension-temperature relation for methanol'. In: *Journal of Chemical and Engineering Data* 53.9 (2008), pp. 2233–2236. DOI: 10.1021/je8003468.

[17] J. Justino et al. 'Unusual interfacial behaviour of mixtures of 2,2,2-Trifluoroethanol with hydrogenated alcohols'. In: *Journal of Molecular Liquids* 393 (2024), p. 123684. DOI: 10.1016/j.molliq.2023.123684.

[18] A. L. S. Gamboa. 'Ordering in Langmuir and Langmuir-Blodgett Films: Effect of the Presence of Fluorocarbon and Hydrocarbon Chains'. PhD thesis. Lisboa, Portugal: Universidade Técnica de Lisboa – Instituto Superior Técnico, 2006.

[19] M. P. Krafft et al. 'Reversible Stepwise Formation of Mono- and Bilayers of a Fluorocarbon/Hydrocarbon Diblock on Top of a Phospholipid Langmuir Monolayer. A Case of Vertical Phase Separation'. In: *Langmuir* 17.21 (2001), pp. 6577–6584. DOI: 10.1021/la010587a.

[20] M. Maaloum, P. Muller and M. P. Krafft. 'Lateral and Vertical Nanophase Separation in Langmuir-Blodgett Films of Phospholipids and Semifluorinated Alkanes'. In: *Langmuir* 20.6 (2004), pp. 2261–2264. DOI: 10.1021/la030312q.

[21] G. M. C. Silva et al. 'Spontaneous self-assembly and structure of perfluoroalkylalkane surfactant hemimicelles by molecular dynamics simulations'. In: *Proceedings of the National Academy of Sciences of the United States of America* 116.30 (2019), pp. 14868–14873. DOI: 10.1073/pnas.1906782116.

[22] W. Humphrey, A. Dalke and K. Schulten. 'VMD: Visual Molecular Dynamics'. In: *Journal of Molecular Graphics & Modelling* 14.1 (1996), pp. 33–38. DOI: 10.1016/0263-7855(96)00018-5.

[23] W. L. Jorgensen, D. S. Maxwell and J. Tirado-Rives. 'Development and Testing of the OPLS All-Atom Force Field on Conformational Energetics and Properties of Organic Liquids'. In: *Journal of the American Chemical Society* 118.45 (1996), pp. 11225–11236. DOI: 10.1021/ja9621760.

[24] E. M. Duffy. PhD thesis. New Haven, CT, USA: Yale University, 1994.

[25] R. Chitra and P. E. Smith. 'A comparison of the properties of 2,2,2-trifluoroethanol and 2,2,2-trifluoroethanol/water mixtures using different force fields'. In: *Journal of Chemical Physics* 115.12 (2001), pp. 5521–5530. DOI: 10.1063/1.1396676.

[26] H. J. C. Berendsen, J. R. Grigera and T. P. Straatsma. 'The Missing Term in Effective Pair Potentials'. In: *Journal of Physical Chemistry* 91.24 (1987), pp. 6269–6271. DOI: 10.1021/j100308a038.

[27] E. K. Watkins and W. L. Jorgensen. 'Perfluoroalkanes: Conformational Analysis and Liquid-State Properties from ab Initio and Monte Carlo Calculations'. In: *Journal of Physical Chemistry A* 105.16 (2001), pp. 4118–4125. DOI: 10.1021/jp004071w.

[28] S. W. I. Siu, K. Pluhackova and R. A. Böckmann. 'Optimization of the OPLS-AA Force Field for Long Hydrocarbons'. In: *Journal of Chemical Theory and Computation* 8.4 (2012), pp. 1459–1470. DOI: 10.1021/ct200908r.

[29] A. A. H. Pádua. 'Torsion Energy Profiles and Force Fields Derived from Ab Initio Calculations for Simulations of Hydrocarbon–Fluorocarbon Diblocks and Perfluoroalkylbromides'. In: *Journal of Physical Chemistry A* 106.43 (2002), pp. 10116–10123. DOI: 10.1021/jp025732n.

[30] L. Martínez et al. 'PACKMOL: A Package for Building Initial Configurations for Molecular Dynamics Simulations'. In: *Journal of Computational Chemistry* 30.13 (2009), pp. 2157–2164. DOI: 10.1002/jcc.21224.

[31] J. D. G. Fonseca. 'Nano Patterned Films involving Hydrogenated and Fluorinated Surfactants'. Online (accessed 30/03/2024): https://fenix.tecnico.ulisboa.pt/cursos/meq/dissertacao/846778572213462. MA thesis. Instituto Superior Técnico, 2021.

[32] J. L. D. Rodrigues. 'Hemimicelles of semifluorinated alkanes at the surface of water: influence of electrolytes and long-chain alcohols'. Online (accessed 30/03/2024): https://fenix.tecnico.ulisboa.pt/cursos/meq21/dissertacao/846778572213962. MA thesis. Instituto Superior Técnico, 2022.

[33] A. C. O. Alves. 'Langmuir Monolayers of Perfluorinated Fatty Acids: a Molecular Dynamics Simulation Study'. Online (accessed 30/03/2024): https://fenix.tecnico.ulisboa.pt/cursos/meq/dissertacao/1691203502343635. MA thesis. Instituto Superior Técnico, 2019.

[34] L. Bardin. 'Monocouches d'alcanes semi-fluorés'. PhD thesis. Paris, France: Université Pierre et Marie Curie, 2010.

[35] D. Nečas and P. Klapetek. 'Gwyddion: an open-source software for SPM data analysis'. In: *Central European Journal of Physics* 10.1 (2012), pp. 181–188. DOI: 10.2478/s11534-011-0096-2.

[36] G. Zhang et al. 'Occurrence, Shape, and Dimensions of Large Surface Hemimicelles Made of Semifluorinated Alkanes. Elongated versus Circular Hemimicelles. Pit- and Tip-Centered Hemimicelles'. In: *Journal of the American Chemical Society* 127.29 (2005), pp. 10412–10419. DOI: 10.1021/ja0510515.

[37] A. González-Pérez, C. Contal and M. P. Krafft. 'Experimental evidence for a surface concentration-dependent mechanism of formation of hemimicelles in Langmuir monolayers of semi-fluorinated alkanes'. In: *Soft Matter* 3.2 (2007), pp. 191–193. DOI: 10.1039/b613265k.

[38] L. Bardin et al. 'Long-Range Nanometer-Scale Organization of Semifluorinated Alkane Monolayers at the Air/Water Interface'. In: *Langmuir* 27.22 (2011), pp. 13497–13505. DOI: 10.1016/10.1021/la201802x.

[39] A. Mourran et al. 'Self-Assembly of the Perfluoroalkyl-Alkane F14H20 in Ultrathin Films'. In: *Langmuir* 21.6 (2005), pp. 2308–2316. DOI: 10.1021/la048069y.

[40] X. Feng et al. 'AFM Study of Gibbs Films of Semifluorinated Alkanes at Liquid Crystal/Air Interfaces'. In: *ChemPhysChem* 14.9 (2013), pp. 1801–1805. DOI: 10.1002/cphc.201300173.

[41] O. Gang et al. 'Surface phases of semi-fluorinated alkane melts'. In: *Europhysics Letters* 49.6 (2000), pp. 761–767. DOI: 10.1209/epl/i2000-00216-4.

[42] F. G. Tournilhac, P. Bassoul and R. Cortès. 'Structure of the Smectic B Phase Formed by Linear and Branched Perfluoroalkyl-Alkanes'. In: *Molecular Crystals and Liquid Crystals* 362 (2001), pp. 45–65. DOI: 10.1080/10587250108025759.

[43] M. O. Gallyamov et al. 'Self-assembly of (perfluoroalkyl)alkanes on a substrate surface from solutions in supercritical carbon dioxide'. In: *Physical Chemistry Chemical Physics* 8.22 (2006), pp. 2642–2649. DOI: 10.1039/b602959k.

[44] J. Alexander, S. Magonov and M. Moeller. 'Topography and surface potential in Kelvin force microscopy of perfluoroalkyl alkanes self-assemblies'. In: *Journal of Vacuum Science and Technology B* 27.2 (2009), pp. 903–911. DOI: 10.1116/1.3079675.

[45] M. Veschgini et al. 'Size, Shape, and Lateral Correlation of Highly Uniform, Mesoscopic, Self-Assembled Domains of Fluorocarbon–Hydrocarbon Diblocks at the Air/Water Interface: A GISAXS Study'. In: *ChemPhysChem* 18.19 (2017), pp. 2791–2798. DOI: 10.1002/cphc.201700325.

[46] P. Fontaine et al. 'Direct Evidence for Highly Organized Networks of Circular Surface Micelles of Surfactant at the Air-Water Interface'. In: *Journal of the American Chemical Society* 127.2 (2005), pp. 512–513. DOI: 10.1021/ja044779e.

[47] P. Fontaine et al. 'Evidence for Interaction with the Water Subphase As the Origin and Stabilization of Nano-Domain in Semi-Fluorinated Alkanes Monolayer at the Air/Water Interface'. In: *Langmuir* 30.50 (2014), pp. 15193–15199. DOI: 10.1021/la5038124.

[48] L. de Viguerie et al. 'Effect of the Molecular Structure on the Hierarchical Self-Assembly of Semifluorinated Alkanes at the Air/Water Interface'. In: *Langmuir* 27.14 (2011), pp. 8776–8786. DOI: 10.1021/la201377f.

[49] P. Silva et al. 'Origin of the central pit in hemimicelles of semifluorinated alkanes: How molecular dipoles and substrate deformation can determine supra-molecular morphology'. In: *Journal of Colloid and Interface Science* 655 (2023), pp. 576–583. DOI: 10.1016/j.jcis.2023.11.007.

[50] M. Maaloum, P. Muller and M. P. Krafft. 'Monodisperse Surface Micelles of Nonpolar Amphiphiles in Langmuir Monolayers'. In: *Angewandte Chemie – International Edition* 41.22 (2002), pp. 4331–4334. DOI: 10.1002/1521-3773(20021115)41:22<4331::AID-ANIE4331>3.0.CO;2-J.

[51] C. Schwieger, X. Liu and M. P. Krafft. 'Self-assembled mesoscopic surface domains of fluorocarbon-hydrocarbon diblocks can form at zero surface pressure: tilting of solid-like hydrocarbon moieties compensates for cross-section mismatch with fluorocarbon moieties'. In: *Physical Chemistry Chemical Physics* 19.35 (2017), pp. 23809–23816. DOI: 10.1039/c7cp02432k.

[52] G. L. Gaines Jr. 'Surface Activity of Semifluorinated Alkanes: $F(CF_2)_m(CH_2)_nH$'. In: *Langmuir* 7.12 (1991), pp. 3054–3056. DOI: 10.1021/la00060a025.

Chapter 11

Structure and stability of mixed binary Langmuir films of PFAAs

11.1 Introduction

The supramolecular organisation of PFAA molecules in the form of hemimicelles at the air–water interface results from a combination of intermolecular dispersion and dipole–dipole interactions. As a first approximation, the latter are constant for a family of FnHm analogues with different chain lengths (different n and/or m). This results from the fact that the main contributions to the molecular dipole of the PFAA molecules arise from the electronically asymmetric CH_2-CF_2 bond, the CF_3 and, to a lesser extent, the CH_3 groups. One way of systematically adjusting the intermolecular dispersion interactions within the film of PFAAs, while maintaining the dipole–dipole interactions approximately constant, is to prepare mixed Langmuir films of two different FnHm, i.e. with different n and/or m. Moreover, given the dissimilarities in molecular structure arising from this difference, the study of geometrical factors affecting the molecular packing can also simultaneously be assessed. This should enable, at the same time, a deeper understanding of the fundamental aspects driving the observed self-assembling process and to assess the effect of an extra variable (the composition of the mixed binary film) on the structural characteristics of the film, envisaging practical applications.

The use of X-ray diffraction-based techniques to probe the structural properties of materials is a ubiquitous procedure in physics. For the structural characterisation of Langmuir films, this is no exception, but it poses some technical challenges to guarantee that the probing is done at the surface and not in volume (i.e. that the diffracted signal originates mostly from the molecules of the thin film rather than from the bulk liquid subphase). Moreover, because the film is very thin, the number of diffracting centres (in other words, the quantity of matter diffracting the light) is very low, so a high-intensity, low-divergence X-ray source is required for these experiments. Synchrotron X-ray radiation sources are thus paramount for these studies. In this chapter, the results from thermodynamic and structural characterisation studies of mixed Langmuir films of F8H14:F8H20 are presented. These molecules were chosen because their pure Langmuir films are well characterised, but also because they display a significant difference in the lengths of their CH chains, which was anticipated to have a strong impact on the structure of the mixed films.

11.2 Methods

11.2.1 Surface Pressure – Molecular Area Isotherms

The π–A isotherms were recorded in compression mode using a custom made Polytetrafluoroethylene (PTFE)-coated Langmuir trough equipped with two mechanical barriers and kept inside a protective plastic case. The trough had a maximum surface area of about 140.4 cm^2, having a minimum surface area of about 8.9 cm^2. Hence, the maximum attainable compression ratio was approximately 15.7. The π was measured with a Riegler & Kirstein GmbH microbalance equipped with a filter paper plate, using the Wilhelmy method. The barriers and the microbalance were connected to a captor which, through a digital interface, enabled the control of the barriers' movement and the recording of the data. The temperature of the subphase was controlled with the aid of an externally circulating water bath to $(12.0 \pm 0.5)\,^{\circ}C$. The isotherms were recorded at constant compression rate, which was in the range of 1 $Å^2$/molecule/min to 2 $Å^2$/molecule/min.

Ultrapure water from a Milli-Q Millipore system (resistivity 18.2 $M\Omega\,cm$ at 25 °C; surface tension 74.1 $mN\,m^{-1}$ at 12 °C) was used as the liquid subphase for all the experiments. Perfluorooctyltetradecane (F8H14) and perfluorooctyleicosane (F8H20) were available at the start of this work, having been synthesised by Doctors Yoann Prado and Kamal Sbargoud at Institut des Nanosciences de Paris according to Reference [1] and purified through repeated crystallisation from methanol. Their purity was confirmed by Nuclear Magnetic Resonance (NMR) and elemental analysis. Spreading solutions of binary mixtures of these PFAAs were prepared by gravimetry in analytical grade chloroform (Carlo Erba, purity ≥99%) with a typical total PFAA concentration of 2 mM, the proportion of each PFAA being adjusted to vary the solution composition. The Langmuir films were prepared by spreading the desired solution on the water surface with a microsyringe (typical volumes were in the 20 µL to 25 µL range, in order to start recording the π–A isotherms at a A of about 0.6 $nm^2\,molecule^{-1}$ to 0.5 $nm^2\,molecule^{-1}$), followed by a 10 min waiting time to allow for solvent evaporation before starting the monolayer compression. At least 3 different and independent π–A isotherms were recorded for each studied system. The π–A isotherms were processed using an adapted version of the Savitzky-Golay filter for the treatment of non-evenly spaced data, using a filtering window of 51 points with a 3^{rd} degree polynomial [2, 3]. Except where mentioned otherwise, the presented results are derived or calculated from the filtered data.

11.2.2 Experiments performed at the ID10 beam line (ESRF)

GISAXS geometry Part of the GISAXS measurements were performed on the ID10 beam line of the European Synchrotron Radiation Facility (ESRF) synchrotron. The dedicated PTFE Langmuir trough was equipped with a single movable barrier (maximum surface area ≈ 680 cm^2; maximum compression ratio ≈ 4.0). The temperature of the subphase was controlled with the aid of an externally circulating water bath to $(12.0 \pm 0.5)\,^{\circ}C$. The surface pressure, which was measured by the Wilhelmy plate method, was actively controlled and kept constant during the scans. The trough was mounted on an active anti-vibration system, was enclosed within a gas-tight box with Kapton windows and was flushed with water-saturated helium. The energy of the incoming

X-ray beam, 8 keV ($\lambda = 0.155$ nm), was selected using a double diamond crystal monochromator. The incident beam was slightly deflected downward by a double mirror setup to an incidence angle with the water surface of 2 mrad (below the critical angle of total reflection on the air–water interface, which is ≈ 2.8 mrad at 8 keV). The incident beam size was fixed by optical slits and set at 23 µm × 28 µm (vertical × horizontal). The resolution of the measurement is defined by mounting a collimator with 2 vertical slits (separated by 650 mm) between the sample and the detector. Such a setup leads to an in-plane angular resolution of about 0.4 mrad. The scattered signal was recorded using a one-dimensional Mythen 2 strip detector. In this configuration, the spectra are obtained by scanning over the in-plane (2θ) angle and, at each detector position at fixed 2θ, the vertical scattered intensity is measured; for the GISAXS measurements presented herein, the vertical distribution of the scattered intensity is integrated along Q_z.

11.2.3 Experiments performed at the SIRIUS beam line (SOLEIL)

Part of the GISAXS and all the GIXD measurements presented herein were performed on the SIRIUS beam line of the Source Optimisée de Lumière d'Énergie Intermédiaire du LURE (SOLEIL) synchrotron. Due to technical constraints, both geometries were not implementable simultaneously, as detailed below. Therefore, the GISAXS and the GIXD experiments were performed separately and on different monolayers. In all cases, the dedicated PTFE Langmuir trough was equipped with a single movable barrier (maximum surface area $\approx 700\,\mathrm{cm}^2$; maximum compression ratio ≈ 3.5). The temperature of the subphase was controlled with the aid of an externally circulating water bath to $(12.0 \pm 0.5)\,^\circ$C. The surface pressure, which was measured by the Wilhelmy plate method, was actively controlled and kept constant during the scans. The trough was mounted on an active anti-vibration system, was enclosed within a gas-tight box with Kapton windows and was flushed with water-saturated helium. The energy of the incoming X-ray beam, 8 keV ($\lambda = 0.155$ nm), was selected using the (111) face of a Si double crystal in reflection geometry (further technical details characterising the SIRIUS beam line can be found in the literature [4]). The incident beam (140 µm × 2000 µm, vertical × horizontal) was defined by a set of mirrors and deflected downward to an incidence angle with the water surface of 2 mrad (below the critical angle of total reflection on the air–water interface, which is ≈ 2.8 mrad at 8 keV). This geometry leads to a probed thickness of about 5 nm beneath the interface by the evanescent refracted wave. The scattered signal was recorded using a two-dimensional Pilatus detector.

GISAXS geometry The resolution of the measurement is improved by mounting a collimator between the sample and the detector with 1 vertical slit (of about 300 µm) at a distance of 537 mm from the detector. The scattered radiation is collected on a 1-pixel wide vertical line of the detector, which functions as a second slit of about 172 µm. In this configuration, the spectra are obtained by scanning over the in-plane (2θ) angle and simultaneously measuring the vertical scattered intensity; for the GISAXS measurements presented herein, the vertical distribution of the scattered intensity is integrated along Q_z.

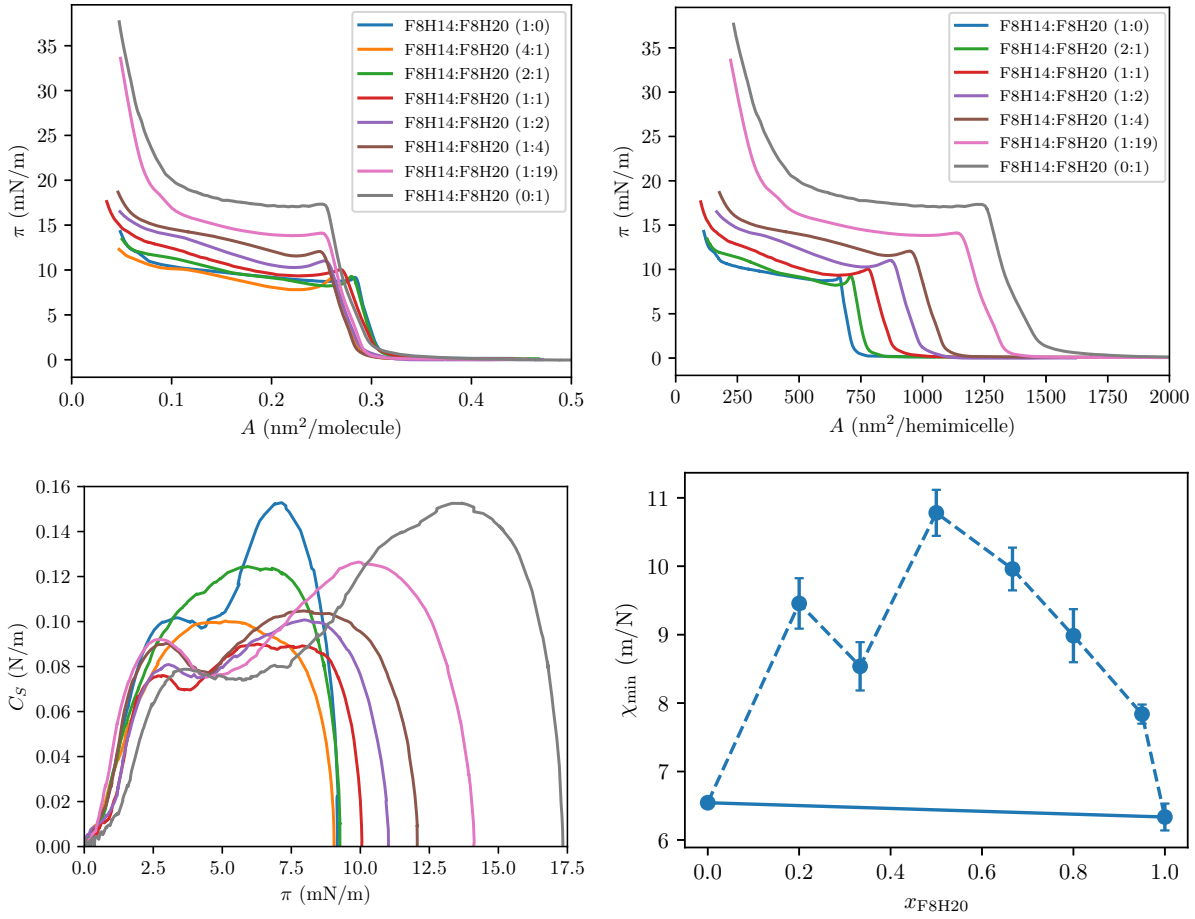

Figure 11.1: Experimental thermodynamic results obtained for the mixed Langmuir films of F8H14:F8H20 at $T = 12\,^{\circ}\mathrm{C}$. Top left: π–A isotherms at different film compositions, indicated in the inset as the molar proportions between the film components. Top right: π as a function of the surface area per hemimicelle (π–$A_{\mathrm{hemimicelle}}$ isotherms) at different film compositions, indicated in the inset as the molar proportions between the film components. $A_{\mathrm{hemimicelle}}$ was estimated based on the lattice parameter a retrieved from the GISAXS experiments performed at $\pi = 5\,\mathrm{mN\,m^{-1}}$. Bottom left: compression modulus (C_S, defined in Equation 1.2) as a function of π; the curves are colour coded similarly to the π–A isotherms presented in the top left image. Bottom right: minimum monolayer compressibility (χ_{min}) calculated from the π–A isotherm data.

GIXD geometry A standard Soller slit collimator was used for these measurements, leading to an in-plane wave vector resolution of $\approx 0.05°$. In this configuration, the spectra are obtained by scanning over the in-plane (2θ) angle and simultaneously measuring the vertical scattered intensity. This permits to record the scattered intensity as a function of the in-plane (Q_{xy}) and off-plane (Q_z) components of the scattering vector. As is detailed in the results section, the scattering intensity distribution is analysed as a function of Q_{xy} and Q_z, is integrated along Q_z or is transformed into polar coordinates and further analysed as such.

11.3 Results and Discussion

Three limit scenarios can be anticipated for the structure of the mixed Langmuir films of F8H14:F8H20: a completely segregated film (scenario "a"); a film mixed at the hemimicellar level, *i.e.* comprising pure (or partially mixed) hemimicelles of two different sizes forming a single 2D lattice (scenario "b"); or a film mixed at the molecular level, *i.e.* comprising mixed monodisperse hemimicelles forming a single 2D lattice (scenario "c"). The characterisation of the mixed Langmuir films resorting to different experimental techniques aimed at discerning between the proposed scenarios.

11.3.1 Thermodynamic Characterisation: π–A Isotherms

The π–A isotherms at $T = 12\,°C$ for the mixed Langmuir films of F8H14:F8H20 with different film compositions (x_{F8H20}) are presented in Figure 11.1 (top left). The T of 12 °C was chosen and kept constant because it has been demonstrated that the F8H14 is unstable at higher T (F8H20 is stable at least up to 18 °C) [5]. The π–A isotherms for the pure compounds are similar to those already reported in the literature [5–11]. For the pure systems, but also for the mixed films, the π remains constant and essentially null upon compression of the film up to a value of A near $0.30\,nm^2\,molecule^{-1}$, the point at which a lift-off occurs and a steep rise in π is observed. This value is slightly larger than that obtained for the tight packing of perfluorinated chains (of about $0.28\,nm^2\,molecule^{-1}$ [12–14]) and this discrepancy has been interpreted as an evidence of lying molecules in between the surface hemimicelles constituting the film [5, 15, 16]. The observed lift-off A values are nevertheless consistent with the existence of a structure of close-packed CF chains, as is further discussed below. Continuing the compression of the film results in its collapse, that is the transition to a post-monomolecular state or a three-dimensional (3D) condition of the film [17, 18]. This is identified as a local maximum in π (Surface Pressure of Collapse ($\pi_{collapse}$); *cf.* Figure 1.1), followed by a plateau which has been interpreted, for the pure films, as a first-order phase transition between the monolayer and a trilayer state [19]. Further compression of the film results in a second lift-off occurring at an A that is approximately one third of the first lift-off A. This supports the occurrence of a monolayer to trilayer transition. The fact that a single $\pi_{collapse}$ is identified permits to exclude scenario "a": for a completely segregated film, it would be expected that the mixed film would exhibit a behaviour similar to the pure compound with the lowest $\pi_{collapse}$ (in this case, F8H14) upon compression until the collapse of the film, followed by a plateau and a second rise in π until the $\pi_{collapse}$ of the second compound would be attained.

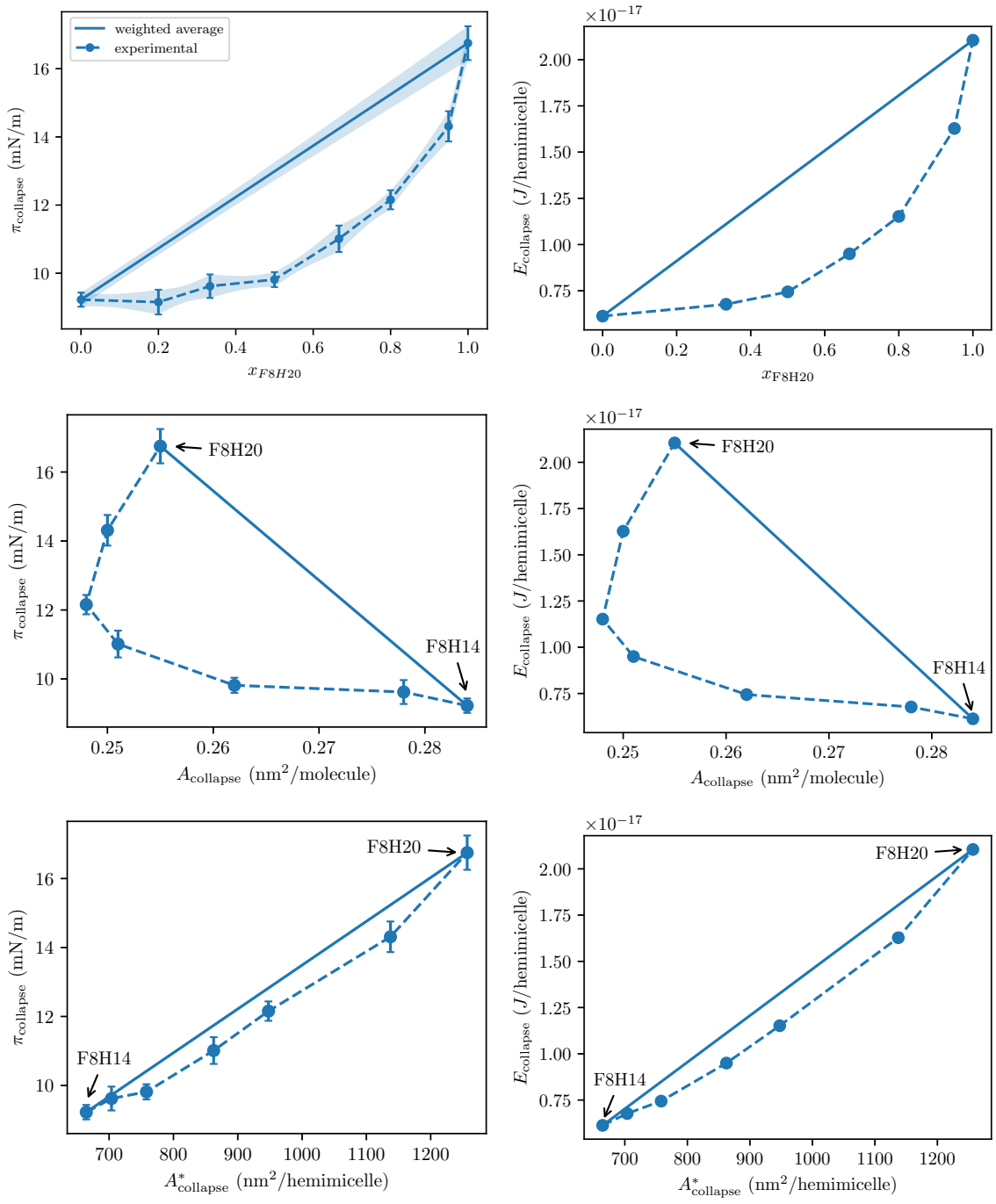

Figure 11.2: Experimental thermodynamic results obtained for the mixed Langmuir films of F8H14:F8H20 at $T = 12\,°C$. Top left: surface pressure of collapse ($\pi_{collapse}$, defined in Figure 1.1) as a function of the film composition (x_{F8H20}). Top right: energy of collapse per surface hemimicelle ($E_{collapse}$) as a function of x_{F8H20}. Middle left: $\pi_{collapse}$ as a function of the surface area per molecule at the onset of the collapse ($A_{collapse}$). Middle right: $E_{collapse}$ as a function of $A_{collapse}$. Bottom left: $\pi_{collapse}$ as a function of the surface area per hemimicelle at the onset of the collapse ($A^*_{collapse}$). Bottom right: $E_{collapse}$ as a function of $A^*_{collapse}$.

The π as a function of the surface area per hemimicelle (π–$A_{\text{hemimicelle}}$ isotherms) at different film compositions is presented in Figure 11.1 (top right). This representation hints at the occurrence of regular changes in the thermodynamic properties of the mixed films of F8H14:F8H20 that are not as striking when the isotherms are plotted as a function of A. In particular, the dependence of π_{collapse} with $A_{\text{hemimicelle}}$ appears to be linear. This result is further detailed in a few paragraphs.

The compressibility of the condensed phase of the mixed films of F8H14:F8H20 was estimated from the π–A isotherms. The compressibility modulus (C_S, defined in Equation 1.2) is represented in Figure 11.1 (bottom left) as a function of π for different x_{F8H20}. Two remarks are general and occur for all the studied systems: C_S is essentially null for $\pi \approx 0\,\text{mN}\,\text{m}^{-1}$ for all systems, because the compression of the monolayers at large A occurs at $\pi \approx 0\,\text{mN}\,\text{m}^{-1}$ and doesn't cause a measurable increase in π (the monolayers are very compressible at this point, which has been interpreted as the equilibrium plateau between a non-condensed, possibly gaseous, and a liquid condensed phases [5]); C_S increases and is highest for intermediate π and it decreases and becomes 0 at $\pi = \pi_{\text{collapse}}$. With the exception of the systems $x_{\text{F8H20}} = 0.2$ and $x_{\text{F8H20}} = 0.33$, all systems display a local minimum for C_S for a π of about $3\,\text{mN}\,\text{m}^{-1}$ to $5\,\text{mN}\,\text{m}^{-1}$. This has been associated to the existence of a subtle change of slope or a "kink" in the π–A isotherms, which has been interpreted as the transition from a dimeric double-helix to a monomeric organisation of the PFAA molecules [20] or the onset of a nucleation process characterising the beginning of the collapse of the monolayer [21]. The latter interpretation can be considered knowing that the PFAAs have a value of Equilibrium Spreading Pressure (ESP) in the order of $3\,\text{mN}\,\text{m}^{-1}$ to $5\,\text{mN}\,\text{m}^{-1}$ [21], that they show some degree of temporal instability at longer timescales and especially for shorter PFAA molecules and at π significantly above these values [5, 8, 11, 21] and that, in general, a Langmuir films can be considered to be in a meta-stable state when compressed to a π above its ESP [22, 23]. However, such kink is suppressed for the systems $x_{\text{F8H20}} = 0.2$ and $x_{\text{F8H20}} = 0.33$, which might be indicative of different dynamics for an intermediate range of x_{F8H20}. That being said, these results should be carefully analysed, since the meta-stability of the films might preclude the attainment of the thermodynamic equilibrium of the film within the time scale during which the compression π–A isotherms are recorded.

The minimum monolayer compressibility (χ_{min}) was estimated from the π–A isotherms and is represented in Figure 11.1 (bottom right) as a function of x_{F8H20}. In absolute terms, all systems present χ_{min} in the range of approximately $6\,\text{m}\,\text{N}^{-1}$ to $11\,\text{m}\,\text{N}^{-1}$. These values are comparable to those reported in the literature for pure PFAA monolayers [5, 7–9, 11, 21] and are characteristic of Liquid Condensed (LC) phases. χ_{min} is higher for the mixed films, compared to both pure compounds, meaning that the mixed films are more compressible than the pure ones. As is further discussed below, this is also consistent with the expulsion of molecules from the interface even before the attainment of π_{collapse}.

The π_{collapse} is represented in Figure 11.2 as a function of: x_{F8H20} (top left); the surface area per molecule at the onset of the collapse (A_{collapse}; middle left); and the surface area per hemimicelle at the onset of the collapse (A^*_{collapse}; bottom left). π_{collapse} is always lower than the average of the pure compounds for the mixed films. Furthermore, the dependence of π_{collapse} with A_{collapse} also deviates significantly from the average of the pure compounds. In the latter case,

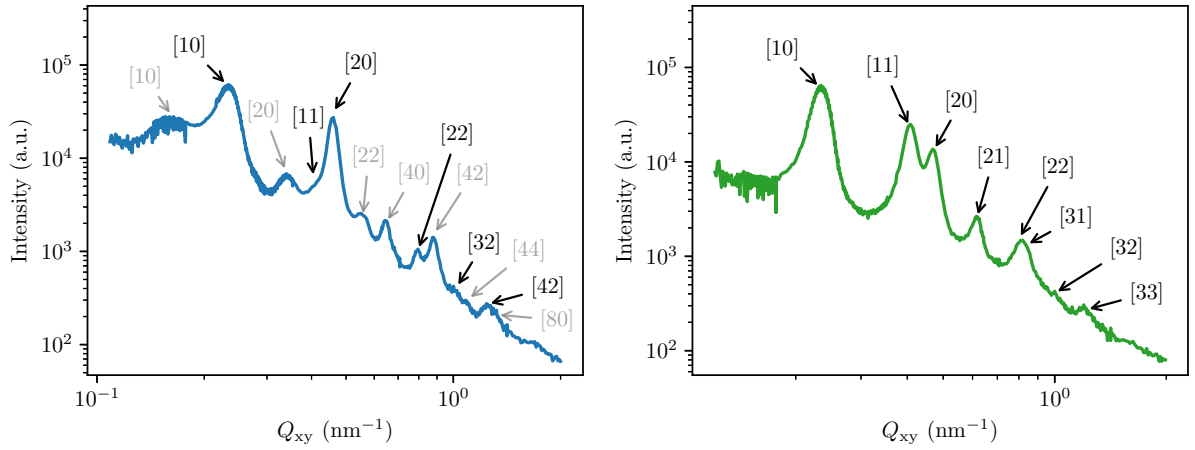

Figure 11.3: Typical GISAXS Q_z-integrated spectra of the F8H14:F8H20 Langmuir films obtained at $T = 12\,°C$ and: $\pi = 0\,mN\,m^{-1}$ with a molar proportion of 1:0 or $x_{F8H20} = 0.00$ (left); $\pi = 5\,mN\,m^{-1}$ with a molar proportion of 2:1 or $x_{F8H20} = 0.33$ (right). The arrows indicate the indexation of the identified diffraction peaks attributed to the main (black) or secondary (light grey) 2D hexagonal lattices.

Table 11.1: Parameters from the fit of Lorentzian curves (after background subtraction) to the experimental dataset presented in Figure 11.3 (right), that is the GISAXS Q_z-integrated spectrum obtained at $T = 12\,°C$ and $\pi = 5\,mN\,m^{-1}$ for the mixed binary Langmuir film of F8H14:F8H20 with a molar proportion of 2:1 ($x_{F8H20} = 0.33$). The parameters of the fit are the peak position (x_c), the peak integrated area (Area) and the FWHM. Ratio indicates the ratio between the peaks' x_c and the position of the first order peak indexed according to a hexagonal lattice as the [10] peak. Ratio_{hex} indicates the corresponding theoretical value expected for Ratio for a hexagonal lattice. Indexation_{hex} indicates the peak indexation according to a hexagonal lattice and a is the corresponding lattice parameter deduced from the corresponding peak x_c and Indexation_{hex}.

x_c (nm^{-1})	Ratio	Ratio_{hex}	Area (a.u.)	FWHM (nm^{-1})	Indexation_{hex}	a (nm)
0.23348	1.000	1.000	2702.7	0.02736	[10]	31.07
0.40695	1.743	1.732	1419.4	0.03713	[11]	30.88
0.47023	2.014	2.000	774.4	0.04013	[20]	30.86
0.61545	2.636	2.646	110.0	0.04205	[21]	31.19
0.79869	3.421	3.464	52.6	0.06022	[22]	31.47
0.83350	3.570	3.606	75.3	0.07148	[31]	31.38
0.99443	4.259	4.359	35.2	0.18290	[32]	31.80
1.20818	5.175	5.196	36.1	0.15910	[33]	31.20

this can be related with the non-linear dependence of both π_{collapse} with x_{F8H20} and of A_{collapse} with x_{F8H20}. Finally, the variation of π_{collapse} with A^*_{collapse} approaches the linear dependence, falling only slightly below the average for the pure compounds. Taken together, these results are indicative that the mechanism of collapse of the mixed monolayers of F8H14:F8H20 is proportional to the area occupied per hemimicelle in the dense film, of which A^*_{collapse} is a good estimation.

The energy of collapse per surface hemimicelle (E_{collapse}) was estimated from π_{collapse} and the GISAXS results (see Subsection 11.3.2), according to Equation 11.1, and is presented in Figure 11.2. E_{collapse} is plotted as a function of: x_{F8H20} (top right); A_{collapse} (middle right); and A^*_{collapse} (bottom right). The unit cell area ($A^{\text{GISAXS}}_{\text{unit cell}} = a^2 \sin(60°)$) was calculated from the hexagonal lattice parameter (a) retrieved from the GISAXS experiments performed at $\pi = 5\,\text{mN}\,\text{m}^{-1}$ and corresponds approximately to the surface area occupied per surface hemimicelle, at that π.

$$E_{\text{collapse}} = \pi_{\text{col}} \times A^{\text{GISAXS}}_{\text{unit cell}} = \pi_{\text{col}} \times a^2 \sin(60°) \tag{11.1}$$

E_{collapse} displays a dependence on the aforementioned variables (x_{F8H20}, A_{collapse}, A^*_{collapse}) that is similar to that described for π_{collapse}. In particular, it is clear that E_{collapse} is almost proportional to A^*_{collapse}, falling just below the average for the pure compounds. E_{collapse} can be thought of as the amount of energy required to detach a hemimicelle from the water surface upon the collapse of the film, assuming the mechanism of collapse consists in the ejection of whole hemimicelles and their detachment from the water subphase rather than the ejection of individual molecules from the film. The fact that E_{collapse} is almost linearly dependent on A^*_{collapse} reiterates the hypothesis that the collapse of the film might occur through the detachment of whole hemimicelles from the liquid surface rather than the ejection of individual molecules. However, the deviations from the average of the pure compounds suggest that the energy of interaction of the hemimicelles with the underlying subphase is altered with varying film composition. This, in turn, suggests that the interactions of the PFAA molecules comprising the hemimicelles depend on the film composition, which is consistent with mixing occurring at the hemimicelle level (scenario "c" described above).

11.3.2 Grazing Incidence Small Angle X-ray Scattering (GISAXS)

The GISAXS experiments permit to determine the organisation of the hemimicelles comprising the mixed binary films of F8H14:F8H20. A typical dataset consists in the diffracted intensity, integrated along Q_z, represented as a function of Q_{xy}, as is depicted in Figure 11.3. These are obtained at varying values of x_{F8H20} and π, at a constant temperature of $T = 12\,°\text{C}$. After subtracting a polynomial function adjusting the background, the diffraction peaks are fitted with peak-shaped functions. Herein, either Lorentzian or Gaussian functions were used, depending on the experimental setup and dataset. It should be noted that for measurements made on the same monolayer, the same peak shape is assumed for the whole experiment. The peak positions (x_c), integrated areas (Area) and FWHMs are retrieved from the fits. For all cases, the peaks can be indexed according to a 2D hexagonal lattice, as it has been observed for the pure cases (at least for non-zero π) [5, 11, 24, 25]. The corresponding peak indexation ($\text{Indexation}_{\text{hex}}$) and

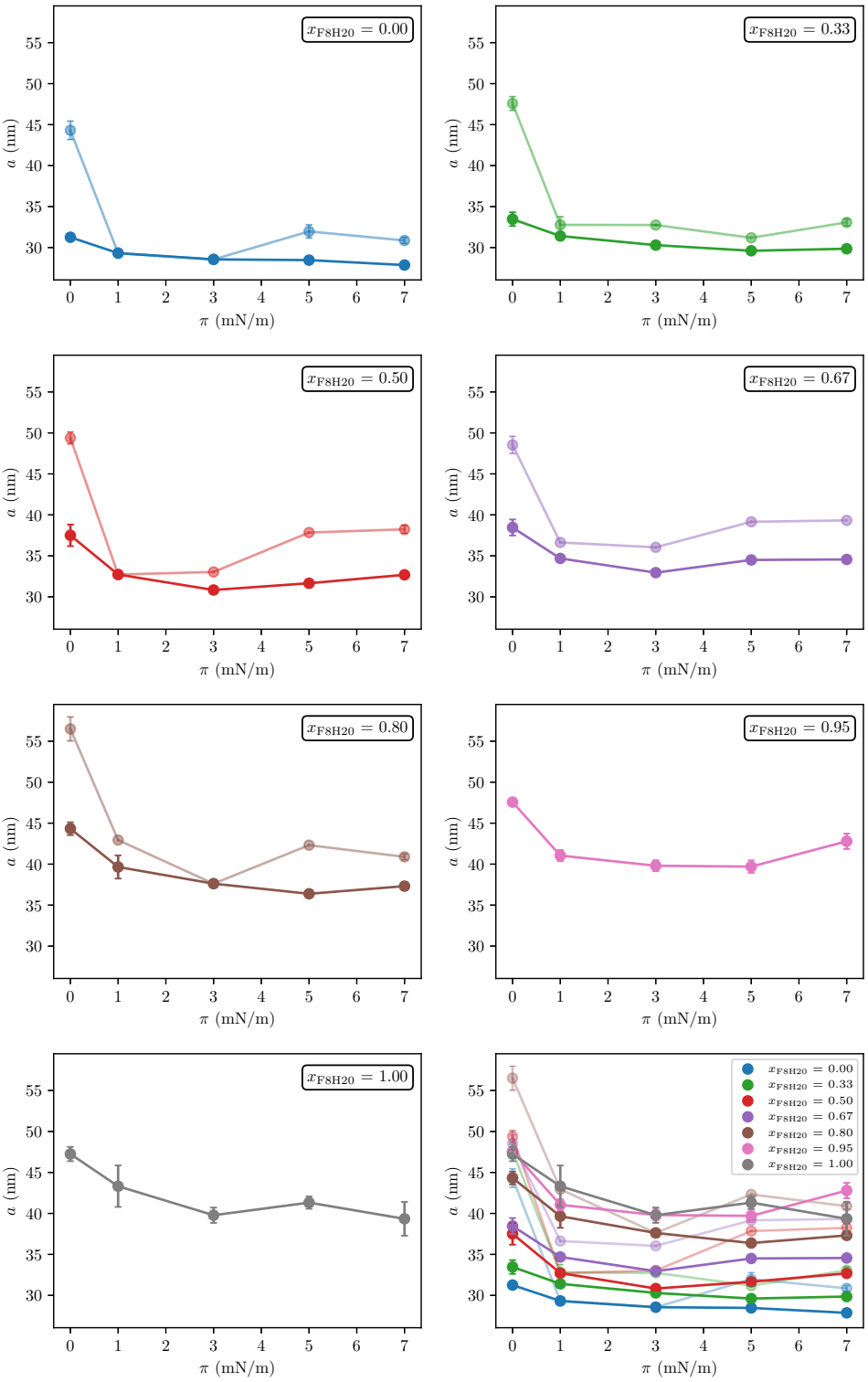

Figure 11.4: Lattice parameter a for the proposed main (blue) and secondary (orange) 2D hexagonal lattices as a function of π calculated from the GISAXS measurements at $T = 12\,^{\circ}\mathrm{C}$ for the mixed binary Langmuir film of F8H14:F8H20 with different compositions (x_{F8H20}, indicated on the inset). The bottom right plot is a compilation of the remaining plots, in which case the lines are colour coded according to x_{F8H20}, indicated on the inset, being the a for the proposed main and secondary 2D hexagonal lattices represented as dark and faded lines, respectively.

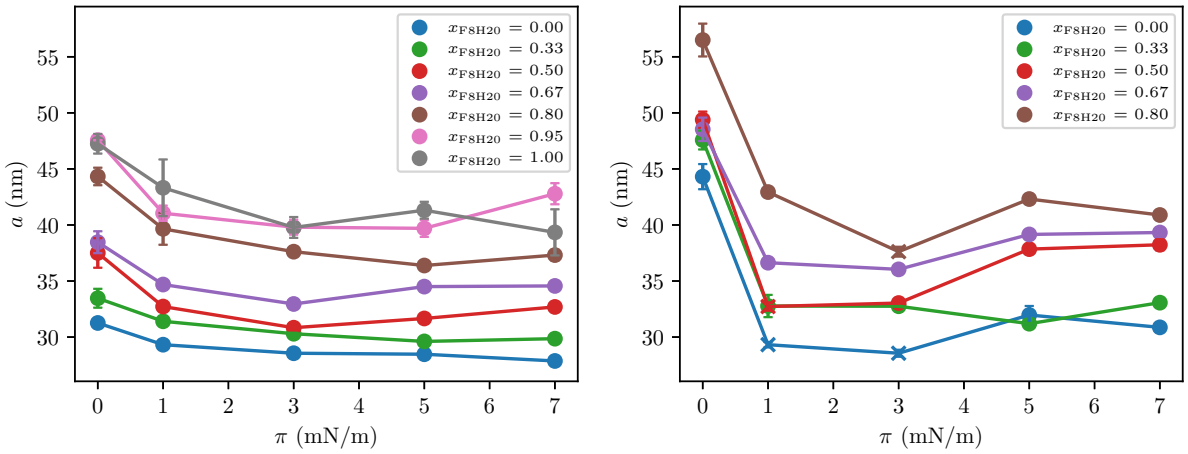

Figure 11.5: Lattice parameter a for the proposed main (left) and secondary (right) 2D hexagonal lattices as a function of π calculated from the GISAXS measurements at $T = 12\,°C$ for the mixed binary Langmuir film of F8H14:F8H20 with different compositions (x_{F8H20}, indicated on the inset). On the rightmost plot, the crosses mark the points for which the presence of only one hexagonal lattice is inferred from the GISAXS spectra at the corresponding π and x_{F8H20}; in those cases, the values of a for the proposed main hexagonal lattice are represented.

the 2D hexagonal lattice parameter (a, inferred from x_c and $\text{Indexation}_{\text{hex}}$) can thus computed. All these quantities are presented in Table 11.1, as an illustrative example for the spectrum in Figure 11.3 (right).

For the studied x_{F8H20} range and π (varying from $0\,\text{mN}\,\text{m}^{-1}$ to $7\,\text{mN}\,\text{m}^{-1}$, always below π_{collapse}), the system is generally organised according to a single 2D hexagonal lattice. However, for some values of x_{F8H20}, two 2D hexagonal lattices are present, as it has been observed in the case of the pure F8H14 film. This is deduced from the fact that the proposed [10] peak for the main structure is markedly asymmetric and a second peak at lower Q_{xy} values is clearly discernible in its vicinity (therefore corresponding to a structure with a larger lattice parameter). An example of such situation is presented in Figure 11.3 (left).

The a for the main and the secondary 2D hexagonal lattices are presented in Figures 11.4 and 11.5, as a function of π and for different x_{F8H20}. These data are presented in tabular form in Tables C.1 and C.2, in Appendix C. Additionally, a and $A_{\text{unit cell}}^{\text{GISAXS}}$ for the main 2D hexagonal lattice are shown as functions of x_{F8H20} and for different π in Figures 11.6 and 11.7, respectively. For the proposed main structure, in general, a decreases with increasing π and increases with increasing x_{F8H20}. Both effects are expected: the first given that the compression of the film would be anticipated to cause the compression of the hemimicelles closer together and consequently the reduction of a; and the second given that, for any given π, the a for the pure F8H20 film is larger than that for the pure F8H14 film [5]. However, considering the dependency of $A_{\text{unit cell}}^{\text{GISAXS}}$ with x_{F8H20}, it is clear that the size of the mixed hemimicelles is systematically smaller than the weighted average of the pure compounds[1]; in other words, the systems present negative deviations to Vegard's law. This suggests that the interactions among hemimicelles in the mixed films are

[1]With the sole exception for the data point for $x_{F8H20} = 0.95$ at $\pi = 7\,\text{mN}\,\text{m}^{-1}$; this point likely falls within the trend, considering the experimental dispersion associated with the measurements.

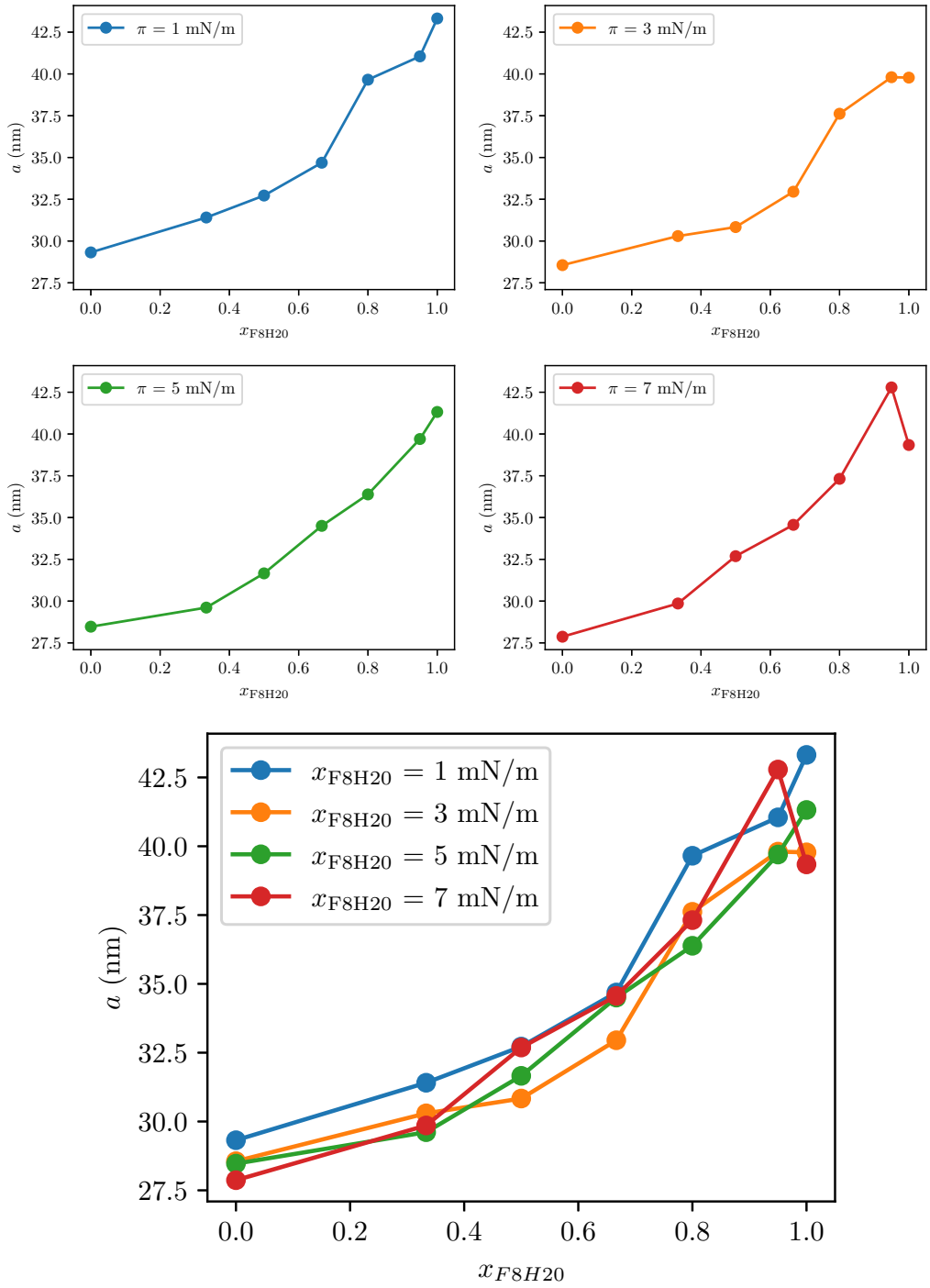

Figure 11.6: Lattice parameter a for the proposed main 2D hexagonal lattice as a function of x_{F8H20} calculated from the GISAXS measurements at $T = 12\,^{\circ}\mathrm{C}$ for the mixed binary Langmuir film of F8H14:F8H20 at different π values, indicated on the insets. The bottom right plot is a compilation of the remaining plots, in which case the lines are colour coded according to π, indicated on the inset.

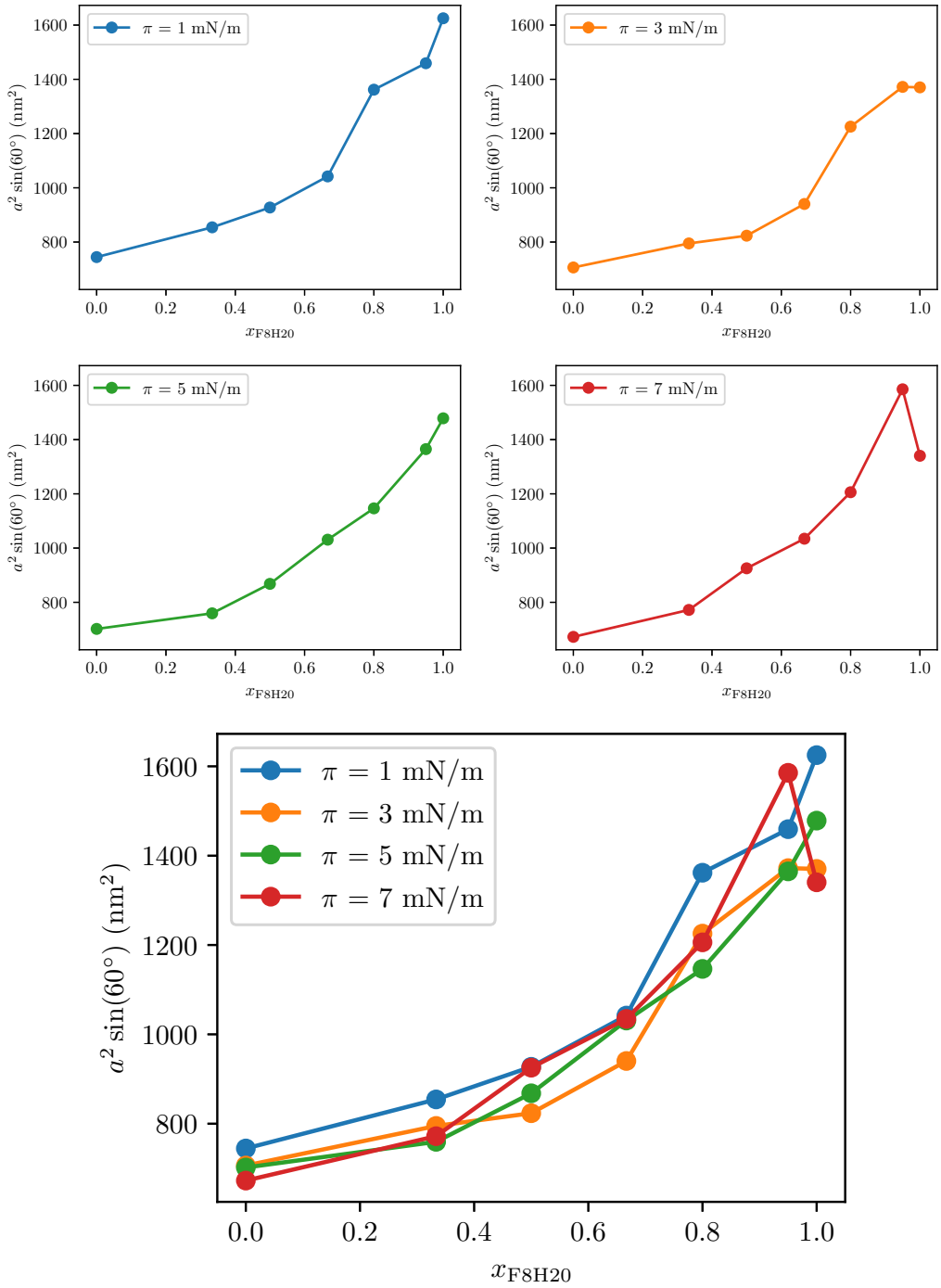

Figure 11.7: Unit cell area ($A^{\text{GISAXS}}_{\text{unit cell}} = a^2 \sin(60°)$) for the proposed main 2D hexagonal lattice as a function of x_{F8H20} calculated from the GISAXS measurements at $T = 12\,°C$ for the mixed binary Langmuir film of F8H14:F8H20 at different π values, indicated on the insets. The bottom plot is a compilation of the remaining plots, in which case the lines are colour coded according to π, indicated on the inset.

different and stronger (more attractive or, conversely, less repulsive), compared to the pure film cases, permitting the tighter packing of the hemimicelles under such circumstances and the consequent reduction in a. Another possibility consists in the deformation of the hemimicelles upon compression of the film, distorting their shape from round to hexagonal. This effect is expected to be more significant for the larger hemimicelles, as these have a lower curvature. This phenomenon would increase the packing fraction of the film and ultimately lead to a reduction in a. This scenario is plausible if one takes into account the results reported in the literature of AFM images of films of PFAAs on a solid substrate. These present round domains when the samples are prepared by transfer onto a solid substrate [8], but comprise hexagonally-faceted domains when the samples are prepared by spin coating [26].

On one hand, in general, the evolution of the films' structure with π results in the shift of the diffraction peaks to larger Q_{xy} values, which translates into the contraction of the diffracting lattice. Moreover, the secondary lattice is completely suppressed or its a approaches that of the main 2D hexagonal lattice. On the other hand, by increasing x_{F8H20} the diffraction peaks are shifted to smaller Q_{xy} values and become broader. This means that the film is formed by larger, but less ordered hemimicelles, with increasing x_{F8H20}. These observations are deepened in the following paragraphs and are illustrated in Figure C.1 in Appendix C.

Concerning the cases for which the coexistence of two 2D hexagonal lattices is proposed and for $\pi = 0\,\mathrm{mN\,m^{-1}}$, the main structure has a a between about 30 nm (pure F8H14) and about 40 nm (for $x_{F8H20} = 0.80$). On one hand, these values resemble the size of the hemimicelles of pure F8H14 or an intermediate size between that of pure F8H14 and pure F8H20, respectively. On the other hand, the secondary structure has a a from about 45 nm to 55 nm, increasing with x_{F8H20}. This is larger than what would be expected to be the size of the hemimicelles of F8H14 or F8H20 and is a particularly unexpected phenomenon to occur for the pure F8H14 monolayer (a monodisperse system would be anticipated in this case). It should be noted that the purity of the used PFAA molecules was thoroughly checked by elemental analysis and ^{1}H and ^{19}F NMR. It is unlikely that the reported phenomena result from the presence of an impurity contaminating the F8H14. Moreover, upon compression of the film to $\pi > 0\,\mathrm{mN\,m^{-1}}$, the a of the secondary lattice is drastically reduced and approaches that of the main lattice. This effect is observed, in general, for the entire studied π range. For some π values, this second structure is even indiscernible or suppressed (e.g. $\pi = 3\,\mathrm{mN\,m^{-1}}$ for $x_{F8H20} = 0.80$). Finally, the intensity of the [10] peak of the main 2D hexagonal lattice is almost always larger than the intensity of the [10] peak of the secondary lattice (*cf.* Table C.3 in Appendix C). Exceptions to this observation were linked to difficulties in the processing of the data, in cases where the [10] peak of the secondary lattice was particularly broad, close to the direct beam and/or overlapped with the [10] peak of the main lattice. Taken together, these results suggest that the secondary lattice might be a metastable or transient structure that is suppressed upon compression of the film. Notwithstanding the importance of such finding, the remainder of the discussion is therefore focused on the results obtained for the proposed main 2D hexagonal lattice of hemimicelles.

Together with the π–A isotherm data presented above and the GIXD results presented in Subsection 11.3.3, the described phenomena hint at the possibility of mixing at a molecular level (*i.e.* within the hemimicelles). The results presented herein are in general agreement liter-

Table 11.2: Monolayer compressibility (χ) estimated from the GISAXS results. χ is defined in Equation 1.1. The subscripts indicate the range of π used to calculate χ.

x_{F8H20}	χ_{1-7} ($\mathrm{m\,N^{-1}}$)	χ_{1-5} ($\mathrm{m\,N^{-1}}$)
0.00	64.3	67.9
0.33	57.2	34.0
0.50	−430.1	60.6
0.67	−284.3	374.1
0.80	46.4	23.2
0.95	−82.1	59.8
1.00	39.8	42.3

ature data (for the pure films, for which values of a are available for comparison; data for $\pi = 5\,\mathrm{mN\,m^{-1}}$): for F8H14, a is reported to be about $(27.8 \pm 0.6)\,\mathrm{nm}$ [11] to about $(28 \pm 4)\,\mathrm{nm}$ [25]; for F8H20, a is reported to be about $(40.7 \pm 1.2)\,\mathrm{nm}$ [11] to about $(36 \pm 7)\,\mathrm{nm}$ [25]. Only the latter value is significantly lower than the ones obtained in this work (although it also presents a higher uncertainty).

The monolayer compressibility (χ) was estimated from the positions of the GISAXS peaks for two windows of π, namely $1\,\mathrm{mN\,m^{-1}}$ to $5\,\mathrm{mN\,m^{-1}}$ (χ_{1-5}) and $1\,\mathrm{mN\,m^{-1}}$ to $7\,\mathrm{mN\,m^{-1}}$ (χ_{1-7}). These results are compiled in Table 11.2. The estimations were carried out this way because, for a number of systems, a appears to stagnate or even increase from $\pi = 5\,\mathrm{mN\,m^{-1}}$ to $\pi = 7\,\mathrm{mN\,m^{-1}}$, which is counterintuitive. As it was mentioned above, this may be an indication that some molecules might be ejected from the film before the attainment of π_{collapse} (most likely F8H14 because of its lower π_{collapse}). This would effectively lead to a film with a higher x_{F8H20} which, knowing that the F8H20 hemimicelles are larger than the F8H14 ones, would be anticipated to result in an increase in a. However, the effect of experimental uncertainty associated with these measurements is difficult to gauge and should not be neglected, prompting a careful analysis of the obtained estimations.

The obtained χ_{1-7} and χ_{1-5}, in absolute values, are of about the same order of magnitude. However, χ_{1-7} is negative for some values of x_{F8H20}, whereas χ_{1-5} is positive for the entire range of x_{F8H20}. This is a consequence of the aforementioned fact that, for some systems, a increases from $\pi = 5\,\mathrm{mN\,m^{-1}}$ to $\pi = 7\,\mathrm{mN\,m^{-1}}$. In the case of χ_{1-5}, the values are all of the same magnitude, bar the one obtained for $x_{\mathrm{F8H20}} = 0.67$ which is one order of magnitude higher. This is probably a consequence of how the calculation is performed[2], which is quite affected by the dispersion of the experimental points. Nevertheless, the χ values calculated from the GISAXS results are in line with those obtained from the π–A isotherms above and are at least 2 orders of magnitude higher than those estimated from the GIXD measurements. All these results are in accord with those reported in the literature for pure monolayers for which data are available [5, 11]: the increase in π upon compression of the film results in the compaction of supramolecular domains and rather than of the molecules within them.

[2]The integration of Equation 1.1, considering a constant χ in the integration range, results in assuming a linear dependence of π with $\ln A$. The slope of such relation is equal to $-\chi^{-1}$, from which χ is retrieved.

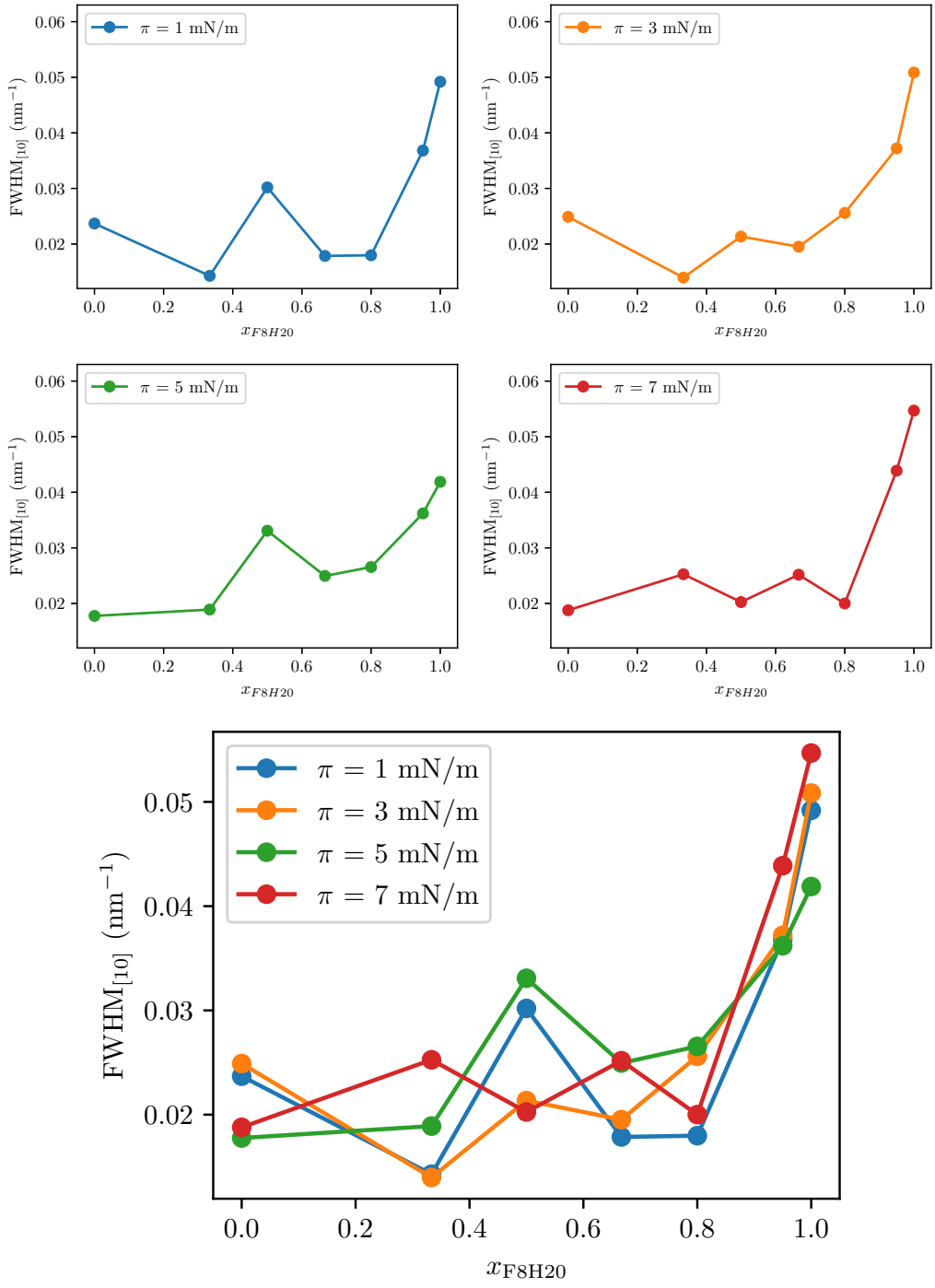

Figure 11.8: FWHM of the [10] peak for the proposed main 2D hexagonal lattice as a function of x_{F8H20} calculated from the GISAXS measurements at $T = 12\,^{\circ}\mathrm{C}$ for the mixed binary Langmuir film of F8H14:F8H20 at different π values, indicated on the insets. The bottom plot is a compilation of the remaining plots, in which case the lines are colour coded according to π, indicated on the inset.

The fact that diffraction peaks are detected at $\pi = 0\,\mathrm{mN\,m^{-1}}$ is not necessarily expected, given that the available literature data is not consensual: these have been reported to be detected (F10H16 [5]; F10H16, F12H16 and F8H20 [25]) and to not be detected (F8H16 [24]). Differences in the attainable experimental resolution in different circumstances might explain the disparate results. The existence of hemimicelles before the lift-off and at $\pi = 0\,\mathrm{mN\,m^{-1}}$ has been demonstrated [9, 27], but whether or not they are organised at the air–water interface has been a matter of debate. Herein, the GISAXS results, obtained at $\pi = 0\,\mathrm{mN\,m^{-1}}$ and for A in the range of $0.36\,\mathrm{nm^2\,molecule^{-1}}$ to $0.40\,\mathrm{nm^2\,molecule^{-1}}$, demonstrate that the onset of the lateral ordering of the film occurs before a non-zero π is attained, for the entire range of x_{F8H20}. However, as explained below, this ordering is relatively weak, in general, and it is difficult to estimate the characteristic length it spans.

The lateral ordering of the hemimicelles can be quantified by computing the coherence length (ξ) from the width of the peaks or FWHM in the GISAXS spectra. However, as explained in Section 7.4, this depends significantly on the experimental setup and on the choice of the peak shape used in the data analysis. The results presented herein are sourced from 3 different experiments, and they were not always fitted with the same peak function. It is expected that the positions of the peaks (and ultimately a) are relatively unaffected by these differences, even if the FWHM is more dependent on the attainable experimental resolution. Moreover, the choice of peak function has a significant impact on ξ: this varies by a factor of approximately 3, depending on whether it is estimated using Equation 7.10 or Equation 7.11. Consequently, for the same data set, ξ can vary significantly based on the choices made for the treatment of the experimental data, even if the obtained FWHMs are similar. To circumvent these limitations and get at least a qualitative grasp on the organisation of the mixed films of F8H14:F8H20, the analysis of the FWHM of the [10] peak ($\mathrm{FWHM_{[10]}}$) can be informative. The organisation of the film is inversely correlated with $\mathrm{FWHM_{[10]}}$. $\mathrm{FWHM_{[10]}}$ is represented as a function of x_{F8H20} and for different π in Figure 11.8. These results are presented as a function of π in Figure C.2 and in tabular form in Table C.4, in Appendix C. No data is presented for $\pi = 0\,\mathrm{mN\,m^{-1}}$ because, in the cases where spectra were recorded at this π, the [10] peak was found to be significantly asymmetric and/or close to the direct beam, precluding an accurate estimation of $\mathrm{FWHM_{[10]}}$.

Focusing on the pure cases, the F8H14 film is more ordered than the F8H20 film. The hemimicelles of pure F8H14 are smaller than those of pure F8H20, and so the former have a bigger curvature than the latter. As it was mentioned before, the deformability (*i.e.* the energetic cost of the deformation) of the hemimicelles upon compression of the film can be anticipated to be inversely correlated with their curvature. In other words, it is expected that larger hemimicelles, which have a smaller curvature, are more deformable than smaller, more curved ones. This way, the less deformable hemimicelles of pure F8H14 are expected to form a more organised lattice than the more deformable ones of pure F8H20. This rationalises the relative order of $\mathrm{FWHM_{[10]}}$ for the pure films. Moreover, and bearing in mind the caveats mentioned in the preceding paragraph, this is anticipated to translate in the order of the F8H14 film being larger than that of the F8H20 in absolute terms but also in relative terms: because of their smaller size, the order of the F8H14 hemimicelles extends over more hemimicelle diameters than the order of the F8H20 hemimicelles. From the literature, ξ values are available for the pure films at $\pi = 5\,\mathrm{mN\,m^{-1}}$ from two sources:

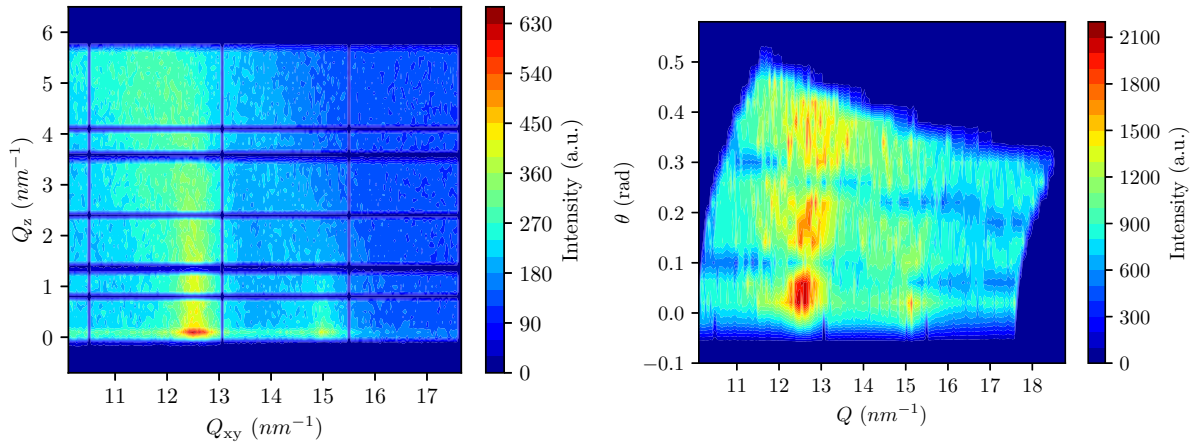

Figure 11.9: Left: contour plot of the diffraction intensity as a function of the in-plane (Q_{xy}) and out-of-plane (Q_z) components of the scattering vector obtained at $T = 12\,°C$ and $\pi = 1\,mN\,m^{-1}$ for the mixed binary Langmuir film of F8H14:F8H20 with a molar proportion of 1:19 ($x_{F8H20} = 0.95$). Right: the same dataset, but represented in polar coordinates, that is the contour plot of the diffraction intensity as a function of the modulus of the scattering vector (Q) and the out-of-plane angle with the interface (θ).

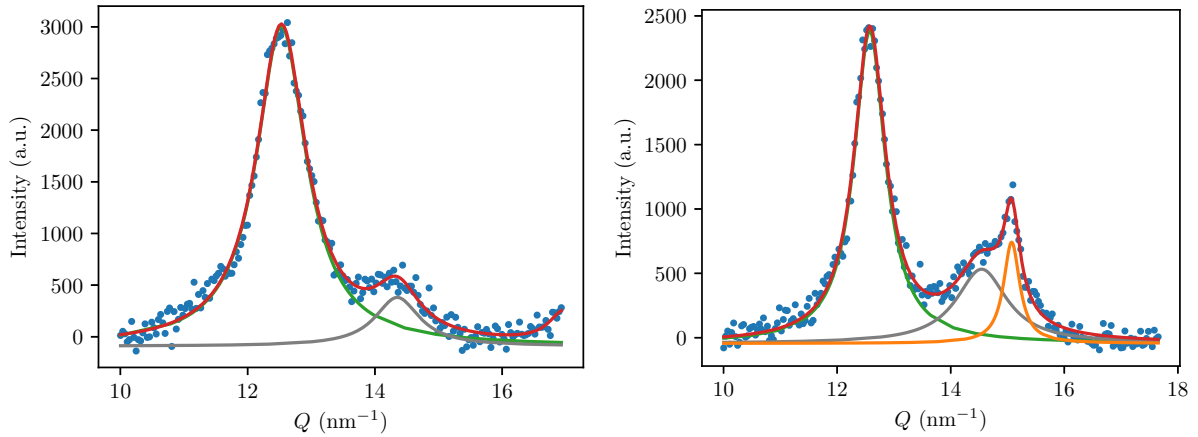

Figure 11.10: GIXD θ-integrated spectra for small values of θ (in the range of 0 rad to 0.1 rad), obtained at $T = 12\,°C$ and $\pi = 5\,mN\,m^{-1}$ for the mixed Langmuir film of F8H14:F8H20 with a molar proportion of 1:0 ($x_{F8H20} = 0.00$ or pure F8H14; left) and of 1:19 ($x_{F8H20} = 0.95$; right). The blue circles represent the experimental data points and the curves represent the fitted Lorentzian peaks corresponding to the proposed structures, labelled "CF chain" (green), "CH chain (generic)" (orange) and "CH chain (F8H20)" (grey) in the text. The red curve is the fitted sum of the remaining curves.

ξ is estimated to be about 7 times the a for F8H14 and about 4 times the a for F8H20 [11]; ξ is estimated to be about 10 times the a for F8H14 and about 28 times the a for F8H20 [25]. The first set of results compares well with the results presented herein, but the second set of results doesn't seem to be in agreement with them. The authors of that study report a much more ordered film than the findings presented in this work. The authors also report that the order within the pure film of hemimicelles increases with increasing m in FnHm, the opposite of what is reported herein.

Concerning the organisation of the mixed films, the $\mathrm{FWHM}_{[10]}$ is approximately minimal for $x_{\mathrm{F8H20}} = 0.00$ and is constant up to about $x_{\mathrm{F8H20}} = 0.80$, increasing by about three-fold for $x_{\mathrm{F8H20}} = 1.00$. This is indicative that the presence of a relatively small amount of F8H14 induces the ordering of the film. Based on the reasoning presented in the previous paragraph, this can be correlated with the smaller size of the hemimicelles in the mixed films (*cf.* Figure 11.6): from the results presented so far, the distinction between the presence of monodisperse hemimicelles or a mixture of hemimicelles with 2 different sizes (scenarios "b" and "c") is not clear; however, in either case, the presence of smaller than pure F8H20 domains is expected, which should have a higher curvature and be less deformable. The fact that $\mathrm{FWHM}_{[10]}$ presents a plateau for $x_{\mathrm{F8H20}} \leq 0.80$ is more puzzling, considering that a varies continually with x_{F8H20}. This may occur if the diffraction peaks for $x_{\mathrm{F8H20}} \leq 0.80$ are resolution-limited. These results are in support of the mixed films of F8H14:F8H20 being mixed rather than completely segregated.

11.3.3 Grazing Incidence X-Ray Diffraction (GIXD)

The GIXD experiments permit to determine the structure and order of the PFAA molecules within the hemimicelles comprising the mixed films of F8H14:F8H20. A typical dataset or spectrum consists in the diffracted intensity as a function of the in-plane (Q_{xy}) and out-of-plane (Q_{z}) components of the scattering vector, as is depicted in Figure 11.9. These measurements are performed at varying values of x_{F8H20} and π, at a constant temperature of $T = 12\,^{\circ}\mathrm{C}$. The diffracted intensity can be integrated along Q_{z} and represented as a function of Q_{xy}. However, a transformation to polar coordinates can be enlightening in the treatment of these datasets, as is discussed below. This is achieved by computing the modulus of the scattering vector (Q) and the out-of-plane angle with the interface (θ) according to Equations 11.2 and 11.3, respectively. The diffraction intensity can be integrated along θ and represented as a function of Q. After subtracting the background, the diffraction peaks are fitted with peak-shaped functions (herein, Lorentzian functions were used). Two illustrative examples of integrated GIXD spectra are presented in Figure 11.10.

$$Q = \sqrt{Q_{\mathrm{xy}}^2 + Q_{\mathrm{z}}^2} \tag{11.2}$$

$$\tan\theta = \frac{Q_{\mathrm{z}}}{Q_{\mathrm{xy}}} \Leftrightarrow \theta = \arctan\left(\frac{Q_{\mathrm{z}}}{Q_{\mathrm{xy}}}\right) \tag{11.3}$$

As can be observed in Figure 11.9 (left), there is a clearly marked peak with maximal intensity in the plane and for Q_{xy} near $12.5\,nm^{-1}$. This can be attributed to the stacking of the CF chains and is in agreement with literature data [5, 11]. However, it can be seen that the coordinates of maximal intensity of this peak are shifted to lower Q_{xy} with increasing Q_z (the peak "turns" counter-clockwise), which can be attributed to the presence of a diffracting structure with a constant lattice parameter (*i.e.* constant distance between the laterally stacked molecules), but with a progressively changing molecular tilt angle. This is consistent with the proposed fan-like arrangement of the molecules inside the hemimicelles. This diffracting structure would present the maximal diffraction intensity for a constant value of Q, as θ is varied. The change of coordinates is illustrated in Figure 11.9 (right): the peak whose intensity varied to lower Q_{xy} with increasing Q_z, in polar coordinates, appears as a rod with a maximal intensity at an approximately constant value of Q. This effect is general and occurs for all the investigated x_{F8H20} and π experimental conditions. The GIXD spectra were thus represented and fitted in polar coordinates, performing the integration for low values of θ, in the range of 0 rad to 0.1 rad.

Concerning the integrated datasets (*cf.* Figure 11.10 (right)), in general, for the studied ranges of x_{F8H20} and π, the spectra present 3 diffraction peaks in the range of Q of about $10\,nm^{-1}$ to $18\,nm^{-1}$: a peak with x_c near $12.5\,nm^{-1}$, which is consistent with the position of a first order peak arising from the close packing of perfluorinated chains [12, 13, 28], herein associated with a structure termed "CF chain"; a peak with x_c near $14.5\,nm^{-1}$, whose position is consistent with a first order peak characteristic of the packing of the hydrogenated chains [5, 11, 28], herein associated with a structure termed "CH chain (generic)"; for F8H20-containing systems, a third, usually narrower peak was identified with x_c near $15.0\,nm^{-1}$, whose position is also consistent with the close packing of the hydrogenated chains, and was herein associated with a structure termed "CH chain (F8H20)". These are identified in Figure 11.10 in green, orange and grey, respectively. The GIXD spectra obtained for the pure F8H14 Langmuir films only present 2 diffraction peaks, which were attributed to the structures "CF chain" and "CH chain (generic)" (*cf.* Figure 11.10 (left)).

All the identified diffraction peaks appear to be in the plane. Based on the position of the "CF chain" peak, it is plausible to consider that the CF chains are tightly packed according to a "hexagonal" lattice. As is further discussed below, this structure is regular and can be anticipated to have some degree of hexagonal symmetry, but it is not strictly crystalline (hence the quotation marks in "hexagonal"). However, for the remaining peaks, the underlying structure is hard to determine unambiguously, as only one peak per structure is clearly observed. This implicitly assumes that peaks "CH chain (generic)" and "CH chain (F8H20)" arise from different structures, and this reasoning is based on the fact that the first of these peaks is always present, whereas the second only appears for F8H20-containing systems. Hydrocarbon chains are known to form tilted organised phases in Langmuir monolayers [23] and the identification of which phase is present usually requires having access to more diffraction peaks. Given only one diffraction peak is observed, a hexagonal packing is assumed. This reasoning has been done before for pure films of PFAAs to interpret the GIXD spectra of F8H16, F8H18 and F8H20 [5, 11]. It should be mentioned that this assumption is plausible given the quantitative analysis detailed below and considering that the packing of the CH chains can be considered *a priori* to be constrained

by the CF chains and frustrated by the mismatch in the chains' cross-sectional areas. In other words, it is plausible to assume that the CF chains impose the hexagonal ordering of the CH chains, at least to some extent.

The intensity of the GIXD diffraction peaks[3] is presented as a function of x_{F8H20} in Figure 11.11. The intensity of the "CF chain" peak appears to be approximately constant with varying x_{F8H20}. This is quite puzzling because, even though F8H14 and F8H20 have a CF chain with the same length, it would be expected that the number of diffracting centres for the pure F8H20 would be higher than that of the pure F8H14: the F8H20 hemimicelles are larger, the molecules are packed closer together (recall that $\Delta_{\mathrm{F8H20}} < \Delta_{\mathrm{F8H14}}$; *cf.* Figure 9.11 on page 106) and the "CF chain" structure displays a characteristic length that increases with x_{F8H20} (see below). The intensity of the "CH chain (generic)" diffraction peak displays a similar trend, except for $\pi = 5\,\mathrm{mN\,m^{-1}}$. It is hard to gauge whether this is an effect of the measurement or of the sample itself: apart from the difficulties in treating the data (*e.g.* the determination of the baseline), the "CF chain" peak is rather intense and significantly overlaps with the "CH chain (generic)" peak, which makes the identification of the latter quite challenging. Regarding the intensity of the "CH chain (F8H20)" diffraction peak, this seems to increase with x_{F8H20}. In this case, this is consistent with the "CH chain (F8H20)" structure being the result of the organisation of the H20 blocks rather than an effect of the mixing of the two molecules in the film. In other words, it seems that the CH chains of the F8H20 molecules organise in a "CH chain (F8H20)" structure already in the pure film, and this structure is present in the mixed film too. However, the "CH chain (F8H20)" peak seems to evolve in time, as sometimes rescanning this peak would result in a significantly reduced intensity. This effect was difficult to explore and was not studied at lengths, although the presence of the "CH chain (F8H20)" peak was very reproducible. This is indicative of an evolution of the organisation of the CH blocks.

Assuming each peak corresponds to a different structure packed according to a hexagonal lattice, the corresponding lattice parameters (a) can be computed with Equation 11.4. The unit cell area ($A^{\mathrm{GIXD}}_{\mathrm{unit\ cell}}$) can be estimated from a according to $A^{\mathrm{GIXD}}_{\mathrm{unit\ cell}} = a^2 \sin(60°)$. The values of $A^{\mathrm{GIXD}}_{\mathrm{unit\ cell}}$ for each structure are presented in Figure 11.12, as a function of x_{F8H20} and for different values of π. These data are presented as a function of x_{F8H20} (in separate plots for each value of π) and as a function of π in Figures C.3 and C.4, as well as in tabular form in Tables C.5, C.6 and C.7, in Appendix C.

$$a = \frac{2\pi}{x_c} \times \frac{2}{\sqrt{3}} \tag{11.4}$$

The obtained values of $A^{\mathrm{GIXD}}_{\mathrm{unit\ cell}}$ are scattered around the values of $0.29\,\mathrm{nm^2\,molecule^{-1}}$ (for "CF chain"), $0.22\,\mathrm{nm^2\,molecule^{-1}}$ (for "CH chain (generic)") and $0.20\,\mathrm{nm^2\,molecule^{-1}}$ (for "CH chain (F8H20)"). It is reiterated that the first value is characteristic of tightly packed CF chains and the second and third values are consistent with the stacking of CH chains [5, 11–13, 17, 28]. Considering the vertical scales of the plots in Figure 11.12, it appears that varying either x_{F8H20}

[3]These results are sourced from 2 different experiments; specifically, the results at $\pi = 5\,\mathrm{mN\,m^{-1}}$ and the remaining ones were obtained in different experiments. To make comparisons possible among them, the intensity of the diffraction peaks was normalised by the average intensity of the "CF chain" peak measured for the pure films, for each value of π.

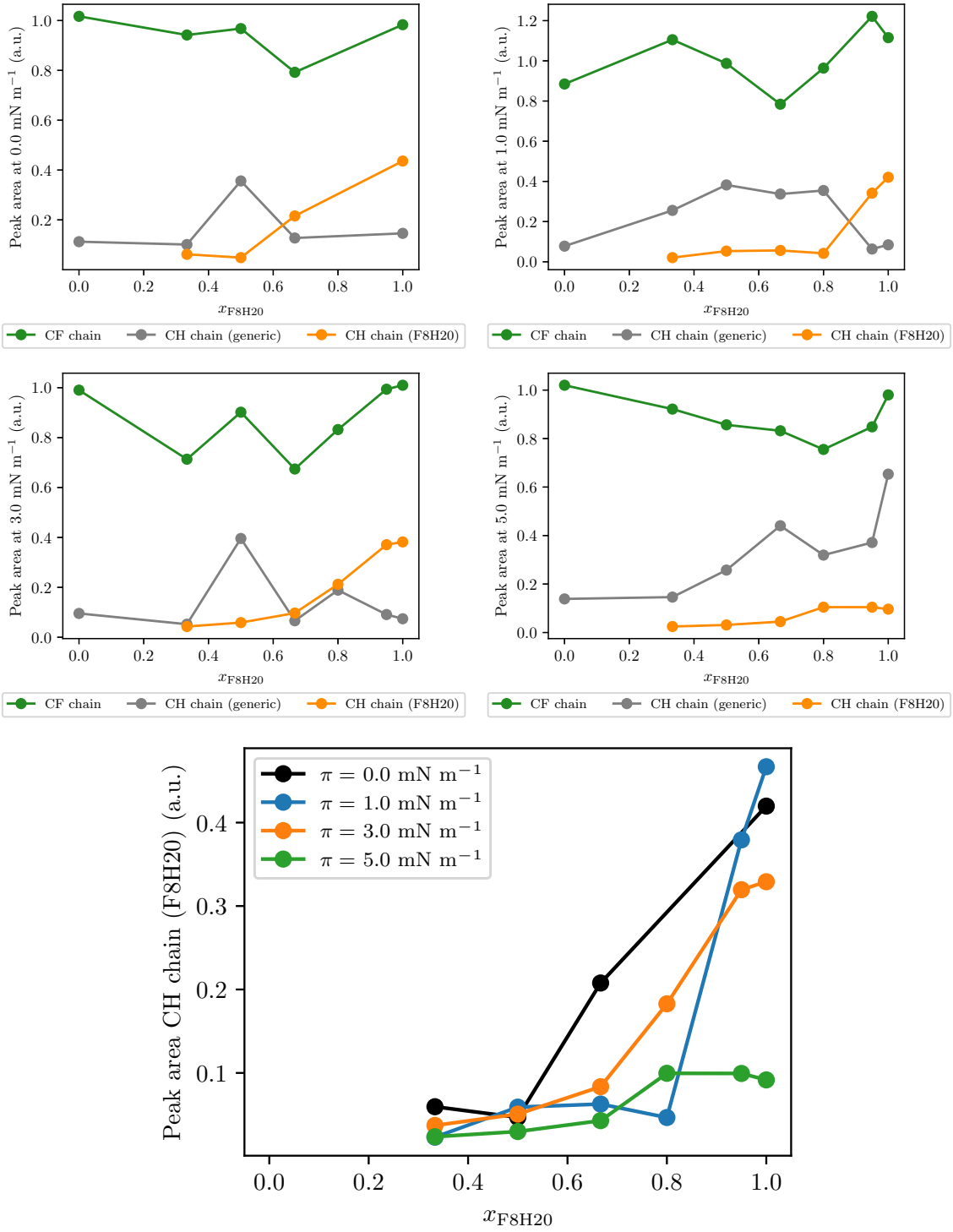

Figure 11.11: Intensity of the GIXD diffraction peaks as a function of x_{F8H20} for different π, indicated on the vertical axis (bottom and middle rows), for the structures "CF chain" (green), "CH chain (generic)" (grey) and "CH chain (F8H20)" (orange). The bottom plot compiles the results obtained at different π for the "CH chain (F8H20)" structure.

or π has a negligible effect on $A^{\text{GIXD}}_{\text{unit cell}}$. This means that the diffracting structures are fairly incompressible: from the positions of the peaks attributed to each structure, χ was estimated to be essentially null. This had been noted previously for the pure films [5, 11] and the behaviour of the mixed films seems to follow the same trend. This can be interpreted as the molecules' chains being tightly packed and, considering the results presented above, the compression of the film results in the compression of the network of hemimicelles rather than the compression of the molecules closer together [5, 11]. In comparison with literature values, in which data can be found for pure films of F8H16, F8H18 and F8H20, only 2 diffraction peaks are reported for each system, one associated with the stacking of the CF chains and the other with the stacking of the CH chains [5, 11]. However, the position of the latter peak is reported to shift to higher Q values when the CH chain is elongated from 16 to 20 carbon atoms, resulting in the decrease of the corresponding lattice parameter and the calculated $A^{\text{GIXD}}_{\text{unit cell}}$ from 0.233 nm^2 to 0.200 nm^2. It is possible that the reported structure for the CH chains of F8H16 corresponds to the "CH chain (generic)" presented herein, whereas the reported structure for the CH chains of F8H20 would result from from an overlap of the diffraction peaks reported here for the "CH chain (generic)" and "CH chain (F8H20)" structures.

The characteristic length for each structure i ($\xi^i_{[10]}$) was estimated from the peak widths (*cf.* Equation 7.10), assuming these correspond to the [10] peak of a hexagonal lattice. The values of $\xi^{\text{CF chain}}_{[10]}$, $\xi^{\text{CH chain (generic)}}_{[10]}$ and $\xi^{\text{CH chain (F8H20)}}_{[10]}$ are presented in Figure 11.13 (left), as a function of x_{F8H20} and for different values of π. These data are presented as a function of x_{F8H20} (in separate plots for each value of π) and as a function of π in Fig-

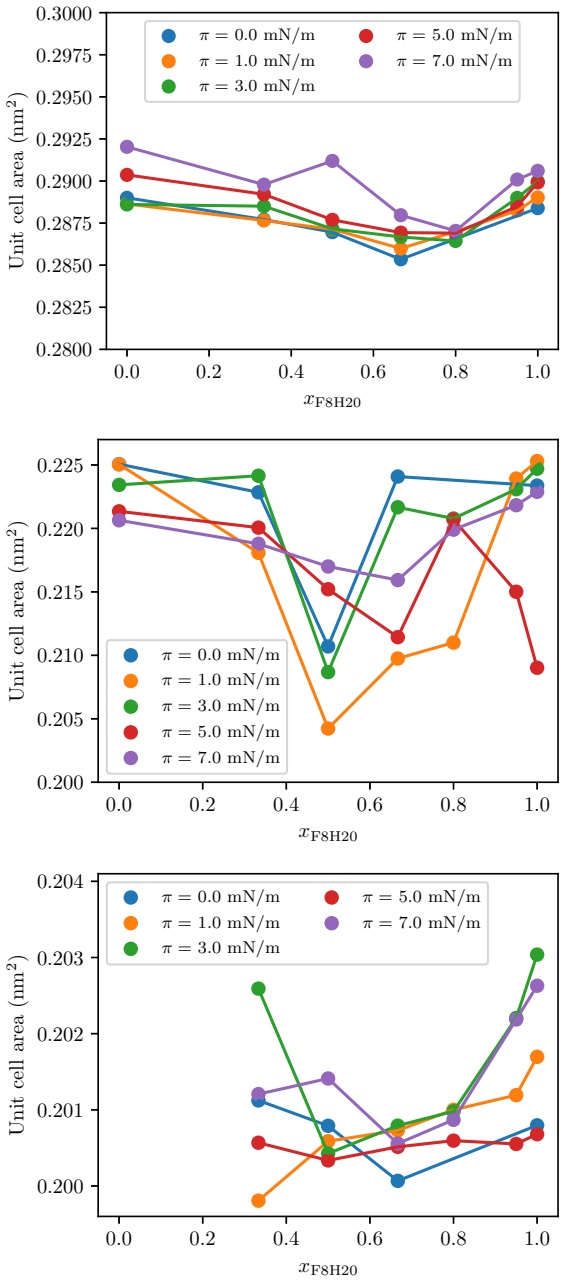

Figure 11.12: Unit cell area ($A^{\text{GIXD}}_{\text{unit cell}}$) as a function of x_{F8H20}, calculated from the GIXD measurements at $T = 12\,^{\circ}$C for the mixed Langmuir film of F8H14:F8H20 at different π values (identified in the insets of each plot), for the lattices corresponding to the "CF chain" (top), "CH chain (generic)" (middle) and "CH chain (F8H20)" (bottom) structures. $A^{\text{GIXD}}_{\text{unit cell}}$ is numerically equal to $a^2 \sin(60°)$, where a is the lattice parameter inferred from the position of the corresponding diffraction peaks in the GIXD spectra.

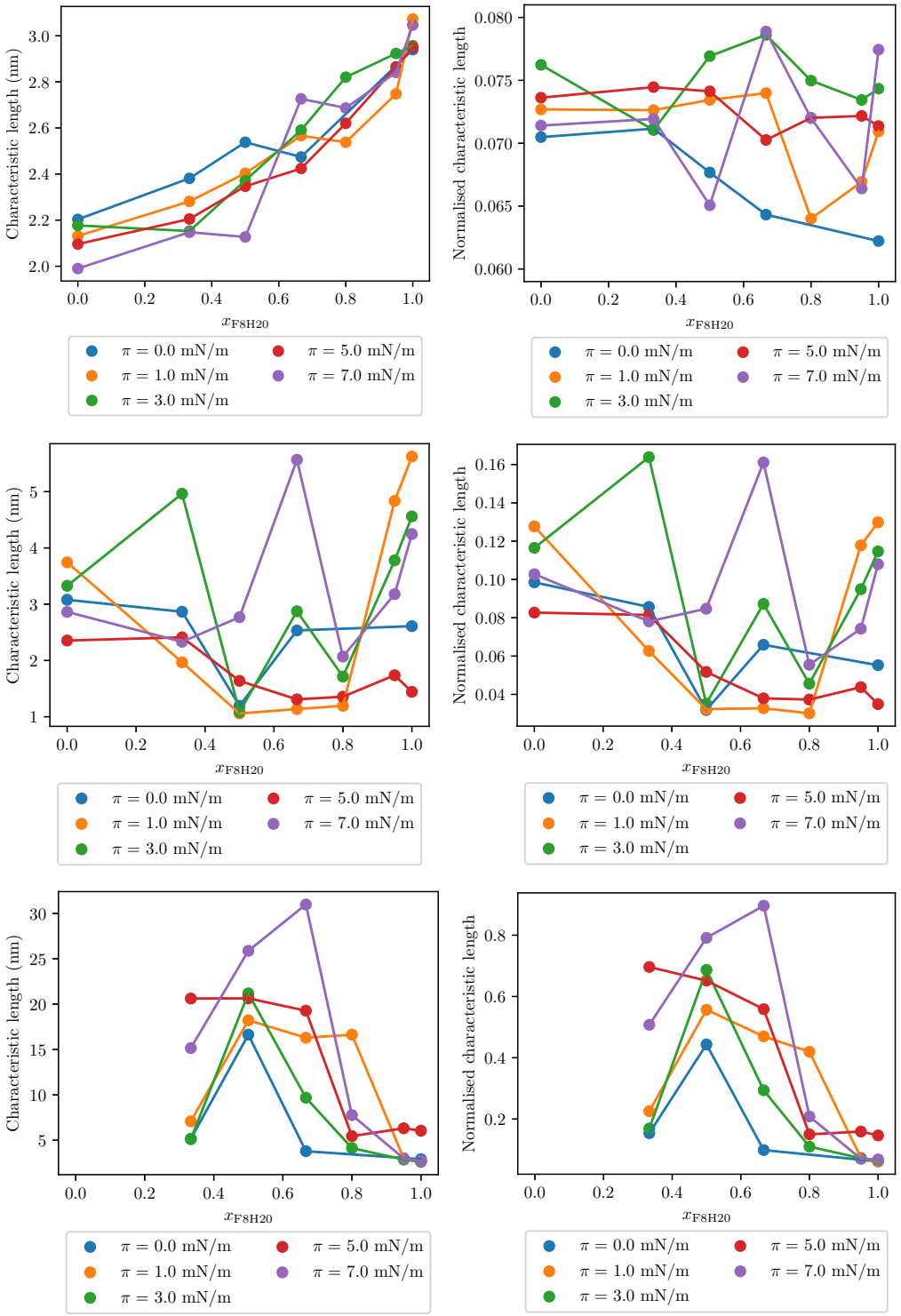

Figure 11.13: Characteristic length as a function of x_{F8H20}, calculated from the width of the corresponding diffraction peak from the GIXD measurements at $T = 12\,°C$, for the mixed Langmuir films of F8H14:F8H20 at different π values (identified in the legends of each plot), for the lattices corresponding to the "CF chain" (top), "CH chain (generic)" (middle) and "CH chain (F8H20)" (bottom) structures. The leftmost plots show the values in nm, whereas the rightmost plots show the values divided (normalised) by the lattice parameter a obtained from the GISAXS measurements at the corresponding values of x_{F8H20} and π.

ures C.5 and C.6, as well as in tabular form in Tables C.8, C.9 and C.10, in Appendix C. To probe the relative length scale of the ordering in these systems, the $\xi^{i}_{[10]}$ values were divided (normalised) by the corresponding lattice parameter obtained from the GISAXS measurements performed at the same experimental conditions of x_{F8H20} and π. These results are presented in Figure 11.13 (right) and, in tabular form, in Tables C.11, C.12 and C.13, in Appendix C.

A comment must be made concerning the terminology employed in this analysis. The term *characteristic length* is used in detriment of *coherence length*. The latter refers to the experimentally accessible estimation of the correlation length of a finite crystal (see Section 7.4). The crystalline state is characterised by the spacial periodicity of its constituting atomic arrangements. In other words, the positions of the atoms in a crystal can be predicted by the translation of a base motif. In the case of a finite crystal, the coherence length provides a measure of the length for which this regularity is maintained and of at least how far apart atoms must be so that this translational order is lost. In the case of the hemimicelles of PFAAs, whose structure has been detailed in the preceding chapters, this translational symmetry is absent: the positions of the molecules are not predictable by applying translations of a motif, so these supramolecular structures are not crystalline, strictly speaking. However, the stacking of the molecules is nonetheless very regular and describable by a mathematical function, which justifies the occurrence of diffraction of X-rays by these structures. Therefore, because the hemimicelles are not strictly crystalline, but are still able to act as diffraction gratings for X-rays, the term characteristic length is used to designate the length scale associated with the width of the diffraction peaks. The characteristic length can still be understood as a measure of the order of the diffracting lattice of molecules inside the hemimicelles.

In absolute terms, the computed values range from a few nm for $\xi^{\text{CF chain}}_{[10]}$ and $\xi^{\text{CH chain (generic)}}_{[10]}$ to a few tens of nm for $\xi^{\text{CH chain (F8H20)}}_{[10]}$, although with variations among the studied systems. The results for $\xi^{\text{CF chain}}_{[10]}$ and $\xi^{\text{CH chain (generic)}}_{[10]}$ are comparable to those reported in the literature obtained for pure films of F8H16, F8H18 and F8H20 [5, 11]. In general, for a fixed x_{F8H20}, the characteristic length is fairly unaffected by π, with few exceptions. Considering the molecular diameters of the CF and CH chains (about 0.58 nm and 0.48 nm, respectively, estimated from the $A^{\text{GIXD}}_{\text{unit cell}}$ above), from the $\xi^{\text{CF chain}}_{[10]}$ and $\xi^{\text{CH chain (generic)}}_{[10]}$ results, it can be said that the CF and the CH chains present local order (up to about 10 times the molecular diameter). Long range order spanning over a few tens of molecular diameters is found for some systems, based on the $\xi^{\text{CH chain (F8H20)}}_{[10]}$ results. Moreover, $\xi^{\text{CF chain}}_{[10]}$ generally increases with increasing x_{F8H20} and $\xi^{\text{CH chain (F8H20)}}_{[10]}$ is highest for intermediate x_{F8H20} values and lowest for pure F8H20. This suggests that the presence of F8H14 molecules increases the lateral ordering of the CH chains of the F8H20 molecules. This is consistent with the existence of mixing at a molecular level, at least to a partial extent.

Taking into consideration the results of normalised $\xi^{i}_{[10]}$ ($\xi^{i'}_{[10]}$; Figure 11.13 (right)), the observations about the length scale at which the order of the chains is maintained are reiterated: local ($\xi^{\text{CF chain'}}_{[10]}$ and $\xi^{\text{CH chain (generic)'}}_{[10]}$ results) and long range ($\xi^{\text{CH chain (F8H20)'}}_{[10]}$ results). It should be remarked, however, that the coherence length is always smaller than the hemimicelle size (roughly similar to the lattice parameter retrieved from the GISAXS experiments), suggesting that the different proposed structures are contained well inside the hemimicelles. The order of

the CF chains (and thus $\xi_{[10]}^{\text{CF chain}}$) increases in absolute terms with increasing x_{F8H20}. However, considering that the size of the hemimicelles also increases with x_{F8H20}, these effects are more or less mutually compensated. In other words, the order of the CF chains in relative terms is approximately constant (given the vertical scale) for the studied x_{F8H20} range and spanning about 6 % to 8 % of the hemimicelle size. The obtained $\xi_{[10]}^{\text{CF chain'}}$ can be related to the fan-like packing of the molecules within the hemimicelles: the molecules are disposed in approximately concentric layers in a CF chain up-CH chain down configuration and with an increasing molecular tilt (from the centre towards the periphery of the aggregate). The rate at which this tilt increases is inversely proportional to the length of the CH chain. Because the PFAA molecules are essentially cone shaped, this constrains the packing of the CF chains, which explains why the order of the latter increases in absolute terms with increasing x_{F8H20}, but remains approximately constant in relative terms. Notwithstanding, this phenomenon could occur whether the F8H14 and F8H20 molecules mix at a molecular level (within the hemimicelles) or not (the diffraction pattern could be the average of the pure cases, resulting in a similar interpretation), so this result alone does not allow for a clear distinction between the two scenarios.

11.3.4 Geometric model applied to mixed films of F8H14:F8H20

11.3.4.1 Prior considerations

In Chapter 9, the internal structure of the hemimicelles of pure PFAAs was studied by MD simulations and rationalised according to a geometrical model, to explain the packing of the molecules. It was found that: the molecular tilt angle (θ_{tilt}) varies approximately linearly with the radial distance from the centre of the hemimicelle (r) at a rate (Δ_{FnHm}) that is characteristic of each FnHm; θ_{tilt} varies between 0° for $r = 0\,\text{nm}$ and a limit value $\theta_{\text{Tilt,F}}$ for $r = R$ (where R is the radius of the hemimicelle). $\theta_{\text{Tilt,F}}$ was found to be approximately constant and independent of the PFAA in study. Based on a few considerations presented in that chapter[4], the diameter of the pure hemimicelles can be predicted based on the knowledge of the molecular geometry (*i.e.* n and m in FnHm), which essentially sets the numerical value of Δ_{FnHm}. However, the prediction of the size of mixed binary hemimicelles is not possible without added information or further assumptions. In that regard, and given that the experimental results hint at the possibility of (at least partial) mixing of F8H14 and F8H20 molecules within the hemimicelles, 3 hypothetical scenarios were put forward to characterise the internal structure of the mixed binary hemimicelles. These are limit cases that serve as a basis for further studies, namely by providing the necessary assumptions for the application of the geometrical model to these systems. These assumptions are further detailed below.

From the MD simulation results presented in Chapter 9, it is known that $\theta_{\text{Tilt,F}} \approx 65°$, $\Delta_{\text{F8H14}} \approx (5.07 \pm 0.05)\,°\,\text{nm}^{-1}$ and $\Delta_{\text{F8H20}} \approx (3.50 \pm 0.05)\,°\,\text{nm}^{-1}$. To minimise the difference between the diameter of the pure hemimicelles predicted with the model and the experimental results, when applying the geometrical model to the mixed hemimicelles, the values of $\theta_{\text{Tilt,F}} = 71°$, $\Delta_{\text{F8H14}} = 5.00\,°\,\text{nm}^{-1}$ and $\Delta_{\text{F8H20}} = 3.44\,°\,\text{nm}^{-1}$ were chosen for the calculations presented herein. These choices are critically assessed in a few paragraphs.

[4]In particular, the reader is referred to Equations 9.9 and 9.10, presented in Subsection 9.3.2, on page 97.

11.3.4.2 Application to 3 different (limit) cases or hypotheses

Hypothesis 1: random mixture of F8H14 and F8H20 molecules within the mixed hemimicelles In a first hypothesis, F8H14 and F8H20 molecules are considered to mix randomly within the hemimicelles. In this case, the rate of variation of θ_{Tilt} with r for a mixed hemimicelle of F8H14:F8H20 is denoted $\Delta_{x_{\text{F8H20}}}$, where x_{F8H20} is the molar fraction of F8H20 in the film. $\Delta_{x_{\text{F8H20}}}$ is assumed to be given by the average of the pure compounds Δ_{F8H14} and Δ_{F8H20}, weighted by x_{F8H20} (Equation 11.5).

$$\begin{aligned}\Delta_{x_{\text{F8H20}}} = (1 - x_{\text{F8H20}}) \times \Delta_{\text{F8H14}} + x_{\text{F8H20}} \times \Delta_{\text{F8H20}} \Leftrightarrow \\ \Leftrightarrow \Delta_{x_{\text{F8H20}}} = \Delta_{\text{F8H14}} + x_{\text{F8H20}} \times (\Delta_{\text{F8H20}} - \Delta_{\text{F8H14}}) \quad (11.5)\end{aligned}$$

Substituting Equation 11.5 in a generalised form of Equation 9.10, the radius of the mixed hemimicelle of F8H14:F8H20, according to hypothesis 1 ($R_{x_{\text{F8H20}},1}$) is given by Equation 11.6:

$$R_{x_{\text{F8H20}},1} = \frac{\theta_{\text{Tilt,F}}}{\Delta_{x_{\text{F8H20}}}} = \frac{\theta_{\text{Tilt,F}}}{\Delta_{\text{F8H14}} + x_{\text{F8H20}} \times (\Delta_{\text{F8H20}} - \Delta_{\text{F8H14}})} \quad (11.6)$$

Hypothesis 2: concentric circle and corona (F8H14 in the centre) In a second limit scenario, it was proposed that each hemimicelle would be formed by both F8H14 and F8H20 molecules, but that these would completely segregate within the hemimicelles. The molecular disposition of the PFAAs within the aggregate, in this case, is characterised by a central circle of tightly packed molecules of one of the PFAAs surrounded by a concentric corona of tightly packed molecules of the other PFAA. Therefore, two possibilities naturally arise, which are that either the F8H14 is placed in the central circle and is surrounded by a corona of F8H20 (hypothesis 2) or the reverse disposition (hypothesis 3).

For hypothesis 2, it is assumed that the mixed hemimicelle displays an internal segregation of the molecules, with the formation of a central circular aggregate of F8H14 of radius R', surrounded by a concentric corona of F8H20 molecules with inner radius R' and outer radius R. It is assumed that $\Delta_{x_{\text{F8H20}}}$, in this case, is equal to Δ_{F8H14} for $r \in [0, R'[$ and equal to Δ_{F8H20} for $r \in [R', R]$. Therefore, it is obtained:

$$\begin{aligned}\theta_{\text{Tilt,F}} = \Delta_{\text{F8H14}} \times R' + \Delta_{\text{F8H20}} \times \left(R - R'\right) \Leftrightarrow \\ \Leftrightarrow \theta_{\text{Tilt,F}} = \Delta_{\text{F8H20}} \times R + (\Delta_{\text{F8H14}} - \Delta_{\text{F8H20}}) \times R' \Leftrightarrow \\ \Leftrightarrow R = \frac{\theta_{\text{Tilt,F}} - (\Delta_{\text{F8H14}} - \Delta_{\text{F8H20}}) \times R'}{\Delta_{\text{F8H20}}} \quad (11.7)\end{aligned}$$

The number of molecules of F8H14 and of F8H20 in the mixed hemimicelle (N_{F8H14} and N_{F8H20}, respectively) can be computed by recalling Equation 9.9:

$$N_{\text{F8H14}} = N\left(R'\right) = \frac{\pi}{A_{\text{CF}}} R'^2$$

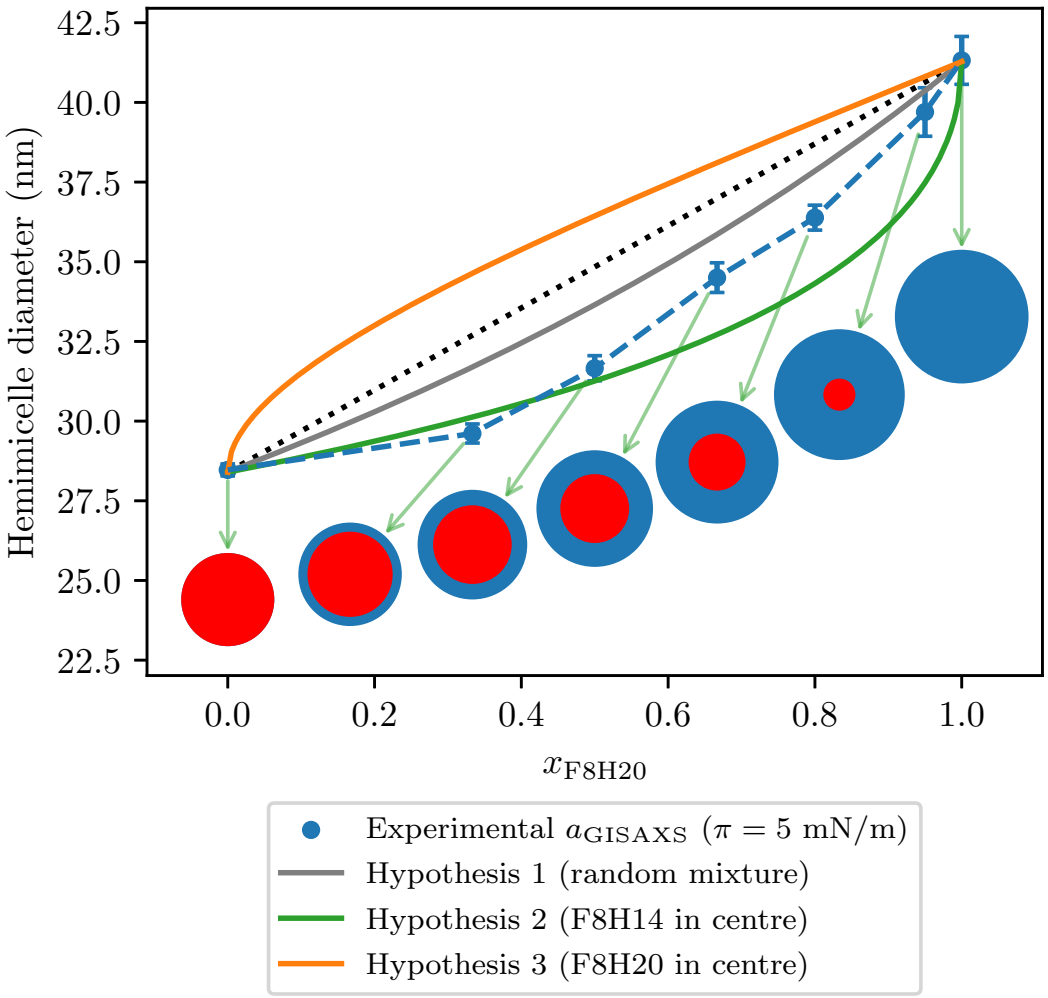

Figure 11.14: Diameter of the mixed binary hemimicelles of F8H14:F8H20 predicted based the geometrical model and considering the different hypotheses presented herein: hypothesis 1 (full grey line; Equation 11.6), hypothesis 2 (full green line; Equation 11.9) and hypothesis 3 (full orange line; Equation 11.10). The experimental values of the lattice parameter obtained from the GISAXS experiments at $\pi = 5\,\mathrm{mN\,m^{-1}}$ and corresponding to the proposed main lattice (a_{GISAXS}) are presented for comparison (blue circles; the connecting dashed blue line is a guide to the eye). The schemes of the concentric circles provide a visual representation to scale of the internal disposition and size of the mixed binary hemimicelles calculated from the model obtained following hypothesis 2 (concentric circle and corona with F8H14, represented in red, in the centre and F8H20, represented in blue, on the rim), for the x_{F8H20} corresponding to the available experimental data indicated by the green arrows. The black dotted line is a straight line connecting the pure hemimicelles' diameters, as a guide to the eye.

$$N_{\mathrm{F8H20}} = N\left(R\right) - N\left(R'\right) = \frac{\pi}{A_{\mathrm{CF}}}R^2 - \frac{\pi}{A_{\mathrm{CF}}}R'^2 = \frac{\pi}{A_{\mathrm{CF}}}\left(R^2 - R'^2\right)$$

It should be noted that the equations above convey an underling, but important, approximation, which is to consider that A_{CF} is constant and independent of the the chemical nature of the PFAA and of r. As the equation below shows, this simplifies the calculations, but requires some comments, as discussed in a few paragraphs. From N_{F8H14} and N_{F8H20}, the composition of the film x_{F8H20} can be computed and a relation between R and R' is found:

$$x_{\mathrm{F8H20}} = \frac{N_{\mathrm{F8H20}}}{N_{\mathrm{F8H14}} + N_{\mathrm{F8H20}}} = \frac{R^2 - R'^2}{R^2} \Leftrightarrow R' = \sqrt{1 - x_{\mathrm{F8H20}}} \times R \tag{11.8}$$

Substituting Equation 11.8 in Equation 11.7 and solving for R ($R_{x_{\mathrm{F8H20}},2}$, hypothesis 2):

$$R_{x_{\mathrm{F8H20}},2} = \frac{\theta_{\mathrm{Tilt,F}} - \left(\Delta_{\mathrm{F8H14}} - \Delta_{\mathrm{F8H20}}\right) \times \sqrt{1 - x_{\mathrm{F8H20}}} \times R}{\Delta_{\mathrm{F8H20}}} \Leftrightarrow$$

$$R_{x_{\mathrm{F8H20}},2} = \frac{\theta_{\mathrm{Tilt,F}}}{\Delta_{\mathrm{F8H20}} + \left(\Delta_{\mathrm{F8H14}} - \Delta_{\mathrm{F8H20}}\right) \times \sqrt{1 - x_{\mathrm{F8H20}}}} \tag{11.9}$$

Hypothesis 3: concentric circle and corona (F8H20 in the centre) Similarly to hypothesis 2, it is assumed that the mixed hemimicelle displays an internal segregation of the molecules, with the formation of a central circular aggregate of F8H20 of radius R', surrounded by a concentric corona of F8H14 molecules with inner radius R' and outer radius R. It is assumed that $\Delta_{x_{\mathrm{F8H20}}}$, in this case, is equal to Δ_{F8H20} for $r \in [0, R'[$ and equal to Δ_{F8H14} for $r \in [R', R]$. Based on a reasoning analogous to the one presented in hypothesis 2, it can be obtained:

$$\theta_{\mathrm{Tilt,F}} = \Delta_{\mathrm{F8H20}} \times R' + \Delta_{\mathrm{F8H14}} \times \left(R - R'\right)$$

$$x_{\mathrm{F8H20}} = \frac{N_{\mathrm{F8H20}}}{N_{\mathrm{F8H14}} + N_{\mathrm{F8H20}}} = \frac{R'^2}{R^2} \Leftrightarrow R' = \sqrt{x_{\mathrm{F8H20}}} \times R$$

From these equations, it can be deduced that the radius of the mixed hemimicelle of F8H14:F8H20, according to hypothesis 3 ($R_{x_{\mathrm{F8H20}},3}$) is given by Equation 11.10:

$$R_{x_{\mathrm{F8H20}},3} = \frac{\theta_{\mathrm{Tilt,F}}}{\Delta_{\mathrm{F8H14}} + \left(\Delta_{\mathrm{F8H20}} - \Delta_{\mathrm{F8H14}}\right) \times \sqrt{x_{\mathrm{F8H20}}}} \tag{11.10}$$

Comparison and critical assessment of the different hypotheses Each of the hypothesis presented above provides an analytical expression for the diameter of the mixed binary hemimicelles of F8H14:F8H20 as a function of x_{F8H20}. These are plotted in Figure 11.14, together with experimental values of the lattice parameter (a_{GISAXS}) of the proposed main lattice obtained from the GISAXS experiments at $\pi = 5\,\mathrm{mN\,m^{-1}}$, for comparison.

Concerning the results presented in Figure 11.14, one first and most striking remark is the fact that hypothesis 3 predicts $R_{x_{\mathrm{F8H20}},3}$ in excess compared to the average of the pure compounds' radii (*i.e.* the values calculated from Equation 11.10 are above the dotted line in Figure 11.14).

This is both quantitatively and qualitatively in disagreement with the available experimental results. Provided the considered approximations are reasonable, this makes the scenario of the internal structuring of the mixed binary hemimicelles as a central circle of tightly packed F8H20 molecules surrounded by a corona of F8H14 molecules implausible. In the case of hypotheses 1 and 2, both models have the merit of being qualitatively in line with the experimental results, inasmuch as they predict a reduction of the hemimicelle diameter compared to the x_{F8H20}-weighted average of the pure compounds' values. Assuming the lateral packing of the mixed hemimicelles would be comparable to the pure cases (*e.g.* it is reasonable to assume the mixed film forms a hexagonal lattice of hemimicelles), this would correctly translate into negative deviations to Vegard's law. However, both models underperform quantitatively, particularly hypothesis 1 for lower x_{F8H20} and hypothesis 2 for higher x_{F8H20}. This can be an indication that the system might present an intermediate behaviour (*e.g.* internal molecular segregation in a circle/corona configuration, but considering partial miscibility), a mixed regimen (*e.g.* the mixing could occur in a manner similar to hypothesis 2 for low x_{F8H20} and similar to hypothesis 1 for high x_{F8H20}) or a scenario that is not predicted within the presented framework (*i.e.* a possible fourth hypothesis).

Concerning the parameters estimated from the MD simulations of the pure hemimicelles ($\theta_{\mathrm{Tilt,F}}$, Δ_{F8H14} and Δ_{F8H20}), these were selected close to the obtained average values and within a reasonable margin of the respective uncertainties, for better agreement with the experimental results available for the pure hemimicelles. However, this agreement is attained for values in the upper ($\theta_{\mathrm{Tilt,F}}$) and lower (Δ_{F8H14} and Δ_{F8H20}) uncertainty intervals. Given what has been discussed in Chapter 9, the diameter of the aggregates increases with increasing $\theta_{\mathrm{Tilt,F}}$ and decreases with increasing Δ_{FnHm}: the chosen parameters permit the attainment of slightly higher values of diameter. This could be explained by the experimentally observed contraction of the lattice parameter being caused by the hemimicelles being more tightly packed and not necessarily just by having smaller hemimicelles *per si*, at least to a partial extent. This situation is not considered within the presented framework, which only looks at the internal structure of the mixed hemimicelles and their individual size.

A_{CF} was considered to be constant and independent of the the chemical nature of the PFAA and of r. This approximation simplifies the analytical set up of the models, but deserves some comments. First, the PFAA molecules are tightly packed within the hemimicelles, but the A attained for a dense film is slightly higher than that corresponding to the cross-sectional area of CF chains (*cf.* Subsection 11.3.1). This has been attributed to the existence of lying molecules in between the hemimicelles [15, 16], but also to the fact that the hemimicelles themselves present a rounded dome shape [29]. In practice, these factors hinder the tight juxtaposition of the CF chains of the PFAA molecules, increasing their A in a way that can be anticipated to vary with n and/or m in FnHm, even if to a moderate extent. Additionally, given that the molecules display a θ_{Tilt} that increases with r, this causes their top-view exposure to vary with r as well. This effect becomes even more intricate knowing that the fan-like arrangement of the molecules results in the partial overlap of the concentric layers of molecules, and thus of a more complex relation between A and r. With all that in mind, with the aim of analysing trends and having a tractable mathematical model, but also drawing from the accumulated experimental and MD simulation knowledge on these systems, considering A_{CF} constant was a careful albeit necessary choice.

11.3.5 General discussion

π–A isotherms The π–A isotherm results hint at the occurrence of mixing within the Langmuir films, possibly at a molecular level (*i.e.* within the hemimicelles; scenario "c"). This reasoning is based on the fact that the π–A isotherms display only one π_{collapse} (that varies with x_{F8H20}). For a completely segregated film, the π–A isotherm would exhibit a behaviour similar to F8H14 (which has the lowest π_{collapse}) upon compression until the collapse of the film, followed by a plateau and a second rise in π until the π_{collapse} of F8H20 is attained, followed by a second plateau. The ratio of the lengths of the plateaus would be proportional to the molar ratio of the two molecules constituting the film. Moreover, E_{collapse} varies non-linearly with $A_{\text{unit cell}}^{\text{GISAXS}}$, meaning that the interaction energy of the hemimicelles with the underlying subphase is altered with varying film composition. Assuming the collapse of the film occurs by ejection of whole hemimicelles rather than by the expulsion of individual molecules from the water surface, this suggests that the interactions between the PFAA molecules forming the hemimicelles and the subphase depend on the film composition.

GISAXS Based on the GISAXS results, the mixed films comprise hemimicelles ordered in a 2D hexagonal lattice. The existence of a completely segregated film is unlikely, given that an intermediate 2D hexagonal lattice parameter (a) is inferred from the GISAXS spectra, rather than the superposition of the 2 pure films' diffraction patterns. A secondary 2D hexagonal lattice is detected for $x_{\text{F8H20}} \leq 0.80$, including for pure F8H14 and already at $\pi = 0\,\text{mN}\,\text{m}^{-1}$. However, given this is essentially suppressed upon compression of the film (it's either no longer detected or its a approaches that of the main lattice), this might be a transient, possibly meta-stable structure. For the main lattice, $A_{\text{unit cell}}^{\text{GISAXS}}$ presents negative deviations to Vegard's law, suggesting that the attractive interactions among the molecules comprising the mixed films are increased (or, conversely, the repulsive interactions are decreased), rendering the packing of the hemimicelles tighter. This is consistent with mixing at a molecular level. Alternatively, the deformation of the hemimicelles in the mixed films and consequent reduction in a might also occur. Mixing at a hemimicelle level (*i.e.* a film comprising mixed pure hemimicelles of 2 different sizes; scenario "b") cannot be ruled out based on the GISAXS results, since these results could also be interpreted in light of this scenario.

GIXD From the GIXD results, the CF chains are tightly packed within the hemimicelles, in a structure ("CF chain") which is anticipated to have some degree of hexagonal symmetry. This result alone, albeit in accord with literature data [5, 11, 28], is not trivial: knowing that the PFAA molecules are disposed in a fan-like arrangement within the hemimicelles [29] (for the pure cases, but a similar structure is assumed for the hemimicelles in the mixed films; see also Chapters 8 and 9 of this work), the diffracting structure is not strictly crystalline because it is not generated by the translation of a repeating motif. Rather, the molecules are packed with a significant degree of order and a regular intermolecular spacing, which are paramount to enable the phenomenon of X-ray diffraction, but they also display regularity in the way the packing changes from one part to another within the hemimicelle. This can be pinned to the proposed fan-line disposition of the molecules inside the hemimicelles, through which the molecular tilt varies regularly (in

fact, approximately linearly) from the centre towards the periphery of the hemimicelles. This is supported by the GIXD results presented herein, for which the maximal diffraction intensity is shifted to lower Q_{xy} with increasing Q_z: the diffraction peaks "turn" counterclockwise. This result is also recovered from the MD simulation results of pure hemimicelles, presented in Chapter 9, in which the obtained fan-like structure of the molecules gives rise to a calculated diffraction spectrum in accord with the experimental one. This, on one hand, validates the simulation methodology and, on the other hand, justifies that the obtained experimental results are in agreement with the proposed structure.

Concerning the stacking of the CH chains, this seems to be associated to 2 underlying structures ("CH chain (generic)" and "CH chain (F8H20)"), for F8H20-containing films, and only 1 for pure F8H14 ("CH chain (generic)"). In all cases, 2D hexagonal symmetry is assumed based on prior knowledge on the pure systems [5, 11] and considering the frustration imposed by the mismatch of the CH and CF chains' cross-sectional areas. In other words, the packing of the CH chains is constrained and imposed by the packing of the CF chains.

In quantifying the extent of the lateral ordering of the molecules, the characteristic lengths ($\xi^i_{[10]}$) computed from the GIXD results show that $\xi^{\text{CF chain}}_{[10]}$ generally increases with x_{F8H20} and, in general, $\xi^{\text{CH chain (F8H20)}}_{[10]}$ is highest for intermediate x_{F8H20} values and lowest for pure F8H20. This hints at the possibility of (at least partial) mixing at a molecular level, inasmuch as the presence of F8H14 molecules appears to increase the lateral ordering of the F8H20 CH chains.

Geometrical model applied to the mixtures Drawing on the accumulated knowledge, both from experiments and from MD simulations, some limit-case hypotheses are considered for the possible molecular arrangement within the mixed binary hemimicelles, each leading to an analytical expression relating the diameter of the hemimicelles with the x_{F8H20}. The obtained models, which can be perceived as the extension of the geometrical model presented for the pure hemimicelles in Chapter 9, rationalise the obtained results and can serve as the starting point for future investigations. In particular, considering some important but reasoned approximations, it was found that the structuring of the mixed hemimicelles in concentric circle+corona of completely segregated molecules (F8H20 molecules in the central circle, surrounded by a corona of F8H14 molecules) is unlikely, as that would likely increase (rather than decrease) of the diameter with x_{F8H20}. On the other hand, the reverse configuration (F8H14 molecules in the central circle, surrounded by a corona of F8H20 molecules) or the complete and random mixture of F8H14 and F8H20 within the hemimicelles would result in the reduction of the mixed hemimicelle diameter. However, the quantitative agreement with the experimental results in either case is poor and only a qualitative (albeit enlightening) trend is highlighted from these efforts.

Ensemble of results Considering the results as a whole, it is clear that the mixed binary Langmuir films of F8H14:F8H20 comprise laterally-ordered hemimicelles. Their size is intermediate to the pure ones' and is lower than what would be expected from Vegard's law, hinting at the occurrence of mixing within the film. From this reasoning, however, it is not clear whether the mixing could occur at a hemimicelle or at a molecular level. The existence of a totally segregated film seems unlikely, which is also supported by the π–A isotherm results.

At the molecular scale, the PFAA molecules have their CF chains stacked in a a pseudo-hexagonal lattice. The CH chains appear to give rise to 2 different diffracting structures. The upper part of the CH chains (*i.e.* the part immediately attached to the CF chain) can be anticipated to be packed more loosely, being constrained by the mismatching cross-sectional areas of the CF and CH chains. The lower parts of the CH chains, being further separated from the CH_2-CF_2 junction, may have their lateral stacking less constrained, thus being able to pack more closely (originating a smaller lattice parameter). This effect must be achievable only for a CH chain of a minimum length, as it is observed for F8H20-containing systems but not for pure F8H14. This could also be linked to the aforementioned rate of tilt change (from the centre towards the periphery of the aggregate): for F8H20 this rate is lower, and so the molecular configurations from one layer to the next change less (and thus may allow for a tighter packing) than in the F8H14 case. Both effects might also act together and synergistically.

Overall, the structure of the hemimicelles in the mixed binary films is not clear, as the results do not permit to unambiguously distinguish between whether the mixing occurs at a molecular or at a hemimicelle level. However, considering that $\xi_{[10]}^{\text{CH chain (F8H20)}}$ increases in the presence of F8H14 molecules (compared to the pure F8H20 case), this hints at the possibility of some degree of intercalation of the F8H14 and F8H20 molecules (and thus of mixing at a molecular level) that would favour a more efficient and ordered packing of the CH chains of the F8H20.

11.4 Concluding remarks

The properties of mixed binary Langmuir films of F8H14:F8H20 were studied at 12 °C as a function of Surface Pressure (π) and film composition (molar fraction of F8H20 or x_{F8H20}) at different length scales: macroscopic (π–Molecular Area (A) isotherms), mesoscopic or supramolecular (Grazing Incidence Small Angle X-Ray Scattering (GISAXS) measurements) and microscopic or intermolecular (Grazing Incidence X-Ray Diffraction (GIXD) experiments). Considering that the pure Langmuir films of F8H14 and of F8H20 comprise laterally organised monodisperse surface hemimicelles, with a size dependent on the Perfluoroalkylalkane (PFAA) molecule [5, 8, 11, 14, 24, 25], three scenarios were proposed for the structure of the mixed films: a) complete segregation of the two molecules and the coexistence of the two lattices, one for each pure compound; b) mixing occurring at a hemimicelle level, with the existence of a single lattice of pure hemimicelles of two different sizes; or c) mixing occurring at a molecular level, with the existence of a single lattice of monodisperse hemimicelles.

Considering the ensemble of the results, the structure of the film is probably characterised by the mixing of F8H14 and F8H20 molecules, although it is not unambiguously clear whether this occurs at a hemimicelle or at a molecular level (*i.e.* distinguishing between scenarios "b" and "c"). The existence of a completely segregated film (scenario "a") seems unlikely. The mixed films present a main diffracting lattice of with a lattice parameter intermediate to that of the pure cases. The presence of a secondary, larger and probably transient or meta-stable lattice is reported for $x_{\text{F8H20}} \leq 0.80$. The contraction of the main two-dimensional (2D) hexagonal lattice for the mixed films relative to the average of the pure cases (*i.e.* negative deviations to Vegard's law) and the possibility of intercalation of the hydrogenated (CH) chains of the F8H14 and

F8H20, at least to some extent and as suggested by the GIXD results, hint at the possibility of mixing occurring at a molecular level.

As for future perspectives, the structure of the mixed binary Langmuir films of F8H14:F8H20 should be investigated by Atomic Force Microscopy (AFM), after transfer onto a solid substrate. This study should probe the structure of films at different x_{F8H20} and assess how the size of the hemimicelles varies. The distinction between scenarios "c" and "b" could be anticipated based on the observation of monodisperse hemimicelles or a bimodal distribution of hemimicelle sizes, respectively, at least for $\pi > 0\,\mathrm{mN\,m^{-1}}$. The transfer and imaging by AFM of a pure monolayer of F8H14 at $\pi = 0\,\mathrm{mN\,m^{-1}}$ (at around $A = 0.40\,\mathrm{nm^2\,molecule^{-1}}$ to $0.36\,\mathrm{nm^2\,molecule^{-1}}$) should be attempted to assess whether the presence of a secondary lattice is detected, although it is not clear whether this could be achieved if it is a transient phenomenon and/or if it is disrupted by the phenomenon of transfer onto a solid substrate. Finally, extending the experimental methodologies applied to the characterisation of Langmuir films of F8H14:F8H20 to other mixed binary films of PFAAs should be considered, envisaging the study of the effects of the molecular architecture on the hemimicelle structure and lateral ordering of the film. In particular, the following conditions should be assessed: varying the perfluorinated (CF) chain length while keeping the CH chain length constant (*e.g.* F8H16:F12H16); and varying both the CF chain and the CH chain lengths while keeping the total molecular length constant (*e.g.* F8H20:F12H16).

References

[1] J. F. Rabolt, T. P. Russell and R. J. Twieg. 'Structural Studies of Semifluorinated *n*-Alkanes. 1. Synthesis and Characterization of $F(CF_2)_m(CH_2)_nH$ in the Solid State'. In: *Macromolecules* 17.12 (1984), pp. 2786–2794. DOI: 10.1021/ma00142a060.

[2] A. Savitzky and M. J. E. Golay. 'Smoothing and Differentiation of Data by Simplified Least Squares Procedures'. In: *Analytical Chemistry* 36.8 (1964), pp. 1627–1939. DOI: 10.1021/ac60214a047.

[3] *Savitzky-Golay smoothing filter for not equally spaced data*. The steps of data processing of the surface pressure–molecular area isotherms presented in this work were loosely based on the open-source code provided in this page. URL: https://dsp.stackexchange.com/questions/1676/savitzky-golay-smoothing-filter-for-not-equally-spaced-data (visited on 13/05/2024).

[4] A. Hemmerle et al. 'Opportunities and new developments for the study of surfaces and interfaces in soft condensed matter at the SIRIUS beamline of Synchrotron SOLEIL'. In: *Journal of Synchrotron Radiation* 31 (2024), pp. 162–176. DOI: 10.1107/S1600577523008810.

[5] L. Bardin. 'Monocouches d'alcanes semi-fluorés'. PhD thesis. Paris, France: Université Pierre et Marie Curie, 2010.

[6] M. Broniatowski et al. 'Two-dimensional miscibility between a semifluorinated hydrocarbon and hydrogenated alcohols'. In: *Colloids and Surfaces A: Physicochemical and Engineering Aspects* 249.1–3 (2004), pp. 3–9. DOI: 10.1016/j.colsurfa.2004.08.039.

[7] M. Broniatowski, I. Sandez Macho and P. Dynarowicz-Łątka. 'Study of perfluorooctyl-*n*-alkanes monolayers at the air–water interface'. In: *Thin Solid Films* 493.1–2 (2005), pp. 249–257. DOI: 10.1016/j.tsf.2005.05.034.

[8] G. Zhang et al. 'Occurrence, Shape, and Dimensions of Large Surface Hemimicelles Made of Semifluorinated Alkanes. Elongated versus Circular Hemimicelles. Pit- and Tip-Centered Hemimicelles'. In: *Journal of the American Chemical Society* 127.29 (2005), pp. 10412–10419. DOI: 10.1021/ja0510515.

[9] A. González-Pérez, C. Contal and M. P. Krafft. 'Experimental evidence for a surface concentration-dependent mechanism of formation of hemimicelles in Langmuir monolayers of semi-fluorinated alkanes'. In: *Soft Matter* 3.2 (2007), pp. 191–193. DOI: 10.1039/b613265k.

[10] C. G. Lux et al. 'Compression of Self-Assembled Nano-Objects: 2D/3D Transitions in Films of (Perfluoroalkyl)Alkanes – Persistence of an Organized Array of Surface Micelles'. In: *Chemistry – A European Journal* 16.24 (2010), pp. 7186–7189. DOI: 10.1002/chem.200903535.

[11] L. Bardin et al. 'Long-Range Nanometer-Scale Organization of Semifluorinated Alkane Monolayers at the Air/Water Interface'. In: *Langmuir* 27.22 (2011), pp. 13497–13505. DOI: 10.1016/10.1021/la201802x.

[12] M. Li et al. 'Formation of an ordered Langmuir monolayer by a non-polar chain molecule'. In: *Nature* 367.6459 (1994), pp. 151–153. DOI: 10.1038/367151a0.

[13] M. Goldmann et al. 'In-plane X-ray diffraction from monolayers of perfluorinated fatty acids: evidence for azimuthal ordering in the condensed phase'. In: *Journal de Physique II* 4.5 (1994), pp. 773–785. DOI: 10.1051/jp2:1994164.

[14] M. P. Krafft and J. G. Riess. 'Chemistry, Physical Chemistry, and Uses of Molecular Fluorocarbon-Hydrocarbon Diblocks, Triblocks, and Related Compounds – Unique "Apolar" Components for Self-Assembled Colloid and Interface Engineering'. In: *Chemical Reviews* 109.5 (2009), pp. 1714–1792. DOI: 10.1021/cr800260k.

[15] P. Fontaine et al. 'Evidence of lying molecules in the structure of the most condensed phase of semi-fluorinated alkane monolayers'. In: *Nanoscale* 10.5 (2018), pp. 2310–2316. DOI: 10.1039/c7nr07415h.

[16] H. O. S. Yadav et al. 'Hemimicelle formation of semi-fluorocarbon chains at air–water interface: coarse-grained molecular dynamics study with an extension of the SPICA force field'. In: *Molecular Physics* 119.19–20 (2021), Article No. e1910355. DOI: 10.1080/00268976.2021.1910355.

[17] A. L. S. Gamboa. 'Ordering in Langmuir and Langmuir-Blodgett Films: Effect of the Presence of Fluorocarbon and Hydrocarbon Chains'. PhD thesis. Lisboa, Portugal: Universidade Técnica de Lisboa – Instituto Superior Técnico, 2006.

[18] A. W. Adamson and A. P. Gast. *Physical Chemistry of Surfaces*. 6th ed. Hoboken, New Jersey, USA: John Wiley & Sons, Inc., 1997. ISBN: 978-0-471-14873-9.

[19] P. Fontaine et al. 'Evidence for Interaction with the Water Subphase As the Origin and Stabilization of Nano-Domain in Semi-Fluorinated Alkanes Monolayer at the Air/Water Interface'. In: *Langmuir* 30.50 (2014), pp. 15193–15199. DOI: 10.1021/la5038124.

[20] P. Dynarowicz-Łatka et al. 'Structural Investigation of Langmuir and Langmuir–Blodgett Monolayers of Semifluorinated Alkanes'. In: *Journal of Physical Chemistry B* 110.12 (2006), pp. 6095–6100. DOI: 10.1021/jp057270u.

[21] M. Broniatowski et al. 'Nucleation and Growth in the Collapsed Langmuir Monolayers from Semifluorinated Alkanes'. In: *Journal of Physical Chemistry B* 111.44 (2007), pp. 12787–12794. DOI: 10.1021/jp0748462.

[22] D. Vollhardt and V. B. Fainerman. 'Progress in charecterization of Langmuir monolayers by consideration of compressibility'. In: *Advances in Colloid and Interface Science* 127.2 (2006), pp. 83–97. DOI: 10.1016/j.cis.2006.11.006.

[23] V. M. Kaganer, H. Möhwald and P. Dutta. 'Structure and phase transitions in Langmuir monolayers'. In: *Reviews of Modern Physics* 71.3 (1999), pp. 779–819. DOI: 10.1103/RevModPhys.71.779.

[24] P. Fontaine et al. 'Direct Evidence for Highly Organized Networks of Circular Surface Micelles of Surfactant at the Air-Water Interface'. In: *Journal of the American Chemical Society* 127.2 (2005), pp. 512–513. DOI: 10.1021/ja044779e.

[25] M. Veschgini et al. 'Size, Shape, and Lateral Correlation of Highly Uniform, Mesoscopic, Self-Assembled Domains of Fluorocarbon–Hydrocarbon Diblocks at the Air/Water Interface: A GISAXS Study'. In: *ChemPhysChem* 18.19 (2017), pp. 2791–2798. DOI: 10.1002/cphc.201700325.

[26] L. Bardin et al. 'Highly organized crystalline monolayer of a semi-fluorinated alkane on a solid substrate obtained by spin-coating'. In: *Thin Solid Films* 519.1 (2010), pp. 414–416. DOI: 10.1016/j.tsf.2010.07.065.

[27] C. Schwieger, X. Liu and M. P. Krafft. 'Self-assembled mesoscopic surface domains of fluorocarbon-hydrocarbon diblocks can form at zero surface pressure: tilting of solid-like hydrocarbon moieties compensates for cross-section mismatch with fluorocarbon moieties'. In: *Physical Chemistry Chemical Physics* 19.35 (2017), pp. 23809–23816. DOI: 10.1039/c7cp02432k.

[28] Z. Huang et al. 'Structural studies of semifluorinated hydrocarbon monolayers at the air/water interface'. In: *Journal of the Chemical Society – Faraday Transactions* 92.4 (1996), pp. 545–552. DOI: 10.1039/ft9969200545.

[29] G. M. C. Silva et al. 'Spontaneous self-assembly and structure of perfluoroalkylalkane surfactant hemimicelles by molecular dynamics simulations'. In: *Proceedings of the National Academy of Sciences of the United States of America* 116.30 (2019), pp. 14868–14873. DOI: 10.1073/pnas.1906782116.

Chapter 12

Interstitial voids in mixtures of hydrogenated and fluorinated chains

The non-ideality of mixtures of CH and CF chains is well known, arising from the mutual phobicity of those two apparently similar, but very unlike moieties. The fact that those chains display different spacial requirements results in some remarkable properties when they mix, including in liquid mixtures of Normal Alkanes (n-As) and Perfluoroalkanes (PFAs) that display large, positive Excess Volume of Mixing (V^E) [1–3]. Such behaviour hints at the connection between alterations of the packing at a molecular level that translate into macroscopically observable properties, which can be related in great part with the differences in molecular volume and preferential conformations and the creation of interstices of essentially empty space among the molecules. The understanding of such phenomena in model systems, and of the characterisation of the interstitial void space in liquid mixtures of CH and CF chains in particular, enables a better understanding of the fundamental principles driving this behaviour. Herein, a methodology based on Molecular Dynamics (MD) simulations is put forward to quantify, locate and characterise the morphology of the empty or void space in liquid mixtures of hexane (H6) and perfluorohexane (F6). This is then applied to the study of those properties in liquid perfluorohexylhexane (F6H6) and perfluorooctylbromide (F8Br), two molecules with interest in fundamental studies, within the scope of this work, and in practical uses in the biomedical field.

12.1 Interstitial voids in computer simulations

12.1.1 Context and motivation

The study of the interstitial void space in molecular models used in MD simulations has many variations and formulations, but the information it permits to retrieve is insightful and complementary to that obtained from the study of the simulated molecules themselves, both from fundamental and practical points of view. To cite a few examples, this characterisation has been done to provide information on the structure of liquids [4–10] and the volumetric properties of lipid membranes [11–13] and protein solutions [14]. The link between the existence of interstitial cavities among molecules in a simulated fluid and the solubility of small molecules (such as respiratory gases) has also been addressed, based on the formalism of statistical mechanics of

the Widom's test-particle insertion method [15–17]. For the specific purpose of the topological characterisation of the interstitial void space, the used methodologies most commonly employed partition the inter-atomic space following different algorithms, such as those based on the Voronoi tessellation formalism [6, 10, 11, 13, 14, 18], the concept of the alpha-shape [4, 5, 7] or on grid-based sampling approaches [9]. Regardless of the employed algorithm, the purpose of such analysis is to locate voids in a condensed-phase simulation, characterise their morphology and quantify their volume. These results can provide valuable information on the processes of dissolution of gases in liquids and the mechanisms of diffusion in liquids and of permeation of small molecules across lipid membranes. However, it is common that these algorithms are used on a frame-by-frame analysis, which precludes their use on several configurations from one same trajectory, for better representativeness and improved statistical treatment, and on large data sets, possibly in an automated manner.

Herein, the interstitial void space in liquid mixtures of hexane (H6) and perfluorohexane (F6) was systematically studied as a function of composition, temperature and the size of the interstitial cavities. This served both as an exploratory analysis and a benchmark of the methodology. The deployed methods were based on the formalism of the Voronoi S-tessellation, which is briefly introduced in the following pages. This work extended the use of this algorithm for the sampling of several configurations (trajectory frames), for better representation and improved statistical treatment based on the automated analysis of large data sets. Additionally, further analyses were implemented to extract information from these results, as detailed below. The data set consisted of a series of simulations carried out systematically by developing a pipeline to automatically and sequentially vary the system composition (numbers of molecules of H6 and of F6), build the starting configurations, equilibrate the system, run the production simulations and analyse the results.

The analyses were then employed to characterise the void space in MD simulations of pure liquid perfluorohexylhexane (F6H6) and perfluorooctylbromide (F8Br). This study was made as part of a larger project that goes beyond the scope of this thesis, but that has significant overlaps that justify its inclusion in the present chapter, namely: methodological (the use of MD simulations, scientific programming and data analysis), chemical (H6 and F6 can be regarded as the building blocks of PFAAs and their mixtures systems for the study of the fundamental principles governing the mutual incompatibility of the CH and CF moieties) and practical (the dissolution of respiratory gases in liquids, particularly in a PFAA on its own (F6H6), which otherwise already finds uses in ophtalmologic settings [19], or in emulsions of F8Br that can be stabilised by the incorporation of PFAAs in their formulations [20]).

12.1.2 The Voronoi S-network and the Voronoi S-tessellation

The concepts of the Voronoi S-network and the Voronoi S-tessellation[1], whose mathematical foundations have been studied by Medvedev *et al.* [11, 12, 18], are useful tools for the analysis of the interstitial void space in molecular models of MD simulations. They are a generalisation of the classical Voronoi-Delaunay approach which, given a set of predefined points in a three-

[1]For systematic reference, a glossary summarising some of the terms appearing throughout the text and their definitions is presented in Subsection 12.1.4.

dimensional space, divides the latter into regions (Voronoi polyhedra), each one containing all the points that are closer to a predefined point of the set than to any other of the predefined points [21]. This algorithm partitions space into regions naturally assigned to each predefined point. This is known as the Voronoi tessellation [12].

The Voronoi polyhedra can also be constructed for a system of balls[2], by taking their centres as the set of predefined points. However, only if the balls have equal radii does this partition keep its physical meaning of naturally dividing space into regions pertaining to each ball [13]. The problem is further complicated if the balls partially overlap [11, 18]. The original physical meaning of the Voronoi tessellation can be preserved if the distance from any point to a ball is measured from its surface rather than from its centre [13, 18]. This partitions the space into regions (Voronoi S-regions) containing all the points closer to the surface of a given ball than to the surfaces of any other ball of the system. The mosaic thus formed is known as the Voronoi S-tessellation [18]. Evidently, in the case of balls with equal radii (including balls with null radii, *i.e.* a system of points), this coincides with the classical Voronoi tessellation. The Voronoi S-tessellation covers the space without overlapping and gaps [12, 18].

The faces of a Voronoi S-region are pieces of hyperboloids, its edges or "bonds" are segments of Voronoi S-channels, and its vertices or "void sites" are the Voronoi S-vertices of the quadruplets of balls whose Voronoi S-regions meet in this vertex [18, 21]. A void site coincides with the centre of the empty sphere inscribed among this quadruplet of balls. The centres of these four mutually neighbouring balls are arranged in a tetrahedron called a Delaunay S-simplex [12]. The mosaic formed by all Delaunay S-simplexes is called the Delaunay S-covering and it is the dual of the corresponding Voronoi S-tessellation. The Delaunay S-covering also covers the entire space without gaps but generally, unlike in the classical case, there may be overlapping Delaunay S-simplexes; therefore, in the strict mathematical sense, they don't form a tessellation [12, 18]. The set of void sites and edges of all the Voronoi S-regions constitutes the Voronoi S-network [12].

A Delaunay S-simplex represents an elementary cavity within its constituent quadruplet of balls. The radius R_i of the empty sphere inscribed among the balls of a Delaunay S-simplex is a measure of the size of the elementary cavity [12, 18]. Each void site corresponds to a Delaunay S-simplex and thus the study of the interstitial cavities can be reduced to the study of clusters of sites on the Voronoi S-network, in what is known as the site-percolation problem [18]. In the context of this work, one such cluster of void sites is called an *interstitial void* or simply *void*.

Neighbour Delaunay S-simplexes share one common face (*i.e.* 3 balls) and the corresponding void sites (Voronoi S-vertices) are connected by a bond (network edge). This bond is a fairway passage between the two void sites and is the locus of the points that are at once most distant from the surfaces of the three balls. In other words, it is the trajectory of the centre point of the empty sphere (of varying radius) simultaneously tangent to this set of three balls [18]. This provides a physical sense to the "tightness" of the bond, linked to the radius of the tangent empty sphere. The point along the bond where the corresponding tangential sphere has the smallest radius is a bottleneck and its radius R_b characterises how "tight" the bond is [12, 18].

[2]For the purpose of the intended analysis, that is the calculation of the three-dimensional Voronoi S-network of a molecular system, the atoms are more generally designated as *balls*. Also, the term *ball* is preferred over the mathematical term *sphere* to avoid the misunderstanding between objects of the system and interstitial empty spheres inscribed between balls (themselves named *void sites* herein) [18].

12.1.3 Study of interstitial voids in molecular systems

From a mathematical point of view, the molecular systems studied by MD simulations can be regarded as a set of partially overlapping balls of different radii [11, 18], each ball representing exactly one atom in the case of atomistic MD simulations. The study of the structure, spatial arrangement and interstitial voids of a computer model of a molecular system can be done systematically using the formalism of the Voronoi S-network [11–13, 18, 21].

Interstitial voids with relevant physical meaning in a molecular system (*e.g.* for the study of solubilisation and diffusion processes of small molecules in a liquid or across a lipid membrane) can be defined as those accessible to a spherical probe of a given radius [12, 22]. Within the mathematical framework of the Voronoi S-network, this corresponds to identifying the void sites with radii larger than a cutoff value R_i^{probe} (a method known as "R_i colouring") or, alternatively, identifying the bonds with bottleneck radii larger than a cutoff value R_b^{probe} (a method known as "R_b colouring"). If a probe of radius R_b^{probe} can move along a bond (*i.e.* pass through its bottleneck) then both sites connected by this bond are also accessible to it [12, 18].

The total empty volume of a void (V_{void}) can be determined simply as the sum of the volumes of its constituting Delaunay S-simplexes minus the volume occupied by the parts of its own atoms [12]. However, this calculation is not trivial, since it may occur that atoms other than those of the quadruplet of the Delaunay S-simplex occupy a part of its volume. Also, problems with multiple overlapping atoms may arise, making the analytical determination of V_{void} intractable. This can be overcome through the numerical calculation of the empty volume of a Delaunay S-simplex (V_S), by sampling (randomly or using a grid-based approach) the fraction of the tetrahedron's volume outside any atoms and obtaining V_S as the product of the obtained fraction by the volume of the tetrahedron.

Delaunay S-simplexes may have a significant overlap for particular configurations of molecular systems [18], which could lead to artefacts in the analyses. Overlaps happen rarely, and pose significant problems only when the volume as the sum of the volumes of all Delaunay S-simplexes is to be calculated. However, even in such cases, the study of the interstitial voids using this methodology is nonetheless possible and adequate [11, 12, 18]. Moreover, it is assumed that the system is non-degenerate, *i.e.* each inscribed empty sphere is simultaneously tangent to no more than 4 balls. This not only significantly simplifies the analysis and the algorithm, but also degenerate configurations can be decomposed into non-degenerate ones by performing infinitesimal shifts of the positions of the degenerate balls or infinitesimal variations of their radii which, for the purpose of this work, convey essentially the same physical information [18].

The position of a void can be defined as the weighted average of the positions of its corresponding void sites [12]. The weight of each void side is taken as the empty volume of the corresponding Delaunay S-simplex (V_S). This is the equivalent of finding the position of the centre of mass (x_{COM}) of a set of massive points in space, each having a mass equal to the corresponding V_S.

Different authors have came up with several concepts and geometrical definitions to get a quantitative grasp on the morphology of the interstitial voids in MD simulations [5, 12]. These vary with the employed definition of voids and the algorithm used to identify them, but they usually purport how deviated the shape of the void is from a perfect sphere (*e.g.* by computing

the surface to volume ratio and comparing it to that of a sphere with the same volume) [5]. Alternatively, the voids can be approximated to spherocylinders, to gain information concerning their elongation and morphology, as well as to obtain information about their orientation relative to the molecules of the system [11, 12]. A spherocylinder is characterised by the length of its cylindrical part (L) and the radius of its spherical caps (R). These can be determined systematically through the following procedure [11, 12]: the tensor of inertia of the void is calculated considering it as a set of massive points in space (the set of void sites, each with a weight equal to the respective V_S), as described above; the axis of the tensor of inertia along which its principal value is minimal corresponds to the direction of the largest extension of the void and it's taken as the axis of the spherocylinder; L is then equal to twice[3] the Root-mean-square Deviation (RMSD) relative to x_{COM} of the coordinates of the void sites projected on this axis. R is determined from the condition of the equality of the volumes of the spherocylinder ($V_{\mathrm{spherocylinder}}$) and the void it represents (V_{void}) [11] (Equation 12.1).

$$V_{\mathrm{void}} = V_{\mathrm{spherocylinder}} = R^2\pi\left(L + \frac{4}{3}R\right) \tag{12.1}$$

The morphology of the voids can by characterised by the void sphericity (α), as defined in Equation 12.2 and based on the geometry of the corresponding spherocylinder [12]. It ranges from 0 for an infinitely long spherocylinder to 1 for a perfect sphere.

$$\alpha = \frac{2R}{2R + L} \tag{12.2}$$

The formalism of Radial Distribution Functions (RDFs) has been used before to study the interstitial void space in molecular models of fluids. For example, in one study, the computation of void–void RDFs uncovered that the interstitial voids in a dense fluid of Lennard-Jones (LJ) particles tend to form a dual network with the LJ particles, in which the positions of the interstitial voids display a periodicity of about the same length scale as the LJ particles themselves [23]. In another study, the structure of liquid water and the corresponding interstitial voids were probed by calculating water–water and water–void RDFs, through which the authors found that the water and the void networks are anti-correlated (*i.e.* water molecules and interstitial voids are intercalated) [5]. However, to the best of our knowledge, the formalism of RDFs has not been used to determine the preferential location of interstitial cavities in organic liquids.

12.1.4 Definitions

Voronoi polyhedron For a set of points in space, a *Voronoi polyhedron* is the region of space containing all the points that are closer to a given point of the set than to any other point of the set [12].

Voronoi surface A *Voronoi surface* is the geometric locus of points in space equidistant to two neighbouring points in space [18]. A Voronoi surface is a plane in a 3D space.

[3] In the original work [11, 12], L is taken as one times the mean square deviation of the projected coordinates.

Voronoi channel A *Voronoi channel* is the geometric locus of points in space equidistant to three mutually neighbouring points in space [18]. A Voronoi channel is a straight line in a 3D space.

Voronoi tessellation The Voronoi polyhedra constructed for an entire set of points form a mosaic, called the *Voronoi tessellation*, which covers the space without overlaps or gaps [12].

Delaunay simplex The Voronoi tessellation defines quadruplets of mutually neighbouring points that form a tetrahedron (with one of such points on each vertex) called a *Delaunay simplex*.

Delaunay tessellation The Delaunay simplexes, similarly to the Voronoi polyhedra, form a mosaic covering the space without overlapping and gaps called the *Delaunay tessellation* [12]. The Voronoi and Delaunay tessellations are duals [12, 24].

Voronoi network The *Voronoi network* is the geometric construction formed by the set of all vertices and edges of the Voronoi polyhedra [12].

Voronoi S-region The *Voronoi S-region* is the region of space containing all the points that are closer to the surface of a given ball than to that of any other ball [12]. It is the generalisation of the Voronoi polyhedron for systems comprising balls of different radii. For a system of balls with equal radii, it coincides with the Voronoi polyhedron [12, 18].

Voronoi S-surface A *Voronoi S-surface* is the geometric locus of points in space equidistant to the surfaces of two balls. If the balls have equal radii, it coincides with the Voronoi surface. For two balls of different radii, it has the shape of an axial-symmetrical hyperboloid [18].

Voronoi S-channel A *Voronoi S-channel* is the generalisation of the *Voronoi channel* to systems of balls of different radii. It is the geometric locus of points in space equidistant to the surfaces of three balls of different radii and, in general, it has the shape of a hyperbole or of an ellipse (respectively if it is open or closed) [18].

Voronoi S-tessellation Analogously to the Voronoi tessellation, the mosaic formed by the Voronoi S-regions constructed for all atoms of the system covers the space without overlaps or gaps and is called *Voronoi S-tessellation* [12].

Voronoi S-network As a generalisation of the classical Voronoi network, the *Voronoi S-network* is the set of the vertices (sites) and edges (bonds) of all the Voronoi S-regions of the system [12].

Delaunay S-simplex The quadruplets of mutually neighbouring balls, the sphere inscribed among which is empty, is called *Delaunay S-simplex* [12]. It has a tetrahedral shape (with one of the four balls on each vertex) and it represents an elementary cavity between the balls. It may or

may not coincide with the classical Delaunay simplexes defined for the atomic centres, depending on the atomic radii [12, 18]. Delaunay S-simplexes corresponding to neighbouring S-network sites have one face (*i.e.* three balls) in common [12].

Delaunay S-covering Similarly to the classical case, the sum total of all Delaunay S-simplexes constructed for a given system of balls forms a mosaic covering the entire space without gaps [18]. However, this does not necessarily constitute a tessellation in the strict mathematical sense since, under certain circumstances, the Delaunay S-simplexes may overlap [12, 18]. This space-covering mosaic is thus preferentially named *Delaunay S-covering*.

Vertex (or site) of a Voronoi network or of a Voronoi S-network Each *vertex* of the Voronoi network corresponds to one Delaunay simplex, being the centre of its inscribed empty sphere [12]. In the context of the determination of the Voronoi S-network for a molecular system, the term "site" is typically used in lieu of "vertex" [18].

Edge (or bond) of a Voronoi network or of a Voronoi S-network Each *edge* of the Voronoi network is a segment of a Voronoi channel connecting two neighbouring sites and represents a fairway passing through the narrow bottleneck between three balls from one site to the other [12]. In other words, it is the trajectory of the centre point of the empty sphere (of varying radius) simultaneously tangent to the three balls [18]. This definition provides a physical sense to the dimensions of the edge, which are directly linked to the radius of the tangent empty sphere. The point along the bond with the smallest radius is called a bottleneck and its radius R_b characterises how "tight" the bond is [12, 18]. The definition is similar when applied to a Voronoi S-network. In the context of the determination of the Voronoi S-network for a molecular system, the term "bond" is typically used in lieu of "edge" [18].

Void site A *void site* or a S-network site is a vertex or site of the Voronoi S-network [18]. It is associated to a quadruplet of balls of a Delaunay S-simplex and it coincides with the centre of the empty sphere inscribed among those balls [12, 18]. A site is characterised by the radius of the corresponding inscribed sphere (*i.e.* the radius of the void site). A void site pins the elementary cavity represented by a Delaunay S-simplex to a single point in space. Therefore, the study of the spatial distribution of interstitial voids can be reduced to studying the characteristics of clusters of sites on the network [18].

Void Within the context of this work, a *void* is defined as the cluster of void sites (or the set of Delaunay S-simplexes these represent) that are simultaneously connected to one another by a number of edges (bonds) of the Voronoi S-network and obey a certain geometric criterion. Herein, the R_b colouring method was used (see Subsection 12.1.3).

12.2 Simulation conditions

Molecular dynamics simulations were performed using the Groningen Machine for Chemical Simulation (GROMACS) open-source software package (v. 5.0.7) [25, 26], for systems consisting of a total of 500 molecules of H6 and of F6 in cubic boxes with periodic boundary conditions in all directions. The number of molecules of each compound was adjusted to vary the molar composition of the system. For each studied system, an initial low-density random molecular configuration was generated and subjected to an energy minimisation using the steepest descent method to relax unphysical high-energy contacts. A random velocity distribution was assigned to the atoms, according to the Maxwell distribution at the desired temperature, and a 10 ns NpT pre-equilibration run was performed at 1000 bar to achieve a dense liquid configuration. The equilibrium volume of each box was then obtained from an 25 ns NpT simulation at 1 bar, of which the first 5 ns was discarded from the analysis. The final configuration from this run was then resized to the average NpT volume and used in a NVT simulation for a further 22 ns, of which the last 20 ns were used to characterise the interstitial voids of the system. The simulations were conducted at a Temperature (T) between 298 K and 338 K.

The equations of motion were integrated in 2 ns timesteps, using the leapfrog algorithm, with all bonds involving hydrogen atoms constrained to their equilibrium distance by the LINCS algorithm [27]. A 1.4 nm cutoff (1.1 nm for the pre-equilibration) was used for both dispersive and electrostatic interactions, applying standard analytic tail corrections for energy and pressure to the dispersion terms and treating the long-range Coulombic interactions using the particle-mesh Ewald method. The Verlet cutoff scheme was used to update the neighbour lists every 10 steps. The Berendsen thermostat and barostat were used during the pre-equilibration stage, whereas the Nosé-Hoover thermostat and the Parrinello-Rahman barostat were applied in the production stage runs. In all cases, the thermostat and barostat coupling constants were 0.5 ps and 10 ps, respectively.

The systems were modelled using an atomistic Force Field (FF) based on the Optimised Potential for Liquid Simulations (OPLS)–All-Atom (AA) framework [28–30]. Following the OPLS–AA framework, the cross interaction dispersion parameters for energy and size were obtained using the geometric mean rule. However, to account for the large positive excess volumes and enthalpies of mixing, the cross-interaction parameters between hydrogen and fluorine atoms were re-scaled [31]: the unlike energy interaction ($\varepsilon_{\mathrm{HF}}$) is reduced by 23 % and the unlike size interaction (σ_{HF}) is increased by 3.5 %.

The same simulation conditions and procedures were employed to perform MD simulations of liquid perfluorohexylhexane (F6H6, 1000 molecules) and liquid perfluorooctylbromide (F8Br, 500 molecules). The FF used in the simulations is also based on the OPLS–AA framework. In the case of the F6H6, the CF and the CH segments use the parameters for perfluoroalkanes [29] and for L-OPLS alkanes [30], respectively. The dihedral torsion parameters modelling the conformations of the CF_2-CF_2-CH_2-CH_2 moiety, as well as the atomic partial charges for the carbon atoms therein, were retrieved from reference [32]. For the F8Br molecules, the FF parameters are the ones reported in reference [32].

12.3 Description of the implemented analyses

For each system, the simulated production trajectory was sampled at regular intervals and about 200 frames were used to analyse the interstitial void spaces. Tests were performed to assess the influence of the system size (*i.e.* the number of particles in the simulation box) and the length of the analysed trajectory (*i.e.* the number of frames used for the analyses). The analyses performed on systems with more particles and/or with more frames yielded similar results. Unless otherwise specified, all analysis were performed using in-house programs written in Python (v. 3.10), which made use of the packages: Matplotlib (v. 3.5.0) [33, 34], NetworkX (v. 2.6.3) [35, 36], NumPy (v. 1.21.4) [37, 38], pandas (v. 2.0.1) [39, 40] and SciPy (v. 1.7.3) [41, 42]. A snippet of code for the generation of a grid of points over the interior of a tetrahedron in 3D was adapted from Ref. [43]. Snapshots from the simulation trajectories, including any representations of the interstitial voids, were rendered using the Visual Molecular Dynamics (VMD) open-source software package (v. 1.9.3) [44].

The analysis pipeline consisted in looping through the frames and, for each frame, calculating the corresponding Voronoi S-network using the algorithm developed by Medvedev *et al.* [11, 12, 18] (available online as a precompiled executable [45]). This work extended the use of this algorithm for the sampling of several configurations (trajectory frames), for better representation and improved statistical treatment based on the automated analysis of large data sets. Additionally, further analyses were implemented to extract information from these results (*e.g.* the computation of RDFs involving void sites). For each atom i, its radius was taken as half the corresponding LJ distance parameter σ_i, within the framework of the FF used in the MD simulations. The interstitial voids were then identified according to the R_b colouring procedure described in Subsection 12.1.3, with a varying R_b^{probe} (specified case by case). The value of $R_b^{\text{probe}} = 0.20\,\text{nm}$ was chosen for the majority of the analysis and it corresponds to a value slightly larger than the radius of a xenon (Xe) atom (for which $\sigma_{\text{Xe}} = 0.394\,78\,\text{nm}$ [46]). This value was chosen due to the interest in studying liquids with dissolved Xe and it permits the systematic identification of relatively large voids in the studied molecular systems (typical R_i^{probe} values lie in the range of 0.12 nm to 0.16 nm [4, 5, 12]; these values are representative of the sizes of smaller probes such as molecular hydrogen (H_2), molecular oxygen (O_2) and water (H_2O)). The empty volume of each Delaunay S-simplex (V_S) was calculated as explained in Subsection 12.1.3 using a grid-based sampling approach.

Because Delaunay S-simplexes may overlap, a consistency check was performed for each frame: the volume of the simulation box, calculated as the sum of the total volume of the Delaunay S-simplexes (the sum of V_S^{total}, *i.e.* the volume of the tetrahedron defined by the quadruplet of atoms), and the box volume given by the product of the box vectors (V_B) were compared. For the analysed frames, the differences in these quantities amounted to less than 0.1 %, *i.e.* $\frac{V_S^{\text{total}} - V_B}{V_B} < 0.001$, which are negligible and do not impair the analyses [11, 12, 18].

The location of the voids relative to the molecules was studied based on the formalism of RDFs, using the coordinates of the void sites to compute distances between these and the atoms in the system. Because the number of void sites (and of voids) may change from frame to frame, the RDFs presented herein are the result of a bin-by-bin average of the RDFs calculated for each frame, weighed by the number of void sites in each frame.

12.4 Nomenclature and notation

For the results and analyses presented herein and following the definitions presented on Table 2.1, the molecules studied in this work are abbreviated as follows: H6 (hexane), F6 (perfluorohexane), F6H6 (perfluorohexylhexane) and F8Br (perfluoroalkylbromide). The atoms in each molecule are labelled and identified as CXY (carbon atoms), XY (hydrogen or flurine atoms) or Br (bromine atom), where X identifies whether the atom is part of a hydrogenated chain (X = H) or fluorinated chain (X = F) and Y identifies the position of the atom in the chain (Y is a capital letter from A to H). Equivalent, indistinguishable atoms share the same label (*e.g.* both carbon atoms on the -CH_3 termini of a H6 molecule are labelled CHA). The nomenclature and notation are summarised in Figure 12.1, including the systematic identification or "Y" for the positions of the atoms.

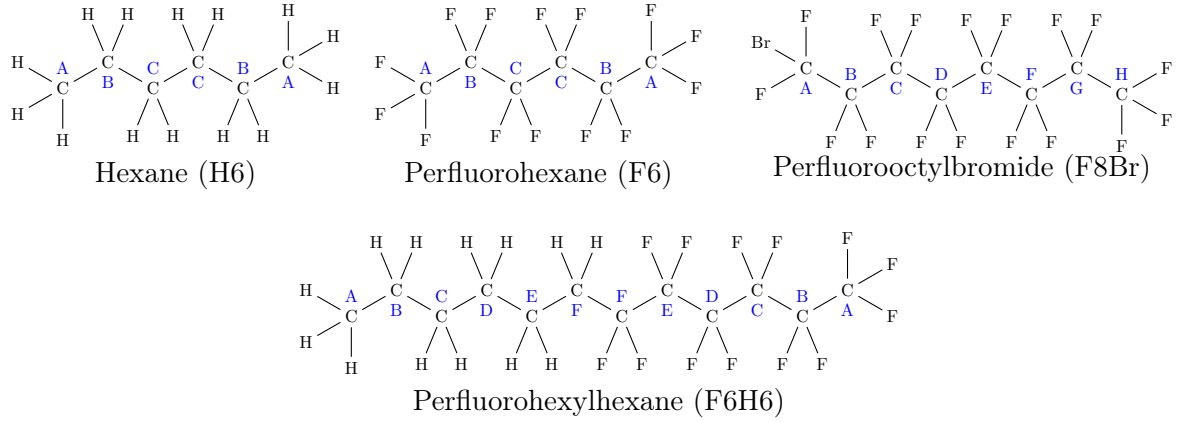

Figure 12.1: Schematic representation of the molecules and the nomenclature used in the characterisation study of the interstitial voids in MD simulations. The carbon atoms are labelled with letters identifying the analogous atoms, for each molecule. For instance: the (hydrogenated) terminal carbon atom of H6 (-$\mathbf{C}H_3$) is identified as CHA; the (fluorinated) second-to-terminal carbon atom of F6 (-$\mathbf{C}F_2CF_3$) is identified as CFB. Likewise, the hydrogen or fluorine atoms share the identifying label with the carbon atom they are bonded to (*e.g.* FA and CFA, for the atoms of the -CF_3 group in F6).

12.5 Results and Discussion

12.5.1 Mixtures of hexane (H6) and perfluorohexane (F6)

The first systems to be studied were liquid mixtures of F6+H6, which were simulated at four different Temperatures (Ts) (298 K, 308 K, 318 K and 328 K) and spanning the entire composition of molar fraction of F6 (x_{F6}) in 0.05 increments. This was a systematic exploratory study that also served as a benchmark for later analyses and investigation of other condensed-phase systems.

12.5.1.1 Quantification of the total void volume in the system

The average total void volume in the simulated systems ($\overline{V_{\mathrm{void,\ total}}}$) is presented in Figure 12.2 (left) as a function of x_{F6} in the mixtures of F6+H6 and for the four studied T. Two data sets are presented: one in which the voids where identified using the R_b colouring method with $R_b^{\mathrm{probe}} = 0.20\,\mathrm{nm}$ (see Subsection 12.1.3) and another one that used $R_b^{\mathrm{probe}} = 0.16\,\mathrm{nm}$. For

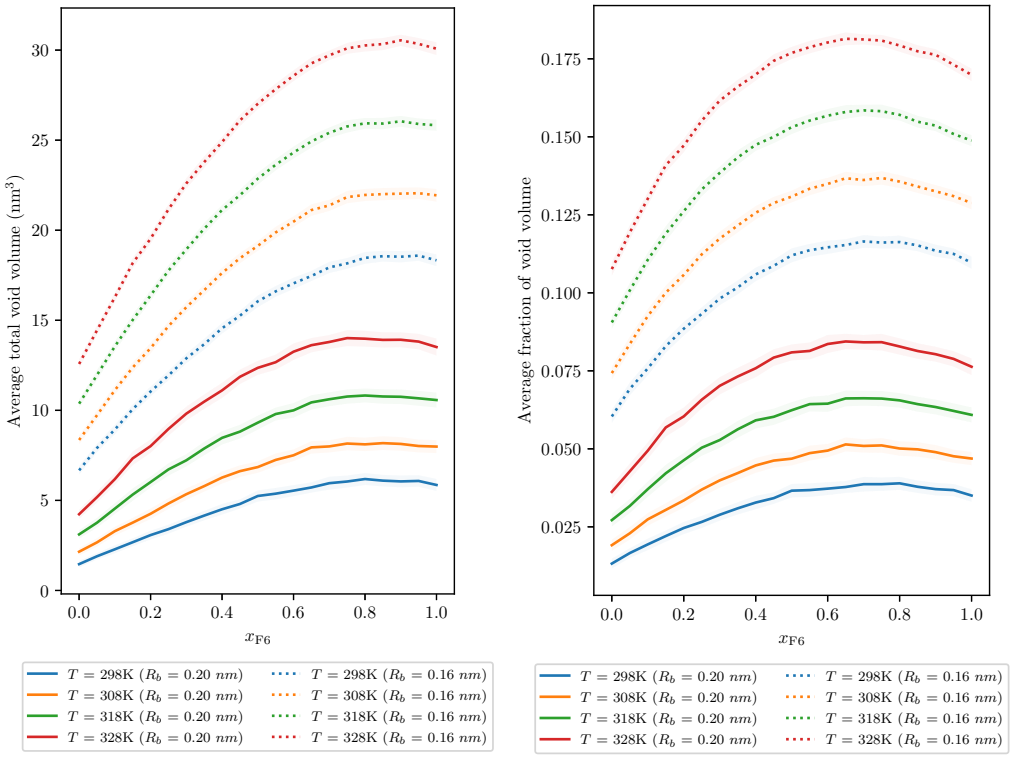

Figure 12.2: Average total void volume ($\overline{V_{\text{void, total}}}$, left) and average fraction of total void volume ($\overline{V_{\text{void, total}}}^{\text{norm}}$, right) as a function of the molar fraction of F6 (x_{F6}) in the mixtures of F6+H6, for the different studied temperatures and the two R_b^{probe} values used in the R_b colouring method. The shaded area represents the interval corresponding to one standard deviation from the mean.

both data sets, the void volume in the simulation box increases with increasing x_{F6}, reaching a maximum near the pure F6, but at a composition lower than $x_{\text{F6}} = 1.00$. $\overline{V_{\text{void, total}}}$ increases with increasing T, at constant x_{F6}. For fixed x_{F6} and T, $\overline{V_{\text{void, total}}}$ is larger for the $R_b^{\text{probe}} = 0.16\,\text{nm}$ data set than for the $R_b^{\text{probe}} = 0.20\,\text{nm}$ data set. This is expected because, in the first case, a smaller probe radius is considered and therefore more void regions of a given configuration are accessible, which translates in a bigger $\overline{V_{\text{void, total}}}$ (and usually, but not necessarily, a larger number of voids, as explained below) compared to the second scenario. This observation is general and should be kept in mind throughout this study.

Because $\overline{V_{\text{void, total}}}$ depends on the volume of the simulation box, and also because the molar volume of the mixtures of F6+H6 does not vary linearly with x_{F6}, the average fraction of total void volume ($\overline{V_{\text{void, total}}}^{\text{norm}}$) was computed and is presented in Figure 12.2 (right). This equates essentially to the average total void volume normalised by the volume of the simulation box. Here, the trend described above is once more observed for both data sets, but the deviation from the average of the pure compounds' values is even more evident. $\overline{V_{\text{void, total}}}^{\text{norm}}$ increases with increasing T, for a fixed x_{F6}. This is the result of the thermal expansion of the system, which naturally results in the increase of the interstitial void space among the molecules. The minimum $\overline{V_{\text{void, total}}}^{\text{norm}}$ occurs for the pure H6 system, at any given temperature. In quantitative terms, the volume of the system accessible to a probe of radius $R_b^{\text{probe}} = 0.20\,\text{nm}$ amounts to about 2 % to 7.5 % of the total volume of the system, depending on x_{F6} and T, whereas about 6 % to 18 % of the total volume of the system are accessible to a probe of radius $R_b^{\text{probe}} = 0.16\,\text{nm}$. Qualitatively, however, the trends observed with varying x_{F6} and T are similar for both cases.

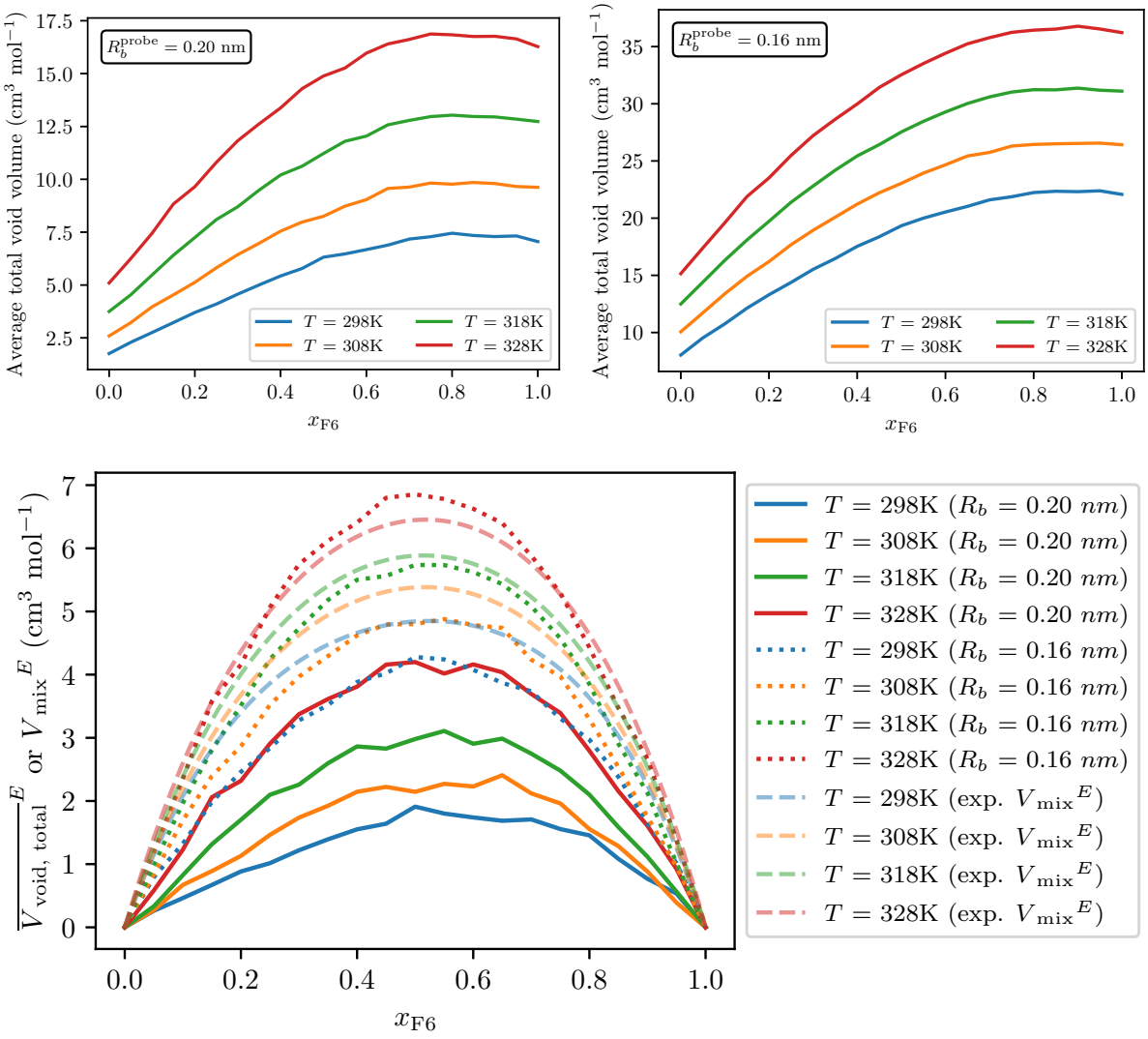

Figure 12.3: Average total void volume per mole as a function of the molar fraction of F6 (x_{F6}) in the simulated mixtures of F6+H6, for the different studied temperatures and $R_b^{\text{probe}} = 0.20$ nm (top left) or $R_b^{\text{probe}} = 0.16$ nm (top right). The bottom plot shows the excess average total void volume per mole ($\overline{V_{\text{void, total}}}^E$) as a function of x_{F6}, for the different studied temperatures and calculated from the MD simulation results (full line: $R_b^{\text{probe}} = 0.20$ nm; dotted line: $R_b^{\text{probe}} = 0.16$ nm), together with experimental data of excess volume of mixing (V_{mix}^E) of mixtures of F6+H6 as a function of x_{F6} and for different temperatures (dashed line; from ref. [1]).

Another way of interpreting these results is considering how much empty volume exists per molecule in the system, which is represented in Figure 12.3 (top). As mentioned above, this varies with T, x_{F6} and R_b^{probe} and ranges from about $2\,\mathrm{cm^3\,mol^{-1}}$ to about $35\,\mathrm{cm^3\,mol^{-1}}$, depending on those variables. These should be compared with the molar volume of pure H6 ($131.55\,\mathrm{cm^3\,mol^{-1}}$ [2]) and the molar volume of pure F6 ($201.64\,\mathrm{cm^3\,mol^{-1}}$ [2]). The trends described earlier are retrieved in these plots once more. Additionally, the excess average total void volume per mole ($\overline{V_{\mathrm{void,\,total}}}^E$), *i.e.* at a given x_{F6} the difference between the calculated $\overline{V_{\mathrm{void,\,total}}}$ and the average of the values obtained for the pure compounds, is represented in Figure 12.3 (bottom). It can be seen that $\overline{V_{\mathrm{void,\,total}}}^E$ is always positive for the entire range of x_{F6}, displaying an upside-down slightly-skewed (towards larger values of x_{F6}) shape for both $R_b^{\mathrm{probe}} = 0.20$ nm and $R_b^{\mathrm{probe}} = 0.16$ nm. It is also visible that $\overline{V_{\mathrm{void,\,total}}}^E$ increases with increasing T, for a fixed x_{F6}.

It has been suggested that the large excess volume of mixing (V_{mix}^E) observed for mixtures of F6+H6 is the result of alterations in the conformation of the molecules within the mixtures that causes a less efficient packing and, ultimately, the creation of interstitial voids among the molecules [31, 47]. The V_{mix}^E is an experimentally accessible quantity [1] and is represented in Figure 12.3 (bottom), for comparison. For both R_b^{probe} data sets, it can be said that the plots of $\overline{V_{\mathrm{void,\,total}}}^E$ as a function of x_{F6} have a curved shape resembling that of the experimental V_{mix}^E. Moreover, the order of magnitude of $\overline{V_{\mathrm{void,\,total}}}^E$ is comparable to that of V_{mix}^E, for both data sets. Quantitative comparisons should be made with caution and bearing in mind that the overlap of $\overline{V_{\mathrm{void,\,total}}}^E$ with V_{mix}^E would not be anticipated or, in the case it would happen, the corresponding R_b^{probe} would be somewhat arbitrary. Regardless, the fact that the shape of those curves is similar and the orders of magnitude of the values are the same are in line with the initial conjecture. It is indeed plausible that interstitial voids are created in excess for mixtures of F6+H6 and that those are of a physically significant size: as mentioned above, the choice of R_b^{probe} was made considering the size of small molecules that can "fit" and dissolve in the interstices of the studied liquids (*e.g.* H_2O, Xe, H_2, O_2, CO_2).

12.5.1.2 Characterisation of the morphology of the interstitial voids

Concerning the morphology and the volume occupied by each interstitial cavity or void, it is useful to recall that these are a construction of sets of interconnected void sites, within the framework of the Voronoi S-network. The distribution of the radii of the existing void sites in the simulated mixtures of F6+H6 provides a simple but useful characterisation of the size of these elementary cavities. These distributions are represented in Figure 12.4 as a function of x_{F6} at $T = 298\,\mathrm{K}$ (left) and as a function of T for $x_{\mathrm{F6}} = 0.50$ (right). It can be said that the shape of the distributions is bell-shaped and skewed, being the most common void site radii in the range 0.05 nm to 0.10 nm. Physically significant void sites (*i.e.* those with radii larger than about 0.12 nm to 0.16 nm [4, 5, 12]) are less common, in relative terms. Their proportion, however, increases with increasing x_{F6}, in line with the results presented above. It is curious to note that the proportion of the smallest voids (with close to null radii) also increases with increasing x_{F6}; this is a consequence of the winding of the F6 chains in a helix, which creates an interstice (a void site, by definition) between fluorine atoms bonded to consecutive carbon atoms. The effect of T on the void site radii distributions is also clear, in which the proportion of physically significant void sites increases with increasing T, also in line with the results presented above.

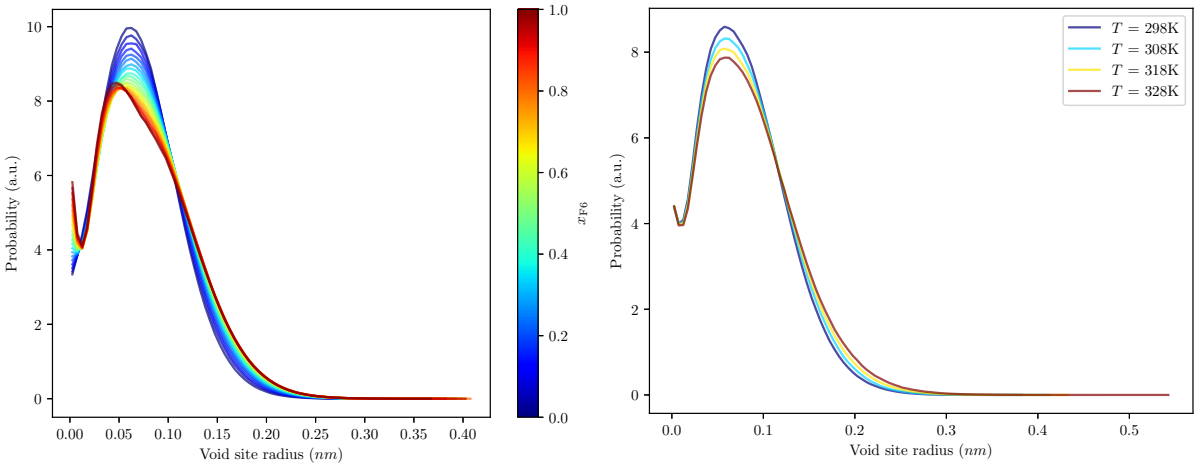

Figure 12.4: Distribution of void site radii as a function of: the molar fraction of F6 (x_{F6}) in the simulated mixtures of F6+H6 and at a constant temperature of $T = 298\,K$ (left); the T for a constant molar fraction of F6 of $x_{F6} = 0.50$ (right).

Figure 12.5 plots the average number of voids ($\overline{n_{voids}}$) in the simulated mixtures of F6+H6 normalised by the total number of molecules in the simulated systems (*i.e.* the average number of voids per molecule), as a function of x_{F6} and T. It can be observed that $\overline{n_{voids}}$ increases with increasing x_{F6} (albeit non-linearly) for both $R_b^{probe} = 0.20$ nm and $R_b^{probe} = 0.16$ nm, although for the former the curves appear to have a maximum for a x_{F6} in the range of 0.5 to 1. This means that, in general, the packing of the CF chains results in a less efficient occupation of space, in the sense that more voids of physically significant size are formed. As discussed above, the mutual incompatibility of the CH and CF chains may also result in the formation of interstitial gaps in excess that could explain the inverted curve shape of the plots (*i.e.* positive deviations from the straight line connecting the pure compounds' values). For both data sets, $\overline{n_{voids}}$ increases with T (at constant x_{F6}), although this behaviour is less clear for $R_b^{probe} = 0.16$ nm considering the overlap of the error (shaded) regions. This is coherent with the aforementioned effect related to the thermal expansion of the system.

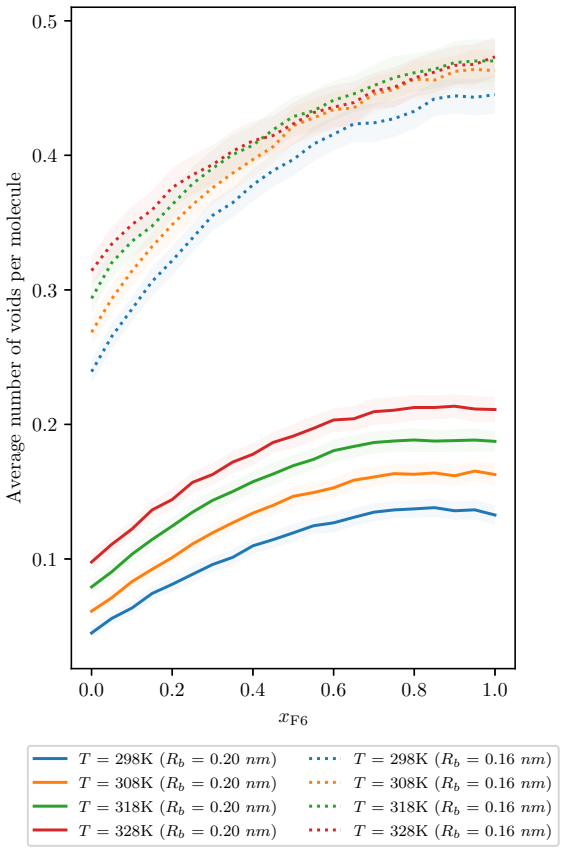

Figure 12.5: Average number of voids per molecule ($\overline{n_{voids}}$) in the simulated mixtures of F6+H6, as a function of the molar fraction of F6 (x_{F6}), for the different studied temperatures and $R_b^{probe} = 0.20$ nm or $R_b^{probe} = 0.16$ nm.

In interpreting the results presented in Figure 12.5, it should be stated that the number of interstitial cavities or voids found in a system will depend on the choice of R_b^{probe}: large values of R_b^{probe} will identify a small number of isolated clusters of void sites, corresponding to the most spacious voids of the system; conversely, decreasing R_b^{probe} will select more voids with more intricate and complex shapes. However, by continuing to decrease R_b^{probe}, the voids start to become interconnected and the void network is said to become percolated. There is a critical value of R_b^{probe} ($R_{b,\text{crit}}^{\text{probe}}$) for which the network is fully percolated and, in effect, only one void spanning the entire system exists [12]. $R_{b,\text{crit}}^{\text{probe}}$ varies from system to system (and, in the context of MD simulations, even the FF, as this will define the size of the atoms and the distances among them, thus the interstitial void network), but it usually takes values in the order of 0.8 nm to 0.9 nm (about half or lower than the values used in the analyses herein). This is indicative that although the process of dissolution of small molecules can be rationalised, at least in part, as the insertion of those molecules in preexisting, sufficiently large cavities among the molecules of solvent, the mechanism of diffusion (and particularly across lipid membranes) requires the interaction between the solute molecules that "push through" the solvent/lipid molecules due to thermal motion [12, 22].

The average volume per void ($\overline{V_{\text{void}}}$) is plotted in Figure 12.6 as a function of x_{F6} and T. For both $R_b^{\text{probe}} = 0.20$ nm and $R_b^{\text{probe}} = 0.16$ nm, $\overline{V_{\text{void}}}$ increases with x_{F6} and a subtle maximum may be discerned for some values of T. This is indicative that the presence of the CF chains results in the opening of more voluminous cavities with physical significance. $\overline{V_{\text{void}}}$ also increases with T, for a fixed x_{F6}. This means that the cavities formed in the systems are, on average, larger with increasing temperature, which is in line with the effects of thermal expansion mentioned above. Additionally, the choice of R_b^{probe} between the two tested values seems to result in the identification of voids with similar $\overline{V_{\text{void}}}$, as can be seen in Figure 12.6 (bottom). This suggests that, even though setting $R_b^{\text{probe}} = 0.16$ nm increases the number of identified voids compared to considering $R_b^{\text{probe}} = 0.20$ nm (*cf.* Figure 12.5), each individual void tends to have, on average, a similar total volume in either case.

Lastly, the morphology of the voids was characterised by the computation of the void sphericity (α), as defined in Equation 12.2. The results are presented in Figure 12.7 as a function of x_{F6} and T. It can be observed that α decreases with increasing x_{F6}, for both $R_b^{\text{probe}} = 0.20$ nm and $R_b^{\text{probe}} = 0.16$ nm, possibly stabilising on a constant value or displaying a shallow minimum for a x_{F6} above the equimolar composition, considering the error (shaded) regions. This means that the voids in systems with a higher content of F6 are less spherical and tend to have more complex shapes. For a given x_{F6}, increasing T decreases α, which can also be interpreted as a consequence of the thermal expansion of the systems: the creation of additional interstitial space on its own, but considering that the cavities will be more interconnected, may result in voids with more complex or elongated shapes, thus with lower α. Finally, at constant x_{F6} and T, the voids identified with $R_b^{\text{probe}} = 0.20$ nm are more spherical than those constructed with $R_b^{\text{probe}} = 0.16$ nm (*cf.* Figure 12.7, bottom). This is expected because the criterion $R_b^{\text{probe}} = 0.20$ nm selects fewer and less connected void sites, which thus tend to cluster closer together, compared to $R_b^{\text{probe}} = 0.16$ nm, ultimately resulting in the observed order in the α values.

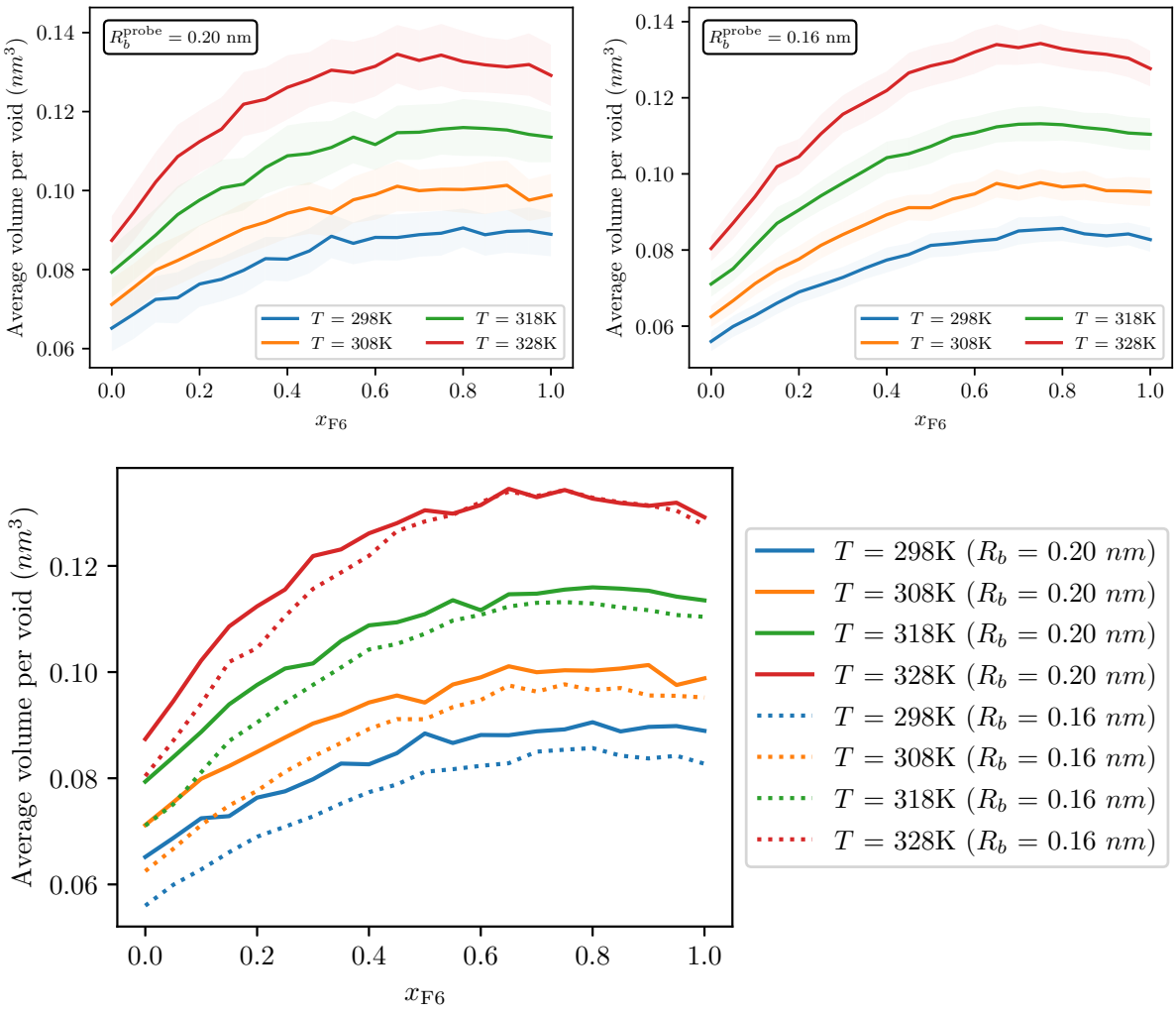

Figure 12.6: Average volume per void as a function of the molar fraction of F6 (x_{F6}) in the simulated mixtures of F6+H6, for the different studied temperatures and $R_b^{\text{probe}} = 0.20$ nm (top left) or $R_b^{\text{probe}} = 0.16$ nm (top right). The shaded area represents the interval corresponding to one standard deviation from the mean, calculated from the trajectory averages. The bottom plot shows both data sets on the same axes, for an easier comparison between them (the shaded areas are omitted for clarity).

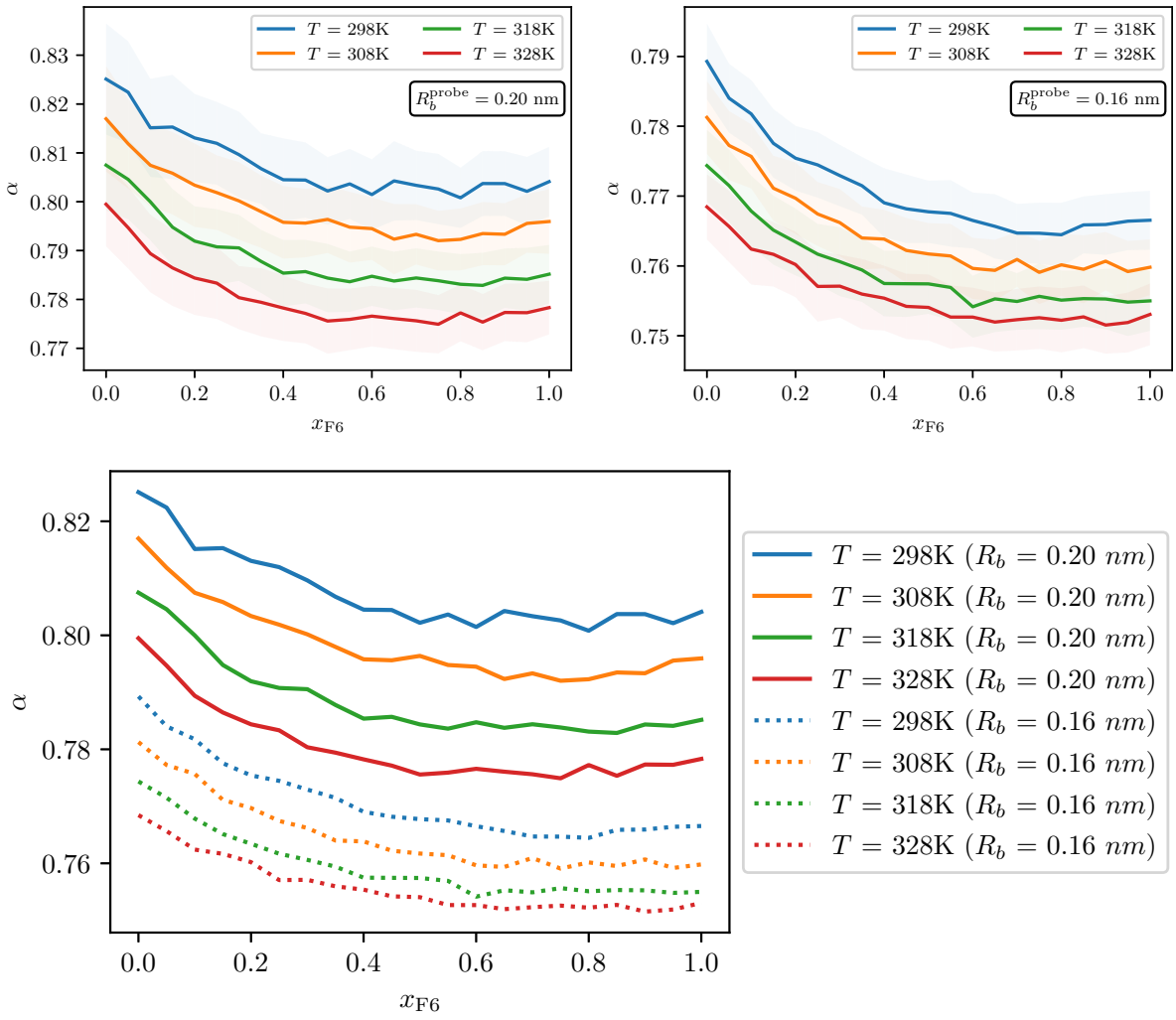

Figure 12.7: Average void sphericity (α) as a function of the molar fraction of F6 (x_{F6}) in the simulated mixtures of F6+H6, for the different studied temperatures and $R_b^{probe} = 0.20$ nm (top left) or $R_b^{probe} = 0.16$ nm (top right). The shaded area represents the interval corresponding to one standard deviation from the mean, calculated from the trajectory averages. The bottom plot shows both data sets on the same axes, for an easier comparison between them (the shaded areas are omitted for clarity).

Overall, taking together the results characterising $\overline{n_{\text{voids}}}$, $\overline{V_{\text{void}}}$ and α (Figures 12.5, 12.6 and 12.7, respectively), it seems that, for a given T, systems with increasing x_{F6} have not only more voids, but these tend to be larger and have more complex (less spherical) shapes. This results in the increase of $\overline{V_{\text{void, total}}}$ and $\overline{V_{\text{void, total}}}^{\text{norm}}$ observed in Figure 12.2. However, as noted before, the behaviour of these metrics is not linear with x_{F6} and is in line with the non-ideal behaviour of the mixtures of F6+H6.

In a more in-depth analysis, each void is characterised by its sphericity (α), void volume (V_{void}) and constituent number of Delaunay S-simplexes ($n_{\text{Delaunay S-simplexes}}$, identical to the number of void sites it comprises). To gain further insights into how these variables depend on one another, Figure 12.8 shows scatter plots of these variables two-by-two, the third variable being represented in a colour scale, for the system of pure H6 ($x_{\text{F6}} = 0.00$) simulated at $T = 298\,\text{K}$ and voids identified with $R_b^{\text{probe}} = 0.20$ nm (each point represents one void). Additional plots showing the results of this analysis for mixtures of F6+H6 with different compositions ($x_{\text{F6}} = 0.00$, $x_{\text{F6}} = 0.50$ and $x_{\text{F6}} = 1.00$) and for both $R_b^{\text{probe}} = 0.20$ nm (Figure D.1) and $R_b^{\text{probe}} = 0.16$ nm (Figure D.2) are presented in Appendix D. These plots clearly show that the majority of the voids found in the systems are small and more spherical. The larger voids tend to be the least spherical, but also those that evidently represent the largest and most significant interstitial cavities. Whilst α and V_{void} seem to be negatively correlated, the latter seems to be positively correlated and vary almost linearly with $n_{\text{Delaunay S-simplexes}}$. The conclusions drawn for systems with different compositions are similar and independent of the chosen value of R_b^{probe}.

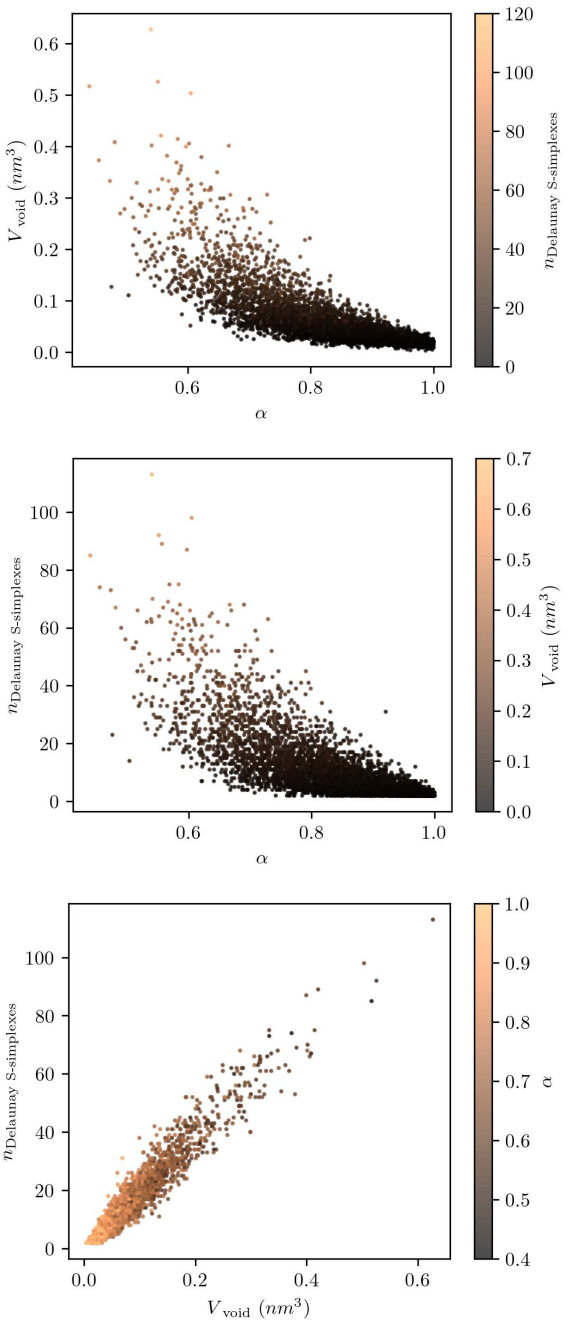

Figure 12.8: Scatter plots relating the void sphericity (α), void volume (V_{void}) and number of Delaunay S-simplexes ($n_{\text{Delaunay S-simplexes}}$) for the analyses of the interstitial void volume in MD simulations of pure liquid H6 ($x_{\text{F6}} = 0.00$) at 298.15 K for $R_b^{\text{probe}} = 0.20$ nm. Top: V_{void} as a function of α (colouring: $n_{\text{Delaunay S-simplexes}}$); middle: $n_{\text{Delaunay S-simplexes}}$ as a function of α (colouring: V_{void}); bottom: $n_{\text{Delaunay S-simplexes}}$ as a function of V_{void} (colouring: α).

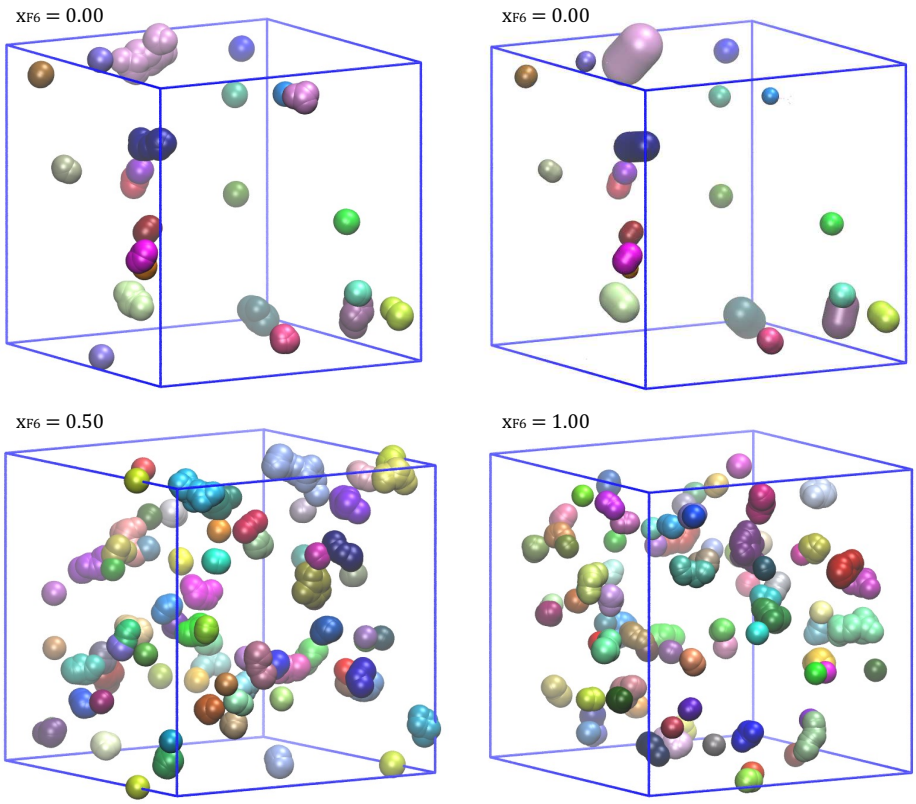

Figure 12.9: Snapshots of representative configurations of the mixtures of F6+H6 with $x_{\mathrm{F6}} = 0.00$ (pure H6; top row), $x_{\mathrm{F6}} = 0.50$ (bottom left) or $x_{\mathrm{F6}} = 1.00$ (pure F6; bottom right), simulated at $T = 298\,\mathrm{K}$, displaying the voids in these systems identified by R_b colouring with $R_b^{\mathrm{probe}} = 0.20$ nm. The F6 and H6 molecules are omitted for clarity. The void spherocylinders are illustrated for $x_{\mathrm{F6}} = 0.00$ (pure H6; top right); the remaining images represent the void sites in a spacefill model to scale. Each void spherocylinder and the corresponding set of void sites, in the different representations, are coloured differently.

Some snapshots illustrating the results discussed above are presented on Figure 12.9 (with additional ones presented in Appendix D in Figures D.3 and D.4). In this Figure, the void sites identified with the R_b colouring method with $R_b^{\mathrm{probe}} = 0.20$ nm are coloured according to the void they are part of. The voids have various shapes and are scattered across the simulation box. They appear more abundant for higher x_{F6}, in line with the average results presented above. An illustration of the representation of the voids as spherocylinders is also presented for $x_{\mathrm{F6}} = 0.00$ (Figure 12.9, top right). It should be highlighted that this representation carries some advantages, in general and for studies falling outside the scope of this work, namely because the spherocylinders are precisely located (they have a geometric centre) and oriented (they possess a direction of elongation) in space. In the present work, the analyses based on the location of the void sites, presented in the next few pages, were sufficient for the intended purposes. The void orientation was not explored because the studied systems do not present anisotropy (unlike lipid membranes, for instance). Finally, the snapshots obtained for $R_b^{\mathrm{probe}} = 0.16$ nm (Figure D.4) provide similar conclusions (Figure D.3 shows snapshots with explicit representation of the molecules, to illustrate the positioning of the voids relative to them).

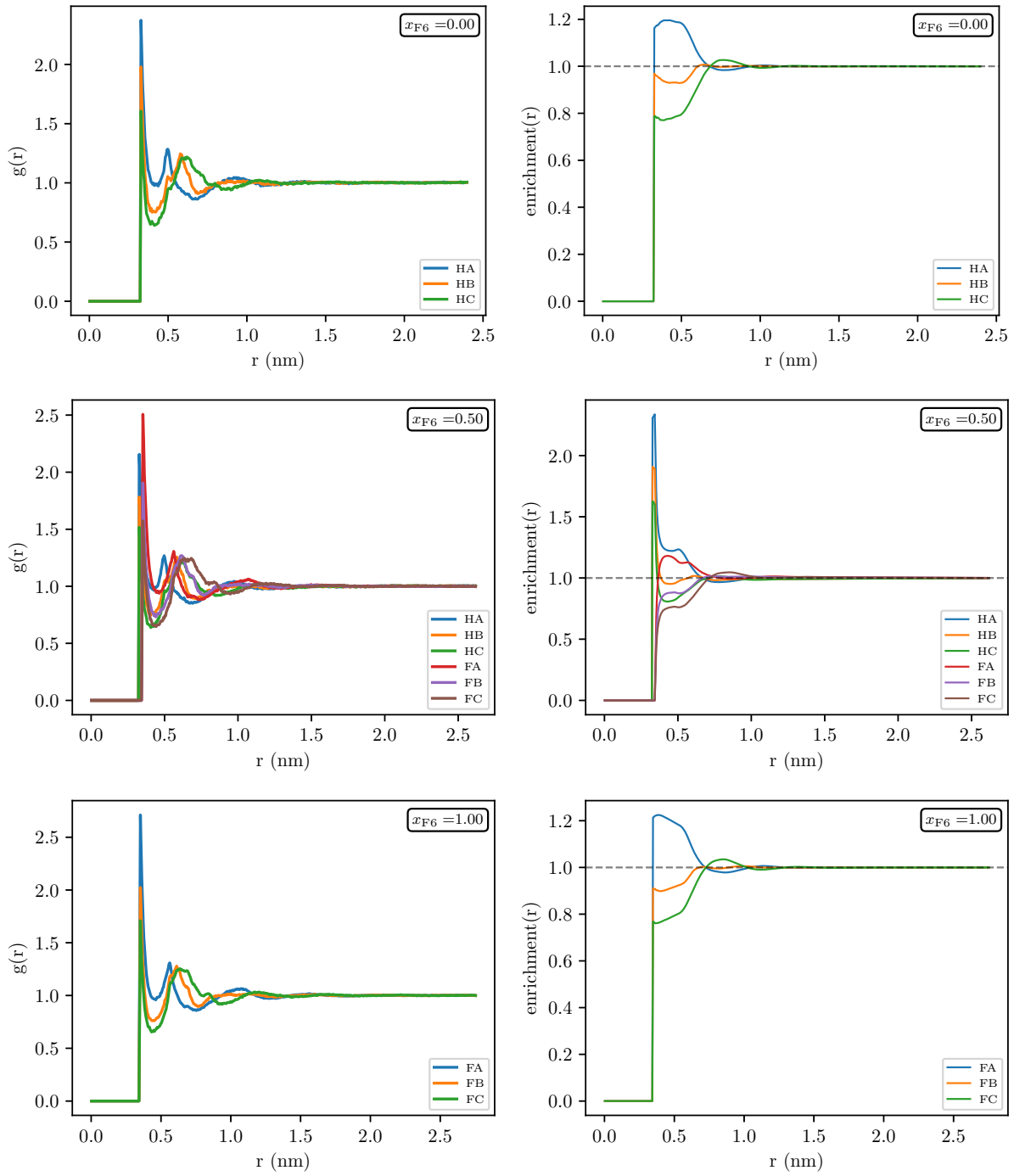

Figure 12.10: RDFs between the void sites having a radius $R_b \geq 0.20$ nm and the hydrogen or the fluorine atoms of F6 or of H6 for $x_{F6} = 0.00$ (pure H6; top left), $x_{F6} = 0.50$ (middle left) or $x_{F6} = 1.00$ (pure F6; bottom left), for $T = 298$ K. The right column shows the corresponding ratio of the local molar fraction of the hydrogen or fluorine atoms around the void sites and their bulk molar fraction (enrichment), as a function of the radial distance from the void sites. The nomenclature used to identify the atoms is presented in Figure 12.1.

12.5.1.3 Location of the interstitial voids in the system

In the previous paragraphs, the void volume and the morphology of the interstitial cavities in simulated mixtures of F6+H6 were discussed. This study aimed at further characterising the voids in these systems by identifying the preferential regions in space where they might be located, relative to the molecules in the system. In the following, some results concerning this matter are presented, based on the formalism of Radial Distribution Functions (RDFs). Most of the results below are based on the analysis of the voids with a physically significant size, identified according to the R_b colouring method with $R_b^{\text{probe}} = 0.20$ nm. This work was focused on the study of such "larger" voids and, as discussed below, the conclusions of the analysis are in essence (*i.e.* qualitatively, even if quantitative differences exist) independent of the choice of R_b^{probe}, for both tested values.

The RDFs between the void sites having a radius $R_b \geq 0.20$ nm and the hydrogen (resp. fluorine) atoms of H6 (resp. F6) in mixtures of F6+H6 with different x_{F6} and at $T = 298\,\text{K}$ are presented in Figure 12.10. The same picture also depicts the enrichment of each atom as a function of the radial distance to the void sites. The enrichment at a distance r of an atom X is obtained by counting the number of atoms of type X that are inside the sphere of radius r centred on a void site and calculating the corresponding mole fraction, repeating the operation for all void sites and averaging the results. This is compared with the average mole fraction of the atom X in the simulation box by computing the ratio between the two quantities (*i.e.* the enrichment). If the void sites (being regarded here as surrogates for the location of the voids *per si*) didn't show any preferential location within the liquid mixture, the enrichment of all atoms should be similar and close to unity. Conversely, this quantity is higher if the void sites are located preferentially near the atom in question [48]. For the pure liquids, it is clear that the first and most intense peak in the calculated RDFs corresponds to the atoms in the chains' termini (HA for H6 and FA for F6). The second and third peaks correspond to the atoms bonded to the second and third carbon atoms in those chains (Hb and HC for H6, FB and FC for F6, respectively). The plots depicting the enrichment for these systems corroborate these observations, meaning that void sites with a radius $R_b \geq 0.20$ nm (and thus large voids) are located preferentially near the termini of the F6 and H6 chains in the pure liquids, then near the second to terminal carbon atom and finally in the middle of the chains.

For the mixed systems, the interpretation is not as direct due to a peculiarity in how the void sites are defined and identified. A void site, by definition, represents the largest empty sphere inscribed among (and tangent to) a set of 4 atoms. Because the hydrogen atoms have a smaller LJ parameter σ than fluorine atoms ($\sigma_{\text{H}} < \sigma_{\text{F}}$), the distance between the centre of an empty sphere of radius R_b and a hydrogen atom tangent to it will be smaller than the distance between the centre of the same sphere and centre of a fluorine atom tangent to it. This translates into the contact peak in the RDFs calculated for the mixtures of F6+H6 being shifted to smaller distances if these are calculated between a void site and a hydrogen atom, compared to those calculated involving a fluorine atom. Because of this, the enrichment plots start at smaller distances and at higher values for the hydrogen atoms of H6 compared to the fluorine atoms of F6, in F6+H6 mixtures. That said, a judicious interpretation of the plots of the enrichment around void sites is still possible. In the case of the equimolar mixture, represented in Figure 12.10, the largest

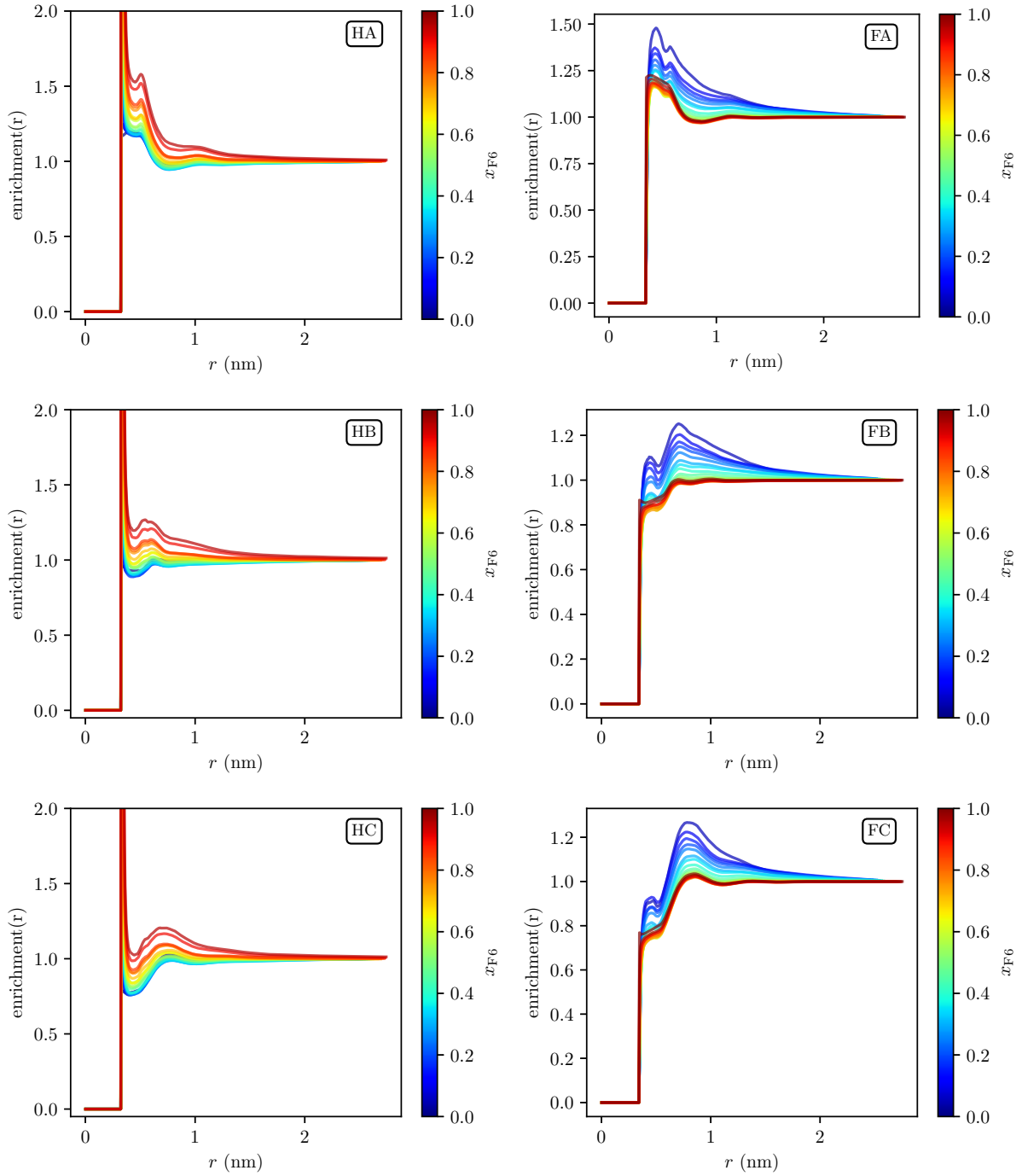

Figure 12.11: Ratio of the local molar fraction of the hydrogenated atoms HA (top left), HB (middle left) and HC (bottom left) of H6 and the fluorinated atoms FA (top right), FB (middle right) and FC (bottom right) of F6 around the void sites and their respective bulk molar fractions (enrichment), as a function of the radial distance from the void sites and for different values of composition (x_{F6}) of the system, for the simulated mixtures of F6+H6 at a temperature $T = 298\,\mathrm{K}$ and for void sites with a radius $R_b \geq 0.20$ nm. The nomenclature used to identify the atoms is presented in Figure 12.1. The corresponding RDFs are presented in Figure D.5 in Appendix D.

enrichment for short distances (*i.e.* reasoning analogously to the coordination sphere [48] of the void sites) corresponds to the atom HA of H6, followed by the atom FA of F6 and then the atoms nearing the middle of the chains of either molecule. Taken together, it can be said that large voids tend to be located at the termini of the chains in mixtures of F6+H6.

Considering the effect of varying x_{F6} on the location of large voids, Figure 12.11 shows the plots of the enrichment around the void sites in hydrogen atoms of H6 (left) and in fluorine atoms of F6 (right), for different values of x_{F6} and at a constant temperature of $T = 298\,\mathrm{K}$, in the simulated mixtures of F6+H6 (the corresponding RDFs are presented in Figure D.5 in Appendix D). It can be observed that, for a given atom and for short distances (analogously of the coordination sphere of the void sites), the enrichment generally increases with decreasing molar fraction of the atom in the bulk. For example, the enrichment in HA around the void sites increases with increasing x_{F6}, whereas the enrichment in FA around the void sites increases with decreasing x_{F6}. This means that the voids are preferentially located near the scarcer molecules in the mixture. This can be interpreted considering that for the mixtures of F6+H6 at the extremes of x_{F6}, the relative impact of adding one molecule of the minority component is more significant that in mixtures near the equimolar composition. In other words, the chemical environment surrounding a molecule of H6 (respectively F6) infinitely diluted in F6 (respectively H6) is the most different it can be in those mixtures, which accentuates the differences in behaviour of both molecules. This can be interpreted by recalling the discussion above concerning the reasoning of the existence of extra void space in mixtures of F6+H6 related to the non-ideal behaviour of these systems (and their large and positive V^{E}_{mix}). Moreover, it is known that *n*-As dissolved in PFA solutions tend to "coil" or preferentially adopt more globular conformations [31], which could be anticipated to originate more packing defects in solution, and thus more and/or larger interstitial voids. Conversely, it has been shown that the partial molar volume at infinite dilution of PFAs in *n*-As (specifically of F6 in H8) is about 10 % larger than the molar volume of the pure PFAs [49]. This can also be interpreted as an effect of the mutual phobicity of the two types of chains, which ultimately originates more and/or larger cavities among the molecules.

One extra comment should be made, at this point, concerning some choices made for the implementation of the analyses. The analyses presented herein are based on the location of the hydrogen or fluorine atoms in the H6 and F6 molecules. However, the same reasoning could be applied based on the corresponding carbon atoms instead. Moreover, the choice of R_b^{probe} affects the identification of the interstitial voids, and may thus condition the conclusions drawn from the analyses. The plots of the enrichment around the void sites in hydrogen, fluorine and carbon atoms of H6 or F6 in the simulated mixtures of F6+H6, for different values of x_{F6} and at a constant temperature of $T = 298\,\mathrm{K}$, have been computed and are presented in Appendix D in Figures D.6 and D.7 (the corresponding RDFs are presented in Figures D.8 and D.9). The choice between $R_b^{\mathrm{probe}} = 0.20$ nm and $R_b^{\mathrm{probe}} = 0.16$ nm originates plots that are qualitatively similar (in particular, the order of the curves is essentially the same, when analysing the dependency on x_{F6}). Moreover, the trends observed for the results calculated for a given carbon atom are similar to those observed for the hydrogen or fluorine atoms bonded to it. The reasoning based on the data collected for hydrogen or fluorine atoms presents the added advantage, compared to reasoning based on the data obtained for the carbon atoms, that those atoms are more exposed

to the environment surrounding the molecules. This means that the voids and the void sites are in more direct contact (from a mathematical perspective) with fluorine and hydrogen atoms compared to the carbon atoms, which facilitates in particular the interpretation of the results and the determination of the preferential location of the voids from the RDFs and the enrichment plots. Therefore, the choice of R_b^{probe} for the selection of large interstitial voids and the choice of the reference atoms for the characterisation of the location of those voids has been validated and was kept throughout the rest of the analyses.

The effect of varying T on the preferential location of large voids was also assessed. Figure 12.12 shows the plots of the enrichment around the void sites in HA atoms of H6 (top) and in FA atoms of F6 (bottom), for the mixtures of F6+H6 with a fixed composition of $x_{\text{F6}} = 0.50$ simulated at different values of T (the corresponding RDFs are presented in Figure D.10, in Appendix D). T seems to have a very mild effect on the preferential location of large voids, as it can be seen that the plots in Figure 12.12 are practically overlapping. For short distances, only a very small increase (respectively decrease) in enrichment is observed with increasing temperature for HA (respectively FA). Similar conclusions were drawn when analysing results from simulations with different x_{F6} and for different atoms (data not shown). This is a probable indication that the thermal expansion of the systems occurs as a whole and the extra interstitial space originating from such phenomenon is more or less evenly distributed in space.

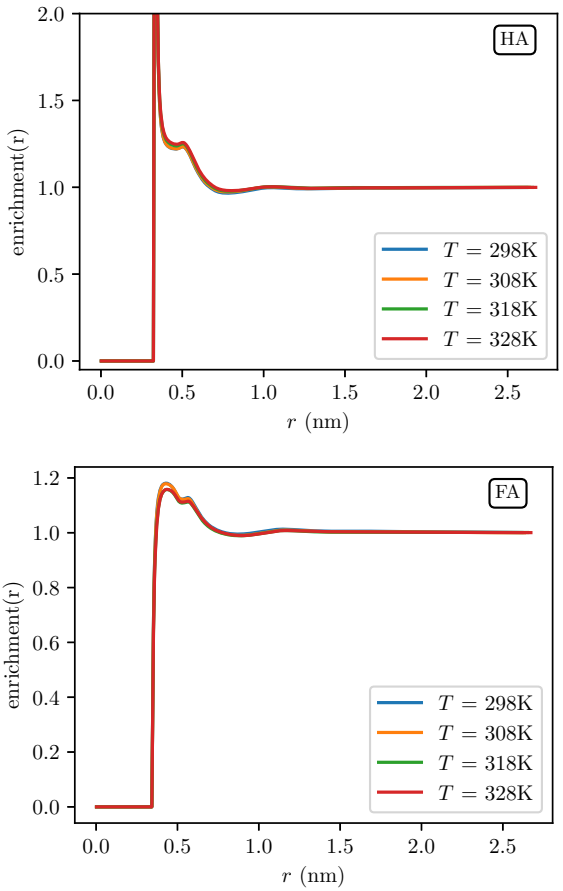

Figure 12.12: Ratio of the local molar fraction of the atoms HA of H6 (top) and FA of F6 (bottom) around the void sites and their respective bulk molar fractions (enrichment), as a function of the radial distance from the void sites and for different values of temperature, for the mixture of F6+H6 with composition $x_{\text{F6}} = 0.50$ and for void sites having a radius $R_b \geq 0.20$ nm. The nomenclature used to identify the atoms is presented in Figure 12.1. The corresponding RDFs are presented in Figure D.10 in Appendix D.

One last analysis was performed to get further insights on the correlation between the size of the void sites and their preferential location in space for mixtures of F6+H6. The rationale behind this was to get a more general picture of the spatial distribution of the interstitial void space in a broader sense, and not just one limited to the location of voids of physically significant size. In this regard, the enrichment around the void sites in hydrogen atoms of H6 (Figure 12.13) and in fluorine atoms of F6 (Figure 12.14), for the mixtures of F6+H6 with a fixed composition of $x_{\text{F6}} = 0.50$ simulated at $T = 298\,\text{K}$, were computed based on different selections of void

sites whose radii were classified (sliced) in ranges or bins of 0.1 nm (the corresponding RDFs are presented in Figures D.11 and D.12 in Appendix D, respectively for the hydrogen atoms of H6 and for the fluorine atoms of F6). In other words, the void sites having a radius R_i in the range of 0.0 nm to 0.1 nm were selected and the enrichment calculations were performed for this slice, and the same was done separately for void sites with R_i in the range of 0.1 nm to 0.2 nm and so on. The last slice contains the voids with $R_i \geq 0.20$ nm, which corresponds to the data set obtained earlier for $R_b^{\text{probe}} = 0.20$ nm. As mentioned before, because the void sites are tangent to the atoms, by definition, the contact peak in the RDF and enrichment plots appears at a well defined distance for each of the slices corresponding to the sum of an atom's radius (or, more specifically, half its LJ σ_i parameter) and the lower boundary of the range of R_i for that slice. This way, to make comparisons easier, the plots in Figures 12.13 and 12.14 (as well as those in Figures D.11 and D.12) were laterally shifted so that the contact peaks are coincident. Additionally, the plots are presented in duplicate, with the colouring of the curves corresponding to each slice in reverse order, for improved readability.

Taking the previous remarks into consideration, the atoms in the termini of the chains (HA and FA) have larger void sites located near them, for short distances: analysing the sequence of slices in decreasing order of R_i for these atoms, the enrichment is highest for $R_i \geq 0.20$ nm and gradually decreases with decreasing R_i. The opposite trend is observed for the atoms HB and FB and even more so for HC and FC. Taken together, these corroborate the results presented above, inasmuch as the largest interstitial voids in the F6+H6 mixtures tend to be located near the chains' termini. Moreover, the interstitial voids that exist near the atoms in the middle of the chains tend to be smaller in size and less physically significant. It should be remarked that the information presented in these Figures is illustrative and representative of the overall trends found for other studied systems at different x_{F6} (data not shown). The existence of large interstitial voids, and especially near the termini of the chains, might explain at least in part the preferential solubilisation of small solutes such as H_2O [48] and Xe [50, 51] in mixtures of F6+H6 in those locations: they are more spacious in the first place to accommodate the solute molecules. Evidently, the analyses performed herein are based just on volumetric arguments and other factors (*e.g.* energetic) should be considered in interpreting solubility and other results.

12.5.2 Perfluorohexylhexane (F6H6) and perfluorooctylbromide (F8Br)

After the benchmark studies focused on the mixtures of F6+H6, the study of the interstitial void space was extended to the systems of liquid F6H6 and of liquid F8Br, which were simulated at $T = 298$ K only. These molecules were chosen for 2 reasons: first, for fundamental reasons and in connection to the rest of the work presented in this thesis (both are highly fluorinated molecules, one of them is a PFAA); second, based on their current and potential uses in the biomedical field, in ophtalmologic and blood substitute formulations, the characterisation of these systems carries practical relevance.

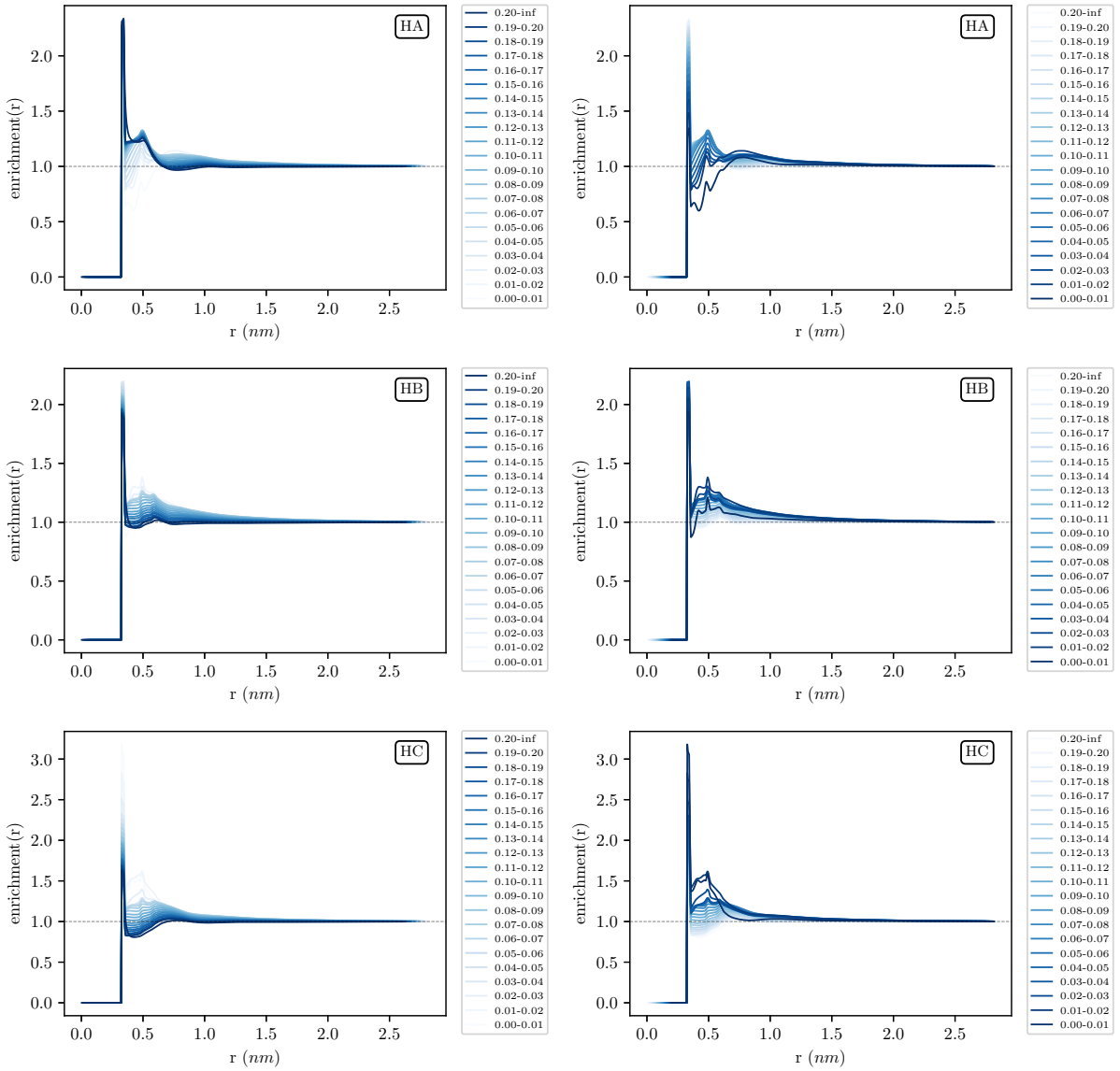

Figure 12.13: Ratio of the local molar fraction of the atoms HA (top row), HB (middle row) and HC (bottom row) around the void sites and their bulk molar fraction (enrichment), as a function of the radial distance from the void sites and for different (sliced) void site radii ranges, for the simulated mixtures of F6+H6 with molar composition $x_{\mathrm{F6}} = 0.50$ and at a temperature $T = 298\,\mathrm{K}$. The plots on both columns contain exactly the same information, but with reverse colour coding: dark to light (left) and light to dark (right), for decreasing order of void site radii ranges. The nomenclature used to identify the atoms is presented in Figure 12.1. The curves in each plot have been laterally shifted so that the contact peaks are coincident (see text for further details). The corresponding RDFs are presented in Figure D.11 in Appendix D.

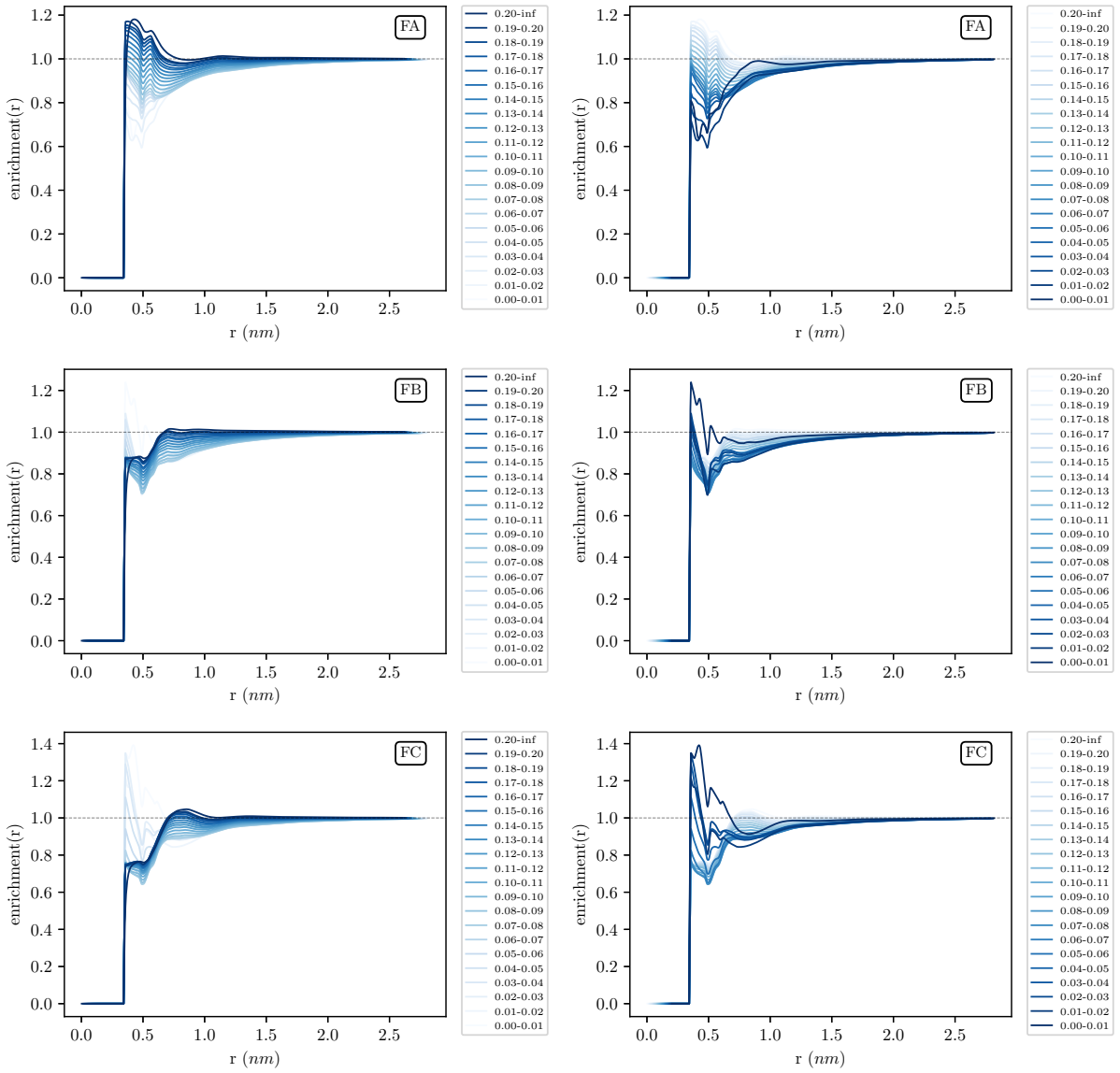

Figure 12.14: Ratio of the local molar fraction of the atoms FA (top row), FB (middle row) and FC (bottom row) around the void sites and their bulk molar fraction (enrichment), as a function of the radial distance from the void sites and for different (sliced) void site radii ranges, for the simulated mixtures of F6+H6 with molar composition $x_{\mathrm{F6}} = 0.50$ and at a temperature $T = 298\,\mathrm{K}$. The plots on both columns contain exactly the same information, but with reverse colour coding: dark to light (left) and light to dark (right), for decreasing order of void site radii ranges. The nomenclature used to identify the atoms is presented in Figure 12.1. The curves in each plot have been laterally shifted so that the contact peaks are coincident (see text for further details). The corresponding RDFs are presented in Figure D.12 in Appendix D.

12.5.2.1 Total void volume and morphology of the interstitial voids

The distributions of the void site radii, computed for the pure F6H6 and pure F8Br at $T = 298\,\mathrm{K}$, are presented in Figure 12.15, together with the analogous distributions for the F6+H6 mixture at the same temperature and for $x_{\mathrm{F6}} = 0.00$, $x_{\mathrm{F6}} = 0.50$ and $x_{\mathrm{F6}} = 1.0$. The distributions display a bell shaped that is similar to the ones reported above, and the peak of the distributions for F6H6 and F8Br occurs near the same range (0.05 nm to 0.10 nm). Curiously, the overall shape of the curve for F6H6 is very similar to the one obtained for pure H6 ($x_{\mathrm{F6}} = 0.00$), except for void sites with near-zero radius. This is intriguing, as it seems that the existence of a fluorinated chain in this case fails to create a higher proportion of interstitial cavities of large dimensions, compared to a mixture of F6+H6 with $x_{\mathrm{F6}} = 0.50$ (*a priori*, the system that would serve as a base for comparison, given that the ratio of CH chains to CF chains is the same as for F6H6). It has been suggested that the chemical bond between the CF and CH chains in PFAAs precludes the relief of their mutual incompatibility by macro-phase separation [52]. In this context, the added cohesiveness that results from the chemical merge of those chains might hinder the formation of large interstitial cavities in liquid F6H6. In the case of F8Br, its void site radii distribution broadly follows the same trends as the curve shown for pure F6 ($x_{\mathrm{F6}} = 1.00$). The fact that pure F6 and F8Br present similar results is unsurprising, given the similarities in the molecular structure of both compounds. The existence of a relatively high number of void sites with near-zero radius is observable for both F6H6 and F8Br, a result which is linked to the aforementioned phenomenon of winding of the CF chains. It should be noted that the proportion of physically significant void sites (recalling these are represented by the tail of the distribution to the right of values in the range of 0.12 nm to 0.16 nm) is remarkable for F8Br and, to a lesser extend, F6H6.

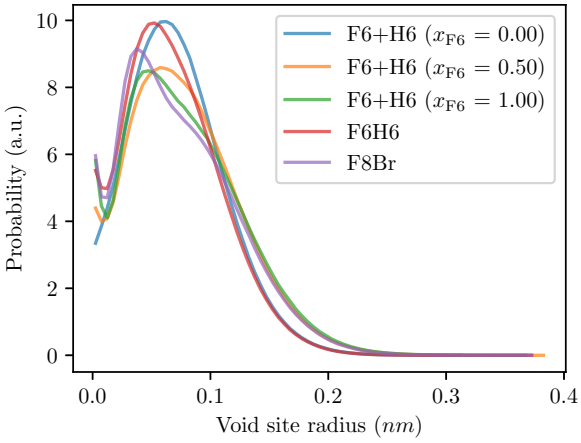

Figure 12.15: Distribution of void site radii at the constant temperature of $T = 298\,\mathrm{K}$ for the simulated systems of mixtures of F6+H6 with compositions $x_{\mathrm{F6}} = 0.00$, $x_{\mathrm{F6}} = 0.50$ and $x_{\mathrm{F6}} = 1.0$, pure F6H6 and pure F8Br.

The average values of fraction of total void volume ($\overline{V_{\mathrm{void,\,total}}}$), average total void volume per mole ($\overline{V_{\mathrm{void,\,total}}}$), average volume per void ($\overline{V_{\mathrm{void}}}$) and average void sphericity ($\overline{\alpha}$) were computed for the pure F6H6 and pure F8Br systems, based on the data collected for voids identified using the R_b colouring method with either $R_b^{\mathrm{probe}} = 0.20$ nm or $R_b^{\mathrm{probe}} = 0.16$ nm. These values are compiled on Table 12.1, together with the values of the same metrics obtained for the mixtures of F6+H6 with compositions $x_{\mathrm{F6}} = 0.00$, $x_{\mathrm{F6}} = 0.50$ and $x_{\mathrm{F6}} = 1.00$, for comparison.

For F6H6, it is clear that the fraction of $\overline{V_{\mathrm{void,\,total}}}$ is the lowest reported for the studied systems. In particular, comparing the systems of pure F6H6 and pure H6 ($x_{\mathrm{F6}} = 0.00$), given the highlighted similarities in their void site radii distributions, the interstitial void volume equates to about $(1.07 \pm 0.13)\,\%$ of the total volume for F6H6, compared to $(1.32 \pm 0.32)\,\%$ for H6 (for $R_b^{\mathrm{probe}} = 0.20$ nm). However, when comparing the molar value of $\overline{V_{\mathrm{void,\,total}}}$ and

Table 12.1: Compilation of average results obtained for the systems simulated at $T = 298\,\mathrm{K}$ of pure F6H6 and pure F8Br together with a recap of some results obtained for the systems of mixtures of F6+H6 with compositions $x_{\mathrm{F6}} = 0.00$, $x_{\mathrm{F6}} = 0.50$ and $x_{\mathrm{F6}} = 1.00$, for comparison. The values of the average fraction of total void volume ($\overline{V_{\mathrm{void,\,total}}}$), average total void volume per mole ($\overline{V_{\mathrm{void,\,total}}}$), average volume per void ($\overline{V_{\mathrm{void}}}$) and average void sphericity ($\overline{\alpha}$) are presented and are based on the data collected for voids identified using the R_b colouring method with either $R_b^{\mathrm{probe}} = 0.20$ nm or $R_b^{\mathrm{probe}} = 0.16$ nm.

R_b^{probe} (nm)	System	Fraction of $\overline{V_{\mathrm{void,\,total}}}$	$\overline{V_{\mathrm{void,\,total}}}$ ($\mathrm{cm^3\,mol^{-1}}$)	$\overline{V_{\mathrm{void}}}$ ($\mathrm{nm^3}$)	$\overline{\alpha}$
0.20	F8Br	0.0294 ± 0.0027	7.6 ± 0.7	0.0875 ± 0.0089	0.807 ± 0.018
	F6H6	0.0107 ± 0.0013	3.1 ± 0.4	0.0660 ± 0.0066	0.831 ± 0.012
	F6+H6 ($x_{\mathrm{F6}} = 0.00$)	0.0132 ± 0.0032	1.8 ± 0.4	0.0652 ± 0.0117	0.825 ± 0.023
	F6+H6 ($x_{\mathrm{F6}} = 0.50$)	0.0366 ± 0.0043	6.3 ± 0.7	0.0884 ± 0.0112	0.802 ± 0.014
	F6+H6 ($x_{\mathrm{F6}} = 1.00$)	0.0350 ± 0.0040	7.1 ± 0.8	0.0889 ± 0.0111	0.804 ± 0.014
0.16	F8Br	0.0958 ± 0.0032	12.4 ± 0.4	0.0803 ± 0.0053	0.770 ± 0.008
	F6H6	0.0514 ± 0.0019	15.1 ± 0.5	0.0560 ± 0.0025	0.792 ± 0.006
	F6+H6 ($x_{\mathrm{F6}} = 0.00$)	0.0604 ± 0.0042	8.0 ± 0.6	0.0560 ± 0.0052	0.789 ± 0.011
	F6+H6 ($x_{\mathrm{F6}} = 0.50$)	0.1120 ± 0.0045	19.3 ± 0.8	0.0812 ± 0.0063	0.768 ± 0.009
	F6+H6 ($x_{\mathrm{F6}} = 1.00$)	0.1097 ± 0.0039	22.1 ± 0.8	0.0827 ± 0.0064	0.767 ± 0.008

simply because the molecular volume of F6H6 is larger than that of H6, the order is reversed: $(3.1 \pm 0.4)\,\mathrm{cm^3\,mol^{-1}}$ for F6H6, versus $(1.8 \pm 0.4)\,\mathrm{cm^3\,mol^{-1}}$ for H6. In terms of void morphology, the voids in F6H6 tend to be smaller and more spherical, compared to the remaining systems (*cf.* Table 12.1). This can be rationalised recalling that larger void sites are scarcer for F6H6 (*cf.* Figure 12.15) and so their connectivity may be impaired. This results in smaller voids (thus the lower $\overline{V_{\mathrm{void}}}$) comprising fewer voids sites that should cluster closer together (thus the higher $\overline{\alpha}$).

In the case of F8Br, the average results for the different metrics show similarities with pure F6 ($x_{\mathrm{F6}} = 1.00$). At this point, the existence of large interstitial cavities among fluorinated molecules molecules has been established, and the fact that these two systems share similar trends in the analyses (*cf.* Table 12.1) should thus not come as a surprise. However, as is explored below, the asymmetry in the molecular structure due to the presence of a Br atom in F8Br (compared to F6, which can be said to be end-to-end symmetric) has important consequences in the preferential location of the voids in this system.

The reasoning presented above for the systems of F6H6 and F8Br is in line with the results obtained regardless of the value of R_b^{probe} used. However, as explained before, reducing R_b^{probe} in the analyses results in an increased fraction of $\overline{V_{\mathrm{void,\,total}}}$ (and $\overline{V_{\mathrm{void,\,total}}}$ itself) and decreased $\overline{V_{\mathrm{void}}}$ and $\overline{\alpha}$. This stems from the fact that, evidently, more void sites are accessible to a probe if $R_b^{\mathrm{probe}} = 0.16$ nm than if $R_b^{\mathrm{probe}} = 0.20$ nm, and the number of voids in the first case is also anticipated (provided $R_b^{\mathrm{probe}} > R_{b,\mathrm{crit}}^{\mathrm{probe}}$) to be higher than in the second case. This is illustrated in the snapshots presented in Figure 12.16, for both the F6H6 and the F8Br systems.

12.5.2.2 Location of the interstitial voids in the system

To assess the location of large void sites in the pure F6H6 and pure F8Br systems, the RDFs between the void sites having a radius $R_b \geq 0.20$ nm and the hydrogen or the fluorine atoms of F6H6 (respectively the fluorine atoms of F8Br) were computed and are presented in Figure 12.17. The corresponding plots depicting the enrichment of those atoms around the void sites are also featured in the same figure.

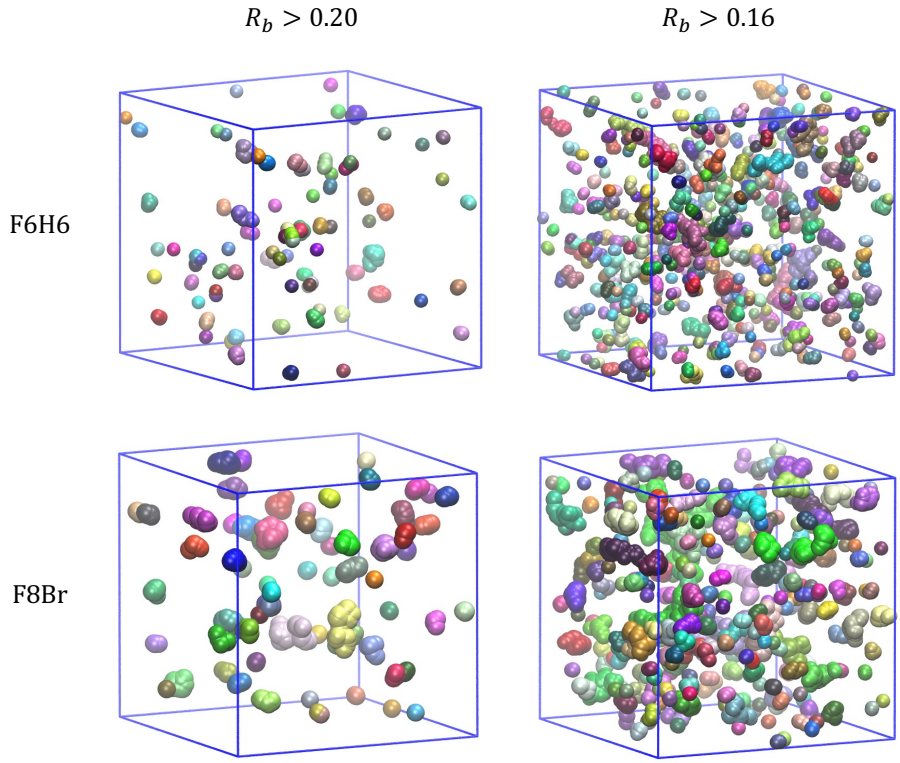

Figure 12.16: Snapshots of representative configurations of the simulated systems of pure F6H6 (top row) and of pure F8Br (bottom row), showcasing the voids in these systems identified by R_b colouring with $R_b^{\text{probe}} = 0.20$ nm (left column) or $R_b^{\text{probe}} = 0.16$ nm (right column). The F6H6 and F8Br molecules are omitted for clarity. The void sites are represented in a spacefill model to scale. Each set of void sites constituting one same void is coloured differently.

Considering the results presented for the F6H6 system, it can be said that, for short distances (once more in an analogy to the coordination sphere of small solutes), the void sites are located preferentially near the hydrogen or fluorine atoms in the following order: HA ≈ FA > HB > FB > HC > FC > HD > FF > FE > FD ≈ HE > HF. This means that large voids are located preferentially near the -CH_3 and -CF_3 termini of F6H6, similarly to what was observed for the mixtures of F6+H6. Moreover, large voids are relatively less likely to be located near the atoms in the middle of the chain, although the enrichment calculated for the central atoms of the CF chain seems slightly higher compared to that for the equivalent atoms of the CH chain.

In the case of F8Br, for short distances, the preferential location of large void sites is near the atoms in the order: FH > FA > FG > FB > FF ≈ FC > FE ≈ FD. Again, this is in line with large voids being preferentially located near the molecules' termini. However, because there is a Br atom bonded to one of the terminal carbon atoms (CFA) in F8Br, the termini are not equivalent and the large voids are preferentially located near the -CF_3 terminus (FH) compared to the -CF_2Br terminus (FA). This can be rationalised considering that, in the latter case, a fluorine atom is replaced with a Br atom, which has a larger atomic radius (compare $\sigma_{\text{Br}} = 0.384\,\text{nm}$ with $\sigma_{\text{F}} = 0.295\,\text{nm}$). This can be anticipated to condition the molecular packing and hinder, to some extent, the formation of interstitial cavities in the -CF_2Br terminus relative to the -CF_3 terminus. Finally, the preferential location of large void sites near the remaining fluorine atoms decreases approximately regularly from the termini towards the centre of the F8Br molecules.

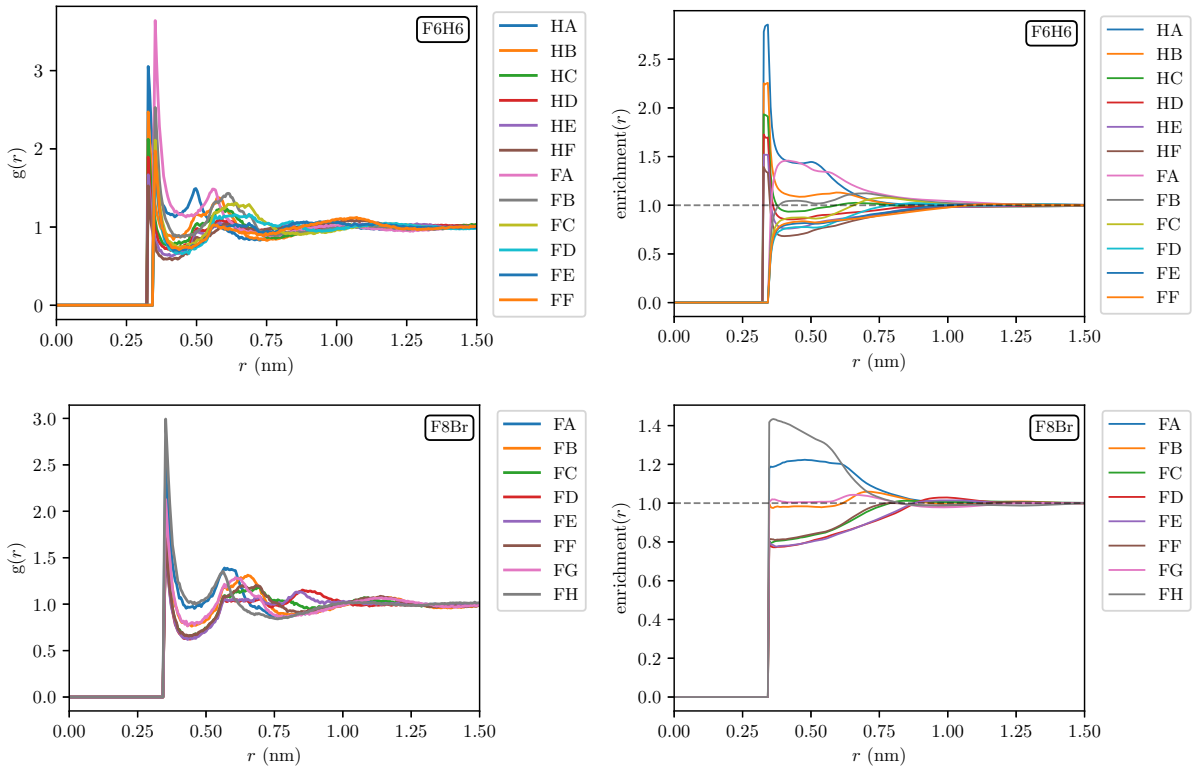

Figure 12.17: RDFs between the void sites having a radius $R_b \geq 0.20$ nm and the hydrogen or the fluorine atoms of F6H6 (top left) and between the void sites and the fluorine atoms of F8Br (bottom left). The right column shows the corresponding ratio of the local molar fraction of the hydrogen or fluorine atoms around the void sites and their bulk molar fraction (enrichment), as a function of the radial distance from the void sites. The nomenclature used to identify the atoms is presented in Figure 12.1.

Similarly to the F6+H6 mixtures, one final analysis was conducted to assess the location of voids of different sizes in pure F6H6 and pure F8Br. Figure 12.18 shows the enrichment around the void sites in some selected atoms (FA, FF, HA and HF) of F6H6 calculated for void sites classified (sliced) in ranges or bins of 0.1 nm. The complete set of plots of enrichment around the void sites in each fluorine atom and in each hydrogen atom of F6H6 is presented in Appendix D in Figures D.13, D.14, D.15 and D.16 (the corresponding RDFs are presented in Figures D.17, D.18, D.19 and D.20, respectively). From these plots, it is clear that large voids tend to be located near the atoms in the molecules' termini (FA and HA), whereas smaller, less physically significant voids can be found preferentially near the atoms in the middle of the chain. These results are in line with and expand the ones presented above.

Figure 12.19 shows the enrichment around the void sites in some selected atoms (FA, FD and FF) of F8Br calculated for void sites classified (sliced) in ranges or bins of 0.1 nm. The complete set of plots of enrichment around the void sites in each fluorine atom of F8Br is presented in Appendix D in Figures D.21 and D.22 (the corresponding RDFs are presented in Figures D.23 and D.24). In line with what was noted before, these results show that the larger interstitial voids are located preferentially near the termini (FA and FH) of the F8Br chains, with a slightly higher preference towards the non-brominated terminus (FH). The smaller and less physically significant voids tend to be located near the middle of the chains.

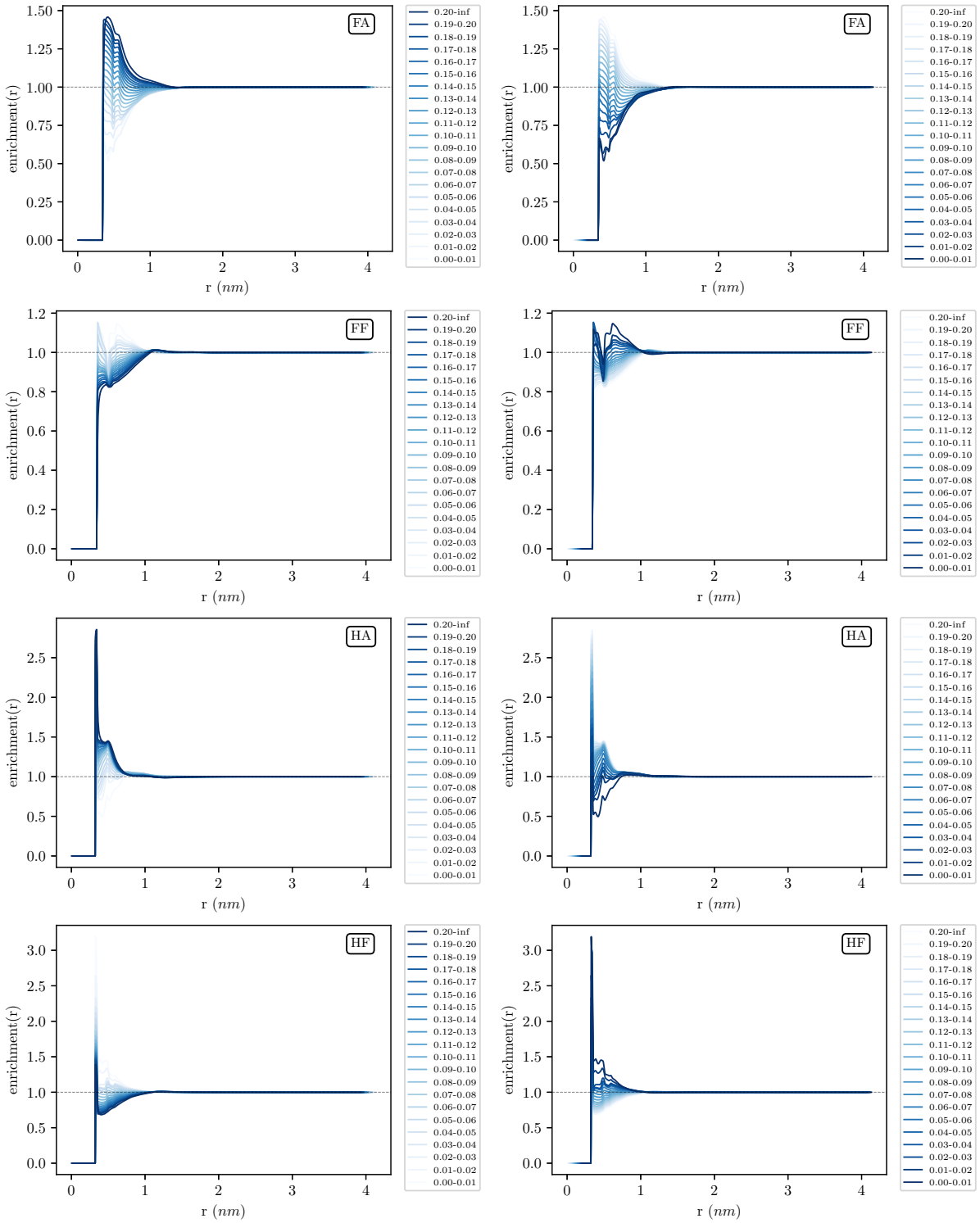

Figure 12.18: Ratio of the local molar fraction of the atoms FA (first row), FF (second row), HA (third row) and HF (fourth row) around the void sites and their bulk molar fraction (enrichment), as a function of the radial distance from the void sites and for different (sliced) void site radii ranges, for the system of pure F6H6 simulated at $T = 298\,\mathrm{K}$. The plots on both columns contain exactly the same information, but with reverse colour coding: dark to light for decreasing order of void site radii ranges (left) and light to dark for decreasing order of void site radii ranges (right). The nomenclature used to identify the atoms is presented in Figure 12.1. The curves in each plot have been laterally shifted so that the contact peaks are coincident (see text for further details). The analogous plots for all the hydrogen atoms of F6H6 are presented in Figures D.15 and D.16 in Appendix D (respectively in Figures D.13 and D.14 for the fluorine atoms), and the corresponding RDFs are presented in Figures D.19 and D.20 (respectively Figure D.17 and D.18 for the fluorine atoms).

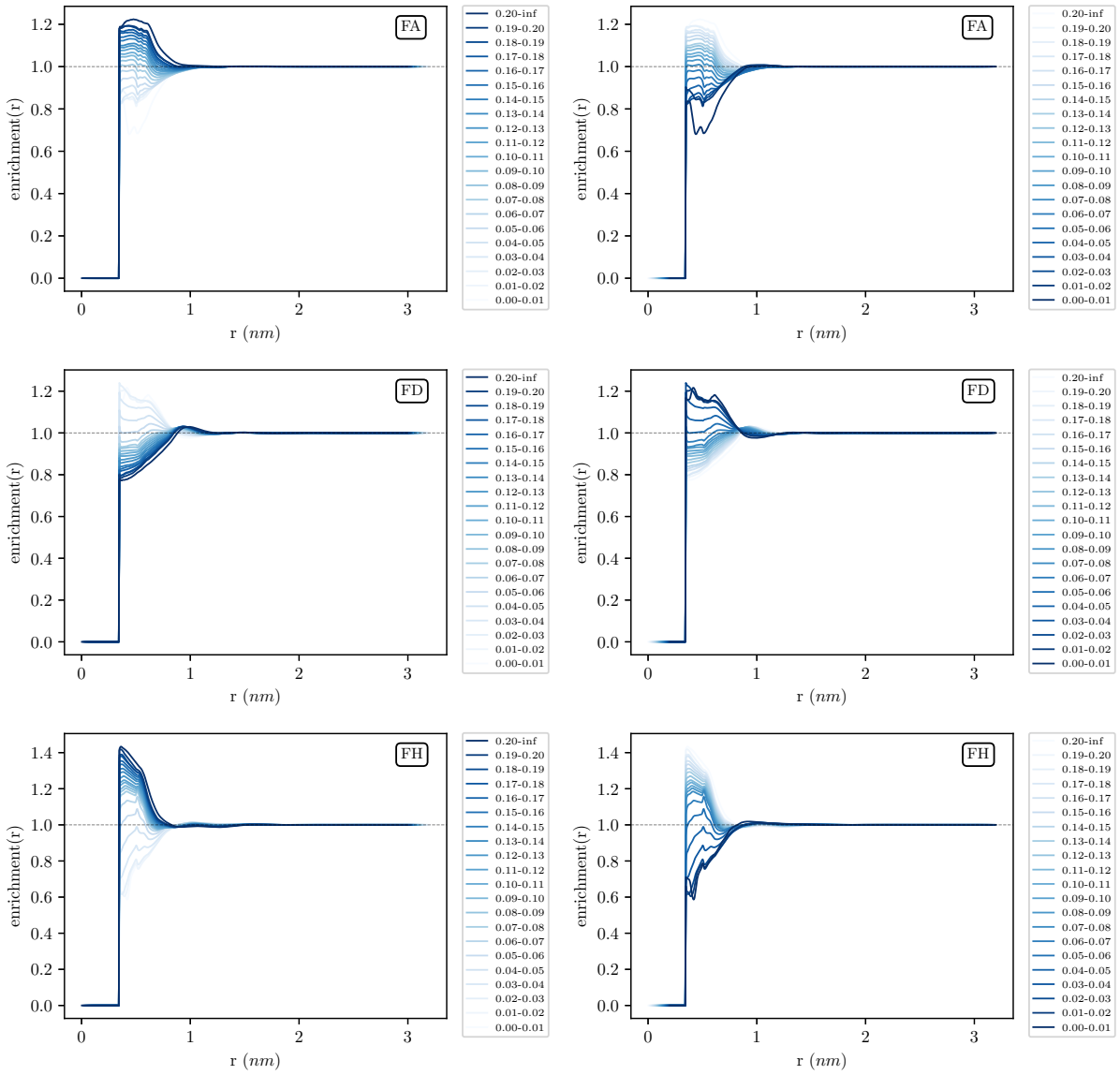

Figure 12.19: Ratio of the local molar fraction of the atoms FA (top row), FD (middle row) and FH (bottom row) around the void sites and their bulk molar fraction (enrichment), as a function of the radial distance from the void sites and for different (sliced) void site radii ranges, for the system of pure F8Br simulated at $T = 298\,\mathrm{K}$. The plots on both columns contain exactly the same information, but with reverse colour coding: dark to light for decreasing order of void site radii ranges (left) and light to dark for decreasing order of void site radii ranges (right). The nomenclature used to identify the atoms is presented in Figure 12.1. The curves in each plot have been laterally shifted so that the contact peaks are coincident (see text for further details). The analogous plots for all the fluorine atoms of F8Br are presented in Figures D.21 and D.22 in Appendix D, and the corresponding RDFs are presented in Figures D.23 and D.24.

12.6 Conclusions

In this work, the interstitial void space in liquid mixtures of hexane (H6) and perfluorohexane (F6) was systematically studied as functions of composition, temperature and the size of the interstitial cavities. The identification of the interstitial voids was done based on the formalism of the Voronoi S-tesselation. The total void volume of the systems, as well as the morphology of the interstitial voids and their preferential location relative to the molecules constituting the system, were investigated. This work was based on the mathematical foundations and algorithm developed by Medvedev *et al.* [11, 12, 18, 45]. Several computational and numerical analysis pipelines were developed to extend the applicability of the algorithm to the sampling of several configurations (trajectory frames), for better representativeness and improved statistical treatment based on the automated analysis of large data sets. This included the development of tools founded on the formalism of Radial Distribution Functions (RDFs) to achieve these goals. Having obtained the results for the mixtures of F6+H6 as a benchmark, the Molecular Dynamics (MD) simulation and analytical methodologies were further employed to characterise the interstitial void space of pure liquid perfluorohexylhexane (F6H6) and perfluorooctylbromide (F8Br). These systems were selected based on the conceptual connection between the present study and the rest of the work presented in this document, as well as on the practical relevance they have for their uses in the biomedical field.

In this regard, for mixtures of F6+H6:

- The total void volume was found to increase with increasing Temperature (T), an effect that was attributed to the thermal expansion of the fluid. The preferential location of the voids within the systems seems practically unaffected by T, suggesting the thermal expansion of the systems occurs as a whole and the extra interstitial space originating from such phenomenon is more or less evenly distributed in space;

- The total void volume was found to display a maximum in its dependency with the molar fraction of F6 (x_{F6}). This phenomenon was interpreted as a consequence of the well-documented non-ideality of the mixtures of Normal Alkanes (n-As) with Perfluoroalkanes (PFAs) and it was rationalised by comparing it to the Excess Volume of Mixing (V^E) of mixtures of F6+H6. The creation of large interstitial voids in mixtures of F6+H6, linked to a less efficient packing of the molecules and alterations in their conformations, has been suggested, at least in part, as the cause of the observed large and positive V^E exhibited by these systems. The results presented herein are in support of this conjecture;

- The void morphology was found to vary with x_{F6}. First, the interstitial cavities tend to be larger with increasing x_{F6}, as assessed by the void site radii distributions. Second, in general, the average number of voids per molecule of the system was found to increase with increasing x_{F6}. Third, the individual voids were found to increase in volume (V_{void}), to be formed by a larger number of void sites ($n_{\mathrm{Delaunay\ S\text{-}simplexes}}$) and decrease in sphericity (α) with increasing x_{F6}. In other words, and although in a non-linear way, increasing x_{F6} causes the interstitial cavities to be, on average, more voluminous, more interconnected (spanning larger regions in space) and less spherical (having more complex shapes);

- A correlation was found between those three variables (V_{void}, $n_{\text{Delaunay S-simplexes}}$ and α), inasmuch as that larger or more extensive ($> n_{\text{Delaunay S-simplexes}}$) voids tend to be bigger ($> V_{\text{void}}$) and less spherical ($< \alpha$). This is in line with other literature results (although the quantitative metrics used therein to characterise the morphology of the voids were different) [7];

- The larger, more physically significant voids were found to be located near the termini of the chains (-CF_3 and -CH_3 groups), and in particular near the termini of the chains of the molecules present in lower quantity in the mixtures of F6+H6. It has been observed that small solutes such as H_2O [48] and Xe [50, 51] are preferentially solubilised in those locations in liquid mixtures of F6+H6. This might have a connection to the fact that, as shown herein, preexisting spacious voids already exist in those locations, although other factors (*e.g.* energetic) should also be taken into consideration;

- The location of voids of different sizes within the mixtures of F6+H6 was also studied. It was reiterated that larger voids tend to be located near the chains' termini, but it was also uncovered that the smaller, less physically relevant voids are preferentially located nearer the middle of the chains;

- The use of a different probe radius (R_b^{probe}) as a criterion for the identification of large voids changes the results quantitatively, but the overall trends and conclusions drawn from the studies with $R_b^{\text{probe}} = 0.20$ nm and $R_b^{\text{probe}} = 0.16$ nm were essentially identical and independent of R_b^{probe}.

Concerning the results obtained for the pure F6H6 and pure F8Br systems:

- Both systems were found to display a large total void volume, which might help explain, based on volumetric arguments, the high gas-dissolving capacities of these classes of fluorinated compounds [53];

- F8Br was found to have a high fraction of large interstitial cavities, based on the assessment of its void site radii distribution, being quite similar to that of pure F6. This was interpreted based on the chemical similarity between the highly fluorinated compounds (F6 and F8Br). On the other hand, the amount of large interstitial cavities was found to be comparatively lower for F6H6, which was interpreted based on the fact that, in this molecule, the mutually incompatible perfluorinated (CF) and hydrogenated (CH) chains are covalently bonded to each other, hindering the propensity to form additional interstitial void space verified in mixtures of F6+H6;

- The results characterising the void morphology in F6H6 and in F8Br were found to be in line with those obtained for the mixtures of F6+H6, inasmuch as the same correlation between V_{void}, $n_{\text{Delaunay S-simplexes}}$ and α was found. The effect of varying R_b^{probe} was assessed and the independence of the conclusions drawn using $R_b^{\text{probe}} = 0.20$ nm and $R_b^{\text{probe}} = 0.16$ nm was reiterated;

- Large voids were found to be preferentially located near the termini of the chains of F6H6, with apparently no significant preference to either the -CF_3 or the -CH_3 termini. Likewise, large voids tend to be located near the termini of the F8Br molecules. However, in this case, it was found that voids tend to be preferentially located near the -CF_3 compared to the -CF_2Br termini. This was rationalised considering the added bulkiness arising from the presence of the Br atom, which might occupy more space and preclude the formation of cavities as large as those existing near the fully fluorinated terminal group;
- The location of voids of different sizes was also studied in pure F6H6 and in pure F8Br. As it was found for the mixtures of F6+H6, it was once again verified that larger and more physically relevant voids are located near the termini of those molecules, whereas smaller voids are located nearer to the middle of the molecules.

In conclusion, this work permitted the development of computational tools and methodologies with a general and broad applicability for the analysis of the interstitial void space in MD simulations of liquids, drawing from preexisting knowledge, mathematical foundations and algorithms based on the Voronoi tessellation formalism [6, 10, 11, 13, 14, 18, 45]. These tools were successfully applied in the characterisation of the interstitial void space in mixtures of F6+H6, pure F6H6 and pure F8Br, including the determination of the preferential location, relative to the molecules, of voids of physically significant size. This work envisages to be a contribution from a fundamental point of view in the characterisation of the structure of these liquids, as well as in the understanding of the mechanisms of dissolution and diffusion of small solutes in liquids. The methodologies are general and may be applied in the future for the study of other molecular models and chemical systems.

References

[1] R. G. Bedford and R. D. Dunlap. 'Solubilities and Volume Changes Attending Mixing for the System: Perfluoro-*n*-hexane–*n*-Hexane'. In: *Journal of the American Chemical Society* 80.2 (1958), pp. 282–285. DOI: 10.1021/ja01535a007.

[2] L. Lepori et al. 'Volume changes on mixing perfluoroalkanes with alkanes or ethers at 298.15 K'. In: *Fluid Phase Equilibria* 201.1 (2002), pp. 119–134. DOI: 10.1016/S0378-3812(02)00069-9.

[3] C. Duce et al. 'VLE and LLE of perfluoroalkane + alkane mixtures'. In: *Fuid Phase Equilibria* 199.1–2 (2002), pp. 197–212. DOI: 10.1016/S0378-3812(01)00815-9.

[4] G. C. Sosso et al. 'On the Role of Nonspherical Cavities in Short Length-Scale Density Fluctuations in Water'. In: *Journal of Physical Chemistry A* 121.1 (2017), pp. 370–380. DOI: 10.1021/acs.jpca.6b11168.

[5] N. Ansari et al. 'High and low density patches in simulated liquid water'. In: *Journal of Chemical Physics* 149.20 (2018), Article No. 204507. DOI: 10.1063/1.5053559.

[6] S. Gehrke, R. Macchieraldo and B. Kirchner. 'Understanding the fluidity of condensed phase systems in terms of voids–novel algorithm, implementation and application'. In: *Physical Chemistry Chemical Physics* 21.9 (2019), pp. 4988–4997. DOI: 10.1039/c8cp07120a.

[7] N. Ansari et al. 'Insights into the Emerging Networks of Voids in Simulated Supercooled Water'. In: *Journal of Physical Chemistry B* 124.11 (2020), pp. 2180–2190. DOI: 10.1021/acs.jpcb.9b10144.

[8] E. A. Shelepova et al. 'Comparing the void space and long-range structure of an ionic liquid with a neutral mixture of similar sized molecules'. In: *Journal of Molecular Liquids* 299 (2020), Article No. 112121. DOI: 10.1016/j.molliq.2019.112121.

[9] N. Ansari, T. Karmakar and M. Parrinello. 'Molecular Mechanism of Gas Solubility in Liquid: Constant Chemical Potential Molecular Dynamics Simulations'. In: *Journal of Chemical Theory and Computation* 16.8 (2020), pp. 5279–5286. DOI: 10.1021/acs.jctc.0c00450.

[10] D. Dudariev et al. 'Insight to the Local Structure of Mixtures of Imidazolium-Based Ionic Liquids and Molecular Solvents from Molecular Dynamics Simulations and Voronoi Analysis'. In: *Journal of Physical Chemistry B* 127.11 (2023), pp. 2534–2545. DOI: 10.1021/acs.jpcb.2c08818.

[11] A. V. Anikeenko et al. 'Implementation of the Voronoi-Delaunay method for analysis of intermolecular voids'. English. In: *Computational Science and its Applications - ICCSA 2004, pt. 3*. Ed. by A. Lagana et al. Vol. 3045. Lecture Notes in Computer Science. 2004, pp. 217–226. ISBN: 3-540-22057-7.

[12] M. G. Alinchenko et al. 'Morphology of Voids in Molecular Systems. A Voronoi-Delaunay Analysis of a Simulated DMPC Membrane'. In: *Journal of Physical Chemistry B* 108.49 (2004), pp. 19056–19067. DOI: 10.1021/jp040386q.

[13] M. G. Alinchenko et al. 'Effect of Cholesterol on the Properties of Phospholipid Membranes. 4. Interatomic Voids'. In: *Journal of Physical Chemistry B* 109.34 (2005), pp. 16490–16502. DOI: 10.1021/jp051832s.

[14] V. P. Voloshin, N. N. Medvedev and A. Geiger. 'Fast Calculation of the Empty Volume in Molecular Systems by the Use of Voronoi-Delaunay Subsimplexes'. In: *Transactions on Computational Science XXII*. Ed. by M. L. Gavrilova and C. J. K. Tan. 2014, pp. 156–172. ISBN: 978-3-642-54212-1.

[15] B. Widom. 'Some Topics in the Theory of Fluids'. In: *Journal of Chemical Physics* 39.11 (1963), pp. 2808–2812. DOI: 10.1063/1.1734110.

[16] M. F. C. Gomes and A. A. H. Pádua. 'Interactions of Carbon Dioxide with Liquid Fluorocarbons'. In: *Journal of Physical Chemistry B* 107.50 (2003), pp. 14020–14024. DOI: 10.1021/jp0356564.

[17] I. Sedov and T. Magsumov. 'The Gibbs free energy of cavity formation in a diverse set of solvents'. In: *Journal of Chemical Physics* 153.13 (2020), p. 134501. DOI: 10.1063/5.0021959.

[18] N. N. Medvedev et al. 'An Algorithm for Three-Dimensional Voronoi S-Network'. In: *Journal of Computational Chemistry* 27.14 (2006), pp. 1676–1692. DOI: 10.1002/jcc.20484.

[19] M. P. Krafft and J. G. Riess. 'Chemistry, Physical Chemistry, and Uses of Molecular Fluorocarbon-Hydrocarbon Diblocks, Triblocks, and Related Compounds – Unique "Apolar" Components for Self-Assembled Colloid and Interface Engineering'. In: *Chemical Reviews* 109.5 (2009), pp. 1714–1792. DOI: 10.1021/cr800260k.

[20] J. G. Riess and J. G. Weers. 'Emulsions for biomedical uses'. In: *Current Opinion in Colloid and Interface Science* 1.5 (1996), pp. 652–659. DOI: 10.1016/S1359-0294(96)80104-X.

[21] A. Okabe et al. *Spatial Tessellations: Concepts and Applications of Voronoi Diagrams*. 2nd ed. Wiley Series in Probability and Mathematical Statistics. New York, USA: John Wiley and Sons, Ltd., 2000. ISBN: 0-471-98635-6.

[22] D. Chakraborty and A. Chandra. 'Voids and Necks in Liquid Ammonia and Their Roles in Diffusion of Ions of Varying Size'. In: *Journal of Computational Chemistry* 33.8 (2012), pp. 843–852. DOI: 10.1002/jcc.22910.

[23] V. P. Voloshin, S. Beaufils and N. N. Medvedev. 'Void space analysis of the structure of liquids'. In: *Journal of Molecular Liquids* 96–97 (2002), pp. 101–112. DOI: 10.1016/S0167-7322(01)00330-0.

[24] F. Aurenhammer. 'Voronoi Diagrams – A Survey of a Fundamental Geometric Data Structure'. In: *Computing Surveys* 23.3 (1991), pp. 345–405. DOI: 10.1145/116873.116880.

[25] D. Van der Spoel et al. 'GROMACS: Fast, Flexible, and Free'. In: *Journal of Computational Chemistry* 26.16 (2005), pp. 1701–1718. DOI: 10.1002/jcc.20291.

[26] M. J. Abraham et al. *GROMACS User Manual version 5.0.7*. URL: https://ftp.gromacs.org/manual/manual-5.0.7.pdf (visited on 10/07/2022).

[27] B. Hess. 'P-LINCS: A Parallel Linear Constraint Solver for Molecular Simulation'. In: *Journal of Chemical Theory and Computation* 4.1 (2008), pp. 116–122. DOI: 10.1021/ct700200b.

[28] W. L. Jorgensen, D. S. Maxwell and J. Tirado-Rives. 'Development and Testing of the OPLS All-Atom Force Field on Conformational Energetics and Properties of Organic Liquids'. In: *Journal of the American Chemical Society* 118.45 (1996), pp. 11225–11236. DOI: 10.1021/ja9621760.

[29] E. K. Watkins and W. L. Jorgensen. 'Perfluoroalkanes: Conformational Analysis and Liquid-State Properties from ab Initio and Monte Carlo Calculations'. In: *Journal of Physical Chemistry A* 105.16 (2001), pp. 4118–4125. DOI: 10.1021/jp004071w.

[30] S. W. I. Siu, K. Pluhackova and R. A. Böckmann. 'Optimization of the OPLS-AA Force Field for Long Hydrocarbons'. In: *Journal of Chemical Theory and Computation* 8.4 (2012), pp. 1459–1470. DOI: 10.1021/ct200908r.

[31] P. Morgado et al. 'Alkane Coiling in Perfluoroalkane Solutions: A New Primitive Solvophobic Effect'. In: *Langmuir* 33.42 (2017), pp. 11429–11435. DOI: 10.1021/acs.langmuir.7b02516.

[32] A. A. H. Pádua. 'Torsion Energy Profiles and Force Fields Derived from Ab Initio Calculations for Simulations of Hydrocarbon–Fluorocarbon Diblocks and Perfluoroalkylbromides'. In: *Journal of Physical Chemistry A* 106.43 (2002), pp. 10116–10123. DOI: 10.1021/jp025732n.

[33] J. D. Hunter. 'Matplotlib: A 2D graphics environment'. In: *Computing in Science & Engineering* 9.3 (2007), pp. 90–95. DOI: 10.1109/MCSE.2007.55.

[34] T. A Caswell et al. *matplotlib/matplotlib: REL: v3.5.0*. Version 3.5.0. Nov. 2021. URL: https://doi.org/10.5281/zenodo.5706396.

[35] A. A. Hagberg, D. A. Schult and P. J. Swart. 'Exploring Network Structure, Dynamics, and Function using NetworkX'. In: *Proceedings of the 7th Python in Science Conference*. Ed. by G. Varoquaux, T. Vaught and J. Millman. Pasadena, CA USA, 2008, pp. 11–15.

[36] A. A. Hagberg et al. *NetworkK 2.6.3*. Version 2.6.3. Sept. 2021. URL: https://pypi.org/project/networkx/2.6.3/.

[37] C. R. Harris et al. 'Array programming with NumPy'. In: *Nature* 585.7825 (2020), pp. 357–362. DOI: 10.1038/s41586-020-2649-2.

[38] T. E. Oliphant *et al. numpy 1.21.4*. Version 1.21.4. Nov. 2021. URL: https://pypi.org/project/numpy/1.21.4/.

[39] W. McKinney. 'Data Structures for Statistical Computing in Python'. In: *Proceedings of the 9th Python in Science Conference*. Ed. by S. van der Walt and J. Millman. 2010, pp. 56–61. DOI: 10.25080/Majora-92bf1922-00a.

[40] The pandas Development Team. *pandas-dev/pandas: Pandas*. Version 2.0.1. Apr. 2023. URL: https://doi.org/10.5281/zenodo.7857418.

[41] P. Virtanen et al. 'SciPy 1.0: Fundamental Algorithms for Scientific Computing in Python'. In: *Nature Methods* 17.3 (2020), pp. 261–272. DOI: 10.1038/s41592-019-0686-2.

[42] P. Virtanen et al. *SciPy 1.7.3*. Version 1.7.3. Nov. 2021. URL: https://pypi.org/project/SciPy/1.7.3/.

[43] J. Burkardt. *Tetrahedral Grid of Points*. The code is distributed under the GNU LGPL license. University of South Carolina. URL: https://people.math.sc.edu/Burkardt/py_src/tetrahedron_grid/tetrahedron_grid_points.py (visited on 16/05/2024).

[44] W. Humphrey, A. Dalke and K. Schulten. 'VMD: Visual Molecular Dynamics'. In: *Journal of Molecular Graphics & Modelling* 14.1 (1996), pp. 33–38. DOI: 10.1016/0263-7855(96)00018-5.

[45] *Voronoi Network Poly (VNP) code*. Institute of Chemical Kinetics and Combustion. URL: http://www.kinetics.nsc.ru/mds/?Software:VNP (visited on 14/10/2021).

[46] M. Bohn et al. 'Excess properties of liquid mixtures from perturbation theory: results for model systems and predictions for real systems'. In: *Fluid Phase Equilibria* 23.2–3 (1985), pp. 137–151. DOI: 10.1016/0378-3812(85)90002-0.

[47] P. Morgado et al. 'Systems Involving Hydrogenated and Fluorinated Chains: Volumetric Properties of Perfluoroalkanes and Perfluoroalkylalkane Surfactants'. In: *Journal of Physical Chemistry B* 115.50 (2011), pp. 15013–15023. DOI: 10.1021/jp207567y.

[48] P. Morgado et al. 'Solubility of water in *n*-alkanes: New experimental measurements and molecular dynamics simulations'. In: *Fluid Phase Equilibria* 503 (2020), Article No. 112322. DOI: 10.1016/j.fluid.2019.112322.

[49] P. Morgado et al. 'Solution Behavior of Perfluoroalkanes and Perfluoroalkylalkane Surfactants in n-Octane'. In: *Journal of Physical Chemistry C* 111.43 (2007), pp. 15962–15968. DOI: 10.1021/jp073758e.

[50] P. Morgado et al. 'Probing the Structure of Liquids with ^{129}Xe NMR Spectroscopy: *n*-Alkanes, Cycloalkanes, and Branched Alkanes'. In: *Journal of Physical Chemistry B* 117.30 (2013), pp. 9014–9024. DOI: 10.1021/jp4060507.

[51] P. Morgado, L. F. G. Martins and E. J. M. Filipe. 'From nano-emulsions to phase separation: evidence of nano-segregation in (alkane + perfluoroalkane) mixtures using ^{129}Xe NMR Spectroscopy'. In: *Physical Chemistry Chemical Physics* 21.7 (2019), pp. 3742–3751. DOI: 10.1039/c8cp06509h.

[52] P. Lo Nostro. 'Aggregates from semifluorinated *n*-alkanes: how incompatibility determines self-assembly'. In: *Current Opinion in Colloid and Interface Science* 8.3 (2003), pp. 223–226. DOI: 10.1016/S1359-0294(03)00052-9.

[53] M. F. C. Gomes, J. Deschamps and D.-H. Menz. 'Solubility of dioxygen in seven fluorinated liquids'. In: *Journal of Fluorine Chemistry* 125.9 (2004), pp. 1325–1329. DOI: 10.1016/j.jfluchem.2004.03.013.

Chapter 13

Final Remarks

Perfluoroalkylalkanes (PFAAs), with a chemical formula $C_nF_{2n+1}C_mH_{2m+1}$ (often abbreviated to FnHm), are diblock molecules formed by a hydrogenated (CH) and a perfluorinated (CF) blocks, both hydrophobic and mutually phobic. The study of these molecules has been spurred by their inertness and biocompatibility, as well as their remarkable self-assembling properties and high gas-dissolving capacities. These molecules present a potential interest as blood substitutes and in other biomedical applications, but also in nanomaterials applications for the fabrication of self-assembled templates for surface nanopatterning. Despite lacking a terminal polar group, these "primitive surfactants" form Langmuir films on water or hydrophilic substrates. The films comprise hexagonally ordered, monodisperse hemimicelles, as shown by Atomic Force Microscopy (AFM) and Grazing Incidence Small Angle X-Ray Scattering (GISAXS). The diameter of the hemimicelles is dependent on the molecular architecture. However, the concrete effects of varying molecular structure (n and/or m), mixing in binary films and the physicochemical properties of the liquid subphase on the structure and ordering of the Langmuir films were still untapped at the start of this work.

13.1 Conclusions

13.1.1 Global conclusions

Prior to this work, it had already been uncovered that the diameter of the hemimicelles of PFAAs depends on the lengths of the CH chain and, to a lesser extent, of the CF chain. Herein, a rational justification for this observation is provided for the pure cases, in Chapter 9. This is a consequence of the geometry of the PFAA molecules, which pack in a **fan-like arrangement** inside the hemimicelles, as is demonstrated experimentally, by Grazing Incidence X-Ray Diffraction (GIXD), and computationally, by Molecular Dynamics (MD) simulation.

The peculiar morphology of the PFAA hemimicelles has been known for decades and has been demonstrated by AFM of the transferred Langmuir films of PFAAs. In particular, these self-assembled supramolecular surface aggregates display a characteristic pit in their centre. In Chapter 8, based on MD simulation results, it is demonstrated that this is a consequence of the **ordering of the CF_2–CH_2 dipoles**, which adopt a preferential head-to-tail orientation, combined with the **possibility to deform the liquid subphase**.

The role of the physicochemical nature of the liquid subphase in the nanostructuring of Langmuir films of PFAAs was investigated, combining computational (MD simulation) and experimental (AFM imaging of samples prepared by spin coating) approaches. The results, presented in Chapter 10, are indicative that ordered films of PFAAs comprising laterally ordered **hemimicelles can be formed at the surface of short-chain CH** (Methanol (MeOH), Ethanol (EtOH), Propanol (PrOH), Butanol (BuOH)) **or CF** (2,2,2-trifluoroethanol (TFE)) **alcohols**. These results demonstrate that water is not paramount for the formation and lateral organisation of hemimicelles of PFAAs. This is in line with the rationale that the formation of hemimicelles of PFAAs can be perceived as a true self-assembling phenomenon driven by factors intrinsic to the PFAAs.

An experimental investigation, combining measurements of Surface Pressure (π)–Molecular Area (A) isotherms, GISAXS and GIXD, probed the structure and thermodynamic properties of mixed Langmuir films of F8H14:F8H20, whose results are presented in Chapter 11. It was found that the molecules are not completely segregated within the binary films. **The PFAA molecules mix, most likely at the molecular level**, *i.e.* the film comprises mixed hemimicelles whose size is intermediate to that of the pure hemimicelles. The geometrical model mentioned above was extended to rationalise the dependence of the hemimicelle size with the film composition.

In Chapter 12, an exploratory study is presented aiming at characterising the morphological and volumetric properties of the interstitial voids in liquid mixtures of CH and CF chains, namely of hexane (H6) and perfluorohexane (F6). The existence of these cavities is related to the processes of solubilisation and diffusion of small molecules in highly fluorinated systems, including of respiratory gases in artificial blood formulations. This investigation also explores the volumetric constraints underlying the mutually phobic behaviour of CH and CF chains, which are determinant for the self-assembling properties of systems containing those moieties, namely in Langmuir films of PFAAs. It was found that **larger, more physically relevant cavities are preferentially located near the termini of the molecules**. The methodology was extended to biomedically relevant systems (liquid F6H6 and liquid perfluorooctylbromide (F8Br)), for which a similar trend was found.

13.1.2 Chapter-by-chapter highlights

Chapter 9 – Modelling the internal structure and size of PFAA hemimicelles MD simulations of water-supported hemimicelles of a series of PFAA molecules were performed, namely of a F8Hm (F8H14, F8H16, F8H18 and F8H20) and of a FnH16 series (F6H16, F8H16, F10H16 and F12H16). These revealed that:

- Hemimicelles whose morphological and structural features resemble the experimentally observed ones are retrieved (round, dome-shaped, with a central pit, with the molecules in a fan-like arrangement in a CF chain up-CH chain down orientation);

- The molecular tilt angle (θ_{Tilt}) increases approximately linearly from the centre to the periphery of the hemimicelles, until a limit value ($\theta_{\mathrm{Tilt,\,F}} \approx 65°$) is attained at the rim of the aggregates. This was found to be approximately similar for all studied systems;

- A model is proposed, based on geometrical arguments, to describe the packing of the molecules and the internal structure of the PFAA hemimicelles. This geometrical model rationalises the fan-like arrangement of the PFAA molecules as a consequence of: the mismatch of the cross-sectional areas of the CH and the CF chains; a constant longitudinal shift of one concentric layer of molecules relative to the next consecutive layer (h), which is linked to the alignment of the CF_2–CH_2 dipoles; and the planarising effect of the high-Surface Tension (γ) liquid water subphase;

- The dependency of the diameter of the PFAA hemimicelles on the length of the CH chain and the CF chain is elucidated, for the hemimicelles of pure PFAAs;

- The central pit of the hemimicelles naturally arises from the combined effects of the lateral disposition of molecules with regularly increasing θ_{Tilt} (from the centre to the periphery of the hemimicelles) and the constant longitudinal shift or h;

- The GIXD spectra were computed from the simulation trajectories. These reproduce the experimentally observed shift of the maximal diffraction intensity to lower Q_{xy} values with increasing Q_{z}. This was linked to the fan-like molecular arrangement within the aggregates and the constant rate of change of θ_{Tilt} with r, validating the simulations and enlightening the experimental results;

- The computational methodology was extended to study other FnHm hemimicelles, namely a F10Hm (F10H14, F10H16, F10H18 and F10H20) and a F12Hm series (F12H16 and F12H20). The geometrical model was deployed in a fully predictive way for the estimation of the aggregation number, limit-size of the hemimicelles and the preparation of the initial configurations to run the simulations.

Chapter 8 – Origin of the central pit in hemimicelles of PFAAs MD simulations of water-supported hemimicelles of PFAAs were performed to assess the role of the CF_2–CH_2 dipole-dipole interactions in the self-assembling phenomenon. The PFAA molecules were modelled using a Force Field (FF) either explicitly considering electrostatic interactions (Optimised Potential for Liquid Simulations (OPLS) All-Atom (AA) FF) or a simplified non-electrostatic FF (Transferable Potentials for Phase Equilibria (TraPPE) Coarse-Grained (CG) FF), effectively "switching" on or off (respectively) the CF_2-CH_2 dipole-dipole interactions. Furthermore, the effect of the substrate deformability on the morphology of the hemimicelles was probed by conducting the simulations using a constrained, plane water subphase and comparing these with the regular, unconstrained water subphase simulations. It was found that:

- The morphology of the PFAA hemimicelles, and particularly the existence of the experimentally observed central depression or pit, was found to result from the ordering of the CF_2–CH_2 dipoles, which adopt a preferential head-to-tail orientation, combined with the possibility to deform the underlying liquid subphase;

- The alignment of the CF_2–CH_2 dipoles ultimately originates the longitudinal shift described in the framework of the geometrical model.

Chapter 10 – Formation of hemimicelles of PFAAs in the presence of long- and short-chain alcohols MD simulations of PFAA aggregates over a liquid subphase of short-chain CH (MeOH, EtOH, PrOH) or CF (TFE) alcohols were performed. The experimental characterisation by AFM of thin films prepared by spin coating solid substrates previously wet with CH (MeOH, EtOH, BuOH) or CF (TFE) alcohols was also done. The combined computational and experimental approach unveiled:

- In the MD simulations, hemimicelles with structural and morphological features similar to those obtained for hemimicelles simulated at the water–vacuum interface were retrieved at the surface of pure MeOH and of pure TFE. Dissolution of the PFAA molecules was observed for the simulations with a subphase of pure EtOH and of pure PrOH, but stable aggregates were retrieved if the subphase was a mixture of alcohol and water (20 % molar of alcohol);
- Experimentally, films comprising hemimicelles of PFAAs are obtained at the surface of silicon wafers previously wet with water, MeOH, EtOH, BuOH or TFE, although with varying degrees of lateral order, as determined by AFM;
- These results support that water is not paramount for the formation and lateral organisation of hemimicelles of PFAAs.

In a parallel MD simulation study, the formation of hemimicelles of PFAAs (F8H16 or F8H18) in mixed films of PFAAs with long-chain alcohols (octadecanol (H18OH) or 1H,1H-perfluorooctadecanol (F171HOH)) was investigated. The obtained results show that:

- It is plausible that the PFAA and alcohol molecules are segregated within the mixed films. The collapse of the monolayers is likely to occur with the gliding of PFAA molecules on top of an alcohol monolayer;
- The existence of structurally resilient hemimicelles that remain organised upon collapse is plausible. These may rest intact upon collapse of the monolayer, causing the deformation of the alcohol film and the water surface beneath it.

Chapter 11 – Structure and stability of mixed binary Langmuir films of PFAAs An experimental study of π–A isotherms, GISAXS and GIXD measurements of mixed Langmuir films of F8H14:F8H20 was performed, to characterise the thermodynamic and structural properties of these films as a function of film composition (x_{F8H20}) and π, at constant Temperature (T). The following conclusions were drawn:

- The π–A isotherms of the mixed films are similar to those obtained for the pure cases. They present only one Surface Pressure of Collapse (π_{collapse}), which was found to be almost proportional (with only minor negative deviations) to the area occupied per hemimicelle at the onset of the collapse (A_{collapse}). The estimated surface energy of collapse follows the same trends as π_{collapse}, in terms of its dependency on A_{collapse}. These results exclude the scenario of complete segregation of the PFAA molecules and imply that the film is mixed, possibly at the molecular level;

- From the GISAXS measurements, it was determined that the films comprise hemimicelles ordered in a two-dimensional (2D) hexagonal lattice with a lattice parameter (a) intermediate to that of the pure compounds. With few exceptions, a was found to increase with x_{F8H20} and to decrease with π. The corresponding unit cell area shows negative deviations to Vegard's law, suggesting stronger intermolecular interactions and/or the deformation of the hemimicelles upon film compression. A secondary lattice, attributed to a meta-stable state of a structure formed by the F8H14 molecules, is detected for the pure F8H14 and the mixed films. These results exclude the scenario of a completely segregated film and are consistent with mixing occurring within the film, although it is not clear whether this happens at a hemimicelle or a molecular level;

- The GIXD results elucidated the structure of the PFAA molecules inside the hemimicelles. The diffraction spectra present 3 peaks: one associated with the stacking of the CF chains and 2 with the stacking of the CH chains, one of which is characteristic of the H20 blocks of F8H20 (being absent for the pure F8H14). The intensity of the CF chain diffraction peak varies with the in-plane (Q_{xy}) and out-of-plane (Q_{z}) components of the scattering vector in a way that is compatible with the fan-like arrangement of molecules. This is in accord with the MD simulation results of pure hemimicelles, validating the computational methodology and supporting the proposed structure for the Langmuir films of PFAAs;

- The geometrical model was extended to the mixed films of F8H14:F8H20 to rationalise the dependence of the hemimicelle size with the film composition. Three limit scenarios are proposed for the structure of the mixed hemimicelles, of which, based on the comparison with available experimental GISAXS data on a: one scenario is deemed unlikely (complete segregation of the molecules within the hemimicelles in a concentric circle of F8H20 molecules and outer corona of F8H14 molecules) and two other scenarios are deemed plausible (concentric circle of F8H14 molecules and outer corona of F8H20 molecules; complete random mixing), given the qualitative agreement of the latter with experiments in predicting a reduction of a compared to the average of the pure compounds' values. This theoretical approach should serve as a starting point for future investigations.

Chapter 12 – Interstitial voids in mixtures of hydrogenated and fluorinated chains
Simulations of liquid mixtures of H6+F6 were performed as a function of the molar composition of the mixture (x_{F6}) and of T. Interstitial cavities were quantitatively characterised, based on the formalism of the Voronoi S-tessellation. Physically relevant voids were identified as those cavities whose dimensions are sufficient to accommodate a molecule of a small solute, in particular of respiratory gases (oxygen). This study uncovered that:

- The number of voids and their volume increase with both x_{F6} and of T;

- The total void volume increases with T (rationalised in terms of the thermal expansion of the fluid) and displays a maximum with x_{F6} and positive deviations to the x_{F6}-weighted average of the pure compounds (which were related to the positive Excess Volume of Mixing (V^E) displayed by mixtures of H6+F6);

- On average, the interstitial voids are smaller and more spherical for low x_{F6} and larger and have more complex shapes for large x_{F6};
- Physically relevant voids are located preferentially near the chains' termini;
- The computational methodology was extended to systems relevant in the biomedical field (liquid F6H6 and liquid F8Br). Similar conclusions were drawn, concerning the morphological and volumetric characterisation of the interstitial cavities in these systems, as well as their preferential location near the molecules' termini.

13.2 Future Perspectives

Despite the encouraging results presented in this thesis, there are several remaining aspects that should be addressed in future investigations. Some of these perspectives for future studies are listed below.

- The experiments (π–A isotherms, GIXD, GISAXS) to characterise the structural and thermodynamic properties of the mixed binary films of PFAAs should be extended to other mixtures. In particular, the effect on such properties of varying the CF chain length while keeping the CH chain length constant (*e.g.* F8H16:F12H16) and varying both the CF chain and the CH chain lengths while keeping the total molecular length constant (*e.g.* F8H20:F12H16) should be addressed;
- The study by MD simulations of the mixed binary films of PFAAs should be attempted, to complement the experimental approaches and provide detailed information on the structure and molecular organisation of these systems. This is expected to be a challenging problem to tackle, due to the slow diffusion of such large molecules at the surface of water, requiring long simulations, and the large number of molecules that are required to build a representative system. The possibility of using a CG FF to circumvent these problems (at least partially) should be pondered and weighed against the possibility of losing important information in such approximation (*e.g.* the use of a non-electrostatic force-field might not provide a complete characterisation of the intermolecular interactions, as discussed in Chapter 8);
- The experimental approach for the characterisation of the Langmuir films of PFAAs at the air–water interface should contemplate the imaging by AFM of films transferred onto an appropriate solid substrate. In particular, the structure of the mixed films should be probed by such means, to unveil whether these are formed by a single lattice of monodisperse, mixed hemimicelles or by a single lattice of 2 types of hemimicelles with distinct sizes (approaching or matching those of the pure components). Furthermore, the structure of the pure F12H16 and pure F12H20 Langmuir films should be further probed, given the discrepancies between the MD simulation and experimental results, described in Chapter 9. Finally, the pure F8H14 Langmuir film should be further characterised to assess whether the existence of the secondary lattice is detected by AFM of the film transferred at low π;

- The structure of the mixed binary films should be studied after the collapse of the monolayer, resorting to the techniques listed above. This should provide valuable insights concerning the molecular organisation within the hemimicelles, for instance if the size of the hemimicelles varies after the collapse of the monolayer. This might be an indication of the preferential ejection of one type of molecules (*e.g.* if the hemimicelle size increases after the monolayer collapse of the mixed Langmuir films of F8H14:F8H20, this might be indicative of the preferential expulsion of the F8H14 molecules, whose pure hemimicelles are smaller, compared to the F8H20 molecules), which in turn might help elucidate whether the hemimicelles are monodisperse or if some sort of intra-hemimicelle segregation occurs;

- The obtained results of thin films of organised hemimicelles of PFAAs prepared by spin coating a solid substrate previously wet with a short-chain alcohol are promising. However, as discussed in Chapter 10, the occurrence of finite-size effects due to the small amount of liquid subphase used for the preparation of the samples prompt a careful analysis of these results. Ideally, a film formed at the surface of liquid alcohol should be prepared using a Langmuir trough and transferred onto a solid substrate, for characterisation by AFM, or probed directly at the liquid–air interface by GIXD and/or GISAXS. The most obvious candidate for such proof-of-concept experiment would be MeOH, since the obtained film is the most ordered one of the tested alcohols and it is anticipated that this alcohol may permit the preparation of the most stable films of all the tested conditions. This note is mentioned here, even though the concretisation of such experiment is highly challenging due to practical and safety limitations in handling large amounts of organic solvents;

- The study of the interstitial voids in simulations of liquids should be extended to other molecules of biomedical interest, such as other fluorinated liquids that may be used in oxygen-carrying formulations. From a fundamental point of view, it would also be interesting expanding the results presented herein for mixtures of H6+F6 to other mixtures with varying chain lengths (*e.g.* pentane (H5) and perfluoropentane (F5); octane (H8) and F6). Analogously, the study of other liquid PFAAs should be performed (*e.g.* F6H8; F4H6);

- Envisaging the unlocking of the potential biomedical applications of the highly fluorinated compounds mentioned throughout this work, the study of emulsions with fluorinated molecules (such as F8Br), stabilised with Phospholipids (PLs) and/or PFAAs should be pursued. The characterisation of the interstitial voids by MD simulation should provide insights into the processes of solubilisation and diffusion of respiratory gases in the emulsion and across the organic/aqueous interface.

Part IV

Appendices

Appendix A

Supplementary Information

The information presented below has been published as supplementary information accompanying the paper presented in Chapter 8 [1]. The MD simulation parameters presented herein are the same as those used to perform the simulations presented in Chapter 9.

A.1 Images

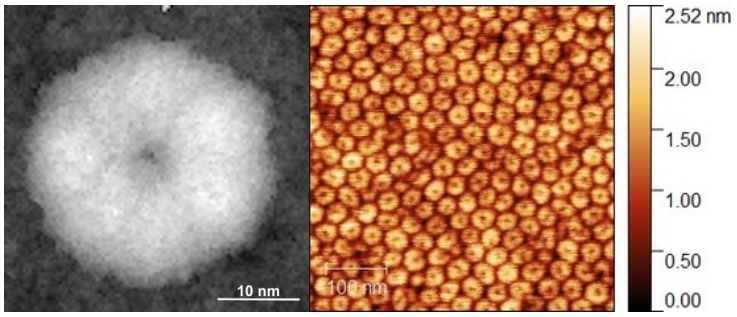

Figure A.1: Left: Top-view topography (AFM-like) image of an F8H16 simulated hemimicelle; right: Experimental topography AFM image of F8H16 hemimicelles.

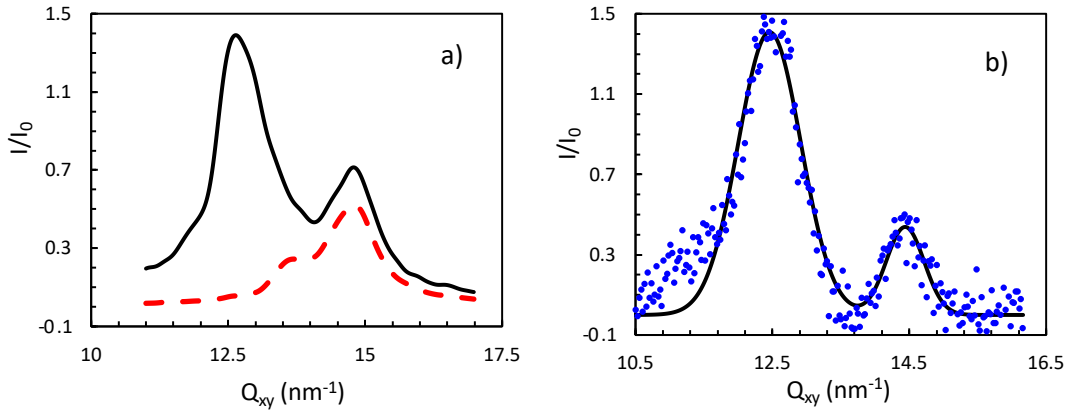

Figure A.2: Grazing Incidence X-Ray Diffraction (GIXD) of a F8H16 monolayer at 298.15 K from (a) MD simulation and (b) experiment. Red dotted line is the contribution of the hydrogenated segments alone to the GIXD spectrum.

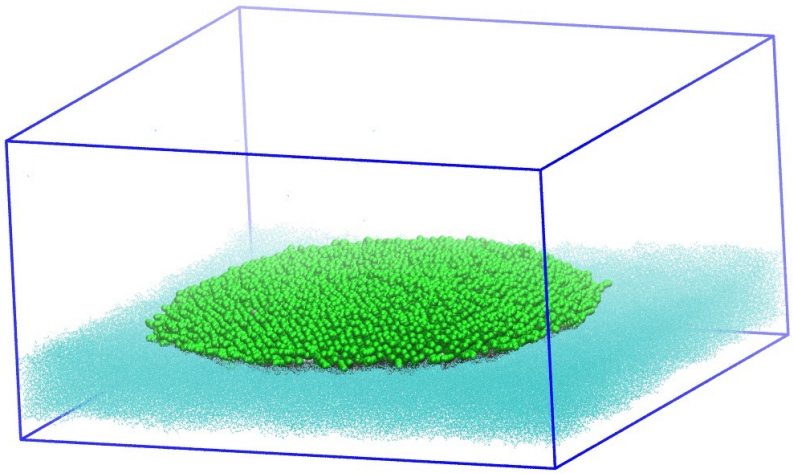

Figure A.3: Snapshot of a typical simulation box displaying the water layer and a hemimicelle.

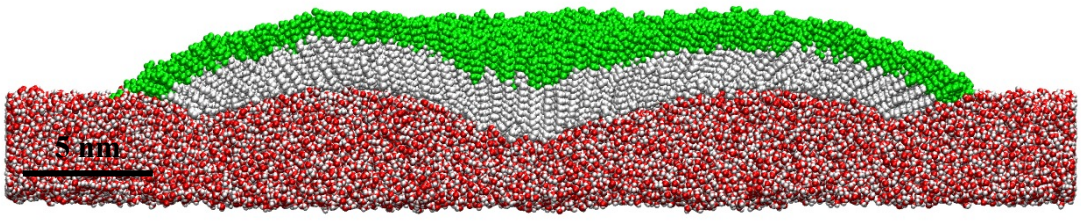

Figure A.4: Representative snapshot of the final state of the MD simulation trajectory, illustrating a side view of a cross-section cut through the middle of the surface aggregate modelled with the OPLS force field at the vacuum TIP4P/2005 interface. The CH and CF chains are coloured white and green, respectively. The water molecules are coloured red and white (oxygen and hydrogen atoms, respectively).

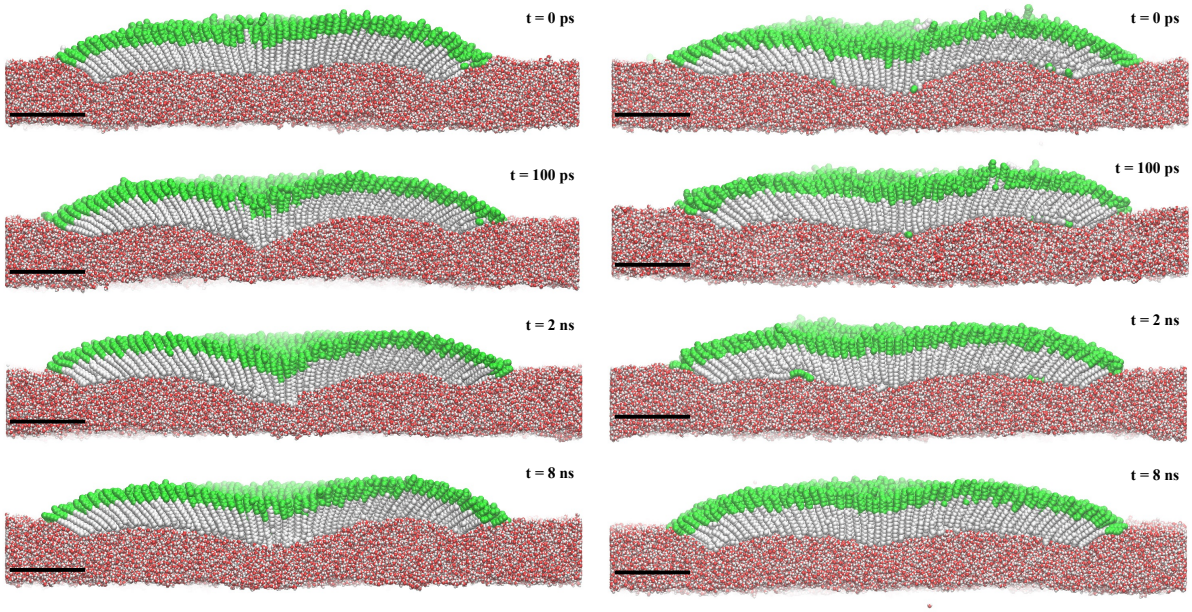

Figure A.5: Sequence of snapshots representative of the inter-conversion of pit-less hemimicelles to hemimicelles with a pit and vice-versa. Pit-less hemimicelles, obtained from a TraPPE simulation (left), developed a pit after including the dipole. Conversely, a pit-centred hemimicelle obtained from a TraPPE + dipole simulation (right) becomes pit-less upon the removal of the dipole. The scale bars are 5 nm long. These results are available in an animated visual representation at https://doi.org/10.1016/j.jcis.2023.11.007 [online: 02/01/2024].

A.2 Parameters used in the Molecular Dynamics simulations

A.2.1 Definitions

The parameters presented below were retrieved from various sources and, whenever necessary, their format and units were converted for compatibility with the GROMACS software package (v. 2020.6) [2]. The attention of the reader is drawn to the fact that, because of this, some parameters might vary by a factor of 2 (after any eventually necessary unit conversions), compared to the values presented in the original sources. This is due to differences in the formal definitions of some potential functions. For clarity, the functional forms of the potential functions used in this work are presented below, together with a reference to the corresponding equations in the GROMACS manual (v. 2020.6) [3]. All notation used herein is customary and is otherwise identical to the one used in this source.

A.2.1.1 Intermolecular interactions

a) Coulomb interaction (Eq. 5.125 in [3])

$$U_{\text{Coulomb}} = \frac{q_i q_j}{4\pi\varepsilon_0 r_{ij}} \tag{A.1}$$

b) Lennard-Jones interaction (Eq. 5.119 in [3])

$$U_{\text{LJ}} = 4\epsilon_{ij}\left(\left(\frac{\sigma_{ij}}{r_{ij}}\right)^{12} - \left(\frac{\sigma_{ij}}{r_{ij}}\right)^{6}\right) \tag{A.2}$$

A.2.1.2 Intramolecular interactions

a) Harmonic bond stretching potential (eq. 5.144 in [3])

$$U_{\text{Bond}} = \frac{1}{2}k^b_{ij}(r_{ij} - r^0_{ij})^2 \tag{A.3}$$

b) Harmonic angle bending potential (eq. 5.159 in [3])

$$U_{\text{Angle}} = \frac{1}{2}k^\theta_{ijk}(\theta_{ijk} - \theta^0_{ijk})^2 \tag{A.4}$$

c) Dihedral potential – Ryckaert-Bellemans (RB) form (eq. 5.174 in [3])

$$U_{\text{RB}} = \sum_{n=0}^{m} C_n(\cos(\psi))^n \tag{A.5}$$

Where m is the order of the highest order term in the series (i.e. $C_i = 0$ for $i > m$).

d) Dihedral potential – Fourier form (eq. 5.175 in [3])

$$U_{\text{Fourier}} = \frac{1}{2}\left[C_1(1+\cos(\phi)) + C_2(1-\cos(2\phi)) + C_3(1+\cos(3\phi)) + C_4(1-\cos(4\phi))\right] \tag{A.6}$$

A.2.2 Parameters

Note: within the framework of the used Force Fields, some bonds and angles are constrained to their equilibrium positions. Those cases are signalled by the word "rigid" in the places where the harmonic bond stretching or angle bending constants would be presented.

A.2.2.1 SPC/E water model

All the parameters for the SPC/E water model were sourced from reference [4].

Table A.1: Notation used for the SPC/E water model.

Interaction centre	**Notation**	**Atomic mass (a.m.u.)**
O	OW	15.9994
H	HW	1.0080

Table A.2: Non-bonded interaction parameters for the SPC/E water model.

Interaction centre	σ_{ii} (nm)	ϵ_{ii} ($\mathrm{kJ\,mol^{-1}}$)	q_i (e)
OW	0.316557	0.650194	-0.8476
HW	0.000000	0.000000	0.4238

Table A.3: Harmonic bond stretching parameters for the SPC/E water model.

Bond	r_{ij}^0 (nm)	k_{ij}^b ($\mathrm{kJ\,nm^2\,mol^{-1}}$)
OW-HW	0.100	rigid

Table A.4: Harmonic angle bending parameters for the SPC/E water model.

Angle	θ_{ijk}^0 (°)	k_{ijk}^θ ($\mathrm{kJ\,rad^2\,mol^{-1}}$)
HW-OW-HW	109.47	rigid

A.2.2.2 TIP4P/2005 water model

All the parameters for the TIP4P/2005 water model were sourced from reference [4].

Table A.5: Notation used for the TIP4P/2005 water model.

Interaction centre	**Notation**	**Atomic mass (a.m.u.)**
O (atom)	OW	15.9994
H (atom)	HW	1.0079
M (virtual interaction site)	MW	0.0000

Table A.6: Non-bonded interaction parameters for the TIP4P/2005 water model.

Interaction centre	σ_{ii} (nm)	ϵ_{ii} (kJ mol^{-1})	q_i (e)
OW	0.31589	0.77490	0.0000
MW	0.00000	0.00000	-1.1128
HW	0.00000	0.00000	0.5564

Table A.7: Harmonic bond stretching parameters for the TIP4P/2005 water model.

Bond	r_{ij}^0 (nm)	k_{ij}^b (kJ nm^2 mol^{-1})
OW-HW	0.09572	rigid
OW-MW	0.01546	rigid

Table A.8: Harmonic angle bending parameters for the TIP4P/2005 water model.

Angle	θ_{ijk}^0 (°)	k_{ijk}^θ (kJ rad^2 mol^{-1})
HW-OW-HW	104.52	rigid

A.2.2.3 F8H16 modelled with the OPLS-based Force Field

The parameters used to model the F8H16 molecules, within the framework of the OPLS Force Field, were sourced from several references (see tables below).

Table A.9: Notation used for the OPLS-based F8H16 molecules.

Interaction centre	**Notation**	**Atomic mass (a.m.u.)**
C (CH3)	CH3	12.0110
C (CH2)	CH2	12.0110
H (CH3)	H3	1.0080
H (CH2)	H2	1.0080
C (CF3)	CF3	12.0110
C (CF2)	CF2	12.0110
F	F	18.9984

Table A.10: Non-bonded interaction parameters for the OPLS-based F8H16 molecules.

Interaction centre	σ_{ii} (nm)	ϵ_{ii} (kJ mol^{-1})	q_i (e)	**Ref.**
CH3	0.350	0.276144	-0.222	[5, 6]
CH2	0.350	0.276144	-0.148	[5, 6]
H3	0.250	0.125520	0.074	[5, 6]
H2	0.250	0.110000	0.074	[5, 6]
CF3	0.350	0.276144	0.360	[7]
CF2	0.350	0.276144	0.240	[7]
F	0.295	0.221752	-0.120	[7]

Table A.11: Partial charges of the carbon atoms in the CF_2-CF_2-CH_2-CH_2 moiety of the OPLS-based F8H16 molecules. These atoms are correspondingly denoted CFB-CFA-CHA-CHB.

Interaction centre	q_i (e)	**Ref.**
CFB	0.205	[8]
CFA	0.135	[8]
CHA	0.037	[8]
CHB	-0.193	[8]

Table A.12: Harmonic bond stretching parameters for the OPLS-based F8H16 molecules.

Bond	r_{ij}^0 (nm)	k_{ij}^b (kJ nm^2 mol^{-1})	**Ref.**
CXx-CXx	0.1529	224262.4	[5–7, 9]
CHx-Hx	0.1090	284512.0	[5, 6, 9]
CFx-F	0.1332	307105.6	[7]

Table A.13: Harmonic angle bending parameters for the OPLS-based F8H16 molecules.

Angle	θ_{ijk}^0 (°)	k_{ijk}^θ (kJ rad^2 mol^{-1})	**Ref.**
CXx-CXx-CXx	112.7	488.273	[5–7, 9]
CXx-CHx-Hx	110.7	313.800	[5–7, 9]
Hx-CHx-Hx	107.8	276.144	[5–7, 9]
CXx-CFx-F	109.5	418.400	[7]
F-CFx-F	109.1	644.336	[5–7, 9]

Table A.14: Dihedral potential function parameters (RB function) for the OPLS-based F8H16 molecules.

Dihedral	**RB function coefficients** ($\mathrm{kJ\,mol^{-1}}$)					**Ref.**
	C_0	C_1	C_2	C_3	C_4	
CFx-CFx-CFx-F	1.46440	1.88280	0.00000	-3.34720	0.00000	[7]
CHx-CHx-CHx-CHx	0.51879	-0.23019	0.89681	-1.49134	0.00000	[6]
CFx-CFx-CFx-CFx	14.91596	-22.56431	-39.41328	11.61479	35.44685	[7]
CHx-CHx-CHx-Hx	0.62760	1.88280	0.00000	-2.51040	0.00000	[6, 9]
Hx-CHx-CHx-Hx	0.62760	1.88280	0.00000	-2.51040	0.00000	[6, 9]
F-CFx-CFx-F	-4.70700	6.79900	0.00000	-2.09200	0.00000	[7]
CHx-CHx-CHx-CFx	-0.98743	0.08368	1.65687	-0.40166	-0.35146	[8]
CHx-CHx-CFx-CFx	-1.21963	-0.18200	-0.50627	0.63596	1.27194	[8]
CHx-CFx-CFx-CFx	4.97059	-11.68591	-7.15045	5.79902	8.06675	[8]
F-CFx-CHx-Hx	0.60668	1.82004	0.00000	-2.42672	0.00000	[8]
F-CFx-CFx-CHx	1.38281	4.14844	0.00000	-5.53125	0.00000	[8]
F-CFx-CHx-CHx	0.96860	2.90579	0.00000	-3.87438	0.00000	[8]
Hx-CHx-CHx-CFx	0.27824	0.83471	0.00000	-1.11294	0.00000	[8]
Hx-CHx-CFx-CFx	0.37865	1.13596	0.00000	-1.51461	0.00000	[8]

A.2.2.4 F8H16 modelled with the TraPPE-based Force Field

The parameters used to model the F8H16 molecules, within the framework of the TraPPE Force Field, were sourced from several references (see tables below). In the case of reference [10], the parameters from the "model-T" presented therein were used.

Table A.15: Notation used for the TraPPE-based F8H16 molecules.

Interaction centre (bead)	**Notation**	**Atomic mass (a.m.u.)**
CH3	CH3	15.0350
CH2	CH2	14.0270
CF3	CF3	69.0062
CF2	CF2	50.0058

Table A.16: Non-bonded interaction parameters for the TraPPE-based F8H16 molecules.

Interaction centre	σ_{ii} (nm)	ϵ_{ii} ($\mathrm{kJ\,mol^{-1}}$)	**Ref.**
CH3	0.3787	0.837682	[11, 12]
CH2	0.4030	0.392443	[11, 12]
CF3	0.4360	0.723358	[13]
CF2	0.4730	0.228648	[13]

Note: the interaction centres are charge-neutral, except for the beads of the CH_2-CF_2 bond

in the case of the TraPPE + dipole aggregate. As explained in the manuscript, in this case, point charges of +0.3785 and −0.3785 were added to the CH2 and CF2 beads, respectively. The forcefield parameters are otherwise identical for the TraPPE and the TraPPE + dipole models.

Table A.17: Harmonic bond stretching parameters for the TraPPE-based F8H16 molecules.

Bond	r_{ij}^0 (nm)	k_{ij}^b ($\mathrm{kJ\,nm^2\,mol^{-1}}$)	**Ref.**
CXx-CXx	0.1540	rigid	[10, 13]

Table A.18: Harmonic angle bending parameters for the TraPPE-based F8H16 molecules.

Angle	θ_{ijk}^0 (°)	k_{ijk}^θ ($\mathrm{kJ\,rad^2\,mol^{-1}}$)	**Ref.**
CXx-CXx-CXx	114.0	519.654	[10, 13]

Table A.19: Dihedral potential function parameters (RB or Fourier functions) for the TraPPE-based F8H16 molecules.

Dihedral	**RB or Fourier function coefficients** ($\mathrm{kJ\,mol^{-1}}$)								**Function**	**Ref.**
	C_0	C_1	C_2	C_3	C_4	C_5	C_6	C_7		
CHx-CHx-CHx-CHx	0.00000	5.57121	-1.13393	13.15886	0.00000	0.00000	0.00000	0.00000	Fourier	[13]
CFx-CFx-CFx-CFx	7.81896	-2.35051	11.26781	56.53860	-65.47918	-117.79984	76.60731	34.28650	RB	[10, 13]

References

[1] P. Silva et al. 'Origin of the central pit in hemimicelles of semifluorinated alkanes: How molecular dipoles and substrate deformation can determine supra-molecular morphology'. In: *Journal of Colloid and Interface Science* 655 (2023), pp. 576–583. DOI: 10.1016/j.jcis.2023.11.007.

[2] M. J. Abraham et al. 'GROMACS: High performance molecular simulations through multi-level parallelism from laptops to supercomputers'. In: *SoftwareX* 1–2 (2015), pp. 19–25. DOI: 10.1016/j.softx.2015.06.001.

[3] E. Lindahl et al. *GROMACS 2020.6 Manual (2020.6)*. 2021. URL: https://doi.org/10.5281/zenodo.4576060 (visited on 25/10/2023).

[4] H. J. C. Berendsen, J. R. Grigera and T. P. Straatsma. 'The Missing Term in Effective Pair Potentials'. In: *Journal of Physical Chemistry* 91.24 (1987), pp. 6269–6271. DOI: 10.1021/j100308a038.

[5] W. L. Jorgensen, D. S. Maxwell and J. Tirado-Rives. 'Development and Testing of the OPLS All-Atom Force Field on Conformational Energetics and Properties of Organic Liquids'. In: *Journal of the American Chemical Society* 118.45 (1996), pp. 11225–11236. DOI: 10.1021/ja9621760.

[6] S. W. I. Siu, K. Pluhackova and R. A. Böckmann. 'Optimization of the OPLS-AA Force Field for Long Hydrocarbons'. In: *Journal of Chemical Theory and Computation* 8.4 (2012), pp. 1459–1470. DOI: 10.1021/ct200908r.

[7] E. K. Watkins and W. L. Jorgensen. 'Perfluoroalkanes: Conformational Analysis and Liquid-State Properties from ab Initio and Monte Carlo Calculations'. In: *Journal of Physical Chemistry A* 105.16 (2001), pp. 4118–4125. DOI: 10.1021/jp004071w.

[8] A. A. H. Pádua. 'Torsion Energy Profiles and Force Fields Derived from Ab Initio Calculations for Simulations of Hydrocarbon–Fluorocarbon Diblocks and Perfluoroalkylbromides'. In: *Journal of Physical Chemistry A* 106.43 (2002), pp. 10116–10123. DOI: 10.1021/jp025732n.

[9] M. L. P. Price, D. Ostrovsky and W. L. Jorgensen. 'Gas-Phase and Liquid-State Properties of Esters, Nitriles, and Nitro Compounds with the OPLS-AA Force Field'. In: *Journal of Computational Chemistry* 22.13 (2001), pp. 1340–1352. DOI: 10.1002/jcc.1092.

[10] S.T. Cui et al. 'Intermolecular potentials and vapor–liquid phase equilibria of perfluorinated alkanes'. In: *Fluid Phase Equilibria* 146.1 (1998), pp. 51–61. DOI: 10.1016/S0378-3812(98)00216-7.

[11] L. F. G. Martins et al. 'Solubility of xenon in liquid *n*-alkanes and cycloalkanes by computer simulation. Towards the perfect anaesthetic'. In: *Journal of Molecular Liquids* 340 (2021), p. 117272. DOI: 10.1016/j.molliq.2021.117272.

[12] M. G. Martin and J. Ilja Siepmann. 'Transferable Potentials for Phase Equilibria. 1. United-Atom Description of *n*-Alkanes'. In: *Journal of Physical Chemistry B* 102.14 (1998), pp. 2569–2577. DOI: 10.1021/jp972543+.

[13] L. Zhang and J. I. Siepmann. 'Pressure Dependence of the Vapor–Liquid–Liquid Phase Behavior in Ternary Mixtures Consisting of *n*-Alkanes, *n*-Perfluoroalkanes, and Carbon Dioxide'. In: *Journal of Physical Chemistry B* 109.7 (2005), pp. 2911–2919. DOI: 10.1021/jp0482114.

Appendix B

Modelling the internal structure and size of PFAA hemimicelles: supplementary results

B.1 Calculated GIXD patterns from the MD simulations of pure hemimicelles

The GIXD pattern was estimated by computing the structure factor or the scattering intensity as a function of the in-plane (Q_{xy}) and out-of-plane (Q_z) components or Cartesian coordinates of the scattering vector calculated from the final configurations of each of the MD simulation trajectories of the pure hemimicelles of the F8Hm and the FnH16 data sets. The results presented herein are supplementary to those presented in Chapter 9. The diffraction intensity was also computed in polar coordinates, that is as a function of the modulus of the scattering vector (Q) and the out-of-plane angle with the interface (θ). In line with the treatment of the experimental data presented in Chapter 11, the θ-integrated diffractograms were obtained for small values of θ (*i.e.* the diffraction intensity integrated along θ in the range of 0 rad to 0.1 rad, or about 0° to 5.73°, and represented as a function of Q). The θ-integrated diffractograms were fitted with Lorentzian curves.

B.1.1 Hemimicelle with 1700 molecules of F8H14

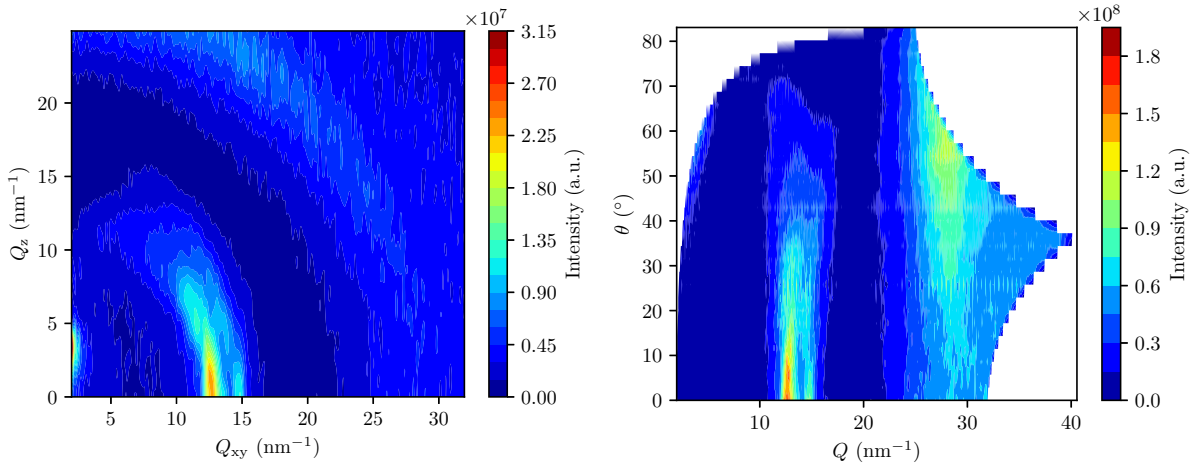

Figure B.1: Left: contour plot of the diffraction intensity as a function of the in-plane (Q_{xy}) and out-of-plane (Q_z) components of the scattering vector calculated from the final configuration of the MD simulation trajectory of the pure F8H14 hemimicelle, which contained 1700 molecules of PFAA. Right: the same dataset, but represented in polar coordinates, that is the contour plot of the diffraction intensity as a function of the modulus of the scattering vector (Q) and the out-of-plane angle with the interface (θ).

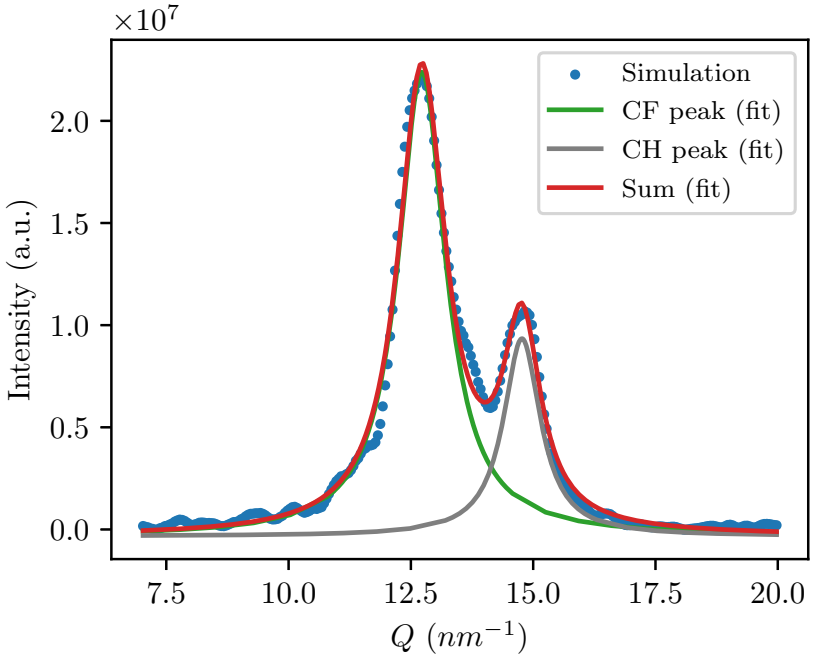

Figure B.2: GIXD θ-integrated diffractogram for small values of θ (*i.e.* the intensity presented in Figure B.1 integrated along θ in the range of 0 rad to 0.1 rad, or about 0° to 5.73°, as a function of Q), calculated from the final configuration of the MD simulation trajectory of the pure F8H14 hemimicelle, which contained 1700 molecules of PFAA. The blue circles represent the data points retrieved from the calculation and the curves represent the fitted Lorentzian peaks corresponding to the proposed structures, labelled "CF peak" (green) and "CH peak" (grey). The red curve is the cumulative sum of the remaining fitted curves.

B.1.2 Hemimicelle with 2500 molecules of F8H16

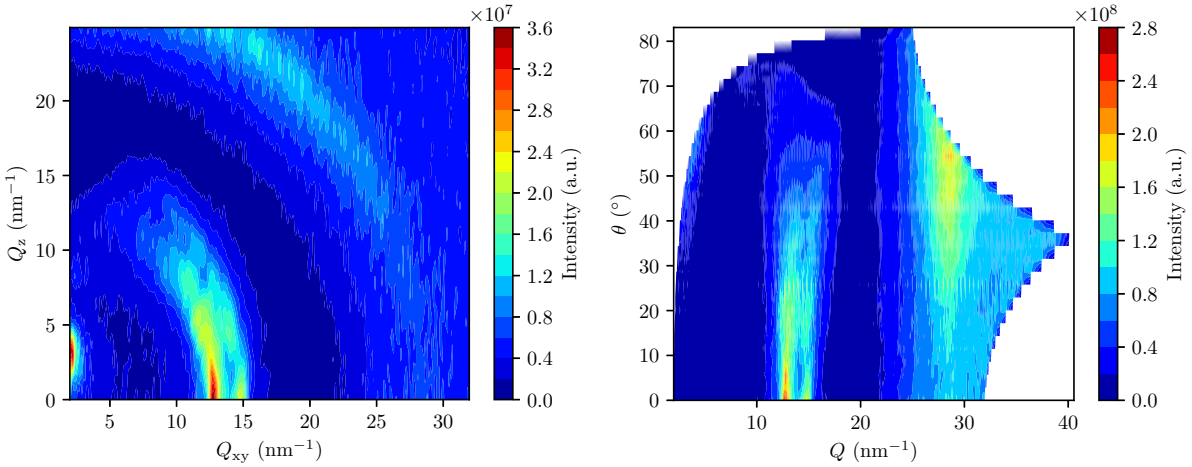

Figure B.3: Left: contour plot of the diffraction intensity as a function of the in-plane (Q_{xy}) and out-of-plane (Q_z) components of the scattering vector calculated from the final configuration of the MD simulation trajectory of the pure F8H16 hemimicelle, which contained 2500 molecules of PFAA. Right: the same dataset, but represented in polar coordinates, that is the contour plot of the diffraction intensity as a function of the modulus of the scattering vector (Q) and the out-of-plane angle with the interface (θ).

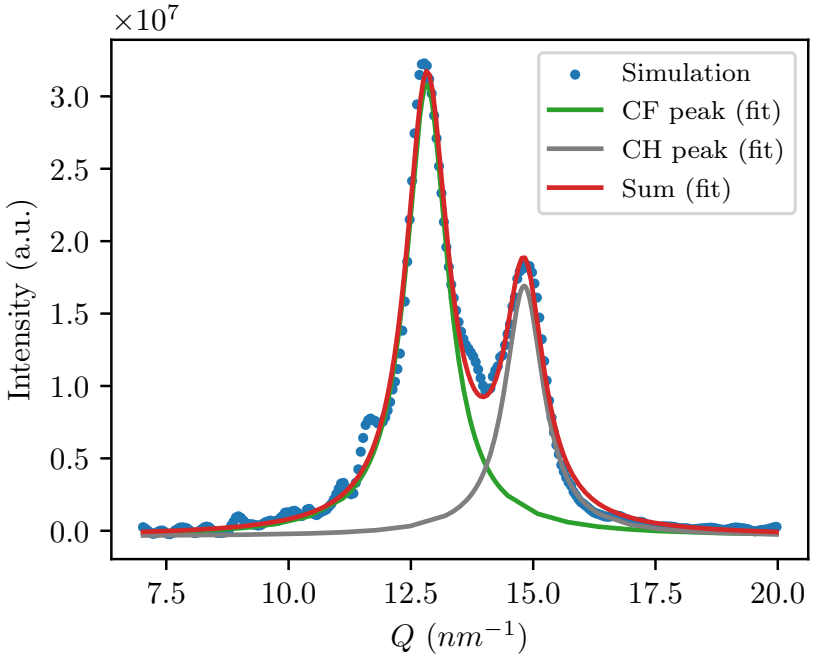

Figure B.4: GIXD θ-integrated diffractogram for small values of θ (*i.e.* the intensity presented in Figure B.3 integrated along θ in the range of 0 rad to 0.1 rad, or about 0° to 5.73°, as a function of Q), calculated from the final configuration of the MD simulation trajectory of the pure F8H16 hemimicelle, which contained 2500 molecules of PFAA. The blue circles represent the data points retrieved from the calculation and the curves represent the fitted Lorentzian peaks corresponding to the proposed structures, labelled "CF peak" (green) and "CH peak" (grey). The red curve is the cumulative sum of the remaining fitted curves.

B.1.3 Hemimicelle with 3200 molecules of F8H18

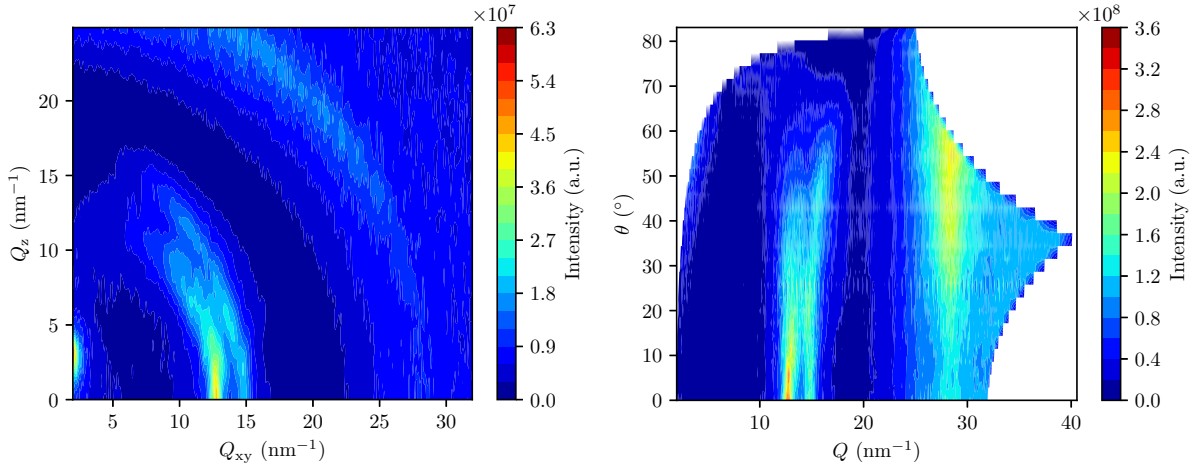

Figure B.5: Left: contour plot of the diffraction intensity as a function of the in-plane (Q_{xy}) and out-of-plane (Q_z) components of the scattering vector calculated from the final configuration of the MD simulation trajectory of the pure F8H18 hemimicelle, which contained 3200 molecules of PFAA. Right: the same dataset, but represented in polar coordinates, that is the contour plot of the diffraction intensity as a function of the modulus of the scattering vector (Q) and the out-of-plane angle with the interface (θ).

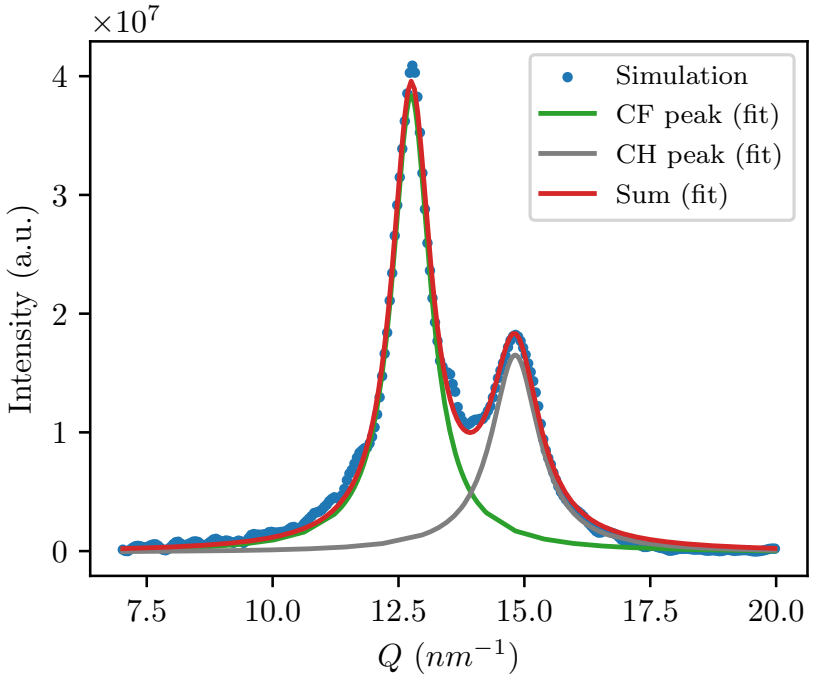

Figure B.6: GIXD θ-integrated diffractogram for small values of θ (*i.e.* the intensity presented in Figure B.3 integrated along θ in the range of 0 rad to 0.1 rad, or about 0° to 5.73°, as a function of Q), calculated from the final configuration of the MD simulation trajectory of the pure F8H18 hemimicelle, which contained 3200 molecules of PFAA. The blue circles represent the data points retrieved from the calculation and the curves represent the fitted Lorentzian peaks corresponding to the proposed structures, labelled "CF peak" (green) and "CH peak" (grey). The red curve is the cumulative sum of the remaining fitted curves.

B.1.4 Hemimicelle with 3900 molecules of F8H20

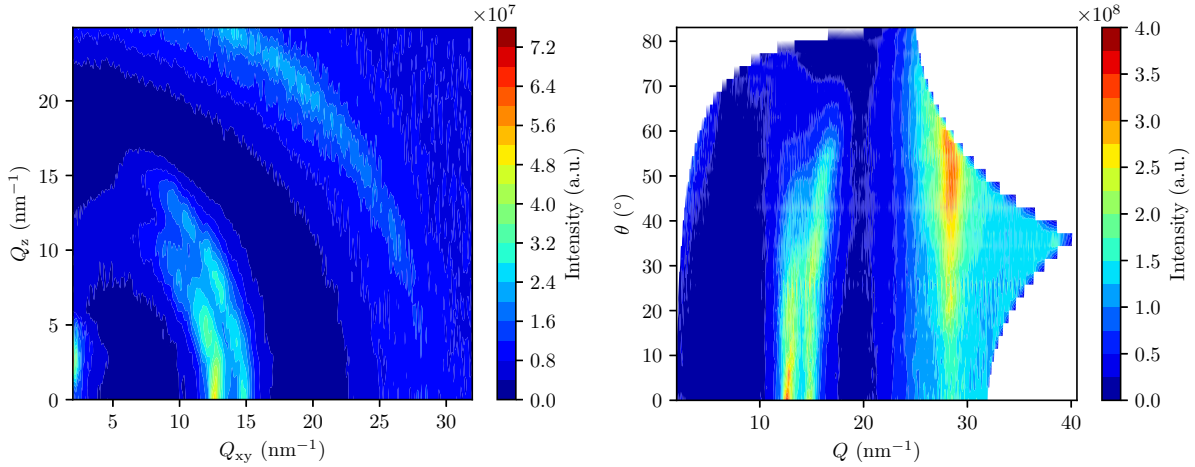

Figure B.7: Left: contour plot of the diffraction intensity as a function of the in-plane (Q_{xy}) and out-of-plane (Q_z) components of the scattering vector calculated from the final configuration of the MD simulation trajectory of the pure F8H20 hemimicelle, which contained 3900 molecules of PFAA. Right: the same dataset, but represented in polar coordinates, that is the contour plot of the diffraction intensity as a function of the modulus of the scattering vector (Q) and the out-of-plane angle with the interface (θ).

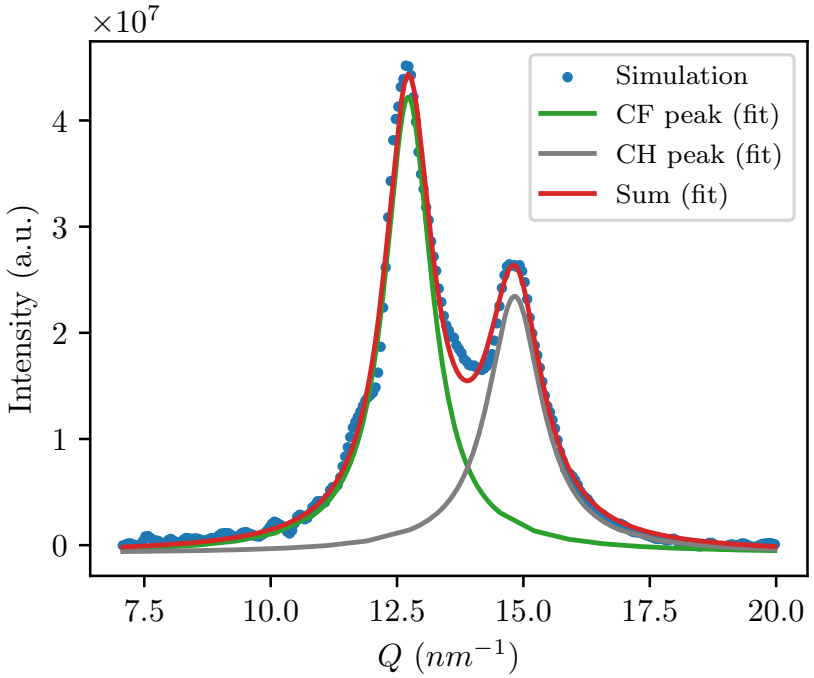

Figure B.8: GIXD θ-integrated diffractogram for small values of θ (*i.e.* the intensity presented in Figure B.3 integrated along θ in the range of 0 rad to 0.1 rad, or about 0° to 5.73°, as a function of Q), calculated from the final configuration of the MD simulation trajectory of the pure F8H20 hemimicelle, which contained 3900 molecules of PFAA. The blue circles represent the data points retrieved from the calculation and the curves represent the fitted Lorentzian peaks corresponding to the proposed structures, labelled "CF peak" (green) and "CH peak" (grey). The red curve is the cumulative sum of the remaining fitted curves.

B.1.5 Hemimicelle with 2486 molecules of F6H16

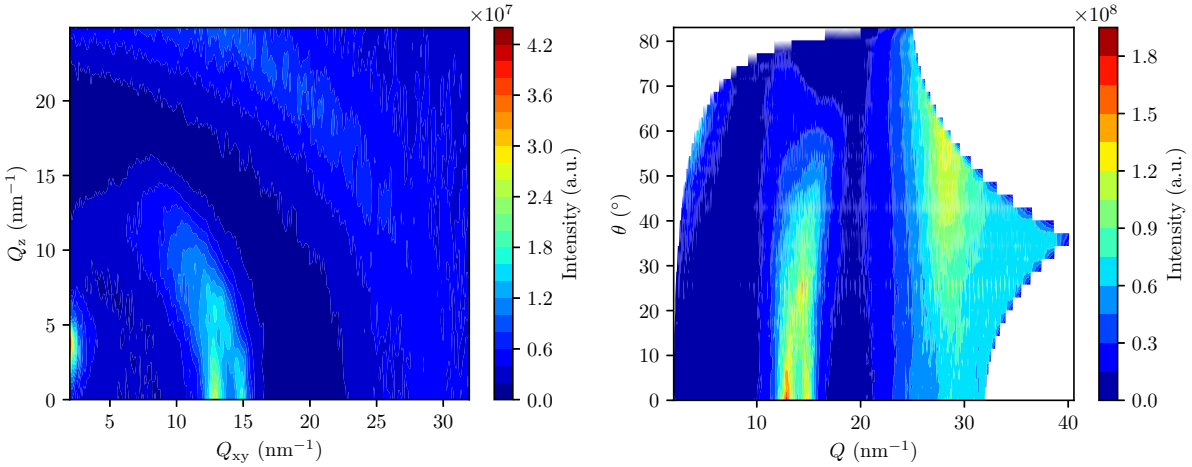

Figure B.9: Left: contour plot of the diffraction intensity as a function of the in-plane (Q_{xy}) and out-of-plane (Q_z) components of the scattering vector calculated from the final configuration of the MD simulation trajectory of the pure F6H16 hemimicelle, which contained 2486 molecules of PFAA. Right: the same dataset, but represented in polar coordinates, that is the contour plot of the diffraction intensity as a function of the modulus of the scattering vector (Q) and the out-of-plane angle with the interface (θ).

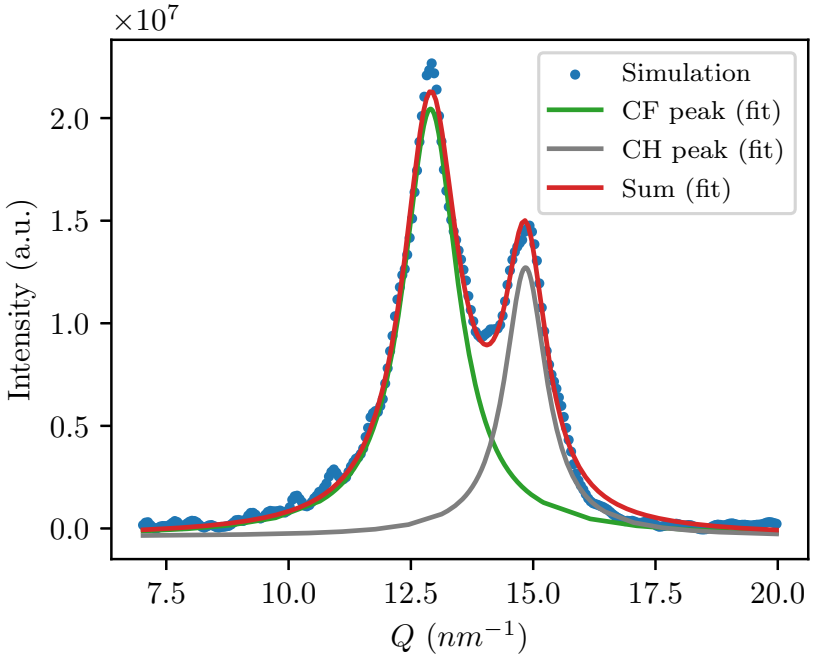

Figure B.10: GIXD θ-integrated diffractogram for small values of θ (*i.e.* the intensity presented in Figure B.3 integrated along θ in the range of 0 rad to 0.1 rad, or about 0° to 5.73°, as a function of Q), calculated from the final configuration of the MD simulation trajectory of the pure F6H16 hemimicelle, which contained 2486 molecules of PFAA. The blue circles represent the data points retrieved from the calculation and the curves represent the fitted Lorentzian peaks corresponding to the proposed structures, labelled "CF peak" (green) and "CH peak" (grey). The red curve is the cumulative sum of the remaining fitted curves.

B.1.6 Hemimicelle with 2550 molecules of F10H16

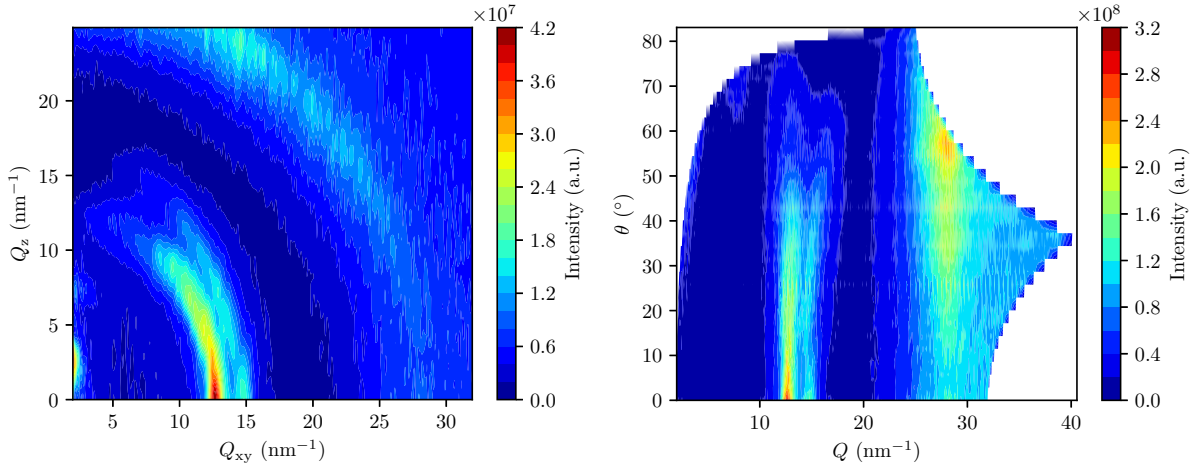

Figure B.11: Left: contour plot of the diffraction intensity as a function of the in-plane (Q_{xy}) and out-of-plane (Q_z) components of the scattering vector calculated from the final configuration of the MD simulation trajectory of the pure F10H16 hemimicelle, which contained 2550 molecules of PFAA. Right: the same dataset, but represented in polar coordinates, that is the contour plot of the diffraction intensity as a function of the modulus of the scattering vector (Q) and the out-of-plane angle with the interface (θ).

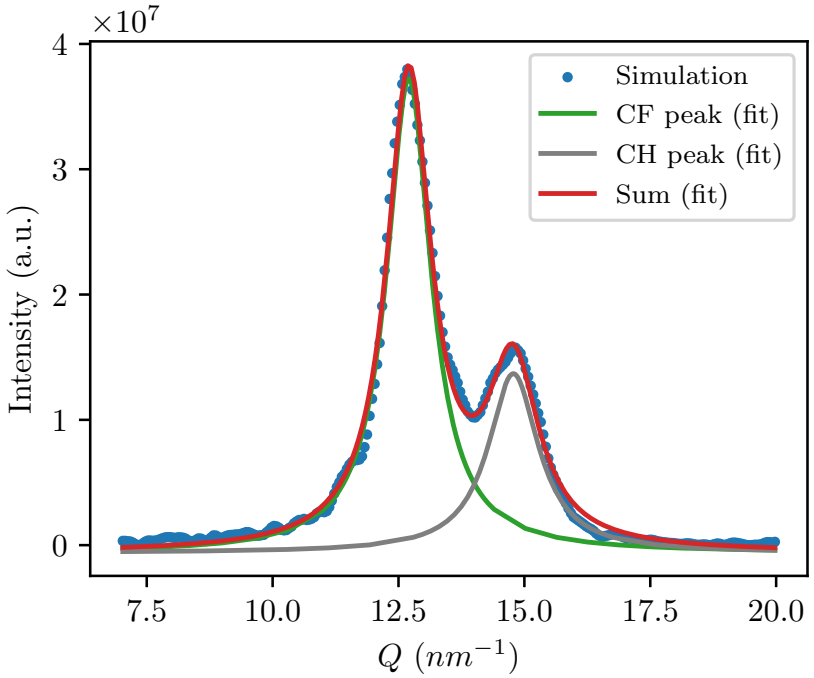

Figure B.12: GIXD θ-integrated diffractogram for small values of θ (*i.e.* the intensity presented in Figure B.3 integrated along θ in the range of 0 rad to 0.1 rad, or about 0° to 5.73°, as a function of Q), calculated from the final configuration of the MD simulation trajectory of the pure F10H16 hemimicelle, which contained 2550 molecules of PFAA. The blue circles represent the data points retrieved from the calculation and the curves represent the fitted Lorentzian peaks corresponding to the proposed structures, labelled "CF peak" (green) and "CH peak" (grey). The red curve is the cumulative sum of the remaining fitted curves.

B.1.7 Hemimicelle with 3200 molecules of F12H16

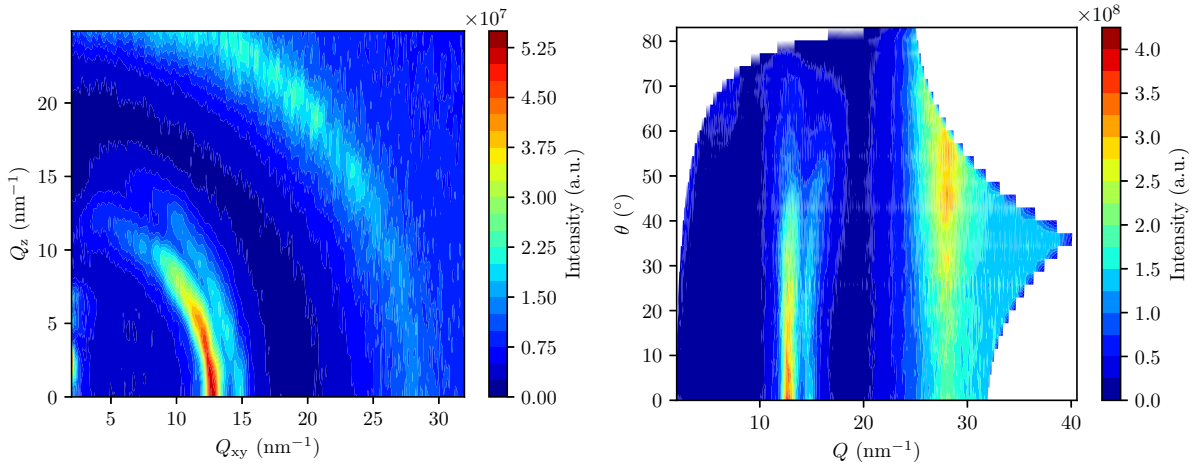

Figure B.13: Left: contour plot of the diffraction intensity as a function of the in-plane (Q_{xy}) and out-of-plane (Q_z) components of the scattering vector calculated from the final configuration of the MD simulation trajectory of the pure F12H16 hemimicelle, which contained 3200 molecules of PFAA. Right: the same dataset, but represented in polar coordinates, that is the contour plot of the diffraction intensity as a function of the modulus of the scattering vector (Q) and the out-of-plane angle with the interface (θ).

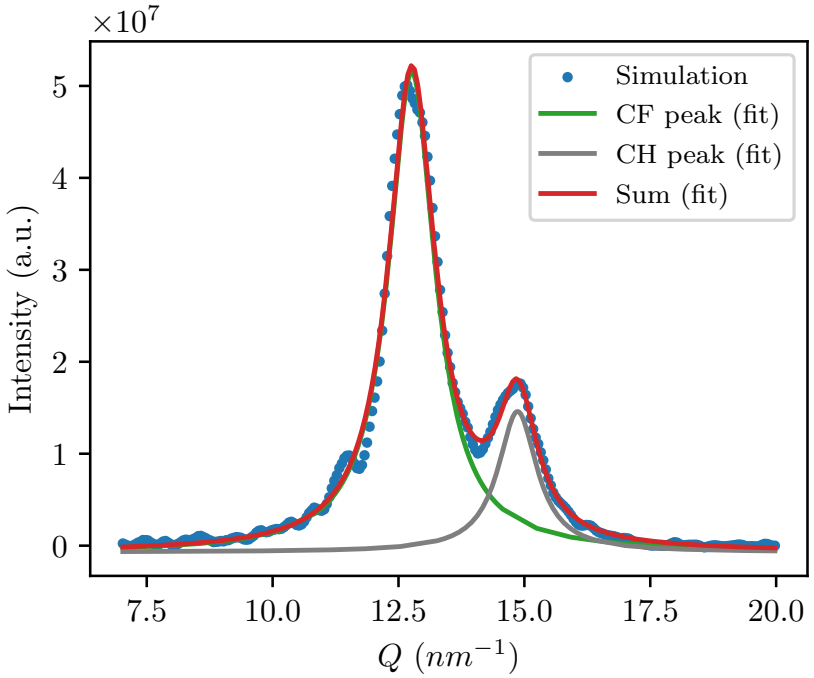

Figure B.14: GIXD θ-integrated diffractogram for small values of θ (*i.e.* the intensity presented in Figure B.3 integrated along θ in the range of 0 rad to 0.1 rad, or about 0° to 5.73°, as a function of Q), calculated from the final configuration of the MD simulation trajectory of the pure F12H16 hemimicelle, which contained 3200 molecules of PFAA. The blue circles represent the data points retrieved from the calculation and the curves represent the fitted Lorentzian peaks corresponding to the proposed structures, labelled "CF peak" (green) and "CH peak" (grey). The red curve is the cumulative sum of the remaining fitted curves.

Table B.1: Parameters for the "CF peak" obtained from the fits to the results of the GIXD pattern calculated from the MD simulation trajectories of the hemimicelles of different PFAA molecules: peak position (Position), peak integrated area (Area), peak Full Width at Half Maximum (FWHM), lattice parameter (a), area of the unit cell ($A^{\text{Unit Cell}}$) and coherence length (ξ).

Molecule	Position (nm^{-1})	Area (a.u.)	FWHM (nm^{-1})	a (nm)	$A^{\text{Unit Cell}}$ (nm^2)	ξ (nm)
F8H14	12.724 ± 0.005	$(4.213 \pm 0.048) \times 10^7$	1.181 ± 0.016	0.570	0.282	1.69
F8H16	12.827 ± 0.005	$(5.105 \pm 0.064) \times 10^7$	1.042 ± 0.016	0.566	0.277	1.92
F8H18	12.753 ± 0.003	$(5.591 \pm 0.046) \times 10^7$	0.925 ± 0.009	0.569	0.280	2.16
F8H20	12.721 ± 0.005	$(7.680 \pm 0.090) \times 10^7$	1.138 ± 0.016	0.570	0.282	1.76
F6H16	12.901 ± 0.005	$(4.456 \pm 0.047) \times 10^7$	1.361 ± 0.016	0.562	0.274	1.47
F10H16	12.705 ± 0.003	$(6.381 \pm 0.057) \times 10^7$	1.075 ± 0.012	0.571	0.282	1.86
F12H16	12.763 ± 0.004	$(9.289 \pm 0.089) \times 10^7$	1.133 ± 0.013	0.568	0.280	1.77

Table B.2: Parameters for the "CH peak" obtained from the fits to the results of the GIXD pattern calculated from the MD simulation trajectories of the hemimicelles of different PFAA molecules: peak position (Position), peak integrated area (Area), peak Full Width at Half Maximum (FWHM), lattice parameter (a), area of the unit cell ($A^{\text{Unit Cell}}$) and coherence length (ξ).

Molecule	Position (nm^{-1})	Area (a.u.)	FWHM (nm^{-1})	a (nm)	$A^{\text{Unit Cell}}$ (nm^2)	ξ (nm)
F8H14	14.770 ± 0.010	$(1.398 \pm 0.040) \times 10^7$	0.920 ± 0.032	0.491	0.209	2.17
F8H16	14.816 ± 0.008	$(2.630 \pm 0.060) \times 10^7$	0.968 ± 0.027	0.490	0.208	2.07
F8H18	14.818 ± 0.008	$(3.031 \pm 0.054) \times 10^7$	1.159 ± 0.025	0.490	0.208	1.73
F8H20	14.828 ± 0.009	$(5.02 \pm 0.10) \times 10^7$	1.319 ± 0.031	0.489	0.207	1.52
F6H16	14.844 ± 0.006	$(2.138 \pm 0.038) \times 10^7$	1.037 ± 0.022	0.489	0.207	1.93
F10H16	14.780 ± 0.010	$(2.732 \pm 0.062) \times 10^7$	1.217 ± 0.033	0.491	0.209	1.64
F12H16	14.864 ± 0.012	$(2.270 \pm 0.078) \times 10^7$	0.945 ± 0.040	0.488	0.206	2.12

B.2 Spatial Distribution Functions from the MD simulations of pure hemimicelles

Following the results presented in Chapters 8 and 9, the Spacial Distribution Functions (SDFs) of the CH and CF carbon atoms in the CH_2–CF_2 bond were computed for all the limit size hemimicelles that were simulated. Several snapshots of the visual representations of these SDFs are presented below, complementing the results presented therein. The pictures display the surfaces of constant particle density corresponding to the presented "Isovalues" (in particles/nm).

B.2.1 Hemimicelle with 3200 molecules of F12H16

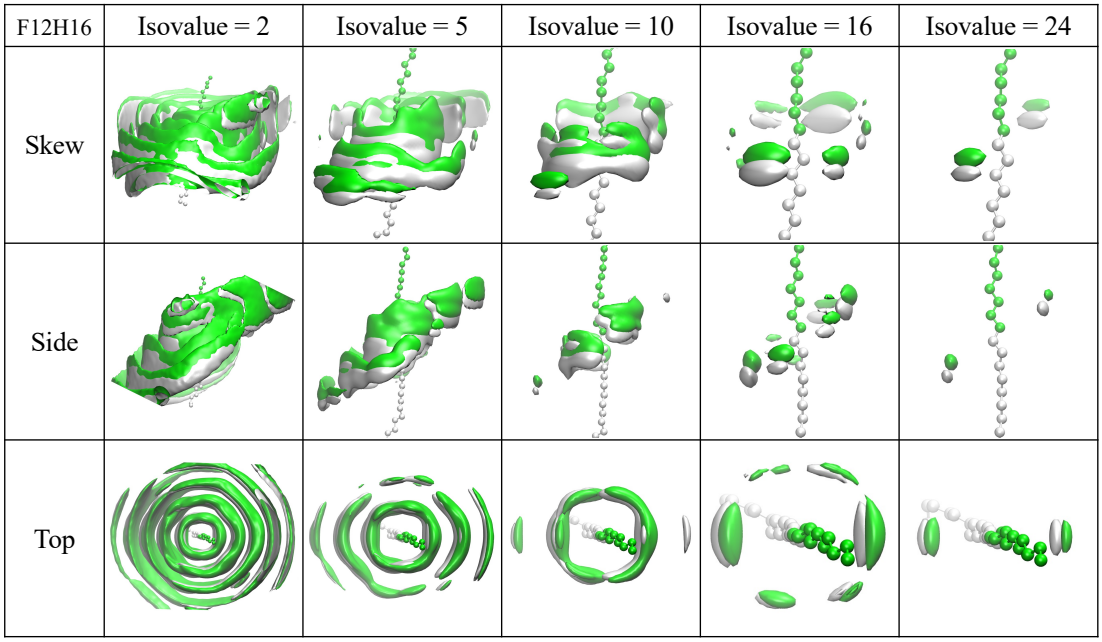

Figure B.15: Spatial Distribution Functions (SDFs) of the CH (white) and CF (green) carbon atoms in the CH_2–CF_2 bond, obtained for the molecules comprising the F12H16 hemimicelle.

B.2.2 Hemimicelle with 1700 molecules of F8H14

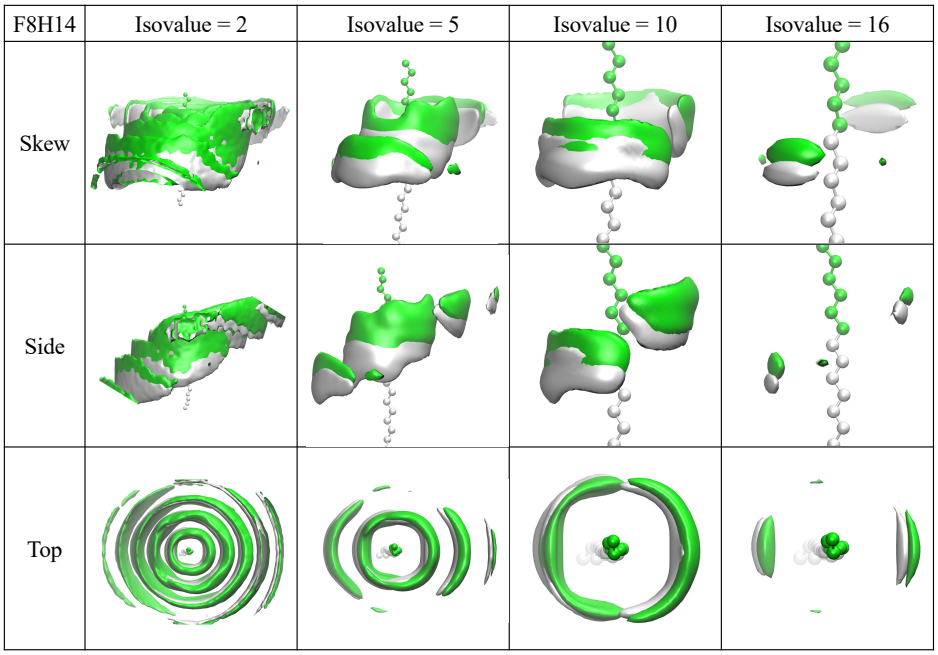

Figure B.16: Spatial Distribution Functions (SDFs) of the CH (white) and CF (green) carbon atoms in the CH_2–CF_2 bond, obtained for the molecules comprising the F8H14 hemimicelle.

B.2.3 Hemimicelle with 2500 molecules of F8H16

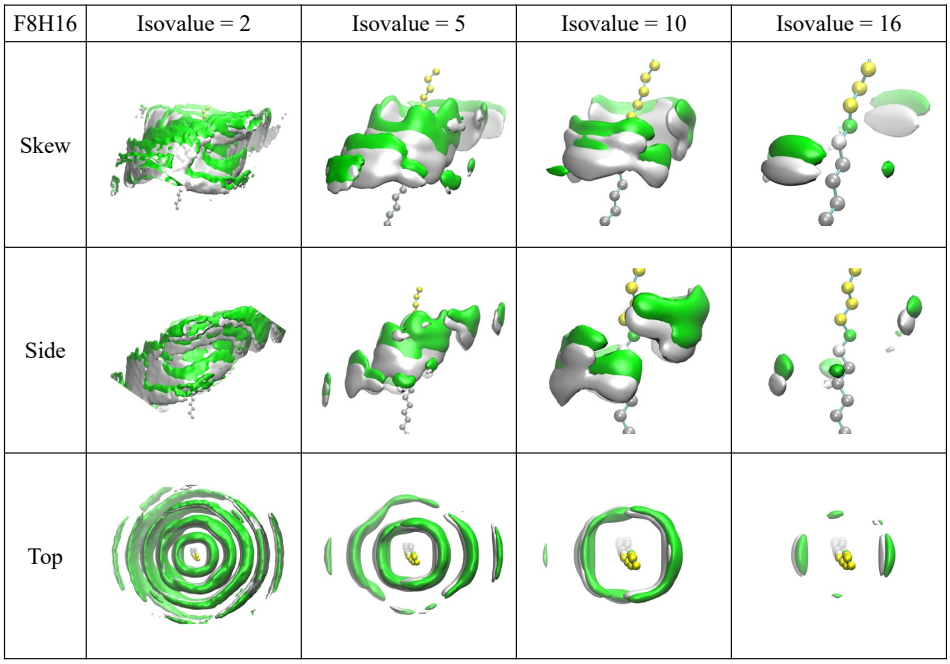

Figure B.17: Spatial Distribution Functions (SDFs) of the CH (white) and CF (green) carbon atoms in the CH_2–CF_2 bond, obtained for the molecules comprising the F8H16 hemimicelle.

B.2.4 Hemimicelle with 3200 molecules of F8H18

F8H18	Isovalue = 2	Isovalue = 5	Isovalue = 10	Isovalue = 16
Skew	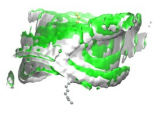	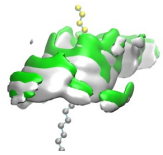	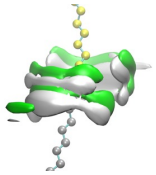	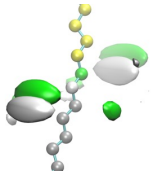
Side	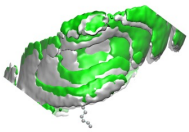	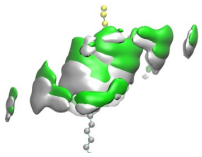	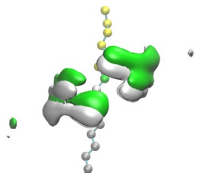	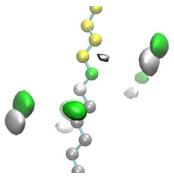
Top	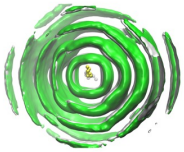			

Figure B.18: Spatial Distribution Functions (SDFs) of the CH (white) and CF (green) carbon atoms in the CH_2–CF_2 bond, obtained for the molecules comprising the F8H18 hemimicelle.

B.2.5 Hemimicelle with 3900 molecules of F8H20

F8H20	Isovalue = 2	Isovalue = 5	Isovalue = 10	Isovalue = 16
Skew	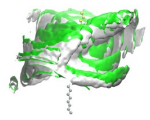	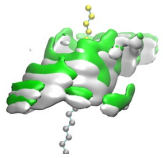	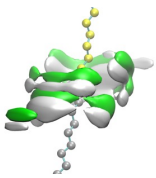	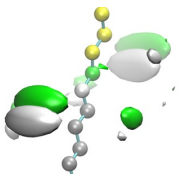
Side	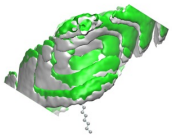	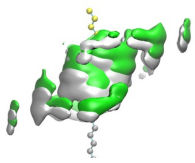	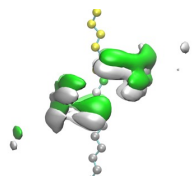	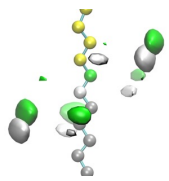
Top	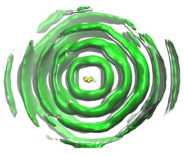	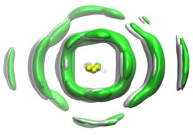		

Figure B.19: Spatial Distribution Functions (SDFs) of the CH (white) and CF (green) carbon atoms in the CH_2–CF_2 bond, obtained for the molecules comprising the F8H20 hemimicelle.

B.2.6 Hemimicelle with 2486 molecules of F6H16

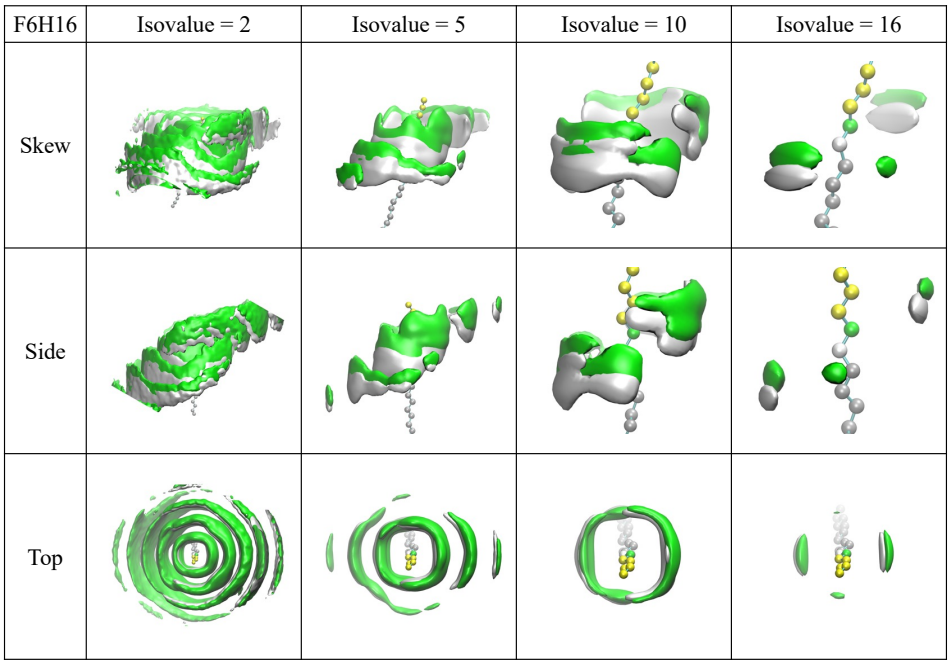

Figure B.20: Spatial Distribution Functions (SDFs) of the CH (white) and CF (green) carbon atoms in the CH_2–CF_2 bond, obtained for the molecules comprising the F6H16 hemimicelle.

B.2.7 Hemimicelle with 2550 molecules of F10H16

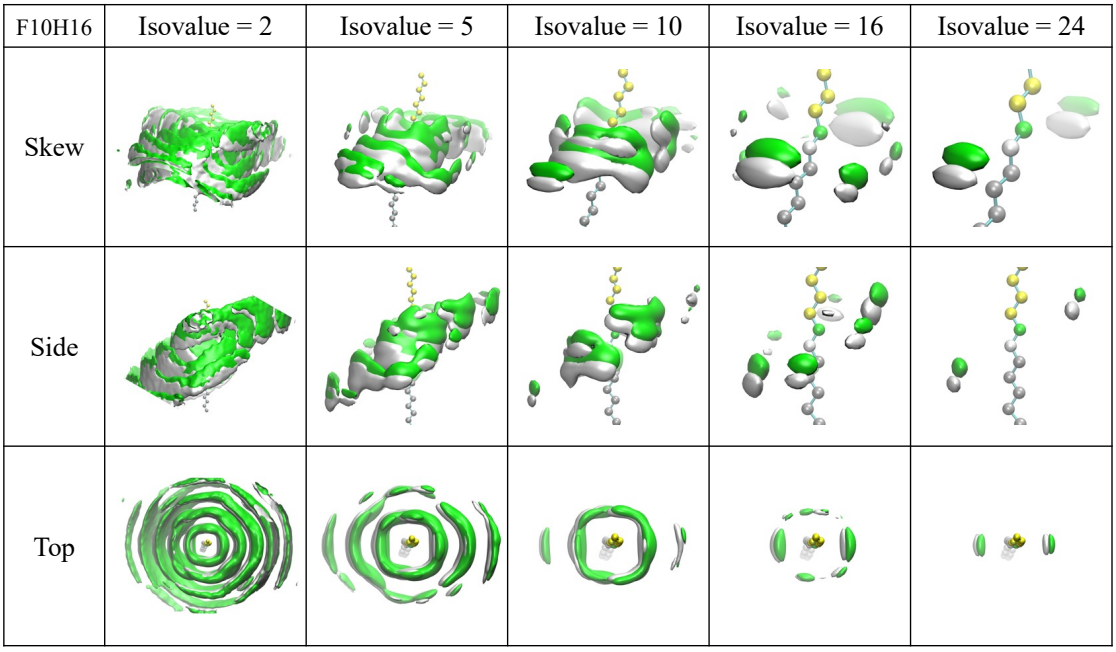

Figure B.21: Spatial Distribution Functions (SDFs) of the CH (white) and CF (green) carbon atoms in the CH_2–CF_2 bond, obtained for the molecules comprising the F10H16 hemimicelle.

B.3 Supplementary results: F10Hm and F12Hm series

B.3.1 C_F–C_F–C_F–C_F dihedral angle ($\theta_{dihedral}$)

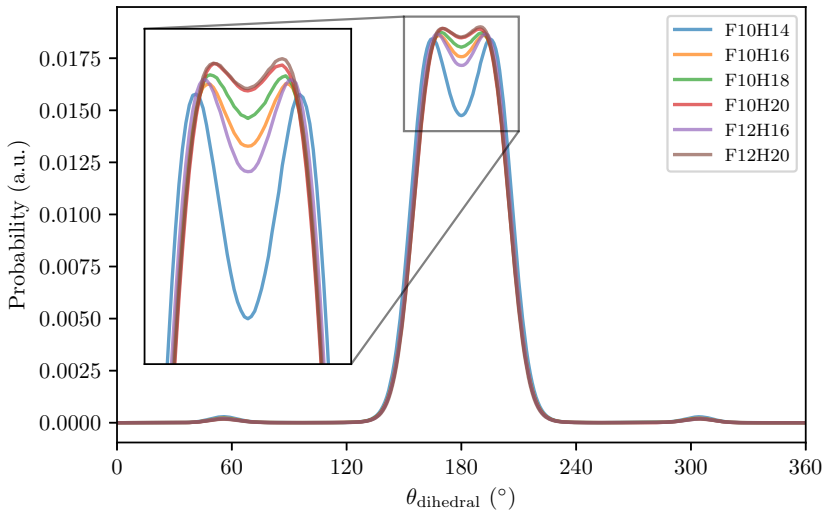

Figure B.22: Distribution of the C_F–C_F–C_F–C_F dihedral angles ($\theta_{dihedral}$) for hemimicelles of different PFAA molecules of the F10Hm and the F12Hm series (FnHm, indicated in brackets in the legend and highlighted in the inset). The $\theta_{dihedral}$ follows the IUPAC convention, for which $\theta_{dihedral} = 0°$ for the *cis* conformation. The symmetry (around 180°) of these distributions are indicative of the attainment of the limit size of the aggregates.

B.3.2 Hemimicelle size and molecular packing

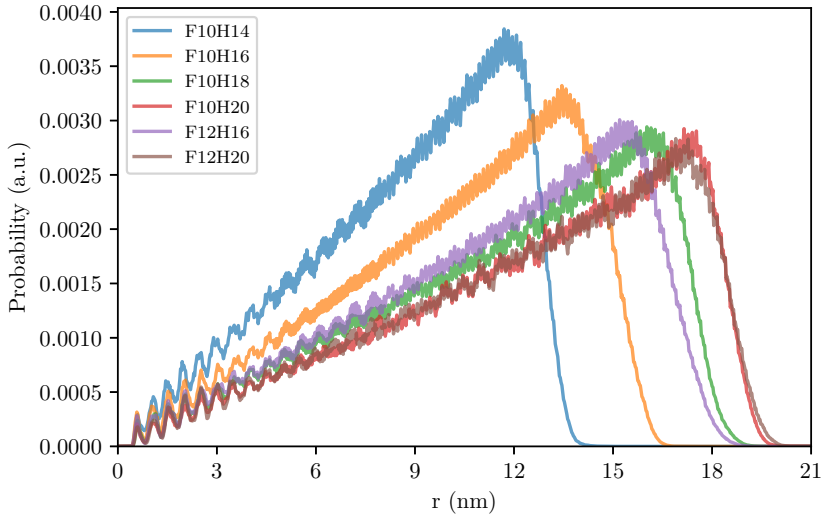

Figure B.23: Distribution of the of the probability of finding a PFAA molecule as a function of the radial distance (r) from the centre of the limit-size aggregates or hemimicelles of the F10Hm and the F12Hm series (FnHm, indicated in brackets in the legend and highlighted in the inset).

B.3.3 Illustrative snapshots of the MD simulations

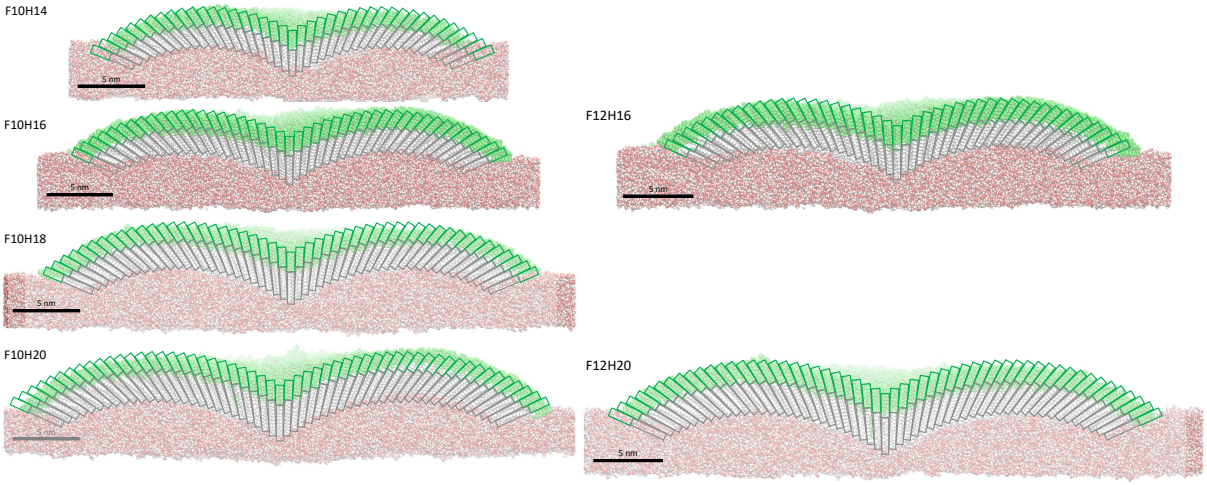

Figure B.24: Snapshots of the final state configurations of the cross-section cuts through the centre of the simulated PFAA limit-size aggregates or hemimicelles, for the F10Hm and the F12Hm series. The atoms pertaining to the CH and CF chains are represented in a space fill model and coloured white and green, respectively. The water molecules are represented in a space fill model and their oxygen and hydrogen atoms are coloured red and white, respectively. The corresponding hemimicelle structures constructed using the geometrical model are superimposed for comparison, representing the CH and CF chains as grey and green rectangles, respectively. All images are to the same scale.

B.3.4 Tilt angle (θ_{Tilt})

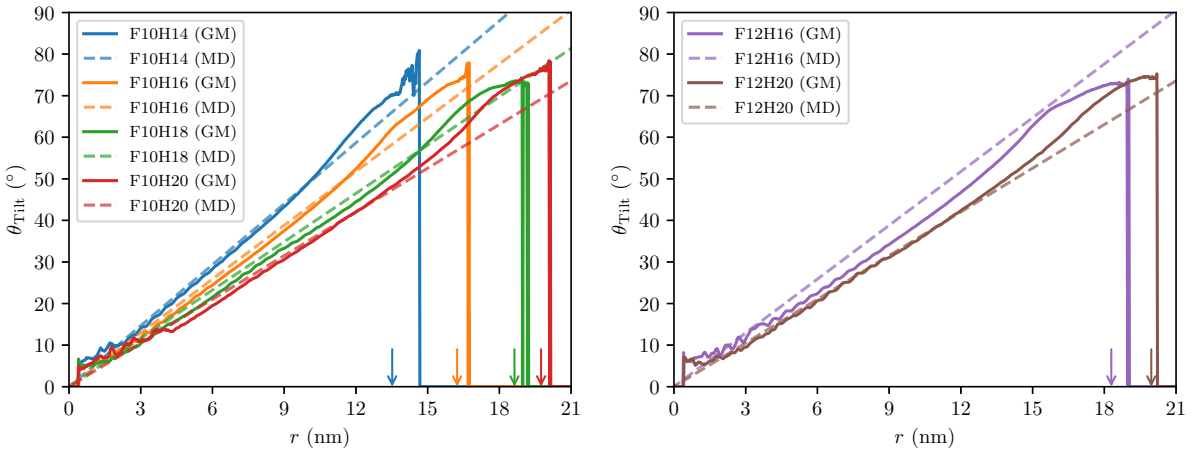

Figure B.25: Average tilt angle (θ_{Tilt}, full lines) as a function of the radial distance to centre of the aggregate (r) for the simulated limit-size aggregates or hemimicelles of F10Hm (m = 14, 16, 18, 20; left) and of F12Hm (m = 16, 20; right). The dashed lines represent the corresponding dependency of θ_{Tilt} on r predicted with the geometrical model. The arrows mark the radii of the hemimicelles computed from the MD simulation trajectories, using the same colour coding as the one presented in the legend.

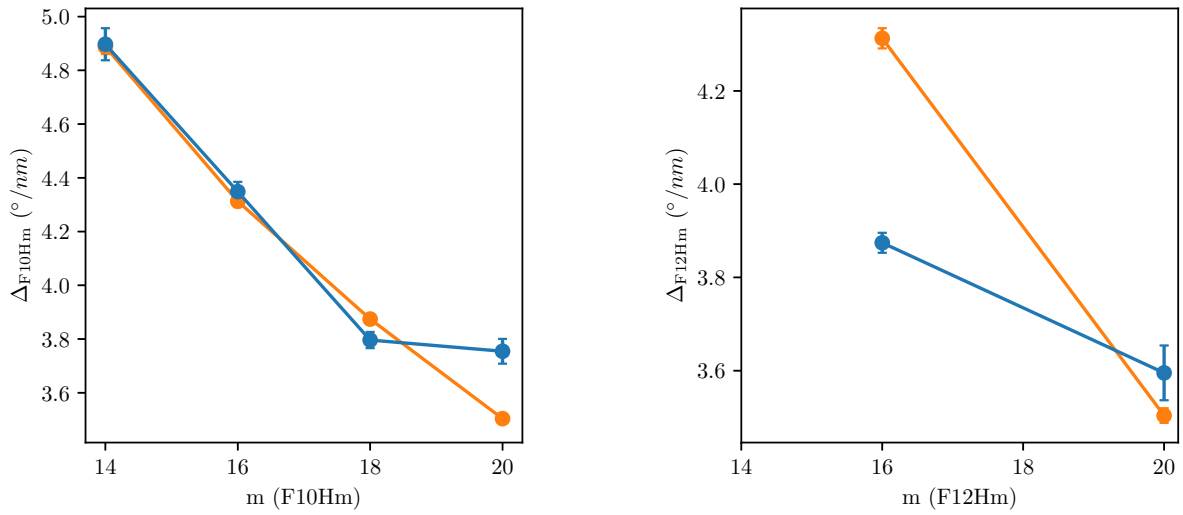

Figure B.26: Slope of the plots of average tilt angle as a function of the radial distance to centre of the aggregate (presented in Figure B.25) for the simulated hemimicelles of F10Hm (m = 14, 16, 18, 20; left) and of F12Hm (m = 16, 20; right): predicted by the geometrical model (orange) and obtained from the MD simulation results (blue).

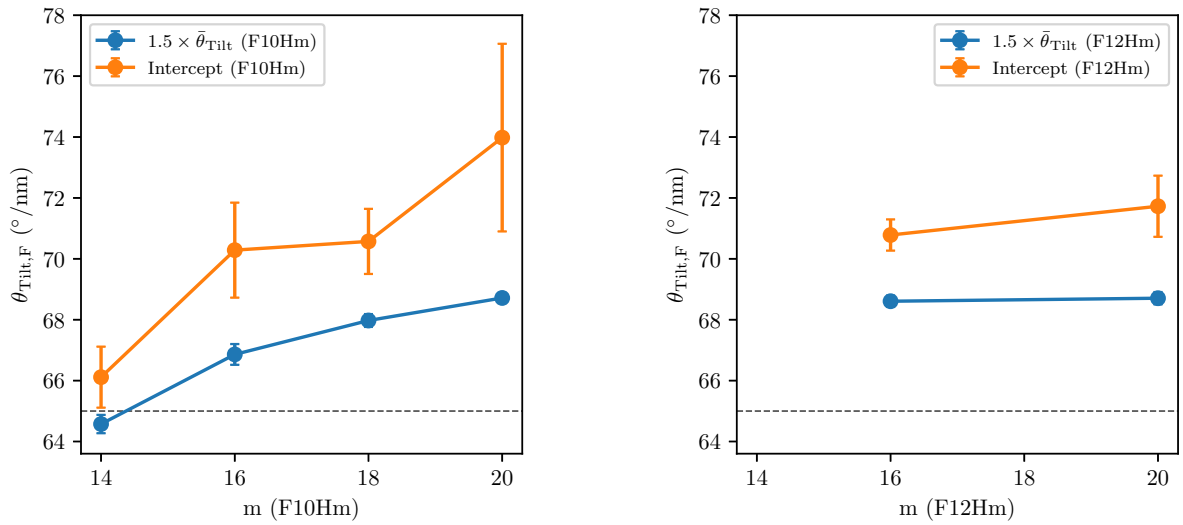

Figure B.27: Final tilt angle ($\theta_{\mathrm{Tilt,F}}$) estimated from the MD simulation results for the hemimicelles of F10Hm (m = 14, 16, 18, 20; left) and of F12Hm (m = 16, 20; right): calculated as the interception of the straight line going through the linear region in Figure 9.10 with the vertical line for the radius of the corresponding hemimicelle ("Intercept"; orange); and calculated as 1.5 times the average θ_{Tilt} ("$1.5 \times \bar{\theta}_{\mathrm{Tilt}}$"; blue), as presented in Equation 9.11. The dashed line marks the $\theta_{\mathrm{Tilt,F}} = 65°$ value that was assumed in the development of the geometrical model (*cf.* Subsection 9.3.2).

B.3.5 Calculated GIXD patterns from the MD simulations of pure hemimicelles

Table B.3: Parameters for the "CF peak" obtained from the fits to the results of the GIXD pattern calculated from the MD simulation trajectories of the hemimicelles of different PFAA molecules: peak position (Position), peak integrated area (Area), peak Full Width at Half Maximum (FWHM), lattice parameter (a), area of the unit cell ($A^{\text{Unit Cell}}$) and coherence length (ξ).

Molecule	Position (nm^{-1})	Area (a.u.)	FWHM (nm^{-1})	a (nm)	$A^{\text{Unit Cell}}$ (nm^2)	ξ (nm)
F10H14	12.760 ± 0.005	$(4.772 \pm 0.052) \times 10^7$	1.304 ± 0.017	0.569	0.280	1.53
F10H16	12.705 ± 0.003	$(6.381 \pm 0.057) \times 10^7$	1.075 ± 0.012	0.571	0.282	1.86
F10H18	12.778 ± 0.003	$(8.922 \pm 0.065) \times 10^7$	1.095 ± 0.010	0.568	0.279	1.83
F10H20	12.736 ± 0.003	$(9.701 \pm 0.073) \times 10^7$	0.986 ± 0.009	0.570	0.281	2.03
F12H16	12.763 ± 0.004	$(9.289 \pm 0.089) \times 10^7$	1.133 ± 0.013	0.568	0.280	1.77
F12H20	12.760 ± 0.004	$(1.036 \pm 0.011) \times 10^8$	0.989 ± 0.013	0.569	0.280	2.02

Table B.4: Parameters for the "CH peak" obtained from the fits to the results of the GIXD pattern calculated from the MD simulation trajectories of the hemimicelles of different PFAA molecules: peak position (Position), peak integrated area (Area), peak Full Width at Half Maximum (FWHM), lattice parameter (a), area of the unit cell ($A^{\text{Unit Cell}}$) and coherence length (ξ).

Molecule	Position (nm^{-1})	Area (a.u.)	FWHM (nm^{-1})	a (nm)	$A^{\text{Unit Cell}}$ (nm^2)	ξ (nm)
F10H14	14.814 ± 0.010	$(1.438 \pm 0.042) \times 10^7$	0.967 ± 0.034	0.490	0.208	2.07
F10H16	14.780 ± 0.010	$(2.732 \pm 0.062) \times 10^7$	1.217 ± 0.033	0.491	0.209	1.64
F10H18	14.907 ± 0.007	$(3.212 \pm 0.060) \times 10^7$	0.989 ± 0.023	0.487	0.205	2.02
F10H20	14.805 ± 0.007	$(4.992 \pm 0.083) \times 10^7$	1.179 ± 0.024	0.490	0.208	1.70
F12H16	14.864 ± 0.012	$(2.270 \pm 0.078) \times 10^7$	0.945 ± 0.040	0.488	0.206	2.12
F12H20	14.781 ± 0.012	$(5.140 \pm 0.140) \times 10^7$	1.296 ± 0.041	0.491	0.209	1.54

B.3.5.1 Hemimicelle with 1850 molecules of F10H14

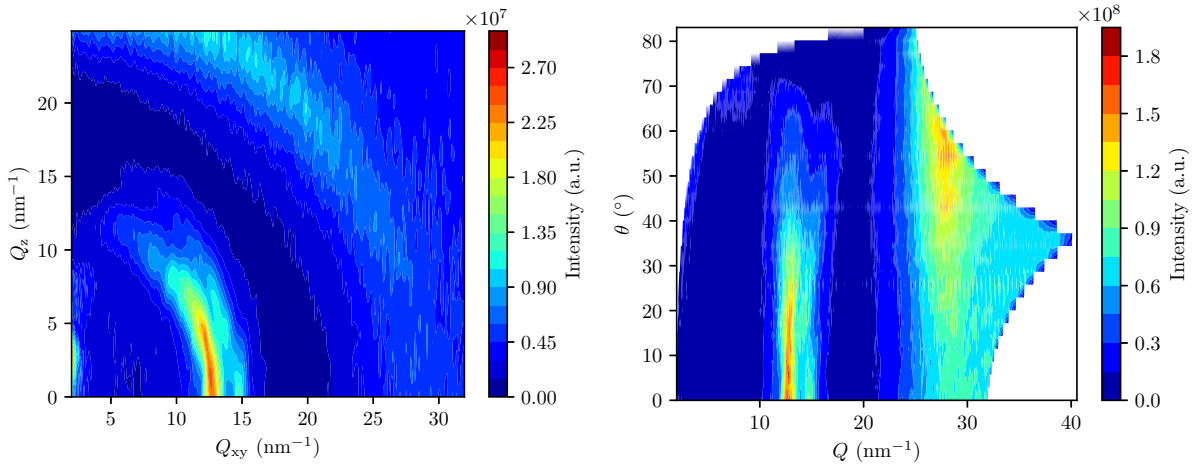

Figure B.28: Left: contour plot of the diffraction intensity as a function of the in-plane (Q_{xy}) and out-of-plane (Q_z) components of the scattering vector calculated from the final configuration of the MD simulation trajectory of the pure F10H14 hemimicelle, which contained 1850 molecules of PFAA. Right: the same dataset, but represented in polar coordinates, that is the contour plot of the diffraction intensity as a function of the modulus of the scattering vector (Q) and the out-of-plane angle with the interface (θ).

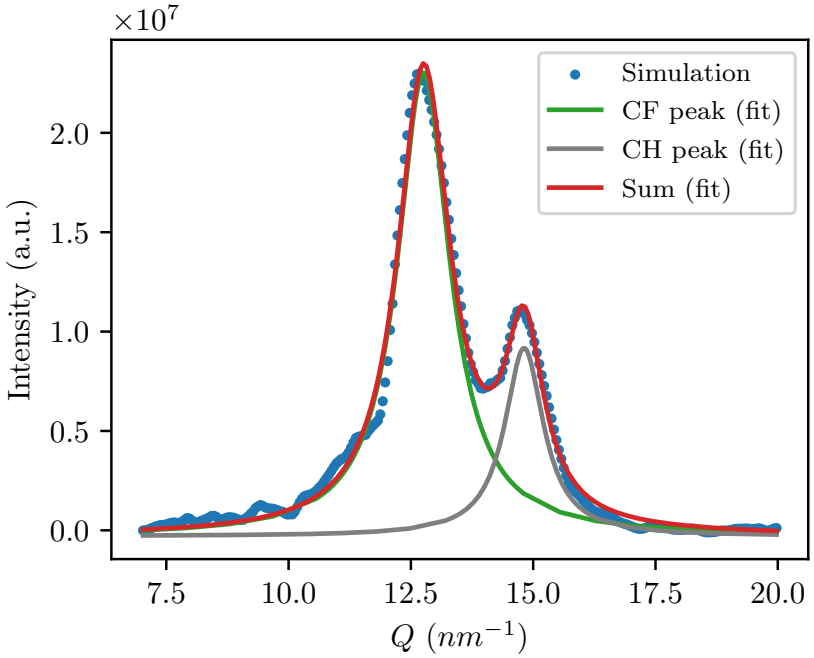

Figure B.29: GIXD θ-integrated diffractogram for small values of θ (*i.e.* the intensity presented in Figure B.1 integrated along θ in the range of 0 rad to 0.1 rad, or about 0° to 5.73°, as a function of Q), calculated from the final configuration of the MD simulation trajectory of the pure F10H14 hemimicelle, which contained 1850 molecules of PFAA. The blue circles represent the data points retrieved from the calculation and the curves represent the fitted Lorentzian peaks corresponding to the proposed structures, labelled "CF peak" (green) and "CH peak" (grey). The red curve is the cumulative sum of the remaining fitted curves.

B.3.5.2 Hemimicelle with 3400 molecules of F10H18

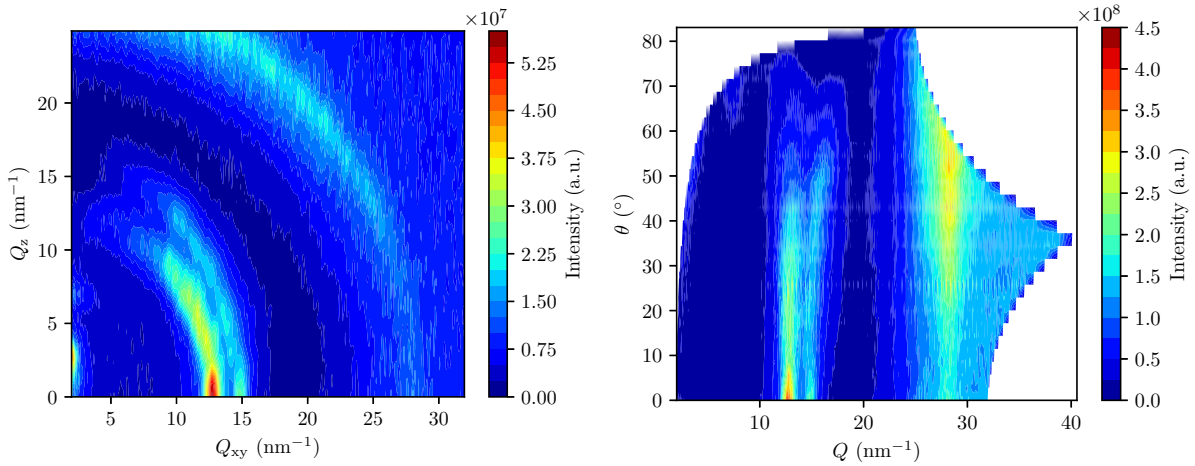

Figure B.30: Left: contour plot of the diffraction intensity as a function of the in-plane (Q_{xy}) and out-of-plane (Q_z) components of the scattering vector calculated from the final configuration of the MD simulation trajectory of the pure F10H18 hemimicelle, which contained 3400 molecules of PFAA. Right: the same dataset, but represented in polar coordinates, that is the contour plot of the diffraction intensity as a function of the modulus of the scattering vector (Q) and the out-of-plane angle with the interface (θ).

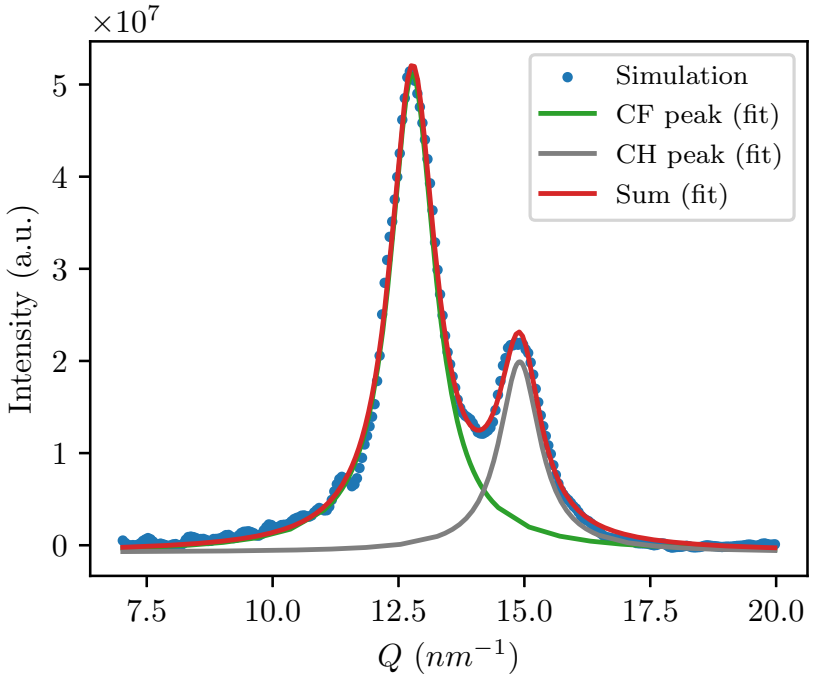

Figure B.31: GIXD θ-integrated diffractogram for small values of θ (*i.e.* the intensity presented in Figure B.1 integrated along θ in the range of 0 rad to 0.1 rad, or about 0° to 5.73°, as a function of Q), calculated from the final configuration of the MD simulation trajectory of the pure F10H18 hemimicelle, which contained 3400 molecules of PFAA. The blue circles represent the data points retrieved from the calculation and the curves represent the fitted Lorentzian peaks corresponding to the proposed structures, labelled "CF peak" (green) and "CH peak" (grey). The red curve is the cumulative sum of the remaining fitted curves.

B.3.5.3 Hemimicelle with 3900 molecules of F10H20

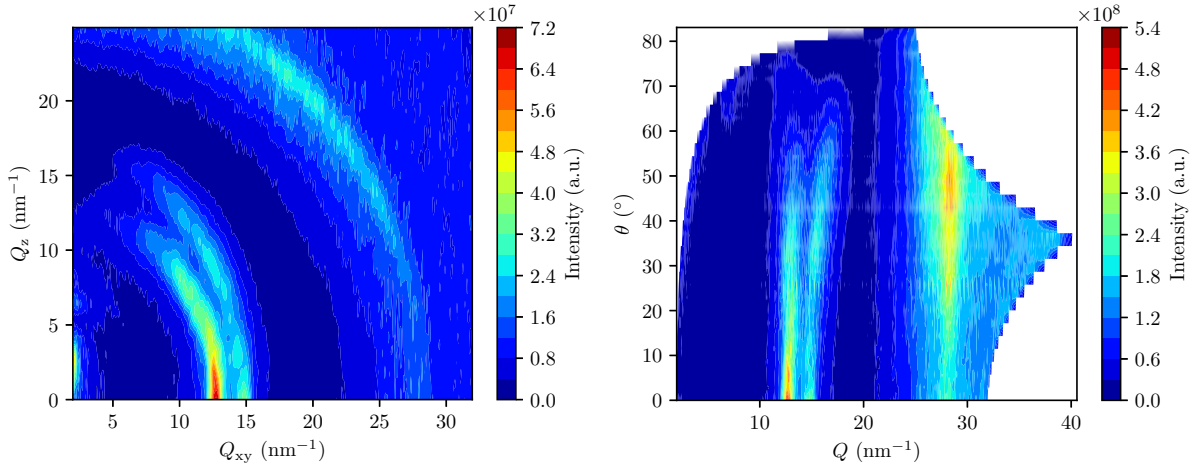

Figure B.32: Left: contour plot of the diffraction intensity as a function of the in-plane (Q_{xy}) and out-of-plane (Q_z) components of the scattering vector calculated from the final configuration of the MD simulation trajectory of the pure F10H20 hemimicelle, which contained 3900 molecules of PFAA. Right: the same dataset, but represented in polar coordinates, that is the contour plot of the diffraction intensity as a function of the modulus of the scattering vector (Q) and the out-of-plane angle with the interface (θ).

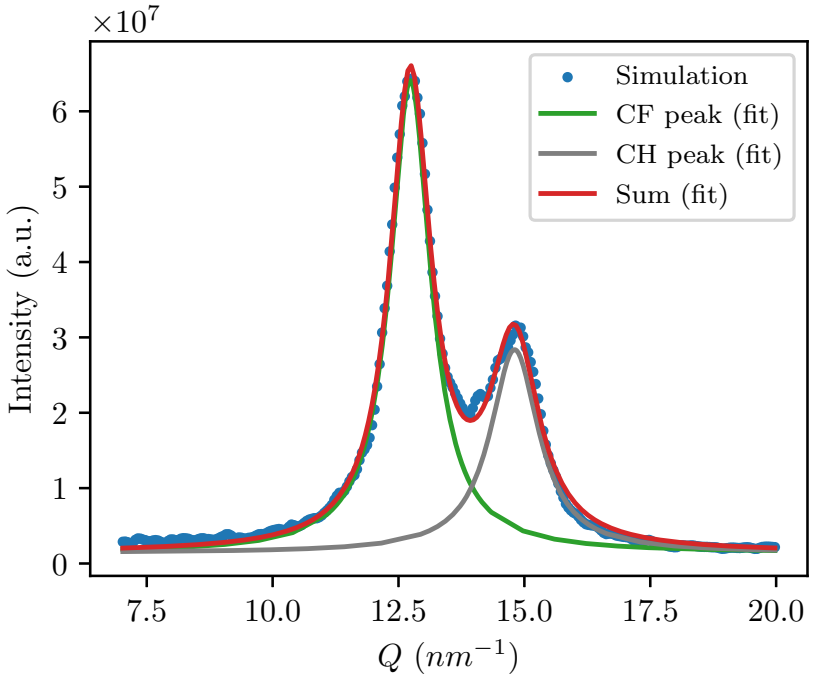

Figure B.33: GIXD θ-integrated diffractogram for small values of θ (*i.e.* the intensity presented in Figure B.1 integrated along θ in the range of 0 rad to 0.1 rad, or about 0° to 5.73°, as a function of Q), calculated from the final configuration of the MD simulation trajectory of the pure F10H20 hemimicelle, which contained 3900 molecules of PFAA. The blue circles represent the data points retrieved from the calculation and the curves represent the fitted Lorentzian peaks corresponding to the proposed structures, labelled "CF peak" (green) and "CH peak" (grey). The red curve is the cumulative sum of the remaining fitted curves.

B.3.5.4 Hemimicelle with 3900 molecules of F12H20

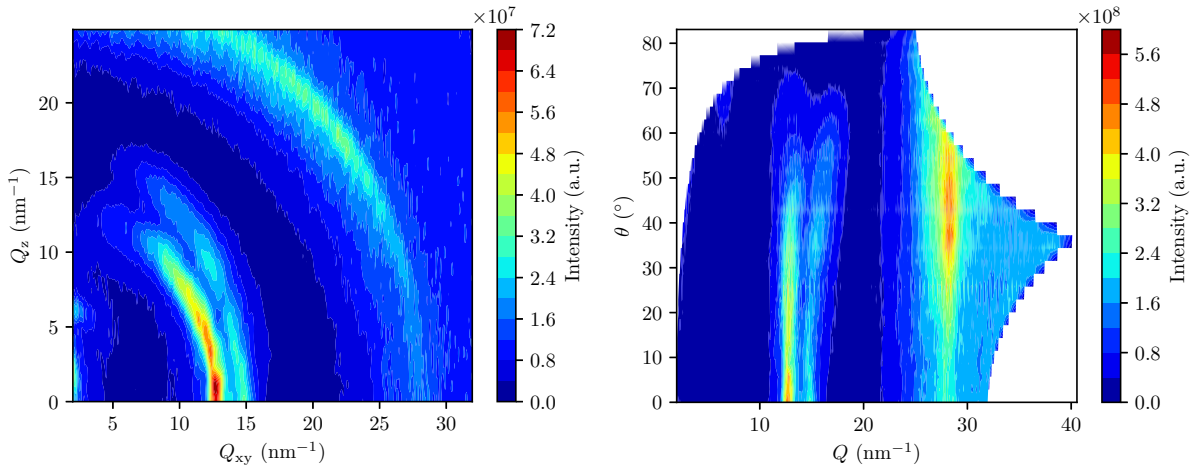

Figure B.34: Left: contour plot of the diffraction intensity as a function of the in-plane (Q_{xy}) and out-of-plane (Q_z) components of the scattering vector calculated from the final configuration of the MD simulation trajectory of the pure F12H20 hemimicelle, which contained 3900 molecules of PFAA. Right: the same dataset, but represented in polar coordinates, that is the contour plot of the diffraction intensity as a function of the modulus of the scattering vector (Q) and the out-of-plane angle with the interface (θ).

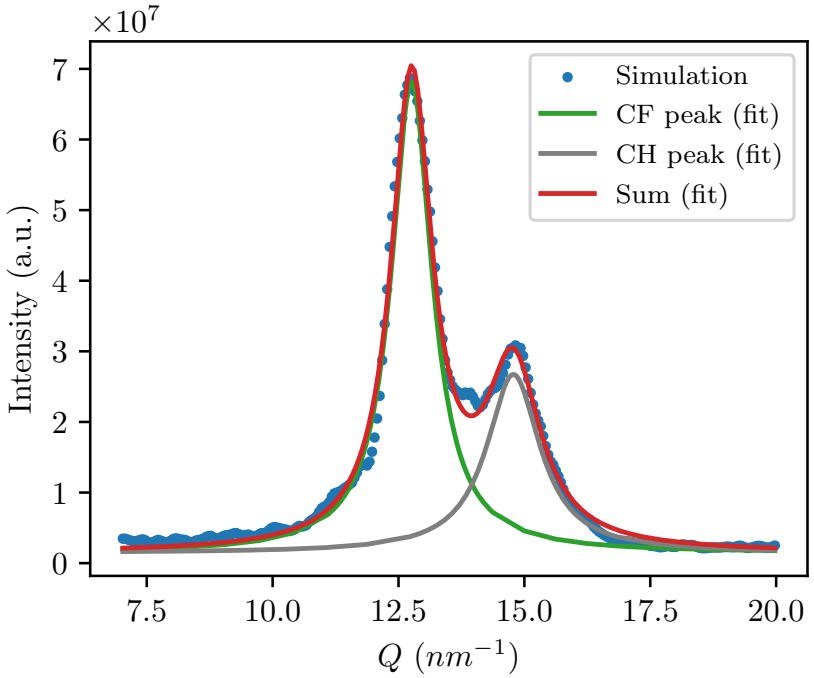

Figure B.35: GIXD θ-integrated diffractogram for small values of θ (*i.e.* the intensity presented in Figure B.1 integrated along θ in the range of 0 rad to 0.1 rad, or about 0° to 5.73°, as a function of Q), calculated from the final configuration of the MD simulation trajectory of the pure F12H20 hemimicelle, which contained 3900 molecules of PFAA. The blue circles represent the data points retrieved from the calculation and the curves represent the fitted Lorentzian peaks corresponding to the proposed structures, labelled "CF peak" (green) and "CH peak" (grey). The red curve is the cumulative sum of the remaining fitted curves.

Appendix C

Mixed Langmuir films of F8H14:F8H20: supplementary results

C.1 GISAXS results: supplementary graphics

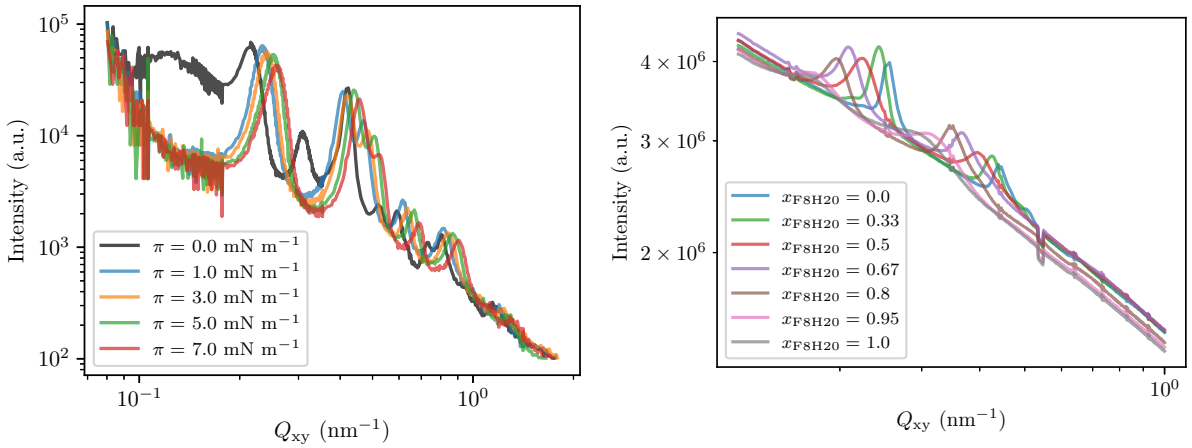

Figure C.1: Typical GISAXS Q_z-integrated spectra of the F8H14:F8H20 Langmuir films obtained at $T = 12\,°C$ and: varying π (indicated in the inset) at a constant film composition of $x_{F8H20} = 0.00$, corresponding to a molar proportion of 1:0 (left); varying x_{F8H20} (indicated in the inset) at a constant $\pi = 5\,\mathrm{mN\,m^{-1}}$ (right).

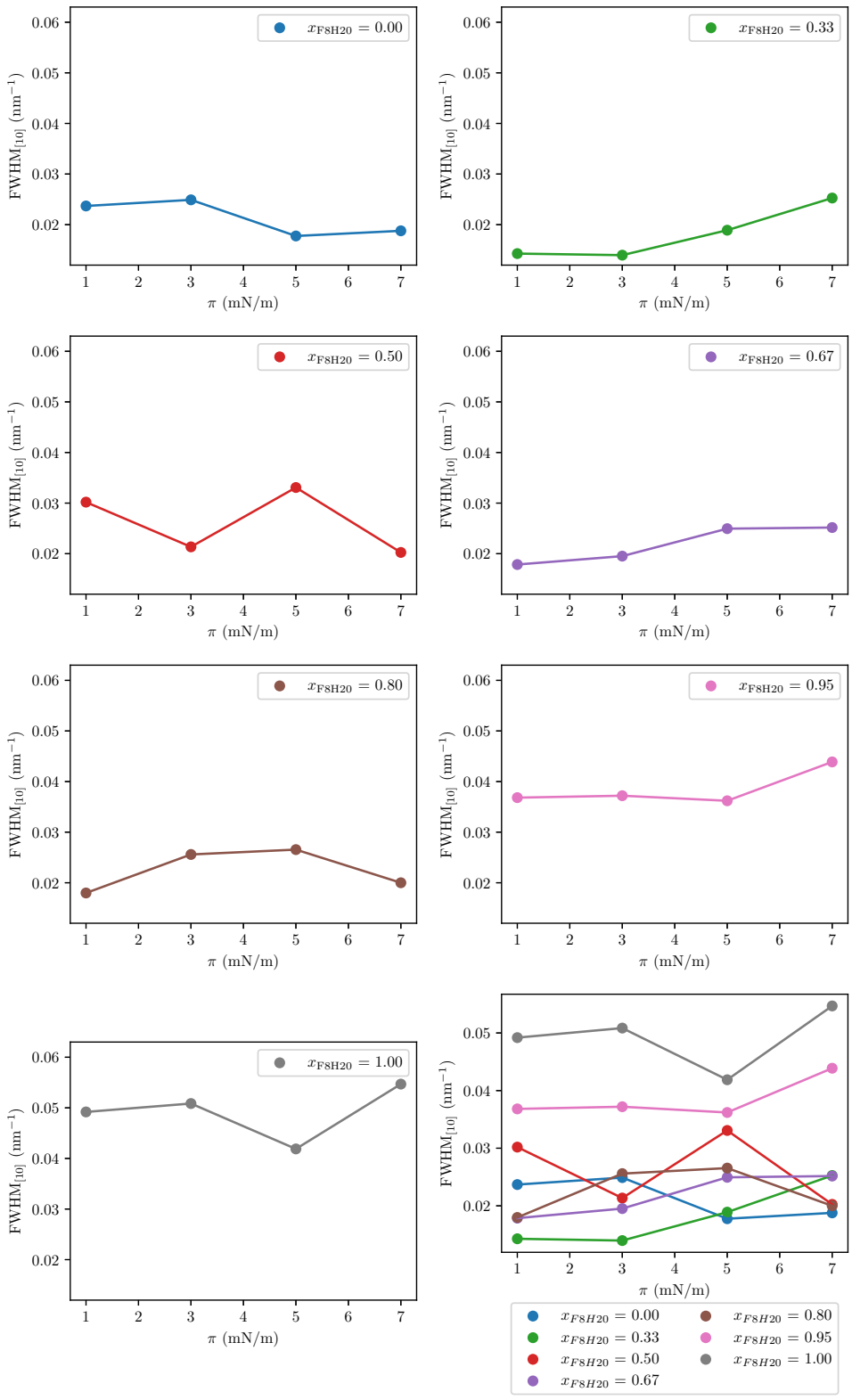

Figure C.2: FWHM of the [10] peak for the proposed main 2D hexagonal lattice as a function of π calculated from the GISAXS measurements at $T = 12\,°C$ for the mixed binary Langmuir film of F8H14:F8H20 at different x_{F8H20} values, indicated on the insets. The bottom right plot is a compilation of the remaining plots, in which case the lines are colour coded according to x_{F8H20}, indicated in the legend.

C.2 GISAXS results: tables

Table C.1: Lattice parameter a (in nm) for the proposed main 2D hexagonal lattice as a function of π calculated from the GISAXS measurements at $T = 12\,^{\circ}\mathrm{C}$ for the mixed Langmuir films of F8H14:F8H20 with different compositions (x_{F8H20}). The reader is referred to Figure 11.4 on page 164 for a graphical representation of these data.

π (mN m^{-1})	x_{F8H20}						
	0.00	0.33	0.50	0.67	0.80	0.95	1.00
0	31.26 ± 0.29	33.46 ± 0.84	37.51 ± 1.32	38.46 ± 0.98	44.33 ± 0.78	47.57 ± 0.01	47.25 ± 0.88
1	29.32 ± 0.24	31.41 ± 0.39	32.72 ± 0.37	34.69 ± 0.17	39.65 ± 1.42	41.05 ± 0.68	43.32 ± 2.53
3	28.56 ± 0.31	30.30 ± 0.11	30.83 ± 0.22	32.95 ± 0.25	37.62 ± 0.44	39.80 ± 0.67	39.78 ± 0.93
5	28.47 ± 0.19	29.61 ± 0.30	31.66 ± 0.39	34.50 ± 0.47	36.38 ± 0.39	39.70 ± 0.76	41.32 ± 0.75
7	27.87 ± 0.29	29.86 ± 0.37	32.69 ± 0.33	34.56 ± 0.19	37.32 ± 0.46	42.79 ± 0.94	39.34 ± 2.06

Table C.2: Lattice parameter a (in nm) for the proposed secondary 2D hexagonal lattice as a function of π calculated from the GISAXS measurements at $T = 12\,^{\circ}\mathrm{C}$ for the mixed Langmuir films of F8H14:F8H20 with different compositions (x_{F8H20}). The table entries with no data correspond to experimental conditions for which the proposed secondary is not discernible (only one set of peaks is identified, corresponding to the main 2D hexagonal lattice). For the values for which no uncertainty is provided, this could not be estimated in a reliable way. The reader is referred to Figure 11.5 on page 165 for a graphical representation of these data.

π (mN m^{-1})	x_{F8H20}						
	0.00	0.33	0.50	0.67	0.80	0.95	1.00
0	44.31 ± 1.12	47.58 ± 0.84	49.39 ± 0.73	48.53 ± 1.05	56.50 ± 1.46	-	-
1	-	32.77 ± 0.99	-	36.64	42.94	-	-
3	-	32.75	33.04	36.04	-	-	-
5	31.97 ± 0.80	31.19	37.85	39.16	42.31	-	-
7	30.87 ± 0.35	33.07 ± 0.40	38.23 ± 0.49	39.33	40.89 ± 0.35	-	-

Table C.3: Ratio of the areas of the [10] peaks corresponding to the proposed secondary and main 2D hexagonal lattices in the mixed Langmuir films of F8H14:F8H20, calculated from the GISAXS results. The table entries with no data correspond to experimental conditions for which the proposed secondary is not discernible (only one set of peaks is identified, corresponding to the main 2D hexagonal lattice). The table entries marked with an asterisk correspond to experimental conditions for which the [10] peak of the secondary lattice is not well defined, as this was found to be very close to the direct beam, which precluded the calculation presented herein.

π (mN m^{-1})	x_{F8H20}						
	0.00	0.33	0.50	0.67	0.80	0.95	1.00
0	*	*	*	*	*	-	-
1	-	0.442	-	1.358	0.743	-	-
3	-	0.000	1.348	0.769	-	-	-
5	0.008	0.517	0.051	0.052	0.097	-	-
7	1.919	0.035	0.164	0.157	0.368	-	-

Table C.4: Peak [10] width (FWHM, in nm^{-1}) for the proposed main 2D hexagonal lattice as a function of π calculated from the GISAXS measurements at $T = 12\,^{\circ}\mathrm{C}$ for the mixed Langmuir films of F8H14:F8H20 with different compositions (x_{F8H20}). The table entries with no data correspond to experimental conditions for which this quantity could not be estimated in a reliable way. The reader is referred to Figure 11.8 on page 170 for a graphical representation of these data.

π (mN m^{-1})	x_{F8H20}						
	0.00	0.33	0.50	0.67	0.80	0.95	1.00
0	-	-	-	-	-	-	-
1	0.023 69	0.014 28	0.030 19	0.017 86	0.017 98	0.036 82	0.049 19
3	0.024 90	0.013 97	0.021 35	0.019 52	0.025 59	0.037 20	0.050 85
5	0.017 76	0.018 90	0.033 08	0.024 95	0.026 55	0.036 20	0.041 88
7	0.018 78	0.025 26	0.020 25	0.025 17	0.020 00	0.043 88	0.054 69

C.3 GIXD results: supplementary graphics

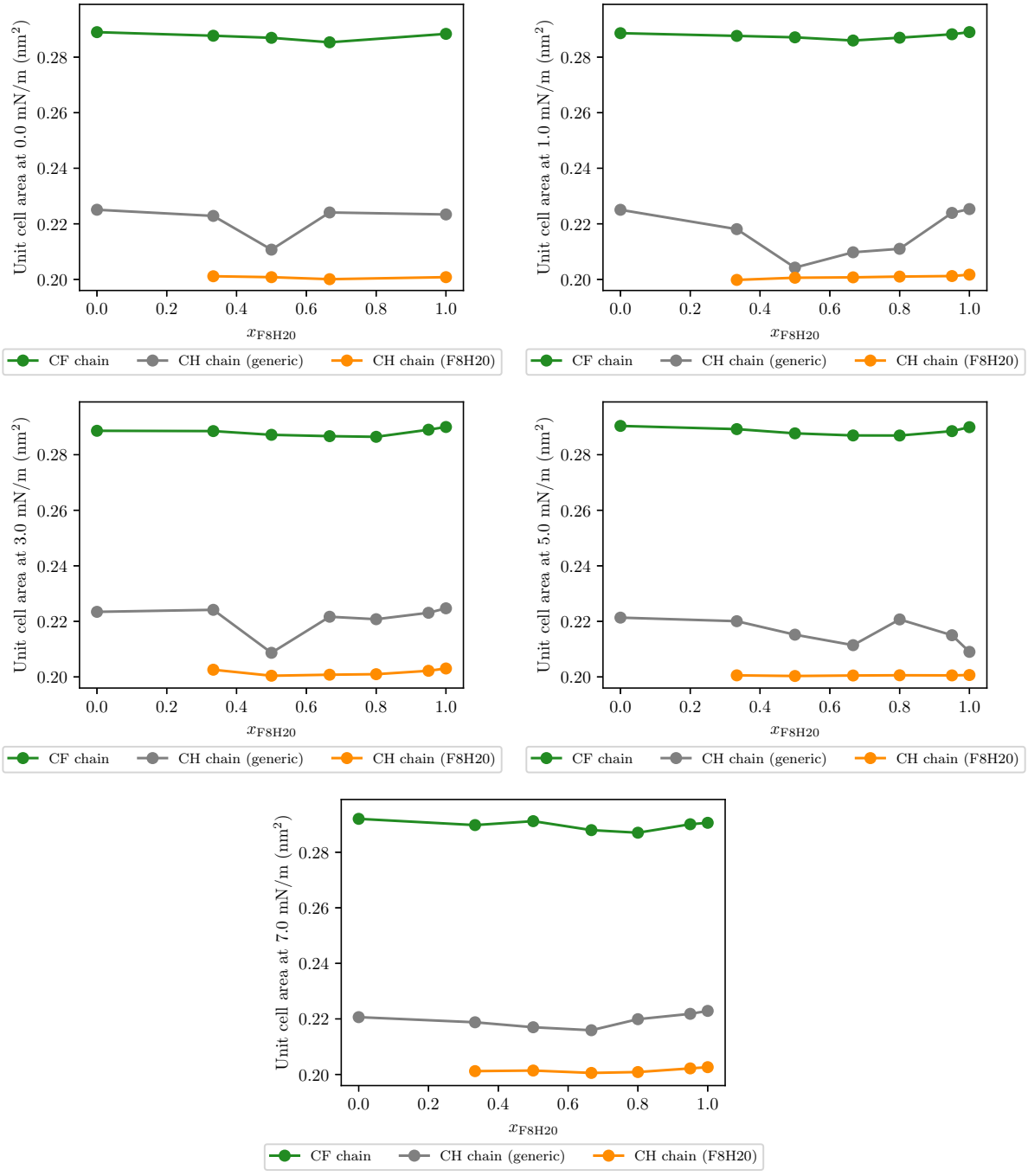

Figure C.3: Unit cell area ($A^{\text{GIXD}}_{\text{unit cell}}$) as a function of x_{F8H20}, calculated from the GIXD measurements at $T = 12\,^{\circ}\text{C}$ for the mixed Langmuir films of F8H14:F8H20 at varying π (identified in the vertical axis of each plot), for the lattices corresponding to the "CF chain" (green), "CH chain (generic)" (grey) and "CH chain (F8H20)" (orange) structures. $A^{\text{GIXD}}_{\text{unit cell}}$ is numerically equal to $a^2 \sin(120°)$, where a is the lattice parameter inferred from the position of the corresponding diffraction peaks in the GIXD spectra.

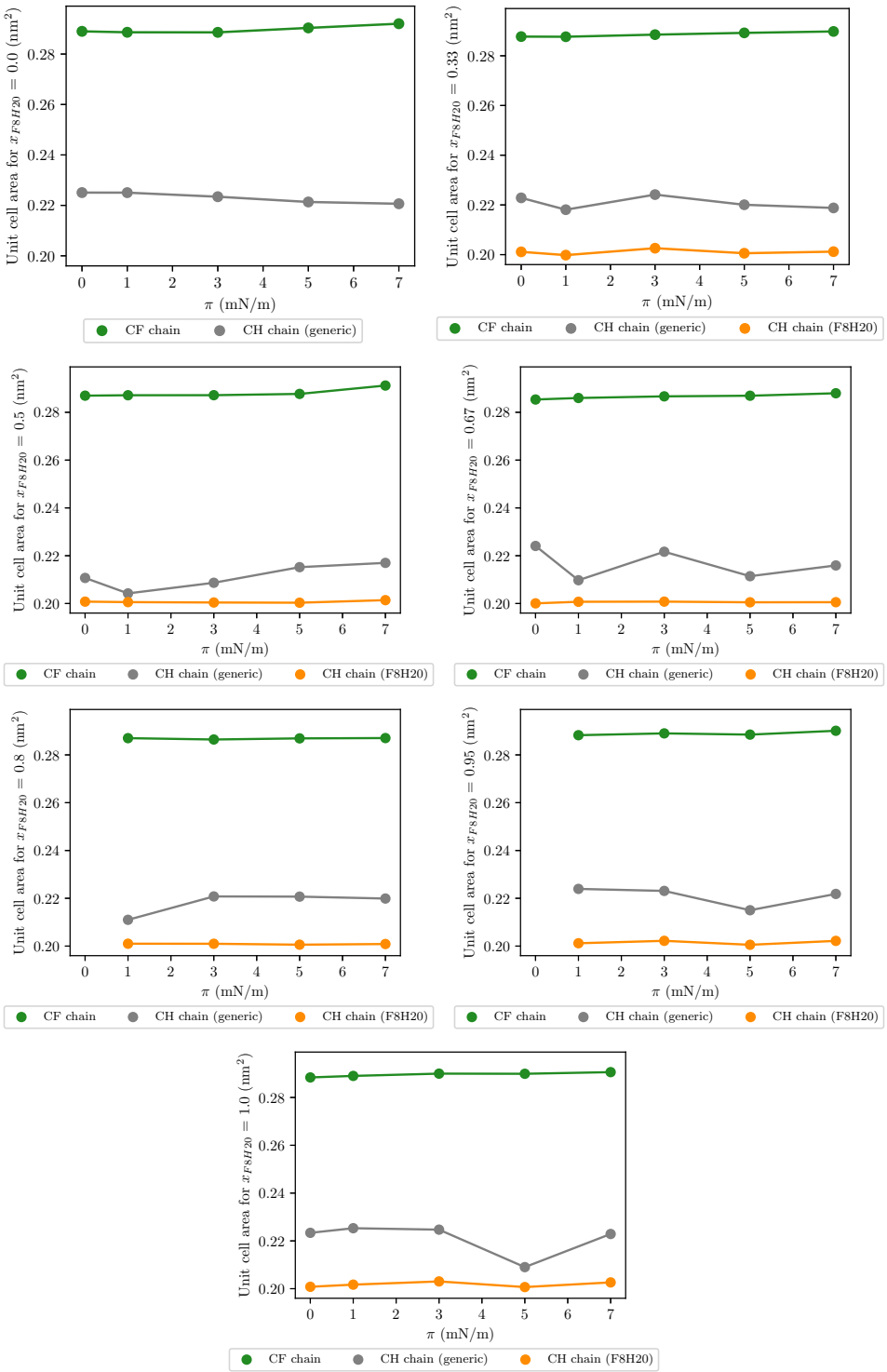

Figure C.4: Unit cell area ($A^{\text{GIXD}}_{\text{unit cell}}$) as a function of π, calculated from the GIXD measurements at $T = 12\,^{\circ}\text{C}$ for the mixed Langmuir films of F8H14:F8H20 with varying composition (x_{F8H20}, identified in the vertical axis of each plot), for the lattices corresponding to the "CF chain" (green), "CH chain (generic)" (grey) and "CH chain (F8H20)" (orange) structures. $A^{\text{GIXD}}_{\text{unit cell}}$ is numerically equal to $a^2 \sin(120^{\circ})$, where a is the lattice parameter inferred from the position of the corresponding diffraction peaks in the GIXD spectra.

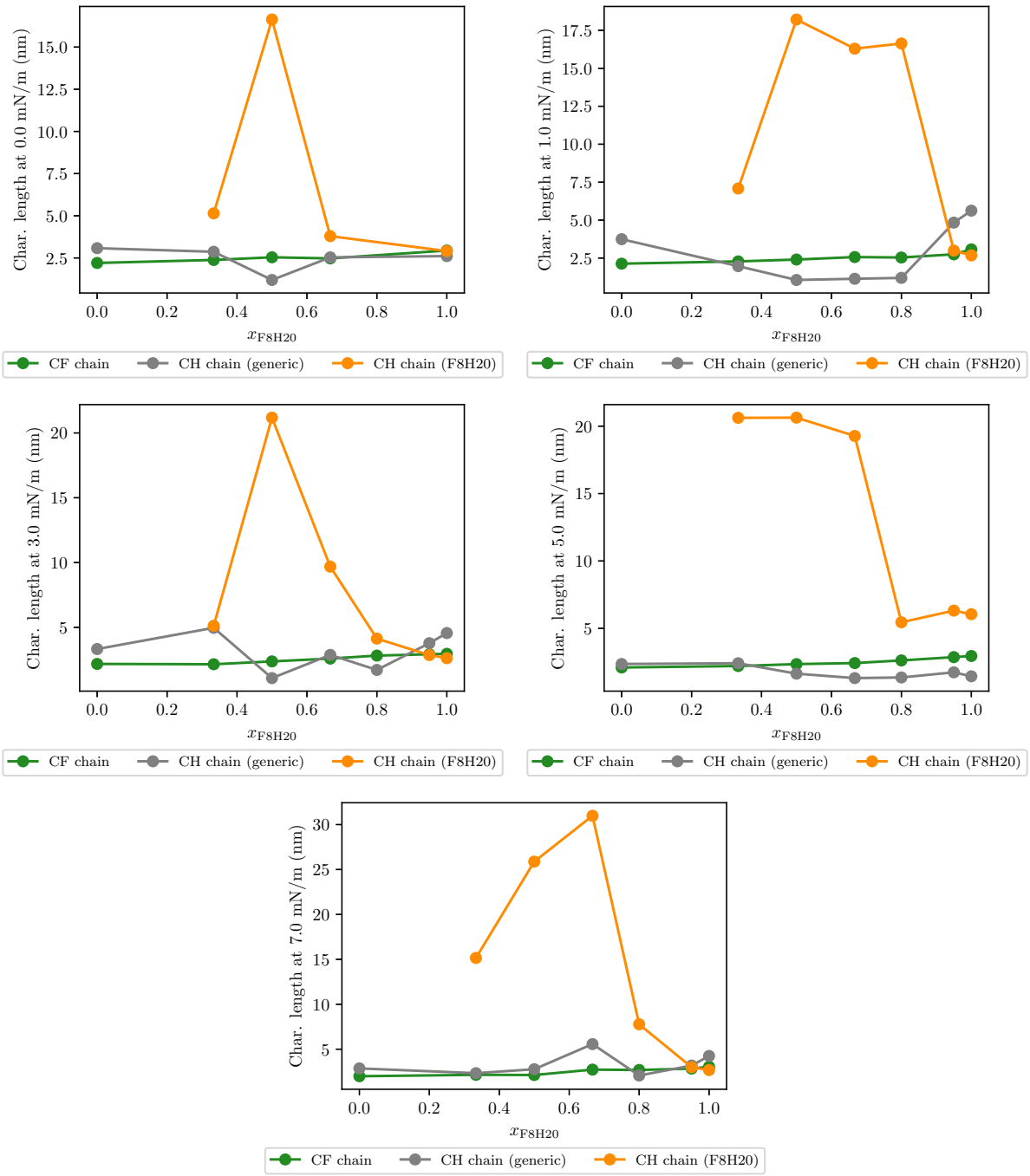

Figure C.5: Characteristic length as a function of x_{F8H20}, calculated from the width of the corresponding diffraction peak from the GIXD measurements at $T = 12\,°C$ for the mixed Langmuir films of F8H14:F8H20 at varying π (identified in the vertical axis of each plot), for the lattices corresponding to the "CF chain" (green), "CH chain (generic)" (grey) and "CH chain (F8H20)" (orange) structures. $A^{GIXD}_{unit\ cell}$ is numerically equal to $a^2 \sin(120°)$, where a is the lattice parameter inferred from the position of the corresponding diffraction peaks in the GIXD spectra.

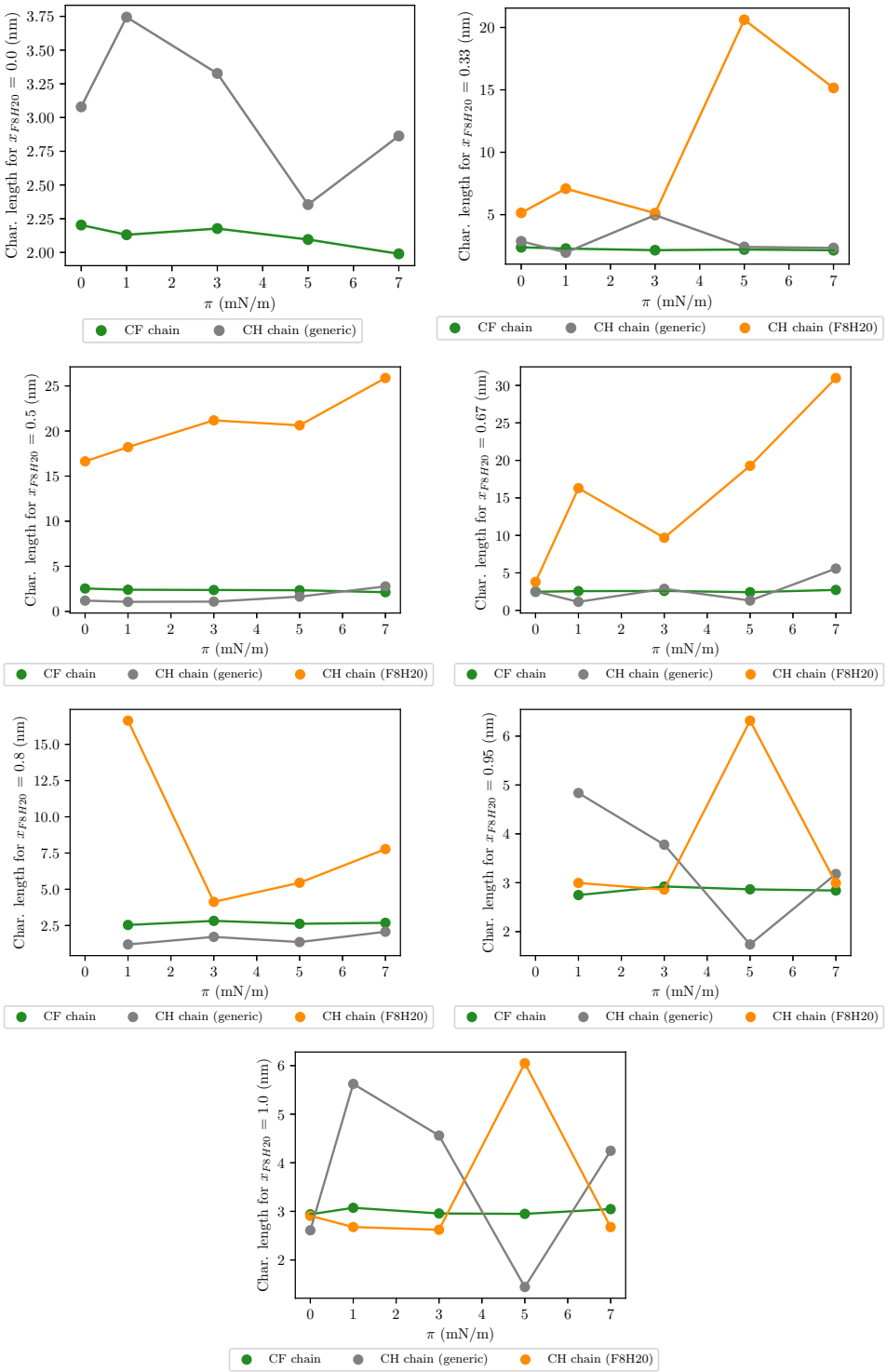

Figure C.6: Characteristic length as a function of π, calculated from the width of the corresponding diffraction peak from the GIXD measurements at $T = 12\,^{\circ}\mathrm{C}$ for the mixed Langmuir films of F8H14:F8H20 with varying composition (x_{F8H20}, identified in the vertical axis of each plot), for the lattices corresponding to the "CF chain" (green), "CH chain (generic)" (grey) and "CH chain (F8H20)" (orange) structures. $A^{\mathrm{GIXD}}_{\mathrm{unit\ cell}}$ is numerically equal to $a^2 \sin(120^{\circ})$, where a is the lattice parameter inferred from the position of the corresponding diffraction peaks in the GIXD spectra.

C.4 GIXD results: tables

Table C.5: Unit cell area ($A^{\mathrm{GIXD}}_{\text{unit cell}}$) as a function of x_{F8H20}, calculated from the GIXD measurements at $T = 12\,^{\circ}\mathrm{C}$ for the mixed binary Langmuir film of F8H14:F8H20 at different π values, for the lattices corresponding to the "CF chain" structure (the reader is referred to Figure 11.12 on page 177 for a graphical representation of these data). The table entries with no data correspond to experimental conditions for which the measurements were not performed.

π (mN m^{-1})	x_{F8H20}						
	0.00	0.33	0.50	0.67	0.80	0.95	1.00
0	0.2890	0.2877	0.2870	0.2853	-	-	0.2884
1	0.2886	0.2877	0.2871	0.2860	0.2870	0.2882	0.2890
3	0.2886	0.2885	0.2872	0.2867	0.2864	0.2890	0.2900
5	0.2904	0.2892	0.2877	0.2869	0.2869	0.2885	0.2899
7	0.2920	0.2898	0.2912	0.2880	0.2870	0.2901	0.2906

Table C.6: Unit cell area ($A^{\mathrm{GIXD}}_{\text{unit cell}}$) as a function of x_{F8H20}, calculated from the GIXD measurements at $T = 12\,^{\circ}\mathrm{C}$ for the mixed binary Langmuir film of F8H14:F8H20 at different π values, for the lattices corresponding to the "CH chain (generic)" structure (the reader is referred to Figure 11.12 on page 177 for a graphical representation of these data). The table entries with no data correspond to experimental conditions for which the measurements were not performed.

π (mN m^{-1})	x_{F8H20}						
	0.00	0.33	0.50	0.67	0.80	0.95	1.00
0	0.2251	0.2228	0.2107	0.2241	-	-	0.2234
1	0.2250	0.2181	0.2042	0.2098	0.2110	0.2239	0.2253
3	0.2234	0.2242	0.2087	0.2217	0.2208	0.2231	0.2247
5	0.2213	0.2201	0.2152	0.2114	0.2207	0.2150	0.2090
7	0.2206	0.2188	0.2170	0.2159	0.2199	0.2218	0.2229

Table C.7: Unit cell area ($A^{\text{GIXD}}_{\text{unit cell}}$) as a function of x_{F8H20}, calculated from the GIXD measurements at $T = 12\,^{\circ}\text{C}$ for the mixed binary Langmuir film of F8H14:F8H20 at different π values, for the lattices corresponding to the "CH chain (F8H20)" structure (the reader is referred to Figure 11.12 on page 177 for a graphical representation of these data). The table entries with no data correspond to experimental conditions for which the measurements were not performed or for which the peaks corresponding to this structure were not discerned.

π (mN m^{-1})	x_{F8H20}						
	0.00	0.33	0.50	0.67	0.80	0.95	1.00
0	-	0.2011	0.2008	0.2001	-	-	0.2008
1	-	0.1998	0.2006	0.2007	0.2010	0.2012	0.2017
3	-	0.2026	0.2004	0.2008	0.2010	0.2022	0.2030
5	-	0.2006	0.2003	0.2005	0.2006	0.2006	0.2007
7	-	0.2012	0.2014	0.2006	0.2009	0.2022	0.2026

Table C.8: Characteristic length as a function of x_{F8H20}, calculated from the width of the corresponding diffraction peak from the GIXD measurements at $T = 12\,^{\circ}\text{C}$ for the mixed binary Langmuir film of F8H14:F8H20 at different π values, for the lattices corresponding to the "CF chain" structure (the reader is referred to Figure 11.13 on page 178 for a graphical representation of these data). The table entries with no data correspond to experimental conditions for which the measurements were not performed.

π (mN m^{-1})	x_{F8H20}						
	0.00	0.33	0.50	0.67	0.80	0.95	1.00
0	2.20	2.38	2.54	2.47	-	-	2.94
1	2.13	2.28	2.40	2.57	2.54	2.75	3.07
3	2.18	2.15	2.37	2.59	2.82	2.92	2.96
5	2.10	2.20	2.35	2.42	2.62	2.87	2.95
7	1.99	2.15	2.13	2.73	2.69	2.84	3.05

Table C.9: Characteristic length as a function of x_{F8H20}, calculated from the width of the corresponding diffraction peak from the GIXD measurements at $T = 12\,^{\circ}\text{C}$ for the mixed binary Langmuir film of F8H14:F8H20 at different π values, for the lattices corresponding to the "CH chain (generic)" structure (the reader is referred to Figure 11.13 on page 178 for a graphical representation of these data). The table entries with no data correspond to experimental conditions for which the measurements were not performed.

π (mN m^{-1})	x_{F8H20}						
	0.00	0.33	0.50	0.67	0.80	0.95	1.00
0	3.08	2.87	1.20	2.53	-	-	2.61
1	3.74	1.97	1.06	1.14	1.20	4.84	5.62
3	3.33	4.96	1.08	2.87	1.71	3.78	4.56
5	2.35	2.41	1.64	1.31	1.36	1.74	1.44
7	2.86	2.33	2.77	5.57	2.07	3.18	4.25

Table C.10: Characteristic length as a function of x_{F8H20}, calculated from the width of the corresponding diffraction peak from the GIXD measurements at $T = 12\,^{\circ}\mathrm{C}$ for the mixed binary Langmuir film of F8H14:F8H20 at different π values, for the lattices corresponding to the "CH chain (F8H20)" structure (the reader is referred to Figure 11.13 on page 178 for a graphical representation of these data). The table entries with no data correspond to experimental conditions for which the measurements were not performed or for which the peaks corresponding to this structure were not discerned.

π (mN m^{-1})	x_{F8H20}						
	0.00	0.33	0.50	0.67	0.80	0.95	1.00
0	-	5.14	16.63	3.79	-	-	2.91
1	-	7.08	18.21	16.29	16.64	2.99	2.68
3	-	5.12	21.18	9.68	4.13	2.86	2.62
5	-	20.62	20.63	19.27	5.45	6.32	6.05
7	-	15.15	25.87	30.98	7.77	2.99	2.68

Table C.11: Characteristic length divided (normalised) by the lattice parameter a obtained from the GISAXS measurements at the corresponding values of x_{F8H20} and π (ξ/a) as a function of x_{F8H20}, calculated from the GIXD results obtained at $T = 12\,^{\circ}\mathrm{C}$ for the mixed binary Langmuir film of F8H14:F8H20 at different π values, for the lattices corresponding to the "CF chain" structure (the reader is referred to Figure 11.13 on page 178 for a graphical representation of these data). The table entries with no data correspond to experimental conditions for which the measurements were not performed.

π (mN m^{-1})	x_{F8H20}						
	0.00	0.33	0.50	0.67	0.80	0.95	1.00
0	0.0705	0.0712	0.0677	0.0643	-	-	0.0622
1	0.0727	0.0726	0.0734	0.0740	0.0640	0.0669	0.0709
3	0.0762	0.0710	0.0769	0.0786	0.0750	0.0734	0.0743
5	0.0736	0.0745	0.0741	0.0703	0.0720	0.0722	0.0714
7	0.0714	0.0719	0.0651	0.0789	0.0720	0.0664	0.0774

Table C.12: Characteristic length divided (normalised) by the lattice parameter a obtained from the GISAXS measurements at the corresponding values of x_{F8H20} and π (ξ/a) as a function of x_{F8H20}, calculated from the GIXD results obtained at $T = 12\,^{\circ}\mathrm{C}$ for the mixed binary Langmuir film of F8H14:F8H20 at different π values, for the lattices corresponding to the "CH chain (generic)" structure (the reader is referred to Figure 11.13 on page 178 for a graphical representation of these data). The table entries with no data correspond to experimental conditions for which the measurements were not performed.

π (mN m^{-1})	x_{F8H20}						
	0.00	0.33	0.50	0.67	0.80	0.95	1.00
0	0.0985	0.0857	0.0319	0.0659	-	-	0.0552
1	0.1277	0.0627	0.0323	0.0328	0.0301	0.1178	0.1298
3	0.1165	0.1638	0.0352	0.0872	0.0456	0.0949	0.1146
5	0.0827	0.0814	0.0517	0.0379	0.0373	0.0438	0.0349
7	0.1027	0.0781	0.0847	0.1611	0.0555	0.0743	0.1080

Table C.13: Characteristic length divided (normalised) by the lattice parameter a obtained from the GISAXS measurements at the corresponding values of x_{F8H20} and π (ξ/a) as a function of x_{F8H20}, calculated from the GIXD results obtained at $T = 12\,^{\circ}\mathrm{C}$ for the mixed binary Langmuir film of F8H14:F8H20 at different π values, for the lattices corresponding to the "CH chain (F8H20)" structure (the reader is referred to Figure 11.13 on page 178 for a graphical representation of these data). The table entries with no data correspond to experimental conditions for which the measurements were not performed or for which the peaks corresponding to this structure were not discerned.

π ($\mathrm{mN\,m^{-1}}$)	x_{F8H20}						
	0.00	0.33	0.50	0.67	0.80	0.95	1.00
0	-	0.1537	0.4435	0.0986	-	-	0.0616
1	-	0.2255	0.5567	0.4697	0.4195	0.0730	0.0618
3	-	0.1691	0.6869	0.2939	0.1098	0.0719	0.0659
5	-	0.6963	0.6517	0.5586	0.1498	0.1591	0.1464
7	-	0.5076	0.7915	0.8963	0.2082	0.0700	0.0680

Appendix D

Void analyses: supplementary results

In this appendix chapter, some supplementary results are presented that complement the study presented in Chapter 12. The notation followed herein is the same as that used in Chapter 12 (and summarised in Figure 12.1, on page 200).

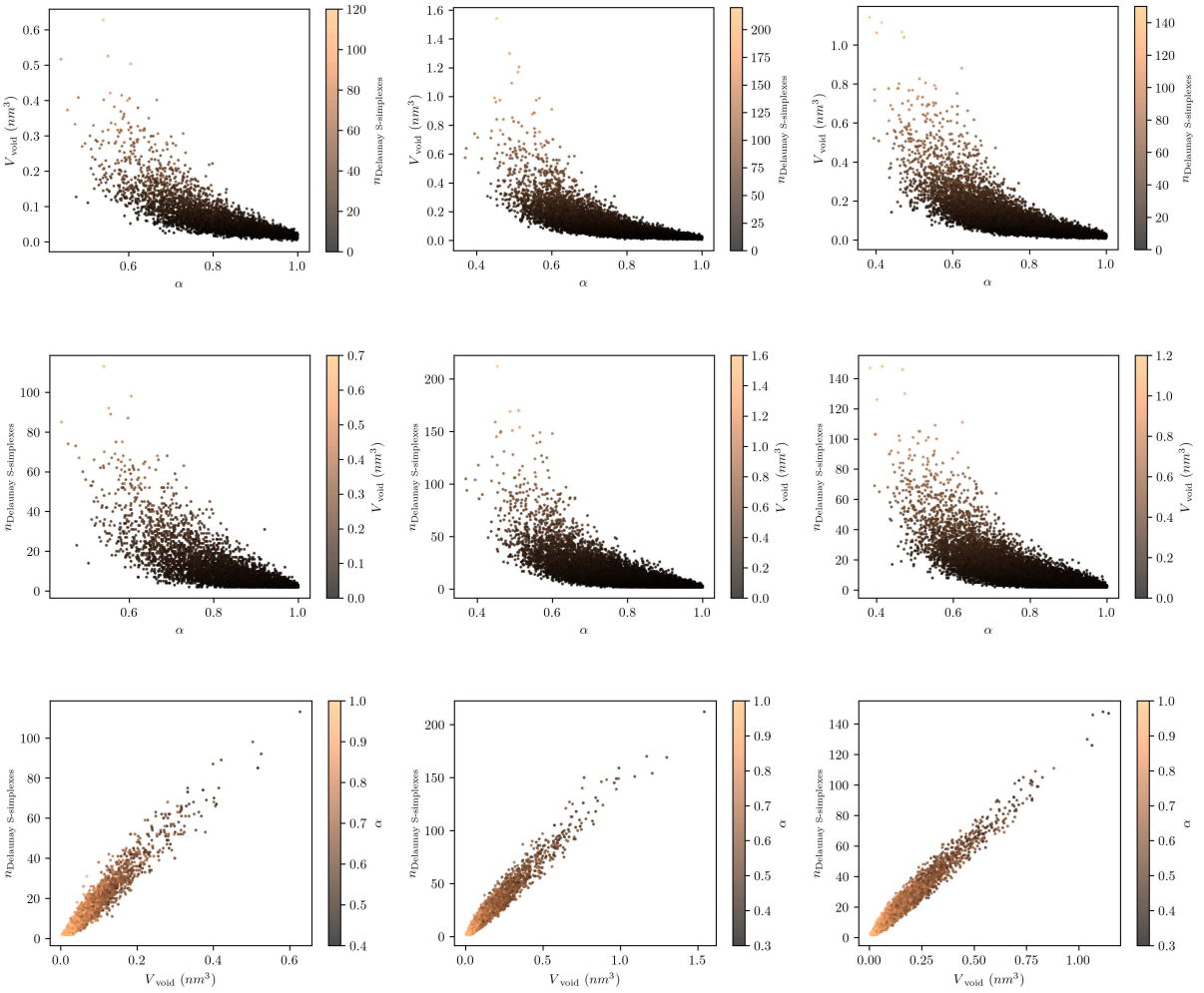

Figure D.1: Scatter plots relating the void sphericity (α), void volume (V_{void}) and number of Delaunay S-simplexes ($n_{\text{Delaunay S-simplexes}}$) for the analyses of the interstitial void volume in MD simulations of liquid mixtures of F6 and H6 at 298.15 K for $R_b^{\text{probe}} = 0.20$ nm. Each column stands for a different composition of the system (x_{F6}): 0.00, 0.50 and 1.00 (from left to right, respectively). The plots in the top row display the V_{void} as a function of α (the points are coloured according to $n_{\text{Delaunay S-simplexes}}$); the plots in the middle row display the $n_{\text{Delaunay S-simplexes}}$ as a function of α (the points are coloured according to V_{void}); the plots in the bottom row display the $n_{\text{Delaunay S-simplexes}}$ as a function of V_{void} (the points are coloured according to α).

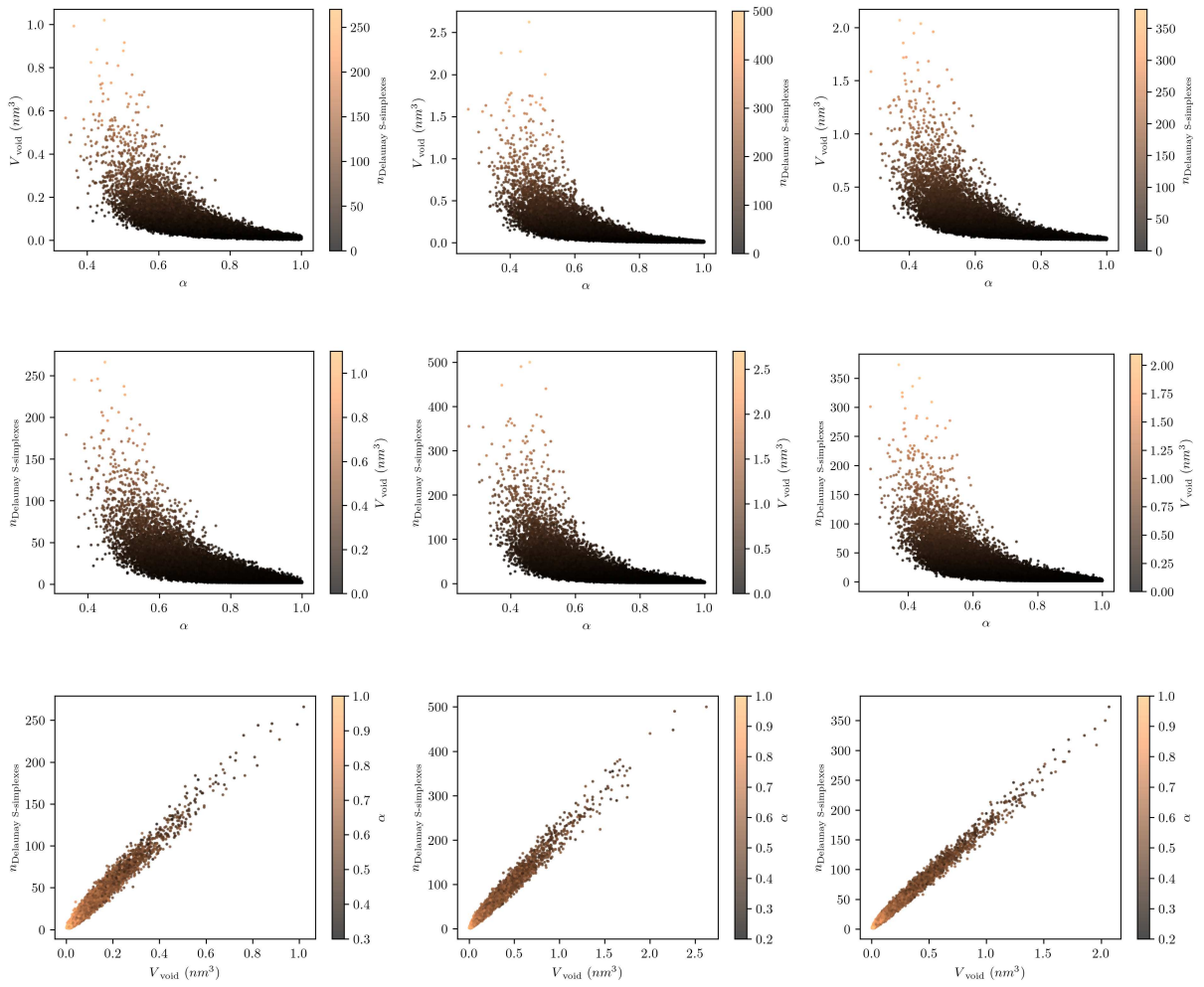

$x_{\text{F6}} = 0.00$ $x_{\text{F6}} = 0.50$ $x_{\text{F6}} = 1.00$

Figure D.2: Scatter plots relating the void sphericity (α), void volume (V_{void}) and number of Delaunay S-simplexes ($n_{\text{Delaunay S-simplexes}}$) for the analyses of the interstitial void volume in MD simulations of liquid mixtures of F6 and H6 at 298.15 K for $R_b^{\text{probe}} = 0.16$ nm. Each column stands for a different composition of the system (x_{F6}): 0.00, 0.50 and 1.00 (from left to right, respectively). The plots in the top row display the V_{void} as a function of α (the points are coloured according to $n_{\text{Delaunay S-simplexes}}$); the plots in the middle row display the $n_{\text{Delaunay S-simplexes}}$ as a function of α (the points are coloured according to V_{void}); the plots in the bottom row display the $n_{\text{Delaunay S-simplexes}}$ as a function of V_{void} (the points are coloured according to α).

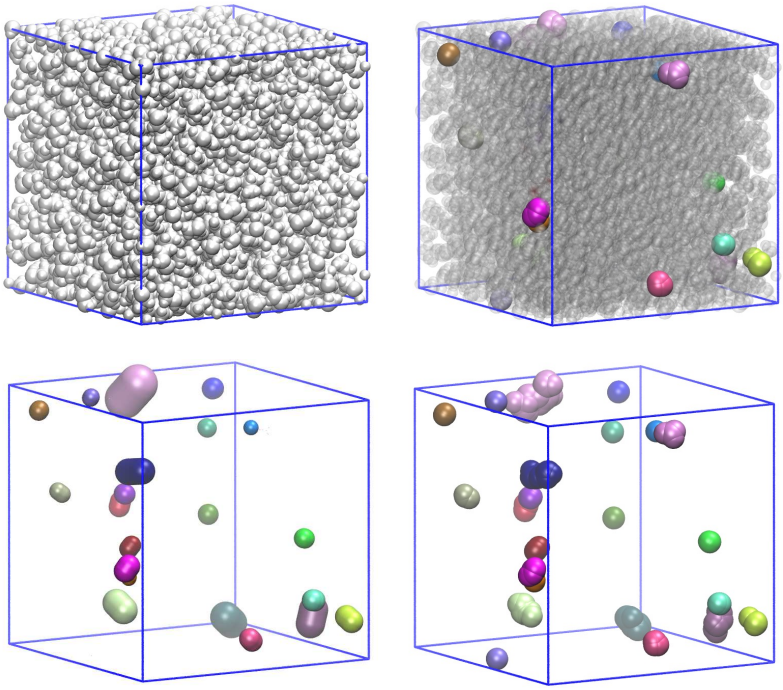

Figure D.3: Snapshots of the same configuration of the simulated mixture of F6+H6 for which $x_{\mathrm{F6}} = 0.00$ (pure H6) illustrating: a spacefill model of the molecules with all atoms of the H6 molecules coloured white (top left); the same view, but with transparent molecules and the void sites represented in a spacefill model to scale (top right); the void sites with the H6 molecules omitted for clarity (bottom right); the void spherocylinders corresponding to each void with the H6 molecules omitted for clarity (bottom left). Each void spherocylinder and the corresponding set of void sites, in the different representations, are coloured differently. In all cases, the voids were identified with $R_b^{\mathrm{probe}} = 0.20$ nm.

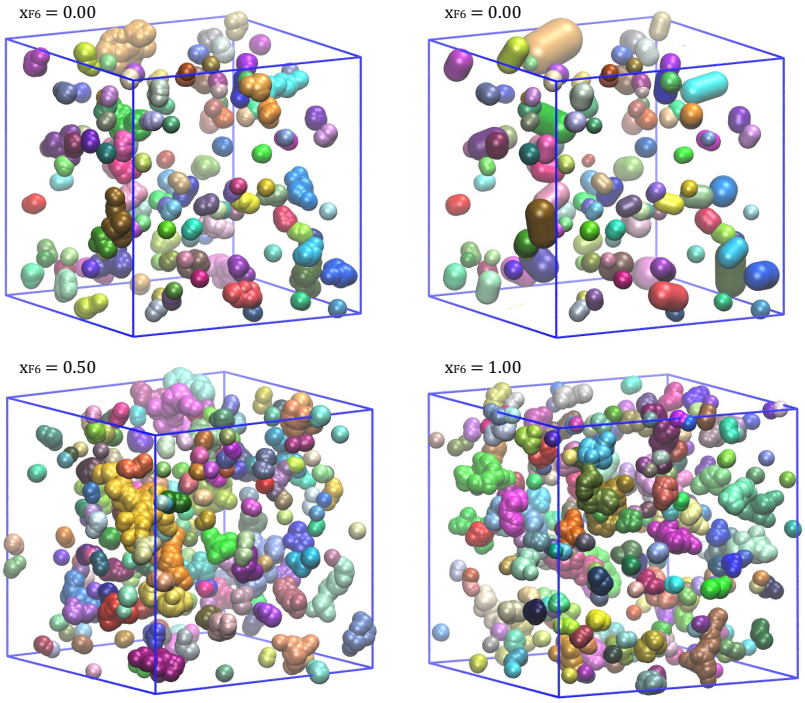

Figure D.4: Snapshots of different configurations of the simulated mixtures of F6+H6 for which $x_{\mathrm{F6}} = 0.00$ (pure H6; top row), $x_{\mathrm{F6}} = 0.50$ (bottom left) or $x_{\mathrm{F6}} = 1.00$ (pure F6; bottom right), representing the voids in these systems identified by R_b colouring with $R_b^{\mathrm{probe}} = 0.16$ nm. The F6 and H6 molecules are omitted for clarity. The void spherocylinders are illustrated for $x_{\mathrm{F6}} = 0.00$ (pure H6; top right); the remaining images represent the void sites in a spacefill model to scale. Each void spherocylinder and the corresponding set of void sites, in the different representations, are coloured differently.

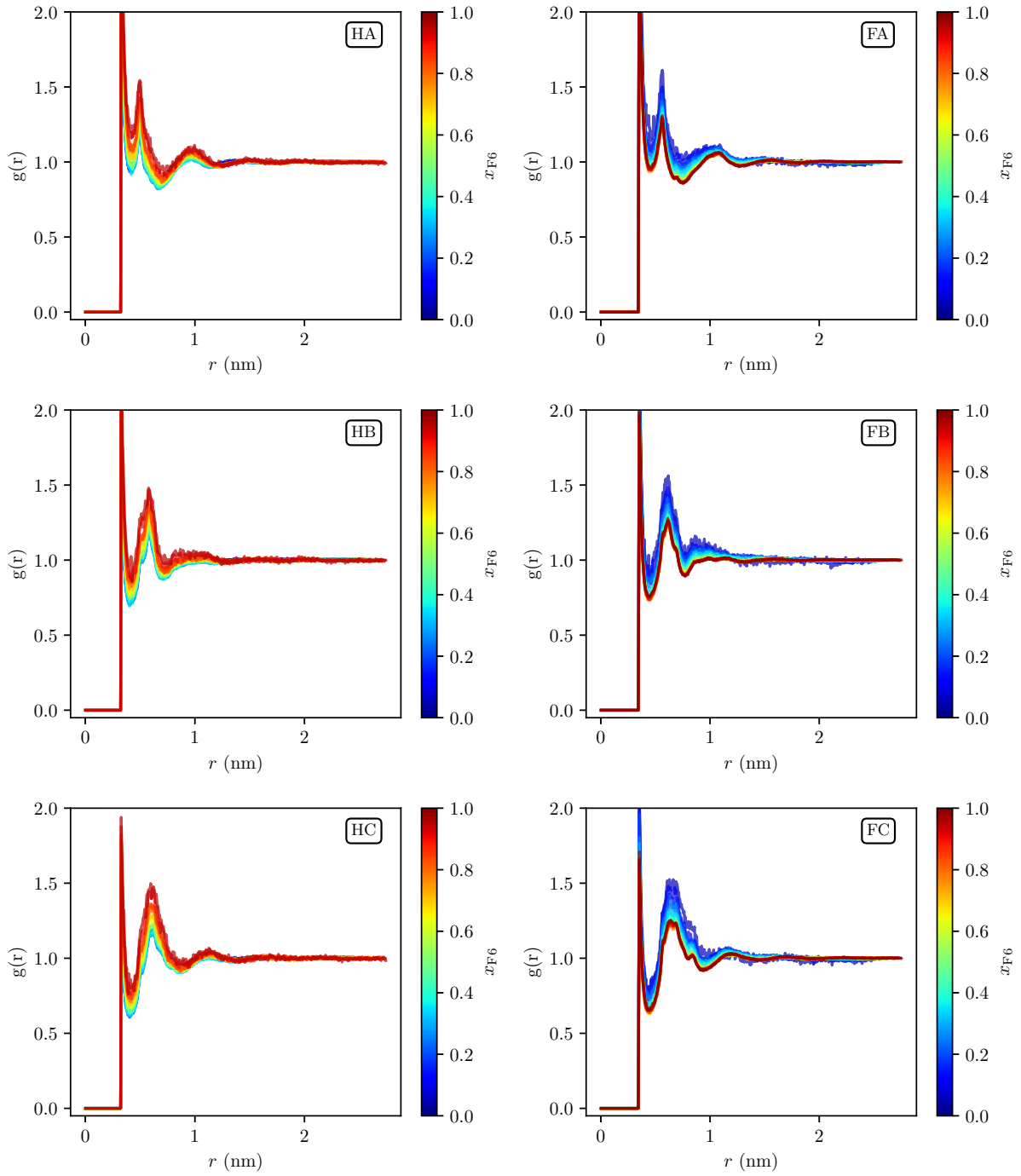

Figure D.5: RDFs between the void sites having a radius $R_b \geq 0.20$ nm and hydrogenated atoms HA (top left), HB (middle left) and HC (bottom left) of H6 and the fluorinated atoms FA (top right), FB (middle right) and FC (bottom right) of F6, for the simulated mixtures of F6+H6 at a temperature $T = 298\,\mathrm{K}$ and for different values of composition (x_{F6}) of the system. The nomenclature used to identify the atoms is presented in Figure 12.1. The corresponding enrichment plots are presented in Figure 12.11.

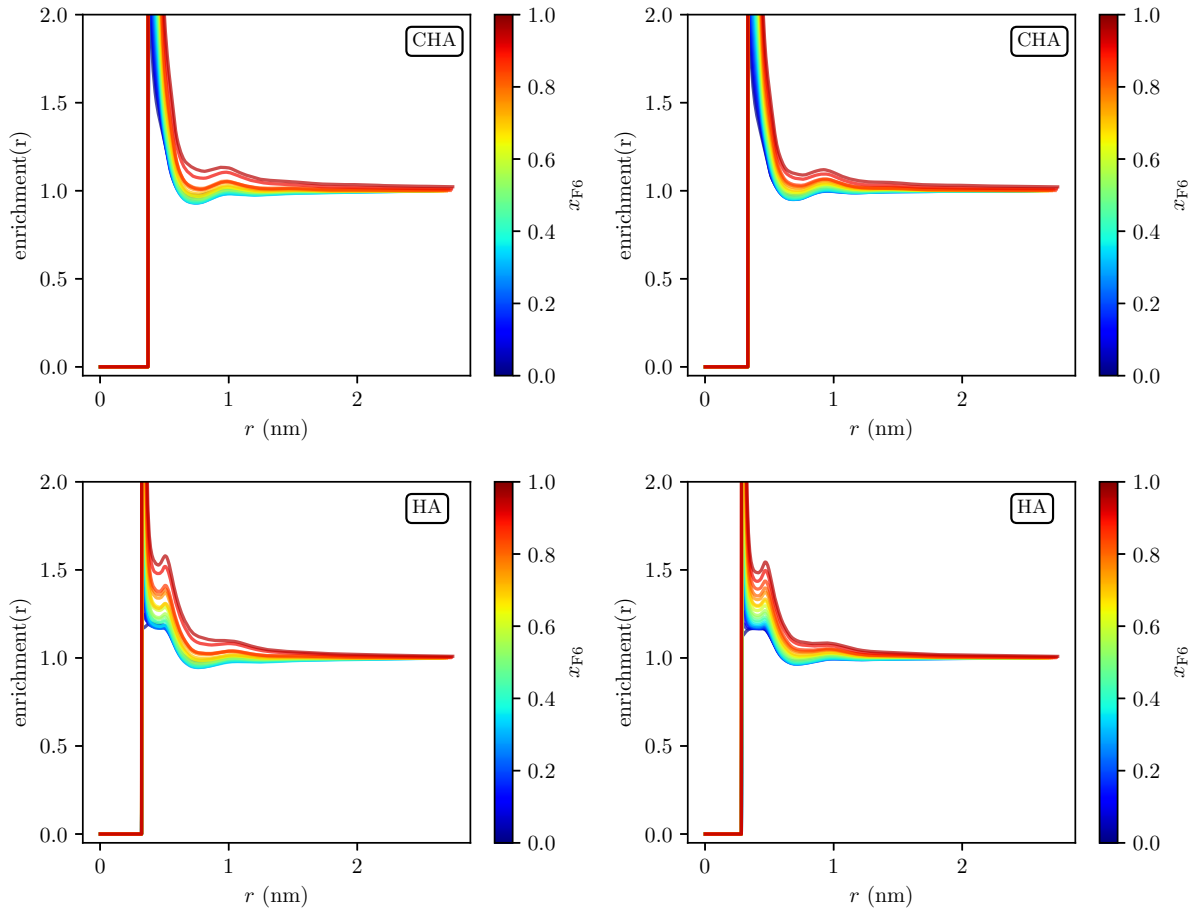

Figure D.6: Ratio of the local molar fraction of the atoms CHA (top row) and HA (bottom row) of H6 around the void sites and their respective bulk molar fractions (enrichment), as a function of the radial distance from the void sites and for different values of composition (x_{F6}) of the system, for the simulated mixtures of F6+H6 at a temperature $T = 298\,K$ and for void sites having a radius $R_b \geq 0.20$ nm (left column) or $R_b \geq 0.16$ nm (right column). The nomenclature used to identify the atoms is presented in Figure 12.1. The corresponding RDFs are presented in Figure D.8.

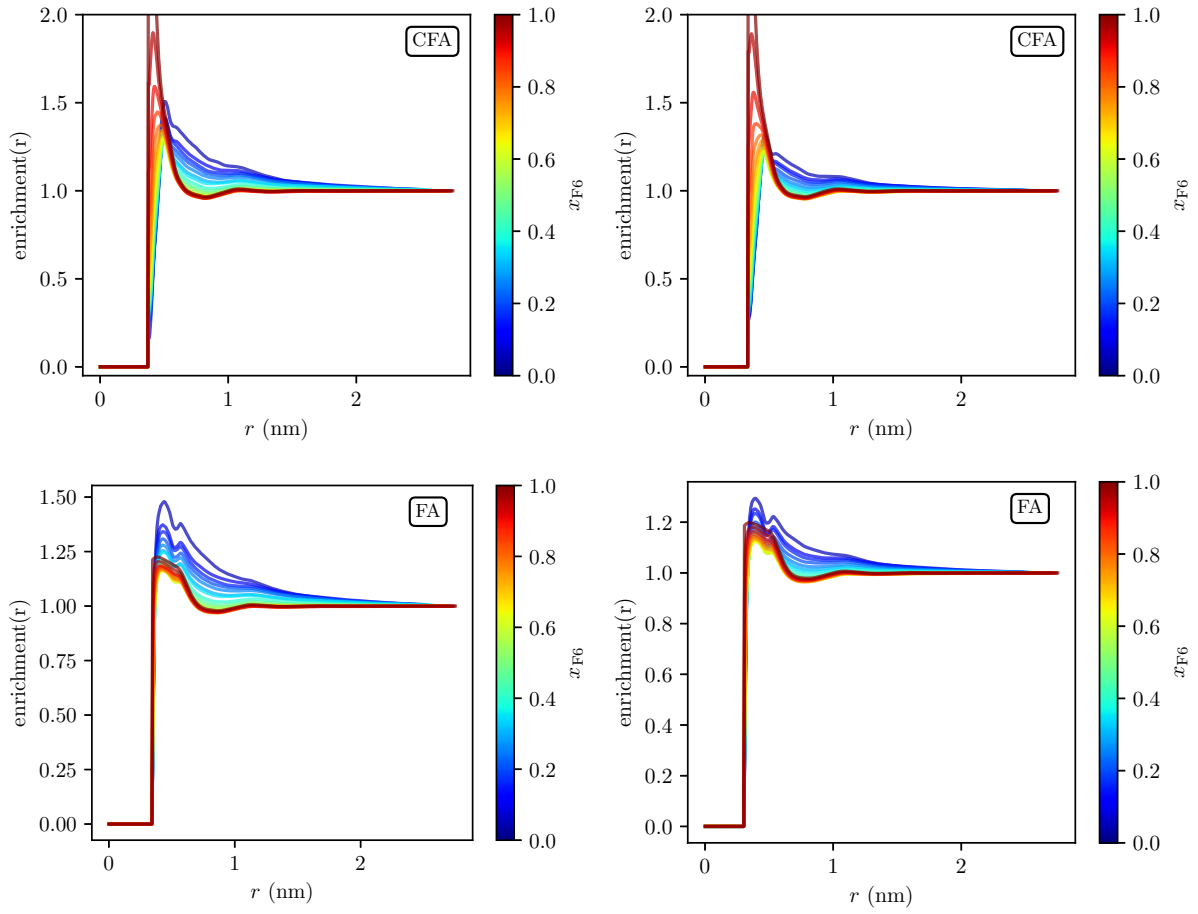

Figure D.7: Ratio of the local molar fraction of the atoms CFA (top row) and FA (bottom row) of F6 around the void sites and their respective bulk molar fractions (enrichment), as a function of the radial distance from the void sites and for different values of composition (x_{F6}) of the system, for the simulated mixtures of F6+H6 at a temperature $T = 298\,K$ and for void sites having a radius $R_b \geq 0.20$ nm (left column) or $R_b \geq 0.16$ nm (right column). The nomenclature used to identify the atoms is presented in Figure 12.1. The corresponding RDFs are presented in Figure D.9.

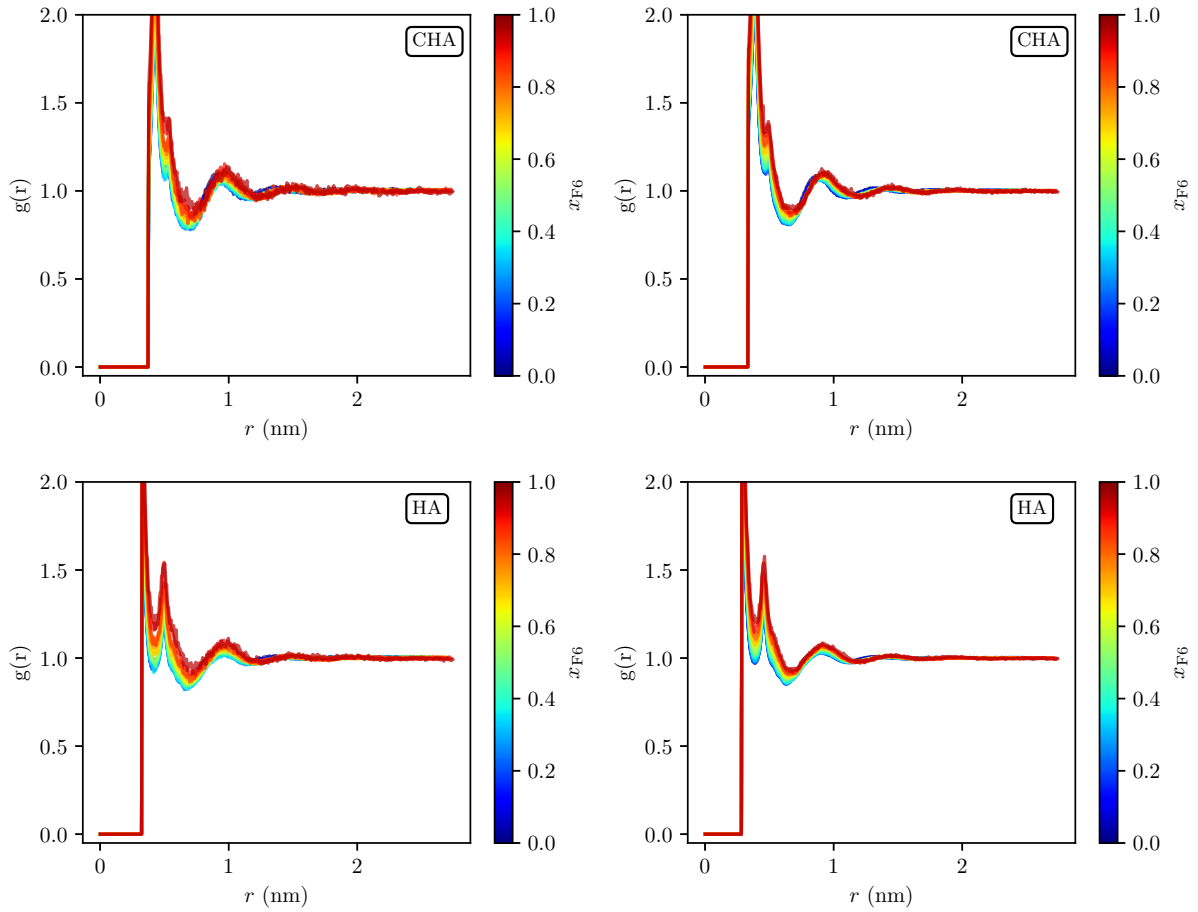

Figure D.8: RDFs between the void sites having a radius $R_b \geq 0.20$ nm (left column) or $R_b \geq 0.16$ nm (right column) and the atoms CHA (top row) and HA (bottom row) of H6 for different values of composition (x_{F6}) of the system, for the simulated mixtures of F6+H6 at a temperature $T = 298\,\mathrm{K}$. The nomenclature used to identify the atoms is presented in Figure 12.1. The corresponding enrichment plots are presented in Figure D.6.

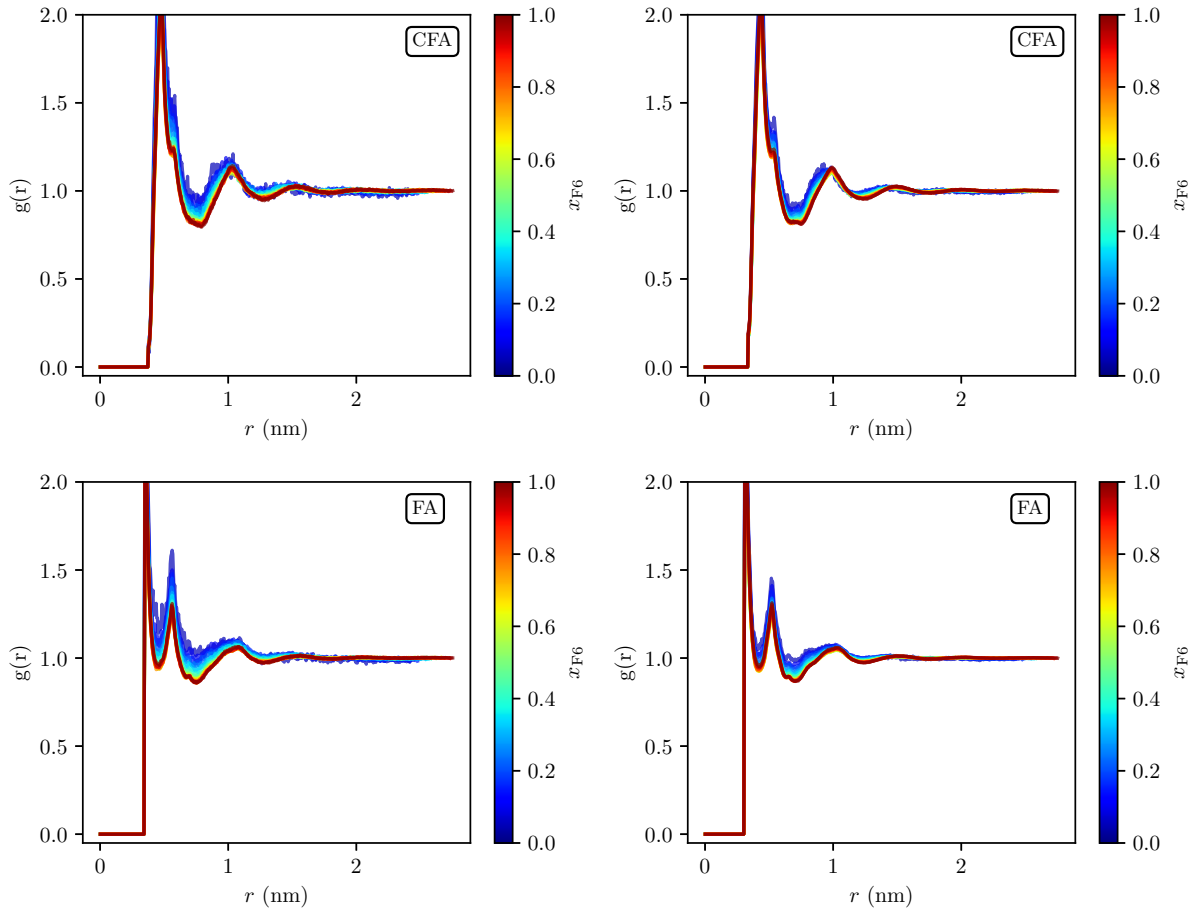

Figure D.9: RDFs between the void sites having a radius $R_b \geq 0.20$ nm (left column) or $R_b \geq 0.16$ nm (right column) and the atoms CFA (top row) and FA (bottom row) of F6 for different values of composition (x_{F6}) of the system, for the simulated mixtures of F6+H6 at a temperature $T = 298\,\mathrm{K}$. The nomenclature used to identify the atoms is presented in Figure 12.1. The corresponding enrichment plots are presented in Figure D.7.

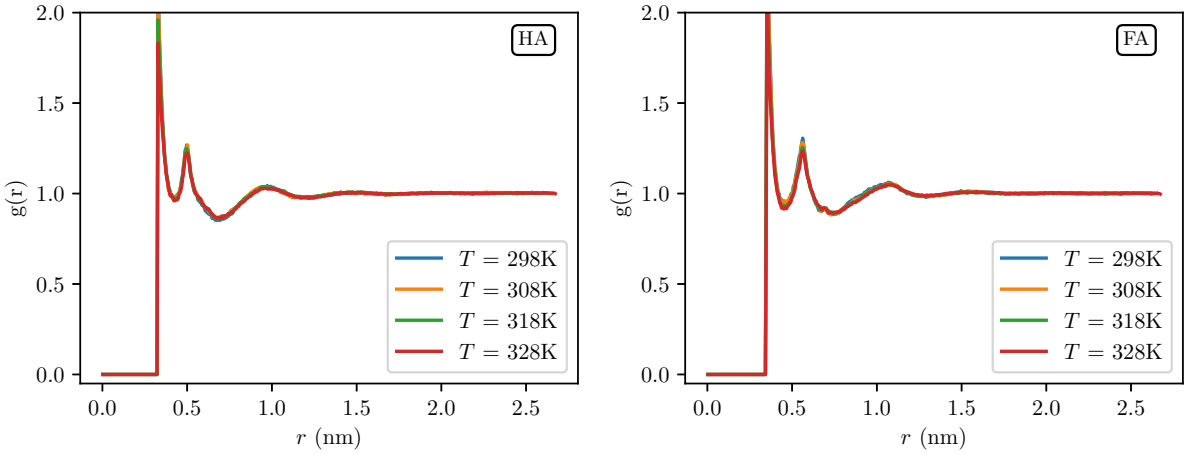

Figure D.10: RDFs between the void sites having a radius $R_b \geq 0.20$ nm and the atoms HA of H6 (left) and FA of F6 (right), for the simulated mixture of F6+H6 with composition $x_{\mathrm{F6}} = 0.50$ at different values of temperature. The nomenclature used to identify the atoms is presented in Figure 12.1. The corresponding enrichment plots are presented in Figure 12.12.

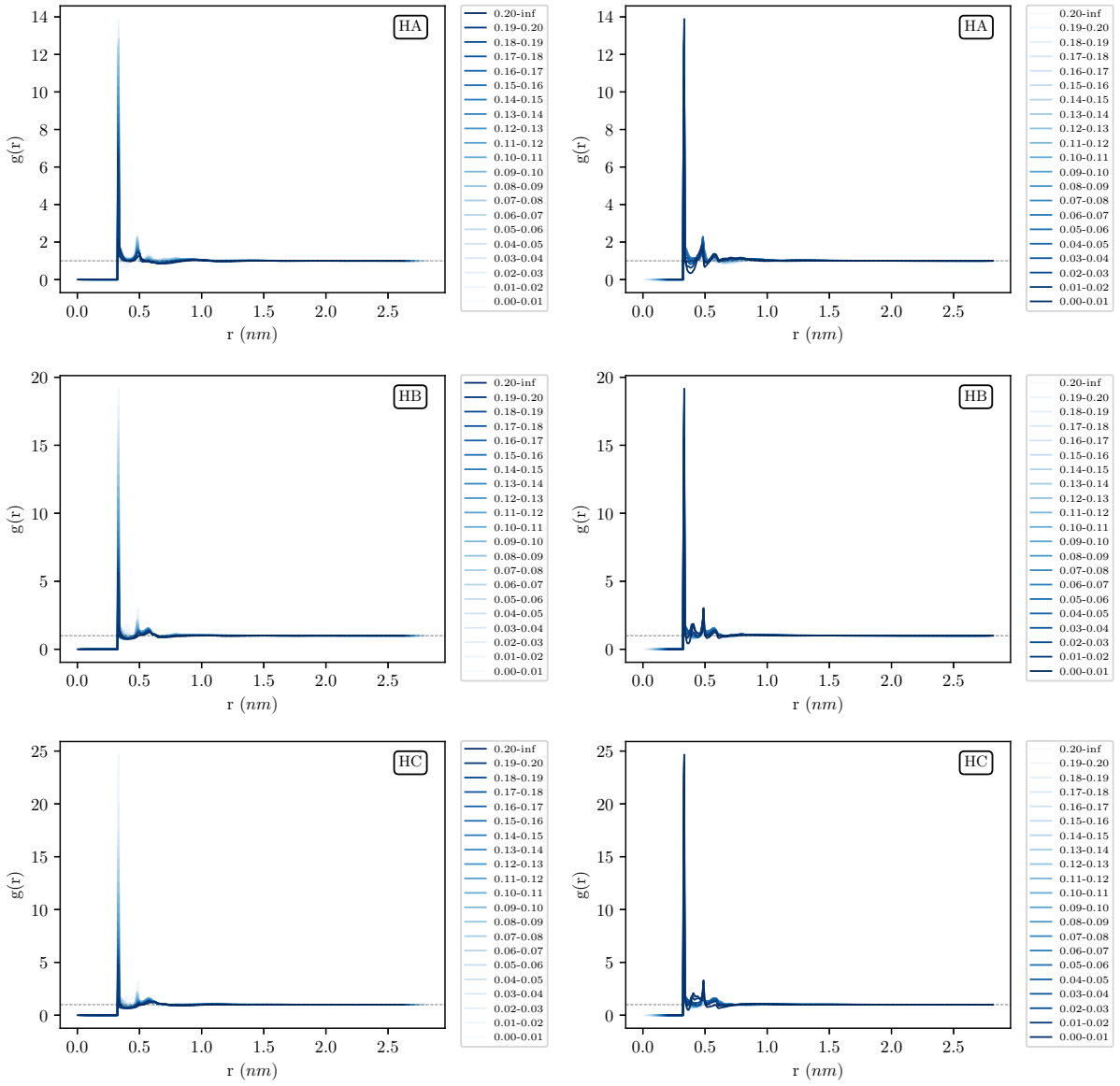

Figure D.11: RDFs between the void sites and the atoms HA (top row), HB (middle row) and HC (bottom row), for different (sliced) void site radii ranges, for the simulated mixtures of F6+H6 with molar composition $x_{F6} = 0.50$ and at a temperature $T = 298\,\mathrm{K}$. The plots on both columns contain exactly the same information, but with reverse colour coding: dark to light for decreasing order of void site radii ranges (left) and light to dark for decreasing order of void site radii ranges (right). The nomenclature used to identify the atoms is presented in Figure 12.1. The curves in each plot have been laterally shifted so that the contact peaks are coincident (see Section 12.5 for further details). The corresponding enrichment plots are presented in Figure 12.13.

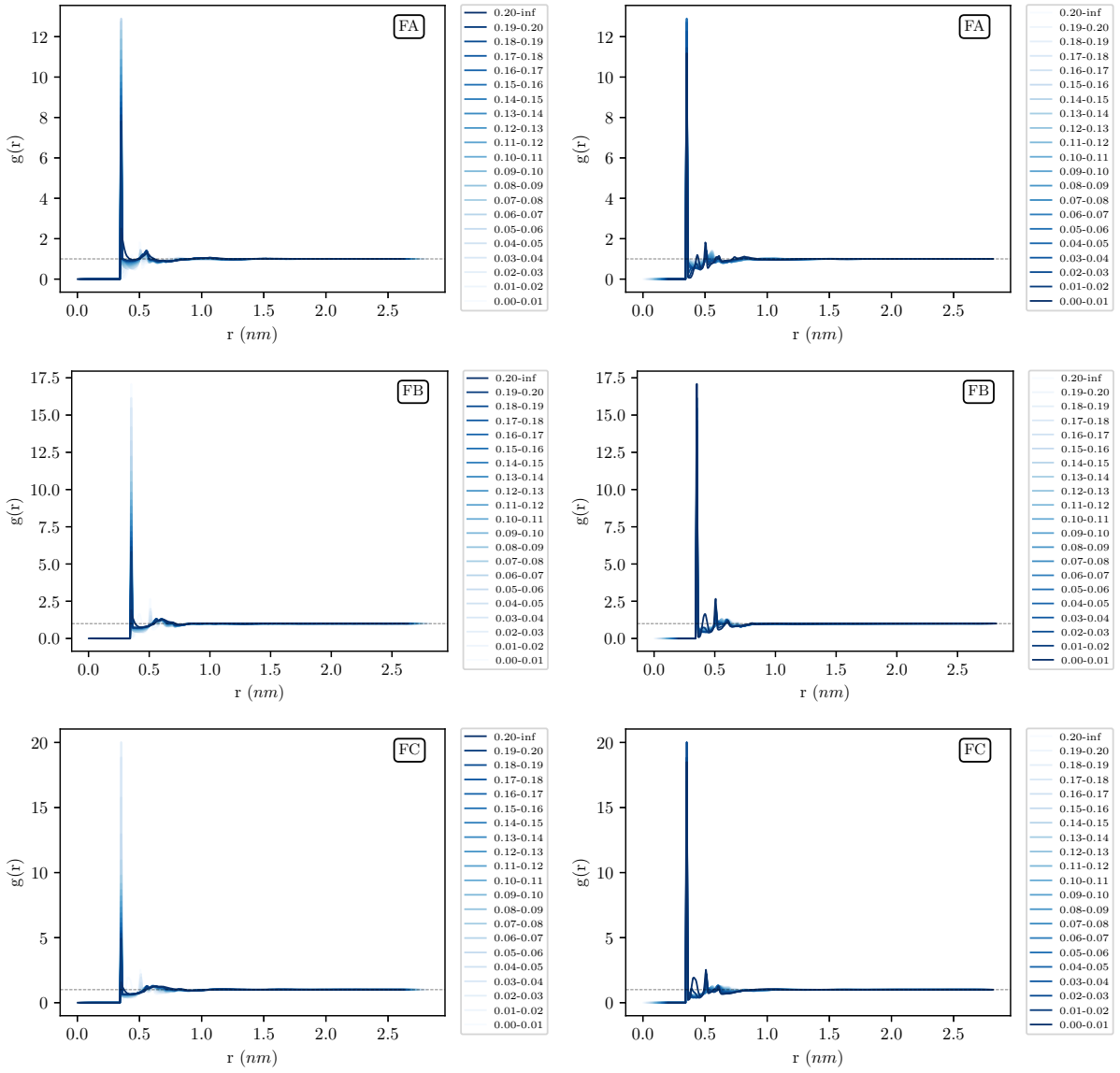

Figure D.12: RDFs between the void sites and the atoms FA (top row), FB (middle row) and FC (bottom row), for different (sliced) void site radii ranges, for the simulated mixtures of F6+H6 with molar composition $x_{\mathrm{F6}} = 0.50$ and at a temperature $T = 298\,\mathrm{K}$. The plots on both columns contain exactly the same information, but with reverse colour coding: dark to light for decreasing order of void site radii ranges (left) and light to dark for decreasing order of void site radii ranges (right). The nomenclature used to identify the atoms is presented in Figure 12.1. The curves in each plot have been laterally shifted so that the contact peaks are coincident (see Section 12.5 for further details). The corresponding enrichment plots are presented in Figure 12.14.

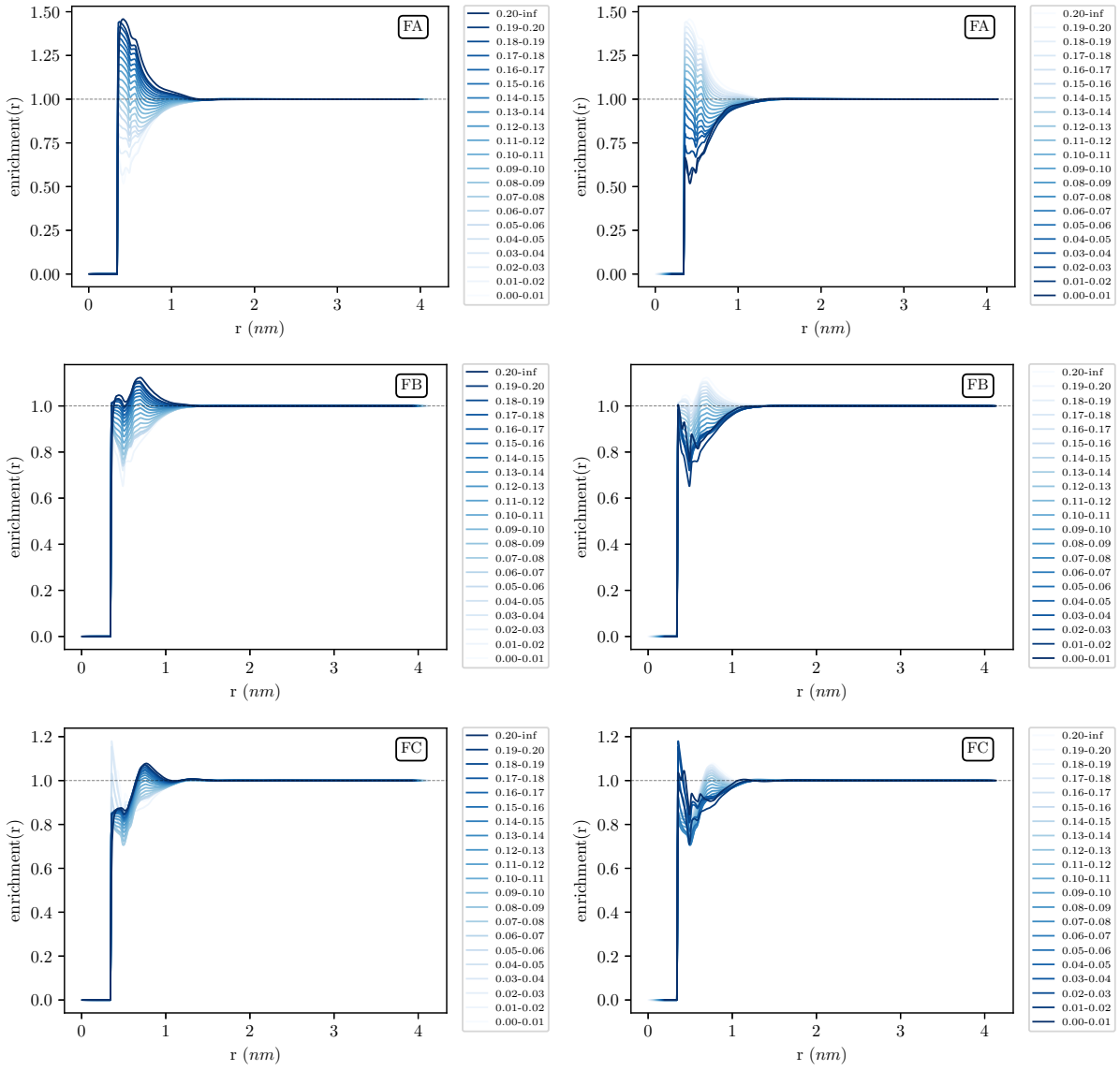

Figure D.13: Ratio of the local molar fraction of the atoms FA, FB and FC (rows, from top to bottom) around the void sites and their respective bulk molar fractions (enrichment), as a function of the radial distance from the void sites and for different (sliced) void site radii ranges, for the system of liquid F6H6 simulated at a temperature $T = 298\,\mathrm{K}$. The plots on both columns contain exactly the same information, but with reverse colour coding: dark to light for decreasing order of void site radii ranges (left) and light to dark for decreasing order of void site radii ranges (right). The nomenclature used to identify the atoms is presented in Figure 12.1. The curves in each plot have been laterally shifted so that the contact peaks are coincident (see Section 12.5 for further details). The corresponding RDFs are presented in Figure D.17.

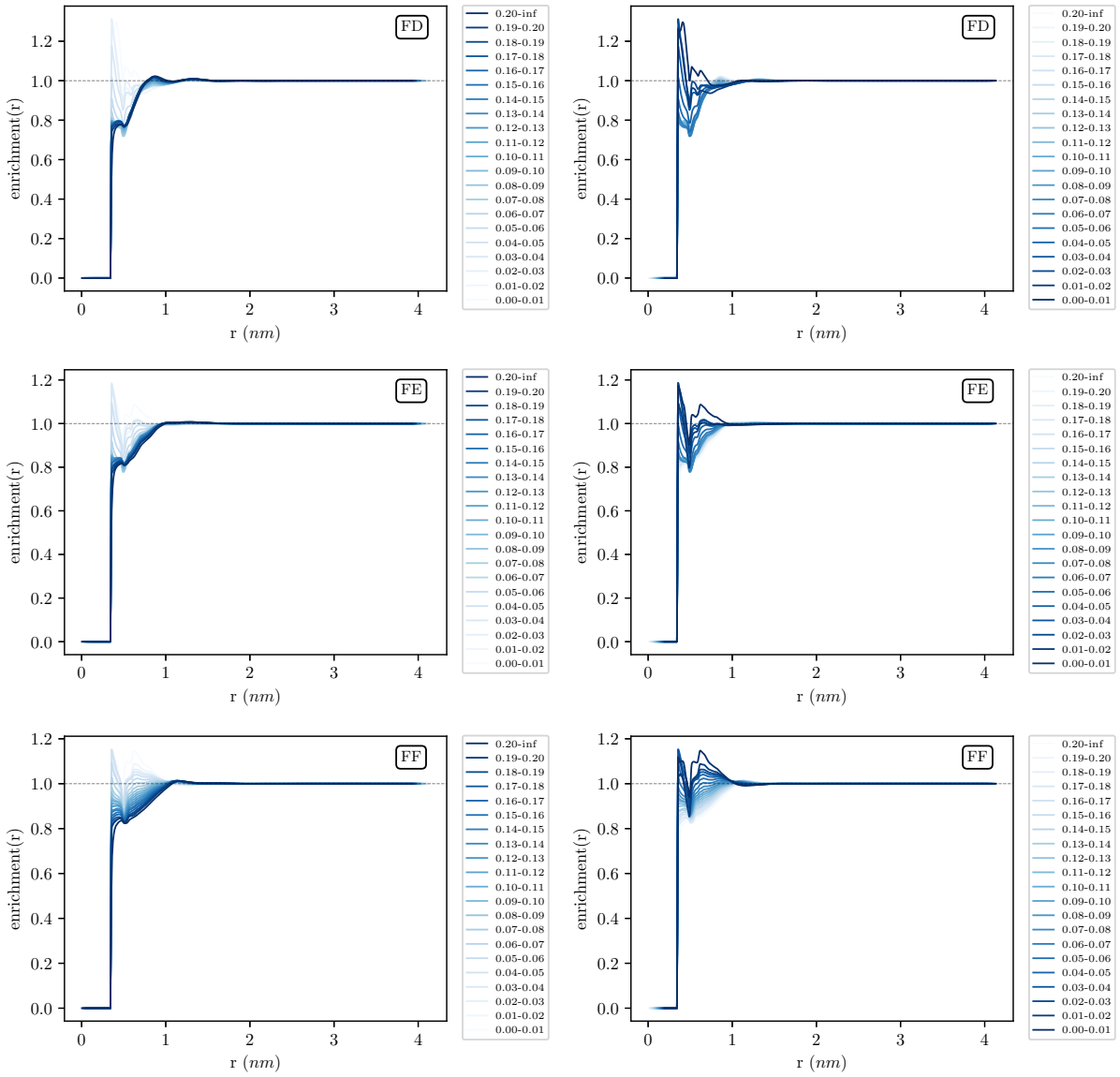

Figure D.14: Ratio of the local molar fraction of the atoms FD, FE and FF (rows, from top to bottom) around the void sites and their respective bulk molar fractions (enrichment), as a function of the radial distance from the void sites and for different (sliced) void site radii ranges, for the system of liquid F6H6 simulated at a temperature $T = 298\,\mathrm{K}$. The plots on both columns contain exactly the same information, but with reverse colour coding: dark to light for decreasing order of void site radii ranges (left) and light to dark for decreasing order of void site radii ranges (right). The nomenclature used to identify the atoms is presented in Figure 12.1. The curves in each plot have been laterally shifted so that the contact peaks are coincident (see Section 12.5 for further details). The corresponding RDFs are presented in Figure D.18.

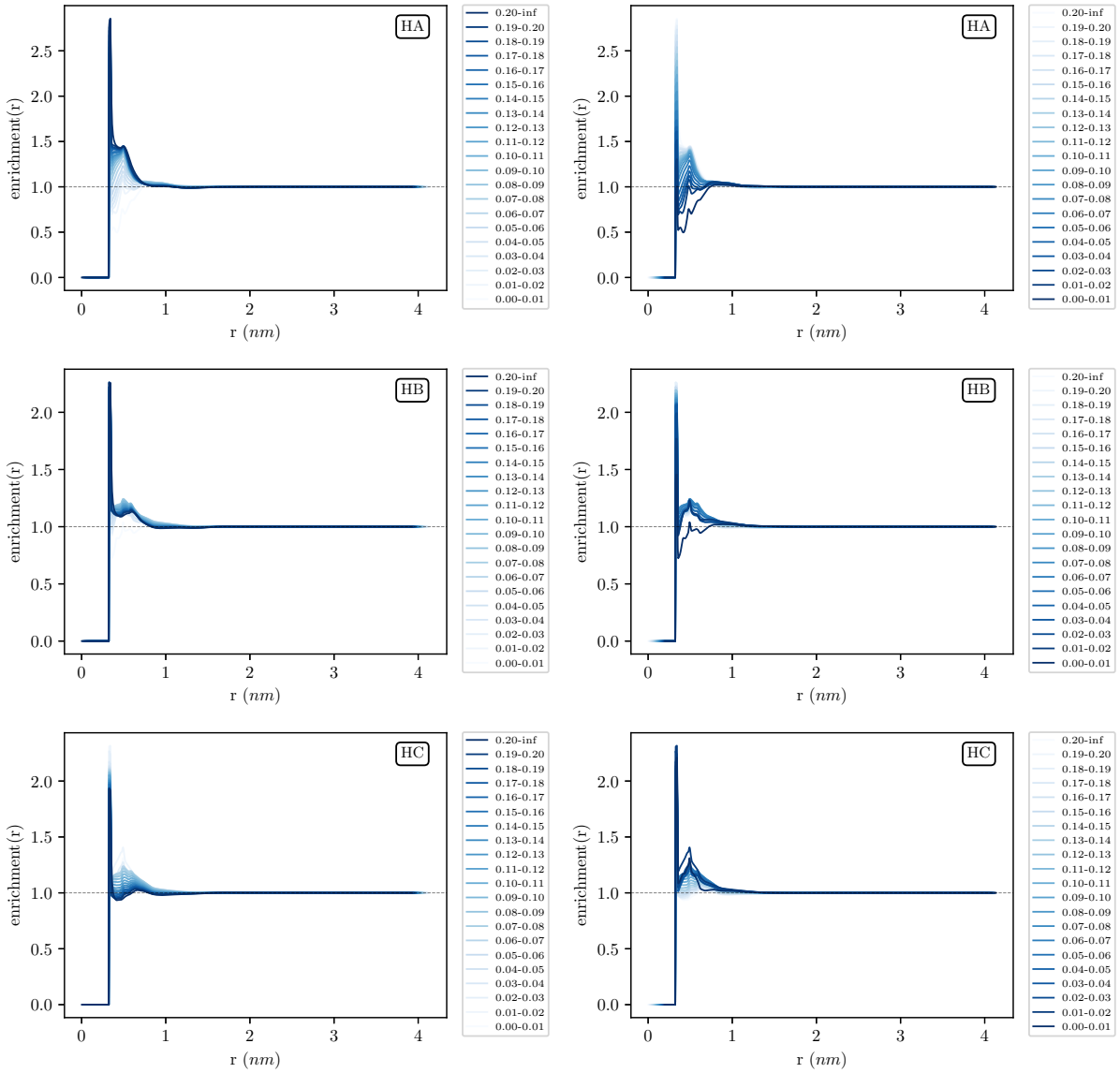

Figure D.15: Ratio of the local molar fraction of the atoms HA, HB and HC (rows, from top to bottom) around the void sites and their respective bulk molar fractions (enrichment), as a function of the radial distance from the void sites and for different (sliced) void site radii ranges, for the system of liquid F6H6 simulated at a temperature $T = 298\,\mathrm{K}$. The plots on both columns contain exactly the same information, but with reverse colour coding: dark to light for decreasing order of void site radii ranges (left) and light to dark for decreasing order of void site radii ranges (right). The nomenclature used to identify the atoms is presented in Figure 12.1. The curves in each plot have been laterally shifted so that the contact peaks are coincident (see Section 12.5 for further details). The corresponding RDFs are presented in Figure D.19.

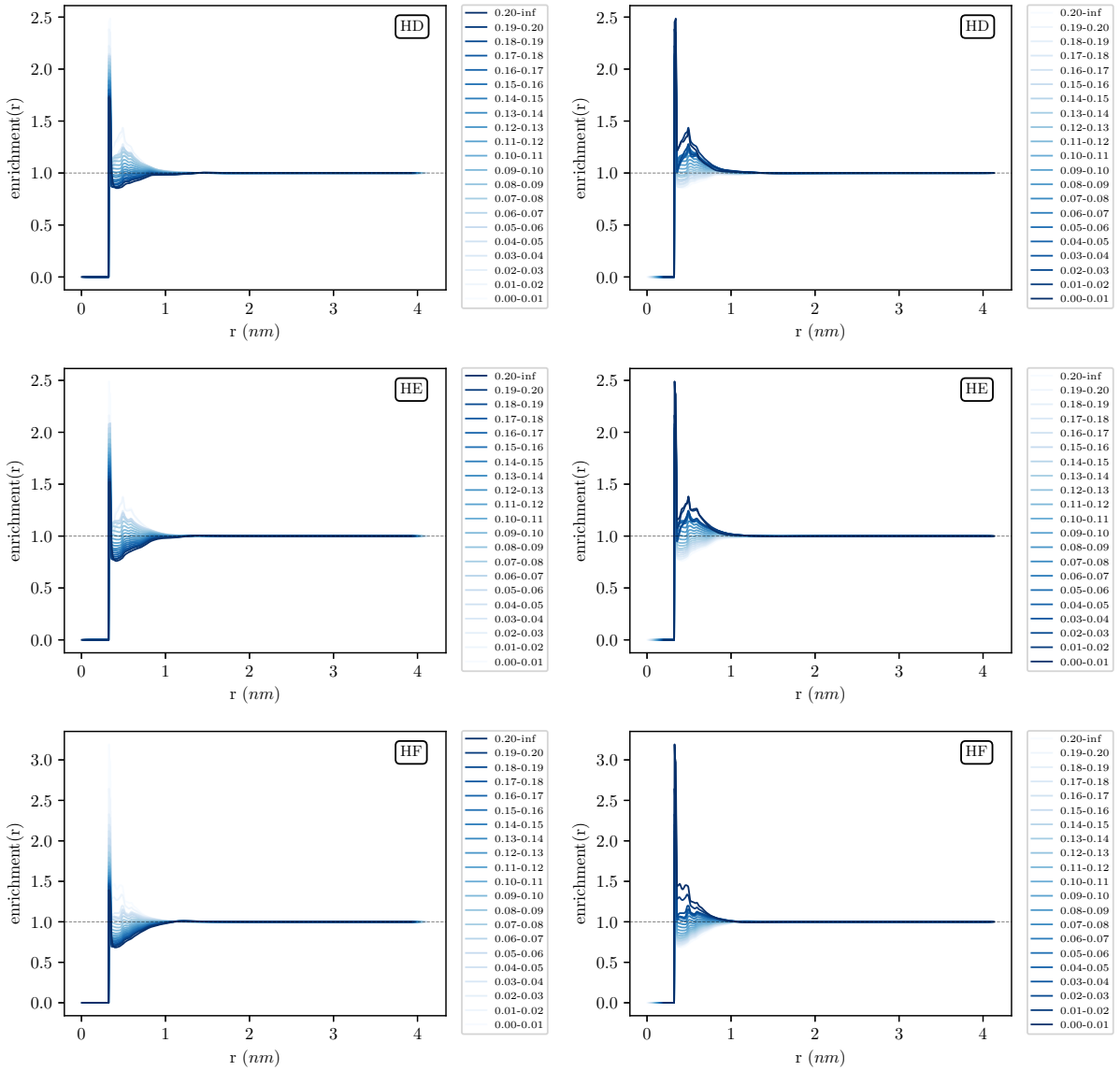

Figure D.16: Ratio of the local molar fraction of the atoms HD, HE and HF (rows, from top to bottom) around the void sites and their respective bulk molar fractions (enrichment), as a function of the radial distance from the void sites and for different (sliced) void site radii ranges, for the system of liquid F6H6 simulated at a temperature $T = 298\,\mathrm{K}$. The plots on both columns contain exactly the same information, but with reverse colour coding: dark to light for decreasing order of void site radii ranges (left) and light to dark for decreasing order of void site radii ranges (right). The nomenclature used to identify the atoms is presented in Figure 12.1. The curves in each plot have been laterally shifted so that the contact peaks are coincident (see Section 12.5 for further details). The corresponding RDFs are presented in Figure D.20.

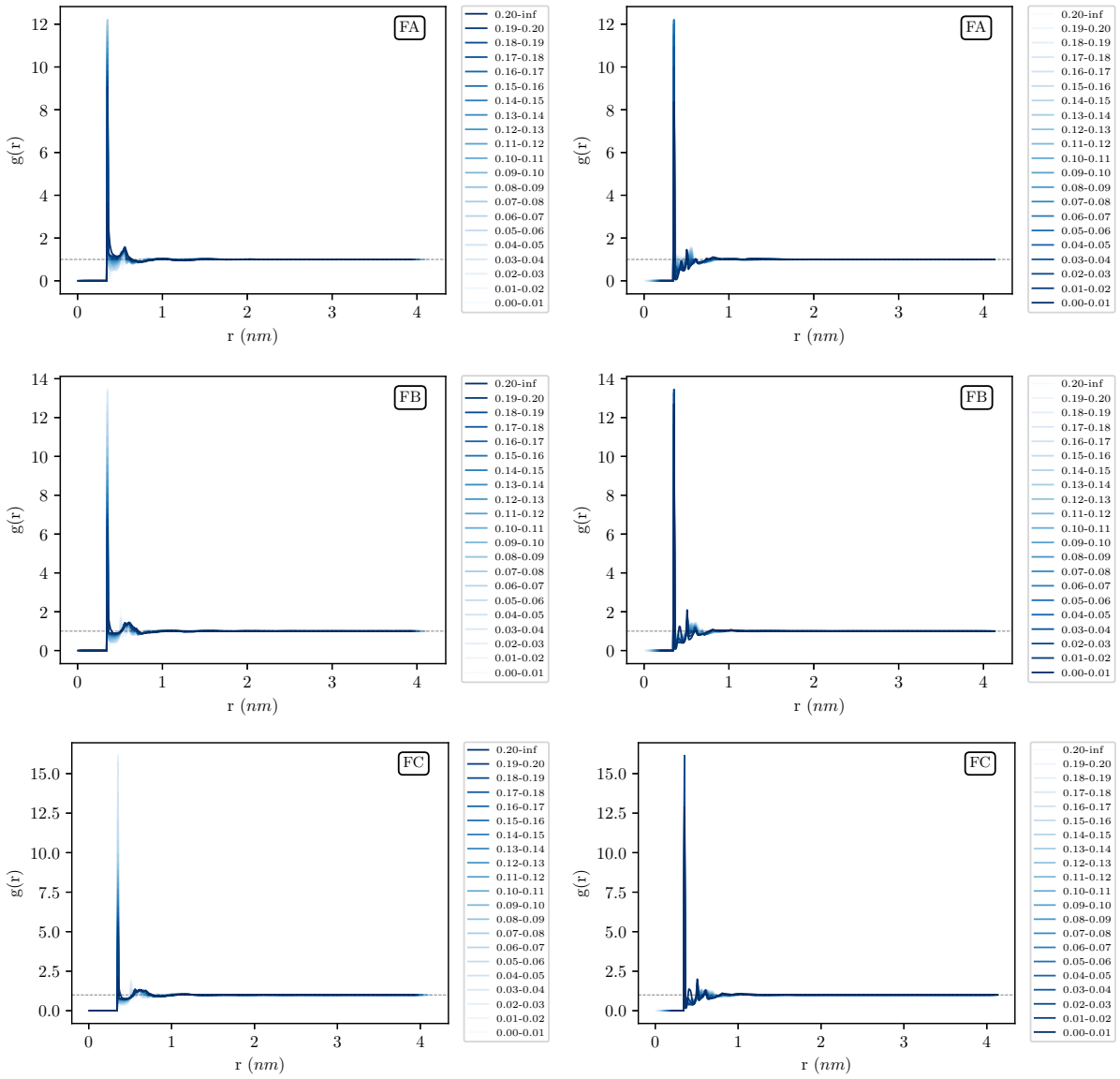

Figure D.17: RDFs between the void sites and the atoms FA, FB and FC (rows, from top to bottom), for different (sliced) void site radii ranges, for the system of liquid F6H6 simulated at a temperature $T = 298\,\mathrm{K}$. The plots on both columns contain exactly the same information, but with reverse colour coding: dark to light for decreasing order of void site radii ranges (left) and light to dark for decreasing order of void site radii ranges (right). The nomenclature used to identify the atoms is presented in Figure 12.1. The curves in each plot have been laterally shifted so that the contact peaks are coincident (see Section 12.5 for further details). The corresponding enrichment plots are presented in Figure D.13.

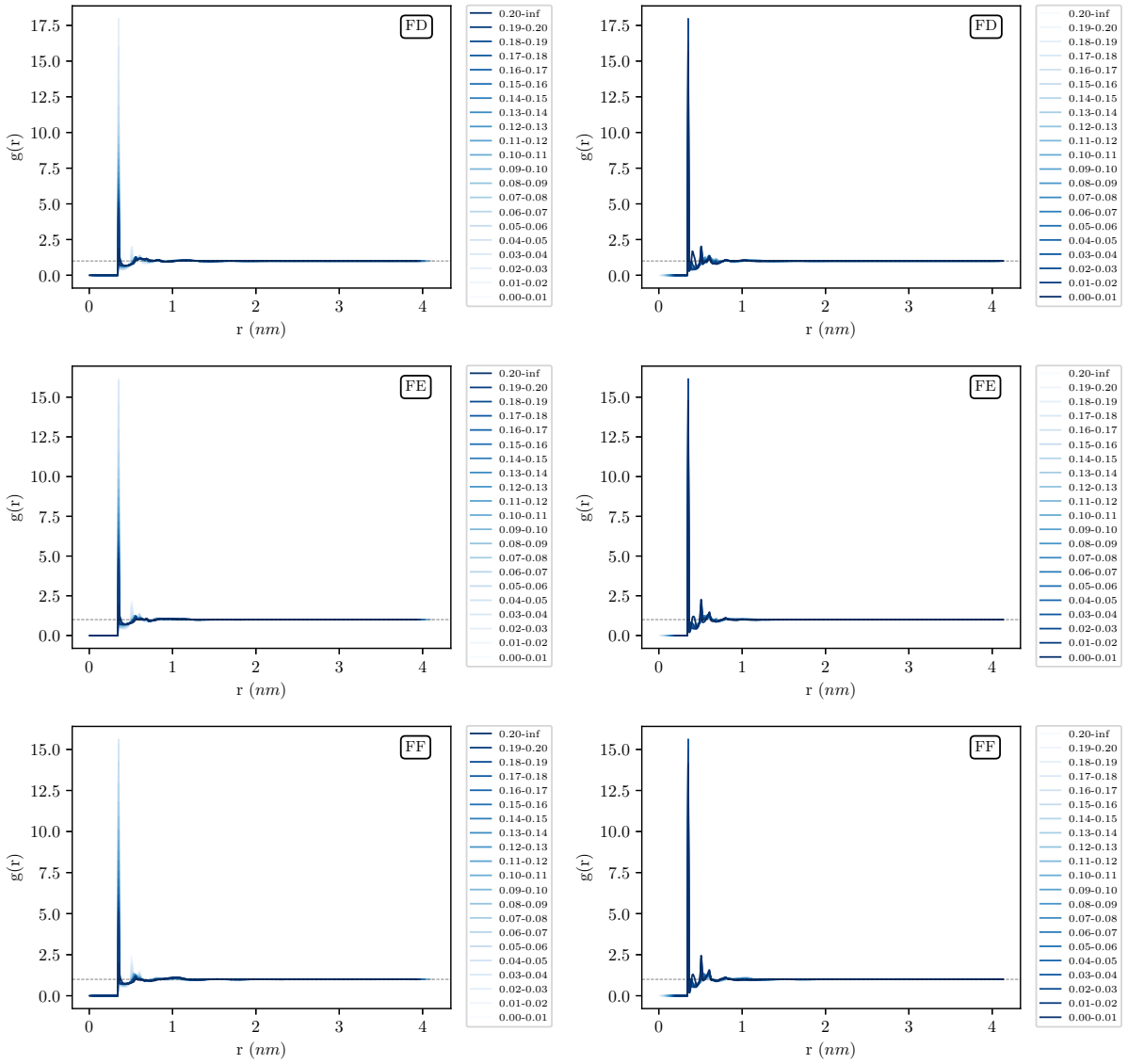

Figure D.18: RDFs between the void sites and the atoms FD, FE and FF (rows, from top to bottom), for different (sliced) void site radii ranges, for the system of liquid F6H6 simulated at a temperature $T = 298\,\mathrm{K}$. The plots on both columns contain exactly the same information, but with reverse colour coding: dark to light for decreasing order of void site radii ranges (left) and light to dark for decreasing order of void site radii ranges (right). The nomenclature used to identify the atoms is presented in Figure 12.1. The curves in each plot have been laterally shifted so that the contact peaks are coincident (see Section 12.5 for further details). The corresponding enrichment plots are presented in Figure D.14.

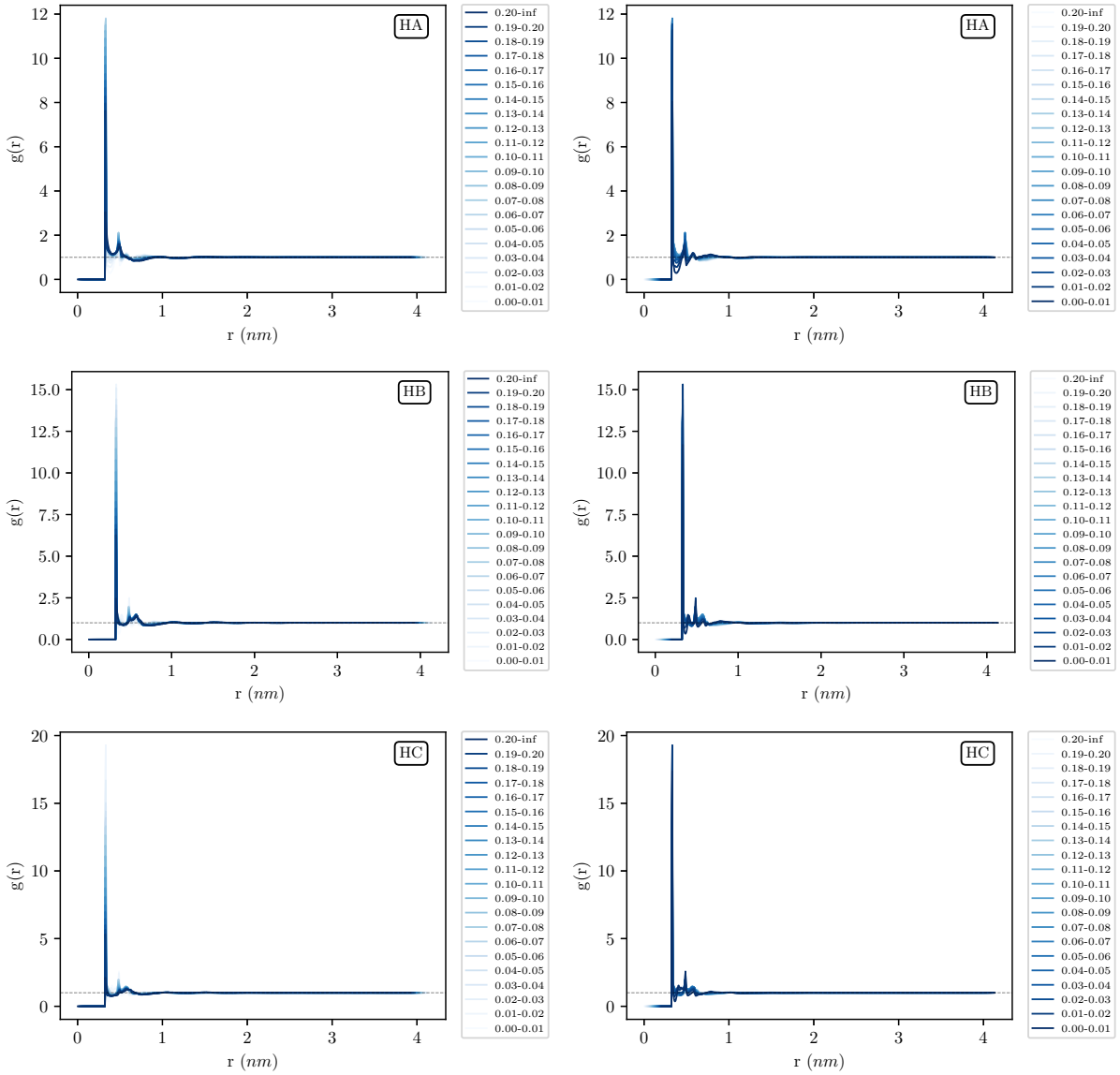

Figure D.19: RDFs between the void sites and the atoms HA, HB and HC (rows, from top to bottom), for different (sliced) void site radii ranges, for the system of liquid F6H6 simulated at a temperature $T = 298\,\mathrm{K}$. The plots on both columns contain exactly the same information, but with reverse colour coding: dark to light for decreasing order of void site radii ranges (left) and light to dark for decreasing order of void site radii ranges (right). The nomenclature used to identify the atoms is presented in Figure 12.1. The curves in each plot have been laterally shifted so that the contact peaks are coincident (see Section 12.5 for further details). The corresponding enrichment plots are presented in Figure D.15.

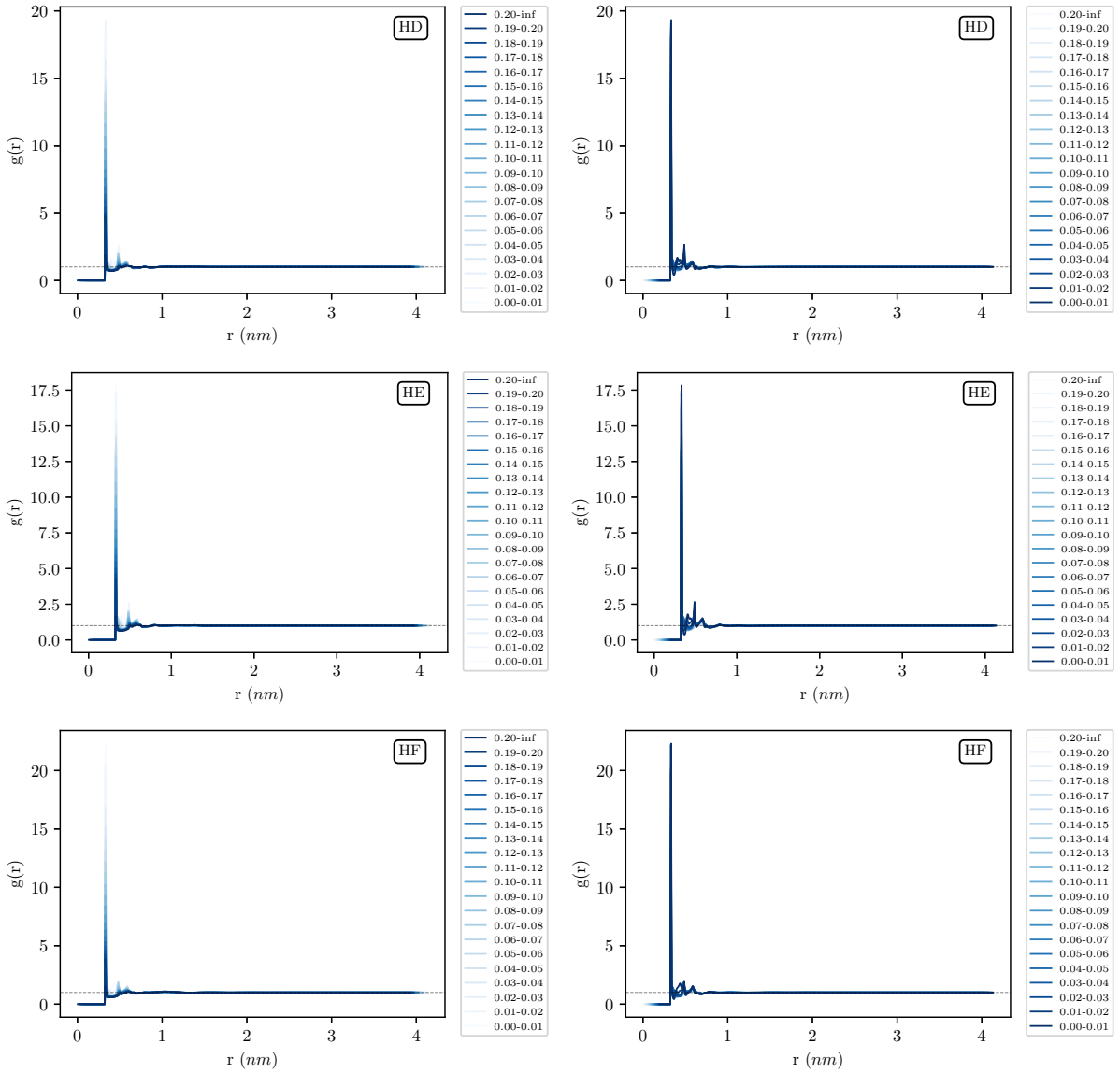

Figure D.20: RDFs between the void sites and the atoms HD, HE and HF (rows, from top to bottom), for different (sliced) void site radii ranges, for the system of liquid F6H6 simulated at a temperature $T = 298\,\mathrm{K}$. The plots on both columns contain exactly the same information, but with reverse colour coding: dark to light for decreasing order of void site radii ranges (left) and light to dark for decreasing order of void site radii ranges (right). The nomenclature used to identify the atoms is presented in Figure 12.1. The curves in each plot have been laterally shifted so that the contact peaks are coincident (see Section 12.5 for further details). The corresponding enrichment plots are presented in Figure D.16.

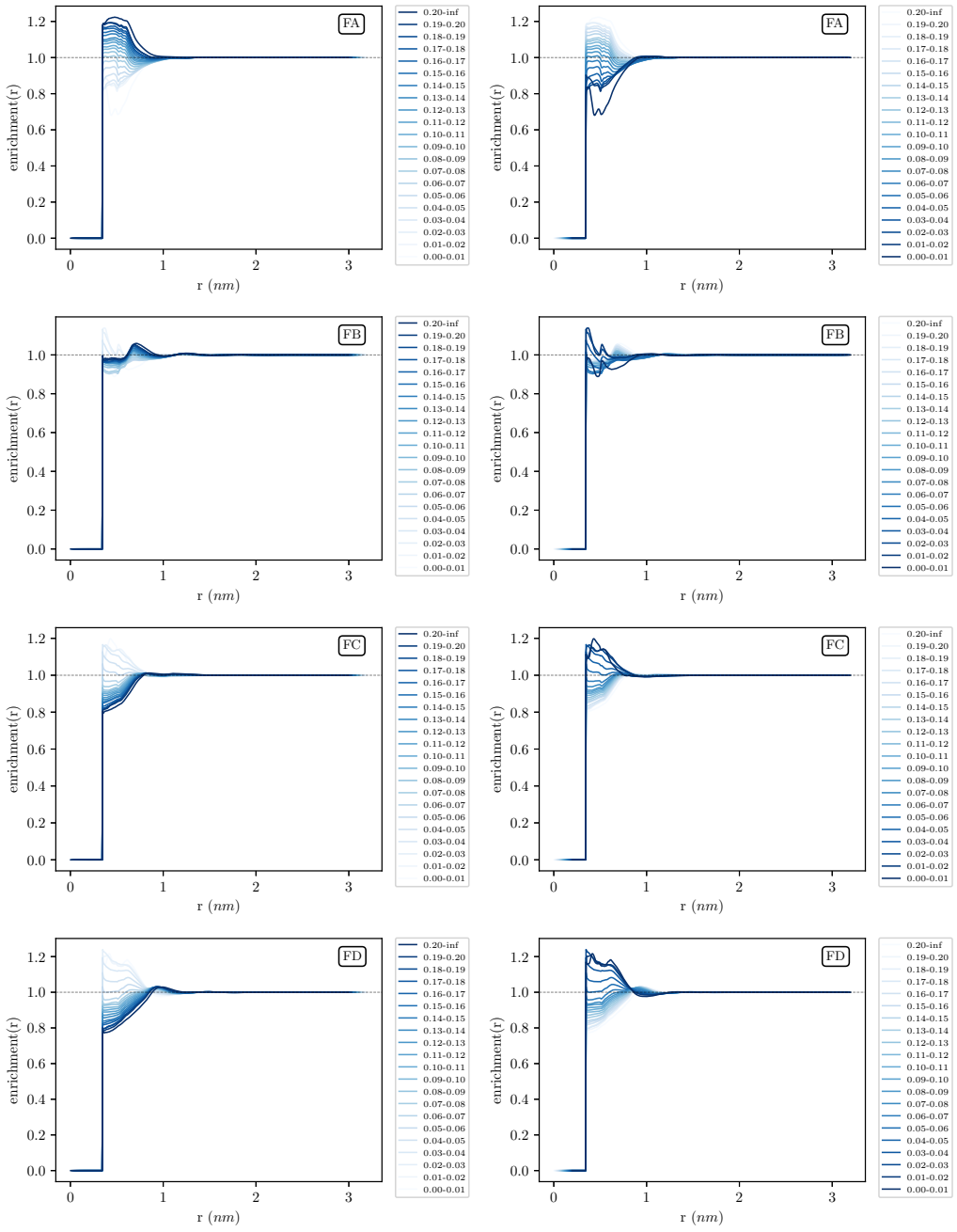

Figure D.21: Ratio of the local molar fraction of the atoms FA, FB, FC and FD (rows, from top to bottom) around the void sites and their respective bulk molar fractions (enrichment), as a function of the radial distance from the void sites and for different (sliced) void site radii ranges, for the system of liquid F8Br simulated at a temperature $T = 298\,\mathrm{K}$. The plots on both columns contain exactly the same information, but with reverse colour coding: dark to light for decreasing order of void site radii ranges (left) and light to dark for decreasing order of void site radii ranges (right). The nomenclature used to identify the atoms is presented in Figure 12.1. The curves in each plot have been laterally shifted so that the contact peaks are coincident (see Section 12.5 for further details). The corresponding RDFs are presented in Figure D.23.

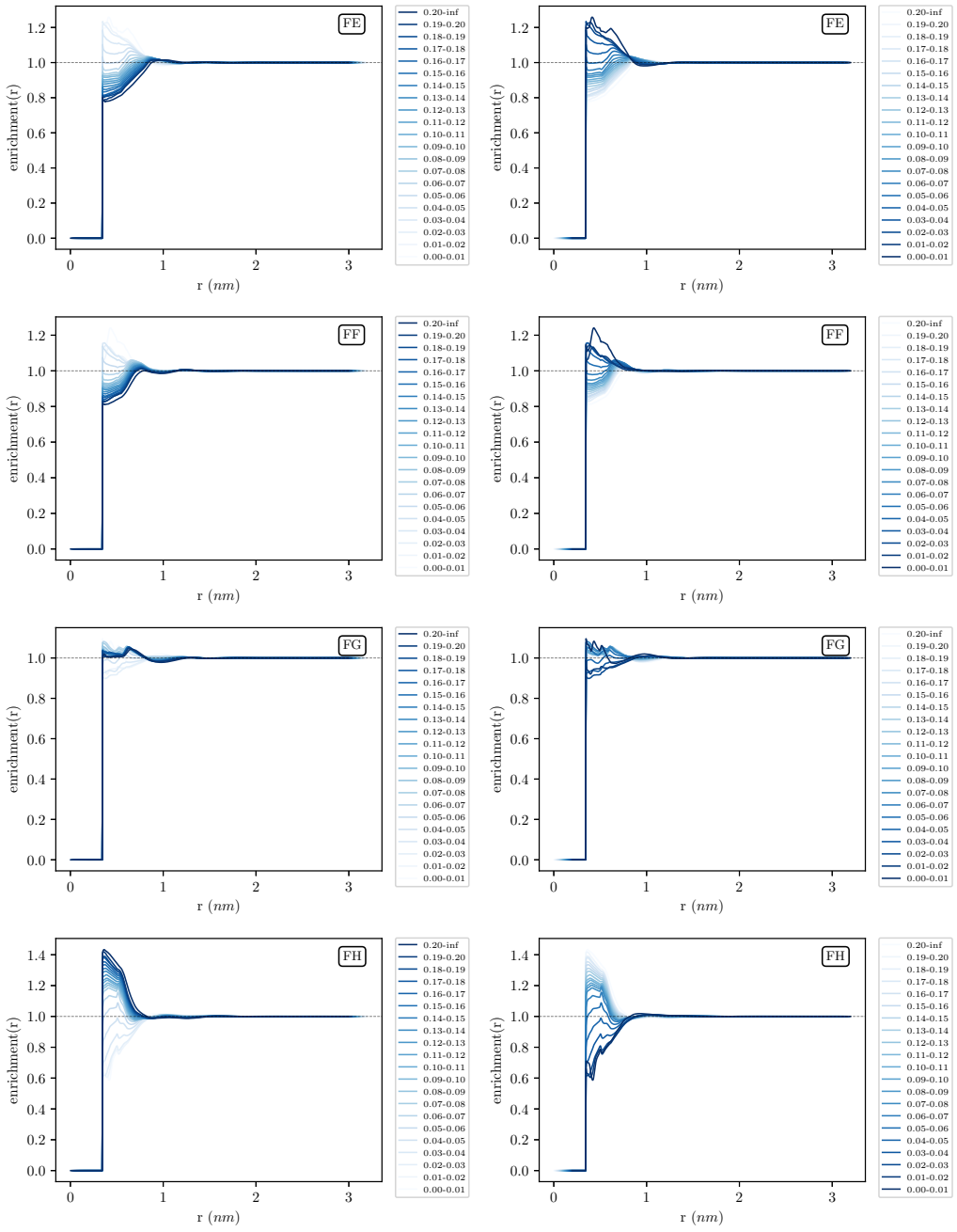

Figure D.22: Ratio of the local molar fraction of the atoms FE, FF, FG and FH (rows, from top to bottom) around the void sites and their respective bulk molar fractions (enrichment), as a function of the radial distance from the void sites and for different (sliced) void site radii ranges, for the system of liquid F8Br simulated at a temperature $T = 298\,\mathrm{K}$. The plots on both columns contain exactly the same information, but with reverse colour coding: dark to light for decreasing order of void site radii ranges (left) and light to dark for decreasing order of void site radii ranges (right). The nomenclature used to identify the atoms is presented in Figure 12.1. The curves in each plot have been laterally shifted so that the contact peaks are coincident (see Section 12.5 for further details). The corresponding RDFs are presented in Figure D.24.

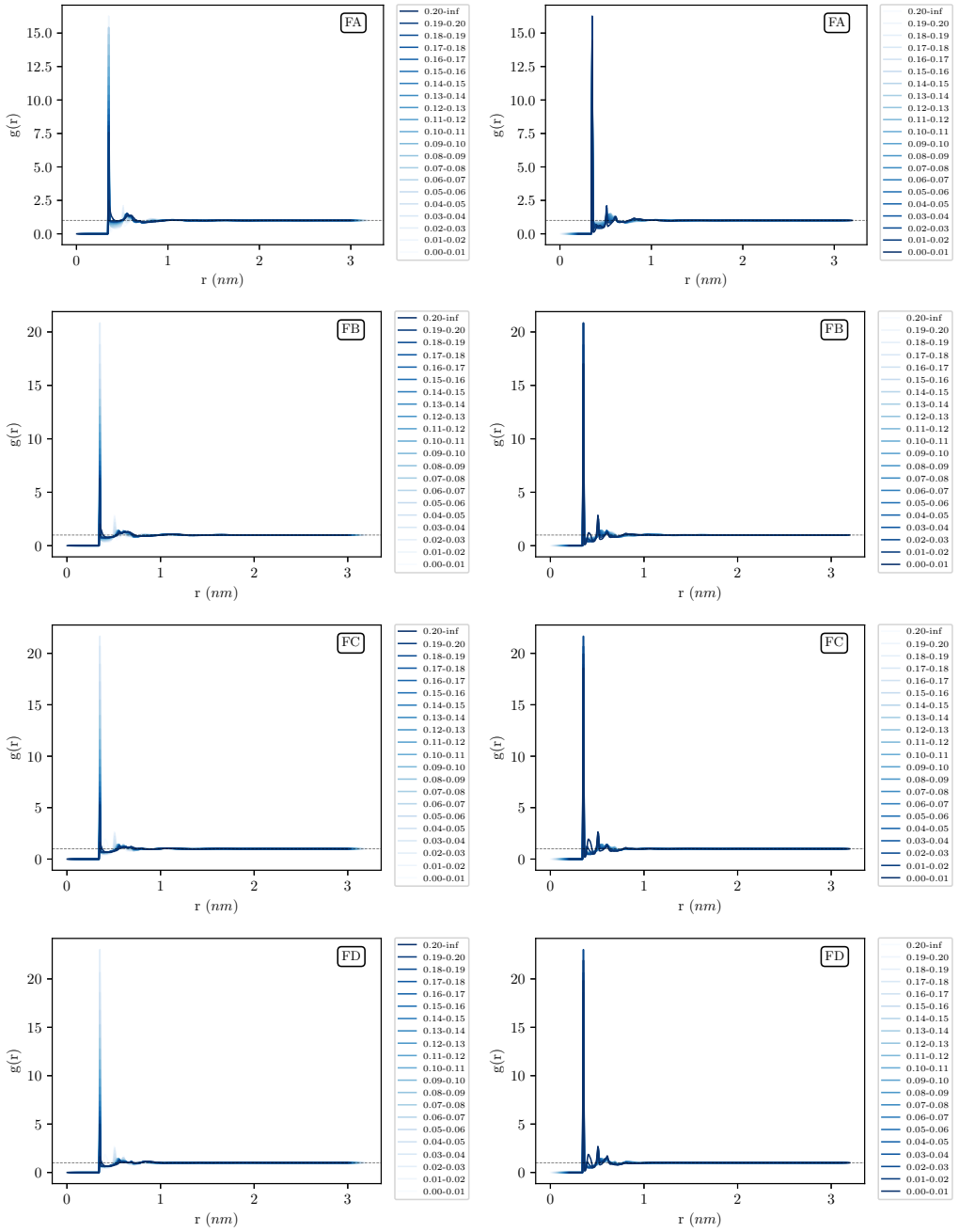

Figure D.23: RDFs between the void sites and the atoms FA, FB, FC and FD (rows, from top to bottom), for different (sliced) void site radii ranges, for the system of liquid F8Br simulated at a temperature $T = 298\,\mathrm{K}$. The plots on both columns contain exactly the same information, but with reverse colour coding: dark to light for decreasing order of void site radii ranges (left) and light to dark for decreasing order of void site radii ranges (right). The nomenclature used to identify the atoms is presented in Figure 12.1. The curves in each plot have been laterally shifted so that the contact peaks are coincident (see Section 12.5 for further details). The corresponding enrichment plots are presented in Figure D.21.

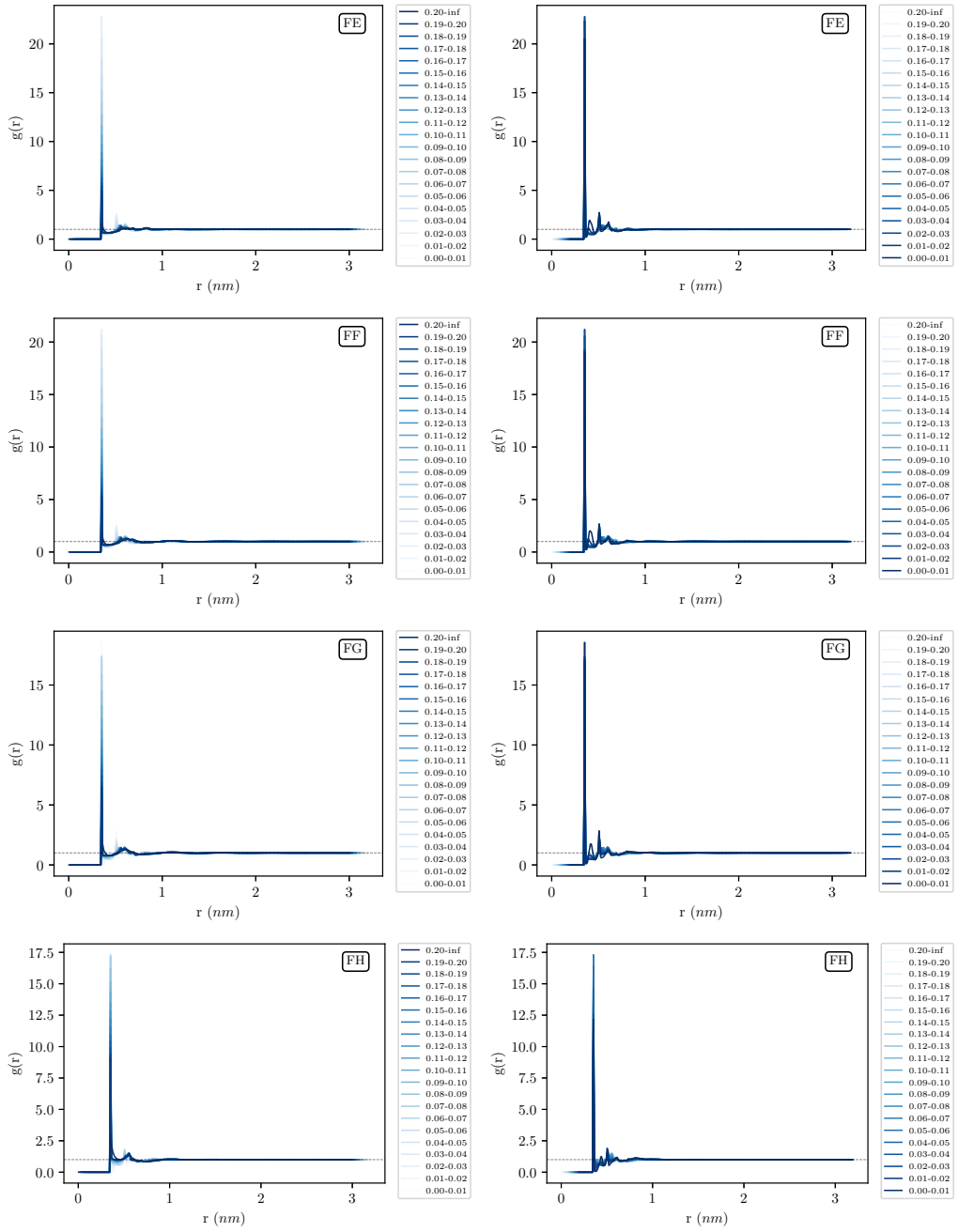

Figure D.24: RDFs between the void sites and the atoms FE, FF, FG and FH (rows, from top to bottom), for different (sliced) void site radii ranges, for the system of liquid F8Br simulated at a temperature $T = 298\,\mathrm{K}$. The plots on both columns contain exactly the same information, but with reverse colour coding: dark to light for decreasing order of void site radii ranges (left) and light to dark for decreasing order of void site radii ranges (right). The nomenclature used to identify the atoms is presented in Figure 12.1. The curves in each plot have been laterally shifted so that the contact peaks are coincident (see Section 12.5 for further details). The corresponding enrichment plots are presented in Figure D.22.